

KURNS

Progress

Report

2021



KURNS Progress Report 2021

APRIL 2021 – MARCH 2022

*Published by
Institute for Integrated Radiation and Nuclear Science,
Kyoto University,
Kumatori-cho, Sennan-gun, Osaka 590-0494, Japan*

Preface for the KURNS Progress Report 2021

It is our pleasure to announce that the KURNS Progress Report 2021 has been published. This report contains all of the accomplishments of research and related activities at the Institute for Integrated Radiation and Nuclear Science, Kyoto University (KURNS) during the fiscal year 2021 (hereafter called as FY2021). Many research subjects have been enrolled also in FY2021, which cover various fields of nuclear science and technology, material science, radiation life science and radiation medical science. It means that our institute continues to play a distinctive role as a Joint Usage/Research Center, promoting an extensive range of studies from fundamental to applied research using research reactors, accelerators, and other facilities.

In FY2020, our joint research was severely restricted due to the declaration of a state of emergency caused by the spread of the COVID-19, but in FY2021, the impact was reduced to a limited extent because of the establishment of measures against the COVID-19. On the other hand, the operation of KUCA has been suspended since the latter half of FY2021 due to various procedures and works associated with the reduction of uranium fuel enrichment, which undertook with US-Japan government agreement. We aim to resume operation of KUCA during FY2023. As a result, KUR was operated for 1029 hours and KUCA was for 234 hours in FY2021. In total, we accepted 3,501 man-day researchers and students for using research facilities.

We strive for safe and stable operations, making it our primary mission to provide scientists the opportunity to conduct research and education. We are happy to dedicate our support to enable users conduct significant interdisciplinary research at KURNS.

Kumatori, July 6, 2022
Ken Nakajima
Director, KURNS

CONTENTS

I. ANNUAL SUMMARY OF EXPERIMENTAL RESEARCH ACTIVITIES		1
I-1. PROJECT RESEARCHES		2
Project 1	The effect of boron neutron capture therapy on normal tissues M. Suzuki (R3P1)	3
PR1-1	The effect of boron neutron capture therapy (BNCT) on normal lung in mice M. Suzuki and Y. Tamari (R3P1-1)	4
PR1-2	Clarification of the normal cell fractionation as a trigger for radiation-induced liver injury Takeno and M. Suzuki (R3P1-2)	5
PR1-3	Examination of the influence on normal liver tissue by Boron neutron capture therapy Y. Tamari <i>et al.</i> (R3P1-4)	6
PR1-4	The Effect of Boron Neutron Capture Therapy to Normal Bones in Mice R. Iwasaki <i>et al.</i> (R3P1-5)	7
PR1-5	The Biological Behavior of Boron Compound in Normal Bone of Young Mice and the Influence of Boron Neutron Capture Therapy on Bone Growth R. Iwasaki <i>et al.</i> (R3P1-6)	8
Project 2	Preclinical studies on gadolinium neutron capture therapy M. Suzuki (R3P2)	10
PR2-1	Investigation of cell killing effect by auger electrons emitted during gadolinium neutron capture therapy (Gd-NCT) M. Suzuki and H. Tanaka (R3P2-1)	11
PR2-2	Development of Nano Carriers Installed with Gd(III)-Thiacalixarene Complex for Gd-NCT N. Iki <i>et al.</i> (R3P2-2)	12
PR2-3	Gadolinium neutron capture therapy as a new treatment for head and neck cancer: tumor-killing effects on a masseter muscle invasion model T. Andoh <i>et al.</i> (R3P2-3)	13
PR2-4	Preparation of drugs targeting cell nucleus with Hoechst unit K. Tanabe <i>et al.</i> (R3P2-4)	14
PR2-5	Development of Gadolinium-loaded mesoporous silica-based nanoparticles and application to cancer radiotherapy F. Tamanoi <i>et al.</i> (R3P2-5)	15
PR2-6	Pathological Findings of Tumor Growth Suppression of GdNCT with Intra-Tumoral Injection of Gadolinium-Polyplex in Pancreatic Cancer Model <i>in vivo</i> H. Yanagie <i>et al.</i> (R3P2-6)	16
PR2-7	Development of gadolinium-containing inorganic nanoparticles with polyglycerol coating for gadolinium neutron capture therapy of cancer L. Zhao <i>et al.</i> (R3P2-7)	17
PR2-8	Study about neutron capture therapy using polymeric drug delivery systems chelating Gd Y. Miura <i>et al.</i> (R3P2-8)	18
PR2-9	Neutron irradiation after administration of Gd-EDTMP to a mouse model of mammary tumor bone metastasis: Effects and distribution of Gd formulation as a novel neutron capture therapy agent T. Matsukawa <i>et al.</i> (R3P2-9)	19
Project 3	Enhancement of research methods for material irradiation and defect analysis A. Kinomura (R3P3)	21

PR3-1	Study to improve transport and measurement performance of a slow positron beamline A. Kinomura <i>et al.</i> (R3P3-1)	22
PR3-2	Doping effect of Cr, Mo, Ta, and Re on defect formation after electron-irradiation T. Toyama <i>et al.</i> (R3P3-2)	23
PR3-3	Hydrogen Thermal Desorption Analysis in Electron-irradiated F82H K. Sato <i>et al.</i> (R3P3-3)	24
PR3-4	Gamma-ray induced photo emission from ZnO single crystal wafer: Comparison with GaN T. Nakamura <i>et al.</i> (R3P3-4)	25
PR3-5	Investigation of Free Volume in Diamond-like Carbon Films Deposited by Various Methods K. Kanda <i>et al.</i> (R3P3-6)	26
PR3-6	Positron annihilation spectroscopy on diamond-like carbon films S. Nakao <i>et al.</i> (R3P3-7)	27
Project 4	Chemical and electronic properties of Actinide compounds and their applications T. Yamamura <i>et al.</i> (R3P4)	29
PR4-1	Study of Magnetic Structure in UIr ₂ Ge ₂ by Resonant X-Ray Scattering Experiments H. Amitsuka <i>et al.</i> (R2P7-2)	30
PR4-2	Bulk thorium separation for ²²⁸ Ac generator K. Shirasaki <i>et al.</i> (R2P7-4)	31
PR4-3	Elution Properties of Re(VII) from Cyclic Monoamide VBPR Resin by Chelating Agents M. Nogami <i>et al.</i> (R2P7-5)	32
PR4-4	Consistency verification between relativistic quantum chemical calculations and experiments in uranium compounds M. Abe <i>et al.</i> (R2P7-6)	33
PR4-5	Evaluation of Phase Diagram of Minor Actinide Oxides with CALPHAD H. Shishido <i>et al.</i> (R2P7-7)	34
PR4-6	Peculiar magnetism in uranium intermetallics with layered structure Y. Haga <i>et al.</i> (R3P4-1)	35
PR4-7	Adsorption Characterization of Actinide Chemical Species on Solid Adsorbents T. Suzuki <i>et al.</i> (R3P4-2)	36
PR4-8	A Study on Effect of Polymer Network on Resins for Separating Actinyl Ions M. Nogami <i>et al.</i> (R3P4-3)	37
PR4-9	XAFS study on the aged deterioration of a simulated fuel debris T. Kobayashi <i>et al.</i> (R3P4-4)	38
PR4-10	Synthesis of noble phthaloyanine derivatives and effect of substituent on recognition of light actinide and chemical property-3 M. Nakase <i>et al.</i> (R3P4-5)	39
Project 5	Development on Neutron Imaging Application Y. Saito (R3P5)	41
PR5-1	Measurements of multiphase flow dynamics using neutron radiography Y. Saito <i>et al.</i> (R3P5-1)	42
PR5-2	Evaluation of Water Distribution and Electrochemical Characteristics in Polymer Electrolyte Fuel Cell H. Murakawa <i>et al.</i> (R3P5-2)	43
PR5-3	Neutron Radiography on the Mixing Behavior of Reaction Solution and Cooling Water at a T-shaped Junction in a Flow-type Supercritical Hydrothermal Reactor. S. Takami <i>et al.</i> (R3P5-3)	44
PR5-4	Visualization of Dynamic Flow Maldistribution in a Microchannel Heat Exchanger H. Umekawa <i>et al.</i> (R3P5-4)	45

PR5-5	Measurement of Frost Distribution by Using X-ray and Neutron Cooperative Imaging R. Matsumoto <i>et al.</i> (R3P5-5)	46
PR5-6	Introduction of contrast agent for X-ray-based visualization of roots planted on organic medium U. Matsushima <i>et al.</i> (R3P5-6)	47
PR5-7	Effect of the water content of high-strength concrete on the spalling phenomenon under fire M. Yoshioka <i>et al.</i> (R3P5-7)	48
PR5-8	Visualization of Lithium Ion Migration in the Solid Electrolyte by Neutron Radiography S. Takai <i>et al.</i> (R3P5-11)	49
PR5-9	Visualization in the Accumulated Curved Rod Arrays M. Kaneda <i>et al.</i> (R3P5-12)	50
Project 6	Advancement of integrated system for dose estimation in BNCT Y. Sakurai (R3P6)	52
PR6-1	Establishment of characterization estimation method in BNCT irradiation field using Bonner sphere and ionization chamber (V) Y. Sakurai <i>et al.</i> (R3P6-1)	53
PR6-2	Study on New Type of Neutron Energy Spectrometer for BNCT K. Watababe <i>et al.</i> (R3P6-2)	54
PR6-3	Development and demonstration of Bonner sphere spectrometer for intense neutrons A. Masuda (R3P6-3)	55
PR6-4	Improvement of the SOF detector system for energy-dependent discrimination and long-term stability M. Ishikawa <i>et al.</i> (R3P6-4)	56
PR6-5	First Direct Observation of Boron Dose Distribution with a Boron-added Liquid Scintillator A. Nohtomi <i>et al.</i> (R3P6-5)	57
PR6-6	Development of Absolute Epi-thermal Neutron Flux Intensity Monitor for BNCT I. Murata <i>et al.</i> (R3P6-6)	58
PR6-7	Study for microdosimetry using silicon-on-insulator microdosimeter in the BNCT irradiation field (V) Y. Sakurai <i>et al.</i> (R3P6-8)	59
PR6-8	Measurement of BNCT beam component fluence with multi imaging plate system K. Tanaka <i>et al.</i> (R3P6-10)	60
PR6-9	Development of 2D Real-Time Neutron Imaging System in the BNCT Irradiation Field S. Uno <i>et al.</i> (R3P6-11)	61
PR6-10	Measurements of Neutron Fluence and Gamma ray Distribution using Thermoluminescence Slabs K. Shinsho <i>et al.</i> (R3P6-12)	62
PR6-11	Development and evaluation of 3D gel dosimeter for the measurement of dose distribution in BNCT S. Hayashi, <i>et al.</i> (R3P6-14)	63
PR6-12	Establishment of beam-quality estimation method in BNCT irradiation field using dual phantom technique (V) Y. Sakurai <i>et al.</i> (R3P6-15)	64
PR6-13	Development of real-time thermal neutron monitor for BNCT H. Tanaka <i>et al.</i> (R3P6-16)	65
PR6-14	Quantitative Measurement of 478 keV Prompt Gamma-rays of Boron-neutron Capture Reaction with the ETCC T. Mizumoto <i>et al.</i> (R3P6-17)	66
PR6-15	Evaluation of neutron irradiation fields for semiconductor device irradiation H. Tanaka <i>et al.</i> (R3P6-19)	67

PR6-16	Optimization of Bolus Shape for Boron Neutron Capture Therapy – Examination Using Simple Shaped Phantom for Experimental Verification — T. Takata <i>et al.</i> (R3P6-20).....	68
PR6-17	Annealing properties of boric acid infused PVA-GTA-I gel irradiated with neutrons H. Yasuda <i>et al.</i> (R3P6-22).....	69
PR6-18	Three dimensional model for pre-clinical assessments in BNCT K. Igawa <i>et al.</i> (R3P6-23).....	70
Project 7	Project Research on Advances in Isotope-Specific Studies Using Multi-Element Mössbauer Spectroscopy M. Seto (R3P7)	72
PR7-1	Intensity tensor of Fe ²⁺ in the M2 site of hypersthene by single crystal Mössbauer microspec-troscopy K. Shinoda <i>et al.</i> (R3P7-1).....	73
PR7-2	Mössbauer Study of the Model Complexes of Heme Enzymes H. Fujii <i>et al.</i> (R3P7-2).....	74
PR7-3	Analysis of Iron-based Products Using Mössbauer Spectroscopy - Iron Oxide Scale Generated in the Boiler Feed-water in Thermal Power Plant - Y. Akiyama <i>et al.</i> (R3P7-3).....	75
PR7-4	Electrical conductivity and the iron valence state of enstatite glasses up to Mbar pressures I. Mashino <i>et al.</i> (R3P7-4).....	76
PR7-5	The role of iron in the differential weathering processes of volcanic fall deposit H. Fukui <i>et al.</i> (R3P7-5).....	77
PR7-6	Rough estimation of Debye temperature for precursor of supported gold cluster catalysts derived from Recoil-free fraction in ¹⁹⁷ Au Mössbauer spectroscopy H. Ohashi <i>et al.</i> (R3P7-6).....	78
PR7-7	Recoilless Fraction on ¹⁹⁷ Au Mossbauer Spectroscopy Y. Kobayashi (R3P7-7).....	79
PR7-8	⁶¹ Ni Mössbauer Spectroscopy for Supramolecular Bridging Cyanide Complexes T. Kitazawa <i>et al.</i> (R3P7-8).....	80
PR7-9	Mössbauer spectroscopy of a perovskite-type iron oxide Ba _{2/3} La _{1/3} FeO ₃ M. Onose <i>et al.</i> (R3P7-9).....	81
PR7-10	Research on magnetism in a novel Kondo Lattice III Y. Kamihara <i>et al.</i> (R3P7-10).....	82
PR7-11	Optimization for the energy standard material for Mössbauer spectroscopy R. Masuda <i>et al.</i> (R3P7-11).....	83
PR7-12	Development of ¹⁸⁰ Hf Mössbauer Spectroscopy S. Kitao <i>et al.</i> (R3P7-12).....	84
PR7-13	Experimental Preliminary Approach on the Precipitation Mechanism of Banded Iron Formation (BIF) K. Yonezu <i>et al.</i> (R3P7-13).....	85
I-2. COLLABORATION RESEARCHES		86
1. Slow Neutron Physics and Neutron Scattering		
CO1-1	Current Status of Versatile Compact Neutron Diffractometer (VCND) on the B–3 Beam Port of KUR, 2021 K. Mori <i>et al.</i> (R3032)	87
CO1-2	Towards to mass production of high- <i>m</i> neutron focusing supermirrors M. Hino <i>et al.</i> (R3087)	88

CO1-3	Development of multilayer mirrors for neutron interferometer M. Kitaguchi <i>et al.</i> (R3094)	89
CO1-4	Development of high-resolution cold/ultracold neutron detectors using nuclear emulsion N. Naganawa <i>et al.</i> (R3113)	90
CO1-5	Development of a Spin Analyzer for Ultra-Cold Neutron S. Kawasaki <i>et al.</i> (R3137)	91
2. Nuclear Physics and Nuclear Data		
CO2-1	Measurement of Energy Resokution in the KURNS-LINAC Pulsed Neutron Facility[2] T. Sano <i>et al.</i> (R3030)	92
CO2-2	Measurements of Thermal-Neutron Capture Cross-Section of the $^{237}\text{Np}(n, \gamma)$ Reaction with TC-Pn in KUR S.Nakamura <i>et al.</i> (R3037)	93
CO2-3	β -decay spectroscopy of rare fission products with a 4π clover detector using an Isotope Separator On-Line KUR-ISOL S. Sakakibara <i>et al.</i> (R3077)	94
CO2-4	Development of a current-mode ^3He gas neutron detectors for BNCT T. Matsumoto <i>et al.</i> (R3088)	95
CO2-5	Quantitation of Gamma Ray Emission from Caputre Reaction of Uranium-238 (3) Y. Nauchi <i>et al.</i> (R3109)	96
CO2-6	Development of a neutron scintillator for a compact NRTA system (Part 2) J. Lee <i>et al.</i> (R3156)	97
CO2-7	Neutron induced fission cross section measurement of ^{233}U J. Hori <i>et al.</i> (R3157)	98
3. Reactor Physics and Reactor Engineering		
CO3-1	Subcriticality measurement by using a small neutron detector (3) T. Misawa <i>et al.</i> (R2CA05)	99
CO3-2	Reactor Noise Power-Spectral Analysis for a Graphite-Moderated and -Reflected Core (III) A. Sakon <i>et al.</i> (R2CA07)	100
CO3-3	Reactor Physics Experiment in a Graphite Moderation System for HTGR (III) Y. Fukaya <i>et al.</i> (R2CA09)	101
CO3-4	Measurement of fundamental characteristics of nuclear reactor at KUCA (VII) Y. Kitamura <i>et al.</i> (R2CA12)	102
CO3-5	Verification of a method to estimate reactivity in a deep subcritical state Y. Yamane <i>et al.</i> (R2CA13)	103
CO3-6	Basic Experiment on Reactor Power Distribution Reconstruction by Ex-core Neutron Detectors T. Sano <i>et al.</i> (R3CA01)	104
CO3-7	Measurement of Neutronics Characteristics for Th loaed core at KUCA (III) T. Sano <i>et al.</i> (R3CA02)	105
CO3-8	Subcriticality measurement by using a small neutron detector (4) T. Misawa <i>et al.</i> (R3CA03)	106
CO3-9	Measurement of Validation Data for Kinetics Parameter and Reactor Kinetics Y. Nauchi <i>et al.</i> (R3CA04)	107
CO3-10	Basic Research for Sophistication of High-power Reactor Noise Analysis (IV) S. Hohara <i>et al.</i> (R3020)	108
CO3-11	Development of Faster Measurement Method of High Neutron Flux with SPND C. H. Pyeon and R. Okumura (R3165)	109

4. Material Science and Radiation Effects

CO4-1	Characterization of Additive Aggregation in Lubricant using Small-Angle X-ray Scattering Y. Oba <i>et al.</i> (R2017)	110
CO4-2	Radiation Tolerance of SiC p+n Junction-Diodes for Beam Monitor Applications T. Kishishita <i>et al.</i> (R2102)	111
CO4-3	TDPAC Spectra of the $^{111}\text{Cd}(\leftarrow^{111\text{m}}\text{Cd})$ and $^{117}\text{In}(\leftarrow^{117}\text{Cd})$ Probes in CdIn_2O_4 W. Sato <i>et al.</i> (R3006)	112
CO4-4	Synthesis of metal nanocomplexes in water solution by γ -ray and electron irradiation reduction F. Hori <i>et al.</i> (R3018)	113
CO4-5	Hydrogen trapping behavior at vacancy in Fe-Al alloy with electron irradiation F. Hori <i>et al.</i> (R3019)	114
CO4-6	Study of resonant frequency change with irradiation dose of piezoelectric PZT element M. Kobayashi <i>et al.</i> (R3041)	115
CO4-7	Concentration Dependence of Local Structures at Cd Sites in $\text{Cd}_x\text{Sr}_{1-x}\text{TiO}_3$ Studied by TDPAC Method S. Komatsuda <i>et al.</i> (R3049)	116
CO4-8	Operation of Field Emission Image Sensor under Gamma-ray Irradiation Y. Gotoh <i>et al.</i> (R3056)	117
CO4-9	Radiochemical Research for the Advancement of $^{99}\text{Mo}/^{99\text{m}}\text{Tc}$ Generator by (n, γ) Method (4) Y. Fujita <i>et al.</i> (R3066)	118
CO4-10	The effect of ion irradiation on yttria stabilized zirconia (YSZ) single crystal substrates using a slow positron beam T. Ozaki <i>et al.</i> (R3072)	119
CO4-11	Study on formation mechanisms of low-fluence ion-irradiation induced damages on semiconductor surfaces J. Yanagisawa <i>et al.</i> (R3078)	120
CO4-12	Complex Structure of Ions Coordinated with Hydrophilic Polymer 22. Ionic Diffusion in Polymeric Structure Utilized by Polyiodide Ions. (3) A. Kawaguchi and Y. Morimoto (R3089)	121
CO4-13	Demagnetization Measurement of Permanent Magnet Materials Against Neutron Irradiation Y. Fuwa <i>et al.</i> (R3096)	122
CO4-14	Evaluation of Deuterated Macromolecular Crowder by Small Angle X-ray Scattering and Dynamic Light Scattering Y. Nagata <i>et al.</i> (R3097)	123
CO4-15	TDPAC Measurement of $^{111}\text{Cd}(\leftarrow^{111}\text{In})$ in Ultrafine Bubble Water M. Taniguchi <i>et al.</i> (R3101)	124
CO4-16	Tritium release behavior from neutron-irradiated FLiNaK mixed with Ti powder K. Katayama <i>et al.</i> (R3106)	125
CO4-17	Tritium recovery behavior for tritium breeder $\text{Li}_4\text{SiO}_4 - \text{Li}_2\text{TiO}_3$ biphasic material Y. Oya <i>et al.</i> (R3115)	126
CO4-18	Vacancy migration energy in CrFeCoNi medium-entropy alloy H. Araki <i>et al.</i> (R3119)	127
CO4-19	A study on destruction of cesium aluminosilicate compounds by gamma irradiation (3) H. Ohashi <i>et al.</i> (R3120)	128
CO4-20	Study on HPLC Elution Behavior of Heavy Lanthanide Metalloufullerenes K. Akiyama <i>et al.</i> (R3123)	129

CO4-21	Glass compositional dependence of radiophotoluminescence in Cu-doped aluminoborosilicate glass Y. Nishi <i>et al.</i> (R3128)	130
CO4-22	Formation of radiation defects on tungsten and their influence on effect of hydrogen isotope retention K. Tokunaga <i>et al.</i> (R3132)	131
CO4-23	Neutron irradiation tests for ITER plasma diagnostics M. Ishikawa <i>et al.</i> (R3133)	132
CO4-24	Vacancy Formation by Al Doping in β -FeSi ₂ Studied by a Reactor-Based Slow Positron Beam A. Yabuuchi (R3140)	133
CO4-25	Change in Fe valence state of Fe and Ni substituted Li ₂ MnO ₃ positive electrode material during different charge and discharge depths by ⁵⁷ Fe Mössbauer spectroscopy M. Tabuchi and Y. Kobayashi (R3166)	134
CO4-26	Evaluation of Structural Vacancies for Semiconducting Quasicrystal Approximant Al-Si-Ru by Positron Annihilation Spectroscopy K. Kitahara <i>et al.</i> (R3174)	135
CO4-27	Effect of gamma radiation on ultra-micro structure of hardwood cell-wall K. Murata <i>et al.</i> (R3176)	136

5. Geochemistry and Environmental Science

CO5-1	Trace elements, halogen, and Ar-Ar/I-Xe analyses of the Hayabusa2 returned samples R. Okazaki <i>et al.</i> (R3007)	137
CO5-2	Track observation in muscovite irradiated by ²⁵² Cf and ²⁴¹ Am sources N. Hasebe <i>et al.</i> (R3008)	138
CO5-3	Volcanic and Tectonic History of Philippine Sea Plate (South of Japan) Revealed by ⁴⁰ Ar/ ³⁹ Ar Dating Technique O. Ishizuka <i>et al.</i> (R3009)	139
CO5-4	Determination of Mercury content using INAA N. Shirai and S. Sekimoto (R3038)	140
CO5-5	Basic research on the trace elements analysis of airborne dust in the environment by INAA & PIXE N. Hagura <i>et al.</i> (R3053)	141
CO5-6	Long term change in soil elements of the atmospheric coarse particle observed at Sakai, Osaka N. Ito, <i>et al.</i> (R3061)	142
CO5-7	Eoarchean gneisses and their thermal histories H. Hyodo <i>et al.</i> (R3090)	143
CO5-8	Absorption of alkali metal ions by white radish sprouts (III) M. Yanaga, <i>et al.</i> (R3093)	144
CO5-9	SEM-EDS analysis of fine particles produced from model debris, (U,Zr)O ₂ , by laser ablation for decommissioning of Fukushima Daiichi Nuclear Power Plant A. Toyoshima <i>et al.</i> (R3110)	145
CO5-10	⁴⁰ Ar- ³⁹ Ar Dating of Extraterrestrial Materials in KURNS N. Iwata <i>et al.</i> (R3121)	146
CO5-11	Ar-Ar and I-Xe Dating for Meteorites and the Hayabusa2 Returned Samples Y. N. Miura <i>et al.</i> (R3127)	147
CO5-12	Neutron Activation Analysis of cosmo- and geo-chemical samples M. Ebihara <i>et al.</i> (R3131)	148
CO5-13	Collisional histories of the LL chondrite parent body revealed by ⁴⁰ Ar/ ³⁹ Ar dating H. Sumino <i>et al.</i> (R3136)	149

CO5-14	Application of the Single Comparator Method to Photon Activation Analysis at KURNS Md. S. Reza and Y. Oura (R3138)	150
CO5-15	Distribution of radiocesium in forestry area in Fukushima T. Ohta <i>et al.</i> (R3139)	151
CO5-16	Determination of Abundance of Rare Metal Elements in Seafloor Hydrothermal Ore Deposits by INAA Techniques-8: Cross check with ICP-QMS analysis (2) J. Ishibashi <i>et al.</i> (R3149)	152
CO5-17	Neutron activation analysis of carbonate reference materials: coral (JCp-1) and giant clam (JCt-1) S. Sekimoto <i>et al.</i> (R3160)	153

6. Life Science and Medical Science

CO6-1	Contribution of indirect actions to cell lethality in mixed neutron and BPA irradiation R. Hirayama <i>et al.</i> (R2P1-4).....	154
CO6-2	The tumor invasion enhanced by the conditioned-medium after X--rays via EGFR pathway H. Yasui <i>et al.</i> (R2P1-8)	155
CO6-3	Physicochemical analysis of protein ILEI, which reduces amyloid- β protein production E. Hibino <i>et al.</i> (R2014)	156
CO6-4	Solution scattering approach for dynamics of Lys48-linked tri-ubiquitin chain M. Yagi-Utsumi <i>et al.</i> (R3003).....	157
CO6-5	Radioresistance Mechanisms Acquired by Adaptive Evolution and their Evolutionary Mechanisms II T. Saito. (R3004).....	158
CO6-6	Oligomeric structural transition of HspB1 from Chinese hamster N. Kurokawa <i>et al.</i> (R3005).....	159
CO6-7	Study of Ku recognition to a DNA DSB end induced by ionizing radiation K. Akamatsu <i>et al.</i> (R3011).....	160
CO6-8	Estimation of trace elements in foods and amounts of intake of wild Japanese macaques M. Fukushima <i>et al.</i> (R3016).....	161
CO6-9	Evaluation of radiation resistance of lens constituent proteins involved in age-related cataract T. Takata and K. Lampi (R3033)	162
CO6-10	Asp racemization/isomerization in shedding products of cell adhesion molecule 1 is potentially involved in the neurodegeneration induced by elevated pressure A. Yoneshige, <i>et al.</i> (R3039)	163
CO6-11	The Study of Boron Neutron Capture Therapy (BNCT) for Primary Central Nervous System Lymphoma (PCNSL) H. Kashiwagi <i>et al.</i> (R3057).....	164
CO6-12	Evaluation of boron neutron capture therapy (BNCT) using brain tumor bearing rats or mice models H. Kashiwagi <i>et al.</i> (R3059).....	165
CO6-13	Establishment of protocol of the preparation of deuterated protein aimed for neutron scattering R. Inoue <i>et al.</i> (R3062)	166
CO6-14	Overall structure of fully assembled cyanobacterial KaiABC circadian clock complex by an integrated experimental-computational approach H. Yagi <i>et al.</i> (R3063).....	167
CO6-15	Analysis of p53 aggregates for elucidation of aggregation mechanism E. Hibino <i>et al.</i> (R3064)	168
CO6-16	Development of hydroponics system for wheat cultivation N. Sato <i>et al.</i> (R3065)	169

CO6-17	Preparation and Characterization of BPA-uridine conjugate for BNCT K. Tanabe <i>et al.</i> (R3067)	170
CO6-18	Analysis of distinct amyloid formation pathways between bovine and human insulin K. Yuzu <i>et al.</i> (R3068)	171
CO6-19	Structural analysis of protein complex using analytical ultracentrifugation and small-angle X-ray scattering. K. Morishima <i>et al.</i> (R3069)	172
CO6-20	Dynamics of copper chaperone for superoxide dismutase studied by small-angle X-ray scattering M. Shimizu <i>et al.</i> (R3071)	173
CO6-21	Structural dynamics of the overlapping di-nucleosome H. Tanaka <i>et al.</i> (R3079)	174
CO6-22	¹¹ C medical-isotope production via the ¹² C(γ ,n) ¹¹ C reaction with carbon nano tube N. Takahashi <i>et al.</i> (R3081)	175
CO6-23	Distribution of the chemical modifications of the amino acid residues in lens structural proteins during development of age-related cataract S. Matsushita <i>et al.</i> (R3084)	176
CO6-24	Molecular dynamics analysis of oxidative folding enzyme ER-60 with solution scattering measurement A. Okuda <i>et al.</i> (R3086)	177
CO6-25	Integrative approach using SAXS / SANS and computational science for understanding the structure-function relationship of IDP T. Oda <i>et al.</i> (R3092)	178
CO6-26	Development of New Treatment Method for Epithelioid Sarcoma by BNCT T. Fujimoto <i>et al.</i> (R3098)	179
CO6-27	Elucidating the Molecular Basis for the Increased Risk of Nuclear Cataract Development with Global Warming T. Takata and N. Yamamoto (R3112)	180
CO6-28	IL-6 suppresses the increase in cell oxidation through phosphorylation of mTOR and is involved in the acquisition of radiation resistance of the human pancreatic cancer-derived cell line Panc-1. Y. Tamari <i>et al.</i> (R3155)	181
CO6-29	Production of medical radioisotopes using electron linear accelerator S. Sekimoto <i>et al.</i> (R3159)	182
CO6-30	Design, Synthesis, and Evaluation of Polyamine-type Boron & Gadlinium Carriers for NCT S. Aoki <i>et al.</i> (R3169)	183
CO6-31	Elucidation of the effects of high dose rate radiation on normal and tumor tissues T. Watanabe <i>et al.</i> (R3170)	184
CO6-32	Theoretical Considerations on Reactor Production of Beta-Emitting Radionuclide ¹⁷⁷ Lu for Targeted Radionuclide Therapy K. Washiyama <i>et al.</i> (R3175)	185
 7. Neutron Capture Therapy		
CO7-1	Synthesis and evaluation of a novel boron neutron capture therapy agent H. Kimura and M. Suzuki (R2134)	186
CO7-2	The evaluation of boron neutron capture therapy (BNCT) to the novel mouse model of pelvic recurrence of colorectal cancer J. Arima <i>et al.</i> (R3001)	187
CO7-3	The abscopal effect as the late influence after the head neutron-irradiation of mice Y. Kinashi <i>et al.</i> (R3028)	188

C07-4	A Fundamental Investigation on Correlation Between Important Elements for Activation and Major Elements in Concrete and Cements for Radiation Shielding K. Kimura <i>et al.</i> (R3031)	189
C07-5	Development of Amino Acid Derivatives Containing ¹⁰ B-Clusters for BNCT A. Niitsu <i>et al.</i> (R3040)	190
C07-6	Enhancement of the cancer cell-killing effects of boron neutron capture therapy by overexpression of <i>LATI</i> in cancer stem cell-like cells K. Ohnishi <i>et al.</i> (R3042)	191
C07-7	Effects of overexpression of <i>LATI</i> in cancer stem cell-like cells on suppression of tumor growth by boron neutron capture therapy K. Ohnishi <i>et al.</i> (R3043)	192
C07-8	Preliminary Experiment of Tumour Growth Suppression by Intra-Tumoral Injection of Boron-Polyplex/Polymer for Boron Neutron Capture Therapy to Pancreatic Cancer Model <i>in vivo</i> H. Yanagie <i>et al.</i> (R3046)	193
C07-9	Enhancement of Tumour Growth Suppression by Electroporation with Intra-Tumoural Injection of Gadolinium-Polyplex for Gadolinium-Neutron Capture Therapy to Pancreatic Cancer Model <i>in vivo</i> H. Yanagie <i>et al.</i> (R3047)	194
C07-10	Identification of host immunostimulatory effects induced by boron neutron capture therapy T. Watanabe <i>et al.</i> (R3048)	195
C07-11	Basic research to expand the indication of neutron capture therapy to non-neoplastic diseases T. Watanabe <i>et al.</i> (R3050)	196
C07-12	Mechanism of Glioma Resistance After BNCT Conferred by Glioma Niche N. Kondo <i>et al.</i> (R3051)	197
C07-13	Solubilization of All-Trans-Retinoic Acid as Macrophage Polarizer by β -1,3-Glucan N. Yasukawa <i>et al.</i> (R3055)	198
C07-14	Carborane bearing pullulan nanogel/boron oxide nanoparticle hybrid for BNCT R. Kawasaki <i>et al.</i> (R3058)	199
C07-15	Optimization of polymeric BPA for non-clinical studies and basic study on its analogues T. Nomoto <i>et al.</i> (R3060)	200
C07-16	Development of Boron-Folic Acid Complex and BNCT Antitumor Effect K. Nishimura <i>et al.</i> (R3073)	201
C07-17	Development of Gadolinium-Boron Complexes for MRI-Guided BNCT S. Okada <i>et al.</i> (R3074)	202
C07-18	Water-soluble dodecaborate-containing pyrazolopyrimidine for BNCT Y. Hattori <i>et al.</i> (R3082)	203
C07-19	Attempts to sensitize tumor cells by exploiting the tumor microenvironment Y. Sanada <i>et al.</i> (R3102)	204
C07-20	Establishment of a method for determining position in alpha autoradiography using CR39 K. Nakai (R3103)	205
C07-21	Screening of Boron / Gadolinium Compounds for BNCT of Malignant Brain Tumors, 2021 M. Takagaki <i>et al.</i> (R3107)	206
C07-22	The effects of radioactivation of animals on the environment for the BNCT to companion animals. Y. Wada <i>et al.</i> (R3114)	207
C07-23	In Vivo Efficacy of BPA-Ionic Liquid as a Novel Compound for BNCT M. Shirakawa <i>et al.</i> (R3117)	208
C07-24	Preliminary study of the anti-tumor effect of BNCT using bubble liposome on the canine hemangiosarcoma model M. Yanagawa <i>et al.</i> (R3122)	209

CO7-25	Development of boron-nutritional diagnostics in the plant using a neutron capture reaction T. Kinouchi (R3126)	210
CO7-26	An Evaluation of the Response of Tumor Cells to BNCT Y. Tong <i>et al.</i> (R3129)	211
CO7-27	Development of ¹⁰ BPA-loaded mesoporous silica-based nanoparticles and evaluation in BNCT mouse experiments F. Tamanoi <i>et al.</i> (R3150)	212
CO7-28	Conjugation of Phenylboronic Acid Moiety through Multistep Organic Transformations on Nanodiamond Surface for an Anticancer Nanodrug of Boron Neutron Capture Therapy M. Nishikawa <i>et al.</i> (R3152)	213
CO7-29	The option of BNCT for oral squamous cell carcinomas K. Igawa <i>et al.</i> (R3154)	214
CO7-30	New boron drug development research targeting pancreatic cancer H. Michiue <i>et al.</i> (R3161)	215
CO7-31	Basic research on new BNCT strategies for melanoma H. Michiue <i>et al.</i> (R3162)	216
CO7-32	Quantitative analysis of the contribution of tumor vascular damage to the antitumor effect of X-ray using BNCR K. Ono <i>et al.</i> (R3163)	217
CO7-33	Study on Intracellular Protein Destruction by Boron Neutron Capture Reaction H. Kakuta <i>et al.</i> (R3167)	218
CO7-34	Observation of Intracellular Boron Neutron Capture Reaction with a Novel Boron Compound H. Kakuta <i>et al.</i> (R3168)	219
CO7-35	Development of immune function targeted boron neutron capture therapy using novel nanoparticles T. Watanabe and M. Suzuki (R3171)	220
CO7-36	Basic Experiment of Boron Neutron Capture Therapy(BNCT) for a Rat Model of Malignant Spinal Cord Glioma R. Kayama <i>et al.</i> (R3172)	221

8. Neutron Radiography and Radiation Application

CO8-1	Demonstration experiment of nuclear material detection using a low-cost assay system M. Komeda <i>et al.</i> (R3CA05)	222
CO8-2	Neutron efficiency of a GEM-based detector H. Ohshita <i>et al.</i> (R3080)	223
CO8-3	Establishment of a novel mutation breeding using Boron Neutron Capture Reaction (BNCR) M.Kirihata <i>et al.</i> (R3083)	224

9. TRU and Nuclear Chemistry

CO9-1	Nuclides sorption onto rock samples in the presence of humic acid T. Sasaki <i>et al.</i> (R3013)	225
CO9-2	Solid phase transformation of lanthanide oxide to hydroxide in aqueous solutions T. Kobayashi <i>et al.</i> (R3015)	226
CO9-3	Electrochemical U dissolution from U-Ru alloy in LiCl-KCl-UCl ₃ melt T. Murakami <i>et al.</i> (R3045)	227
CO9-4	The solvent extraction behavior of Eu and Tb in nitric acid solution using TDdDGA M. Ikeno <i>et al.</i> (R3054)	228
CO9-5	Solid-liquid extraction of Ca, Sr, Ba, Ra with crown ether toward the chemical study of nobelium E. Watanabe <i>et al.</i> (R3099)	229

CO9-6	Determination of Uranium in Fallout Using Fission-Track Analysis K. Takamiya <i>et al.</i> (R3124)	230
CO9-7	Measurement of X-ray of Pd-103 with a CdZnTe semiconductor detector T. Kubota <i>et al.</i> (R3130)	231
CO9-8	Effect of Coexistence of Adsorptive Metal Ions on γ -Ray Irradiation for Crown Ether Resin in HNO ₃ M. Nogami <i>et al.</i> (R3151)	232
CO9-9	Fundamental study on reactor production and separation and purification of β -radioactive materials including Ce-141 for nuclear medicine therapy T. Yamamura <i>et al.</i> (R3173)	233
 10. Health Physics and Waste Management		
CO10-1	Effective Measures on Safety, Security, Hygiene and Disaster Prevention in Laboratories T. Iimoto <i>et al.</i> (R3002)	234
CO10-2	Investigation of a method for analyzing chlorine and bromine in volatile liquid samples in neutron activation analysis K. Ito <i>et al.</i> (R3017)	235
CO10-3	Development of the Evaluation Method of Dose Reduction Effects by Reverse Tillage in the Forest Using the Point-Kernel Integration Method Y. Sogabe <i>et al.</i> (R3076)	236
CO10-4	Application of KURAMA-II to Radiation Monitoring of Public Facilities in Fukushima Prefecture A. Maekawa <i>et al.</i> (R3085)	237
CO10-5	Study of FP contamination behavior on structural materials using neutron activation analysis – Study of penetration and elution behavior of Cs - K. Kondo <i>et al.</i> (R3104)	238
 12. Others		
CO12-1	Determination of natural cobalt content as impurity in iron cyclotron yokes G. Yoshida <i>et al.</i> (R2080)	239
CO12-2	Neutron Resonance Spectrometry for Nuclear Security and Safeguards Education J. Kawarabayashi <i>et al.</i> (R3024)	240
CO12-3	Structural Analysis of Additives in Lubricants by Small-Angle X-ray Scattering T. Hirayama <i>et al.</i> (R3025)	241
CO12-4	Visualization of Lubricant Behavior in Machine Elements by Neutron Phase Imaging T. Hirayama <i>et al.</i> (R3026)	242
CO12-5	Neutron Activation Analysis of Neodymium Oxide T. Miura <i>et al.</i> (R3029)	243
CO12-6	Observation of Superposition of Coherent Transition Radiation Using an Extra Ring Resonator N. Sei, and T. Takahashi (R3035)	244
CO12-7	Another Trial to Analyze the Texture of Roof-tile: Toward Detailed Provenancial Studies of Excavated Ceramics by INAA M. Tomii <i>et al.</i> (R3075)	245
CO12-8	Development of high-count rate two-dimensional neutron detector system S. Sato <i>et al.</i> (R3091)	246
CO12-9	Study for activity measurement technique of radioactive noble gases using a plastic scintillator T. Yamada <i>et al.</i> (R3100)	247
CO12-10	Fiber-reading Radiation Monitoring System with an Optical Fiber and Red-emitting Scintillator at the ⁶⁰ Co Radiation Facility II S. Kurosawa <i>et al.</i> (R3105)	248

CO12-11	Size Measurement of Radioactive Aerosol Particles Using a Diffusion Battery and Imaging Plates in an Electron LINAC Facility Y. Oki <i>et al.</i> (R3134)	249
CO12-12	Study of Isotope Separation via Chemical Exchange Reaction R. Hazama <i>et al.</i> (R3135)	250
CO12-13	Beam Test of a Micro-Cell MWPC for a Muon-Electron Conversion Search Experiment, DeeMe M. Aoki <i>et al.</i> (R3158)	251
CO12-14	Determination of Impurity Metals in the Uranium Oxide by ICP-MS T. Miura <i>et al.</i> (R3164)	252
CO12-15	Neutron activation of medicines for development of new imaging methodology A. Toyoshima <i>et al.</i> (R3177)	253
CO12-16	Evaluation Test of Quantitative 3-D Measurement of Gamma Dose in the Reactor Building by ETCC T. Tanimori <i>et al.</i> (R3178)	254
II. PUBLICATION LIST (April 2021 – March 2022)	255

**I. ANNUAL SUMMARY OF EXPERIMENTAL
RESEARCH ACTIVITIES**

I-1. PROJECT RESEARCHES

Project 1

PR1 The effect of boron neutron capture therapy on normal tissues

M. Suzuki

Institute for Integrated Radiation and Nuclear Science, Kyoto University

In this research project, six research projects were included. One research project (P1-3 could not be reported due to delay of the analysis).

The effect of normal tissues including lung, liver, brain, and bone were investigated in this study. Details of each project is referred to the following contents.

P1-1: “The effect of boron neutron capture therapy (BNCT) on normal lung in mice.”

The effect of boron neutron capture therapy (BNCT) on normal lung was analyzed with reference to the survival. The whole thorax irradiation (WTI) with thermal neutron beam was carried out at 1 hour after subcutaneous administration of boronophenylalanine (BPA) at the dose of 500mg/kg. The mice were sorted into four treatment groups, 10-minutes (min), 15-min, 20-min, and 25-min irradiation groups. In each group, three to six mice were irradiated. In 25-min irradiation group, all the mice died within 10 days. To compare the result of BNCT-treated group with those of thermal neutron beam irradiation group and X-ray irradiation group, further observation is needed.

P1-2: “Clarification of the normal cell fractionation as a trigger for radiation-induced liver injury.”

To clarify the mechanism of radiation-induced liver disease, we used the following boron cluster-sugar chain-conjugated albumin.

- Asialo-N-glycan-MID*-albumin (targeting hepatocytes)
- Mannose-N-glycan-MID*-albumin (targeting non-parenchymal cells)

*MID: maleimide combined with *closo*-dodecarborate

These boron compounds were administered subcutaneously at 1.5 hour before sacrifice the mice for sampling their blood and livers. The boron concentrations in the blood and liver were measured and spatial distributions of these compound in the liver were analyzed using α -autoradiography technique. The liver/blood boron concentration ratio for asialo-N-glycan-MID-albumin was higher than that for mannose-N-glycan-MID-albumin. The spatial distribution of these compounds detected on α -autoradiography were visually almost the same.

P1-4: “Examination of the influence on normal liver tissue by boron neutron capture therapy.”

The purpose of this study is to find the early indicator or surrogate marker which cause fibrosis in the normal liver tissue after BNCT. The degree of the steatosis in the normal liver and the expression level of Sonic Hedgehog protein were investigated at the seven days after thermal beam irradiation with or without boronophenylalanine (BPA). The degree of liver fibrosis was evaluated with Masson trichrome staining at six months after the irradiation. The degree of stenosis, expression of Sonic Hedgehog protein and liver fibrosis in BNCT cohort was higher compared with these in control and thermal neutron beam.

P1-5: “The Effect of Boron Neutron Capture Therapy to Normal Bones in Mice.”

The purpose of this project is to elucidate the compound biological effectiveness (CBE) factor of normal bone by evaluating the influence on bone strength in mice. In this year, the ^{10}B bio-distribution in the bone was investigated after boronophenylalanine (BPA) administration using α -autoradiography and laser ablation (LA) ICP-NS. The higher accumulation of ^{10}B were seen in the growth plate, the trabecular bone, and the bone marrow.

P1-6: “The biological behavior of boron compound in normal bone of young mice and the influence of boron neutron capture therapy on bone growth.”

The purpose of this project is to investigate the biological behavior of boron compound in the normal tibia of young mice, including the analysis of the boron concentration and the bio-distribution of administered boron compound. Furthermore, BNCT was performed on the bones of four-week-old C3H/He mice. The results in this study showed that the tibial growth in the young mice was slightly suppressed in the higher doses of BNCT.

PR1-1 The effect of boron neutron capture therapy (BNCT) on normal lung in mice

M. Suzuki and Y. Tamari

*Institute for Integrated Radiation and Nuclear Science
Kyoto University*

INTRODUCTION: We have reported the results of overall survival (OS) following whole thoracic irradiation (WTI) with X-ray and thermal neutron beams derived from Kyoto University Research Reactor (KUR) in previous reports of “Progress Reports.”. In this year, we have carried out the experiment of WTI with boron neutron capture irradiation (BNCR) using boronophenylalanine (BPA).

In this report, we reported the result of WTI with BNCR using BPA.

EXPERIMENTS:

Mice

Ten- to twelve-week-old female C3H/He mice were used. The mice were purchased from Japan SLC, Inc.

Treatments

The mice were sorted into four treatment groups, 10-minututs (min), 15 min, 20 min, and 30 min irradiation (IR) groups. Three to six mice were included in each cohort. The thermal neutron flux was measured at the surface of the acryl box in which the mice was contained. The WTI with BNCR were carried out at the 5MW reactor power which was the same condition as that in the WTI with thermal neutron beam. BPA was administered subcutaneously at the dose of 500 mg/kg at 1hour (hr) before WTI.

RESULTS: The acryl box containing mice were irradiated with thermal neutron beam at the thermal neutron flux of $4.8E+09$ n/cm²/s which was measured by analysis of activation of gold foil attached to the surface of the box. The observation of the cohort irradiated with thermal neutron irradiation was finished since all the mice were dead.

Figures 1 and 2 shows OSs of WTI with thermal neutron beams and with BNCR using BPA.

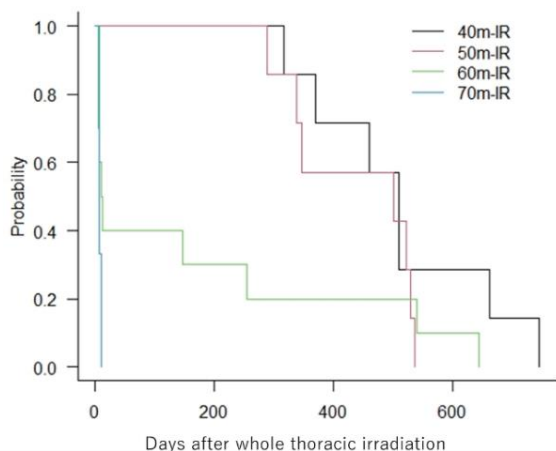


Fig.1 OS of WTI by thermal neutron beam

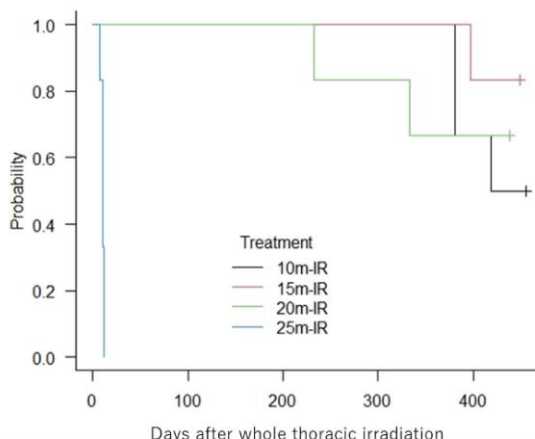


Fig. 2 OS of WTI by BNCR using BPA

Within 10 days after WTI with thermal neutron beam, all the mice in the 70 min IR group and 60 % of mice in the 60 min IR group were dead. Within 10 days after WHI with BNCR, all the mice in the 25 min IR groups are dead.

The cause of acute death following WTI within 10 days is supposed to be dysfunction of esophagus since the basal epithelium cells in esophagus decreased substantially in number within 5 days after WTI.

Figure 3 shows the OS of WTI with thermal neutron beam using the data in which the number of the mice were omitted.

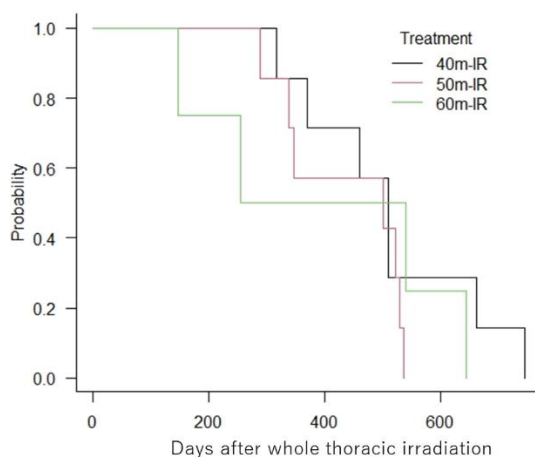


Fig. 3. OS of WTI by thermal neutron irradiation

Further observation is needed to compare the results of WTI with thermal neutron beam and WTI with BNCR.

PR1-2 Clarification of the normal cell fractionation as a trigger for radiation-induced liver injury

S. Takeno¹ and M. Suzuki²

¹Graduate School of Science, Kyoto University

²Institute for Integrated Radiation and Nuclear Science, Kyoto University

INTRODUCTION:

Radiation-induced liver disease (RILD) is one of the fatal adverse events in radiation therapy. The mechanism of the RILD is still not clear. Boron neutron capture radiation (BNCR) can irradiate the cell fractions in which boron compounds distribute selectively since the path of heavy particles (⁴He and ⁷Li atoms) derived from boron neutron capture reaction are noticeably short ones less than 10 μm. To investigate the mechanism of the RILD, BNCR is available for detecting the normal cell fractions which triggered to cause RILD. The objective of our study is to clarify the mechanism of radiation-induced liver injury using BNCR with boron compounds selectively accumulating in normal cell fractions.

EXPERIMENTS:

Boron compounds

In this experiment, we used two boron compounds. These consist of albumin conjugated with two functionalized portions which are maleimide combined with *closo*-dodecaborate (MID) and sugar chain targeting normal cell fractions in liver. The boron compounds are as follows

Asialo-N-glycan-MID-albumin (distributes in hepatocytes)

- Mannose-N-glycan-MID-albumin (distributes in non-parenchymal cells)

Mice

We used seven-week female BALB/c mice which were purchased from CLEA Japan, Inc.

Treatments

The two boron compounds were administered intravenously via tail vein at the dose of 100 μl. At 1.5 hour (hr) later, the blood was sampled, and the liver were resected. Liver tissue sections were divided into two portions. The one portion was put onto CR-39 (solid state nuclear track detector) and irradiated with thermal neutron to analyze boron spatial distribution using α-autoradiography (ARG) technique de-

scribed in our previous study [1]. The ¹⁰B concentrations of the blood and liver were analyzed with inductively coupled plasma atomic emission spectroscopy.

RESULTS:

The ¹⁰B concentrations in the liver and blood

The ¹⁰B concentrations in the blood and liver at 1.5 hr after administration of two boron compounds are shown in Table 1.

Boron compounds	Liver	Blood	Liver/Blood ratio
	mean ± SD	mean ± SD	
Asialo-N-glycan-MID-albumin	18.4 ± 3.6	20.8 ± 3.7	0.89 ± 0.06
Mannose-N-glycan-MID-albumin	13.3 ± 1.1	20.8 ± 4.0	0.67 ± 0.14

The value of the liver/blood of Asialo-N-glycan-MID-albumin was higher than that of Mannose-N-glycan-MID-albumin.

Distribution of ¹⁰B in the liver

The ARGs of each boron compound in liver is shown in Figs. 1 and 2.

Fig.1 ARG of Asialo-N-glycan-MID albumin

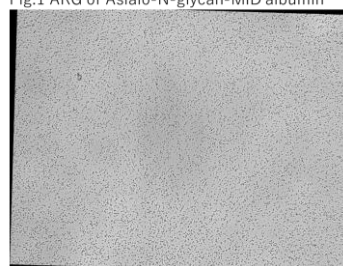
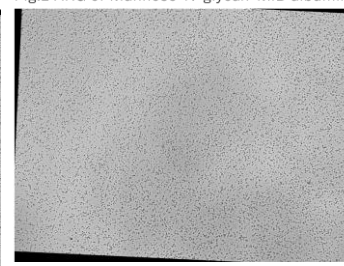


Fig.2 ARG of Mannose-N-glycan-MID albumin



Visually, no apparent difference of ¹⁰B distribution was observed. As shown in Table 1, the ¹⁰B concentrations in the blood were high, which might obscure the difference of ¹⁰B distribution of each boron compound in normal cell fractions of liver.

The further study is necessary to detect the optimal point in time at which the ¹⁰B concentration ratio of liver to blood is higher compared to that in this study.

REFERENCES:

- [1] S.Takeno, H.Tanaka, T. Watanabe, T. Mizowaki, M. Suzuki, Quantitative autoradiography in boron neutron capture therapy considering the particle ranges in the samples. *Phys Medica* 2021;82:306–20. <https://doi.org/10.1016/j.ejmp.2021.02.012>.

PR1-3 Examination of the influence on normal liver tissue by Boron neutron capture therapy

Y. Tamari^{1,2}, T. Takata², S. Takeno², H. Tanaka², H. Yamazaki¹, K. Yamada¹, M. Suzuki²

¹Department of Radiology, Kyoto Prefectural University of Medicine

²Institute for Integrated Radiation and Nuclear Science, Kyoto University

INTRODUCTION: Boron neutron capture therapy (BNCT) for liver tumor, which has been conducted up to the present, has used the compound effectiveness factor (CBE) determined by using genotoxicity for hepatocytes as an indicator, which has been clarified by Suzuki et al [1]. But there is a problem whether it is appropriate as a real clinical endpoint. Fundamental researches of liver fibrosis that are the late effect of radiation therapy are necessary. It is necessary to do basic research that uses liver fibrosis, which is a late radiation injury to the liver, as an evaluation index. The hedgehog signaling pathway is one of the important processes involved in animal development, and has been implicated in the maintenance and regeneration of adult tissues. The hedgehog signaling pathway is activated in the damaged liver and affects tissue remodeling. It has also been reported that cell proliferation is promoted and epithelial-mesenchymal transition leading to fibrosis is induced [2]. A purpose of this study is to find the early indicator or surrogate marker which cause fibrosis in the normal liver tissue after BNCT.

EXPERIMENTS: Female C57BL6 mice at 6 weeks of age were injected 1,000 mg/kg p-boronophenylalanine (BPA) solution subcutaneously 2 hours before neutron irradiation. The mice were irradiated for 60 minutes at the 1MW output. One week after irradiation, mice were sacrificed and the blood and livers were analyzed. Blood and liver boron concentrations 2 hours and 3 hours after the administration of 1,000 mg/kg BPA were quantified using Inductively Coupled Plasma-Atomic Emission Spectrometry (ICP-AES). In addition, Masson trichrome staining was performed to determine the degree of liver fibrosis six months after neutron irradiation. Hematoxylin Eosin (HE) staining and triglyceride quantification were performed to investigate degree of the steatosis in the mouse normal liver tissue after BNCT. Western blotting was performed to determine the expression level of Sonic Hedgehog protein.

RESULTS: Two hours after the administration of BPA, the liver boron concentration was about 8.1 $\mu\text{g/g}$, and the blood boron concentration was about 9.2 $\mu\text{g/g}$.

Three hours after BPA administration, the liver boron concentration was about 4.1 $\mu\text{g/g}$, and the blood boron concentration was about 4.4 $\mu\text{g/g}$. As shown in Fig. 1, Masson trichrome staining showed a tendency for increased liver fibrosis in the neutron-irradiated group receiving BPA (BNCT group). The result of HE staining demonstrated that the steatosis of the BNCT group was increased (Fig. 2). Triglycerides in mouse normal liver tissue after BNCT tended to be increased compared to control. Furthermore, as a result of Western blotting, the expression of Sonic Hedgehog protein in the BNCT group was higher than in the group only irradiated with neutrons (Fig. 3).

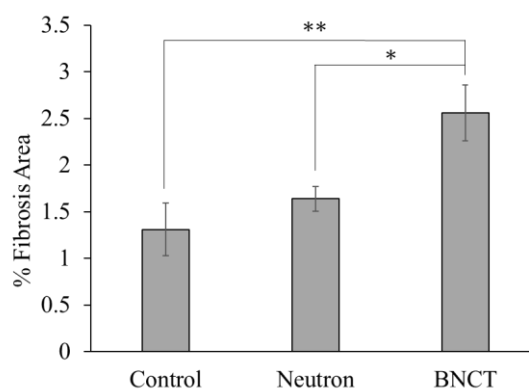


Fig. 1. Fibrosis of mouse liver by BNCT six months after neutron irradiation.

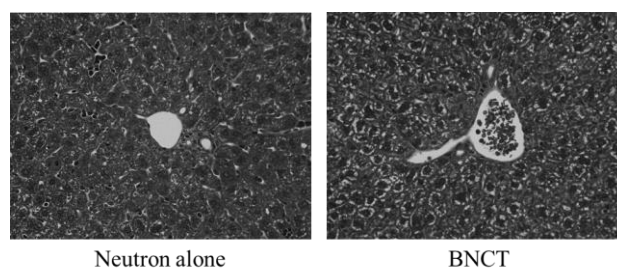


Fig.2 Fatty degeneration of mouse liver by BNCT one week after neutron irradiation.

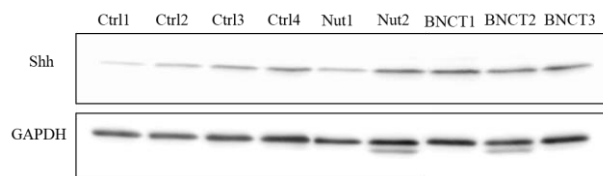


Fig. 3. Shh expression of mouse liver by BNCT. Ctrl: control, Nut: neutron alone, BNCT: BNCT treated.

REFERENCES:

- [1] M. Suzuki *et al.*, *Jpn. J. Cancer Res.*, **91** (2000) 1058-1064.
- [2] Y. Jung *et al.*, *Gut*, **59** (2010) 655-665.

PR1-4 The Effect of Boron Neutron Capture Therapy to Normal Bones in Mice

R. Iwasaki, R. Yoshikawa¹, T. Mori, Y. Sakurai², M. Suzuki² and K. Ono³

Faculty of Applied Biological Sciences, Gifu University
¹United Graduate School of Veterinary Sciences, Gifu University

²Institute for Integrated Radiation and Nuclear Science, Kyoto University

³Kansai BNCT Medical Center, Osaka Medical College

INTRODUCTION:

There are various tumors in which normal bone is included in the irradiation field, such as bone and soft tissue sarcoma, head and neck cancer, gynecologic cancer, prostate cancer, and tumors that have metastasized to the bone. As a result, radiation-induced bone toxicity, such as fracture, necrosis, and impairment of skeletal growth, can be occurred.

On the other hand, compared with the X-ray irradiation, boron neutron capture therapy (BNCT), a tumor cell-selective particle radiation therapy, is considered to be more effective without any late effects to the normal bone. However, to apply BNCT to the clinical practice, accurate dosimetry is essential. And the compound biological effectiveness (CBE) factor, the value which is necessary when converting to the X-ray equivalent dose, is significant for this purpose.

In this project, we had elucidated the CBE factor of normal bone by evaluating the influence on bone strength in mice. Furthermore, the boron concentrations in whole bones after the administration of the boron compound were analyzed. In this year, we visualized the ¹⁰B bio-distribution to investigate the BNCT-specific reduction of bending strength.

EXPERIMENTS: Female eight-week-old C3H/He mice were used for the study (n = 3 in each group). As boron compound, p-boronophenylalanine (BPA) was prepared at a dose of 30 mg/ml.

Bone sample preparation 60 minutes after 125, 250, and 500 mg/kg of BPA were subcutaneously injected into mice, tibias in each mouse were collected. Then, each sample was cut as thin sections of 5 μm-thickness by Kawamoto method, which is a non-demineralized frozen section preparation method.

α-autoradiography The sections were pasted onto CR-39 and irradiated with thermal neutrons at KURNS at a fluence of $6.32 \times 10^{11} \text{ n/cm}^2 - 1.36 \times 10^{12} \text{ n/cm}^2$ for 7–15 minutes. The irradiated CR-39 was etched with a PEW solution at 50 °C for 8 minutes. The obtained macroscopic pit images were accurately superimposed on the tissue section, and the distribution of α-ray tracks in the tibia was observed with an optical microscope.

Laser ablation (LA) ICP-MS After the sample introduction by LA using the NWR213, analysis by ICP-MS was conducted using the Agilent 8800. The localization of boron was imaged semi-quantitatively based on the previously obtained boron concentration.

RESULTS: Fig. 1 shows the ¹⁰B bio-distribution in the tibia evaluated by the α-autoradiography. The higher accumulations of ¹⁰B were seen in the growth plate (a), the trabecular bone (b), and the bone marrow (c). On the other hand, the lower accumulation was seen in the cortical bone (d), although the ¹⁰B was localized a little in the periosteum and endosteum. In each region, the figures clearly show that the boron accumulation is dose dependent. LA-ICP-MS also showed the same results (Fig. 2).

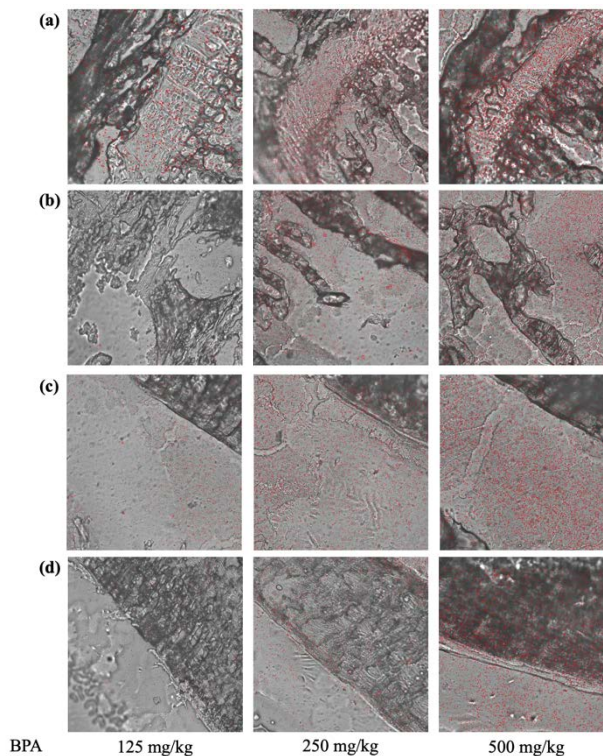


Fig. 1. ¹⁰B distribution in the tibia by α-autoradiography. Red dots representing the presence of boron. (a) growth plate, (b) trabecular bone, (c) bone marrow, and (d) cortical bone.

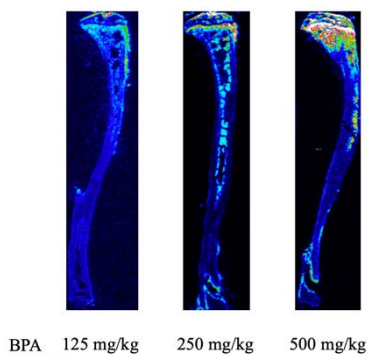


Fig. 2. ¹⁰B distribution in the tibia by LA-ICP-MS. Regions of high concentrations of boron are colored white, red, and green.

CONCLUSION: The results showed that ¹⁰B was mainly distributed in regions with abundant blood flow, such as cartilage, bone marrow, and trabecular bone. It is necessary to perform the morphological analysis using micro-CT and the histopathological examination to investigate the relationship between the decrease in bone strength by BNCT and the ¹⁰B distribution in the normal bone.

PR1-5 The Biological Behavior of Boron Compound in Normal Bone of Young Mice and the Influence of Boron Neutron Capture Therapy on Bone Growth

R. Iwasaki, R. Yoshikawa, R. Kido, T. Mori, Y. Sakurai¹, and M. Suzuki¹

Faculty of Applied Biological Sciences, Gifu University
¹Institute for Integrated Radiation and Nuclear Science, Kyoto University

INTRODUCTION:

There are various tumors in which normal bone is included in the irradiation field, such as bone and soft tissue sarcoma, head and neck cancer, gynecologic cancer, prostate cancer, and tumors that have metastasized to the bone. In particular, there is a high incidence of bone tumors such as osteosarcoma, chondrosarcoma and Ewing's sarcoma in the adolescent and young adult generation. As a result, radiation-induced bone toxicity, such as fracture, necrosis, and impairment of skeletal growth, can be occurred.

On the other hand, compared with the X-ray irradiation, boron neutron capture therapy (BNCT), a tumor cell-selective particle radiation therapy, is considered to be more effective without any late effects to the normal bone. However, in our previous study using the adult mice, the higher accumulation was seen in the epiphyseal cartilage including the growth plate. This finding indicates that the higher radiation doses might be delivered to the growth plate and may cause the impairment of skeletal growth.

In this project, we investigate the biological behavior of boron compound in the normal tibia of young mice, including the analysis of the boron concentration and the bio-distribution of administered boron compound. Furthermore, BNCT was performed on the bones of young mice to evaluate their influence 3 months after the irradiation.

EXPERIMENTS: Female four-week-old C3H/He mice were used for the study (n = 5 in each group). As boron compound, p-boronophenylalanine (BPA) was prepared at a dose of 30 mg/ml. The X-ray and neutron irradiation was performed at Gifu University and Kyoto University Reactor, respectively.

Boron concentration measurement After subcutaneously injected into mice at doses of 125, 250, 500 mg/kg of BPA, the boron concentrations at each time point (30, 60 and 90 min after administration) in the tibia were measured by ICP-AES.

X-ray irradiation Mice were irradiated at a dose rate of 250 cGy/min to their right hind limb at single doses of 4, 8, 12, 16, 20, 24, 28, 32 and 36 Gy.

Neutron irradiation Each neutron irradiation at a power of 1 MW was carried out as follows; neutron beam only (for 30, and 60 min), neutron beam for 30 and 60 min after subcutaneously injected into mice at doses of 125, 250, and 500 mg/kg of BPA. Based on the results of the biodistribution of BPA, irradiation was started at 30 min after the injection.

Bone growth measurement Tibias were collected at 12 weeks post-irradiation. Subsequently, the length of the tibia in each group was measured using a caliper. The

obtained data were shown as relative values to the length of the non-irradiated left tibia.

RESULTS:

Fig. 1 shows the boron concentration in the tibia after BPA administration. The results shows that the boron concentration in the tibia was maintained in a dose-dependent manner at measurement times up to 90 min after BPA administration.

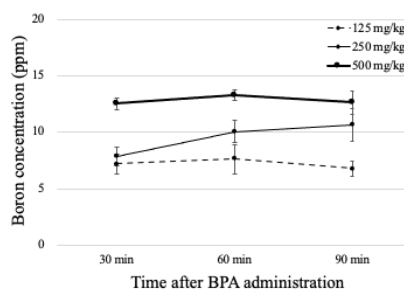


Fig. 1. Boron concentration changes in the tibia after 125, 250 and 500 mg/kg of BPA administration by ICP-AES.

Subsequently, the irradiation experiments to the right hind limb of young mice were performed. Fig. 2 shows the tibias sampled 12 weeks after neutron-irradiation with 500 mg/kg of BPA administration. The growth in the irradiated tibia was slightly suppressed compared with that in the non-irradiated tibia. Fig. 3 shows the changes in the tibial length according to the irradiated dose and the irradiation time. Similar to the X-ray irradiation, higher dose of BNCT mildly suppressed the bone growth.



Fig. 2. The length of the tibias 12 weeks after irradiation. Irradiated and non-irradiated tibias are shown as (+) and (-), respectively.

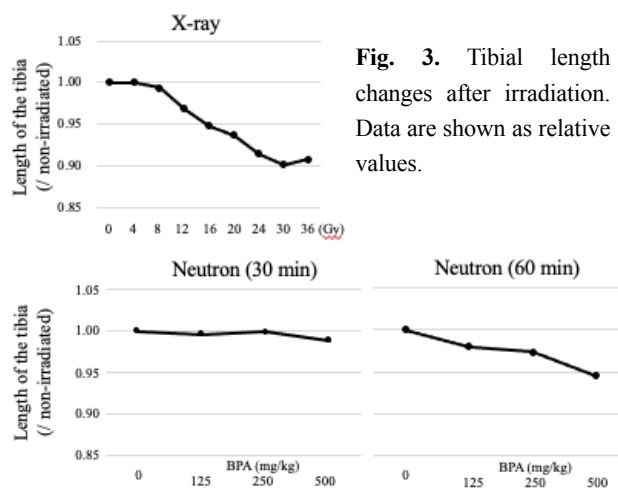


Fig. 3. Tibial length changes after irradiation. Data are shown as relative values.

CONCLUSION: The results showed that the tibial growth in the young mice was slightly suppressed in the higher doses of BNCT. Further investigations such as ¹⁰B bio-distribution, the morphological and the pathological analysis are necessary to elucidate its mechanism.

I-1. PROJECT RESEARCHES

Project 2

PR2 Preclinical studies on gadolinium neutron capture therapy

M. Suzuki

Institute for Integrated Radiation and Nuclear Science, Kyoto University

In this research project, nine research projects were included. Details of each project is referred to the following contents.

P2-1: Investigation of cell killing effect by auger electrons emitted during gadolinium neutron capture therapy (Gd-NCT)

In this year, we developed a new irradiation method to investigate the cell killing effect by auger electrons in Gd-NCT. Using the positive-charged Gd-nanoparticles, the cell killing effect of Gd-NCT was assayed by colony formation assay. In this study, no additive cell killing effect by Gd-NCT was yielded. The Gd concentration of thirty ppm was supposed to be too low. Further study is needed to elucidate the cell killing effect of auger electrons.

P2-2: Development of Nano Carriers Installed with Gd (III)-Thiacalixarene Complex for Gd-NCT

In this year, the cell killing effect of Gd-NCT with Gd₃TCAS₂-installed albumin nanoparticles (NP) was investigated by comparison with those of Gd₃TCAS₂, Gd-DTPA, and PBS control. The results of this study showed that even though the delivery efficiency of Gd₃TCAS₂-installed albumin NP to the cells was lower than that of free Gd₃TCAS₂, Gd₃TCAS₂-installed albumin NP showed higher NCT effect.

P2-3: Gadolinium neutron capture therapy as new treatment for head and neck cancer.

In this study, using masseter muscle invasion model, *in vivo* tumor-killing effects of Gd-NCT with Gd-loaded chitosan nanoparticles (Gd-nanoCPs) was investigated. The tumor-loaded model was developed by injection of SCC-VII (1x10⁶ cell/mouse) into the left masseter muscle. The result showed that decrease in tumor volume in Gd-NCT group was observed without damage to the normal surrounding mucosa.

P2-4: Preparation of drugs targeting cell nucleus with Hoechst unit

In this study, the synthesized BPA-Hoechst collecting in the nucleus was subjected to cellular experiments.

Experiments using F-Hoechst shows that the unit take functional molecules into cell nucleus. The cytotoxic effect of thermal neutron beam irradiation was significantly enhanced when the cells were irradiated in the presence of BPA-Hoechst. BPA-Hoechst conjugate is a potent candidate agent for BNCT.

P2-5: Development of Gadolinium-loaded mesoporous silica-based nanoparticles and application to cancer radiotherapy.

In this study, preliminary evaluation of Gd-

biodegradable periodic mesoporous organosilica (BMPO) using the chicken chorioallantoic membrane (CAM) model that was established by transplanting human ovarian cancer cells.

Preliminary investigation of tumor growth inhibition efficacy Gd-BPMO in the CAM model showed that the tumor growth was significantly inhibited when Gd-BPMO was injected compared to no injection or empty BPMO.

P2-6: Pathological findings of tumor growth suppression of GdNCT with intra-tumoral injection of gadolinium-polyplex in pancreatic cancer model *in vivo*.

In this study, the gadolinium/ hyaluronic acid/ protamine-mixed with cationic liposome (¹⁵⁷Gd-plex) was prepared and its efficacy as the compound of GD-NCT was estimated with Human Pancreas Adenocarcinoma cell line (AsPC-1) bearing mice. HE dyeing & apoptotic assay was performed for evaluating the mechanism for cancer cell cytotoxicity by GdNCT. Cancer cell hyalini- zation and degeneration and apoptotic changes were observed in the GdNCT treated group with ¹⁵⁷Gd-plex.

P2-7: Development of gadolinium-coating inorganic nanoparticles with polyglycerol coating for gadolinium neutron capture therapy of cancer.

In this study, Gd-containing inorganic nanoparticles grafted with polyglycerol (Gd-NP-PG) was evaluated as the agent of Gd-NCT using CT26-bearing mice. Gd-NP-PG nanoparticles-mediated Gd-NCT significantly suppressed the growth of CT26 tumors

P2-8: Study about neutron capture therapy using polymeric drug delivery systems chelating Gd.

In this study, new class of Gd-DOTA introduced polymers (polymer-drug) were used for evaluating its efficacy of the Gd-related therapeutic performance thorough neutron irradiation using CT26 bearing Balb/c mice. The result showed that the low-molecular drug and polymer drug exhibited antitumor efficacy with no significant difference. In the next year, modification of experimental designs and polymer structure will be planned.

P2-9: Neutron irradiation after administration of Gd-EDTMP to a mouse mode of mammary tumor bone metastasis: Effects and distribution of Gd formulation as a novel neutron capture therapy agent.

In this year, after neutron irradiation of the tumor-bearing mice with Gd tetra (methylene phosphonic acid) chelate (Gd-EDTMP), the distribution of ¹⁵⁷Gd in and around the bone was imaged using laser ablation inductively coupled plasma mass spectrometry (LA-ICP-MS). The weight of the right leg in the Gd-NCT group tended to be lower than the control groups. LA-ICP-MS Gd imaging of the legs in the Gd-EDTMP administration groups showed extremely high Gd signal intensity in bone.

PR2-1 Investigation of cell killing effect by auger electrons emitted during gadolinium neutron capture therapy (Gd-NCT)

M. Suzuki and H. Tanaka

*Institute for Integrated Radiation and Nuclear Science
Kyoto University*

INTRODUCTION:

We reported the feasibility of the irradiation system to investigate the cell killing effect by auger electrons in Gd-NCT by micronucleus assay.

In this year, we developed another irradiation system which can irradiate the cells attached to the flasks with horizontal thermal neutron beam derived from the Kyoto University Research Reactor.

Using a new system, we evaluated the cell killing effect of the Gd-containing nanoparticles.

EXPERIMENTS:

Cell line: The V79 cells were maintained in E-MEM supplemented with L-glutamine and 10% fetal bovine serum (FBS).

Gd-nanoparticles: The Gd-nanoparticles which were used in this study were provided from Dr. T. Ando. The surface of Gd-nanoparticles has positive charge which makes the particles adhere to the tumor cells.

Irradiation system: To irradiate the cells attached to the flasks with horizontal thermal neutron beam, the flasks which are processed for transporting cells were used in this study. The flasks are separated with a partition to reduce the volume of medium for filling the space including the bottom.

As shown in Fig. 1, two flasks filled with 30 ml medium were set vertically to be irradiated with horizontal thermal neutron beam.

RESULTS

Dosimetry: The flasks were irradiated with thermal neutron fluence of $1.9E+12$, $3.7E+12$ and $5.8E+12$ n/cm² which was measured by analysis of activation of gold foil attached to the surface of the bottom of flasks.

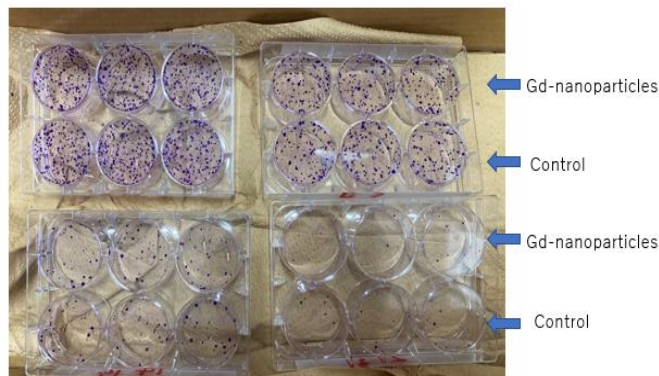


Fig. 1 Picture of setting of two flasks for irradiation

Colony formation assay

Figure 2 shows the picture of stained colonies dispersed into the six wells on the microplates.

Fig. 2 Picture of colony formation assay



No apparent difference of numbers of colonies between the cells irradiated with Gd-nanoparticles and those of control was observed. This experiment was repeated three times. In all the experiments, Gd-nanoparticles did not yield the additive cell killing effect.

DISCUSSION: The feasibility of new irradiation system was confirmed in this study. In this system, no leakage of medium during irradiation occurred since the flasks were sealed tightly with caps. Gd-neutron capture reaction using the positive charged Gd-particles which adhere to the cells during irradiation are supposed to emit auger electrons on the cell membrane. The damage of the cell membrane leads to the apoptosis of the cell.

In this study, no cell killing effect by irradiation derived from Gd-neutron capture reaction was observed. The possibility of this result is that the concentration of Gd (30 ppm) was too low to cause the cell killing effect. Further study is needed to investigate the cell killing effect of auger electrons using this system.

N. Iki¹, M. Komiya¹, T. Nagasaki², and M. Suzuki³

¹Graduate School of Environmental Studies, Tohoku University

²Graduate School of Engineering, Osaka City University

³Institute for Integrated Radiation and Nuclear Science, Kyoto University

INTRODUCTION: Owing to a large thermal neutron capture cross section and total kinetic energy of $^{157}\text{Gd}(n,\text{g})^{158}\text{Gd}$ larger than that of $^{10}\text{B}(n,\text{a})^7\text{Li}$, gadolinium attracts growing attention as an alternative to boron in neutron capture therapy [1]. Because free gadolinium ($\text{Gd}(\text{OH}_2)_9$) has toxicity, a safe carrier of Gd to tumor not to release free Gd is required. We recently found that thiacalix[4]arene-p-tetrasulfonate (TCAS) self-assembled three lanthanide (Ln) cores including Gd to form a sandwich-type complex, Ln_3TCAS_2 (Fig. 1) [2], the characteristic features of which are high kinetic stability, luminescence signal [3], and 1H relaxation arising from the Ln center [4]. Nano-sized particles are frequently used as a drug carrier toward tumor by enhanced permeability and retention (EPR) effect. We have so far studied nano-carriers for Gd_3TCAS_2 such as silica nanoparticle [5] and albumin NP (AlbNP) [6] aiming at Gd-NCT. Here we report the ability of Gd_3TCAS_2 -installed AlbNP to kill cancer cells upon neutron irradiation by comparison with the cases of Gd_3TCAS_2 , Gd-DTPA, and PBS control.



Fig. 1 Structure of Ln_3TCAS_2 complex.

EXPERIMENTS: *Preparation of AlbNP installed with Gd.* The trinuclear complex Gd_3TCAS_2 was prepared as reported elsewhere [2]. The AlbNP was prepared by a method reported [7]. Briefly, BSA solution was added EtOH, followed by addition of glutaraldehyde to obtain the particle containing solution. This was mixed with Gd_3TCAS_2 to afford Gd_3TCAS_2 -installed AlbNP (denoted as Gd_3TCAS_2 -AlbNP(EtOH)).

Cell experiment 1. MCF-7 cells were seeded in a 6-well plate at a cell concentration of 1.0×10^5 cells/mL and incubated for 24 h. After supernatant was removed, RPMI medium and solution containing Gd in a form of 1) Gd_3TCAS_2 -AlbNP(EtOH), 2) free Gd_3TCAS_2 , 3) Gd-DTPA, and 4) PBS (as control) were added to each well and incubated for 24 hr. The concentration of Gd in the medium to incubate MCF-7 was set to be $25 \mu\text{M}$ for 1–3). After washing with PBS, the cells were detached from the well and transferred to tubes to be irradiated with thermal neutron for 20 min.

Cell experiment 2. MCF-7 cells were mixed with RPMI medium containing Gd_3TCAS_2 -AlbNP(EtOH), the absolute amount of which was adjusted to the same value of one delivered into the cells in the experiment 1. Afterward, the cell was irradiated with thermal neutron for 20 min.

Assay. To the wells containing 2 mL of RPMI medium in 6-well plates, irradiated cells were seeded at the concentration of 1,000 cells/well. After incubation for 14 days, the colony was stained with crystalviolet.

RESULTS:

In Experiment 1, the absolute amount of Gd into 2.0×10^4 cells was estimated to be 1) 9.8, 2) 73.6, and 3) 2.6 pmol by using ICP-AES. The colony formation units (CFU) normalized with one for no irradiation is shown in Fig. 2a. As can be seen, there seems appreciable difference between CFU for 1) and others 2–4). Thus, despite the fact that the delivery efficiency of Gd_3TCAS_2 -installed AlbNP to the cells was lower than that of free Gd_3TCAS_2 , Gd_3TCAS_2 -installed AlbNP showed higher NCT effect. In Experiment 2, neutron was irradiated to a sample containing the same amount of Gd in the medium but outside the cells. The CFU showed that the NCT effect is lower than that attained by Experiment 1 (Fig. 2b). This unambiguously shows that internalization of Gd_3TCAS_2 -installed AlbNP in the cells is essential to show the NCT effect.

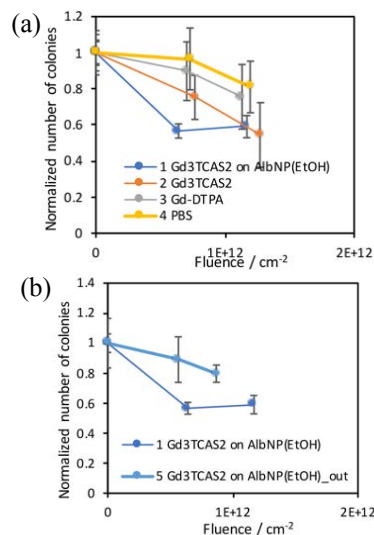


Fig. 2 Dependence of neutron fluence on the colony formation rate ($n = 3$). a) Comparison among the Gd-agents 1–3) internalized in MCF-7 cells. b) Comparison between internalized and outside Gd_3TCAS_2 -installed AlbNP.

REFERENCES:

- [1] M. Takagaki *et al.*, Future Application of Boron and Gadolinium Neutron Capture Therapy, in *Boron Science*, Ed N. S. Hosmane (CRC Press) (2012) 243.
- [2] N. Iki *et al.*, *Eur. J. Inorg. Chem.*, **2016** (2016) 5020-5027.
- [3] R. Karashimada *et al.*, *Chem. Commun.* **52** (2016) 3139-3142.
- [4] N. Iki *et al.*, *Inorg. Chem.* **55** (2016) 4000-4005.
- [5] T. Yamatoya *et al.*, 31P11-8, p. 105, *KURNS Progress Report 2019*.
- [6] N. Iki *et al.*, R2P5-2, *KURNS Progress Report 2020*.
- [7] C. Weber, C. Coester, J. Kreuter, K. Langer, *Int. J. Pharm.*, 194 (2000) 91–102.

PR2-3 Gadolinium neutron capture therapy as a new treatment for head and neck cancer: tumor-killing effects on a masseter muscle invasion model

T. Andoh¹, T. Fujimoto², M. Suzuki³, T. Takata⁴, Y. Sakurai⁴ and H. Ichikawa¹.

¹Faculty of Pharmaceutical Sciences, Kobe Gakuin University, Japan.

²Department of Orthopaedic Surgery, Hyogo Cancer Center, Japan.

³Particle Radiation Oncology Research Center, Institute for Integrated Radiation and Nuclear Science, Kyoto University, Japan.

⁴Division of Radiation Life Science, Institute for Integrated Radiation and Nuclear Science, Kyoto University, Japan

INTRODUCTION: Neutron-capture therapy using nonradioactive ¹⁵⁷Gd (Gd-NCT) is currently under development as a potential radiation therapy option for cancer. Gd-NCT with ¹⁵⁷Gd has several potential advantages over boron (¹⁰B) neutron capture therapy (BNCT). The deep tissue penetration (100 μm) of γ-rays from the ¹⁵⁷Gd (n, γ) ¹⁵⁸Gd reaction is expected to provide tumor-killing efficacy within bulky tumors such as head and neck cancers. Furthermore, oral mucositis caused by BNCT using p-boronophenylalanine could be a potential dose-limiting consideration for head and neck tumors [1]. We have previously developed gadolinium-loaded chitosan nanoparticles (Gd-nanoCPs) for controlled Gd delivery in Gd-NCT. These nanoparticles were composed of Gd-diethylenetriaminepentaacetic acid (Gd-DTPA, an MRI contrast agent), and chitosan (a naturally abundant biodegradable polysaccharide with good biocompatibility and bioadhesive characteristics). In the present study, we investigate the *in vivo* tumor-killing effects after NCT with intra-tumoral injected nanoparticulate formulations on a masseter muscle invasion model close to the oral mucosa.

EXPERIMENTS: Gd-nanoCP was prepared by using chitosan with molecular weights of 10 k and Gd-DTPA through the previously developed w/o emulsion-droplet coalescence technique [2]. Mean particle size and zeta potential of the resultant Gd-nanoCPs were measured by Zetasizer® (Malvern Instruments Ltd, UK) in water at 25°C. Gd content in Gd-nanoCPs was determined by inductively coupled plasma atomic emission spectrometry (ICP-AES, SPS3100, Hitachi High-Tech Science Corporation, Japan) followed by incineration of each sample. In the NCT trial, male 5-week-old C3H/HeN mice were used. SCC-VII (1 × 10⁶ cells/mouse) were injected into the left masseter muscle [3]. The mice were divided into NCT group and HOT control group. Before injection, Gd-nanoCPs were concentrated to 6000 μg Gd/mL by centrifugation. Gd-nanoCPs incorporating 1.2 mg of natural Gd were injected intratumorally twice (2.4 mg Gd/kg) to the mice. The tumors were exposed to thermal

neutron irradiation at the Institute for Integrated Radiation and Nuclear Science, Kyoto University. For determining the tumor volume, two bisecting diameters of the tumor were measured with a slide caliper and calculated with the longest and shortest length of the tumor in millimeters (mm). The tumor-growth suppressing effect was assessed by the ratio of tumor volume before and after neutron irradiation.

RESULTS: Mean particle diameter, Gd content, and zeta potential of the Gd-nanoCP were 178 nm, 19%, and +24 mV, respectively. In the NCT trial, thermal neutron irradiation was applied to mouse tumors 8 h after the last administration. Remarkable tumor growth was observed in the HOT control group, whereas the NCT group showed tumor growth suppression (Fig. 1). Decreases in tumor volume were similar to those observed in our previous study using a transplanted tumor-bearing mouse model [4]. The tumor mass was selectively suppressed without damage to the normal surrounding mucosa because Gd-nanoCPs could not penetrate the surrounding tissue. These results indicate that Gd-nanoCPs displayed potent tumor tissue affinity after intratumoral injection, reduced tumor tissue volume, and did not damage the mucosa. GdNCT using Gd-nanoCPs could thus be a promising therapeutic option to shrink tumors occurring close to the mucosa.

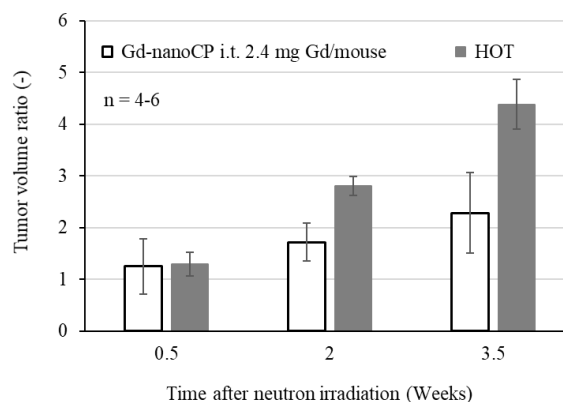


Fig. 1. Tumor volumes after thermal neutron beam irradiation of NCT and HOT control groups.

REFERENCES:

- [1] J. A. Coderre *et al.*, *Radiat. Res.*, 152, 113-118 (1999).
- [2] H. Tokumitsu *et al.*, *Pharm. Res.*, 16, 1830-1835 (1999).
- [3] T. Nomura *et al.*, 5th Asian Conference on Oral and Maxillofacial Surgery: 111-115 (2002).
- [4] H. Ichikawa *et al.*, *Appl. Radiat. Isot.*, 88, 109-113 (2014).

PR2-4 Preparation of drugs targeting cell nucleus with Hoechst unit

K. Tanabe¹, M. Suzuki², T. Nishihara¹ and M. Mizutani¹

¹*Department of Chemistry and Biological Science, College of Science and Engineering, Aoyama Gakuin University*

²*Institute for Integrated Radiation and Nuclear Science, Kyoto University*

INTRODUCTION:

In recent years, Boron Neutron Capture Therapy (BNCT) has been attracting attention as the fifth cancer treatment method next to surgery, chemotherapy, radiation, and immunotherapy. BNCT is a treatment that selectively destroys cancer cells by accumulating ¹⁰B compounds, which cause nuclear reaction with neutrons, on the cancer cells and irradiating them with neutrons. However, at present, there are only two types of boron drugs available for BNCT: BPA and BSH. Therefore, it is an urgent issue to develop drugs that accumulate in the tumor tissue with high selectivity and show effective therapeutic effects. In this study, we attempted to construct the molecular system to take the complex into cell nucleus by using Hoechst molecules. Since the Hoechst group has high DNA-binding function and accumulates in the cell nucleus,¹ it was expected that this molecule act as a courier molecule to deliver drugs into the nucleus. We expected that by collecting the drug in the nucleus, we could achieve an effective DNA-targeted attack in tumor cells. We attempted to modify the conventional drug, BPA, for BNCT and the gadolinium complexes. The synthesized BPA-Hoechst was subjected to cellular experiments, and we confirmed that BPA-Hoechst exhibited effective cytotoxic effects under irradiation conditions of thermal neutrons.

EXPERIMENTS:

Huisgen cycloaddition reaction between A-Hoechst and BPA to form BPA-Hoechst. A-Hoechst (1.0 mg, 2.2 μmol) was added to the solution of BPA with azide unit (0.5 mg, 2.1 μmol) in DMF-H₂O. Then, CuSO₄, TBTA and sodium ascorbate were added to the solution. The resulting mixture was stirred for 20 h at ambient temperature. After the reaction, the mixture was extracted with ethyl acetate. The organic layer was washed with brine, dried over MgSO₄, filtered and concentrated in vacuo. The crude product was purified by silica gel column chromatography to give BPA derivative with Hoechst unit (BPA-Hoechst).

Cellular experiments using BPA-Hoechst. A549 cells were seeded in 96 well plates at a density of 4.5 × 10³ cells per well in DMEM and allowed to grow at 37 °C for 24 hours. The cells were incubated with 0, 10, 100 μM BPA-Hoechst in DMEM (DMSO 1%) for 3 h. After incubation, the cells were irradiated with neutron for 45 min at KUR (1 MW). Then, the cell was cultured for 2 days in the fresh DMEM at 37 °C. Then, cell viability assay was performed Cell Counting Kit-8 (Dojindo) and

microplate reader (Absorbance at 450 nm).

RESULTS:

Preparation of BPA-Hoechst was achieved as shown in Figure 1A. Initially, we conducted the Huisgen reaction of A-Hoechst and BPA derivative bearing azide group. The reaction was proceeded at ambient temperature in the presence of catalytic CuSO₄ and ascorbic acid. Efficiently, the triazole ring formation occurred, and BPA with Hoechst unit (BPA-Hoechst) was formed. On the other hand, the modification of gadolinium complexes is still ongoing. Using cyclic amine **3** as starting material, two amino groups were protected with Boc groups and the remaining amino groups were alkylated. The removal of the protecting groups and the Huisgen reaction are currently under investigation.

For understanding of the biological activity of BPA-Hoechst, we measured its cytotoxic effect against A549 cells, which were exposed to neutron (1 MW) in the presence of aqueous solution of BPA-Hoechst and then incubated at 37 °C. Cell survival was determined by WST assay. Figure 1C compares cell survivals in the presence and absence of BPA-Hoechst after irradiation. The cytotoxic effect of radiation was significantly enhanced when the cells were irradiated in the presence of BPA-uridine. It is likely that BPA is effectively activated in the cell nucleus and thereby exhibits high cytotoxicity against tumor cells upon irradiation. In a separate experiment, we evaluated the cytotoxic effect of BPA in the presence of fluctose that complexed with BPA to dissolve into water. The cytotoxic assay revealed that BPA-fluctose conjugate showed similar cytotoxic effect upon irradiation. Thus, it is reasonable to conclude that BPA-Hoechst conjugate is a potent candidate agents for BNCT. In vivo experiments to evaluate the function of BPA-uridine is in progress.

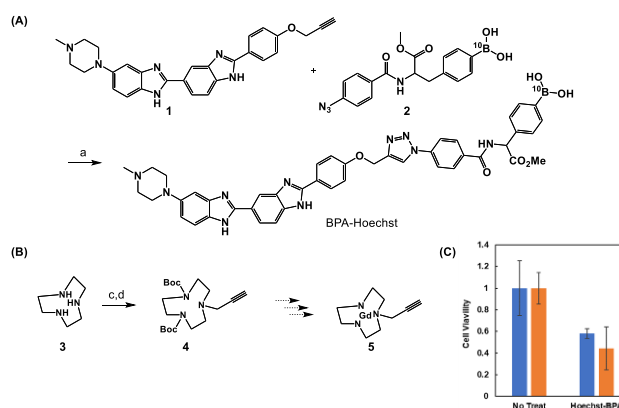


Figure 1. (A,B) Synthesis of BPA-Hoechst (A) and ligand of gadolinium ion (B). (C) Cytotoxic effect of BPA-Hoechst conjugate upon thermal neutron irradiation (1 MW, 45 min).

REFERENCES:

[1] K. Tanabe *et al.*, *ChemBioChem*. **19** (2018), 956–962.

PR2-5 Development of Gadolinium-loaded mesoporous silica-based nanoparticles and application to cancer radiotherapy

F. Tamanoi¹, K. Matsumoto¹ and M. Suzuki²

¹*Institute for Advanced Study
Institute for Integrated Cell-Materials Sciences, Kyoto
University*

²*Institute for Integrated Radiation and Nuclear Science,
Kyoto University*

INTRODUCTION: Boron phenylalanine (BPA) has been developed as useful boron compound which is available for Boron neutron capture therapy (BNCT) therapy. We have developed two types of mesoporous silica-based nanoparticles that are loaded with BPA and found that the BPA-loaded nanoparticles have ability of improving the BNCT efficacy [1]. On the other hand, we have recently developed novel type of biodegradable periodic mesoporous organosilica (BPMO) which was loaded Gadolinium instead of BPA (Gd-BPMO). We assumed this Gd-BPMO could be applied to Gadolinium neutron capture therapy (GdNCT). GdNCT has been devised as a less invasive cancer therapy as well as BNCT. Gd-BPMO has a large surface area where Gd can be attached for GdNCT application. We preliminary evaluated the GdNCT efficacy with Gd-BPMO in chicken chorioallantoic membrane (CAM) model that was transplanted ovarian cancer cells.

EXPERIMENTS:

BPMO was synthesized by sol-gel synthesis of two precursors, bis[3-(triethoxysilyl) propyl] tetrasulfide and 1, 2-bis(triethoxysilyl) ethane. This resulted in the incorporation of tetrasulfide bonds into the framework of the nanoparticles. BPMO was then modified with amino group. Gadolinium diethylenetriamine penta-acetic acid (DTPA) was then mixed with amine-modified BPMO to couple Gd on BPMO by electrostatic interaction between positively charged NH_3^+ and negatively charged COO^- of DTPA. The synthesized nanoparticles were characterized by using SEM and EDX-TEM. The amount of Gd attached on the nanoparticles was examined by ICP-AES, and Gd content was determined.

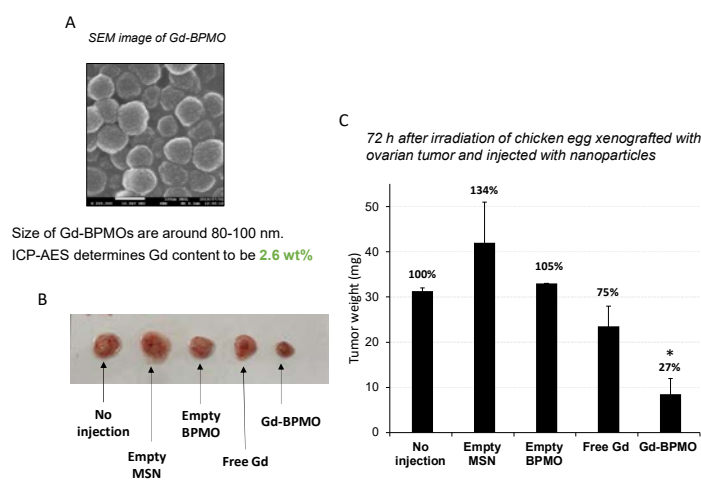
CAM model was established by transplanting human ovarian cancer cells OVAR8 on the CAM in fertilized chicken egg. After intravenously injection of Gd-BPMO, the eggs were placed at the center of emerging neutron beam. Eggs were irradiated with thermal neutron for 1 h at an operating power of 1MW. After the irradiation, eggs were incubated for 3 days at 37°C with 65% humidity. Tumors were then cut out to evaluate the tumor size.

RESULTS: As seen in Fig. A, Gd-BPMO synthesized had approximately 80-100 nm of diameter and homogeneous shapes examined by SEM microscopy (TEM image is not shown). After coupling of Gd to BPMO, we detected the amount of Gd that was coupled with BPMO by ICP. The 2.6% of Gd were coupled with BPMO.

As seen in Fig. B and C, Investigation of tumor growth inhibition effect of Gd-BPMO was preliminary resulted that the tumor growth was significantly inhibited when Gd-BPMO was injected compared to no injection or empty BPMO (27% tumor growth inhibition effect compared to No injection). We have been carrying out further experiments about the characterization and biodistribution of Gd-BPMO, and their tumor growth inhibition efficacy by neutron irradiation is currently ongoing.

REFERENCES:

[1] F. Tamanoi *et al.*, *Int. J. Mol. Sci.* **22**, 2251 (2021).



PR2-6 Pathological Findings of Tumor Growth Suppression of GdNCT with Intra-Tumoral Injection of Gadolinium-Polyplex in Pancreatic Cancer Model *in vivo*

Hironobu Yanagie^{1,2,3}, Yoshiteru Yanagie⁴, Xuan Hou⁵, Masashi Yanagawa⁶, Yuriko Sakurai^{1,2,3}, Kikue Mouri³, Yasuyuki Morishita⁷, Takehisa Matsukawa⁸, Ayano Kubota⁸, Minoru Suzuki⁹, Yoshinori Sakurai⁹, Hiroki Tanaka⁹, Takeshi Nagasaki¹⁰, Kazuhito Yokoyama⁸, Takefumi Hirata¹¹, Masayuki Nashimoto³, Jun Nakajima^{2,12}, Minoru Ono^{2,13}, Takumichi Sugihara³, and Hiroyuki Takahashi^{1,2,5}

¹Institute of Engineering Innovation, School of Engineering, Univ of Tokyo, ²Cooperative Unit of Medicine & Engineering, Univ of Tokyo Hospital, ³Niigata Univ of Pharmacy & Applied Life Sciences, ⁴Faculty of Medicine, Teikyo University, ⁵Dept of Bioengineering, School of Engineering, Univ of Tokyo, ⁶Obihiro Univ of Agriculture and Veterinary Medicine, ⁷Dept of Human & Molecular Pathology, Graduate School of Medicine, The University of Tokyo, ⁸Department of Hygiene, Faculty of Medicine, Juntendo University, ⁹Kyoto Univ Institute for Integrated Radiation & Nuclear Science, ¹⁰Osaka City University Graduate School of Engineering, ¹¹Geochemical Research Center, School of Science, The University of Tokyo, ¹²Dept. of Pulmonary Surgery, The University of Tokyo Hospital, ¹³Dept. of Cardiac Surgery, The University of Tokyo Hospital, JAPAN

INTRODUCTION:

Gadolinium atoms react thermal neutron and offers cytotoxic effect by 1 μ m-range high LET Auger electron, and long-range gamma rays on Gadolinium-neutron capture therapy(GdNCT) [1, 2, 3]. For effective GdNCT, it is necessary to accumulate Gadolinium atoms into the tumor tissues selectively, so we prepared the gadolinium / hyaluronic acid / protamine-mixed with cationic liposome (¹⁵⁷Gd-plex) as neutron capture agent. In this study, we evaluated the mechanism for cancer cell cytotoxicity by GdNCT performing with HE dyeing & Apoptotic analysis using tumor tissues after GdNCT *in vivo*.

EXPERIMENTS:

We prepared nanoparticles mixed with 1.5mL of Gadolinium compound “Gadovist” (MW: 604.71), 0.2mL of a solution of 10mg/mL-hyaluronic acid sodium, and 0.1mL of 20mg/mL of protamine incubating at room temperature for 30min. Then, these mixing solutions were poured into Coatsome EL-C. Human pancreatic cancer AsPC-1 cell was used for the *in vivo* anti-tumor effect evaluation. We prepared AsPC-1(5x10⁵) model by transplanting to right lower leg. Twelve hours after intra-tumoral injection of 0.1mL of ¹⁵⁷Gd-plex, we performed thermal neutron irradiation at Institute for Integrated Radiation and Nuclear Science, Kyoto University (average neutron fluence of 3.0 × 10¹² n/cm²). The change in tumor growth and survival rate of the mice reflected the anti-tumor effect of ¹⁵⁷Gd-plex. We obtained a tumor and various organs (heart, the lungs, liver, kidney, spleen) one month after

irradiation, and performed a formalin fixation and the freeze fixation using the OCT compound and examined the pathological cell cytotoxic effects. We performed apoptotic analysis using the TUNEL dyeing to analyze the mechanism of the antitumor effect (Apoptosis in situ detection Kit Wako, 293-71501, Osaka, Japan) [4].

RESULTS:

The nuclear dysplasia of the cancer cell was strong in the non-irradiation group, but the degeneration was not seen. The degeneration was not seen in the groups with only irradiation, but the cancer cell hyalinization and degeneration were seen in the ¹⁵⁷Gd solution and ¹⁵⁷Gd-plex treated groups(Figure 1). The apoptotic changes of the cancer cells were not seen in the non-irradiation group. There were few apoptotic changes in the control group with irradiation, but the apoptotic changes were dominant in the GdNCT treated group with ¹⁵⁷Gd-plex (Figure 2).

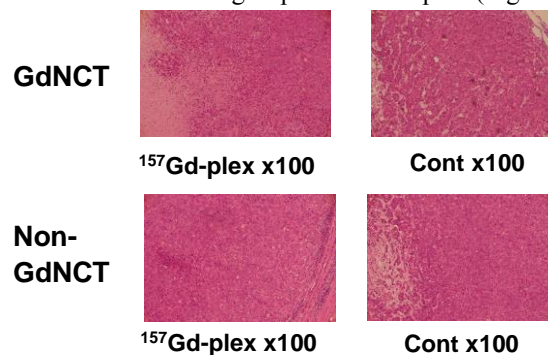


Figure 1. HE staining of tumor growth suppression by ¹⁵⁷Gd-plex on GdNCT

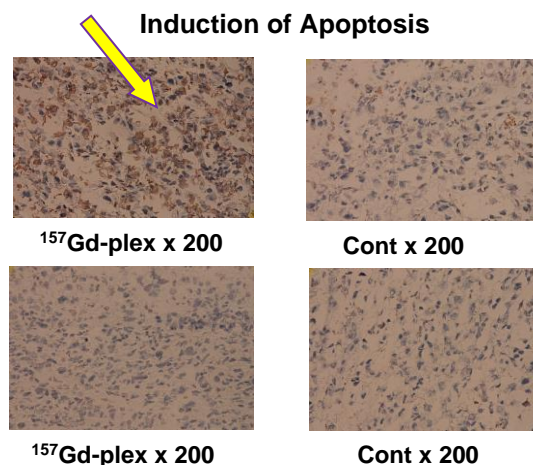


Figure 2. TUNEL staining of tumor growth suppression by ¹⁵⁷Gd-plex on GdNCT

REFERENCES:

- [1] Dewi N *et al.*, Biomed & Pharmacother (2013) 67:451-7.
- [2] Dewi N *et al.*, J Can.Res.Clin.Oncol. (2016) 142(4):767-75.
- [3] Mi P, *et al.* : J Cont. Release (2014) 174:63-71.
- [4] Yanagie H, *et al.* : Br J Radiol (2017), PMID: 28406315 DOI: 10.1259/bjr.20170004.

PR2-7 Development of gadolinium-containing inorganic nanoparticles with polyglycerol coating for gadolinium neutron capture therapy of cancer

Li Zhao¹, Heon Gyu Kang², Masahiro Nishikawa², Minoru Suzuki³ and Komatsu Naoki²

¹ School for Radiological and Interdisciplinary Sciences (RAD-X) and Collaborative Innovation Center of Radiation Medicine of Jiangsu Higher Education Institutions, Soochow University, P. R. China

² Graduate School of Human and Environmental Studies, Kyoto University

³ Institute for Integrated Radiation and Nuclear Science, Kyoto University

Neutron capture therapy (NCT) that employs boron or gadolinium isotopes as sensitizers holds great promise for cancer treatment. ¹⁵⁷Gd is the most effective isotope in terms of thermal neutron capture, holding a large cross-section of 254000 barn. The Gd neutron capture reaction, ¹⁵⁷Gd(n, γ)¹⁵⁸Gd, is capable of generating high linear energy transfer (LET) Auger-Coster-Kronig (ACK) electrons as well as low LET γ photons to damage cancer cells. Another advantage of GdNCT is that Gd(III) is an efficient contrast agent for magnetic resonance imaging (MRI), which enables noninvasive detection of Gd content in the tumor and can guide GdNCT.^[1] Unfortunately, because of the lack of appropriate tumor-selective Gd agents, the GdNCT concept has thus far not been clinically tested.

Gd-containing inorganic nanoparticles (Gd-NP) carrying a large number of Gd atoms in a single particle are considered as a potential Gd agent for GdNCT. We have recently prepared a kind of Gd-NP, which were further grafted with polyglycerol (PG) to increase the colloidal stability and dispersibility in physiological

media.^[2] The resulting Gd-NP-PG nanoparticles were characterized and investigated as a Gd agent for GdNCT of murine CT26 colon cancer. The results showed that Gd-NP-PG nanoparticles can disperse in phosphate buffer saline (PBS) at a fairly high concentration of > 10 mg Gd/mL, showing no aggregation and precipitation over 3 months. Upon intravenous administration, Gd-NP-PG nanoparticles circulated in the mouse blood for a relatively long time, and accumulated in CT26 tumor through enhanced permeability and re-tention (EPR) effect, reaching a high Gd concentration of about 150 μ g/g at 24 h postinjection. As expected, Gd-NP-PG nanoparticles-mediated GdNCT (thermal neutrons: 1 MW for 50 min) significantly suppressed the growth of CT26 tumor as compared to the control groups, suggesting that the nanoparticles can be a potential Gd agent.

We are going to study the MRI of tumor using Gd-NP-PG nanoparticles as a contrast agent, with an aim to realize MRI-guided GdNCT (Figure 1), which can not only help optimize the GdNCT plan, but also enhance the accuracy and efficacy of GdNCT. In addition, the therapeutic mechanism of Gd-NP-PG nanoparticles-mediated GdNCT will also be explored.

Reference:

[1] P. Mi, N. Dewi, H. Yanagie, D. Kokuryo, M. Suzuki, Y. Sakurai, Y. Li, I. Aoki, K. Ono, H. Takahashi, H. Cabral, N. Nishiyama, K. Kataoka, *ACS Nano*, 9 (6), 5913-5921 (2015).

[2] L. Zhao, T. Chano, S. Morikawa, Y. Saito, A. Shiino, S. Shimizu, T. Maeda, T. Irie, S. Aonuma, H. Okabe, T. Kimura, T. Inubushi, N. Komatsu, *Adv. Funct. Mater.*, 22 (24), 5107- 5117 (2012).

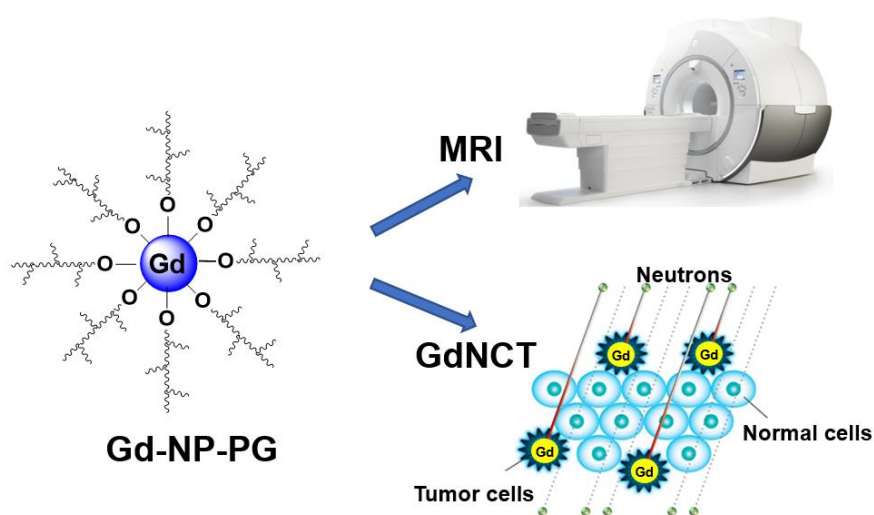


Figure 1. MRI-guided GdNCT using Gd-NP-PG as a Gd agent.

PR2-8 Study about neutron capture therapy using polymeric drug delivery systems chelating Gd

Y. Miura¹, T. Nomoto¹, K. Konarita¹, D. Tokura¹, Y. Sakurai², M. Suzuki², N. Nishiyama¹

¹*Institute of Innovative Research, Tokyo Institute of Technology*

²*Institute for Integrated Radiation and Nuclear Science, Kyoto University*

INTRODUCTION: ¹⁵⁷Gd has the high neutron capture cross section and can generate Auger electrons and γ -rays upon thermal neutron irradiation. Thus, Gd has been expected to be a promising atom in neutron capture therapy. We previously synthesized the inorganic-organic hybrid nanoparticle encapsulating Gd and demonstrated strong antitumor efficiency in subcutaneous tumor models [1]. However, the tumor accumulation level of Gd and ultimate antitumor efficiency was not always well correlated [2]. To improve the tumor accumulation and penetration performance of drug carriers, we designed and synthesized new class of Gd-DOTA introduced polymers (polymer-drug) by using controlled polymerization techniques and selective polymer modifications. According to *in vivo* biodistribution study, obtained polymer-drug enable selective Gd delivery against targeted tumors. Thus, in this year, we tried to confirm the Gd-related therapeutic performance of the polymer-drug through neutron irradiation.

EXPERIMENTS: BALB/c mice bearing subcutaneous CT26 tumors were prepared by subcutaneous injection of the cell suspension. The polymer drug or the low-molecular drug (Gd-DOTA) as a control were intravenously injected to the mouse, and the thermal neutrons were irradiated to the tumor using KUR at 5 MW for 10 min. The tumor volume (V) was calculated using the following equation:

$$V = 1/2 \times a \times b^2$$

where a and b denote major and minor axes of a tumor, respectively.

RESULTS: As shown in Fig. 1, the low-molecular drug and polymer drug exhibited antitumor efficacy, suggesting the successful neutron capture therapy and the appropriate irradiation condition. However, the two samples did not exhibit a significant difference for tumor growth inhibitory effect, suggesting that the dosage of polymeric drug and/or administration schedule were insufficient. In the next fiscal year, we will improve the therapeutic efficacy by modification of experimental designs and polymer structure.

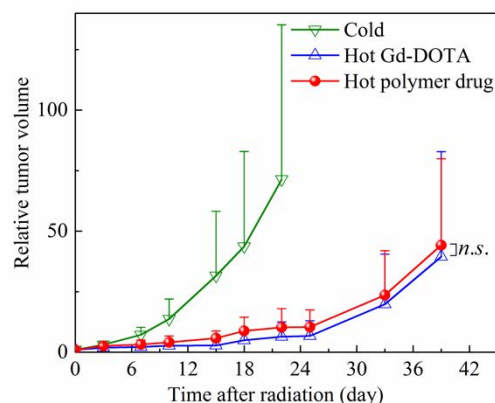


Fig. 1. Antitumor efficacy to subcutaneous CT26 tumor models.

REFERENCES:

- [1] P. Mi *et al.*, ACS Nano, **9** (2015) 5913-5921.
- [2] N. Dewi *et al.*, J. Cancer Res. Clin. Oncol., **142** (2016) 767-775.

PR2-9 Neutron irradiation after administration of Gd-EDTMP to a mouse model of mammary tumor bone metastasis: Effects and distribution of Gd formulation as a novel neutron capture therapy agent

T. Matsukawa¹, M. Suzuki², A. Kubota¹, A. Shinohara^{1,3}, K. Yokoyama^{1,4}

¹ Juntendo University Faculty of Medicine

² Institute for Integrated Radiation and Nuclear Science, Kyoto University

³ Research Institute for Cultural Studies, Seisen University

⁴ International University of Health and Welfare

INTRODUCTION: To develop the next generation of cancer radiation therapy, we evaluated the tissue distribution of Gd tetra (methylene phosphonic acid) chelate (Gd-EDTMP), a gadolinium-containing neutron capture therapy preparation, and the effects of thermal neutron irradiation on animal tumor models. Previous our experiments with a single intraperitoneal administration of Gd-EDTMP in young mice suggested that Gd-EDTMP has a high dose distribution in parts of the femur, especially in bones with epiphyseal line. In this study, mice model of carcinogenesis was created in elderly mice with a closed epiphyseal line to investigate the basis for neutron capture therapy. After neutron irradiation of the mice, the distribution of ¹⁵⁷Gd in and around the bone was imaged using laser ablation inductively coupled plasma mass spectrometry (LA-ICP-MS).

EXPERIMENTS: Gd-EDTMP solution was prepared from gadolinium chloride and EDTMP. BALB/cAJcl female mice (12 weeks old) were acclimated for 1 week and then transplanted Luciferase stably expressing cell line 4T1; mouse mammary tumor cell line JCRB1447 into the right tibia. After acclimation for another week and confirmation of tumor formation, mice were divided into three groups: (n=3 or 4): Gd-EDTMP treated and neutron-irradiated (Gd+/Nu+), Gd-EDTMP treated and not neutron-irradiated (Gd+/Nu-), and phosphate-buffered saline treated and neutron-irradiated (Gd-/Nu+). Gd+/Nu+ and Gd+/Nu- mice were administered a single intraperitoneal dose of 20 mg/kg body weight of Gd-EDTMP (1 mg-Gd/ml PBS) (n=3). Gd-/Nu+ mice (n=4) were administered only PBS equivalent to the same dose as the previous two groups. Twenty-four hours after Gd-EDTMP or PBS administration, Gd+/Nu+ and Gd-/Nu+ mice the lower limbs were irradiated with thermal neutrons for 15 minutes at the Kyoto University Research Reactor (KUR, 5MW). The irradiate fluence of thermal neutron was $3.6 \times 10^{12} \text{ cm}^{-2}$. After irradiation, mice were allowed free access to food and water until 14 days, and their general condition was monitored. After euthanasia, the right thighs and shins were harvested and weighed for tumor weight. The right thighs and shins were thinned to 5 μm by the Kawamoto method, a non-decalcified frozen section preparation method, and the distribution of ¹⁵⁷Gd was imaged by LA-ICP-MS (LA: NWR213, ICP-MS: Agilent 8800) by

the methods previously mentioned [1]. The tumor status was also evaluated by micrographs of Hematoxylin Eosin (H.E.) stained sections of the lower limbs.

RESULTS and DISCUSSION: syu

Comparing the weight of the right legs, including the tumor (Fig. 1), the Gd+/Nu+ group ($822 \pm 27 \text{ mg}$) tended to be lower than the Gd+/Nu- ($1255 \pm 390 \text{ mg}$) or Gd-/Nu+ ($1147 \pm 173 \text{ mg}$) groups. This may suggest that tumor growth in the Gd+/Nu+ mice was suppressed. LA-ICP-MS Gd imaging of the legs of Gd +/Nu + and Gd +/Nu - showed extremely high Gd signal intensity in bone. In 4T1 tumor areas, Gd signal intensity was higher than in surrounding muscle tissue (Fig. 1). It was suggested that 4T1 cells may uptake Gd-EDTMP.

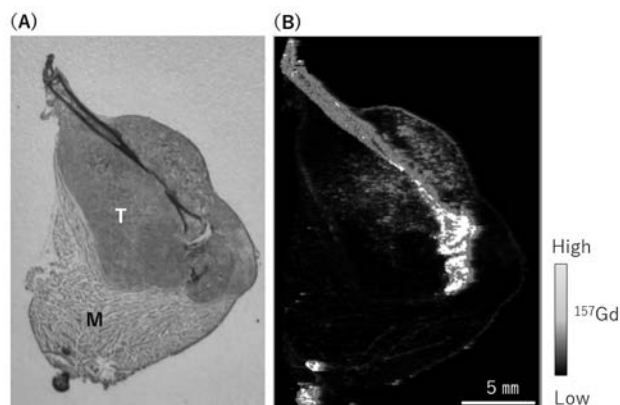


Fig. 1. Leg section of a 4T1 mammary tumor cell transplanted mouse 14 days after treatment with Gd tetra (methylene phosphonic acid) chelate (Gd-EDTMP) (20 mg/kg). (A) Hematoxylin Eosin stained microscopic image: T indicating tumor area and M indicating muscle area. (B) Imaging of ¹⁵⁷Gd distribution by laser ablation inductively coupled plasma mass spectrometry (LA-ICP-MS). In the figure (B), white areas indicate areas of high ¹⁵⁷Gd signal intensity.

REFERENCES:

[1] A. Kubota *et al.*, Juntendo Medical Journal., **65** (2019): 461-467.

I-1. PROJECT RESEARCHES

Project 3

PR3 Enhancement of research methods for material irradiation and defect analysis

A. Kinomura

*Institute for Integrated Radiation and Nuclear Science,
Kyoto University*

OBJECTIVES: Irradiation facilities of high-energy particles for neutrons (Material Controlled irradiation Facility), ions (e.g., Heavy ion irradiation facility) and electrons (Temperature-controlled irradiation facilities of KUR-LINAC) have been extensively developed at the Institute for Integrated Radiation and Nuclear Science. The developed facilities have been in operation and opened for joint research projects. One of the objectives of this project is to further improve or optimize irradiation facilities for advanced irradiation experiments.

As characterization techniques for irradiated materials, a slow positron-beam system and a focused ion beam system have been developed and introduced, respectively, in addition to previous characterization facilities such as an electron microscope, an electron-spin-resonance spectrometer, a bulk positron annihilation spectrometer and a thermal desorption spectrometer. Another objective is to introduce new experimental methods or reconsider analytical methods of previously used characterization techniques.

Based on these two objectives, we expect the enhancement of previous studies and the attraction of new users for the joint research program.

The allotted research subjects (ARS) and co-researchers are listed below. The titles of research subjects are taken from the individual reports.

ARS-1:

Study to improve transport and measurement performance of a slow positron beamline (A. Kinomura et al.)

ARS-2:

Doping effect of Cr, Mo, Ta, and Re on defect formation after electron irradiation (T. Toyama et al.)

ARS-3:

Hydrogen Thermal Desorption Analysis in Electron-irradiated F82H (K. Sato et al.)

ARS-4:

Gamma-ray induced photo emission from ZnO single crystal wafer: Comparison with GaN (T. Nakamura et al.)

ARS-5:

Irradiation technique for study on corrosion resistance of fusion divertor materials to liquid metal during irradiation (M. Akiyoshi et al.)

ARS-6:

Investigation of free volume in diamond like carbon films deposited by various methods (K. Kanda et al.)

ARS-7

Positron annihilation spectroscopy on diamond-like carbon films (S. Nakao et al.)

RESULTS:

In ARS-1, a brightness enhancement system have been

developed for the KUR slow positron beamline as well as measurement systems for positron annihilation lifetime spectroscopy. In this year, positron annihilation lifetime measurements were successfully demonstrated with a brightness enhanced beam in the KUR slow positron beam system. A spot size evaluated by a knife edge method using sample edges was 2.3 mm (FWHM).

In ARS-2, electron irradiation to pure W, W-5%Re (in weight %), W-0.3%Cr, W-1.5%Mo, and W-5%Ta was performed at LINAC at KUR at 8 MeV. After electron irradiation, the average lifetime increased, showing positron trapping to vacancy type defects. Average lifetimes for W-0.3%Cr and W-5%Re remained relatively short compared with the W-1.5%Mo and W-5%Ta alloys, suggesting that the formation of irradiation induced defects was suppressed.

In ARS-3, the TDA of electron-irradiated F82H was conducted after electrolysis hydrogen charging. The hydrogen atom trapping sites in materials were investigated using simulation program for TDA. The TDA curve of electron-irradiated F82H showed a main peak around 320 K and a shoulder peak from 370 K to 420 K. The simulation curve corresponds well to the experimental one except for the shoulder around 420 K.

In ARS-4, although ZnO and GaN have the wurtzite structure and direct bandgap with almost the same bandgap values, peak intensities of the gamma-ray induced photo emission were different. It is considered to be due to the difference in the light emitting mechanism between YL of GaN and GL of ZnO.

In ARS-5, the planned experiments were not performed this year for the influence of infectious disease countermeasures.

In ARS-6, S parameters showed good correlation with film density and hardness. As the density and hardness decrease, the S parameter increases, since the increase in S parameter is considered to mean the increase in free volume. Positron lifetimes increased with decreasing of the density and hardness as well. On the other hand, it was found that the S parameter and positron lifetime have no direct correlation to the hydrogen content estimated from ERDA or NEXAFS measurements.

In ARS-7, Si-DLC and Si-PLC films were deposited on Si substrates by a bipolar-type plasma-based ion implantation and deposition (PBII) system, followed by annealing at 400 °C and 800 °C in vacuum to investigate the thermal stability of the films. The results of positron annihilation spectroscopy suggested that Si incorporation may promote to increase porosity in the films and prevent structural changes due to H release by ion bombardment or thermal annealing at high temperature.

SUMMARY: Several new irradiation (electron-beam and gamma-rays) and analytical (slow-beam and conventional positron measurements) techniques for various materials have been developed and improved for the objectives of this project. Such studies may enhance developments of new techniques and materials research on irradiation effects.

PR3-1 Study to improve transport and measurement performance of a slow positron beamline

A. Kinomura, N. Oshima¹, A. Uedono² and A. Yabuuchi

*Institute for Integrated Radiation and Nuclear Science,
Kyoto University*

¹*National Institute of Advanced Industrial Science and
Technology (AIST)*

²*University of Tsukuba*

INTRODUCTION: Positron annihilation spectroscopy is an important analytical method to detect vacancy-type defects and vacant spaces of materials. Energy-variable mono-energetic positron beams (slow positron beams) are essential to perform depth-dependent positron annihilation spectroscopy of surface layers such as ion-implanted layers or thin films formed on substrates. Intense positron sources are necessary to obtain slow positron beams for practical use. In general, positron sources based on pair creation can provide higher intensity than radioisotope-based positron sources. A positron source using pair-creation by gamma-rays from a nuclear reactor have been developed by using Kyoto University research Reactor (KUR) to obtain a slow positron beam for materials analysis. In the KUR slow positron beamline, the source size (converter and moderator assembly) is approximately 30 mm in diameter. For typical sample sizes of materials analysis (≤ 10 mm), it is necessary to reduce beam sizes efficiently while keeping beam intensity as high as possible. For this purpose, a brightness enhancement system have been developed for the KUR slow positron beamline [1]. In addition, measurement systems for positron annihilation lifetime spectroscopy have been optimized in this study.

EXPERIMENTS: In previous studies, the brightness enhancement system of the KUR slow positron beam line has been evaluated using beam-spot images on phosphor screens attached to microchannel plates. In addition, a knife-edge method using a brightness enhanced beam was examined over samples edges with Doppler broadening measurements. During the brightness enhancement operation, a positron pulsing system and a sample holder need to be biased with an extraction voltage (typically 5 keV). As pulsing signals are required for the lifetime measurement circuit located at the ground state (0 V), pulsing signals were transported through an isolation transformer from the high voltage state to the ground state.

RESULTS: After the positron pulsing system with a normal setup [2] was optimized for a Kapton sheet at 2 keV, the brightness enhancement system was then operated. The Ni re-moderator was inserted in the beam trajectory and additional optics with a magnetic lens and solenoid coils were excited. An extraction voltage of the beam from the Ni re-moderator was 5 keV. As a result, the high voltage of the sample was adjusted to 7 keV to obtain an acceleration voltage of 2 keV.

Fig. 1 shows the positron annihilation lifetime spectra of the Kapton sheet measured with and without the

brightness enhancement (B.E.) system. A satellite peak around 8 ns in Fig. 1(a) is one of the background peaks corresponding to the bunching period of the pulsing system. On the other hand, no satellite peak was observed around 8 ns in fig. 2(b). This difference is attributed to the narrower energy spread of the brightness enhanced beam.

Fig. 2 shows the result of position-dependent intensities of the Kapton lifetime component. The positron beam was moved across the edges of a YSZ sample placed on the Kapton sheet. The positron lifetime spectra were collected at each position. The intensities of the lifetime component of the Kapton was plotted. This procedure can be used as a knife-edge method. The fitting of a Gauss function gave a spot size of 2.3 mm (Full width half maximum: FWHM).

In summary, positron annihilation lifetime measurements were successfully demonstrated with a brightness enhanced beam in the KUR slow positron beam system. A spot size evaluated by a knife-edge method using sample edges was 2.3 mm (FWHM).

REFERENCES:

- [1] Y. Kuzuya *et al.* J. Phys. Conf. Series 791 (2017) 012012.
- [2] M. Nakajima *et al.* Rev. Sci. Instrum. 91 (2020) 125109.

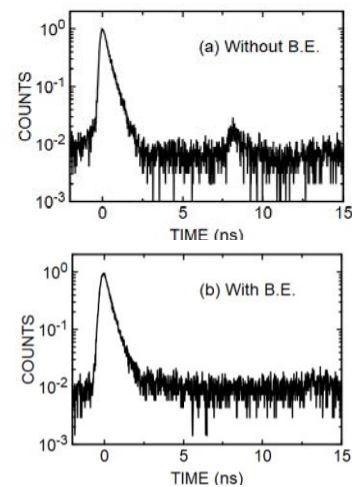


Fig. 1 Positron annihilation lifetime spectrum of a Kapton sheet measured without (a) and with (b) the brightness enhancement system.

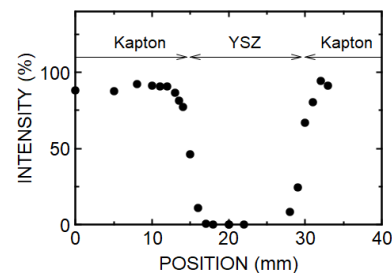


Fig. 2 Position dependence of intensities of the Kapton lifetime component across sample edges.

PR3-2 Doping effect of Cr, Mo, Ta, and Re on defect formation after electron-irradiation

T. Toyama¹, Y. Hatano², T. Suzudo¹, A. Yabuuchi³, A. Kinomura³, K. Inoue¹, Y. Nagai¹

¹*Institute for Materials Research, Tohoku University*

²*Organization for Promotion of Research, University of Toyama*

³*Institute for Integrated Radiation and Nuclear Science, Kyoto University*

INTRODUCTION: Tungsten (W) is a first-candidate material as plasma-facing materials for fusion reactors thank to its high melting point, high sputtering resistance to energetic particles, and the very low solubility of hydrogen isotopes which is a notable advantage in reducing tritium (T) retention. However, recent studies have reported that neutron-irradiation and ion-irradiation cause significant enhancement of hydrogen isotope retention in W, due to hydrogen trapping at irradiation-induced defects such as vacancies, vacancy clusters, and dislocation loops. Recently it was found that the addition of rhenium (Re) to W drastically reduces the hydrogen isotope accumulation [1]. As a mechanism for this, quantum chemical calculation has been performed [2]; it is suggested that Re is strongly bound to interstitial atoms, so that recombination of interstitial atoms and vacancies is promoted, and the formation of vacancy-type defects that become hydrogen capture sites is suppressed. However, no experimental studies on this have been obtained. In this study, we performed electron-irradiation to introduce only a simple Frenkel pair to W or W-Re alloy. The effect of Re addition on the defect formation is investigated by the positron annihilation method. In addition, the effect of Cr, Mo, and Ta is investigated as well.

EXPERIMENTS: Electron-irradiation to pure W, W-5%Re (in weight %), W-0.3%Cr, W-1.5%Mo, and W-5%Ta was performed at LINAC at KUR at 8 MeV, at temperature of < 100 °C to the fluence of $\sim 4E+23$ e⁻/m². Positron annihilation measurements (lifetime measurement and coincidence Doppler broadening measurement) were performed.

RESULTS: Figure 1 shows results of average positron lifetime before and after electron-irradiation for the samples. In pure W, the average lifetime was about 120 ps before electron-irradiation, which is close to the value in W bulk. After electron-irradiation, the average lifetime increased, showing positron trapping to vacancy-type defects induced by electron-irradiation. In W-1.5%Mo and W-5%Ta alloys, the trends were almost similar to that for pure W, indicating that the effect of these elements on the formation of irradiation-induced defects are not significant. In contrast, the average lifetime for W-0.3%Cr and W-5%Re remained relatively short compared with the other alloys, suggesting that the formation of irradiation-induced defects was suppressed. The possible candidate for positron trapping site for W-0.3%Cr and W-5%Re after irradiation could be dislocations in which positron life-time value may be shorter than

mono-vacancy. Figure 2 shows the deuterium (D) retention in W and W alloys before/after 6.4 MeV Fe ion irradiation at DuET at Kyoto University. For pure W, W-2.5Mo, and W-5Ta, significant increases in D retention were observed, which is attributed to the irradiation-induced defects after ion irradiation. On the other hand, the increase in D retention after irradiation was not significant for W-0.3%Cr and W-5%Re. This is due to the suppression of defect formation after irradiation, which is well-confirmed by the present positron lifetime measurements shown in Fig. 1.

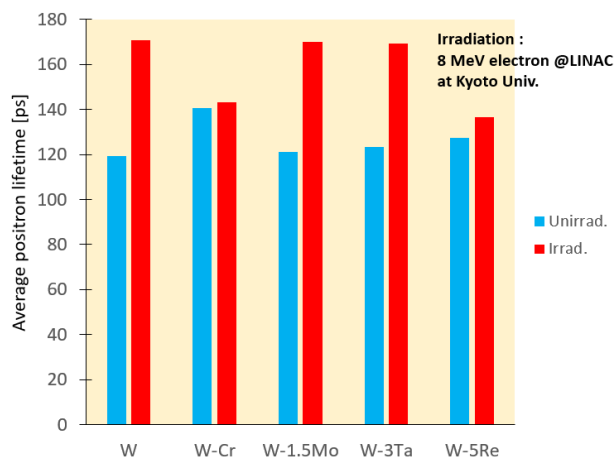


Fig. 1 : Average positron lifetime in W alloys before/after electron irradiation at LINAC.

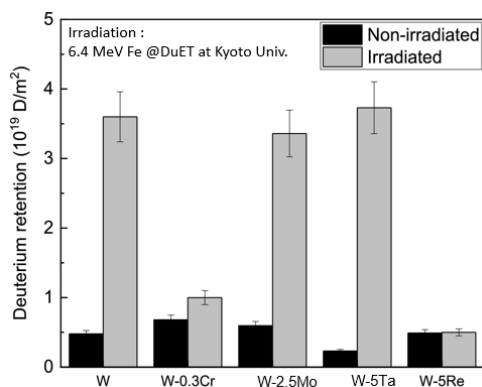


Fig. 2 : Deuterium retention in W alloys before/after 6.4 MeV Fe ion irradiation (Reproduced from J. Wang et al., J. Nucl. Mater. **545** (2021) 15274).

REFERENCES:

- [1] Y. Hatano *et al.*, Nucl. Mater. Energy **9** (2016) 93.
- [2] T. Suzudo, A. Hasegawa, Sci. Rep. **6** (2016) 36738.
- [3] J. Wang *et al.*, J. Nucl. Mater. **545** (2021) 152749.

PR3-3 Hydrogen Thermal Desorption Analysis in Electron-irradiated F82H

K. Sato, T. Kamimura, S. Komazaki, Q. Xu¹, A. Yabuuchi¹, A. Kinomura¹

Graduate School of Science and Engineering, Kagoshima University

¹*Institute for Integrated Radiation and Nuclear Science, Kyoto University*

INTRODUCTION: Thermal desorption analysis (TDA) is widely used to identify the gas atom trapping sites in the field of spallation neutron source materials [1], fusion reactor materials [2] and hydrogen embrittlement [3] and so on. To know the interaction between gas atoms and defects, which has an influence on microstructural evolution, is very important to develop the performance of their materials. TDA curves change if defects grow in the material (size or density change). Therefore, using the TDA, Komazaki et al. detected the formation and growth processes of defects during creep test of high Cr ferritic steels, and estimated the remaining life of the structural materials [4, 5].

In TDA, to obtain the binding energy of gas atoms to defects, three experiments under different rate of temperature increase should be performed [6]. However, it is often difficult to prepare multiple samples irradiated in spallation neutron sources or fusion reactors under same irradiation condition. Therefore, the simulations were also carried out to identify the gas atom trapping sites [2, 7]. In this study, the TDA of electron-irradiated F82H was conducted after electrolysis hydrogen charging. The hydrogen atom trapping sites in materials were investigated using simulation program for TDA.

EXPERIMENTS AND SIMULATIONS: IEA heat F82H [8] was used in this study. Disk samples with a diameter of 5 mm and thickness of 0.5 mm were fabricated using a wire electric discharge machine. Defects were introduced by irradiation with electrons at 8 MeV using the electron linear accelerator of Institute for Integrated Radiation and Nuclear Science, Kyoto University. The irradiation temperature was 333 ± 10 K, and irradiation dose was 1.4×10^{-4} dpa. Hydrogen was charged to the samples using a cathodic electrolysis charging method; also, 0.1 mol/L NaOH with 0.5 mass% NH_4SCN was used. The current density and the charging temperature were 50 A/m^2 and 303 K, respectively. The charging time was for 4 h. The hydrogen molecules were counted at intervals of 5 min using a gas chromatograph, and the system was calibrated with a standard mixture of hydrogen and argon gas with a heating rate of 100 K/h. Simulation program for TDA developed by Kamimura et al. [9] was used in this study.

RESULTS: In unirradiated F82H, when we used the values obtained in the previous study (hydrogen migration energy of 0.145 eV, the defect density of $1.6 \times 10^{23} /\text{m}^3$ (1.9×10^{-6}), and binding energy of 0.580 eV) [10]

(case 1), the density was too low and the binding energy was too high to fit the simulation curve to the experimental one. When we used the hydrogen migration energy of 0.145 eV, the trapping site density of $4.65 \times 10^{24} /\text{m}^3$ (5.52×10^{-5}), and binding energy of 0.373 eV (case 2), the curve fitted to the experimental one was obtained. It is expected that trapping sites are interface of precipitates, dislocations, and block/packet/lath boundaries. Jia et al. observed dislocations of approximately $10^{14} /\text{m}^2$ (density of atoms which compose dislocation core: 8.2×10^{-6}) by transmission electron microscopy in F82H [11]. Therefore, the defect density of $1.6 \times 10^{23} /\text{m}^3$ (1.9×10^{-6}) in the previous work [10] is too low. The hydrogen migration energy in α -Fe of 0.058 eV [12] is lower than that in F82H. As F82H includes many kinds of solute atoms, they capture hydrogen atoms, and slow the diffusion of hydrogen in F82H [13].

In the experimental TDA curve of electron-irradiated F82H, we can see a main peak around 320 K and a shoulder peak from 370 K to 420 K. The hydrogen migration energy, density, and binding energy of pre-existing defects were the same as case 2. The irradiation-induced defect is identified by positron annihilation lifetime measurements, di-vacancies were formed, and their density was 3.03×10^{-5} . The binding energy of hydrogen to vacancy clusters changes with the occupancy of hydrogen [14] and this changed according to the equation: $E_b = -0.631\theta^2 + 0.110\theta + 0.628$ (eV) (θ : occupancy of hydrogen to vacancy clusters). When the defect density is assumed as constant during the temperature increase, the curve does not fit to the experimental one. Therefore, it is assumed that the density of vacancy clusters monotonically decreases with increasing the annealing temperature. The simulation curve corresponds well to the experimental one except for the shoulder around 420 K. If the growth of the vacancy clusters is considered, better fitting curves will be obtained.

REFERENCES:

- [1] B.M. Oliver *et al.*, J. Nucl. Mater. 356 (2006) 148.
- [2] M. Poon *et al.*, J. Nucl. Mater. 374 (2008) 390.
- [3] T. Nagase *et al.*, ISIJ Int. 58 (2018) 349.
- [4] S. Komazaki *et al.*, Tetsu-To-Hagane, 96 (2010) 614.
- [5] H. Yamashita *et al.*, Tetsu-To-Hagane, 102 (2016) 630.
- [6] C.D. Doyle *et al.*, J. Appl. Poly. Sci. 5 (1961) 285.
- [7] Y. Oya *et al.*, J. Nucl. Mater. 461 (2015) 336.
- [8] A. Hishinuma *et al.*, J. Nucl. Mater. 258-263 (1998) 193.
- [9] T. Kamimura *et al.*, Mater. Sci. Forum, 1024 (2021) 135.
- [10] E. Serra *et al.*, J. Sci. Commun. 163 (2000) 51.
- [11] X. Jia and Y. Dai, J. Nucl. Mater. 318 (2003) 207.
- [12] W. Beck *et al.*, Proc. Royal Soc. A 290 (1966) 220.
- [13] H.S. Zhou *et al.*, J. Nucl. Mater. 455 (2014) 470.
- [14] J. Maisonneuve *et al.*, Fusion Sci. Tech. 60 (2011) 1507.

PR3-4 Gamma-ray induced photo emission from ZnO single crystal wafer: Comparison with GaN

T. Nakamura¹, T. Nishimura¹, K. Kuriyama¹, Atsushi Kinomura²

¹Research Center of Ion Beam Technology, Hosei University, Koganei, Tokyo 184-8584, Japan

²Institute for Integrated Radiation and Nuclear Science, Kyoto University, Kumatori, Osaka 590-0494, Japan

INTRODUCTION: Emission characteristics for native and radiation induced defects of wide-gap semiconductors such as ZnO and GaN have been studied by cathode-luminescence using an electron beam and photoluminescence using a He–Cd laser. We recently observed gamma-ray induced photo emission from GaN single crystal wafers [1]. This observed emission corresponds to yellow luminescence (YL). We have also reported that the high resistive ZnO bulk single crystals became low resistive due to the Zn interstitials induced by gamma-ray irradiation of 170 kGy [2]. Whether the luminescence by the excitation of gamma rays is observed in ZnO is important as it may be used as an application as a gamma ray detector. The gamma-ray generates a Compton electron, causing the material to undergo internal bombardment by MeV electrons [3].

EXPERIMENTS: Undoped ZnO single crystal wafers with a size of 1 cm square and a thickness of several 100 μm meters were used for the present study. The resistivity measured by van der Pauw method was 104 $\Omega\text{ cm}$ for an un-irradiated ZnO and varied to 30 $\Omega\text{ cm}$ for ZnO irradiated with the total gamma-ray dose of 170 kGy [2]. Therefore, the resistance change of the ZnO crystal does not occur in the short-time during gamma-ray irradiation emission measurement of about 20 min, corresponding to the gamma-ray dose of ~ 0.59 kGy. That is, short-time irradiation will not produce detectable lattice defects. The crystals were irradiated at room temperature with gamma-rays of 1.17 and 1.33 MeV from a cobalt-60 source of Institute for Integrated Radiation and Nuclear Science, Kyoto University. The gamma-ray irradiation induced photo emission measurements were performed by using a charge coupled device (CCD) equipped spectrometer (QE Pro, Ocean Insight Co. Ltd.). Each measurement was performed under 20 min, gamma-ray irradiation and each spectrum was acquired for 2 min, CCD exposure time.

RESULTS: Fig. 1 shows the gamma-ray induced photo emission spectra of ZnO and GaN single crystal wafers. These spectra were measured at room temperature by the absorption dose rate of about 1.4 kGy/h using wafer thickness of 0.5 mm for ZnO and 0.25 mm for GaN. The GL peak intensity of ZnO is about 1/60 of gamma-ray induced YL observed in GaN single crystal wafers [1]. Note that this peak intensity ratio was corrected by the thickness of the wafer. Although ZnO and GaN are the wurtzite structure, direct bandgap, and have almost the same bandgap values, the difference in peak intensity of the gamma-ray induced photo emission observed in the present study is considered to be due to the difference in

the light emitting mechanism between YL of GaN and GL of ZnO. YL of GaN has been proposed as a transition from a shallow donor to gallium vacancy (VGa) located at about 1.1 eV above the valence band [4]. Our previous study [5] reported that the low-dose gamma-ray irradiation of 160 kGy mainly induces N vacancies (VN) located at about 50 meV below the conduction band. Therefore, the gamma-ray induced YL observed in GaN is attributed to a shallow donor to VGa transition due to the excitation from valence band to conduction band by Compton electrons. On the other hand, GL in ZnO is the recombination of electrons in singly ionized oxygen vacancy (Vo^+) with photo-excited holes in valence band. However, it is suggested that a part of the electrons in Vo^+ in ZnO are excited in the conduction band by the Compton electrons and Vo^+ become the doubly ionized states (Vo^{++}), reducing their contribution to GL. As in the previous report [2], this situation is similar to the Vo^+ signal observed in the electron paramagnetic resonance measurements of ZnO irradiated with the total gamma-ray dose of 170 KGy disappears with red LED illumination.

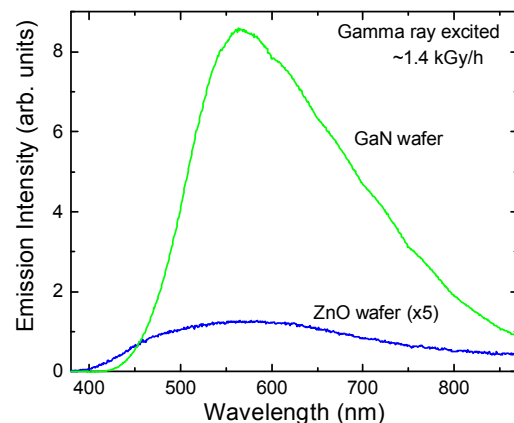


Fig. 1. Gamma-ray induced photo emission spectra from GaN and ZnO single crystal wafer.

Part of this research was published in Solid State Communications 336, 114413 (2021).

REFERENCES:

- [1] T. Nakamura, T. Nishimura, K. Kuriyama, T. Nakamura, A. Kinomura, Appl. Phys. Lett. 118 (2021), 032106.
- [2] J. Tashiro, Y. Torita, T. Nishimura, K. Kuriyama, K. Kushida, Q. Xu, A. Kinomura, Solid State Commun. 292 (2019) 24.
- [3] L.E. Rehn, R.C. Birtcher, J. Nucl. Mater. 205 (1993) 31.
- [4] J. Neugebauer J, C.G. Van de Walle, Appl. Phys. Lett. 69 (1996) 503.
- [5] Y. Torita, N. Nishikata, K. Kuriyama, K. Kushida, A. Kinomura, Q. Xu, J. Phys.: Conf. Series 864 (2017), 012016.

PR3-5 Investigation of Free Volume in Diamond-like Carbon Films Deposited by Various Methods

K. Kanda, T. Mishima, F. Hori¹, A. Yabuuchi² and A. Kinomura²

Laboratory of Advanced Science and Technology for Industry, University of Hyogo

¹Department of Materials Science, Osaka Prefecture University

²Institute for Integrated Radiation and Nuclear Science, Kyoto University

INTRODUCTION: As diamond-like carbon (DLC) has the lowest friction coefficient among various coating materials and its aggressiveness toward other materials is much less, its practical use have wide spread applications in, for instance, automobile parts, magnetic storage disks, implant parts, and food containers [1]. The film properties of DLC film is depended on its three kinds of structural factors, that is, sp^2/sp^3 ratio of carbon atom, hydrogen content, and free volume. The free volume in DLC film strongly related to the several physical properties of the DLC films, especially important ones such as hardness, Young's modulus, electrical conductivity, and gas barrier properties. In this study, the free volume of DLC films was discussed from the positron annihilation spectroscopy (PAS) study using a slow positron beam.

EXPERIMENTS: Eight kinds of DLC films were prepared. The following five methods were used for film deposition, ion plating, unbalanced magnetron sputtering, plasma-enhanced chemical-vapor-deposition, DC sputtering, and filtered cathodic vacuum arc (FCVA) method. In FCVA method, four types of films were produced by varying the voltage. The measurements of Doppler broadening (DB) and positron annihilation lifetime spectroscopy (PALS) were carried out using a slow positron beam installed in the B-1 hole of KUR. Doppler broadening profiles of annihilation γ -rays were obtained using a Ge detector in the voltage range up to 30 kV. The Doppler broadening is characterized by the S - and W -parameters, corresponding to the annihilation with low and high momentum electrons, respectively. PALS was performed at an energy of 2 keV, corresponding to the DLC film on Si. The film density and the hardness were determined from X-ray reflectivity (XRR) measurements, and nanoindentation method, respectively.

RESULTS: The W -parameters were plotted as a function of the S -parameter in Fig. 1. The W -parameter of various DLC decreased linearly with increasing of the S -parameter. This indicated that the same types of positron trapping sites are present. In other words, different types of vacancies were not created with different deposition methods or under different film deposition conditions. In addition, the PAL and the S -parameter show very good correlation, except for the DLC film with specifically high hydrogen content.

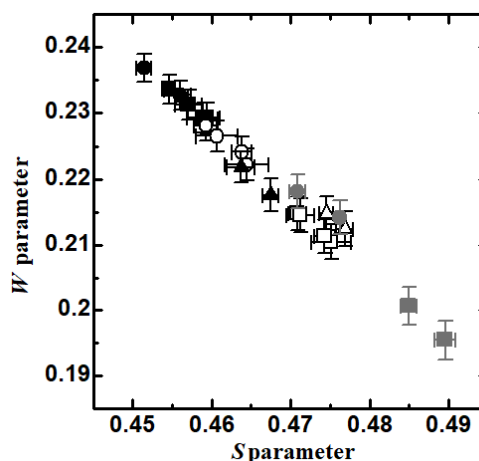


Fig. 1 The core annihilation parameter W versus the valence parameter S , in various DLC films.

Figure 2 shows the correlations between the S -parameters of various DLC films and the density and Martens hardness of DLC films. S -parameter shows good correlation with film density and the hardness. As the density and hardness decrease, the S -parameter increases, since the increase in S -parameter is considered to mean the increase in free volume. As well as, PAL increased with decreasing of the density and hardness. On the other hand, it was found that the S -parameter and PAL have no direct correlation to the hydrogen content, which was estimated from the ERDA analysis, or the sp^2/sp^3 ratio of carbon in the DLC film, which was obtained from the NEXAFS measurements. This is because the magnitude of the S -parameter and PAL depends first of all on the size of the free volume, and the influence of the chemical environment around the free volume is a secondary factor.

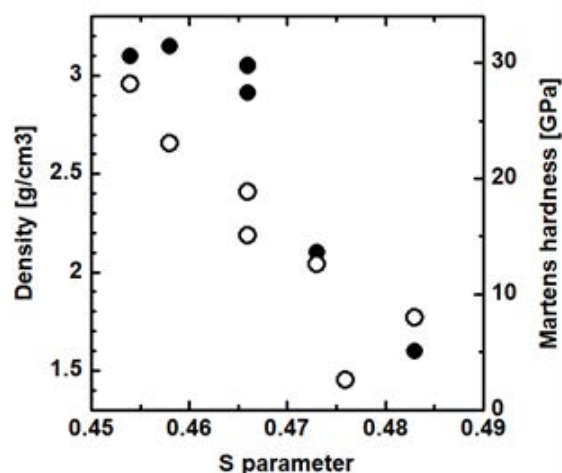


Fig. 2 Correlations between density, hardness and S -parameters of DLC films. ●: Density [g/cm³], ○: Hardness [GPa]

REFERENCES:

[1] N. Ohtake *et al.*, Materials **14** (2021) 315.

PR3-6 Positron annihilation spectroscopy on diamond-like carbon films

S. Nakao, X. Qu¹, A. Yabuuchi¹ and A. Kinomura¹

Innovative Functional Materials Research Institute, National Institute of Advanced Industrial Science and Technology

¹*Institute for Integrated Radiation and Nuclear Science, Kyoto University*

INTRODUCTION: Diamond-like carbon (DLC) films have attracted much attention because of their excellent mechanical properties. However, the properties strongly depend on the microstructure of the films which is varied by the deposition conditions and methods. Recently, DLC or carbon films are categorized from type I to VI, which includes graphite-like carbon (GLC) and polymer-like carbon (PLC).

The thermal stability of the films is of importance for practical applications. However, the thermal stability is not always enough at high temperature. It is considered that the degradation of the properties should be caused by the changes of the microstructure at high temperature. The structural changes may be related to hydrogen (H) desorption and the creation of defects at high temperature. Many studies have been carried out on the thermal stability of DLC films. However, the principal phenomena, such as defect behavior, are not always clear. Therefore, to make clear the behavior of defects is necessary for every type of DLC films (type I to VI) because of different microstructure and hydrogen content. The positron annihilation spectroscopy (PAS) is one of the useful methods to clarify the defect behavior of materials. The aim of this study is to examine the relationship between the thermal stability and the behavior of defects in several types of DLC films by PAS measurement.

It is known that the thermal stability of DLC films may be improved by the incorporation of Si element into the amorphous network of the films (Si-DLC). However, the reason is not always clear. In this study, Si-DLC and Si-PLC films are prepared and annealed up to 800°C, and the samples are examined by PAS measurement.

EXPERIMENTS: Si-DLC and Si-PLC films were deposited on Si (100) substrates by bipolar-type plasma-based ion implantation and deposition (PBII) system. A mixture of trimethylsilane (TMS) and acetylene gases was used. Negative pulse voltage (V_n) was changed from -0.4 to -5 kV to change the structure from polymer-like to diamond-like in the films. The details on the PBII system were reported elsewhere [1].

Samples were annealed at 400°C and 800°C in vacuum by an infrared image furnace. In the PAS measurement, the S-parameter was obtained at different positron energies ranging from 0 to 30 keV. The S-parameters of single crystal diamond, Si wafer and highly oriented pyrolytic graphite (HOPG) were also measured as a reference.

RESULTS: Figure 1 shows the change in S-parameter obtained from the PAS spectra of the samples prepared at

different V_n (a), and the samples after annealed (b). The sample of -0.4kV is categorized to Si-PLC and the others of -2.6 and -5kV are categorized to Si-DLC. The Si and H concentration was decreased with increasing V_n . The S-parameters of the references, diamond, Si and HOPG were ~ 0.48 , ~ 0.51 and ~ 0.47 , respectively. It is clearly seen in the Fig.1 that the S-parameters of ~ 0.51 at higher energies correspond to Si substrates. The S-parameters of the films should correspond to the low energy portion at least less than 5keV. The S-parameters of Si-PLC reaches ~ 0.53 which is higher than that of Si wafer. With increasing V_n , the parameters decrease to ~ 0.49 , possibly due to densification by ion bombardment. Further increase of V_n may cause the increase of defects in the films so that the S-parameter slightly increases to ~ 0.5 . On the other hand, thermal annealing causes the S-parameters decrease to ~ 0.51 in the sample of Si-PLC. It was noted that the S-parameter of PLC was like that of DLC and decreased from ~ 0.49 to ~ 0.475 after annealed at 800°C (not shown). These results suggest that Si incorporation may promote to increase porosity in the films and prevent structural changes due to H release by ion bombardment at high V_n or thermal annealing at high temperature.

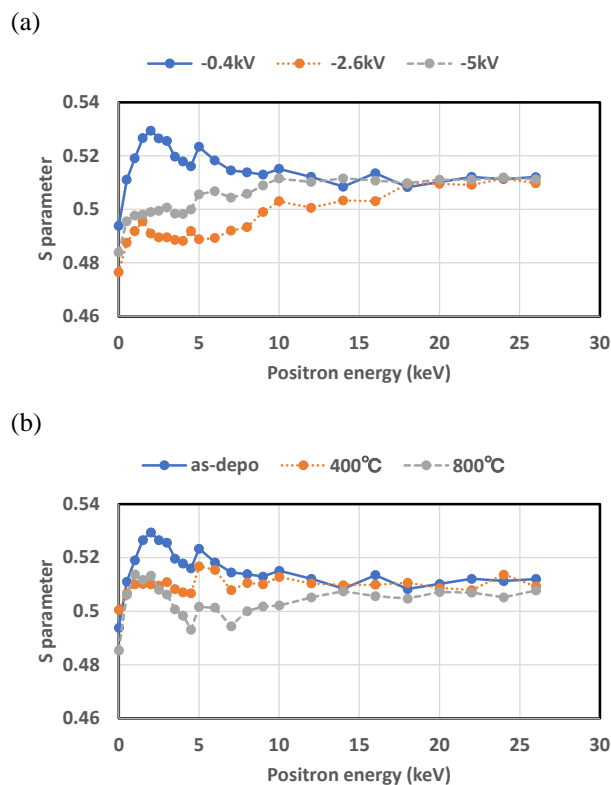


Fig.1. The change in S-parameter of samples at (a) different negative pulse voltage and (b) different annealing temperature.

REFERENCES:

[1] S. Miyagawa *et al.*, Surf. Coat. Technol., **156** (2002) 322-327.

I-1. PROJECT RESEARCHES

Project 4

T. Yamamura¹, Y. Haga², H. Amitsuka³, T. Suzuki⁴, K. Shirasaki⁵, M. Nogami⁶, M. Abe⁷, H. Shishido⁸, M. Nakase⁹, H. Nakai¹⁰, T. Kobayashi¹¹

¹KURNS, Kyoto University

²Advanced Science Research Center, JAEA

³Graduate School of Science, Hokkaido University

⁴Nagaoka University of Technology

⁵Institute for Materials Research, Tohoku University

⁶Graduate school of Electronic Eng., Kindai University

⁷Department of Chemistry, Tokyo Metropolitan University

⁸Graduate School of Engineering, Tohoku University

⁹Lab. for Adv. Nuclear Energy, Tokyo Inst. of Tech.

¹⁰Faculty of Science and Engineering, Kindai University

¹¹Material Science Research Center, JAEA

INTRODUCTION:

Actinide compounds shows a unique chemical and electronic nature due to the partial and insufficient shield of 5f orbital electrons as inner transition elements. We have a deep interest in the aspect of the electronic properties of the actinide compounds and formed the group consisting of three major fields: (1) inorganic and coordination chemistry, (2) electronic properties and (3) theoretical chemistry and its users. These studies will be also useful for application research area such as the handling of the 1F debris and developments of nuclear medicines.

Such research environments to handle actinides elements are extremely difficult to build in ordinary university institutes. The hot laboratory of the KURNS offers unique opportunities for the above-mentioned characteristic research activities.

EXPERIMENTS:

The last fiscal year of the project has been devoted to the setting up the experimental environment and initial test experiments. Each of research fields has made their progress as followings:

(1) T. Suzuki *et al.* has the investigated adsorption behaviors of actinides on polyvinylpyrrolidone (PVPP) in nitric acid and hydrochloric acid solutions. The adsorption behaviors were evaluated through measurements of the distribution coefficient.

(2) Y. Haga *et al.* has synthesized the novel uranium intermetallic compound $U_2Pt_6Ga_{15}$. The single-crystalline samples of this compound have been investigated by the measurements of crystallographic, thermodynamic, and transport properties.

(3) M. Nakase *et al.* has studied properties of Phthalocyanine (Pc) as a ligand for an effective extraction of U. The Pc-Zn complex was sublimely purified in a self-made apparatus that was maintained last year. The pure product was found to be solid (powder), but slightly moistened by moisture in the air. Powder X-ray diffraction (PXRD) and Raman spectrophotometry were used.

(4) Kobayashi *et al.* has studied changes in the chemical state and structure of simulated fuel debris were studied under a controlled environment simulating the environment inside and outside a nuclear reactor were investigated

by XAFS. conducted at the JAEA beamline BL22XU at SPring-8.

(5) Abe *et al.* calculated isotopic fractionation factors (ϵ) for 64 U(VI), U(V), and U(IV) species with various ligands using an exact relativistic quantum chemistry method.

U isotopic fractionation is important and widely discussed in geochemistry [1]. We validated the accuracy of our method by comparing it with experimental results for U isotope fractionation.

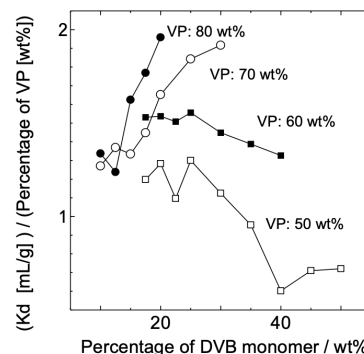


Fig.1 Cross-linkage effects on adsorption of uranyl ion on pyrrolidone resin in HNO_3 .

RESULTS:

(1) From the distribution coefficients measured for uranyl ions on PVPP, T. Suzuki *et al.* confirmed that the thorium is strongly adsorbed on PVPP in higher concentration of HNO_3 , and the cross-linkage effects on adsorption of uranyl ion on pyrrolidone resin. They found that this tendency change is related with the surface potential of resin.

(2) Uranium layers embedded in Pt-Al(Ga) metal blocks exhibit a variety of magnetic properties [2]. Although the transition temperatures are almost the same, the behavior at low temperatures is quite different: $U_2Pt_6Ga_{15}$ exhibits typical antiferromagnetic, whereas $U_2Pt_6Al_{15}$ shows a rapid expansion of magnetization in the ordered state.

(3) The purified Pc-Zn sample and its XRD pattern are shown in Fig. 2. the XRD pattern shows a large halo peak due to the use of ethanol and a glass plate, but also some sharp diffraction due to Pc. Therefore, we conclude that the purification by sublimation was successful.

(4) Immersion in water and γ -ray irradiation has found to oxidize uranium on the sample surface from tetravalent to hexavalent and the U-O distance was shortened. No change in uranium valence or local structure was observed when the samples were removed from the water and exposed to atmospheric air, suggesting that the debris may be stable in the air.

(4) Obtained values of ϵ were almost $U(VI) > U(V) > U(IV)$ for both HF and DFT. The X2C-HF method seems to be more reliable for the calculation between U(VI)-U(IV). On the other hand, when the isotopic fraction of the U(VI)-U(VI) ligand exchange system is considered, the values obtained at the DFT level are generally in better agreement with experiments than the HF values.

REFERENCES:

- [1] T. Yamamizu, *et al.*, Jpn. J. Polymer Sci. Technol., 47 (1990)49-56.
- [2] Y. Matsumoto, Y. Haga *et al.*, J. Phys. Soc. Jpn. 90, 074707 (2021).

PR4-1 Study of Magnetic Structure in UIr_2Ge_2 by Resonant X-Ray Scattering Experiments

H. Amitsuka, F. Kon, C. Tabata¹, H. Nakao², Y. Shimizu³, D. Aoki³, A. Koriki, H. Hidaka, and T. Yanagisawa

Graduate School of Science, Hokkaido University

¹Institute for Integrated Radiation and Nuclear Science, Kyoto University

²Institute Materials Structure Science, CMRC, KEK

³Institute for Materials Research, Tohoku University

INTRODUCTION: The magnetic structure of the uranium compound UIr_2Ge_2 has been investigated for the first time by resonant X-ray scattering experiments using a single crystal sample. This compound has a tetragonal CaBe_2Ge_2 -type structure (space group: $P4/nmm$, D_{4h}^7 , No. 129) [1,2], which is characterized by an inversion-symmetric pairing of two U ions occupying a site lacking spatial inversion symmetry in the unit cell. When an antiferromagnetic order with order wavenumber $\mathbf{Q} = 0$ is induced in such a U ion, the global spatial inversion symmetry of the system is broken and cross-correlated responses such as current-induced magnetization are predicted. For this reason, CaBe_2Ge_2 -type magnetic materials have attracted much attention in recent years because they may provide the simplest example of a system in which odd-parity magnetic multipoles can be active.

On the basis of bulk property measurements on single-crystal sample of UIr_2Ge_2 , we have confirmed that the system exhibits a phase transition suggestive of antiferromagnetic ordering at 18.3 K ($\equiv T_N$), strong magnetic anisotropy with the c -axis as the easy magnetization axis [3]. In the present study, we performed resonant X-ray scattering experiments to identify the magnetic structure of this order.

EXPERIMENTS: The measurements were carried out at BL-11B of KEK PF using soft X-rays of 3.70 ~ 3.75 keV. The sample was a single crystal with a diameter of about 2 mm formed into a plate. The temperature range was 6 K to 24 K. A ^4He flow refrigerator was used for cooling.

RESULTS and DISCUSSION: By searching for magnetic reflections in the a^*-c^* plane, it was confirmed that the superlattice reflections due to resonant scattering at the M_4 edge of U ($3d \rightarrow 5f$ transition: 3.723 keV) grow continuously at (reciprocal lattice points) $(0, 0, 1/2)$ at lower temperatures than near T_N (Fig. 1) [5]. The fact that the magnetic susceptibility of this material shows a cusp anomaly at T_N suggests that an antiferromagnetic ordered state with an ordered wavenumber vector $\mathbf{Q} = (0, 0, 1/2)$ is realized below T_N . For the space group $P4/nmm$, there are three maximal magnetic subgroups where the U ion has a magnetic moment and $\mathbf{Q} = (0, 0, 1/2)$: $P_{2c}A/nmm$ (No. 129.13.1087), $C_{2c}mma$ (No. 67.11.587), and $P_{2c}mmn$ (No. 59.9.486). Among these, only $P_{2c}A/nmm$ has the magnetic easy axis at c -axis.

In order to identify the direction of the magnetic moment, we measured the azimuth angle dependence of the magnetic scattering intensity. The diffractometer is fixed to the Bragg condition with the magnetic scattering vector $\mathbf{q} = (2,$

$0, 1/2)$, the sample is rotated around \mathbf{q} , and the change in scattering intensity is measured. The rotation angle is φ , and the range of $-100^\circ \leq \varphi \leq 90^\circ$ is investigated by setting $\varphi = 0$ so that the $(0, 1, 0)$ direction of the sample is perpendicular to the scattering plane.

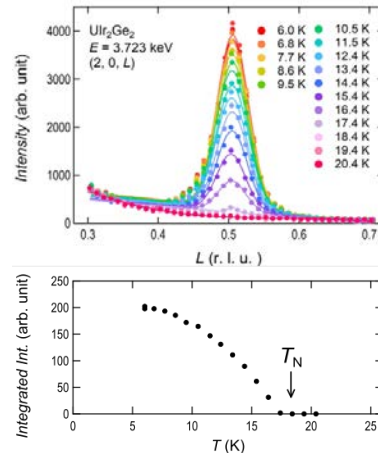


Fig. 1. Temperature profiles of magnetic reflections $(2, 0, 1/2)$ and results of Gaussian-fit (solid line) (top) and temperature dependence of integrated intensity (bottom).

The φ -dependence of the integrated intensity of the magnetic reflections show maxima and minima near $\varphi \sim \pm 90^\circ$ and $\varphi \sim 0$, respectively. The results suggest scattering by magnetic dipoles lying in the c direction, showing a good agreement with calculations based on the magnetic structures belonging to $P_{2c}A/nmm$.

SUMMARY: In this study, we confirmed that the magnetically ordered structure in UIr_2Ge_2 is antiferromagnetic with $\mathbf{Q} = (0, 0, 1/2)$ due to the magnetic dipole parallel to the c -axis. It was found that the system is not an antiferromagnet with $\mathbf{Q} = 0$, as expected for the original purpose. However, the ferriocly ordered layers of the odd-parity multipoles may be antiferromagnetically stacked in the c direction due to weak interlayer interactions, which is of interest in relation to a variety of unusual physical properties of this system.

ACKNOWLEDGEMENT:

The present work was supported by JSPS KAKENHI Grant Number JP15H05882, JP15H05885 and JP15K21732 (J-Physics).

REFERENCES:

- [1] B. Lloret *et al.*, J. Magn. Magn. Mater. **67**, 232 (1987).
- [2] A. A. Menovsky, J. Magn. Magn. Mater. **76** and **77**, 631 (1988).
- [3] F. Kon *et al.*, Physical Society of Japan, Autumn Meeting 2019 (Gifu Univ.), 12pB12-13, September 12, 2019.
- [4] A. Bienenstock, J. Appl. Phys. **37**, 1459 (1966).
- [5] F. Kon *et al.*, Physical Society of Japan, The 75th Annual Meeting, 16pB22-9, March 2020 (Local meeting cancelled to prevent spread of infection COVID-19).

PR4-2 Bulk thorium separation for ^{228}Ac generator

K. Shirasaki, H. Kikunaga¹, K. Washiyama², A. Shinohara³, T. Yoshimura⁴, K. Nagata⁴, C. Tabata⁵, and T. Yamamura⁵

Institute for Materials Research, Tohoku University

¹*Research Center for Electron Photon Science, Tohoku University*

²*Advanced Clinical Research Center, Fukushima Medical University*

³*Department of Chemistry, Graduate School of Science, Osaka University*

⁴*Radioisotope Research Center, Institute for Radiation Sciences, Osaka University*

⁵*Institute for Integrated Radiation and Nuclear Science, Kyoto University*

INTRODUCTION: Actinium chelation chemistry has been drawn attention from not only chemists but also medical workers, who are relevant to nuclear medicine. Because ^{225}Ac ($T_{1/2} = 10$ d) which decays through a chain of four α -emissions and two β -emissions to the stable ^{209}Bi , are of great interest for a targeted alpha therapy nuclide due to its ability to kill considerably high efficiency of tumor cell [1]. However, γ -ray spectrometry, which is a convenient method for identification of radionuclides, has an uncertainty about the application to ^{225}Ac due to its low emission ratios. In contrast, ^{228}Ac ($T_{1/2} = 6.15$ h, daughter nuclide of ^{228}Ra) has potential value because it emits well-defined and intense γ -rays that are easily resolved from the daughter nuclides. Havelka reported the preparation method of ^{228}Ra standard solution from natural thorium nitrate salt [2]. Aldrich *et al.* also reported the preparation method of ^{228}Ac generator from natural thorium salts in 2020 [3]. Their method was composed of two parts with the bulk thorium separation by the precipitation of thorium hydroxide, and purification of ^{228}Ra by the column chromatography using ion-exchange resins. In the handling of thorium hydroxide, the voluminous slurry precipitate complicates the convenient separation from the daughter nuclides.

Hence, we studied precipitation behavior of thorium hydroxide by titration method.

EXPERIMENTS: The precipitation method was based on a technique used in ^{228}Ac separation from natural thorium salts [3]. Thorium oxide (9.95 g) was dissolved in 30 mL of conc. HCl spiked with 0.1 mL of conc. HF with heating ($\sim 150^\circ\text{C}$) for a few minutes. The solution was evaporated near dryness and added mili-Q water (18.2 M Ω , repeated two times). Then, the solution was brought to dryness and dissolved in 0.1 M (mol/L) HCl. Finally, the solution volume was adjusted to 100 mL by the addition of mili-Q water.

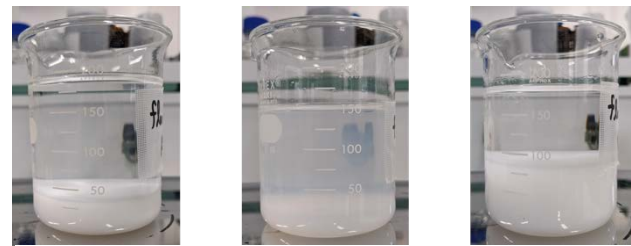
The bulk thorium separation by NaOH titration was processed according to the following steps. The 20 mL of Th stock solution was diluted to 100 mL with mili-Q water and transferred to a beaker of 250 mL. The solution was

intensely stirred and titrated with NaOH solution under pH measuring (Condition A was adjusted to pH12, then reversed by HCl until pH7, refer to previous study [3]: condition B and C were adjusted to pH5 and pH8, respectively.). After the titration, the solution was stayed at several hours (Fig. 1), then the solution passed through a PES filter (0.2 μm filter size). The filtrate was collected, then an additional 20 mL of mili-Q water was passed through for washing the residual (repeated 3 times). These were also corrected in the same bottle. This solution was subjected to the γ -ray spectrometry using a high-pure Ge-detector (ORTEC). The ^{228}Ac activity was determined by γ -emission of 911 keV. The distribution ratio (D) of ^{228}Ra in the solution was calculated by the equation:

$$D = A_{\text{sep}}/A_{\text{ini}} \quad (1)$$

Here, A_{sep} and A_{ini} are activities obtained from γ -ray spectrometry of the separated solution and Th stock solution, respectively. Th concentration of the solution was also measured by ICP-AES (ICPS-7500, Shimadzu).

RESULTS: As shown in Fig. 1, supernatant liquids were found in Condition A and C, which was assumed to be contained thorium as a major precipitated hydroxide.



Condition A

Condition B

Condition C

Fig. 1. photos of titrated samples after titration.

The initial ^{228}Ra atomicity (N_1) of each fraction can be estimated by the equation:

$$N_2' = \lambda_1/(\lambda_2 - \lambda_1) \cdot N_1(e^{-\lambda_1 t} - e^{-\lambda_2 t}) + N_2 e^{-\lambda_2 t} \quad (2)$$

Here, N_2 and N_2' are the number of ^{228}Ac atom at initial and elapsed time t , respectively, λ_1 and λ_2 are the decay constant of ^{228}Ra and ^{228}Ac , respectively. The distribution ratios (D) of ^{228}Ra in the solutions were determined by ^{228}Ac activities and summarized in Table 1. This result indicates that over 90% of ^{228}Ra is remained in the solution and successful bulk thorium separation is realized in the titration condition both A and C.

Table 1 ^{228}Ra distribution ratio (D) and Th concentration.

Condition no.	A	B*	C
D	0.99	-	0.93
Th conc. (ppm)	5.9	-	< 5.1

*Hard to filtrate the solution

REFERENCES:

- [1] C. Kratochwil *et al.*, J. Nucl. Med., **57** (2016) 1941-1944.
- [2] M. Havelka, Appl. Rad. Isotopes, **109** (2015) 222-225.
- [3] K. E. Aldrich *et al.*, Inorg. Chem., **59** (2020) 3200-3206.

PR4-3 Elution Properties of Re(VII) from Cyclic Monoamide VBPR Resin by Chelating Agents

M. Nogami¹, N. Mori¹, C. Tabata², and T. Yamamura²

¹Faculty of Science and Engineering, Kindai University

²Institute for Integrated Radiation and Nuclear Science, Kyoto University

INTRODUCTION: Development of highly selective compounds for actinyl ions in aqueous media (extractants, precipitants, resins, etc.) has been important. We have been focusing on monoamide compounds (Fig. 1) as promising candidates for nitric acid media, considering the possibility of complete incineration of waste compounds (so-called “CHON principle”[1]). For monoamide resins, not a few have been newly synthesized, and adsorptivity to metal ions has been examined, where uranium(VI) was used as the representative of actinyl ions.



Fig. 1. Chemical structure of monoamide compounds. (R, R', R'' : hydrocarbon group) .

Effective elution of the adsorbed metal ions is necessary for recycle use of resins. Many of the monoamide resins are found to adsorb more U(VI) species with increasing concentration of HNO₃. Selective U(VI) recovery would be, therefore, achieved by adsorbing U(VI) under relatively higher concentration of HNO₃ (e.g. 3 to 6 mol/dm³ (=M)) followed by elution of the adsorbed U(VI) by using H₂O or diluted HNO₃ (e.g. 0.1 M). On the other hand, it has been revealed that some metal ions except U(VI) are also adsorbed to monoamide resins. Adsorptivity for many of the ions are lower than that of U(VI), but some ions are adsorbed in almost all HNO₃ concentration range. In this case, the adsorbed metal ions can't be eluted only by changing the concentration of HNO₃, and use of chelating agents is necessary.

In the present study, a monoamide resin consisting of 1-(4-vinylbenzyl)pyrrolidin-2-one (VBPR) was taken. As can be seen in Fig. 2, it has a cyclic monoamide structure with a long spacer between the functional monoamide group and the main polymer chain. VBPR resin shows adsorptivity to Re(VII) (simulant of Tc(VII)) in all HNO₃ concentration range and the distribution ratio, *K_d*, is higher under lower concentration of HNO₃. Based on the above, elution properties Re(VII) by some chelating agents were investigated.



Fig. 2. Chemical structure of VBPR resin

EXPERIMENTS: VBPR resin is a silica-supported type and was synthesized by following the earlier study[2]. Three chelating agents, ethylenediaminetetraacetic acid tetrasodium salt (EDTA-4Na), oxalic acid (Ox), and trisodium citrate dihydrate (Cit-3Na) were used as the candidate eluents. Elution experiments were carried out by batch method. As the first step, 0.1 M HNO₃ containing 10 mM Re(VII) was mixed with VBPR resin (wet 3.0 g) at 25 °C for 24 h in order that VBPR resin might adsorb Re(VII). Next the mixture underwent solid-liquid separation. The solid was air-dried and the concentration of Re in HNO₃ was measured by ICP-OES. The dried VBPR resin (0.15 g) was mixed with solutions containing 0.1 M chelating agents mentioned above and H₂O for reference, respectively (3 cm³ each), at 25 °C for 24 h. The mixture underwent solid-liquid separation again and the concentration of Re in HNO₃ was measured by ICP-OES. Elution ratios were calculated by the eluted amount of Re divided by the adsorbed one.

RESULTS: Elution ratios of Re(VII) by each chelating agent are shown in Table 1. All examined chelating agents are found to elute Re(VII) more effectively than H₂O. Above all, elution ratio by Cit-3Na is highest. The reason still remains unclear and further investigations are necessary.

Table 1. Elution ratio of Re(VII) by each chelating agent.

	EDTA-4Na	Ox	Cit-3Na	H ₂ O
Elution ratio / %	7.8	24.4	32.6	3.6

Following the above result, dependence of Cit-3Na concentration on elution ratio was examined. The result is shown in Fig. 3. The data for H₂O in Table 1 is used for [Cit-3Na] = 0 M. The elution ratio is increased with increasing concentration of Cit-3Na up to 0.1 M and almost constant over 0.1 M. This suggests that ca. 0.1 M is the most appropriate concentration of Cit-3Na for eluting Re(VII) under the present experimental condition.

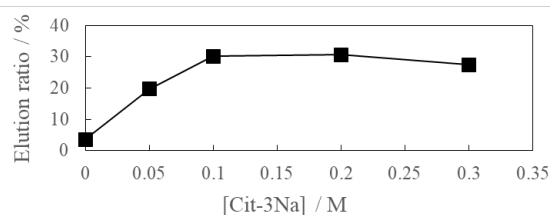


Fig. 3. dependence of Cit-3Na concentration on elution ratio of Re(VII).

REFERENCES:

- [1] M. G. B. Drew *et al.*, Dalton Trans. (2007) 244-251.
- [2] Y. Yoshimura *et al.*, KURRI Progress Report 2019 (2020).

PR4-4 Consistency verification between relativistic quantum chemical calculations and experiments in uranium compounds

M. Abe^{1,2}, M. Hada², A. Sato², A. Yoshida², T. Yamamura², A. Sunaga³, C. Tabata³

¹Department of Chemistry, Hiroshima University

²Department of Chemistry, Tokyo Metropolitan University

³Institute for Integrated Radiation and Nuclear Science, Kyoto University

INTRODUCTION: Theoretical calculations of actinide compounds are very important to understand or predict new phenomenon in these compounds. We have developed computational methods based on relativistic quantum chemistry, which can describe electronic states of actinide compounds. In this work, we calculated equilibrium isotope fractionation coefficients (ε) for 64 U species in U(VI), U(V), and U(IV) states with various ligands (e.g., H₂O, CO₃²⁻, CH₃COO⁻, Cl⁻, NO₃⁻, etc.) using accurate relativistic quantum chemical methods. The U isotope fractionations are important and widely discussed in geochemistry [1]. We verify the accuracy of the computational methods by comparing to some experimental results of U isotope fractionations.

METHODS: We calculated ε between ²³⁵U and ²³⁸U as the sum of the nuclear volume term ($\ln K_{nv}$) and the nuclear mass term ($\ln K_{nm}$) [2-4]. $\ln K_{nv}$ is due to the electronic energy difference caused by the different size and shape of nucleus of isotopes [2,3], while $\ln K_{nm}$ is due to the vibrational level caused by the different reduced mass of isotopologues [4]. In the heavy element system, $\ln K_{nv}$ is dominant in ε . Because $\ln K_{nv}$ is highly affected by relativity, we used the exact two-component (X2C) relativistic method with the Gaussian finite nucleus model, implemented in the DIRAC16 program. We performed both the Hartree-Fock (HF) and density functional theory calculations using the B3LYP functional to discuss the electron correlation effects in $\ln K_{nv}$.

RESULTS: Fig. 1 (a) and (b) show the calculated results, and the magnitude of ε obtained is approximately U(VI) > U(V) > U(IV) for both the HF and DFT cases. The ε values between U(VI)-U(IV) were obtained in the range of 0.96~3.00‰ for X2C-HF, and 0.53~1.94‰ for X2C-B3LYP; thus, the results between HF and DFT are different. The equilibrium ε between U(VI)-U(IV) in hydrochloric acid was estimated as 1.70‰ from X2C-HF and 0.92‰ from X2C-B3LYP, while the experimental counterpart was reported as 1.64‰ [5]. Therefore, the X2C-HF method seems to be more reliable for the ε calculation between U(VI)-U(IV).

On the other hand, if we consider the isotope fractionations in the U(VI)-U(VI) ligand exchange systems, the ε values obtained at the DFT level show generally better agreements with experiments [6,7] than those for HF. This indicates that the DFT calculations are accurate for U(VI) species, which are closed-shell systems, but not for

U(IV) species, which are open-shell systems. Recently, we found that the DFT calculations in the DRAC program do not automatically adopt the average-of-configuration (AOC) open-shell algorithm, whereas our HF calculations adopt it. Hence, recalculations including AOC for DFT is ongoing to improve the description for the open-shell U(IV) electronic states.

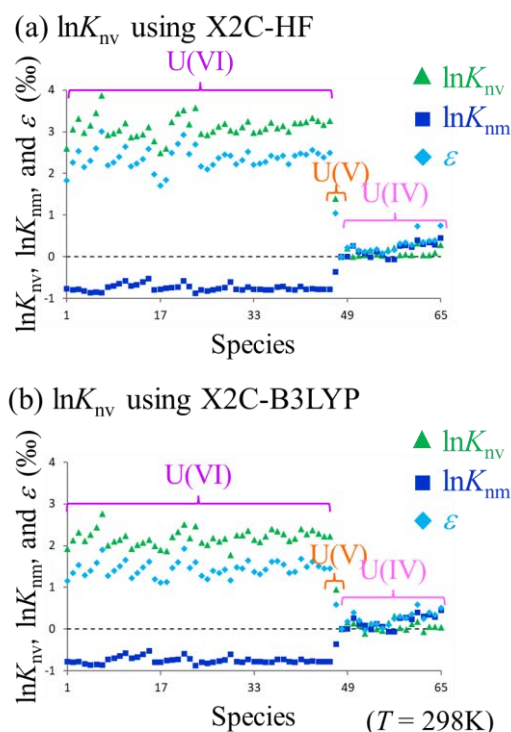


Fig. 1. $\ln K_{nv}$, $\ln K_{nm}$, and ε of 64 U species, calculated (a) at the HF level and (b) at the B3LYP levels for $\ln K_{nv}$. The light blue, green, and deep blue plots represent ε , $\ln K_{nv}$, and $\ln K_{nm}$, respectively. These plots for U(VI), U(V), and U(IV) species are surrounded by the purple, orange, and pink rounded squares, respectively. [8]

REFERENCES:

- [1] C. H. Stirling *et al.*, *Geochim. Cosmochim. Acta*, **163** (2015) 200-218.
- [2] M. Nomura *et al.*, *J. Am. Chem. Soc.*, **118** (1996) 9127-9130.
- [3] J. Bigeleisen, *J. Am. Chem. Soc.*, **118** (1996) 3676-3680.
- [4] J. Bigeleisen and M. G. Mayer, *J. Chem. Phys.*, **15** (1947) 261-267.
- [5] Wang *et al.* *Geochim. Cosmochim. Acta*, **158**, 262 (2015)
- [6] Kim *et al.* *J. Chem. Phys.* **81**, 6266 (1984).
- [7] Aoyama *et al.* *J. Phys. Chem.*, **93**, 2666 (1989).
- [8] A. Sato, R. Bernier-Latmani, M. Hada, and M. Abe, to be submitted.

PR4-5 Evaluation of Phase Diagram of Minor Actinide Oxides with CALPHAD

H. Shishido, H. Hashizume, C. Tabata¹, T. Yamamura¹

Graduate School of Engineering, Tohoku University

¹Institute for Integrated Radiation and Nuclear Science, Kyoto University

INTRODUCTION: Partitioning and transmuting is presently regarded as an effective method to address the issue of high-level radioactive waste disposal [1]. We have proposed to transmute MA rather moderately, namely with a low fission reaction rate to avoid imposing severe engineering challenges on the system design [2]. This concept has considered MA mixed oxides (e.g., Np–Am–O) to be loaded into limited space in fusion reactors. Whereas some studies have reported the phase diagram of U or Pu based MA oxides, no reports have provided the diagrams of the MA-only mixed oxides.

The objective of this study is to evaluate the thermodynamic values and phase diagram of the MA-only mixed oxides. Measurement of the phase diagrams is not a straightforward task; we thus aim to develop a method to evaluate the phase diagrams.

In the current fiscal year, we have performed the electronic structure calculations of NpO₂ and AmO₂ mixed oxide based on the method obtained in the previous year. Because there are no reported crystal structure data for the mixed oxide, crystal structures were prepared assuming appropriate atomic configurations, and structural optimization calculations were performed on them.

METHODS: The calculated crystal structure of (Np, Am)O₂ is shown in Fig. 1. The composition ratio of Np to Am is 1:1, and the atomic arrangement of Np and Am is assumed to have the two crystal structures shown in Fig. 1. The crystal groups are P4/mmm and R-3m, respectively. We performed the structural optimization for these crystals. We used WIEN2k to calculate the electronic state [3]. The generalized gradient approximation (GGA) developed by Perdew, Burke, and Ernzerhof was used as the exchange–correlation functional. The product of the muffin-tin radius and the K vector ($R_{\text{mt}}K_{\text{max}}$) was 8.5 Ry, and the sampling k points were set to 5,000. The calculation was performed as a non-magnetic material without considering the matters related to the electron spin.

RESULTS: The Energy–Volume curves for the two crystal structures of (Np, Am)O₂ are shown in Fig. 2. The curves show Murnaghan's fitting curves. Whereas there is no significant difference between the two crystal structures, the total energy is slightly lower for the R-3m crystal structure.

REFERENCES:

- [1] S. L. Beaman *et al.*, NR-CONF-001, United States Nuclear Regulatory Commission, (1976).
[2] Y. Furudate *et al.*, Prog. Nucl. Energ. **103** (2018) 28-32.

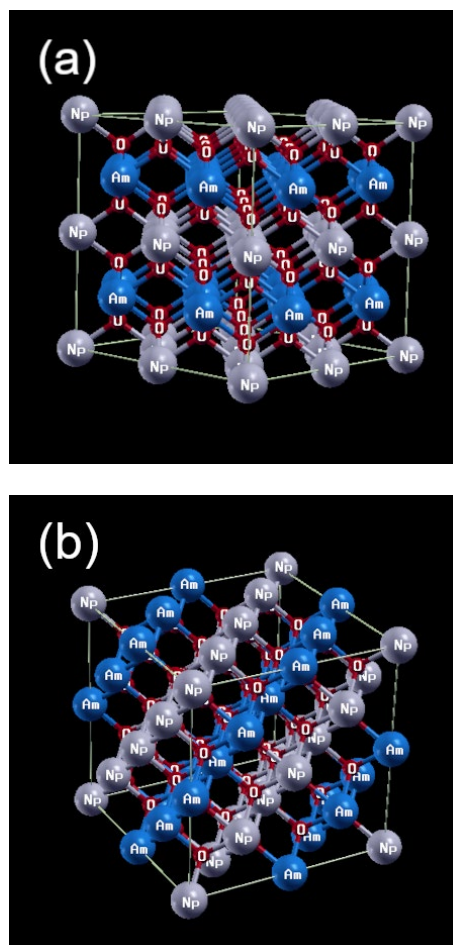


Fig. 1. Crystal structure of (Np, Am)O₂: (a) P4/mmm; (b) R-3m.

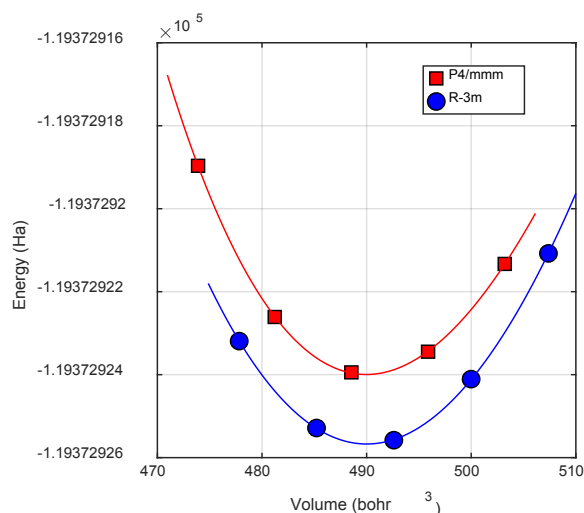


Fig. 2. Energy volume curve of (Np, Am)O₂.

- [3] P. Blaha, K.Schwarz *et al.*, J. Chem. Phys. **152** (2020) 074101.

PR4-6 Peculiar magnetism in uranium intermetallics with layered structure

Y. Haga¹, C. Tabata² and Y. Matsumoto³

¹Advanced Science Research Center, JAEA

²Institute for Integrated Radiation and Nuclear Science, Kyoto University

³Faculty of Science, Toyama University

INTRODUCTION: Unusual physical properties arising from geometrical characteristics of magnetic moments are now attracting active research interests. In particular, the situations where magnetic interactions are frustrating can result in highly unconventional ground states as demonstrated historically by the spin-glass or, more recently, skyrmions formations involving a number of spins. Here, we investigate uranium compounds where the uranium atoms form honeycomb layers. The target materials in this study are a series of compounds having $\text{Sr}_{0.6}\text{Fe}_2\text{Si}_{4.9}$ -type structure where uranium atoms are located at Sr position. Although earlier study suggested atomic disorder inside the uranium layer, our investigation on a U-Pt-Ga ternary analogue showed that a honeycomb arrangement of uranium atoms is likely. The resulting formula should therefore be $\text{U}_2\text{Pt}_6\text{Ga}_{15}$. In this study we further investigated uranium intermetallics with the same crystal structure.

EXPERIMENTS: Single crystals were grown from the self-flux method. The chemical composition of the samples was characterized by the electron-probe microanalysis. Crystal structure was determined using the single-crystal X-ray diffraction.

RESULTS: We have successfully grown single crystals of $\text{U}_2\text{Pt}_6\text{Al}_{15}$ [2] and $\text{U}_2\text{Pt}_6\text{Ga}_{15}$ [3]. Reflecting the different atomic radius of Al and Ga, the lattice parameters of these compounds differ as shown in Table 1. The reduction of the lattice parameters would modify the electronic interaction through the change in the interatomic distances. In f-electron system in general, the smaller the interatomic distance increases the hybridization and leads to a modification of magnetic interaction. Considering the same valence electron count in Al and Ga, the substitution effect would result primarily in chemical pressure effect.

Temperature dependence of magnetization divided by magnetic field applied along the c-direction is shown in Fig. 1 for both $\text{U}_2\text{Pt}_6\text{Al}_{15}$ and $\text{U}_2\text{Pt}_6\text{Ga}_{15}$. Both compounds show an anomaly in M/H corresponding to the magnetic phase transition at around 25 K as shown by arrows in Fig. 1.

	a (Å)	c (Å)
$\text{U}_2\text{Pt}_6\text{Al}_{15}$	4.2957(7)	16.2211(14)
$\text{U}_2\text{Pt}_6\text{Ga}_{15}$	4.3038(5)	16.297(2)

Table. 1. Lattice parameters of $\text{U}_2\text{Pt}_6\text{Al}_{15}$ and $\text{U}_2\text{Pt}_6\text{Ga}_{15}$.

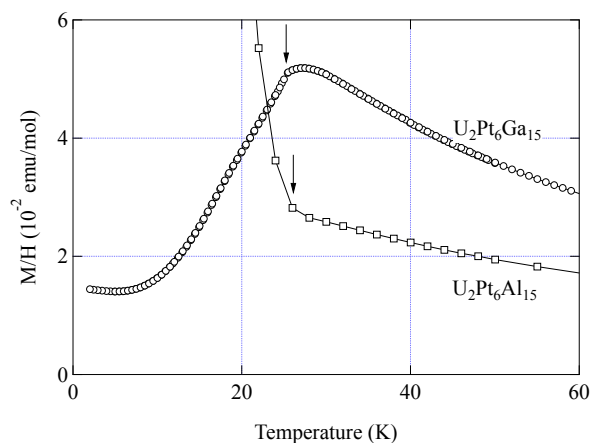


Figure 1. Temperature dependence of magnetization divided by magnetic field for $\text{U}_2\text{Pt}_6\text{Al}_{15}$ and $\text{U}_2\text{Pt}_6\text{Ga}_{15}$.

This result demonstrates that the magnetic properties are drastically modified by substituting Al to Ga. Although the transition temperature is almost the same, the low temperature behavior is completely different. While $\text{U}_2\text{Pt}_6\text{Ga}_{15}$ shows a typical antiferromagnetic behavior, $\text{U}_2\text{Pt}_6\text{Al}_{15}$ shows a steep enhancement of magnetization in the ordered state. Detailed investigation on $\text{U}_2\text{Pt}_6\text{Al}_{15}$ (not shown) further suggests existence of multiple magnetically ordered phases as functions of temperature and applied magnetic field, which cannot be explained by a simple antiferromagnetic ordering.

Present results demonstrate that uranium layers embedded in the metallic Pt-Al(Ga) block show a variety of magnetic characteristics.

REFERENCES:

- [1] Y. Haga *et al.*, JPS Conf. Ser., **29** (2020) 013003-1-5.
- [2] Y. Matsumoto, Y. Haga *et al.*, J. Phys. Soc. Jpn. **90**, 074707 (2021).

PR4-7 Adsorption Characterization of Actinide Chemical Species on Solid Adsorbents

T. Suzuki¹, F. Yin¹, R. Murayama¹, S. Fukutani², A. Sunaga², C. Tabata² and T. Yamamura²

¹Department of Nuclear System Safety Engineering,
Nagaoka University of Technology

²Institute for Integrated Radiation and Nuclear Science,
Kyoto University

INTRODUCTION: We have been studying the solid adsorbents for separation and recovery of actinides [1], and actinide analysis [2]. Recently, the supply of α -nuclides for α -therapy is becoming increasingly important. For the purpose, the actinides separation from the decay series is required. In this year, the adsorption behaviors of actinides on polyvinylpyrrolidone (PVPP) and styrene (Sty)-divinylbenzene (DVB) type pyrrolidone resin were investigated. Especially, we obtained the extended data about adsorption of thorium ion on PVPP, and investigated the cross-linkage effects on the adsorption. In addition, we studied the dissolution methods of thoria.

EXPERIMENTS: We used the commercially available type PVPP (Alfa Aesar) and synthesized pyrrolidone resin in our laboratory. The synthesized resins are *N*-vinylpyrrolidone (VP)/ Sty/DVB copolymers. These resins were synthesized with the different mixing ratio of monomers by the bulk -polymerization method. The proportion of DVB and total monomer is same to cross-linkage degree. The thorium ion was used in ICP-MS standard solution (XSTC-311, SPEX) and uranyl ion was used in XSTC-289. The adsorption behaviors were discussed by using distribution coefficient, K_d [mL/g]. K_d s were obtained by batch experiment.

RESULTS: The adsorption behavior of thorium ion in HNO_3 solution is shown in Fig.2. We confirmed that the thorium is strongly adsorbed on PVPP in higher concentration of HNO_3 , while thorium is weakly adsorbed in lower concentration of HNO_3 . The results of the dependence of adsorption on the mixing ratio of monomers are shown in Fig. 2. Percentage of DVB means the cross-linkage degree. K_d s are standardized by percentage of VP. We confirmed the cross-linkage effects on adsorption of uranyl ion on pyrrolidone resin in HNO_3 solution. The difference of adsorption behaviors by VP-ratio can be explained by the difference of permittivity and hydrophobicity of resins. The normalized distribution coefficient increases or decreases depending on cross-linkage degree in the case of constant VP percentages. The adsorption tendency is varied between the VP percentage of 70% and 60%. We found that this tendency change is related with the surface potential of resin. However, the mechanism of surface potential change is not clarified, although we infer this effect due to the swelling-shrinking tendency of resin [3].

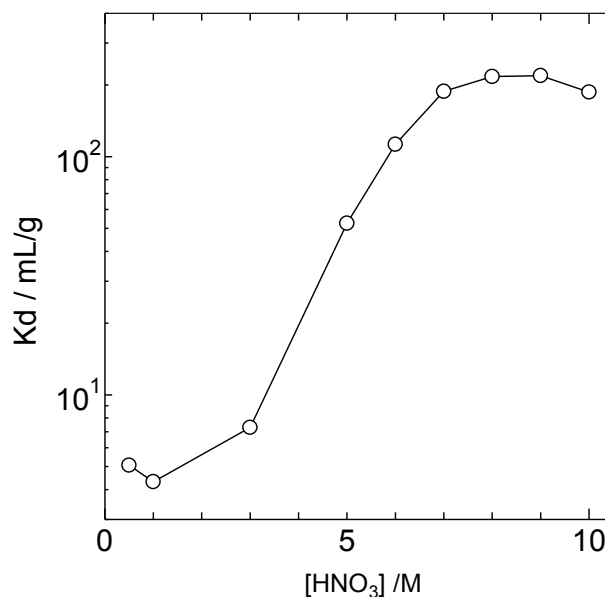


Fig. 1. Adsorption behavior of thorium ion on PVPP in HNO_3 solution.

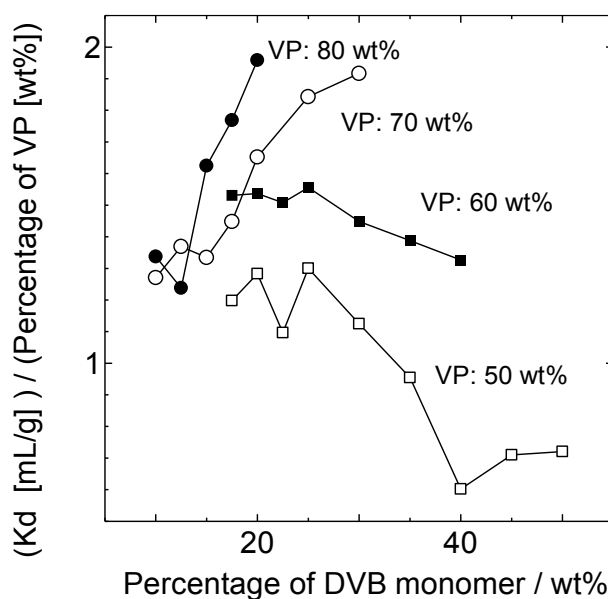


Fig. 2. Cross-linkage effects on adsorption of uranyl ion on pyrrolidone resin in HNO_3 solution.

REFERENCES:

- [1] 鈴木達也, 日本イオン交換学会誌, 30 (2019) 33-38.
- [2] T. Suzuki, *et al.* J. Radioanal. Nucl. Chem., 318 (2018) 221-225.
- [3] T. Yamamizu, *et al.*, Jpn. J. Polymer Sci. Technol., 47 (1990)49-56. (in Japanese)

PR4-8 A Study on Effect of Polymer Network on Resins for Separating Actinyl Ions

M. Nogami¹, C. Tabata², M. Yokota¹, H. Kita¹, and T. Yamamura²

¹Faculty of Science and Engineering, Kindai University

²Institute for Integrated Radiation and Nuclear Science, Kyoto University

INTRODUCTION: Development of highly selective compounds for actinyl ions in aqueous media (extractants, precipitants, resins, etc.) has been important. We have been focusing on monoamide compounds (Fig. 1) as promising candidates for nitric acid media, considering the possibility of complete incineration of waste compounds (so-called "CHON principle"[1]). For the resins, we have taken two factors into accounts for selective interaction between functional monoamide groups and actinyl ions; one is "chelating effect" of the ring formed by polymer monoamides and actinyl ion(s), and the other is "flexibility" of monoamide. Our previous experimental results suggest that the contribution of "chelating effect" is predominant. This report describes our past one year's activity in the above research field.



Fig. 1. Chemical structure of monoamide compounds (R, R', R'' : hydrocarbon group)

RESULTS: We made fruitful discussions with other research groups especially through symposiums organized by IIRNS. For developing our resins, we have devoted our attention to the interaction between functional monoamide groups and actinyl ions as described above. However, we were given a comment on the importance of "component except functional monoamide groups", namely, "chemical structure of polymer network" in the resin. In our resins, divinylbenzene (DVB) is basically used as the crosslinking agent. Also, many resins with a longer chain between the functional monoamide group and the main polymer chain consist of derivatives of polychloromethylstyrene. The point of the comment was that the benzene ring included in the above-described compounds might decrease adsorptivity to metal ions, and that, therefore, it would be worth trying for us to newly synthesize resins without benzene rings as the component.

For the suggestion, we have already partially tried. Diethyleneglycoldimethacrylate (DEGDMA : Fig. 2) was used as a crosslinking agent except DVB. DEGDMA consists of methacrylate ester and ether, and has no benzene rings as can be seen. In the earlier study in the field of actinide chemistry by another research group, such crosslinking agents as methacrylate ester system have been investigated for application to those for suspension polymerization of amidoxime resin (Fig. 3) which is well known as the resin for recovery of U from seawater. According to the literature, by mixing one of

these methacrylate esters with DVB, improvement of adsorption capacity and rate have been found compared with the case where only DVB was used as the crosslinking agent. It is basically because addition of methacrylate ester compounds increases hydrophilicity of resins. On the contrary, mechanical strength and acid/base resistance has been found decreased[2].

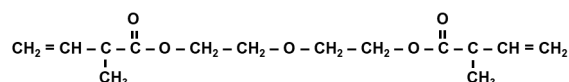


Fig. 2. Chemical structure of DEGDMA

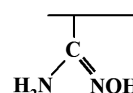


Fig. 3. Chemical structure of amidoxime resin

In our research on crosslinking agents, we synthesized "diamide" resin, not monoamide one, by similarly using the mixture of DEGDMA and DVB. Diamide compounds are famous for the separation of actinide(III) and lanthanide(III) species as well as actinide(IV) and (VI) ones[3]. The applied functional diamide compound was *N,N,N',N'*-tetramethylmalonamide (TMMA : Fig. 4) and the resin was derived from polychloromethylstyrene like monoamide resins with a longer chain. The "TMMA resin" was examined for a column adsorption/elution experiment using Nd(III) under the following conditions ; column : 8 mmφ x 50 mmH, packed resin volume : 2.5 cm³, feed solution : 3 mol/dm³ (=M) HNO₃ containing 10 mM Nd(III), eluent : 0.05 M HNO₃, temperature : 50 °C, SV : 24 h⁻¹. As the result, a distinguished tendency was obtained from the elution experiment. Namely, only ca. 38 % of adsorbed Nd(III) was eluted against our expectation of almost 100 % elution. This strongly suggests that esters in DEGDMA underwent acid hydrolysis followed by the formation of carboxyl and hydroxyl groups which have adsorptivity under low HNO₃ concentration of 0.05 M. Considering the above, applicability of compounds with esters to the component of monoamide resins would be difficult due to unstable characteristics under relatively higher concentration of HNO₃.

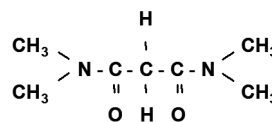


Fig. 4. Chemical structure of TMMA

REFERENCES:

- [1] M. G. B. Drew *et al.*, Dalton Trans. (2007) 244-251.
- [2] H. Egawa *et al.*, J. Atomic Energy Soc. Jpn., **29** (1987) 1079-1086 (In Japanese).
- [3] C. Madic *et al.*, *European Report, EUR19149*; European Commission: Brussels (2000) 9-82.

PR4-9 XAFS study on the aged deterioration of a simulated fuel debris

T. Kobayashi¹, T. Yaita¹, C. Tabata², T. Kubota³, T. Yamamura²

¹Materials Sciences Research Center, Japan Atomic Energy Agency

²Institute for Integrated Radiation and Nuclear Science, Kyoto University

³Agency for Health, Safety and Environment, Kyoto University

INTRODUCTION: For decommissioning the Fukushima-Daiichi Nuclear Power Plant, it is necessary to understand the characteristics of fuel debris. Particularly, for safe and reliable removing of the debris, estimation of the aged deterioration of a debris with changes in environmental conditions could be required. Thus, this study is aiming to investigate the changes in chemical state and structure of a simulated fuel debris under controlled environment simulating conditions inside and/or outside the reactor by XAFS method.

EXPERIMENTS: Currently, the fuel debris inside the reactor is expected to be placed in a high radiation environment and reductive atmosphere while being immersed in water. Thus, in this study, a simulated debris samples prepared by sintering UO_2 and ZrO_2 was immersed in water and the samples were irradiated with γ -ray to simulate the high radiation environment inside the reactor. The samples were prepared at Nuclear Science Research Institute of JAEA and Hot Laboratory of Institute for Integrated Radiation and Nuclear Science, Kyoto University. The γ -ray irradiation was performed at LINAC of Institute for Integrated Radiation and Nuclear Science, Kyoto University. The XAFS measurement was performed at JAEA beamline BL22XU of SPring-8.

RESULTS: As a result, it was found that the uranium on the surface of the sample was oxidized from tetravalent to hexavalent and the U-O distance was shortened, by immersing samples in water and irradiating it with γ -rays (Fig. 1). From the comparison of the samples in which the immersion time and the γ irradiation time were varied, it was revealed that the oxidation reaction mainly occurred during the γ -ray irradiation. Furthermore, even if the sample was picked out from water and exposed to the air atmosphere, no change was observed in the valence or local structure of uranium, suggesting that debris may be stable in the atmosphere.

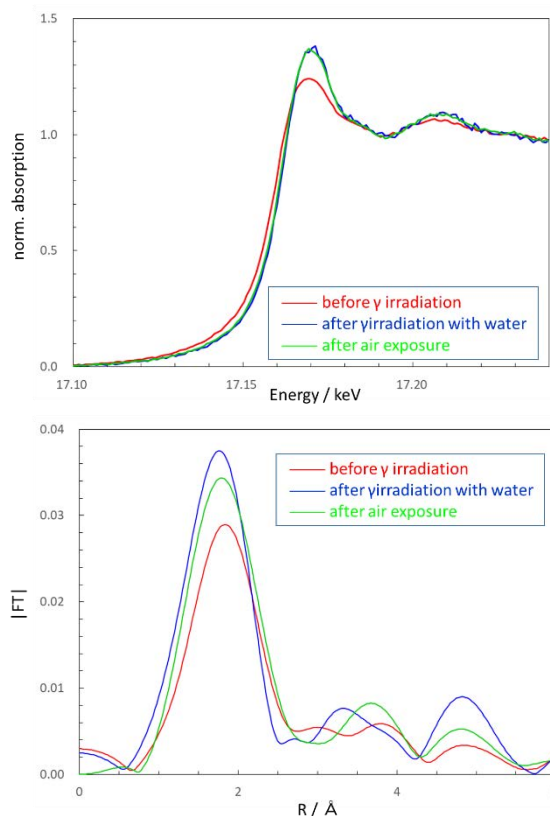


Fig. 1 XANES spectra (upper) and radial structure functions (lower) of simulated fuel debris under several conditions.

PR4-10 Synthesis of nobel phthaloyanine derivatives and effect of substituent on recognition of light actinide and chemical property-3

M. Nakase¹, M. Harigai¹, C. Tabata², T. Yamamura²

¹Institute of Innovative Research, Tokyo Institute of Technology

²Institute for Integrated Radiation and Nuclear Science, Kyoto University

INTRODUCTION: Effective separation of U from Th and other fission products in spent Th fuels is needed in Th fuel cycle. To enable the separation, thorium–uranium extraction (THOREX) process, like the plutonium–uranium redox extraction (PUREX) process, has been studied [1]. In the THOREX process, UO_2^{2+} is extracted by tri-*n*-butyl phosphate (TBP) with the aid of $\text{Al}(\text{NO}_3)_3$. Some of the other extractant which consisted of C, H, O, N atoms (CHON principle) such as monoamide is recently reported for U/Th separation [2]. In this study, Phthalocyanine (Pc) was selected as the main structure of the extractant which also satisfy the CHON principle. To make the solubility of Pc in organic solvent higher, the Pc derivatization is ongoing. The Pc-metal complex in organic solvent itself is interesting to investigate. To obtain the complex with actinide, the purification technique with minimized waste production is highly desirable. In FY2021, some of the purification techniques were tested including chromatography, Solxlet extraction and sublimation. This year, some of the purified samples, mainly Pc-Zn compounds were characterized as well as the other samples.

EXPERIMENTS: The Pc-Zn complex was purified by sublimation by the hand-made apparatus equipped last year as shown in **Figure 1**. The pure product was supposed to be solid (powder), but the obtained product was slightly wet maybe due to the moisture in the air since the Pc-Zn sample was exposed in the hot temperature. By the ¹H-NMR, judgement of purification condition was difficult due to the similarity of the Pc and the substructure of Pc such as phthalonitrile. Therefore, powder x-ray diffraction (PXRD) and Raman spectrophotometry were implemented as well as further purification test. The Laser Raman Spectrophotometer (NRS-3100) is shown in Figure 3

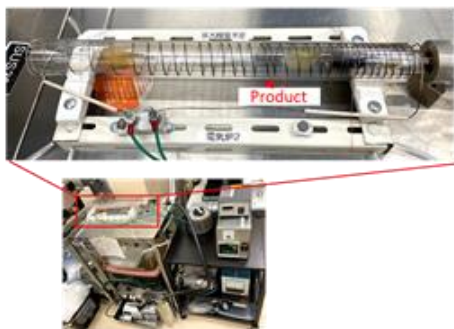


Figure 1 Sublimation setup equipped at Kyoto University.



Figure 2 Laser Raman Spectrophotometer (NRS-3100) .

RESULTS: The Purified Pc-Zn sample and its XRD pattern are shown in Figure 3 and 4. In the XRD pattern, large hallow peak was seen due to the use of ethanol and glass plate, but some of the sharp diffraction attributed to Pc are seen. Therefore, we decide that the purification by sublimation was successful. The Raman spectra in good quality was also obtained and the evaluation by database is ongoing. Raman spectra of other phosphate samples (simulated waste generated in Fukushima Daiichi nuclear Power Station, synthesized in Tokyo Tech) were also measured properly. Due to the strong laser, it seems that the sealed samples can also be measured by adjusting the measurement conditions.



Figure 3 Purified Pc-Zn (left; after sublimation, right; Pc-Zn spread by ethanol for PXRD) .

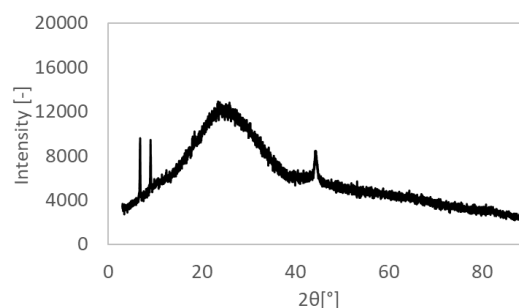


Figure 4 PXRD pattern of sublimated Pc-Zn.

PLANS: We accelerate the synthesis of Pc derivatives and Pc-Actinide complex in both solid and in solution in next year. In addition, some of the irradiated samples such as phosphate waste forms will be shipped to Kyoto University for further characterization.

REFERENCES:

- [1] R.H.Rainey and J.G.Moore, *Nucl Sci Eng*, 10(4), 367–371, 1961.
- [2] P.N.Pathak, *Solv Ext Ion Exch*, 20(3), 293–311, 2002.

I-1. PROJECT RESEARCHES

Project 5

Y. Saito

*Institute for Integrated Radiation and Nuclear Science,
Kyoto University*

1. Objectives and Allotted Research Subjects: Neutron imaging provides valuable information which cannot be obtained from an optical or X-ray imaging. The purpose of this project is to develop the imaging method itself and also the experimental environment for expanding the application area of the neutron imaging. The allotted research subjects are as follows:

- ARS-1: Measurements of Multiphase Flow Dynamics using Neutron Radiography (Y. Saito et al.)
- ARS-2: Evaluation of Water Distribution and Electrochemical Characteristics in Polymer Electrolyte Fuel Cell (H. Asano et al.)
- ARS-3: Neutron Radiography on the Mixing Behavior of Reaction Solution and Cooling (S. Takami et al.)
- ARS-4: Visualization of Dynamic Flow Maldistribution in a Microchannel Heat Exchanger (H. Umekawa et al.)
- ARS-5: Measurement of Frost Distribution by Using X-ray and Neutron Cooperative Imaging (R. Matsumoto et al.)
- ARS-6: Introduction of contrast agent for X-ray-based visualization of roots planted on organic medium (U. Matsushima)
- ARS-7: Effect of the water content of high-strength concrete on the spalling phenomenon under fire (M. Kanematsu et al.)
- ARS-8: Visualization of Excimer cluster tracers by using Neutrons (Y. Tsuji et al.)
- ARS-9: Dynamic Visualization of Hydrogen Accumulation Behavior in Metallic Materials via Neutron Imaging (K. Shimizu et al.)
- ARS-10: In-situ Lithium diffusion behavior in NASICON-Type Structured Lithium Ion Conductive Composite by Means of Neutron Radiography (S. Takai et al.)
- ARS-11 Visualization in the Accumulated Curved Rod Arrays (M. Kaneda)

2. Main results and the contents of this report: To develop neutron imaging, our imaging system was developed so that high-speed imaging could be performed at thermal neutron flux of 10^7 n/cm²s. Such improved system was shared with all of the project members and valuable results were obtained as follows:

ARS-1 improved the above-mentioned high-speed imaging system at the B4 port. In this study, 1-D total variation denoising was applied to image sequences measured by using a system with a high-speed camera and an image intensifier. Such denoising was applied to detect a falling sphere in the air. By applying the 1-D denoising with a parameter $\lambda = 500$, only the noise can be removed.

In addition, a neutron CT system was tested in the E-2 port. In the CT reconstruction process, TomoPy, which is an open-sourced Python toolbox. Developed system was applied to aluminum plates with holes and slits so that the CT reconstruction results could be compared to those at other neutron imaging facilities.

ARS-2 In this study, neutron radiography and electrochemical impedance spectroscopy (EIS) were employed to clarify the relationship between the water contents and the sources of polarization loss in a PEFC. As a result, the relation between the water contents in the PEM and the ionic conductivity is discussed.

ARS-3 applied neutron imaging to the flow visualization of mixing behavior of reactant streams during hydrothermal synthesis. In the synthesis process, cooling of the reaction solution may affect the particle size. In this study, temperature distribution was measured by changing the flow rate of the cooling water. From measurement results, it was confirmed that faster cooling resulted in the production of smaller nanorods.

ARS-4 applied the neutron imaging to visualization of dynamic maldistribution in a microchannel heat exchanger under non-uniformly heated conditions. The effect of heat flux distributions on the maldistribution of liquids was estimated.

ARS-5 applied neutron imaging to frosting behavior in cooling heat exchange system. Simultaneous X-ray and neutron imaging was performed to clarify the 3D frost deposition at the B4 port.

ARS-6 X-ray imaging is not suitable for plant root visualization because of its low sensitivity for biological samples. However, by introducing a contrast agent into the plant roots and increasing the absorption of X-rays compared to rice husk medium, roots in the rice husk medium could be observed. Therefore, this study established a method to locate roots in culture medium with high organic matter using X-ray imaging.

ARS-7 applied neutron to measurement of effect of the water content of high-strength concrete on the spalling phenomenon under fire. In this study, the effect of moisture content on the spalling phenomena of high-strength concrete was investigated by using the neutron imaging technique.

ARS-10 applied to in-situ Lithium diffusion behavior in NASICON-Type structured Lithium Ion conductive composite. From measurement results, it indicates that the material should be changed.

ARS-11 applied to measurement of coolant distribution in the curved rod arrays simulating the stator coil for the future vehicle electro devices. In this study, the coolant visualization inside the simplified stator coil structure is carried out by using the neutron radiography. The coil structure is made of aluminum and composed by layered curved rod array.

ARS-8, 9 were not performed due to the COVID19.

PR5-1 Measurements of multiphase flow dynamics using neutron radiography

Y. Saito, D. Ito and N. Odaira

*Institute for Integrated Radiation and Nuclear Science,
Kyoto University*

INTRODUCTION: Enhancement of the spatial and temporal resolutions in neutron radiography (NRG) is very important for multiphase flow visualization. In this work, image denoising for high-speed neutron imaging was evaluated to observe the dynamic phenomena, and the neutron computed tomography (CT) system was improved to enhance spatial resolution.

IMAGE RESTORATION FOR HIGH-SPEED IMAGING: In high-speed neutron imaging, image noise reduction is very important to understand the phenomena from the acquired images. A lot of filtering methods have been tested to improve the neutron transmission image quality so far. In this study, 1-D total variation denoising [1] was applied to image sequences measured by using a system with a high-speed camera and an image intensifier. Figure 1 shows neutron transmission images of a free-falling metallic sphere in the air. The frame rate is 2000 fps and the exposure time is 1/3000 sec. Although the motion of the sphere can be observed, the images include many noises. The result of denoising is shown in Fig. 2. The change of the grayscale at the center point of the image in Fig. 1 is plotted. The original signal represents the large fluctuation. By applying the 1-D denoising with a parameter $\lambda = 500$, only the noise can be removed. However, the signal of the falling sphere is lost as increasing the denoising parameter. Thus, optimization of the parameter should be done for each measurement object.

IMPROVEMENT OF CT SYSTEM: To increase the spatial resolution in neutron CT, a fine rotation angle and sufficient statistical accuracy are required. So, it takes a long time to get a good result. In this study, our CT system was improved to optimize the CT parameter like rotation angle and exposure time in the E-2 port. The schematic diagram of the system is illustrated in Fig. 3. A CCD camera and a rotation stage are controlled by the same software, which is developed by LabVIEW (National Instruments), on a PC. In the CT reconstruction process, TomoPy [2] which is an open-sourced Python toolbox is used. This library has a lot of reconstruction algorithms, and the grid reconstruction is chosen in the present process. The example of the CT reconstruction of measured images at the E-2 port is shown in Fig. 4. The sample is aluminum circular plates with small holes and slits. The rotation angle is 0.6 degree and the exposure time is 150 sec. As a result, it takes about 13 hours for a measurement. The location and size of the small holes could be observed clearly from the reconstructed images.

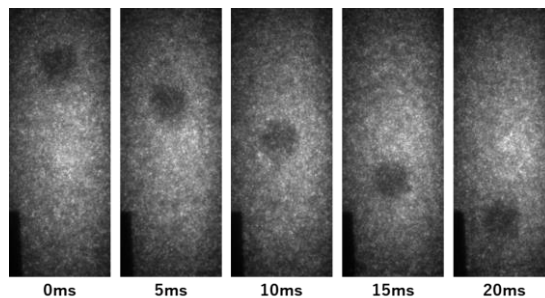


Fig. 1 Neutron transmission images of a free-falling sphere.

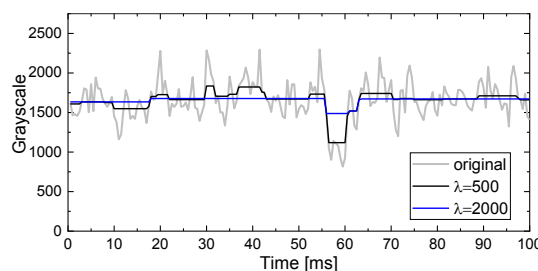


Fig. 2 Time-series grayscale value of the original and denoised signals.

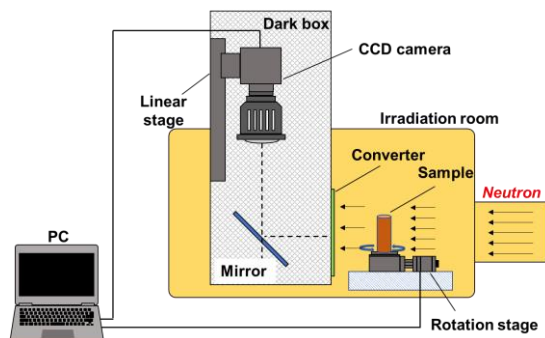


Fig. 3 Improved CT system in E-2 port.

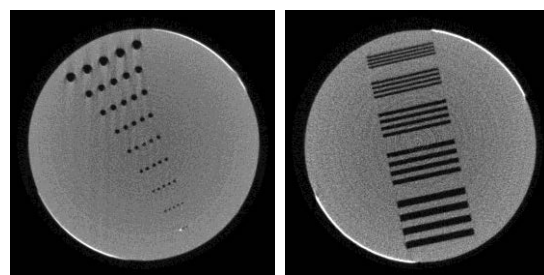


Fig. 4 Neutron CT reconstruction results of aluminum plates with holes and slits.

REFERENCES:

- [1] S.J. Kim, K. Koh, S. Boyd and D. Gorinevsky, L1 Trend Filtering, *SIAM Review*, **51-2** (2009) 339-360.
- [2] <https://github.com/tomopy/tomopy>

PR5-2 Evaluation of Water Distribution and Electrochemical Characteristics in Polymer Electrolyte Fuel Cell

H. Murakawa, K. Mine, K. Mizushima, K. Sugimoto, H. Asano, D. Ito¹ and Y. Saito¹

Graduate School of Engineering, Kobe University
¹Institute for Integrated Radiation and Nuclear Science, Kyoto University

INTRODUCTION: Water management is a key topic of a polymer electrolyte fuel cell (PEFC). It is well known that the water accumulation in the gas diffusion layer (GDL) increases the polarization resistance, whereas the increase in the water content in the proton exchange membrane (PEM) decreases the proton conductivity in the PEM. The water distribution may change during the PEFC operation because of the water generation. However, the effect of water distribution and the water contents in the GDL and the membrane on the resistances has not been fully understood because of the difficulty of measuring water distributions in the PEFC. In this study, neutron radiography and electrochemical impedance spectroscopy (EIS) were employed to clarify the relationship between the water contents and the sources of polarization loss in a PEFC. As a result, the relation between the water contents in the PEM and the ionic conductivity is discussed.

EXPERIMENTS: A small size PEFC having a single-serpentine gas channel with a cross-sectional area of $1 \times 1 \text{ mm}^2$ was used for measuring two-dimensional water distribution and the electrochemical characteristics. Nafion® NR-212 was used as the PEM with a thickness of approximately $90 \text{ }\mu\text{m}$ having catalyst layers on both the anode and cathode sides. Two-dimensional water distributions were obtained every 60 sec during the PEFC operation using neutron radiography. The EIS measurements were simultaneously carried out with the neutron radiography for evaluating the PEM resistance and the reaction resistance. The experiments were carried out at room temperature.

RESULTS: Fig. 1(a) shows an example of the two-dimensional water distribution at a current density, i , of 158 mA/cm^2 with MPL in the parallel channels at 20 min after the start of the PEFC power generation. Condensation water is confirmed as indicated black color. It can be confirmed that the condensed water remains in the flow channels. The relation between the ionic conductivity, σ , and the water contents in the PEM, λ , was evaluated based on the experimental results. Since it was difficult to evaluate the absolute value of λ , the difference in water content, $\Delta\lambda$, was evaluated.

Fig. 1(b) shows the relationship between $\Delta\sigma$ and $\Delta\lambda$ obtained under various experimental conditions, *i.e.* single-serpentine or nine-parallel gas channels, and current density. It is clear that $\Delta\sigma$ almost linearly increases with $\Delta\lambda$. It is thought that the ionic conductivity can be evaluated as a function of the water content in the PEM re-

gardless of the difference in the experimental conditions. Springer et al. [1] proposed a correlation between the ionic conductivity of the PEM and the water content in the PEM. In our experiment, the ionic conductivity was less affected by the water content than in Springer's model. It is thought that Springer's model cannot be applied under low λ conditions such as at the beginning of the PEFC operation. Based on the experimental results, an empirical equation regarding the water content and the ionic conductivity is proposed particularly for lower λ . Numerical analysis was carried out for predicting the cell voltage to compare with Springer's model and the empirical equation. The results are compared as shown in Fig. 2. By applying the equation to the numerical analysis, the difference in the cell voltage is large until 30 min from the PEFC operation. At the beginning of the PEFC operation, the water content in the PEM is low. Therefore, the difference in the ionic conductivity model affects the prediction of the cell voltage.

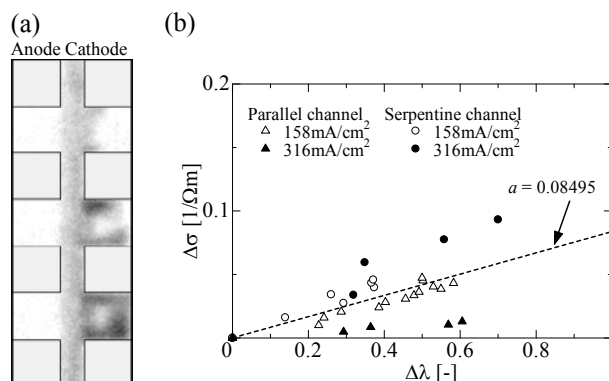


Fig. 1. Examples of the experimental results; (a) Two-dimensional water distributions obtained by neutron radiography; (b) Relation between the change of the water contents in the PEM, $\Delta\lambda$, and the change of the ionic conductivity, $\Delta\sigma$.

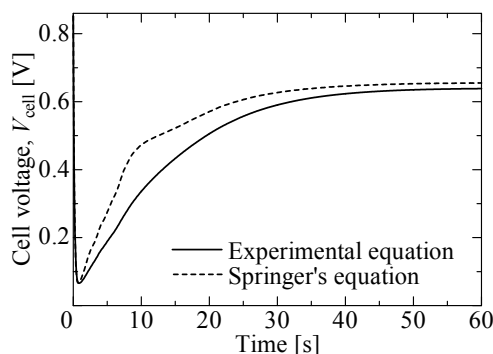


Fig. 2. Effect of the ionic conductivity models on the prediction of the cell voltage by the numerical analysis.

REFERENCES:

[1] T.E. Springer, T.A. Zawadzinski, S. Gottesfeld, J. Electrochemical Society, **138** (1991) 2334–2342.

PR5-3 Neutron Radiography on the Mixing Behavior of Reaction Solution and Cooling Water at a T-shaped Junction in a Flow-type Supercritical Hydrothermal Reactor.

S. Takami, K. Sato, R. Sasaki, B. Xie, M. Kubo¹, T. Tsukada¹, K. Sugimoto², N. Odaira³, D. Ito³, and Y. Saito³

Graduate School of Engineering, Nagoya University

¹ Graduate School of Engineering, Tohoku University

² Graduate School of Engineering, Kobe University

³ Institute for Integrated Radiation and Nuclear Science, Kyoto University

INTRODUCTION: We have synthesized metal oxide nanoparticles by mixing a stream of an aqueous reactant solution with another stream of supercritical water in a flow-type reactor. The mixed reaction solution was gradually cooled to room temperature by using a jacket cooler and released from a back pressure regulator. However, the gradual cooling might result in the production of larger nanoparticles with broader size distribution. In this study, we proposed quicker cooling of the reaction solution by mixing cooling water and observed the cooling process by neutron radiography.

EXPERIMENTS: Fig. 1 shows the schematics of the experimental apparatus. A stream of water was fed using a high-pressure pump and heated by an external heater. Simultaneously, another high-pressure pump fed a stream of room temperature water. The two streams were mixed at the mixing point to mimic the cooling process of the reaction solution by mixing. Toward this mixing point, a neutron beam was irradiated and radiography images were obtained using ⁶LiF/ZnS scintillator screen.

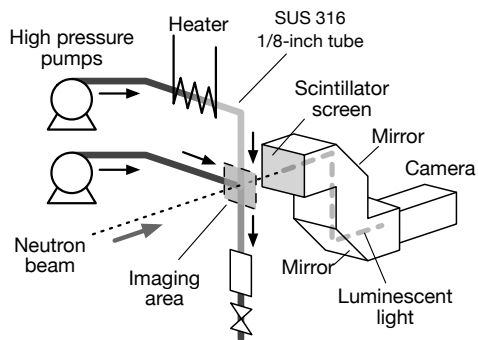


Fig. 1. Schematics of the experimental apparatus.

RESULTS: Fig. 2 shows the averaged water density in the flow channel around the T-shaped junction. The heated water (380°C, 12 g/min) was supplied from the top while the cooling water was supplied from the side (12~36 g/min). When the flow rate of the cooling water was 12 g/min, the cooling water gradually mixed with the heated water in the vertical tube. On the other hand, faster cooling was expected when the flow rate of cooling water was 24 and 36 g/min. To evaluate the change in the temperature of the heated water from the top, we evalu-

ated the density of water at the center of the vertical flow channel and estimated the temperature. Figure 3 shows the change in the temperature in the vertical tube.

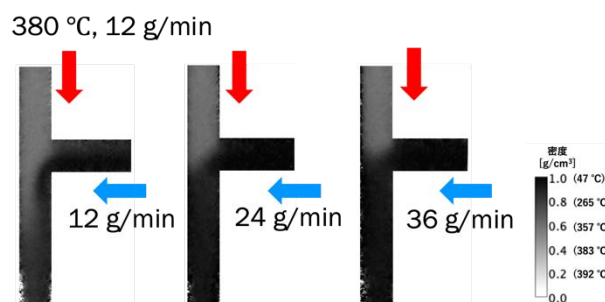


Fig. 2. Averaged water density in the flow channel. Heated water (reactant solution) and cooling water came from the top and the side, respectively.

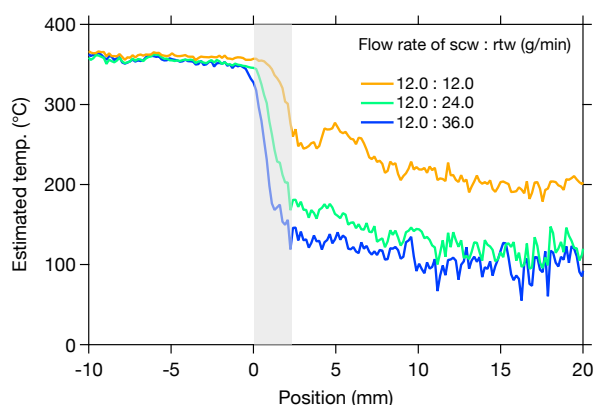


Fig. 3. Estimated temperature of the heated water in the vertical tube around the T-junction. Cooling water was mixed where the position was between 0~2.3 mm.

When the flow rate of cooling water was 24 and 36 g/min, much faster cooling was realized. We then synthesized ZnO nanorods while supplying cooling water. The results showed that nanorods with thinner diameters were obtained as we increased the rate of cooling water. These results confirmed that the size of the product by a flow-type reactor can be controlled by the rate of cooling of the reacted solution.

CONCLUSION: By performing neutron radiography measurements, we evaluated the rate of cooling of the reactant solution in the flow-type reactor and confirmed that faster cooling resulted in the production of smaller nanorods.

REFERENCES:

- [1] S. Takami *et al.*, *J. Supercrit. Fluids*, **63** (2012) 46-51.
- [2] K. Sugioka *et al.*, *AIChE J.*, **60** (2014) 1168-1175.
- [3] S. Takami *et al.*, *Phys. Proc.*, **69** (2015) 564-569.
- [4] K. Sugioka *et al.*, *J. Supercrit. Fluids*, **109** (2016) 43-50.

PR5-4 Visualization of Dynamic Flow Maldistribution in a Microchannel Heat Exchanger

H. Umekawa¹, T. Ami¹, R. Funakura¹, K. Orido¹, K. Akiyama¹, Y. Saito², D. Ito² and N. Odaira²

¹Department of Mechanical Engineering, Kansai University

²Institute for Integrated Radiation and Nuclear Science, Kyoto University

INTRODUCTION: Microchannel heat exchanger has several advantages against the conventional fin-tube heat exchanger, thus recently it has been widely used as the heat exchanger of air-conditioning unit. But the structure of microchannel fundamentally causes the flow oscillation especially under non-uniform heat flux condition.

In this series of investigation[1-3], heat and flow characteristics has been evaluated by using a single plate microchannel heat exchanger.

In this report, the quantitatively visualization of a dynamic flow maldistribution by using neutron radiography will be briefly explained.

EXPERIMENTS: The experimental apparatus is a forced convective boiling system, and the working fluid is Methanol. It has low viscosity similar with actual refrigerant (R32), and has enough attenuation coefficient for visualization. The cross section of the test-section is shown in Fig.1, and it has 9 channels with a 1.6mm diameter. The test-section is heated by Joule heating by using nichrome foils attached to the plate surface with 200 mm heating length and it can generate the nonuniform heat flux distribution. The detail construction and procedures can be shown elsewhere[1-3].

RESULTS: Figure 2(a) is a example of the time averaged visualization image under uniform heating condition. In this report, $\exp(-\mu\rho\delta)$ is used as simple image processing.

As shown in this figure, flow maldistribution can be observed visually. In the former experiment[1-3], it was difficult to evaluate the detail flow movement in each channel owing to the lack of the spacial resolution, but in this experiment which used slightly wide channel, the each channel can be clearly distinguished. Then, it can make the time strip image of each flow channel as shown in Fig.2(b). This time strip image is the stacked of time sequence images of each channel, and Fig.3 is the same data at the inlet of the visualization area is plotted against time. On the basis on these data, the propagation of wet/dry area and also correlation of flow fluctuation among each channel will be evaluated. These characteristics will be correlated with the heat transfer characteristics.

REFERENCES:

[1] H. Umekawa *et al.*, The 25th National Symposium on Power and Energy Systems (2021) B135.
 [2] R.Funakura *et al.*, Thermal Engineering Conference (2021) B123.



Fig.1 Cross section of Microchannel.

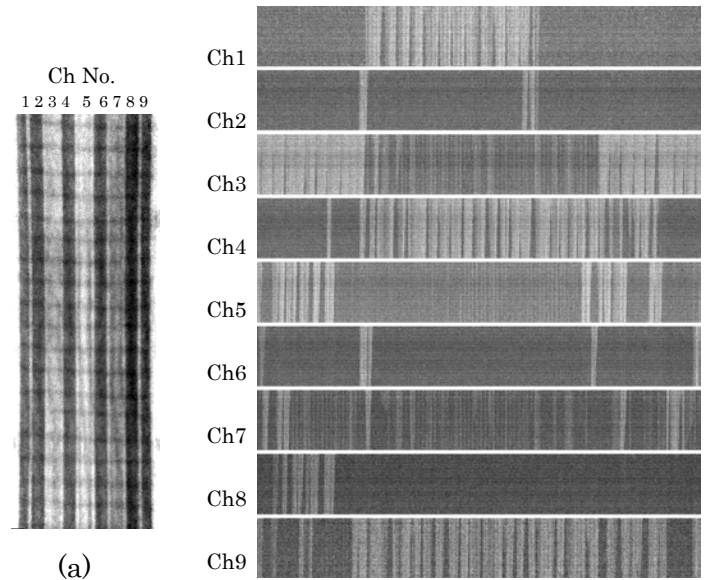


Fig.2 Visualization image ($x_{ex}=0.1$ - $G=50\text{kg/m}^2\text{s}$).
 (a) Time average image (b)Time strip image

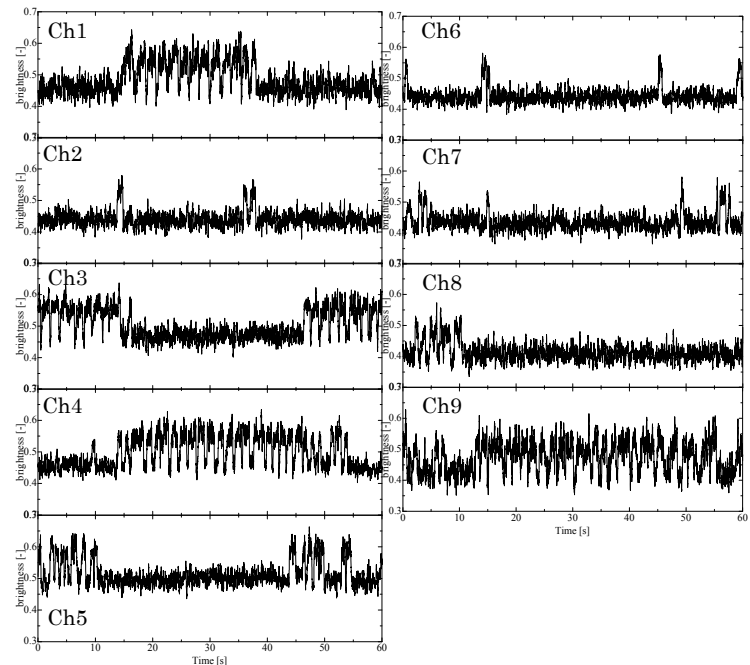


Fig.3 Image processing results in each channel.
 ($x_{ex}=0.1$ - $G=50\text{kg/m}^2\text{s}$)

[3] Sakai Master Thesis, Kansai Univ. (2021).

PR5-5 Measurement of Frost Distribution by Using X-ray and Neutron Cooperative Imaging

R. Matsumoto¹, R. Kuroda², K. Kida², A. Fukai²,
Y. Saito³, D. Ito³ and N. Odaira³

¹Faculty of Engineering Science, Kansai University
²Graduate School of Science and Engineering, Kansai University
³Institute for Integrated Radiation and Nuclear Science, Kyoto University

INTRODUCTION: Recently, heat pumps have been proposed as an effective air conditioning system of heating operation for electric vehicles, because of the inability to use the engine heat as in the conventional vehicles. However, during the heating operation, frosting occurs on the outdoor heat exchanger of the air conditioning system. The frost formation causes a serious energy loss on the battery due to the heat transfer performance degradation by increasing the thermal resistance. In addition, the corrugated fin tube heat exchanger which is mainly used as an automotive heat exchanger has a more complicated structure than conventional one, hence it is difficult to capture the frosting situation. In this study, the frost deposition on the corrugated fin tube heat exchanger was evaluated by X-ray and neutron cooperative radiography imaging in a pseudo-three-dimensional measurement. Last year, the radiography images were obtained by the image intensifier. In this experiment, the scintillator is used for observing the detail frost distribution on the corrugated heat exchanger.

EXPERIMENTAL PROCEDURE: Figure 1 shows the schematic view of the experimental setup. The frost deposition between the fins is measured by irradiating X-ray parallel to the fins of the heat exchanger. The heat exchanger is made of aluminum. Thus, the frost deposition inside of the heat exchanger can be measured by irradiating neutron beam perpendicularly to the fins through the heat exchanger. Flow velocity of cooled humid air adjusted to at 1 m/sec is supplied to the test section. The test section consists of the styrofoam block duct with the corrugated fin tube heat exchanger. The heat exchanger was cooled by circulating the -21 °C fluorinert. The frost deposition on the heat exchanger was observed by CCD camera (Princeton Inst., 16-bit, 1024 × 1024 pixels and 512 × 512 pixels) with scintillator (Fujifilm Co., HR-Ultra Fast HR-16 and Chichibu Fuji Co., ZNSL-L100-AL1016) in every 10 sec for 1200 sec frosting duration. Exposure time is 8 sec for X-ray and 6 sec for neutron beam.

RESULTS: Figure 2 shows the front view of the corrugated fin tube heat exchanger. The heat exchanger consists of flat tubes and the brazed corrugated louver fins. The coolant flows in the parallel flat tubes and the humid air flows in the small fin channels formed by the corrugated louver fins. Figure 3 shows the frost deposition distributions on the heat exchanger using by the scintillator or the image intensifier. X-ray images show the frost formation observed from the front view of the heat exchanger. Last year, the frost deposition was overestimated by using image intensifier on the X-ray imaging. The detailed frost-deposition distribution can be measured by using the scintillator. clearly. The neutron images show the frost deposition inside of the heat exchanger. The main flow direction is left to right on the neutron images in Fig. 3. At 1200 sec, the frost deposits on the

fin front edge. Frost deposition decreases along the flow direction. There is no frost deposition in the downstream of area of the heat exchanger. This result shows the frost deposition distribution in the corrugated fin heat exchanger more clearly by X-ray and neutron cooperative imaging.

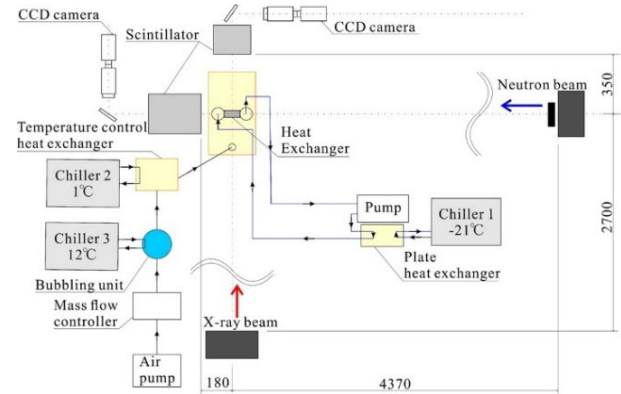


Fig. 1 Schematic view of the experimental setup.



Fig. 2 Front view of the corrugated fin heat exchanger.

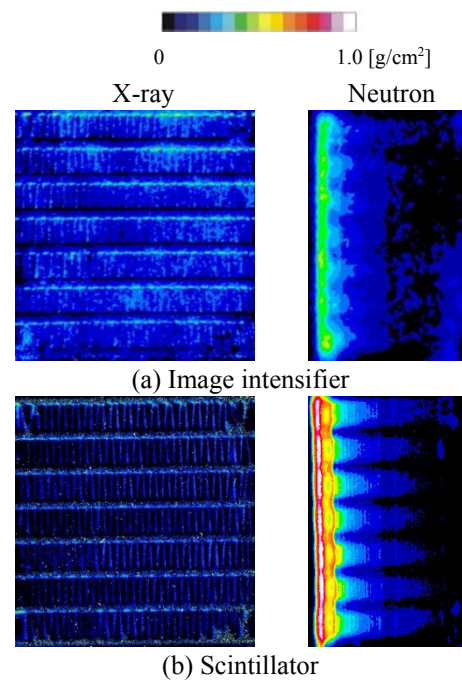


Fig. 3 Frost deposition distributions observed by X-ray and neutron radiography at 1200 sec.

PR5-6 Introduction of contrast agent for X-ray-based visualization of roots planted on organic medium

Uzuki Matsushima¹, Daisuke Ito²,
Yasushi Saito²

¹ Faculty of Agriculture, Iwate University

² Institute for Integrated Radiation and Nuclear Science, Kyoto University

INTRODUCTION: Rice husks are considered an industrial waste product and have been used in rice husk medium, which is a mixture of rice husks and soil at a 3:1 ratio by volume. This inexpensive medium has the advantage of being lightweight, easy to carry, and offers good drainage and resistance to plant root rot. Even if the bottom portion of a potted plant filled with rice husk medium were flooded with water, the capillary rise of the water was less than 8 cm. Therefore, the medium remained dry 8 cm above the waterlogged surface. We investigated the phenomenon of water movement by roots into the arid zone formed in the rice husk medium. This arid region is believed to be a key factor in the development of the plant's ability to tolerate salt. Neutron imaging is sensitive to water, but not minerals, making it suitable for studying water transfer from the soil to the roots. However, in media with high organic matter, such as the rice husk medium, it is difficult to distinguish between roots and the medium, which leads to inconclusive images. X-ray imaging is not suitable for plant root visualization because of its low sensitivity for biological samples. However, by introducing a contrast agent into the plant roots and increasing the absorption of X-rays compared to rice husk medium, roots in the rice husk medium could be observed. Therefore, this study established a method to locate roots in culture medium with high organic matter using X-ray imaging.

MATERIALS and METHODS: Common beans (*Phaseolus vulgaris* L.) were sown in aluminum containers (200 mm height, 25 mm width, and 25 mm depth) filled with rice husk medium and grown until the first true leaf developed. The shoot was cut off leaving approximately 20 mm from the root tip to introduce the iodine solution. To dehydrate the rice husk medium, the bottom of the aluminum container was opened to allow water to evaporate from the roots and nearby medium (Fig. 1). Three iodine solution concentrations of 0.10, 0.25 and 0.05 mol/L were used as treatments, and water was used as a control. The aluminum container was inverted to immerse the stem cut ends into the beaker containing the iodine solution, as shown in Fig. 1. After the cut ends of the sample stems were immersed in the contrast media for 24 hours, they were each packed in a plastic bag and shipped to KURNS, Kyoto University. X-ray imaging was performed at the B4 experimental chamber of the Kyoto University Reactor.

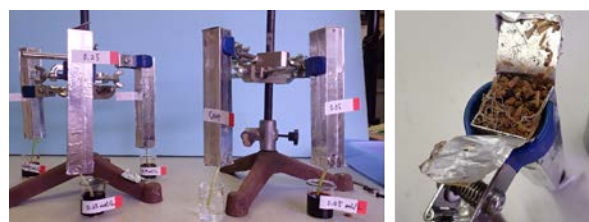


Fig. 1. Introduction of iodine solution into the sample. Left: at the time of introduction; Right: the bottom of the aluminum container is opened.

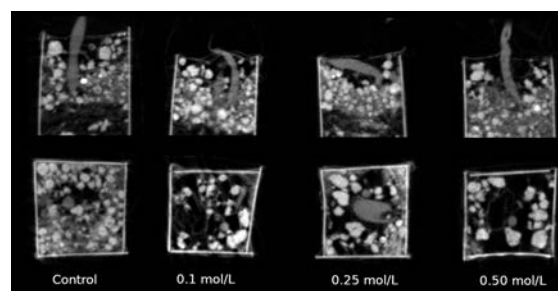


Fig. 2. X-ray CT image. The upper panel is a longitudinal section, and the lower panel is a transverse section. The brighter the pixel, the higher the X-ray absorption at that location.

RESULTS: The stems of the common bean plants turned brown all the way to the root tips after immersion in the iodine solution, confirming that the iodine solution had been introduced into the visible stem and root before the X-ray images were taken. In this experiment, the bottom of the aluminum container was opened to expose the medium and sample roots to air. This exposure caused the water potential of the roots to decrease due to the water vapor pressure difference between the sample root system and the surrounding air. The change created a difference between the root water potential and the osmotic potential of the iodine solution, which was sufficient to introduce the iodine solution into the plant body. The degree of darkness in the X-ray computed tomography (CT) image increased with the degree of the material's absorption of X-rays. The images of the sample stems and roots containing various concentrations of iodine solution were slightly brighter than that of the control sample root (Fig. 2). This indicated that the iodine solution in the plant roots was not sufficient to enhance the X-ray absorption. The contrast agent must contain elements with higher X-ray absorptivity than the iodine solution. The increased X-ray absorption of the plant roots approached that of the soil in the rice husk medium, which made it difficult to distinguish between the roots and the soil in the image. For future studies, it will be necessary to track the visualized roots to determine their shape.

PR5-7 Effect of the water content of high-strength concrete on the spalling phenomenon under fire

M. Yoshioka, T. Hosokawa, A. You, A. Yasue, K. Kobayashi, J. Kim, M. Kanematsu, Y. Nishio¹, N. Odira², D. Ito² and Y. Saito²

Graduate School of Science and Technology, Department of Architecture, Tokyo University of Science

¹*Graduate School of Engineering, Department of Architecture, The University of Tokyo*

²*Institute for Integrated Radiation and Nuclear Science, Kyoto University*

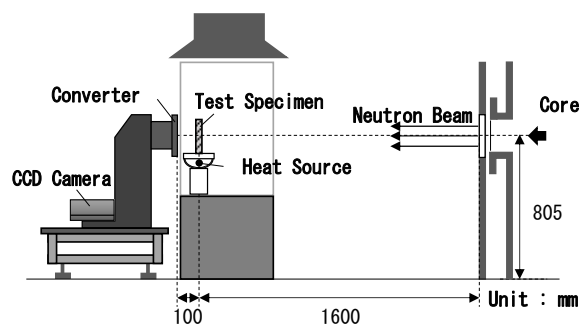


Fig. 1 Schematic diagram of the heating experiment.

INTRODUCTION: In general, reinforced concrete buildings are fireproof structures because they have cover concrete to resist heat from a fire. However, spalling [1] phenomena may occur to lose their cover concrete when the structures were heated by fire, especially in case of using high strength concrete. In the past research, the explanations for this phenomenon have been widely accepted by thermal stress and water vapor pressure, or both. On the other hand, it has been pointed out that the spalling does not occur at the low water content but at the high moisture content. In this study, the effect of moisture content on the spalling phenomena of high-strength concrete was investigated by using the neutron imaging technique.

EXPERIMENTS: Heating experiments were performed on test specimens with target relative moisture contents of 20%, 40%, 60%, 80%, and 100%, in the KUR-B4 port of KURNS. Transmission images were obtained using neutron radiography to detect the moisture behavior inside the specimens to determine the moisture behavior inside the concrete. And at the same time, temperatures at 10 mm and 20 mm from the heating surface were measured by thermocouples. Fig.1 shows the schematic diagram of the test equipment used in the experiment. The specimens are 100×70×30 mm (width × height × thickness) of reinforcing rebar with a cover depth of 30mm. For comparison, two types of cement, Ordinary Portland Cement (OPC) and High-early Strength Cement (HSC), were used. The compressive strength of concrete measured on the day (18 days after the mixing) of the heating experiments was 153N/mm².

RESULTS: It observed the different trends in the spalling phenomenon by the hydrous condition between the specimens of OPC and HSC.

Fig.2 shows an example of a change in the amount of moisture content inside the concrete. Fig.3. shows the relative moisture content inside the concrete just before the explosion. The moisture contents in the specimens tend to increase as the distance from the heating surface increases, regardless of the type of cement or the moisture content. On the other hand, the increase in the moisture content was

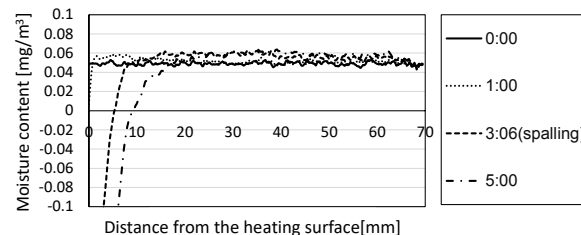


Fig. 2 Changes in the amount of moisture content.

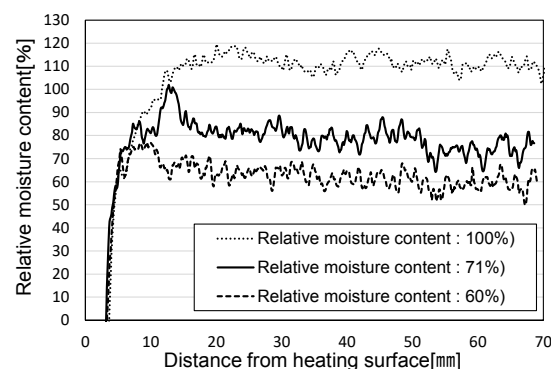


Fig. 3 The effect of initial relative moisture content on the relative moisture distribution just before the spalling.

only at most 0.02mg/mm³, which is equivalent to about 30% of the initial relative moisture content. In addition, in this experiment, no localized increase in moisture content reported as “moisture clog” in previous studies was observed in the relative moisture distribution just before the spalling observed.

Cracks, which were thought to be due to the restraint of reinforcing bars during heating, were observed, however, the effect on the spalling phenomenon due to the presence or absence of reinforcing bars was not confirmed.

Considering the timing of spalling and cracking at the position of the reinforcing bar, it can be said that no cracks were observed in the specimens where thermal stresses were released by the spalling, suggesting that thermal stress may have contributed to the spalling phenomenon.

REFERENCES:

[1] JCI, (2017). “Committee Reports: JCI-TC-154A

S. Takai¹, F. Song¹, H. Chen¹, K. Ota¹, T. Yamamoto¹,
T. Yabutsuka¹, T. Yao², D. Saito³, Y. Saito³

¹Graduate School of Energy Science, Kyoto University

²Kyoto University

³Institute for Integrated Radiation and Nuclear Science,
Kyoto University

INTRODUCTION: Enhancement of lithium ion conduction in oxide-based solid electrolyte is one of the focused issues for the development of All Solid-State Batteries. We have revealed that LaPO₄ dielectric particle dispersion in NASICON-type solid electrolyte LAMP (Li_{1.3}Al_{0.3}Ti_{1.7}(PO₄)₃) improves the conductivity by 3 times [1-3]. The conductivity enhancement is thought to be due to the formation of space charge layer in the vicinity of LaPO₄ / solid electrolyte interface, in which the defect concentration is higher and thus the lithium diffusion occur faster [4]. We have recently measured the tracer diffusion coefficient of lithium ion in pristine and LaPO₄ dispersed LAMP by means of neutron radiography [5]. Due to large neutron attenuation factor of ⁶Li, diffusion profile has been obtained for LAMPs consisting of ⁷Li using ⁶Li as the tracer.

In above experiments, diffusion process has been achieved by simply annealing after applying the tracer. On the other hand, in terms of the battery application, visualization of lithium migration in the solid electrolyte is also significant. In the last year, we have constructed MnO₂ / ⁷Li-LAMP / ^NLi-LAMP / Li_{1.33}Ti_{1.67}O₄ cells to electrolyze for the neutron imaging. Herein, ^NLi indicates the natural isotope ratio of ⁶Li / ⁷Li. However, the lithium transfer at the interface is relatively difficult to observe the lithium migration in ⁷Li-LAMP. Then, in the present study, we changed the cell configuration as LiMn₂O₄ / ⁷Li-LAMP / LiMn₂O₄ symmetry cell to reduce the solid-solid interface.

EXPERIMENTS: ⁷Li-LAMP (Li_{1.3}Al_{0.3}Ti_{1.7}(PO₄)₃) and ^NLi-LiMn₂O₄ pellets were prepared by high-temperature solid-state reaction method. The surfaces of the samples were polished at the both sides of surface to ensure the flat plane with mirror finish. These samples were stacked as the illustration of Fig. 1, heated up to 300 °C to facilitate the lithium migration across the interface, and subjected 0.25 μA of DC current to lead the solid-state electrolysis. The photograph of the apparatus is also shown in Fig. 1. After the electrolysis was started, the entire apparatus was subjected to direct neutron beam for 45 minutes at B4 port of KUR (generated at 1MW). Neutron radiography images were taken by the CCD camera (5 min exposure) every 15 minutes.

RESULTS: Fig. 2 shows the typical radiography images of the symmetrical cell. Since the natural isotope abundance was employed for LiMn₂O₄, the image shows

darker in comparison with LAMP. On the other hand, LAMP shows the whiter image. Comparing the two images of LiMn₂O₄ / ⁷Li-LAMP / LiMn₂O₄ symmetry cell, no significant change was observed for LAMP region, and the trace of lithium migration toward ⁷Li-LAMP cannot be detected. This would be due to the solid – solid interface between LiMn₂O₄ and LAMP is rather severe, restricting DC current down to 1 μA. We are planning to paste LiMn₂O₄ slurry to resolve the difficulty in lithium migration across the interface.

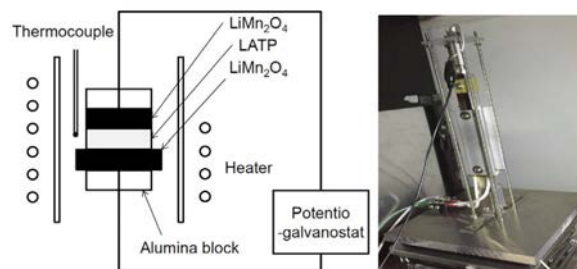


Figure 1 Schematic view and photograph of the apparatus.

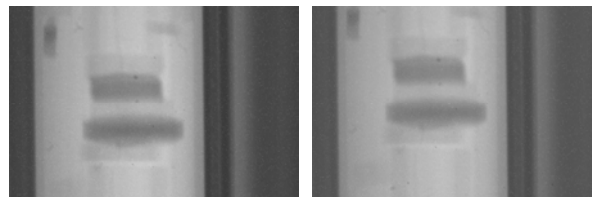


Figure 2 Radiography images of LiMn₂O₄ / ⁷Li-LAMP / LiMn₂O₄ symmetry cell after electrolyzed for (left) 1 h and (right) 3 h.

REFERENCES:

- [1] H. Onishi *et al. Electrochemistry*. 84 (2016) 967.
- [2] F. Song *et al. J. Alloys Compds.* 853(2021)157089.
- [3] F. Song *et al., Materials* 14 (2021) 3502.
- [4] C. C Liang. *J. Electrochemical Soc.* 120 (1973) 1289.
- [5] F. Song *et al., Solid State Ionics* 377 (2022) 115873.

PR5-9 Visualization in the Accumulated Curved Rod Arrays

M. Kaneda, Z. Li, M. Sugimoto

Department of Mechanical Engineering, Osaka Prefecture University

INTRODUCTION: Electrification of vehicles has been promoted to reduce greenhouse gas. The powertrain of the vehicles is the electric motors which is required to have high performance, more power, and compactness [1]. This leads to the higher emission heat density from the motor package and the effective cooling scheme of the heated stator coil has been important. The stator coil in the motor is cooled by the coolant poured from a nozzle above. Although there have been some studies of the temperature measurement [2, 3], the coolant profile inside the coil has not been clarified yet and the pouring conditions are decided empirically. In this study, therefore, the coolant visualization inside the simplified stator coil structure is carried out by using the neutron radiography. The coil structure is made of aluminum and composed by layered curved rod array.

EXPERIMENTS: The schematic model of the experiment is shown in Fig.1(a). The stator coil is presumed by the accumulated curved rod arrays shown in Fig.1(b) where the coolant is directly poured from above. Each square rod is made of aluminum and aligned with a gap of 1mm. This roughly corresponds to the enlarged stator coil structure.

The flow rate of the coolant is 0.5-0.65L/min and the temperature of the coolant is varied from 20-50 degree C. The neutron beam is in horizontal and coaxial direction to the curved coil structure.

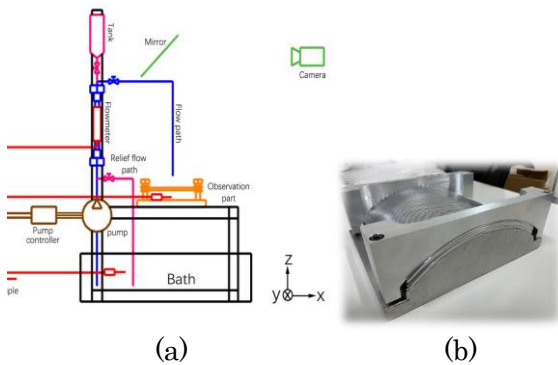


Figure 1. Experimental setup. (a) schematics (b) enlarged stator coil structure

RESULTS: The visualized image of one condition is shown in Fig. 2(a). As expected, the fluid spreads along the structure at lower layer. The rest of the fluid goes down vertically. This profile is converted to the cylindrical coordinate to investigate the fluid volume inside the structure as shown in Fig. 2(b). The fluid profile depends on the flow rate and temperature. Since the fluid viscosity decreases at higher temperature, the fluid area decreases. The higher the flow rate results in the large fluid area.



Figure 2. Visualized coolant profile. (a) snapshot (b) converted to cylindrical coordinate.

By using the neutron attenuation factor of the fluid, the local fluid volume in the spanwise direction can be estimated, which is shown in Figure 3 at 500mL/min. This supports the quantitative temperature dependence.

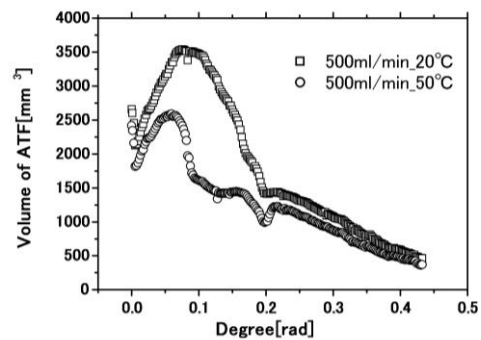


Figure 3. Volume profile of the fluid at 0.5L/min along the circular direction.

The total fluid volume in the structure can be calculated by the integration of the local profile. The flow rate and the temperature dependency can be regarded as the dimensionless number in the horizontal axis and the volume can be normalized by the nozzle diameter, which is partially shown in Figure 4. This yields the linear correlation successfully.

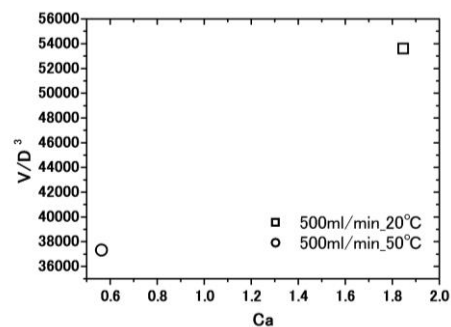


Figure 4. Dimensionless volume versus Capillary number at 0.5L/min.

REFERENCES:

- [1] N. Kobayashi and T. Ikegami, Thermal Sci. Eng., **15**, 2 (2007) 49-54.
- [2] T. Davin *et al.*, Applied Thermal Eng., **75** (2015) 1-13.
- [3] S. Onimaru *et al.*, Denso Technical Review, **13** (2008) 19-25.

I-1. PROJECT RESEARCHES

Project 6

PR6 Advancement of integrated system for dose estimation in BNCT

Y. Sakurai

*Institute for Integrated Radiation and Nuclear Science,
Kyoto University*

BACKGROUNDS AND PURPOSES:

Several types of accelerator-based irradiation system for boron neutron capture therapy (BNCT) are under development at present. But, there are a number of subjects, which should be improved for the further advance and generalization of BNCT.

In the viewpoints of medical physics and engineering, the advance for dose estimation is one of the important subjects. For the characterization of irradiation field, quality assurance and quality control (QA/QC), clinical irradiation to actual patient, and so on, an ultimate goal is to perform the three-dimensional and real-time dose estimation in discriminating for thermal, epi-thermal and fast neutron doses, gamma-ray dose, and boron dose, with simplicity and low effort. Considering about this ultimate dose estimation, several kinds of dose estimation method are studied. It is so difficult to realize the ultimate dose estimation using only one method, but it is necessary to use simultaneously more than two methods.

The purposes of this project research are the advance for various dose estimation methods, and the establishment of an integrated system for dose estimation in BNCT.

In the second year of this research project, 2021, the advancement for the respective dose estimation methods were forwarded mainly using Heavy Water Neutron Irradiation Facility (HWNIF) and E-3 Neutron Guide Tube (E-3) at KUR. The integrated system was considered for the simultaneous usage of several dose estimation methods, same as the previous year.

RESEARCH SUBJECTS:

The collaboration and allotted research subjects (ARS) were organized as follows;

ARS-1 (R3P6-1): Establishment of characterization estimation method in BNCT irradiation field using Bonner sphere and ionization chamber (V). (Y. Sakurai, S. Shiraishi, A. Sasaki, N. Matsubayashi, M. Nojiri, R. Narita, H. Kato, D. Fu, T. Takata, H. Tanaka)

ARS-2 (R3P6-2): Study on new type of neutron energy spectrometer for BNCT. (K. Watanabe, Y. Oshima, A. Ishikawa, A. Uritani, S. Yoshihashi, A. Yamazaki, Y. Sakurai)

ARS-3 (R3P6-3): Development and demonstration of Bonner sphere spectrometer for intense neutrons. (A. Masuda, T. Matsumoto, S. Manabe, H. Tanaka, H. Harano, Y. Sakurai, T. Takata)

ARS-4 (R3P6-4): Improvement of the SOF detector system for energy-dependent discrimination and long-term stability. (M. Ishikawa1, S. Ishiguri, H. Handa, K. Baba, K. Takamiya, Y. Sakurai)

ARS-5 (R3P6-5): First direct observation of boron dose distribution with a boron-added liquid scintillator. (A. Nohtomi, H. Maeda, N. Sakamoto, G. Wakabayashi, Y. Sakurai, T. Takata)

ARS-6 (R3P6-6): Development of absolute epi-thermal neutron flux intensity monitor for BNCT (I. Murata, S. Tada, D. Hatano, S. Tamaki, S. Kusaka, H. Tanaka, Y. Sakurai, T. Takada)

ARS-8 (R3P6-8): Study for microdosimetry using silicon-on-insulator microdosimeter in the BNCT irradiation field (V). (Y. Sakurai, N. Ko, T. Takata, H. Tanaka, T. L. Tran, J. Davis, S. Guatelli, A. Rozenfeld, N. Kondo, M. Suzuki)

ARS-10 (R3P6-10): Measurement of BNCT beam component fluence with multi imaging plate system. (K. Tanaka, Y. Sakurai, C. Hatori, T. Kajimoto, H. Tanaka, T. Takata, G. Bengua, S. Endo)

ARS-11 (R3P6-11): Development of 2D real-time neutron imaging system in the BNCT irradiation field. (S. Uno, T. Koike, K. Miyamoto, R. Hosoya, H. Tanaka)

ARS-12 (R3P6-12): Measurements of neutron fluence and gamma ray distribution using thermoluminescence slabs. (K. Shinsho, M. Tanaka, N. Sugioka, H. Tanaka, T. Takata, G. Wakabayashi, W. Chang, Y. Koba)

ARS-14 (R3P6-14): Development and evaluation of 3D gel dosimeter for the measurement of dose distribution in BNCT. (S. Hayashi, Y. Sakurai, M. Suzuki, T. Takata)

ARS-15 (R3P6-15): Establishment of beam-quality estimation method in BNCT irradiation field using dual phantom technique (V). (Y. Sakurai, N. Kondo, D. Fu, T. Takata, H. Tanaka, M. Suzuki)

ARS-16 (R3P6-16): Development of real-time thermal neutron monitor for BNCT. (H. Tanaka, N. Matsubayashi, S. Kurosawa, T. Takata, Y. Sakurai)

ARS-17 (R3P6-17): Quantitative measurement of 478 keV prompt gamma-rays of boron-neutron capture reaction with the ETCC. (T. Mizumoto, S. Komura, Y. Sakurai, T. Takata, T. Tanimori, A. Takada)

ARS-19 (R3P6-19): Evaluation of neutron irradiation fields for semiconductor device irradiation. (H. Tanaka, N. Matsubayashi, T. Takata, Y. Sakurai)

ARS-20 (R3P6-20): Optimization of bolus shape for boron neutron capture therapy - examination using simple shaped phantom for experimental verification -. (T. Takata, H. Tanaka, A. Sasaki, N. Matsubayashi, M. Nojiri, Y. Sakurai, M. Suzuki)

ARS-22 (R3P6-22): Annealing properties of boric acid infused PVA-GTA-I gel irradiated with neutrons. (H. Yasuda, JE. Taño, CAB. Gonzales, Y. Sakurai)

ARS-23 (R3P6-23): Three dimensional model for pre-clinical assessments in BNCT. (K. Igawa, A. Sasaki, K. Izumi, E. Naito, M. Suzuki, N. Kondo, Y. Sakurai)

ARS-7, ARS-9, ARS-13, ARS-18 and ARS-21 could not be performed because of the influence of COVID-19 infection.

PR6-1 Establishment of characterization estimation method in BNCT irradiation field using Bonner sphere and ionization chamber (V)

Y. Sakurai, S. Shiraishi¹, A. Sasaki¹, N. Matsubayashi¹, M. Nojiri¹, R. Narita¹, H. Kato¹, D. Fu¹, T. Takata and H. Tanaka

*Institute for Integrated Radiation and Nuclear Science,
Kyoto University*

¹*Graduate School of Engineering, Kyoto University*

INTRODUCTION: Development in accelerator-based irradiation systems for BNCT is underway. In the near future, BNCT using these newly developed systems may be carried out at multiple facilities across the world. Considering this situation, it is important that the estimations for dose quantity and quality are performed consistently among several irradiation fields, and that the equivalency of BNCT is guaranteed, within and across BNCT systems. Then, we are establishing QA/QC system for BNCT.

As part of the QA/QC system, we are developing estimation method for neutron energy spectrum using Bonner sphere [1]. For our spectrometer using Bonner sphere, liquid such as pure water and/or boric acid solution is used as the moderator. A multi-layer concentric-sphere case with several sphere shells is prepared. The moderator and its diameter are changeable without entering the irradiation room, by the remote supply and drainage of liquid moderator in the several layers. For the detector, activation foils are remotely changed, or online measurement is performed using SOF detector, etc.

In 2021, the prototype Remote-changeable Bonner-sphere Spectrometer (RBS) was revised. An experiment was performed for the characteristic verification of the prototype RBS at Heavy Water Neutron Irradiation Facility of Kyoto University Reactor (KUR-HWNIF) [2].

MATERIALS AND METHODS: In the neutron energy spectrometry by Bonner-sphere, the combinations of the moderator material and diameter should be previously decided and prepared. Of course, the more information can be obtained as the more moderators and detectors are prepared. However, the information number from those measured data is less than the combination number, because of the overlapped regions among the combinations. The selection is important, in which the more information number is obtained for the combination number.

The combination of moderator and detector is decided, for that the response functions cannot be approximated by the linear functions of the other response functions. The accuracy and precision for the spectrometry can be higher, because the independent information can be obtained from the measurement by the respective combinations. We were developed the selection method, High Independence Selection (HIS) [3].

On the assumption of the application in the standard epi-thermal neutron irradiation mode of KUR-HWNIF, the combination of the moderators for boron-10 concentration and diameter was optimized by HIS. Based on this optimization, the prototype RBS was revised. Some ex-

periments were performed for the characteristic verification of the revised prototype RBS at KUR-HWNIF.

RESULTS: The configuration of the revised RBS was decided as follows. A five-layer concentric spherical acrylic shell is used as a container. Each acrylic wall is 1 mm in thickness. The moderator injection part is 9 mm in thickness for each layer. Pure water and 0.12-wt% boric acid water for boron-10 were used as liquid moderators. Gold wire was used as the detectors. Figure 1. shows the revised prototype RBS.

Unfolding was performed by GRAVEL using the response function of each Bonner sphere corrected by multiplying the ratio for measured/calculated values. The nominal spectrum of the epi-thermal neutron irradiation mode was input as an initial guess.

The comparison between the nominal spectrum and unfolded spectrum was performed. The spectrum obtained by the unfolding reproduced the nominal spectrum relatively well, but the absolute value was overestimated almost one and a half times.

The accuracy of the revised prototype RBS was improved compared with the first prototype RBS. However, the overestimation was not resolved. It is considered that the possible reasons for the overestimation are the differences in sizes between the actually prepared spectrometer, field size, beam directionality, etc..

CONCLUSION: We have the plans to perform (1) the further revision of the prototype RBS and (2) the preparation of a Bonner sphere spectrometer including the remote mechanism for the supply and drainage of the liquid moderators.

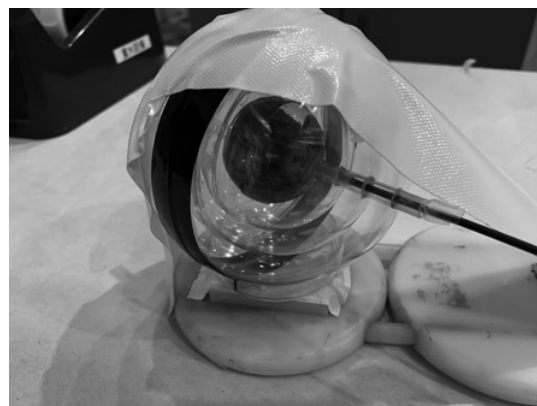


Figure 1. The revised prototype RBS.

REFERENCES:

- [1] S. Shiraishi *et al.*, *Appl. Radiat. Isot.* **163** (2020) 109213.
- [2] Y. Sakurai and T. Kobayashi, *Nucl. Instr. Meth. A* **453** (2000) 569-596.
- [3] H. Ueda, *Doctoral Thesis* (2016).

PR6-2 Study on New Type of Neutron Energy Spectrometer for BNCT

K. Watababe, Y. Oshima, A. Ishikawa¹, A. Uritani¹, S. Yoshihashi¹, A. Yamazaki¹ and Y. Sakurai²

Graduate School of Engineering, Kyushu University
¹ Graduate School of Engineering, Nagoya University
² Institute for Integrated Radiation and Nuclear Science, Kyoto University

INTRODUCTION: Boron neutron capture therapy (BNCT) is one of the radiotherapies. This is a combined modality of radiotherapy and chemotherapy for cancer treatment. In the BNCT, a boron-containing agent, which is concentrated into tumor cells, are irradiated with thermal neutrons and $^{10}\text{B}(n,\alpha)$ reactions are induced. The BNCT is radiotherapy using neutrons. Recently, an accelerator-driven neutron source has actively been developed instead of nuclear reactors, owing to its simplicity of management. The energy spectrum of neutrons, which is irradiated to patients, should be evaluated in order to assure safety of patients.

The conventional technique for neutron spectrometry is the Bonner sphere method. The similar concept is the liquid moderator type neutron spectrometer, in which a small neutron detector can be moved and various neutron responses can be acquired. In this study, we are developing a new neutron detector using an optical fiber. So far, in order to realize the optical fiber type neutron detector showing a neutron peak in the pulse height spectrum, bright neutron scintillators, such as $\text{Eu}:\text{LiCaAlF}_6$ or $\text{LiF}/\text{Eu}:\text{CaF}_2$ eutectics, have been used [1]. Recently, we attempted to replace them with the faster Li glass scintillator[2]. For the both cases, we have never controlled a shape of scintillators because the scintillator size have been too small. Since they had random shapes, the Monte-Carlo simulation based study was difficult to be conducted. In order to evaluate the accurate detector response, the scintillator shape is required to be controlled.

We proposed that a transparent composite Li glass scintillator, in which fine Li glass scintillator powder and resin are mixed. This type of scintillator is expected to be easily shaped because it is a resin-based material. In this study, we fabricate the transparent composite Li glass scintillator and evaluate its response to thermal neutron irradiation.

EXPERIMENTS: We fabricated the transparent composite Li glass scintillator. First, a Li glass scintillator was crushed and grinded in a mortar. And then, fine powder of the Li glass and UV curable resin were mixed. We prepared two types of transparent composite scintillator with different mixing ratio. One of them has the mixing ratio of the UV resin to Li glass powder of 1:2 in weight percent. Other one has the ratio of 2:5. Finally, the mixed resin was irradiated with UV light to solidify the resin. Figure 1 shows a photograph of the fabricated transparent composite Li glass scintillator. They were semi-transparent. A small piece of the fabricated trans-

parent composite Li glass scintillator was mounted at a photocathode of a photomultiplier tube(PMT). The scintillator and PMT were shielded with a black sheet against an ambient light. The signal of the PMT was fed into the digital multichannel analyzer, in which the signal pulse height spectrum was created.



Fig. 1 Photograph of the fabricated transparent composite Li glass scintillator.

RESULTS: Figure 2 shows signal pulse height spectra obtained when the fabricated transparent composite Li glass scintillators were irradiated with thermal neutrons. The neutron source was a Cf-252 source surrounded with a polyethylene moderator. The fabricated transparent composite Li glass scintillator shows a clear neutron peak in the signal pulse height spectrum. The peak pulse height was smaller than that of the bulk Li glass scintillator. There is no difference between the composite scintillators with the different mixing ratio.

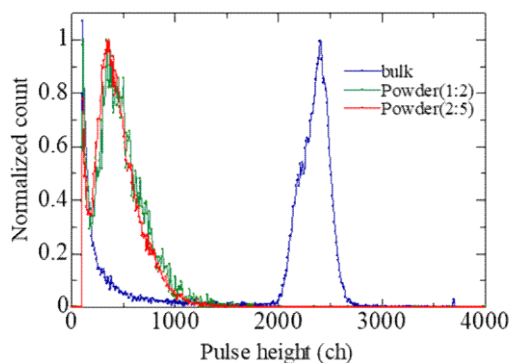


Fig. 2 Signal pulse height spectra obtained when the fabricated transparent composite Li glass scintillator was irradiated with thermal neutrons. The pulse height spectrum obtained by a bulk Li glass scintillator was also plotted.

REFERENCES:

- [1] K. Watanabe *et al.*, Nuclear Instruments and Methods in Physics Research Section A, **802**, 1 (2015).
- [2] A. Ishikawa *et al.*, Sensors and Materials, **32**, 1489-1495 (2020).

PR6-3 Development and demonstration of Bonner sphere spectrometer for intense neutrons

A. Masuda, T. Matsumoto, S. Manabe, H. Tanaka¹,
H. Harano, Y. Sakurai¹ and T. Takata¹

*National Metrology Institute of Japan, National Institute of Advanced Industrial Science and Technology
¹Institute for Integrated Radiation and Nuclear Science, Kyoto University*

INTRODUCTION: Spectrometers for intense neutrons are desired to ensure the performance and safety of boron neutron capture therapy (BNCT). Unfolding method using Bonner sphere spectrometer (BSS) is one of the effective solutions [1]. In this study, two types of Bonner sphere detectors were developed in AIST and demonstrative measurements were carried out at the KURNS.

EXPERIMENTS: Two types of BSS were irradiated by the standard mixed neutron in the heavy water irradiation facility of the KUR [2], as shown in Fig. 1. The first Bonner sphere detectors consist of HDPE moderators and a pair of lithium-glass scintillators, the GS20 and the GS30, coupled with current-integration-operated PMTs [3] [4].

The second ones consist of HDPE moderators and a spherical ³He proportional counter surrounded by a ⁶LiF-loaded neutron absorber. Since the ⁶LiF-loaded layer reduces moderated thermal neutrons just around the thermal neutron detector, detection efficiency is reduced, and the relative response characteristic is not so different from that of the ordinary Bonner sphere detector without the ⁶LiF-loaded layer.



Fig. 1. BSS with a pair of lithium-glass scintillators (left) and BSS with a ⁶LiF-shielded ³He proportional counter (right).

RESULTS: Fig. 2 shows results of the measurements using the scintillator-based BSS. Output values are within the operating range of the system. Net neutron-induced current is derived by subtracting the GS30 current from the GS20 current without correction factors, because the correction factors have not been evaluated for used detectors yet. The results will be corrected using the correction factors [3] and neutron spectral fluence will be derived by the Bonner unfolding method [1].

Fig.3 shows output pulse-height spectra from the BSS with the ⁶LiF-loaded layer. The extent of the pile up was limited within the allowance. Large sphere shows less neutron signals and more γ -ray signals, which resulting

from the neutron capture on hydrogen. The results show that the sensitivity-reduced Bonner sphere detector with the ⁶LiF-loaded layer is acceptable for the BNCT intense neutron beams. Characteristics of the Bonner sphere detectors will be investigated in more detail at AIST and possible combination with neutron detection element will be explored.

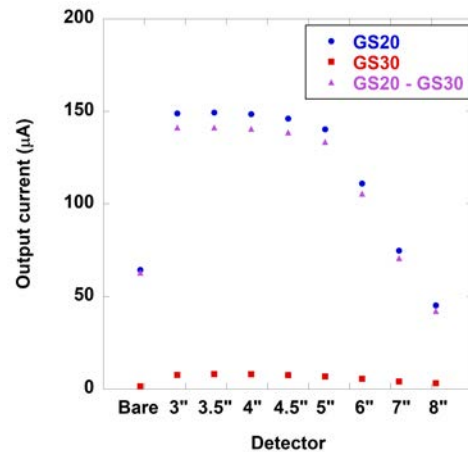


Fig. 2. Measurement results of the scintillator-based BSS.

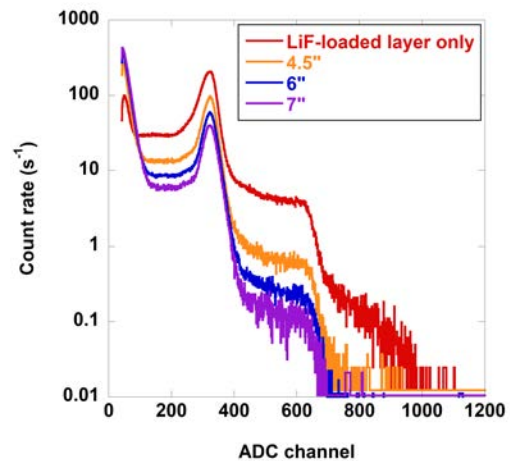


Fig. 3. Pulse height spectra of the BSS with the ⁶LiF-loaded layer.

REFERENCES:

- [1] A. Masuda *et al.*, Appl. Radiat. Isot., **127** (2017) 47-51.
- [2] Y. Sakurai and T. Kobayashi, Nucl. Instr. Mes. Phys. Res. A, **453** (2000).
- [3] T. Matsumoto *et al.*, Radiat. Prot. Dosim., **188** (2020) 117-122.
- [4] A. Masuda *et al.*, 2018 IEEE NSS/MIC Proceedings (2019) 10.1109/NSSMIC.2018.8824697.

This study is supported by Grand-in-Aid for Scientific Research, Japan Society for the Promotion of Science (JSPS KAKENHI Grant Number 19K12638).

PR6-4 Improvement of the SOF detector system for energy-dependent discrimination and long-term stability

M. Ishikawa^{1,2}, Shu Ishiguri², H. Handa², K. Baba², K. Takamiya³ and Y. Sakurai³

¹Faculty of Health Sciences, Hokkaido University

²Graduate School of Biomedical Science and Engineering, Hokkaido University

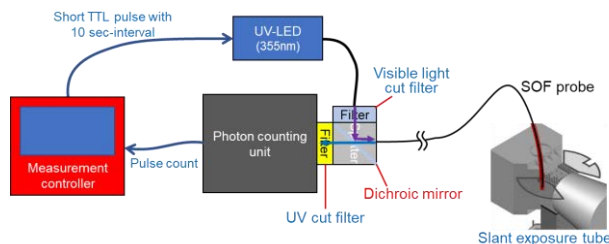
³Institute for Integrated Radiation and Nuclear Science, Kyoto University

INTRODUCTION: In the conventional BNCT, thermal neutron flux and thermal neutron fluence during treatment could not be measured in real time because gold wire activation was used to evaluate thermal neutron fluence. Therefore, we developed a detector (SOF detector; Scintillator with Optical Fiber Detector) with a plastic scintillator attached to the tip of the optical fiber, tried real-time measurement of thermal neutron flux in neutron capture therapy, and got good results. The long-term stability of the SOF detector and the wide measurement dynamic range (linearity of 10^4 to 10^{10} n/cm²/s) have been confirmed in previous collaborative experiments. [1,2] However, signal degradation of SOF detector in long-term exposure was reported [3]. The signal degradation might not be a significant problem in case that calibration can be performed before use. However, signal degradation greatly affects measurement accuracy in case of long-term monitoring because calibration prior to use is difficult. From the previous experiment, it is presumed that the main cause of deterioration of the SOF detector is due to deterioration of the plastic optical fiber, so we tried to conduct two experiments: (A) monitoring deterioration of the SOF probe by using external UV excited signal and (B) the deterioration-accelerated experiment with an SOF detector probe using a quartz optical fiber.

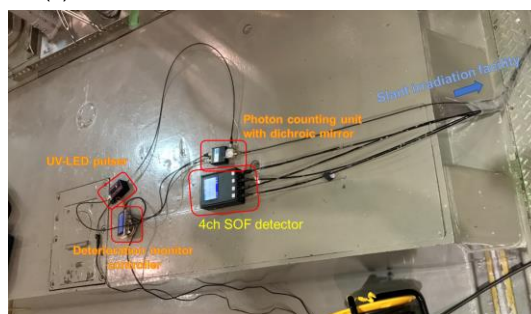
EXPERIMENTS: From the previous experiment, it was presumed that the main cause of deterioration of the SOF detector is due to deterioration of the plastic optical fiber. In order to monitor the SOF probe deterioration, a pulsed UV-LED was used to excite scintillation signals. The decrease of scintillation signals was treated as a comprehensive deterioration including a plastic optical fiber and a scintillator.

Figure 1 shows the deterioration monitoring system using pulsed UV-LED. In addition to the 1-second interval measurement by the SOF detector, the scintillation light excited by the UV-LED was measured once every 10 seconds to assess the deterioration of the SOF probe. Figure 2 shows the SOF signal count rate change during irradiation at the Slant exposure tube with 5 MW. The output of the SOF detector gradually decreases from the start of irradiation and drops to 80% at the end of irradiation. On the other hand, the output of the SOF detector corrected by the measurement by the deterioration monitor system keeps a constant output for 5 hours, indicating that the deterioration correction by the deterioration monitor system is possible.

In addition, as shown in Fig. 3, no deterioration was confirmed in any of the scintillator, the neutron sensitizer (⁶LiF), and the reflector in the measurement using the quartz fiber.



(a) Schematic illustration of deterioration monitor



(b) Experimental setup at the Slant exposure tube

Fig. 1. Deterioration monitor using pulsed UV-LED.

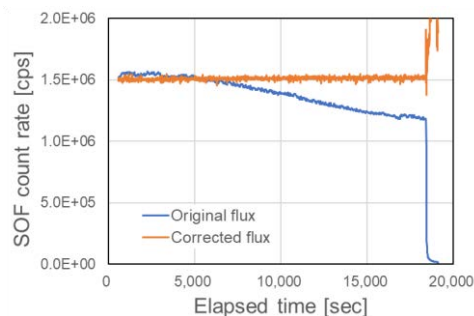


Fig. 2. SOF detector measurement w/ and w/o correction with deterioration monitor system.

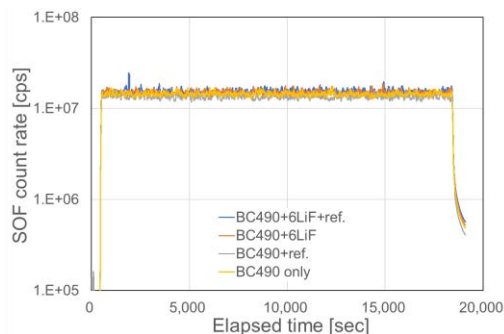


Fig. 3. Deterioration assessment for SOF detector component using a quartz optical fiber.

REFERENCES:

- [1] M. Ishikawa *et al.*, Appl. Radiat. Isot., **61** (2004) 775-779.
- [2] M. Ishikawa *et al.*, Nucl. Instr. Meth., A **551** (2005) 448-457.
- [3] M. Komeda *et al.*, Appl. Radiat. Isot., **67** (2009) 254-257.

PR6-5 First Direct Observation of Boron Dose Distribution with a Boron-added Liquid Scintillator

A. Nohtomi, H. Maeda, N. Sakamoto G. Wakabayashi¹, Y. Sakurai² and T. Takata²

Graduate School of Medicine, Kyushu University

¹Atomic Energy Research Institute, Kindai University

²Institute for Integrated Radiation and Nuclear Science, Kyoto University

INTRODUCTION: For the boron-neutron capture therapy (BNCT), boron dose plays a significant role to kill tumor cells. However, it is very difficult and almost impossible to measure the boron dose distribution directly due to the short ranges of Li and alpha particles in tissue ($\sim 10 \mu\text{m}$) generated by ^{10}B -neutron capture reactions. Instead, the distribution is usually evaluated by calculations with an information of thermal neutron flux. In the present work, direct observation of ^{10}B -neutron capture reactions (so called “boron dose”) was carried out by using a boron-added liquid scintillator [1].

EXPERIMENTS: We dissolved trimethyl borate in a commercially-available liquid scintillator (InstaGel Plus) approximately 1 wt% and 0.25 wt% in natural boron concentration. The boron-added liquid scintillator was filled in a quartz bottle phantom and was irradiated by thermal neutrons ($\sim 10^5 \text{ n/cm}^2/\text{s}$) during 150, 300 and 600 seconds at E-3 irradiation port [2]. Luminescence of the liquid scintillator was observed by a cooled CCD (SBIG, STF8300M) camera during the irradiation in a black box.

RESULTS: As shown in Fig. 1, the luminescence distribution showed a good agreement with that of the energy deposition of Li and alpha particles from ^{10}B -neutron capture reactions calculated by Monte Carlo simulations (PHITS). When trimethyl borate was not dissolved in the liquid scintillator (0 wt%), no visible luminescence was observed even for 600 seconds irradiation. The luminance value recorded by the CCD camera was simply proportional to the irradiation time of thermal neutrons as indicated in Fig. 2.

From the facts mentioned above, it is evident that the observed luminance is originated from Li and alpha particles generated by ^{10}B -neutron capture reactions. This means the luminescence distribution is directly related to so called “boron dose” to liquid scintillator. To the best knowledge of authors, direct optical observation of the boron-dose distribution has not been reported yet experimentally.

This novel technique will be useful for the quality assurance (QA) purposes of BNCT, because instantaneous neutron irradiation may be enough for observation of the actual intense neutron beam of clinical BNCT ($\sim 10^9 \text{ n/cm}^2/\text{s}$) with less amount of addition of trimethyl borate. A quick check of the boron-dose distribution will be promising instead of the conventional gold-wire activation method which is generally very time-consuming task.

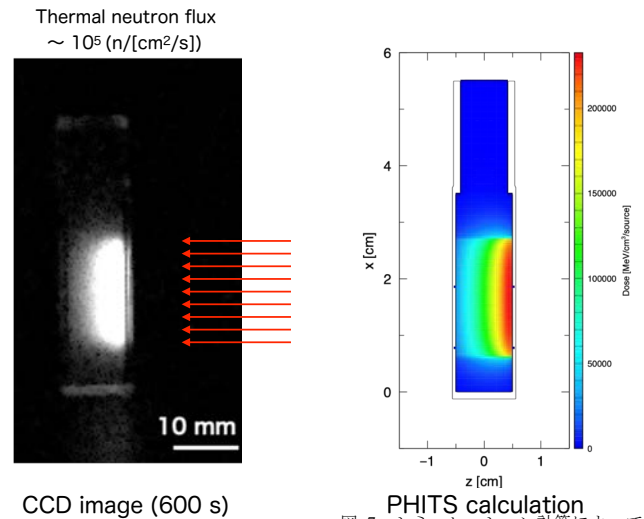


Fig. 1 Visualized boron dose distribution observed by a CCD camera (left) and calculated dose distribution deposited by α and Li particles (right).

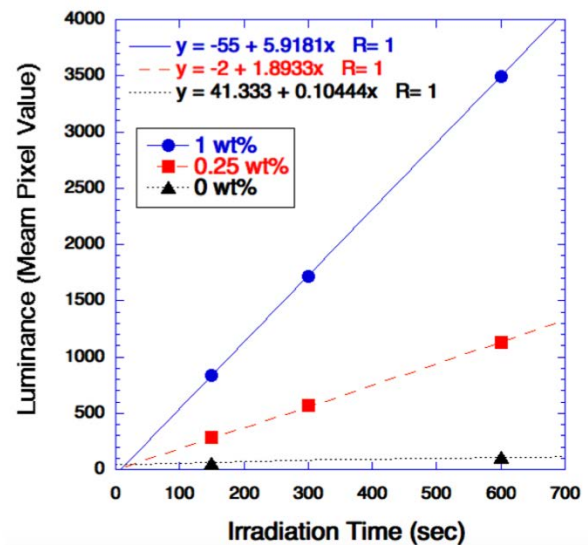


Fig. 2 Luminance value of boron-added liquid scintillator as a function of neutron irradiation time.

ACKNOWLEDGEMENT: This work was partially supported by JSPS KAKENHI Grant Number JP19K08202.

REFERENCES:

- [1] A. Nohtomi *et al.*, Radiol. Phys. Technol., **15** (2022) 37-44.
- [2] T. Kobayashi and, K. Kanda. Nucl. Instrum. Meth., **204** (1983) 525-531.

PR6-6 Development of Absolute Epi-thermal Neutron Flux Intensity Monitor for BNCT

I. Murata, S. Tada, D. Hatano, S. Tamaki, S. Kusaka, H. Tanaka¹, Y. Sakurai¹, T. Takada¹

Graduate School of Engineering, Osaka University
¹Institute for Integrated Radiation and Nuclear Science, Kyoto University

INTRODUCTION: BNCT is a promising cancer therapy which kills tumor cells while suppressing exposure dose to normal tissues. Normally, the neutron field of BNCT has an energy distribution spreading within thermal, epi-thermal and fast neutron regions. Because epi-thermal neutrons are generally used for BNCT, we must measure the epi-thermal neutron flux intensity to evaluate the therapeutic effect and patient's exposure dose. In addition, we also have to evaluate the exposure dose of the fast neutrons that may be harmful to the human body. However, it is quite difficult to know such intensities directly and accurately, because there is no suitable neutron spectrometer or no activation material covering epi-thermal or fast neutrons separately. We are therefore developing new monitors to precisely measure the absolute integral flux intensities of epi-thermal (0.5 eV ~ 10 keV), called first monitor, and fast neutrons (10 keV ~ 1 MeV), called second monitor.[1] The objective of this work is to design and develop the two new detectors and to validate them experimentally.

EXPERIMENTS: The first monitor measures the absolute epi-thermal neutron flux intensity from ⁷²Ga activity created via ⁷¹Ga(n, γ)⁷²Ga reaction by setting a cubic polyethylene (PE) in which a GaN foil is placed at the center. Fig. 1 shows the sensitivity of the first monitor. For the second monitor, two detectors are used, one of which consists of a cubic PE and a GaN foil covered with a Cd sheet is placed at the center (PE type), and the other one is a similar shape to the first monitor, but with a B₄C sheet surrounding the cubic PE (B₄C type). By making difference of the two ⁷²Ga activities, the absolute fast neutron flux intensity is estimated. Fig. 2 shows the sensitivity of the second monitor. In the present study, the performance of the epi-thermal and fast neutron monitors were verified experimentally at KUR, Kyoto University. Irradiations were carried out for 5 and 15 min. in 5 MW operation for the first and second monitors, respectively.

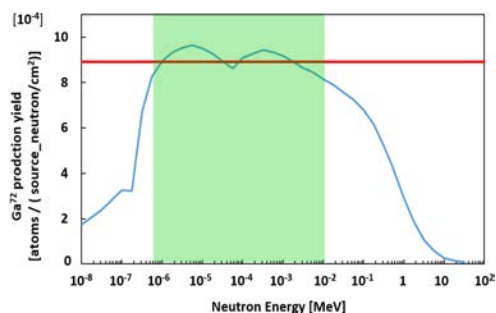


Fig. 1 Sensitivity of the first monitor.

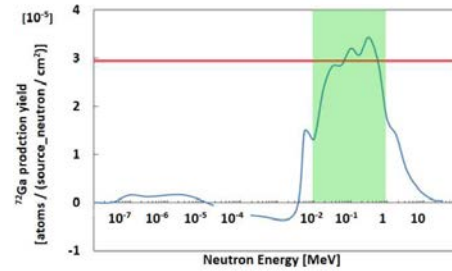


Fig. 2 Sensitivity of the second monitor.

RESULTS: The activities of ⁷²Ga in the monitors were carried out just after their irradiations. The measurements were performed with an HpGe detector. Absolute fluxes were deduced from the obtained activities with the sensitivities shown in Figs. 1 and 2. The results are summarized in Tables 1 and 2. In the tables, the nominal value means the value evaluated at KUR.

Table 1 Absolute epi-thermal neutron flux intensity obtained by the first monitor.

	Experimental value (E)	Nominal value (C)	C/E
⁷² Ga activity [kBq]	$(3.31 \pm 0.05) \times 10^3$	—	—
ϕ_{epi} [n/cm ² /sec]	$(8.67 \pm 0.13) \times 10^8$	7.26×10^8	0.84

Table 2 Absolute fast neutron flux intensity obtained by the second monitor.

	Experimental value (E)	Nominal value (C)	C/E
⁷² Ga activity ^{*1} [kBq]	$(1.32 \pm 0.02) \times 10^3$	—	—
⁷² Ga activity ^{*2} [kBq]	$(1.56 \pm 0.02) \times 10^3$	—	—
ϕ_{epi} [n/cm ² /sec]	0.6×10^7 ^{*3}	4.94×10^7	7.8

*1 For the PE type detector.

*2 For the B₄C type detector.

*3 The estimated error is larger than 100%.

From Table 1, the experimental result of the first monitor is a little larger than the nominal value of KUR. This experimental value was already corrected considering the high energy part of the neutron spectrum. The bare estimation is 5% larger than this value. The first monitor was confirmed to work properly from the present result. On the other hand, as for the second monitor the experimental value shows very small compared to the nominal value. This is due to subtraction of the two activities, namely, as the result the difference is very small and is beyond the statistical errors of the activity measurements. The point is that though the high energy neutron contribution in the neutron spectrum is so small, the sensitivity below 10 keV is not perfectly zero. Now we are modifying the design. Practically, the sensitivity is revised so as to realize zero sensitivity below 10 keV.

REFERENCES:

- [1] Y. Kashiwagi *et al.*, "Development of epi-thermal neutron beam intensity detector with ⁷¹Ga(n,γ)⁷²Ga reaction for boron neutron capture therapy." *Appl. Radiat. Isot.*, **151**, pp.145-149, 2019.

PR6-7 Study for microdosimetry using silicon-on-insulator microdosimeter in the BNCT irradiation field (V)

Y. Sakurai, N. Ko¹, T. Takata, H. Tanaka, T. L. Tran¹, J. Davis¹, S. Guatelli¹, A. Rozenfeld¹, N. Kondo and M. Suzuki

Institute for Integrated Radiation and Nuclear Science, Kyoto University

¹*Kansai BNCT Medical Center, Osaka Medical College*

²*Centre for Medical Radiation Physics, University of Wollongong*

INTRODUCTION: Research and development into several types of accelerator-based irradiation systems for boron neutron capture therapy (BNCT) is underway [1,2]. In the near future, BNCT using these newly developed irradiation systems may be carried out at multiple facilities across the world. In contrast to conventional radiotherapy, the types of radiation present in BNCT consists of many distinct radiation components, each having a different biological weighting factor.

Microdosimetry is an effective dosimetry technique in a mixed radiation environment. Using this technique, it is possible to derive the relative contributions of different radiation modalities. The feasibility study of a novel 3D mesa bridge silicon-on-insulator microdosimeter (SIM) in BNCT [3], developed by University of Wollongong (UOW).

A new-type silicon microdosimeter and its application for boron neutron capture therapy (BNCT) are continuously investigated mainly by Monte Carlo simulation.

MATERIALS AND METHODS: Two detector configurations were investigated, based on the current 3D mushroom microdosimeter. The first structure consists of a cylindrical p+ core electrode through the center of the SV with n+ ring electrode wrapped around the outside of the SV. The second structure consists of a cylindrical n+ core electrode through the center of the SV with p+ ring electrode wrapped around the outside of the SV. Each SV has a diameter and height of 10 μm and the pitch between each individual SV is 40 μm to reduce cross talk between neighboring row of detectors. A total of 2500 individual SVs were connected in an array with odd and even detector row readout channels.

PHITS was used for this study. The T-deposit tally, which scores dose and event-by-event deposition energy distribution was used to calculate the energy deposited inside the SV of the mushroom microdosimeter. The microdosimetric spectrum (frequency mean and dose mean lineal energy distribution) were calculated by dividing the deposited energy by the average chord length of the SV.

The neutron response of the new-type detector were investigated using the neutron source for the mixed neutron irradiation mode of Heavy Water Neutron Irradiation Facility installed in Kyoto University Reactor (KUR-HWNIF) [4].

RESULTS: The ion track of 840 keV Li-7 ions produced inside the p+ region is shown in Figure 1. Similarly,

with the alpha particles, higher number of Li-7 ions were deposited inside the SV with the p+ core through the center.

The number of Li-7 depositing its full energy (840 keV) was also found to be higher with the p+ core design, shown in Figure 2. The range of 840 keV Li-7 ions inside silicon is approximately 2.5 μm . Most of the Li-7 generated inside the p+ core will deposit all its energy inside the SV. However, the Li-7 ions generated inside the p+ ring will only deposit a portion of its energy inside the SV before escaping.

CONCLUSION: It was found that the absorbed dose was approximately 2.4 times more with the p+ core design. No dose was deposited to the surrounding PMMA with the p+ core design.

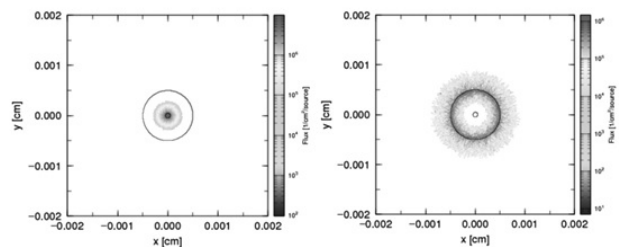


Fig. 1. Ion track of 840 keV Li-7 ions inside a single SV. Left) p+ core through the centre of the SV. Right) p+ ring around the outside of SV.

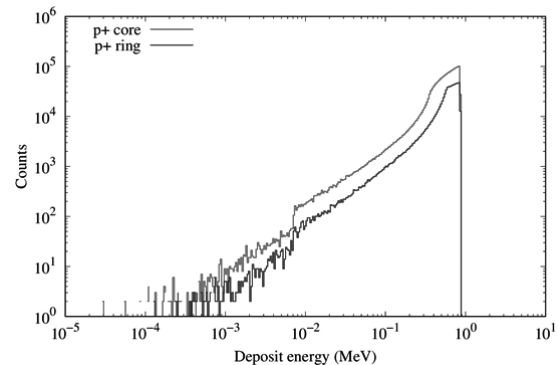


Fig. 2. Deposit energy of 840 keV Li-7 ions inside the SV for p+ core and p+ ring.

REFERENCES:

- [1] H. Tanaka *et al.*, Nucl. Instr. Meth. B **267** (2009) 1970-1977.
- [2] H. Kumada *et al.*, Appl. Radiat. Isot. **88** (2014) 211-215.
- [3] L. T. Tran *et al.*, IEEE Trans. Nucl. Sci. **62** (2015) 3027-3033.
- [4] Y. Sakurai and T. Kobayashi, Nucl. Instr. Meth. A **453** (2000) 569-596.

PR6-8 Measurement of BNCT beam component fluence with multi imaging plate system.

Kenichi Tanaka, Yoshinori Sakurai¹, Chiharu Hatori²,
Tsuyoshi Kajimoto², Hiroki Tanaka¹, Takushi Takata¹,
Gerard Bengua³, Satoru Endo²

*Division of Liberal Arts Sciences, Kyoto Pharmaceutical
University*

¹*Graduate School of Advanced Science and Engineering,
Hiroshima University*

²*Institute for Integrated Radiation and Nuclear Science,,
Kyoto University*

³*Auckland City Hospital*

INTRODUCTION: Measurement of beam fluence spatial distribution is required for quality assurance in the irradiation field for boron neutron capture therapy. This study investigated the use of the multi imaging plate (IP) system which consists of IPs and beam component converters.

EXPERIMENTS: The converter configuration is shown in Fig. 1. The IP is BAS-TR from Fuji Film corporation, Japan. The IP #1 in carbon is to detect gamma rays via secondary electrons, #2 for epithermal neutrons via secondary particles of ${}^6\text{Li}(n,\alpha){}^3\text{H}$ reactions, and #3 for fast neutrons via recoiled protons. Here, material #2 is polyethylene. Material #1 is polyethylene infused with LiF, where ${}^6\text{Li}$ is enriched up to 95 at%. The concentration of ${}^6\text{Li}$ in Material #1 is 10 wt%. The details of the converter was described previously [1].

The experiment was performed with the standard epithermal neutron irradiation mode of KUR-HWNIF [2] at 1 MW. The beam size was set to about $120 \times 120 \text{ mm}^2$ using the collimator. The irradiation for 2 minutes was performed 3 times..

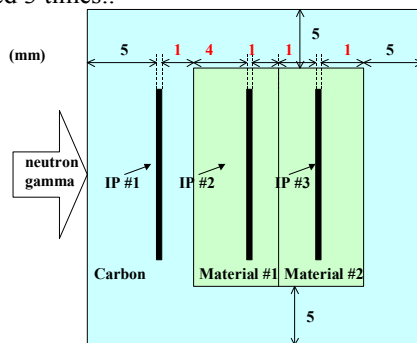


Fig. 1 Converter configuration.
The figure is not in scale.

The fluence ϕ_j of each component was determined using the following model;

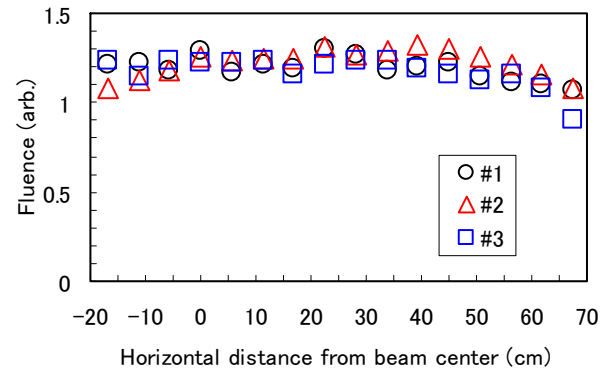
$$PSL = \begin{pmatrix} PSL_1 \\ PSL_2 \\ PSL_3 \end{pmatrix} = \begin{pmatrix} a_{11} & a_{12} & a_{13} \\ a_{21} & a_{22} & a_{23} \\ a_{31} & a_{32} & a_{33} \end{pmatrix} \begin{pmatrix} \phi_1 \\ \phi_2 \\ \phi_3 \end{pmatrix} = A \cdot \phi \quad (1),$$

$$\phi = A^{-1} \cdot PSL \quad (2),$$

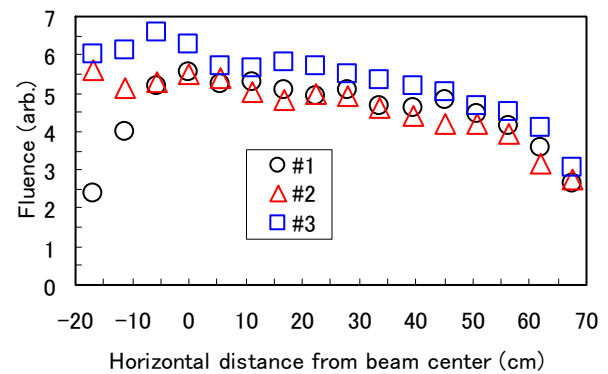
where a_{ij} denotes the response function of the i th IP for the component j estimated by the PHITS simulation [3]

RESULTS: The fluence estimated using the results for the three IPs are shown in Fig. 2. All of three beam components yielded positive values successfully. The reproducibility of the results is about 10-30% in standard deviation. The reduction of the deviation is planned to be investigated.

(a) Gamma rays



(b) Epithermal neutrons



(c) Fast neutrons

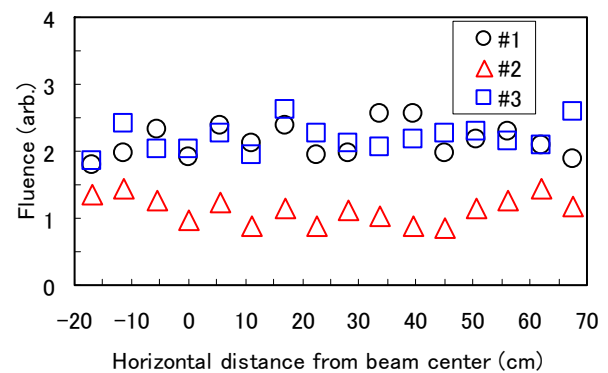


Fig. 1 Estimated fluence distribution.

REFERENCES:

- [1] K.Tanaka *et al.* Appl. Rad. Isot. **115** (2016)212-220.
- [2] Y.Sakurai and T.Kobayashi *Nucl. Instr. Meth.* **A453** (2000)569-596.
- [3] T.Sato *et al.* J. Nucl. Sci. Technol. **50** (2013)913-923.

S. Uno¹, T. Koike², K. Miyamoto³, R. Hosoya³ and H. Tanaka⁴

¹ High Energy Accelerator Research Organization (KEK)

² Faculty of Health Sciences, Kyorin University

³ BeeBeans Technologies Co.Ltd

⁴ Institute for Integrated Radiation and Nuclear Science, Kyoto University (KURNS)

INTRODUCTION: We have been developing a 2D real-time neutron imaging system using a gas electron multiplier (GEM) [1]. Boron neutron capture therapy (BNCT) is a radiation therapy that selectively destroyed tumor cells by means of high linear energy transfer charged particles released by nuclear reaction caused by thermal neutrons irradiation of ¹⁰B. In order to irradiate tumor cells that have taken up ¹⁰B efficiently with thermal neutrons, neutron attenuation by the tissue must be taken into account, so an epithermal neutrons irradiation field are required. For the higher accuracy of BNCT, it is important to quality assurance and control of the irradiation field, such as properly evaluate to spatial distribution and fluence rate of the epithermal neutron beams. In this study, the performance of our system were evaluated using E-3 Neutron Guide Tube (E-3) and Heavy Water Neutron Irradiation Facility (HWNIF) of the Kyoto University Research Reactor.

EXPERIMENTS: Our real-time neutron imaging system consists of a detector module (GEM chamber and readout electronics board) and a PC that controls the detector and processing/display the acquisition data [2]. The detector module has a compact size with dimensions, 444mm × 270mm × 41mm. The effective detection area is 100mm × 100mm. These signals are processed by an FPGA-based data acquisition board, and the resulting digitized neutron event data is recorded to PC via Gigabit Ethernet. The GEM chamber works as a gas radiation detector for neutrons by detecting the charged particles emitted through a ¹⁰B(n, α)⁷Li nuclear reaction. It is incorporates a cathode plane coated with a thin layer (0.05μm thickness) of ¹⁰B, a single GEM used to amplify the charge deposited in the gas of the detector (Ar-CO₂, 70:30, 1atm), and 128 X and 128 Y strips with a 0.8mm pitch strip planes with 2D readout. Detection efficiency for thermal neutrons is 0.2%. Our system have a feature of a spatial resolution of approximately 1 mm (FWHM), an excellent time resolution of 15 ns, low sensitivity to gamma-ray, and Mcps rate capability. The GEM is the double-side printed circuit board, which consists of low temperature co-fired ceramic (LTCC) with 100μm thickness as an insulator and gold layers with 6μm thickness on both sides as an electrode. It has also a large number of holes with 100μm diameter and 200μm pitch (LTCC-GEM) [3]. The LTCC-GEM is quite robust and stability against the large discharge, it is employed to prevent the breakdown of short-circuit between two electrodes of the GEM by abnormal discharge. To evaluate whether this system can image the neutron distribution in real-time, experiments were performed on thermal neutrons at E-3 and epithermal neutrons at HWNIF, and the system response to increased neutron fluence were also evaluated.

tribution in real-time, experiments were performed on thermal neutrons at E-3 and epithermal neutrons at HWNIF, and the system response to increased neutron fluence were also evaluated.

RESULTS: Figure 1 shows real-time spatial distribution of the thermal neutron beam, and its beam profiles. From the measurement (FWTM) of the obtained images, the horizontal and vertical lengths were 14.2mm and 20.6mm, respectively. Those are almost consistent with the actual physical dimension of the collimator (beam collimator aperture H: 14mm, V: 18mm), but the horizontal beam profile was asymmetric (at the base), which shows a tendency similar to the result of Nohtomi et al [4]. The thermal neutron fluence rate was estimated to be $0.5 \times 10^6 \text{ n/cm}^2 \text{ s}$ at a reactor output of 1MW. In the future, it will be necessary to compare it with the evaluation of thermal neutron fluence rate by the activation analysis using gold foil.

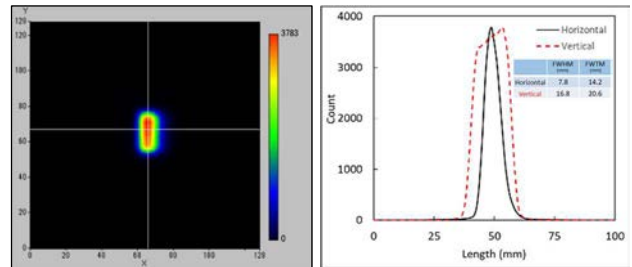


Fig.1. Real-time spatial distribution of the thermal neutron beam, and its beam profiles at E-3.

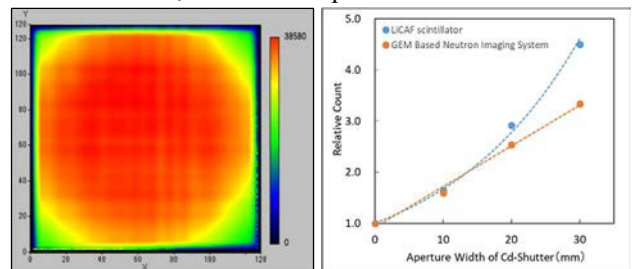


Fig.2. Real-time spatial distribution of the neutron beam and the variation of relative counts on aperture width of Cd-Shutter at HWNIF.

Fig. 2 shows the neutron spatial distribution at the collimator surface at HWNIF. The beam condition of the neutron irradiation field could be evaluated in real-time and the collimator shape could be clearly seen. As a result of changing the aperture width of the Cd-Shutter to increase the neutron fluence, we found that our system showed good counts linearity. It is presumed that the exponential increase in the compared scintillation monitor was due to the location of the detector, and it is necessary to make a more accurate comparison in a similar arrangement.

REFERENCES:

[1] F. Sauli, Nucl. Instrum. Meth. A 386 (1997)531.
 [2] S. Uno *et al*, Physics Procedia 26 (2012)142.
 [3] K.Komiya *et al*, J. Jpn. Soc. Prec. Eng.84.11 (2018)936.
 [4] A.Nohtomi *et al*, KURNS.Prog.Rep.2018 (2019)68.

PR6-10 Measurements of Neutron Fluence and Gamma ray Distribution using Thermoluminescence Slabs

K. Shinsho, M. Tanaka, N. Sugioka, H. Tanaka¹, T. Takata¹, G. Wakabayashi², W. Chang, Y. Koba³

Graduate School of Human Health Science, Tokyo Metropolitan University

¹ KURNS

² Graduate school of Science and Engineering Research, Kindai University

³ Center for Radiation Protection Knowledge, QST-NIRS

INTRODUCTION: Boron Neutron Capture Therapy (BNCT) is one of the radiation therapies using neutrons and ¹⁰B drugs which are attracted to tumors. BNCT is expected to be next-generation cancer therapy which will improve the QOL of patient because it is able to irradiate a cancer cell at the molecular level selectively. However, dosimetry techniques in mixed neutron-gamma fields have not been established yet. Therefore, we focused on neutron and gamma ray measurements using two-dimensional thermoluminescence dosimeter (2D-TLD). The 2D-TLD which we used is thermoluminescence (TL) phosphor Cr doped Al₂O₃ ceramic plate (2-D Al₂O₃: Cr TLD) [1] and BeO ceramics plate.

In this study, we investigated that neutron imaging using 2-D Al₂O₃: Cr TLD and Cd neutron-gamma ray converter technique, and gamma ray dosimetry using BeO ceramics plate in mixed neutron-gamma fields.

EXPERIMENTS:

1. Thermal neutron fluence distribution measurements. Low melting point Al₂O₃ of Chibacera MFG Co. LTD., which was composed of Al₂O₃ > 99.5 wt% was used. The bulk density of the plates was 3.7g·cm⁻¹. The dimensions used for the glow curve measurements were 80 × 80 × 0.7 mm³. The concentration of Cr₂O₃ in the present study was 0.05 wt%. Fig.1 shows the Diagram of neutron imaging using 2-D Al₂O₃: Cr TLD and Cd neutron-gamma ray converter technique. Collimator sizes were 5 mm, 10 mm, and 20 mm. The Two-dimensional TL measurement system consists of a CMOS camera, 80 × 80 mm² heater, and a dark box. After exposure, the TL slabs were heated to 400 °C for 5 min. The TL images were captured using a CMOS camera equipped with a thermal cut filter.

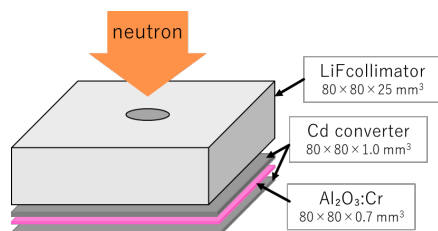


Fig.1 Diagram of neutron imaging using 2-D Al₂O₃: Cr TLD and Cd neutron-gamma ray converter technique. curve measurements.

2. Gamma ray dosimetry

The BeO ceramic TLD (Thermalox® 995, Materion

Corp.) and Na-doped BeO powder TLD (UD-170LS, Panasonic) were used. BeO ceramic TLD content of at least 99.5 wt% and were 10 × 10 × 1.0 mm³. Na-doped BeO powder TLDs were encapsulated in a ø2 mm × 12 mm quartz glass tube. Both TL phosphors were compared to evaluate the usefulness of ceramic BeO for distribution measurement.

In both experiments the irradiation fields are the mixed neutron irradiation mode in KUR-HWNIF, with a power of 1MW.

RESULTS: Figure 2 shows the OCR of Al₂O₃: Cr using Cd converter at mixed neutron irradiation mode in KUR-HWNIF. This 2-D Al₂O₃: Cr TLD and Cd neutron-gamma ray converter technique was found to obtain thermal neutron fluence distributions with high spatial resolution. In the future, we will proceed with the verification by theoretical analysis to improve the accuracy of the measurement in the penumbra region.

Figure 3 shows the Gamma ray dose for irradiation time of BeO ceramic TLD and Na-doped BeO powder TLD. The BeO ceramic TLDs showed the same characteristics as Na-doped BeO powder TLDs in the BNCT irradiation field. It was suggested that γ-ray dose distribution measurement is possible by using BeO ceramic, which can be made large area.

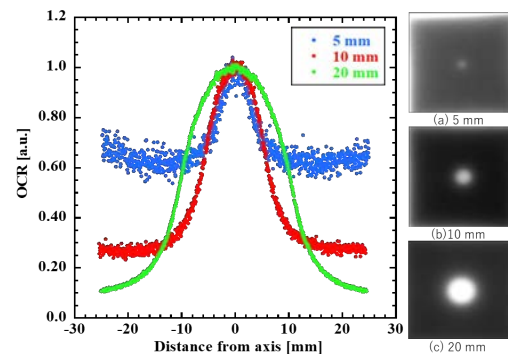


Fig.2 OCR of Al₂O₃: Cr using Cd converter at mixed neutron irradiation mode in KUR-HWNIF.

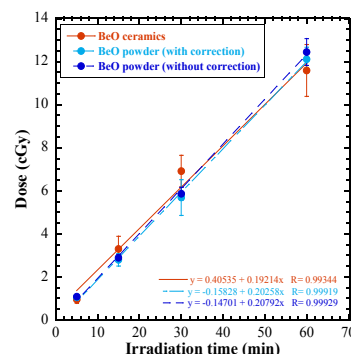


Fig.3 Gamma ray dose for irradiation time of BeO ceramic TLD and Na-doped BeO powder TLD.

REFERENCES: [1] K. Shinsho *et al.*, Sensors and Materials., 30 (2018) 1591-1598

PR6-11 Development and evaluation of 3D gel dosimeter for the measurement of dose distribution in BNCT

S. Hayashi, Y. Sakurai¹, M. Suzuki¹, and T. Takata¹

Department of Clinical Radiology, Hiroshima International University

¹ Institute for Integrated Radiation and Nuclear Science, Kyoto University

INTRODUCTION: Three-dimensional (3D) gel dosimeters have been developed for the 3D dose measurement of the complex dose distributions in clinical applications [1]. These devices utilize radiation-induced chemical reactions in the gel to preserve information about the radiation dose. The 3D absorbed dose distribution is deduced from the distribution of the reactant measured by imaging modalities, such as MRI (magnetic resonance imaging), X-ray CT (computed tomography), and optical CT. These gel dosimeters have excellent dose properties such as high sensitivity, dose rate independence, and a wide dose range, on X- and gamma-rays and the potential as a 3D dosimeter has been suggested.

In recent years, we have been studying the application of radiochromic gel dosimeters to dose evaluation in neutron irradiation. Up to last year, the optical dose-response of the PVA-I (PVA-GTA-I) radiochromic gel dosimeters [2, 3] on the irradiation of neutron beams with different energy spectra from a nuclear reactor was examined and its availability was investigated. In the results, the significant dose response improved by the addition of the hydrated electron scavenger as a sensitizer was demonstrated while the undesirable dose dependence was also observed.

So, this year, we investigated the dose-response and the potential of another type of radiochromic gel dosimeter that utilizes organic dye, leuco crystal violet (LCV) [4].

EXPERIMENTS: As sensitizers, boric acid, $B(OH)_3$, containing ^{10}B of 20% naturally, were added into the LCV radiochromic gel dosimeter. The concentrations in the gel were 0, 25, and 50 mM of $^{10}B(OH)_3$. The resulting solution was subdivided by pouring into PMMA cuvettes (4.5 mL, 1 cm path length). The neutron irradiations were performed using Heavy Water Neutron Irradiation Facility (HWNIF) of Kyoto University Research Reactor (KUR, power of 1 MW). The samples were irradiated in air at room temperature. The three different modes (thermal neutron rich for 30 min, epi-thermal and fast neutron rich for 50 min, and the mixed modes for 20 min) of neutron beams made by heavy water spectrum

shifter and cadmium thermal-neutron filters were applied to the samples. The measurements were performed at room temperature using an UV-Vis spectrophotometer (SHIMADZU, UV-1600PC, Japan). The change in the absorbance ($\Delta Abs.$) at the peak wavelength (600 nm) was investigated as the dose response.

RESULTS: Figures 1(a) and 1(b) show the absorption spectra and the dose responses of the gel samples containing different concentration of boric acid exposed to neutron beam of mix, thermal, epi-thermal and fast modes, respectively.

In the result, the sensitizing effect of ^{10}B was observed as in the gel dosimeter investigated earlier such as PVA-I gel dosimeter. However, its sensitivity was significantly lower than that of the other gel dosimeters. It was suggested that when using the LCV gel dosimeter, it is necessary to add the other sensitizer such as a radical generator.

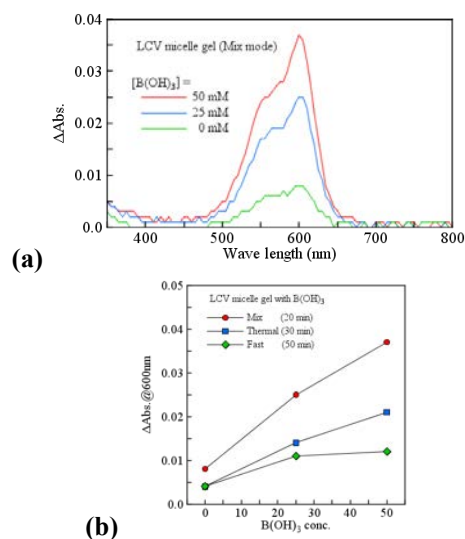


Figure 1 (a) Absorption spectra of the samples containing different concentrations of boric acid irradiated by the mix mode. (b) The dose enhancement with ^{10}B at each mode.

REFERENCES:

- [1] M. Marrale and F. d'Errico, *Gels* **7** (2021) 74.
- [2] S. Hayashi *et al.*, *Radiat. Meas.* **131** (2020) 106226.
- [3] S. Hayashi *et al.*, *J.Phys.; Conf. Ser.* **2167** (2022) 012014.
- [4] A. T. Nasr *et al.*, *Phys. Med. Biol.* **60** (2015) 4685-704.

PR6-12 Establishment of beam-quality estimation method in BNCT irradiation field using dual phantom technique (V)

Y. Sakurai, N. Kondo, D. Fu¹, T. Takata, H. Tanaka and M. Suzuki

*Institute for Integrated Radiation and Nuclear Science,
Kyoto University*

¹*Graduate School of Engineering, Kyoto University*

INTRODUCTION: Development in several types of accelerator-based irradiation systems for boron neutron capture therapy (BNCT) is underway. Many of these systems are nearing or have started clinical trials. Before the start of treatment with BNCT, the relative biological effectiveness (RBE) for the fast neutrons (over 10 keV) incident to the irradiation field must be estimated.

Measurements of RBE are typically performed by biological experiments with a phantom. Although the dose deposition due to secondary gamma rays is dominant, the relative contributions of thermal neutrons and fast neutrons are virtually equivalent under typical irradiation conditions in a water and/or acrylic phantom. Uniform contributions to the dose deposited from thermal and fast neutrons are based in part on relatively inaccurate dose information for fast neutrons.

The aim of this study is the establishment of accurate beam-quality estimation method mainly for fast neutrons by using two phantoms made of different materials, in which the dose components can be separated according to differences in the interaction cross-sections. The fundamental study of a “dual phantom technique” for measuring the fast neutron component of dose is reported [1].

In 2021, verification experiments for the dual phantom technique were performed using Heavy Water Neutron Irradiation Facility installed in Kyoto University Reactor (KUR-HWNIF) as in the previous year. Biological experiments were performed using the solid phantoms, which were made based on the simulation results.

MATERIALS AND METHODS: One of the dual solid phantoms was made of polyethylene with natural lithium fluoride for 30 weight percent (LiF-polyethylene phantom), and the other phantom was made of polyethylene with 95%-enriched lithium-6 fluoride for 30 weight percent (⁶LiF-polyethylene phantom).

Glioblastoma U87MG ΔEGFR cells were cultured in Dulbecco Modified Eagle medium (DMEM) with 10 % fetal bovine serum in 5 % CO₂ incubator at 37 °C. The cells were divided in two groups. One was p-boronophenylalanine (BPA, consisting of ¹⁰B) treated group, and the other was non-treated group. The treatment group was cultured with 25 ppm BPA containing medium overnight.

The neutron flux and gamma-ray dose rate were measured using activation foils and thermo-luminescent dosimeter, respectively. The depth dose distributions for the thermal neutron, fast neutron and gamma-ray components were determined based on the simulation calculation results normalized referring to the measured values.

The epi-thermal neutron irradiation mode was used for the phantom experiments.

RESULTS: Figure 1 shows the depth distributions of the cell survival for the BPA administration group, BPA(+), and the non-administration group, BPA(-), in the LiF-polyethylene phantom. The survival rates compared to non-irradiated control was higher in Non-treated cells than those in BPA-treated cells in LiF-polyethylene phantom.

Figure 2 shows the depth distributions of the cell survival in the ⁶LiF-polyethylene phantom. The survival rates compared to non-irradiated control showed no difference between non-treated cells and BPA-treated cells in ⁶LiF-polyethylene phantom.

CONCLUSION: The ⁶LiF-polyethylene phantom absorbs thermal neutrons although it has not significant effect in fast neutron dose. No difference in survival rates between non-treated cells and BPA-treated cells with ⁶LiF-polyethylene phantom indicated fast neutrons might not effect cell survival. On the other hand, due to mixture of thermal neutron in LiF-polyethylene phantom, BPA-treated cells were killed effectively compared with non-treated cells through n-alpha reactions. In addition, colony forming assays will be performed to confirm the effect of fast neutrons on cell survival.

ACKNOWLEDGMENT: This work was supported by JSPS KAKENHI Grant Number JP 16H05237.

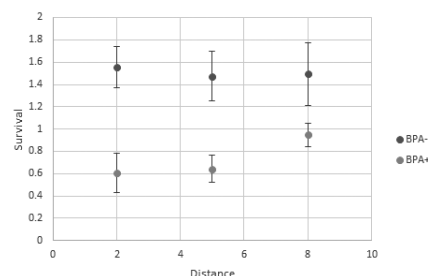


Fig. 1. Depth distributions for the cell survival in the LiF-polyethylene phantom.

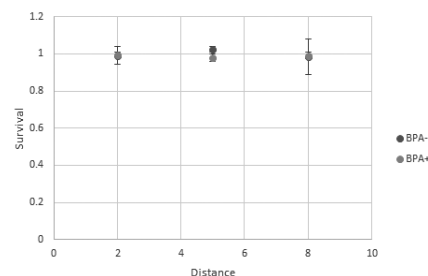


Fig. 2. Depth distributions for the cell survival in the ⁶LiF-polyethylene phantom.

REFERENCES:

[1] Y. Sakurai *et al.*, Med. Phys. **42** (2015) 6651-6657.

PR6-13 Development of real-time thermal neutron monitor for BNCT

H. Tanaka¹, N. Matsubayashi¹, S. Kurosawa², T. Takushi¹, Y. Sakurai¹

¹Institute for Integrated Radiation and Nuclear Science, Kyoto University

²Institute for Materials Research, Tohoku University

INTRODUCTION: Treatment of head and neck cancers with the accelerator-based BNCT system is now available at medical institutions [1]. It is necessary to assure the quality of the therapeutic beam before treatment can be performed. Until now, thermal neutron flux has been measured using the activation method that has been used in research reactors. This method does not provide real-time information. In medical institutions, it is desired to perform quality assurance quickly and accurately, and there is an urgent need to develop a real-time thermal neutron detector.

A thermal neutron monitor using a combination of Eu:LiCaAlF₆(LiCAF) scintillator and an optical fiber has been developed [2]. However, since LiCAF scintillator have a long decay time, it is important to develop a fast-response scintillator to measure thermal neutron flux in the BNCT irradiation field with a high dynamic range.

In this study, fast-response Cs₂LiYCl(Ce)(CLYC) scintillator crystals were prepared, and neutron irradiation tests were performed in the E-3 guide tube.

EXPERIMENTS: Because CLYC scintillators were deliquescent, the crystals were encapsulated in quartz glass. The crystals were placed in a photomultiplier tube, and the output waveform was obtained with an oscilloscope. The neutron and gamma-ray components can be discriminated based on the relationship between the counts integrated over the entire pulse time (Total : T) and the counts integrated from a certain point after a certain time to the final point of the pulse (Decay component : D).

RESULTS: The relationship between T and 1-D/T is shown in the results in Fig. 1. The data projected in the y-axis direction are also shown in Fig. 2. The two-dimensional plot confirms that the events below about 0.2 are neutron events. On the other hand, the projected figure confirms that the neutrons and γ -rays are sufficiently discriminated.

CONCLUSION: The neutron and gamma-ray discrimination ability of the CLYC scintillator was confirmed in the E-3 guide tube. In the future, we aim to install them in optical fibers and adapt them to the irradiation field of BNCT.

Acknowledgements

We thank Prof. Akira Yoshikawa's laboratory staff of Institute for Materials Research, Tohoku University for their guidance in the fabrication and evaluation of scintillator crystals.

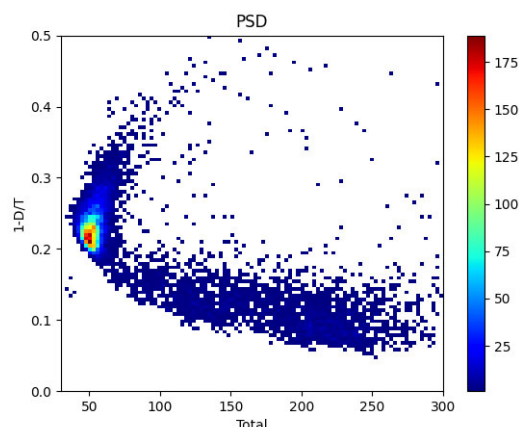


Fig. 1. Relationship between total components and decay components of pulse shape.

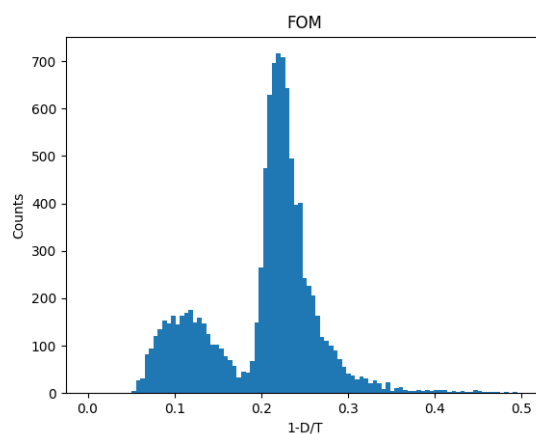


Fig. 2. Pulse shape discrimination of CLYC scintillators.

REFERENCES :

- [1] Hirose K., Konno A., Hiratsuka J., Yoshimoto S., Kato T., Ono K., Otsuki N., Hatazawa J., Tanaka H., Takayama K., Wada H., Suzuki M., Sato M., Yamaguchi H., Seto I., Ueki Y., Iketani S., Imai S., Nakamura T., Ono T., Endo H., Azami Y., Kikuchi Y., Murakami M., Takai Y. Boron neutron capture therapy using cyclotron-based epithermal neutron source and borofalan (10B) for recurrent or locally advanced head and neck cancer (JHN002): An open-label phase II trial, *Radiotherapy and Oncology*, 155, pp. 182 – 187(2021).
- [2] Tanaka H., Sakurai Y., Takata T., Watanabe T., Kawabata S., Suzuki M., Masunaga S.-I., Taki K., Akabori K., Watanabe K., Ono K. Note: Development of real-time epithermal neutron detector for boron neutron capture therapy, (2017) *Review of Scientific Instruments*, 88 (5), art. no. 056101.

PR6-14 Quantitative Measurement of 478 keV Prompt Gamma-rays of Boron-neutron Capture Reaction with the ETCC

T. Mizumoto, S. Komura, Y. Sakurai¹, T. Takata¹, H. Kimura², A. Takada³ and T. Tanimori³

Fukushima SiC Applied Engineering Inc.

¹*Institute for Integrated Radiation and Nuclear Science, Kyoto University*

²*Kyoto Pharmaceutical University*

³*Graduate School of Science, Kyoto University*

INTRODUCTION: Boron neutron capture therapy (BNCT) is one of the promising cancer treatment methods. However, we have not yet obtained a good monitoring method of the treatment effect in real-time during BNCT. If we get images of 478 keV gamma rays generated by the boron-neutron capture reaction, and measure their intensity and generation positions, we can check the treatment effect on BNCT. As such imaging detector, we have been developing electron tracking Compton cameras (ETCCs). ETCCs are advanced Compton cameras which take the information of the recoil direction of electrons and can uniquely determine the arrival direction of sub-MeV/MeV gamma ray event by event. In the present study, we carried out the following three types of experiments based on previous studies to confirm the performance of our ETCC [1].

EXPERIMENTS AND RESULTS:

Exp. 1: We carried out the prompt gamma-ray imaging tests for a boron containing solution in a 4.5 mm diameter tube which simulates a small tumor tissue. The tube was located just above the ETCC and was irradiated with thermal neutrons at E-3 at the 1-MW operation. This experiment was performed for four tubes with different ¹⁰B concentrations (0, 462, 926, 1385 ppm). The experimental setup is shown in Fig. 1. The ETCC measured the prompt gamma rays emitted from the solution during irradiation time. As the result, high quality 478 keV gamma-ray images with a spatial resolution of less than 1 cm. As shown in Fig.1, we also confirmed that the relationship between the detection rate of 478 keV gamma-rays and B-10 concentrations relatively matches well with simulation result.

Exp. 2: We carried out the prompt gamma-ray imaging studies on U87 MG tumor-bearing mice treated with BPA with neutron irradiation with E-3 neutron beam line at the 5-MW operation. Each mouse was anesthetized and administered 1000 mg/kg of BPA by tail vein injection, then fixed in a plastic case. We carried out the measurement with an ETCC and a mouse placed just above it. We also carried out another measurement of a mouse with two ETCCs installed facing each other. Analysing data of an

ETCC, we confirmed that the bright position in the back-projection image of 478 keV gamma-rays shows just the irradiation position of the mouse. The analysis of stereo-ETCC data is in progress.

Exp. 3: We also carried out performance test of the ETCC in a BNCT environment using Heavy Water Neutron Irradiation Facility of KUR at the 1-MW operation. As shown in Fig. 2, we set a 10-cm cubic boron containing solution in the irradiation room. The ETCC measures the 478 keV prompt gamma rays which emit from the solution and pass through the cylindrical hole in the ceiling. This experiment was performed with solution with several B-10 concentrations (0, 46, 93, 230 ppm). We obtained 478 keV gamma-ray backprojection images in which the position of the solution appears brighter. We also obtained that the relationship between the detection rate of 478 keV gamma-rays and ¹⁰B concentrations matches well with simulation result.

These results show that the ETCC has the high potential of the quantitative imaging and monitoring of 478 keV prompt gamma-rays of Boron-neutron capture reaction.

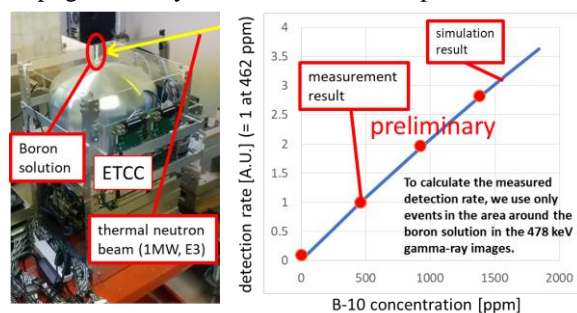


Fig.1 Left: Photograph on Exp.1. Right: The relationship between 478keV gamma-ray detection rate of the ETCC and B-10 concentration of the solution.

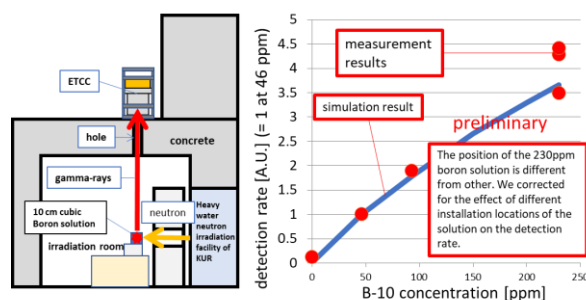


Fig.2 Left: Schematic view on Exp.3. Right: The obtained result of the relationship between 478keV gamma-ray detection rate of the ETCC and B-10 concentration of the solution.

REFERENCES:

[1] S. Komura *et al.*, KURNS Progress Report 2020.

PR6-15 Evaluation of neutron irradiation fields for semiconductor device irradiation

H. Tanaka¹, N. Matsubayashi¹, T. Takushi¹, Y. Sakurai¹

¹Institute for Integrated Radiation and Nuclear Science, Kyoto University

INTRODUCTION: In the irradiation field of BNCT, electronic devices with semiconductor devices such as neutron monitors, patient monitoring cameras, and implantable pacemakers may be irradiated. If semiconductor devices contain nuclides that have a large capture cross section for thermal neutrons, charged particles are generated in the semiconductor devices when they are irradiated by thermal neutrons. The charged particles generate electron-hole pairs in their trajectories, and this charge becomes a noise current in the semiconductor device. This current can cause semiconductor devices to fail. In addition, semiconductor devices are becoming finer and finer every year, and the signal current is becoming smaller and smaller. In other words, they tend to be more sensitive to noise.

For thermal neutrons, systematic data are lacking [1]. It is also important to investigate the effects of neutron and gamma radiation doses. In this study, we evaluated the neutron and gamma-ray doses in the thermal neutron irradiation field, which is necessary to investigate the effects of thermal neutrons on this semiconductor device.

EXPERIMENTS: The heavy water neutron irradiation facility (HWNIF) of KUR moderates the fast neutrons generated in the reactor core to thermal neutron energy using heavy water and aluminum. The HWNIF has a cadmium shutter behind the heavy water moderator to change the neutron energy. In addition, semiconductor devices are installed on substrates, and to observe semiconductor errors in real time, it is necessary to install a measurement device on a large carrier and irradiate it while acquiring data. Although changes in thermal neutron flux on a bismuth surface using rail device have been reported, no evaluation of neutron doses has been performed using a large carrier in combination with a collimator. Here, neutron and gamma-ray doses at the exit of the collimator with a collimator diameter of 300 mm x 300 mm were evaluated using the paired-ionization chamber method.

RESULTS: The figure 1 shows the neutron and gamma-ray dose results at the center of the collimator exit when the cadmium shutter aperture was varied. When the cadmium shutter is 0 mm, the dose rate was 190 mGy/hr/1 MW, with the majority of the dose coming from epithermal and fast neutrons. The gamma-ray dose also tends to increase with increasing thermal neutron flux due to the presence of secondary gamma rays generated by the collimator and other sources.

CONCLUSION: In the HWNIF, the relationship between cadmium shutter aperture and neutron and gamma-ray doses were derived in an irradiation field combining

a large carrier and a collimator. Based on this information, irradiation of semiconductor devices will be carried out in the future.

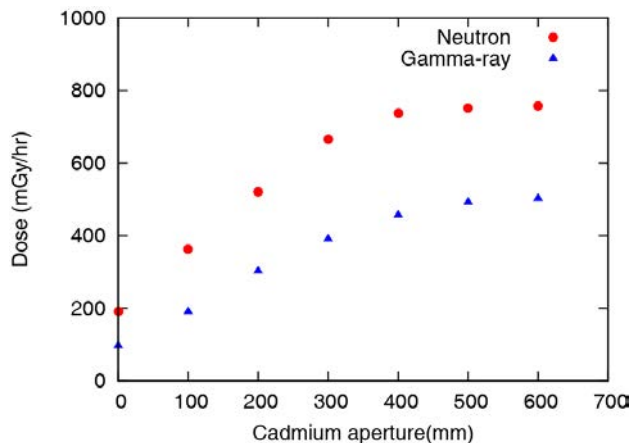


Fig. 1. Relationship between cadmium aperture and neutron and gamma-ray doses.

REFERENCES :

[1] Takashi Kato, Motonobu Tampo, Soshi Takeshita, Hiroki Tanaka, Hideya Matsuyama, Masanori Hashimoto, Yasuhiro Miyake, Muon-Induced Single-Event Upsets in 20-nm SRAMs: Comparative Characterization with Neutrons and Alpha Particles, IEEE Transactions on Nuclear Science, 68,1436-1444,2021.

PR6-16 Optimization of Bolus Shape for Boron Neutron Capture Therapy — Examination Using Simple Shaped Phantom for Experimental Verification —

T. Takata, M. Nojiri¹, A. Sasaki¹, Y. Sakurai, H. Tanaka and M. Suzuki

*Institute for Integrated Radiation and Nuclear Science,
Kyoto University*

¹*Graduate School of Engineering, Kyoto University*

INTRODUCTION: In Boron Neutron Capture Therapy (BNCT), an epithermal neutron beam has been utilized to penetrate a deep site of a patient's body based on its thermalization. However, thermal neutron buildup near a beam incident surface, associated with the use of epithermal neutron, causes dose deficiency in a case where a tumor extends to the vicinity of the patient surface. For such a case, a thermal neutron compensation bolus consisting of a hydrogen-rich material has been utilized to improve the dose distribution. In the present clinical BNCT, a bolus with a uniform thickness and a simple shape has been adopted. This study aims to increase the dose ratio of tumor to normal tissues more aggressively, by optimizing the bolus shape. An overview of the optimizing method was described in the previous report [1]. In addition, a verification using a water phantom has been attempted through experimental measurements [2]. As a part of the verification, the experiments using the phantom with/without a simple-shaped bolus were conducted before comparisons to the optimized one.

MATERIALS AND METHODS: A cylindrical water phantom with a height of 20 cm and diameter of 20 cm was used, assuming a head-and-neck case with a parotid gland cancer irradiated from the lateral direction. A spherical volume with a 4-cm diameter centered at a 2-cm depth from the side surface of the cylinder was defined as a planning target volume (PTV), assuming a tumor extended to a subcutaneous region. A tubular volume with a 3-cm diameter along the center axis of the cylinder was defined as an organ at risk (OAR), assuming a mucosal tissue of the oral cavity and pharynx [2].

The simple-shaped bolus was fabricated using a water bag with an acrylic container. The rectangular container with an outer dimension of $7.5 \times 7.5 \times 1.1$ cm³, filled with the water bag was attached to the beam incident surface (mid-height position of cylinder side) of the phantom (Figure 1).

In-phantom distributions of thermal neutron fluence with/without the bolus were measured using an activation method using gold wires. The gold wires were located in the phantoms to cover the PTV and OAR regions, and irradiated with the epithermal neutron beam of KUR Heavy Water Neutron Irradiation Facility (CO-0000F mode). After the irradiation, the gold wires were placed on an imaging plate (BAS-MS) to obtain the relative distributions of induced activities along the wires. Also, the absolute activities of some positions were determined by a well-type NaI(Tl) detector (SP-20, Ohyo Koken) or an

HP-Ge detector to normalize the relative distribution obtained by the imaging plate.

RESULTS: Figure 2 shows the depth distributions of thermal neutron fluence along the beam axis for the cases with/without the rectangular bolus. In the case with the bolus, a shift in the distribution was observed toward the incident surface by the bolus thickness (1.1 cm). The distributions along other wires, covering the PTV and OAR, will be derived in the same way. Also, the measurement with the optimized bolus will be conducted and analyzed to evaluate the improvement in volume-specific parameters of the thermal neutron fluence distribution.

ACKNOWLEDGMENT: This work was supported by JSPS KAKENHI Grant Number JP 17K17838. We thank Dr. Ken-ichi Tanaka of Kyoto Pharmaceutical University for allowing us to use the imaging plate reader with his helpful support.

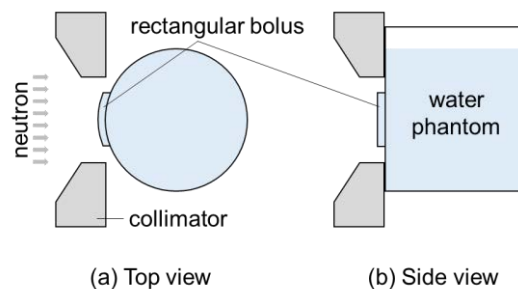


Fig. 1 Schematic layout of irradiation experiment using water phantom with rectangular bolus.

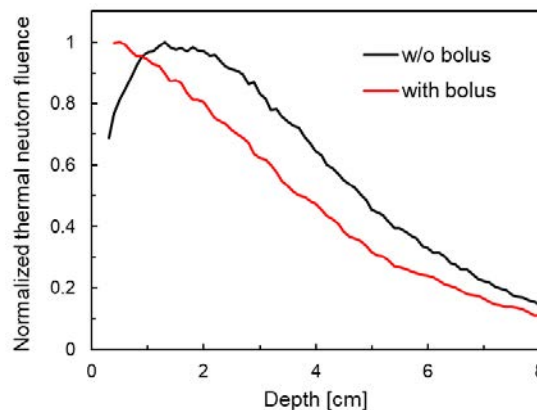


Fig. 2 Depth distributions of thermal neutron fluence for cases with/without bolus.

REFERENCES:

- [1] T. Takata *et al.*, KURNS Progress Report 2019 (2020), 56.
- [2] T. Takata *et al.*, KURNS Progress Report 2020 (2021), 83.

PR6-17 Annealing properties of boric acid infused PVA-GTA-I gel irradiated with neutrons

H. Yasuda¹, JE. Taño^{1,2,3}, CAB. Gonzales¹, Y. Sakurai⁴

¹Department of Radiation Biophysics, RIRBM, Hiroshima University

²Graduate School of Biomedical and Health Sciences, Hiroshima University

³Phoenix Leader Education Program for Renaissance from Radiation Disaster, Hiroshima University

⁴Institute for Integrated Radiation and Nuclear Science, Kyoto University (KURNS)

INTRODUCTION: Since 2019, the authors have investigated the feasibility of infusing boric acid to an original radiochromic gel formula made of polyvinyl alcohol (PVA), glutaraldehyde (GTA), and iodide (I) [1,2], named “PGI gel” herewith. The results of the study demonstrated that addition of boric acid to the PGI gel worked to increase its sensitivity of response to neutron irradiation. We reported that the standard formula PGI gel was capable of reuse through annealing, that is, the irradiated gel samples were reverted by heating from red to clear with the initial absorbance values before irradiation [2]. In the present study, we tried to examine if the reversibility of PGI gels can be achieved with infusion of boric acid after a certain-period storage after irradiation with thermal neutron beams used for the boron neutron capture therapy.

EXPERIMENTS: All samples of PGI gel were prepared using ultrapure water and analytical grade chemicals purchased from FUJIFILM Wako Pure Chemical Corporation (Osaka, Japan). The standard formula of the PVA-GTA-I formula was infused with different boric acid concentrations of 0, 25 and 50 mM. The liquid mixtures were poured into PMMA cuvettes and stored inside a vacuum chamber (-0.08 MPa) for 3-hours. The cuvette samples were then covered with PE lids and stored inside a sterilizing oven at 50°C for 12 hours to convert from liquid to gel. The neutron irradiations of the samples were performed at the Heavy Water Neutron Irradiation Facility (HWNIF) of Kyoto University Reactor (KUR) with a 1MW nominal power. The samples were fixed on a rail system and irradiated at different periods: 20-, 40-, 80-, and 120-min. After irradiation, the samples were stored at room temperature and measured 55 days after irradiation. The optical absorbances were obtained using the NanoDrop OneC™ UV-Vis spectrometer (Thermo Fisher Scientific Inc., USA). After the initial reading, the gel samples were annealed in the oven at 50°C at time intervals of 24, 48, 72, and 96 hours. It should be noted that after each annealing time interval, the samples were stabilized at room temperature for 2 hours before measurement.

RESULTS: Good linearities were confirmed in the dose responses of the PGI gels having different boron concentrations. While, different levels of natural oxidation were observed among the different formula gels after a certain storage period (~55 days). As to the effects of annealing

process at 50°C, it was found that the PGI gels infused with boric acid needed longer time to become clear than the standard one. Also, the time for completely erasing the radiation-induced color tended to be longer in the samples with higher boric acid concentration.

The time changes of decolorization process were well approximated with an exponential function below for all the cases:

$$A(t) = A_0 \times e^{-\lambda t} \quad (1)$$

where $A(t)$ is the absorbance of a PGI gel at the wavelength of 490 nm at the annealing time t ; A_0 is initial absorbance ($=A(0)$); and λ is an empirically determined parameter indicating the speed of color decay. The estimated values of A_0 and λ are shown in Fig.1 as function of the time of neutron irradiation. Notable dependence of those fitting parameter values on boric acid concentration were seen. These findings imply that addition of boric acid can improve the sensitivity of the PGI gel but lower the practicality as it makes longer the annealing time. Further investigation to confirm the reusability is to be continued.

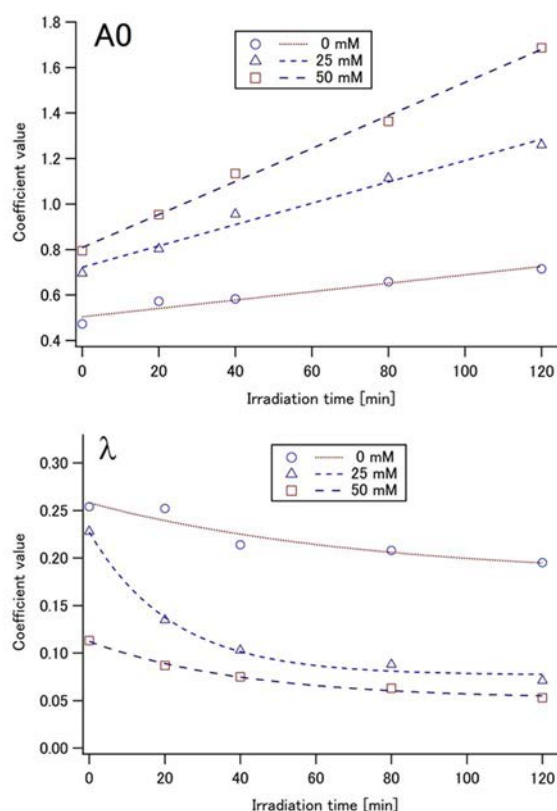


Fig. 1 The estimated parameter values: A_0 (above) and λ (below) obtained through fitting with eq.1 as function of neutron irradiation time for the PGI cells with different boric acid concentrations.

REFERENCES:

- [1] Taño JE *et al.* 2020. *Radiat Meas.* **134** 106311.
- [2] Taño JE *et al.* 2021. *Radiat Meas.* **149** 106674.

PR6-18 Three dimensional model for pre-clinical assessments in BNCT

K.Igawa,¹ A.Sasaki,² K.Izumi,² E.Naito,³ M.Suzuki,³ N.Kondo,³ Y.Sakurai

Neutron Therapy Research Center, Okayama University

¹Department of Oral Maxillofacial Surgery, Okayama University

²Graduate School of Medical and Dental Sciences Oral Life, Niigata University

³Institute for Integrated Radiation and Nuclear Science, Kyoto University

INTRODUCTION: In Boron Neutron Capture Therapy (BNCT), the Boron dose and neutron dose in tumor cells are the key factors. The development of boron agents for BNCT requires the evaluation system bridging the gap between in vivo and in vitro research. Also, from the viewpoint of the guiding principles for animal experiments (3Rs: Replacement, Reduction and Refinement), the alternative research methods that do not use animals, are required for BNCT. On the other hand, three-dimensional (3D) models have been widely used in cancer research due to their ability to mimic multiple features of the tumor microenvironment [1]. Therefore, the validity of the 3D in vitro oral cancer model for pre-clinical investigations in BNCT is examined in this study.

EXPERIMENTS: First, we fabricated 3D in vitro oral cancer and normal oral mucosa models. For the facilitation of 3D in vitro oral cancer model, normal oral mucosa fibroblasts (Niigata University) were embedded and cultured in type I collagen matrix (Niita-gelatin, Japan) for 7 days under a humidified atmosphere of 5% CO₂ at 37 °C. Oral squamous carcinoma cells (HSC3, Riken Cell Bank) were seeded on top of the surface of 3D collagen matrix, and then, the composite was cultured under a submerged condition for additional 7 days in DMEM medium (Wako, Japan) supplemented with 10 % fetal bovine serum (Sigma -Aldrich, USA) and 100 unit/ml penicillin and 100 µg/ml streptomycin (1% p/s) (Thermo Fisher Scientific, USA) (Fig.1) [2]. Similarly, the 3D normal oral mucosa model was manufactured by seeding normal oral keratinocyte (Niigata University) on the top of the collagen matrix with normal oral fibroblasts using complete EpiLife® medium containing 0.06 mM Ca²⁺ [3]. The fabrication of both models was completed by culturing at an air-liquid interface for another 7 days (total 21 days in culture). After the infusion of Boron (Steboronine®, Stella pharma, Japan) or Phosphate Buffered Saline (PBS, Sigma -Aldrich, USA), 3D in vitro models were incubated for 2 hours, washed by PBS, and irradiated by neutron for 20 minutes. After irradiation, they were cultured for another 7 days (Fig. 2). Finally, the 3D models were fixed with 10 % formalin, embedded in paraffin, cut in 5 µm sections and stained with hematoxylin and eosin.

RESULTS: The histological examinations of the 3D oral cancer model after neutron irradiation revealed that the cancer cell layer appeared to be apoptotic after neutron irradiation. More remarkably, the thickness of the underlying fibroblasts-embedded collagen matrix was significantly thinner in BNCT group, compared with control group as shown in Fig.3(a). In contrast, in the normal oral mucosa model, the epithelial layer did not seem to be different after neutron irradiation, except moderate irregular cellular arrangement of the basal cells layer. (Fig.3b). Additionally, the thickness of the underlying collagen matrix did not change after neutron irradiation. These results suggest that our 3D in vitro models could be useful to evaluate cellular response to BNCT for oral cancer cells as well as the surrounding normal oral mucosa, and would be an alternative tool to animal test for BNCT.

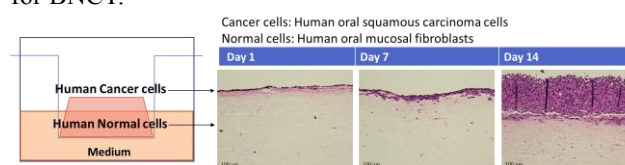


Fig. 1. Diagram of manufacturing 3D oral cancer model

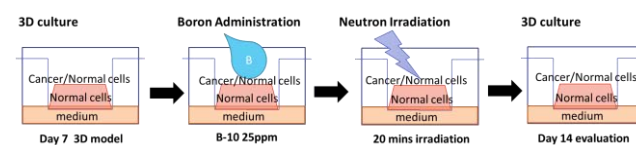


Fig. 2. BNCT protocol for 3D in vitro models

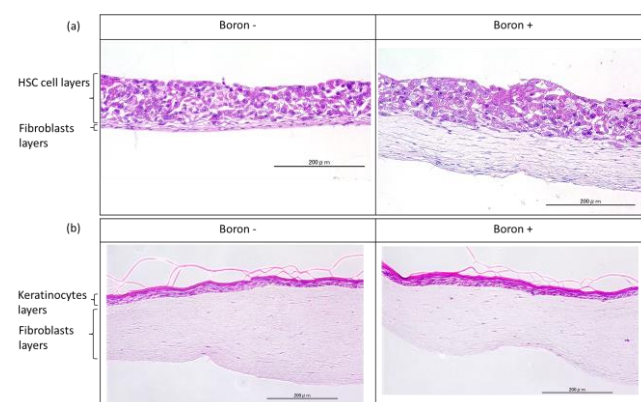


Fig.3. Histology of the 3D cancer model at 7 days after neutron irradiation. (a) 3D oral cancer model (b) 3D normal oral mucosa model.

REFERENCES:

- [1] D Corallo *et al.*, *frontiers in Immunology* vol.11 (2020) <https://doi.org/10.3389/fimmu.2020.584214>.
- [2] K Haga *et al.*, *Translational Oncology* 12 (2021) DOI: 10.1016/j.tranon.2021.101236.
- [3] A Uenoyama *et al.*, *Biosci, Biotechnol, and Biochem*, 80 (2016) DOI:10.1080/09168451.2016.1153957.

I-1. PROJECT RESEARCHES

Project 7

PR7 Project Research on Advances in Isotope-Specific Studies Using Multi-Element Mössbauer Spectroscopy

M. Seto

*Institute for Integrated Radiation and Nuclear Science,
Kyoto University*

OBJECTIVES OF RESEARCH PROJECT:

One of the most irreplaceable features of the Mössbauer spectroscopy is to extract several information such as electronic states for a specific isotope. The main objectives of this project research are the investigation in the frontier of the materials science and the development of advanced experimental methods by using multi-element Mössbauer spectroscopy. Promotion of variety of Mössbauer isotope provides more useful and valuable methods in modern materials science even for complicated systems.

In this project research, each group performed their research by specific isotopes:

^{57}Fe in P7-1, P7-2, P7-3, P7-4, P7-5, P7-9, and P7-13

^{61}Ni in P7-8

^{119}Sn in P2-5, P7-7 and P7-10

^{151}Eu in P2-5, P7-9, P7-10 and P7-11

^{197}Au in P7-6 and P7-7

Other isotopes in P7-11 and P7-12

MAIN SUBJECTS AND RESULTS OF THIS REPORT:

Main subjects and results from these researches are as follows:

(P7-1, K. Shinoda) Intensity Tensor of Fe^{2+} in the M2 Site of Hypersthene by Single Crystal Mössbauer Microspectroscopy

K. Shinoda *et al.* characterized the electric field gradient tensor of single crystals of hypersthene as small as 1mm^3 by developed Mössbauer microspectrometer.

(P7-2, H. Fujii) Mössbauer Study of the Model Complexes of Heme Enzymes

H. Fujii *et al.* investigated model complexes of cytochrome P450 in different solvents of acetonitrile, tetrahydrofuran and methanol to obtain comparable results from the EPR experiments.

(P7-3, Y. Akiyama) Analysis of Iron-based Products Using Mössbauer Spectroscopy - Iron Oxide Scale Generated in the Boiler Feed-water in Thermal Power Plant -

Y. Akiyama *et al.* are investigating a design for the magnetic separation system of the iron oxide scale from power plant through evaluation of ferromagnetic and paramagnetic components.

(P7-4, I. Mashino) Electrical Conductivity and the Iron Valence State of Enstatite Glasses up to Mbar

Pressures

I. Mashino *et al.* investigated pressure dependence of electrical conductivity of Fe-bearing enstatite glasses. The Mössbauer spectroscopy is used to determine the composition ratio of Fe^{2+} and Fe^{3+} components.

(P7-5, Y. Matsushi) The Role of Iron in the Differential Weathering Processes of Volcanic Fall Deposit

H. Fukui *et al.* investigated several soil samples with different weathering pattern to reveal the crucial role of iron in the weathering process.

(P7-6, H. Ohashi) Rough Estimation of Debye Temperature for Precursor of Supported Gold Cluster Catalysts Derived from Recoil-Free Fraction in ^{197}Au Mössbauer Spectroscopy

H. Ohashi *et al.* investigated Au_2S_x , a precursor of supported Au cluster and evaluated its Debye temperature, which was quite low but appropriate as Au catalysts.

(P7-7, Y. Kobayashi) Recoilless Fraction on ^{197}Au Mössbauer Spectroscopy

Y. Kobayashi has investigated the evaluation method of the Debye temperature for Au compounds.

(P7-8, T. Kitazawa) ^{61}Ni Mössbauer Spectroscopy for Supramolecular Bridging Cyanide Complexes

T. Kitazawa *et al.* have investigated several Ni cyanides to evaluate slight difference of Ni environments.

(P7-9, H. Wadachi) Mössbauer Spectroscopy of a Perovskite-Type Iron Oxide $\text{Ba}_{2/3}\text{La}_{1/3}\text{FeO}_3$

M. Onose *et al.* have revealed the temperature dependence of Mössbauer spectra of $\text{Ba}_{2/3}\text{La}_{1/3}\text{FeO}_3$ to find the magnetic structure of spin charge ordering.

(P7-10, Y. Kamihara) Research on Magnetism in a Novel Kondo Lattice III

Y. Kamihara *et al.* studied the temperature dependence of EuSn_2P_2 by using both ^{151}Eu and ^{119}Sn Mössbauer spectroscopy to elucidate its magnetic ordering.

(P7-11, R. Masuda) Optimization for the Energy Standard Material for Mössbauer Spectroscopy

R. Masuda *et al.* evaluated the efficiency of a standard material for Mössbauer spectroscopy using EuF_3 .

(P7-12, S. Kitao) Development of ^{180}Hf Mössbauer Spectroscopy

S. Kitao *et al.* have attempted to observe ^{180}Hf Mössbauer spectra using a HfC source material.

(P7-13, K. Yonezu) Experimental Preliminary Approach on the Precipitation Mechanism of Banded Iron Formation (BIF)

K. Yonezu *et al.* are investigating sedimentary rock to understand its formation mechanism.

PR7-1 Intensity tensor of Fe²⁺ in the M2 site of hypersthene by single crystal Mössbauer microspec-troscopy

K. Shinoda¹, K. Onoue¹, Y. Kobayashi²

¹Department of Geosciences, Graduate School of Science, Osaka Metropolitan University

²Institute for Integrated Radiation and Nuclear Science, Kyoto University

INTRODUCTION: Pyroxene is a major rock-forming mineral and a typical multi-site solid solution. Common chemical formula of natural pyroxene is (Ca, Fe, Mg)₂Si₂O₆. Occupying sites of divalent cations are the M1 and M2 sites. In pyroxene, Fe²⁺ in M1, Fe²⁺ in M2 and Fe³⁺ in M1 sites are possible. Fe²⁺ in the M1 site shows a little wider quadrupole doublet than Fe²⁺ in the M2 site in Mössbauer spectra. Fe³⁺ in the M1 site shows the narrower quadrupole doublet than Fe²⁺. Intensities of component peaks in a quadrupole doublet of a thin section as a single crystal are asymmetric and vary depending on the angle between the direction of incident γ -rays and the crystallographic orientation of the thin section. Intensity of quadrupole doublet (I^h / I^{total}) means a ratio between area of the peak of the higher energy (I^h) and total area of the doublet ($I^{total} = I^h + I^l$) (sum of I^h and area of the lower energy (I^l)). Intensity of quadrupole doublet can be calculated from the intensity tensor. In Mössbauer spectrum of pyroxene in which three doublets are overlapping, it is important to know intensity tensors of the three doublets to separate overlapping doublets. Zimmermann (1975, 1983) showed relationships between the intensity tensor and electric field gradient (EFG) tensor and introduced experimental determination of the intensity tensor from the Mössbauer spectrum of a single crystal. Shinoda and Kobayashi (2019) revealed EFG tensor due to Fe²⁺ in M2 site of ortho-enstatite, which is orthorhombic Fe-poor pyroxene of chemical formula (Mg_{2.03}, Fe_{0.16}) (Si_{1.78}, Al_{0.13}) O₆. However, the intensity tensor of Fe-rich orthopyroxene has not been revealed. In this study, the intensity tensor of Fe²⁺ at the M2 site of hypersthene (Ca_{0.06}, Mg_{1.26}, Fe_{0.68}) (Si_{1.95}, Al_{0.05}) O₆ by EDS analyses were determined by single crystal ⁵⁷Fe Mössbauer spectra using crystallographically oriented thin sections.

EXPERIMENTS and RESULTS: Single crystals of hypersthene as small as 1mm³ from Inawashiro-ko, Aizuwakamatsu, Fukushima, Japan were used for this study. Three crystallographically oriented thin sections perpendicular to a^* , b^* and c^* were prepared by measuring X-ray diffraction using Laue and precession camera. Seven Mössbauer spectra of oriented thin sections were measured. In this study, Cartesian coordinate ($X Y Z$) is set as $X//c^*$, $Y//a^*$, $Z//b^*$, where a^* , b^* , c^* are reciprocal lattice vectors

of hypersthene. Mössbauer measurements were carried out in transmission mode on a constant acceleration spectrometer with an Si-PIN semiconductor detector (XR-100CR, AMPTEK Inc.) and multi-channel analyzer of 1024 channels. A 3.7GBq ⁵⁷Co/Rh of 4mm ϕ in diameter was used as γ -ray source. An ⁵⁷Fe-enriched iron foil was used as velocity calibrant. The two symmetric spectra were folded and velocity range was ± 4 mm/s. Thickness corrections of raw spectra were not done.

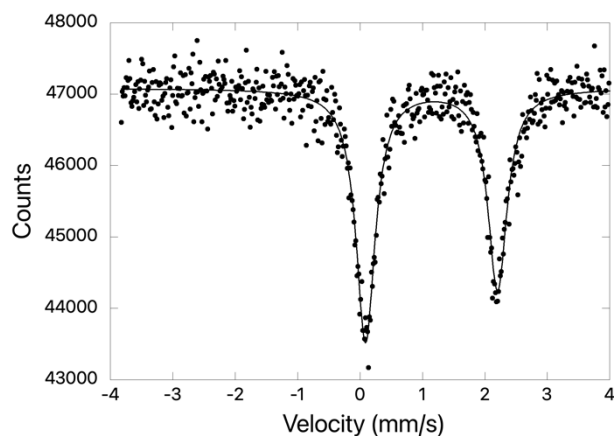


Fig.1 Mössbauer spectrum of hypersthene measured under γ -ray parallel to the a^* -axis.

Fig.1 shows Mössbauer spectrum of hypersthene measured under incident γ -ray parallel to a^* -axis. A doublet due to Fe²⁺ in M2 site of hypersthene was observed. Averages of isomer shift, Q-splitting, and line width were 1.15 2.13 and 0.39 mm/s, respectively. From seven sets of intensity of quadrupole doublet, three components (I_{XX} , I_{YY} , and I_{ZZ}) of the intensity tensor of Fe²⁺ in the M2 site of hypersthene are obtained as 0.577, 0.453 and 0.470. three components of the intensity tensor of Fe²⁺ in the M2 site of ortho-enstatite were 0.615, 0.455 and 0.424 (Shinoda and Kobayashi, 2019). Three components of the intensity tensor of Fe-poor and Fe-rich ortho-pyroxene suggest that I_{XX} and I_{ZZ} show weak chemical dependence of Fe²⁺ and I_{YY} is independent of Fe²⁺ components.

REFERENCES

- [1] Zimmermann, R. (1983) Advances in Mössbauer spectroscopy (Thosar, B.V. Ed.). pp.273-315, Elsevier Scientific Publishing Co. Amsterdam.
- [2] Zimmermann, R. (1975) Nucl. Instr. and Meth. **128**, 537-543.
- [3] Shinoda and Kobayashi (2019) KURNS Progress Report 2019.

PR7-2 Mössbauer Study of the Model Complexes of Heme Enzymes

H. Fujii, Y. Kobayashi¹, A. Takeda, S. Iwamoto

Graduate School of Science, Nara Women's University
¹Graduate School of Science, Kyoto University

INTRODUCTION: Iron porphyrin complexes are active sites of many heme proteins in nature. For example, cytochrome P450 generates a high-valent oxoiron(IV) porphyrin π -cation radical species called compound I in the catalytic cycle. The oxidation state and the spin state of the compound I are key for controlling the function of cytochrome P450. In this project, we prepared a model complex (FeS) of cytochrome P450 and studied the oxidation state and the spin state of FeS by using Mössbauer spectroscopy.

EXPERIMENTS: Mössbauer spectroscopy was conducted in conventional transmission geometry by using ⁵⁷Co-in-Rh(50 mCi) as γ -ray source. The Doppler velocity scale was calibrated using an Fe metal foil at room temperature. ⁵⁷Fe was purchased from commercial as a powder and changed to iron(II) acetate. Synthesis of FeS and its iron(III) chloride complex will be reported in elsewhere.

RESULTS: EPR spectra of FeS indicated that FeS is a mixture of ferric high spin state and ferric low spin state in acetonitrile (AC) at 4K while FeS is a ferric low spin complex in tetrahydrofuran (THF) and methanol. These results can be interpreted by the coordination of THF and methanol, which work as oxygen donor ligand for the heme iron, in THF and methanol, respectively. The binding of THF or methanol is consistent to the coordination of water ligand in cytochrome P450. To confirm the change of the spin state of FeS with coordination of these solvent ligand, we measured Mössbauer spectra of FeS in AC, THF, and methanol at 6K (Figure 1). Mössbauer parameters are listed in Table 1. We found that the Mössbauer peaks from all of these samples are extremely broad, compared with those of other ferric porphyrin complexes. This is also close to the nature of cytochrome P450, for which extremely broad Mössbauer peaks have been reported. These results suggest that FeS can mimic the active site of cytochrome P450. We found two Mössbauer peaks in AC, but one peak in THF and methanol. We tentatively assigned these peaks on the basis of the EPR results. The two peaks in AC result from high spin state and low spin state of FeS; the peak around 0 mm/s results from high spin state and the peak around 1.5 mm/s results from low spin state. On the other hand, the peaks in THF and methanol are assignable to the low spin state. These assignments were further supported by Mössbauer spectrum in AC at 77 K.

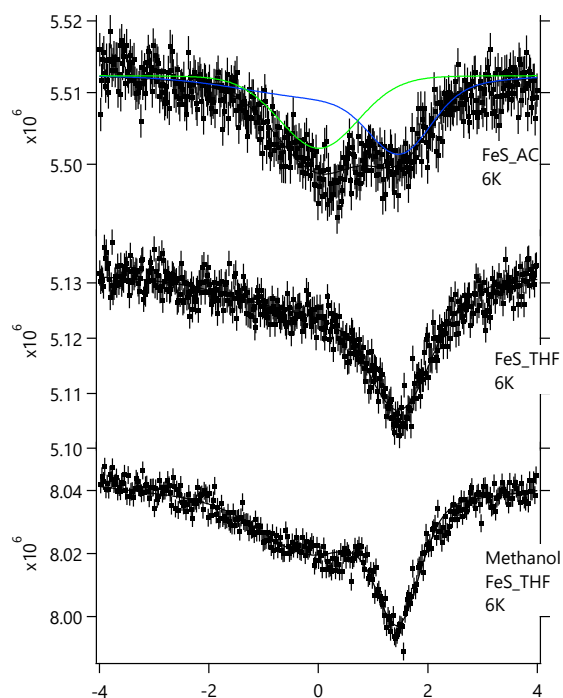


Fig 1. Mössbauer spectra (6 K) of FeS in acetonitrile (top), in THF (middle), and in methanol (bottom).

Table 1. Mössbauer parameters of FeS at 6 K.

	Ratio	IS	QS	FWHM1	FWHM2
AC	57.0%	0.891	1.213	3.658	1.209
	43.0%	0.011		1.607	
THF		0.891	1.213	3.658	1.209
methanol THF		0.674	1.575	2.041	0.824

REFERENCES:

- [1] H. Fujii, in *Heme Peroxidases*, edited by E. Ravan, and B. Dunford (The Royal Society of Chemistry: London, 2016), pp 183-217.
- [2] M. Sharrock *et al.*, *Biochemistry*, **12** (1973) 258-265.
- [3] P. G. Debrunner *et al.*, *Proc. Natl. Acad. Sci.*, **93** (1996) 12791-12798.

PR7-3 Analysis of Iron-based Products Using Mössbauer Spectroscopy - Iron Oxide Scale Generated in the Boiler Feed-water in Thermal Power Plant -

Y. Akiyama, M. Okumura, K. F. Mishima¹, S. Nishijima¹,
H. Okada², N. Hirota², T. Yamaji³, H. Matsuura³,
S. Namba³, T. Sekine⁴, Y. Kobayashi⁵, M. Seto⁵

Graduate School of Engineering, Osaka University

¹ *Department of Nuclear Technology and Applied Engineering, Fukui University of Technology*

² *National Institute for Materials Science*

³ *Shikoku Research Institute Inc.,*

⁴ *Ebara Industrial Cleaning Co., Ltd.,*

⁵ *Institute for Integrated Radiation and Nuclear Science, Kyoto University*

INTRODUCTION: The power generation efficiency of thermal power plants decreases due to corrosion products (iron oxide scale) formed in the feed-water system. In this study, removal of iron oxide scale from thermal power plants applying oxygen treatment (OT) using high gradient magnetic separation (HGMS) was investigated.

While the scale of thermal power plants applying all volatile treatment (AVT) is mainly composed of ferromagnetic particles, the OT scale is mainly composed of paramagnetic particles, which are difficult to capture by magnetic force. Our previous analysis of the scale collected from actual OT-adopted thermal power plant using Mössbauer spectroscopy showed that the OT scale contains up to 20% ferromagnetic particles, while the other components are paramagnetic particles, and these particles do not form co-crystal [1].

Based on the results, we proposed the two-stage magnetic separation system shown in Fig.1, that captures ferromagnetic particles in the first stage and paramagnetic particles in the second stage [2]. To design the magnetic separation system for an actual thermal power plant used at high temperature, we focused on the second stage and investigated the change in the capture performance of paramagnetic scale by the temperature.

EXPERIMENTS: High-gradient magnetic separation using superconducting solenoidal magnet was conducted targeting hematite (Fe_2O_3), which is the main component of OT scale. Suspension of 20.0 g of hematite particles at 500 ppm was prepared, and the experiment was conducted at 25-80 °C under the conditions of magnetic field of 6 T, flow velocity of 20 cm/s, and pH=4. These conditions assume the installation of separation equipment in the chemical cleaning line of a thermal power plant boiler feedwater system. The filters made of ferromagnetic stainless steel were installed inside the superconducting magnet. In case the fluid passing through the superconducting magnet was hot, cooling water was flowed between the magnet and the piping to prevent the magnet from temperature increasing. The results were compared with simulations based on particle trajectory calculations based on the magnetic field and flow velocity distributions around the ferromagnetic filter wire.

RESULTS: Fig. 2 shows the captured amount for each of the five filters. The captured amount increased as the temperature increased. In comparison with the simulation results, the measured value was lower than the estimated value, and the difference tended to increase as the temperature increased [3]. The reason is thought to be the increase in thermal motion of hematite particles and the decrease in fluid temperature due to the cooling water in the magnetic separation section. Based on this, the captured amount was re-calculated considering these effects. As a result, it was estimated that 90 % of the generated paramagnetic particles could be captured by installing 2745 filters in the practical scale. Based on the results, we were able to design the magnetic separation system and conditions for the introduction of a two-stage magnetic separation system for the practical use.

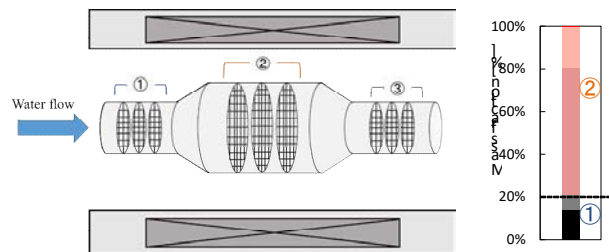


Fig.1 Composition of the scale collected at low-pressure heater drain measured by the Mössbauer spectroscopy and the two-stage magnetic separation system. based on it.

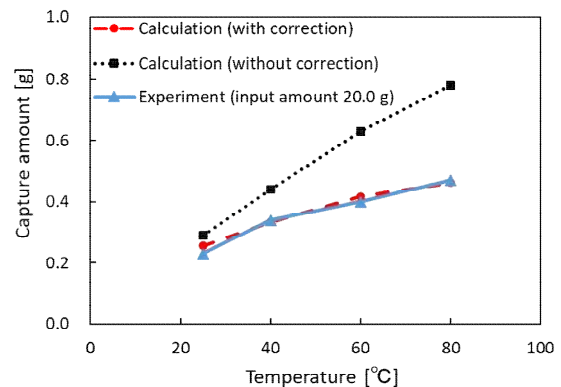


Fig.1 Temperature dependence of capture amount of hematite per a filter.

REFERENCES:

- [1] M. Hiramatsu *et al.*, J. Phys. Conf. Ser., 1293 (2019) 012079.
- [2] K. Akiyama *et al.*, IEEE Transactions on Applied Superconductivity, Vol. 31, No. 5, (2021) 3700204.
- [3] M. Okumura, *et al.*, IEEE Transactions on Applied Superconductivity, in press.

PR7-4 Electrical conductivity and the iron valence state of enstatite glasses up to Mbar pressures

I. Mashino, T. Yoshino, S. Kitao¹, T. Mitsui², R. Masuda³

Institute for Planetary Materials, Okayama University

¹*Institute for Integrated Radiation and Nuclear Science, Kyoto University*

²*Synchrotron Radiation Research Center, Kansai Photon Science Institute, Quantum Beam Science Research Directorate, National Institutes for Quantum and Radiological Science and Technology*

³*Graduate School of Science and Technology, Hirosaki University*

INTRODUCTION: The existence of gravitationally stabilized melts at the bottom of the Earth's mantle has been proposed because a density crossover between melts and crystals is expected to occur. However, whether the crossover occurs in the lower mantle or not strongly depends on the chemical composition of both the melt and crystals. The valence and spin states of iron are believed to affect the iron partitioning between melts and crystals, thus also control a depth of the density crossover [1]. In order to understand the valence/spin states of iron in silicate melts, we firstly conducted high-pressure electrical conductivity measurements of iron-bearing enstatite glass which has a representative composition of the mantle, because silicate glasses have been considered as good analogues of silicate melts.

EXPERIMENTS: ⁵⁷Fe-bearing enstatite glasses (hereafter Fe-enstatite glass) were synthesized from reagent MgO, ⁵⁷Fe₂O₃ and SiO₂ powders. The mixtures of oxides were placed in a platinum crucible and melted at 1650 °C, and subsequently quenched by immersing the base of the crucible in water. The conventional ⁵⁷Fe-Mössbauer spectroscopy was performed using a ⁵⁷Co source in Rh matrix with nominal activity of 1.85 GBq at Institute for Integrated Radiation and Nuclear Science, Kyoto University. The velocity scale is referenced to α -Fe. According to the Mössbauer spectroscopy, iron in the synthesized glasses was found to be present as shown in Table 1. Compared with hyperfine parameters in silicate glasses previously reported at ambient condition [2, 3], doublet 1 and doublet 2 can be associated with Fe³⁺ and Fe²⁺ in octahedral site, respectively.

Table 1.

Fitting results of the ambient conventional Mössbauer spectra of Fe-enstatite glasses

	Doublet 1 (Fe ³⁺)			Doublet 2 (Fe ²⁺)		
	CS (mm/s)	QS (mm/s)	Aria ratio (%)	CS (mm/s)	QS (mm/s)	Aria ratio (%)
13 mol% Fe-bearing enstatite glass						
	0.36	1.27	57	1.04	1.98	43
19 mol% Fe-bearing enstatite glass						
	0.34	1.25	65.2	1.05	2.01	34.8
10 mol% Fe, 10 mol% Al-bearing enstatite glass						
	0.34	1.24	43	1.03	1.91	57

The synthesized glasses were loaded into a diamond anvil cell with 150 and 300 μ m culets. The gold foils electrically insulated by Al₂O₃ layer were attached to the sample and connected to platinum electrodes outside the sample hole. Electrical conductivity measurements were performed at Institute for Planetary Materials, Okayama University using the two-wire terminal method with an

alternating current signal, an amplitude of 1 V and within a frequency range of 0.1–1 MHz.

RESULTS: Fig. 1 shows the obtained electrical conductivity of Fe-enstatite glasses with various iron contents as a function of pressure at 300 K in this study. At lower pressure, the electrical conductivity of Fe-enstatite glasses gradually increases with increasing pressure. At pressures above 70 GPa, the conductivity decreases once and then increases in higher pressure (shaded areas in Fig. 1). Previous studies observed the trend change in electrical conductivity of (Mg,Fe)O ferropericlase between 25 and 40 GPa, which is likely associated with spin transition from high-spin to low-spin states of iron [4, 5]. The trend change in Fe-enstatite glasses is similar to the previous results. Therefore, the spin transition of iron is one possibility to account for the trend change. Another possibility is that Fe³⁺/ Σ Fe ratio changes under high pressure. In previous Mössbauer spectroscopic study of Na, Fe-bearing silicate glass, the Fe³⁺/ Σ Fe slightly increases around 60 GPa [6]. Generally, the electrical conductivity changes depending on Fe³⁺/ Σ Fe ratio. The trend change can be also explained by the change of Fe³⁺/ Σ Fe ratio with increasing pressure. Besides the ambient conventional Mössbauer data, a high-pressure synchrotron Mössbauer spectroscopic experiment was performed for the enstatite glass with 13 mol% Fe. Geophysical discussion is now ongoing.

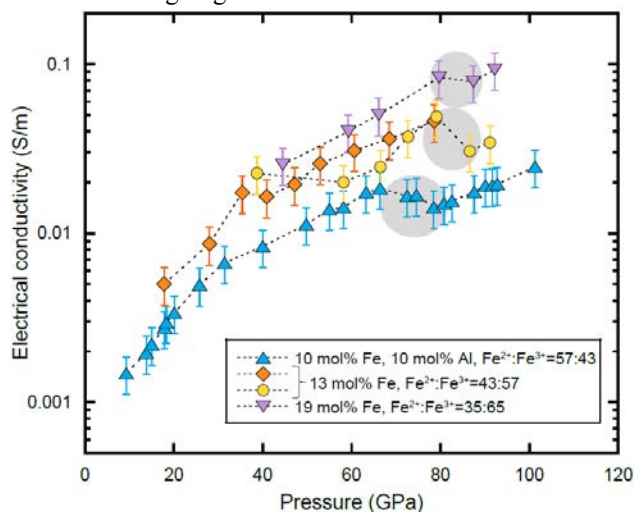


Fig. 1. Electrical conductivities of Fe-bearing enstatite glasses as a function of pressure at 300 K.

REFERENCES:

- [1] R. Nomura *et al.*, *Nature* **473**, 199 (2011).
- [2] M. Dyar, *Am. Mineral.* **70**, 304 (1985).
- [3] B. Mysen and P. Richet, *Silicate Glasses and Melts* (Elsevier, 2019).
- [4] K. Ohta *et al.*, *Proc. Japan Acad. Ser. B* **83**, 97 (2007).
- [5] T. Yoshino *et al.*, *J. Geophys. Res.* **116**, 1 (2011).
- [6] C. Prescher *et al.*, *Earth Planet. Sci. Lett.* **385**, 130 (2014).

PR7-5 The role of iron in the differential weathering processes of volcanic fall deposit

H. Fukui, Y. Matsushi¹, S. Kitao², Y. Kobayashi², K. Shinoda³, T. Watanabe⁴

Graduate School of Science, Kyoto University

¹Disaster Prevention Research Institute, Kyoto University

²Institute for Integrated Radiation and Nuclear Science, Kyoto University

³Graduate School of Science, Osaka city University

⁴Graduate School of Agriculture, Kyoto University

INTRODUCTION: During the alteration of volcanic material into secondary mineral, iron plays an important role. Iron is easy to precipitate under an oxidizing condition, whereas under a relatively reducing condition, because the divalent cation is present in liquid phase, it could contribute to the formation of aluminosilicate [1]. Moreover, halloysite, one of the clay minerals, could be easy to form under the condition in which ferrous iron is present [2]. The aim of the study is to evaluate the role of iron in the weathering processes of volcanic material by examining the chemical state using ⁵⁷Fe Mossbauer spectroscopic analysis.

EXPERIMENTS: We collected soil samples containing an Andesitic pumice, Ta-d2, at Atsuma town, southern part of Hokkaido, Northern Japan. The soil has altered into the three weathering pattern, reddish-weathered pumice (RP), white-weathered pumice (WP), and greyish-weathered pumice (GP) [3]. To examine the valence and chemical-bonding state of iron included in the soil, we conducted room-temperature (300 K) and cryogenic (22K) ⁵⁷Fe Mossbauer spectroscopic analysis. We measured Mossbauer spectra using ⁵⁷Co with Rh matrix as a radiation source for 6 representative powder samples. In addition to the powder samples, to examine the weathering condition within a single pumice, we conducted in-situ Mossbauer analysis for a thin section of the pumice using 0.5 mm diameter pinhole.

RESULTS AND DISCUSSIONS:

Ferrous/ferric ratio in the representative powder samples at GP, RP and WP were shown in Fig. 1A. GP contained the largest amount of ferrous ion, 56.6%, whereas RP

contained smaller amount and WP did the lowest amount of ferrous iron. Clay fraction obtained from WP sample had no divalent iron. Also, both S3-50 and S1-60 located at shallower part of Ta-d2 showed less amount of ferrous iron and more amount of ferric iron than both S3-80 and S1-80 located at deeper part of Ta-d2.

Fig. 1B indicates the ferrous/ferric ratio of 8 locations, P1 to P8, for in-situ pinhole Mossbauer analysis within a single pumice. The greyish cores of pumice, P4 and P6, have the highest amount of ferrous iron, whose values were similar to the powder sample of GP (Fig. 1A). On the other hand, the white rind of pumice, P3 and P5, showed no ferrous iron, all of which have altered into trivalent state. On the reddish band located in between the core and rind, P1 and P2 have an intermediate content of ferrous ion. P6 located just inside the reddish band contained much larger amount of ferrous ion, whereas P7 and P8 just outside the reddish band contained no ferrous iron.

The results revealed that iron in the Ta-d2 pumice follow a different reaction path; under an oxidizing condition of RP, the pumice altered into iron (hydr)oxides such as goethite and hematite, whereas under a relatively reduced condition of WP and GP, halloysite could be easy to form because divalent iron would be present in the solution. Although iron takes trivalent state both in RP and WP, the value of QS (quadrupole splitting) was completely different, 0.75 mm/sec for RP and 0.58 mm/sec for WP, indicating that chemical-bonding state of iron plays a crucial role on the differential weathering of Ta-d2.

REFERENCES:

- [1] Gainey *et al.*, Nat. Commun., **8** (2017) 1230.
- [2] Churchman *et al.*, Clay Miner., **51**(2016) 395-416.
- [3] Fukui *et al.*, Catena (in preparation).

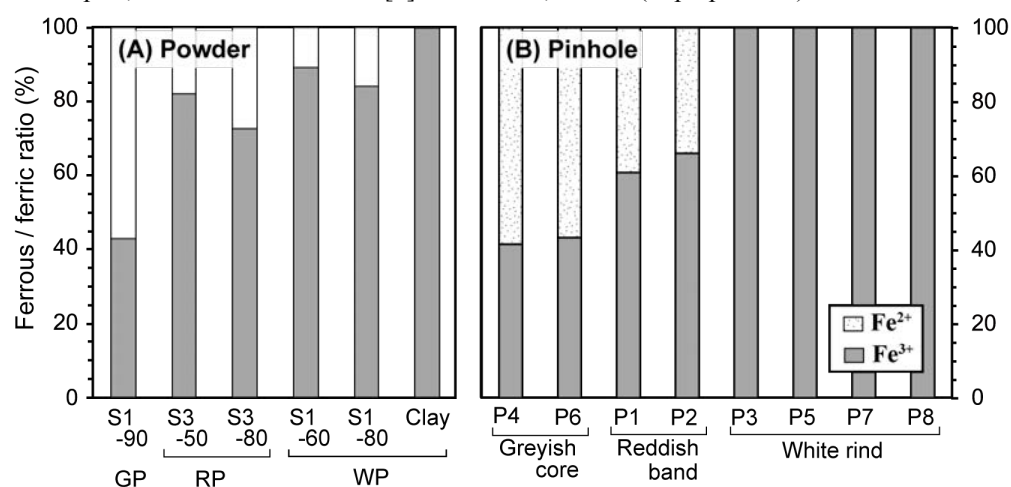


Fig. 1. Ferrous/ferric ratio of (A) 6 powder samples and (B) 8 in-situ Mossbauer analysis of a thin section. Sampling locations of powder samples (A) and position ID, P1 to P8 (B), are indicated in the referenced paper [3] in preparation.

PR7-6 Rough estimation of Debye temperature for precursor of supported gold cluster catalysts derived from Recoil-free fraction in ^{197}Au Mössbauer spectroscopy

H. Ohashi, T. Sai, R. Tawatari, K. Kikuchi, H. Murayama¹, T. Ishida², D. Kawamoto³, Y. Kobayashi⁴, S. Kitao⁴

Faculty of Symbiotic Systems Science, Fukushima University

¹Faculty of Sciences, Kyushu University

²Department of Applied Chemistry for Environment, Tokyo Metropolitan University

³Faculty of Sciences, Okayama University of Science

⁴Institute for Integrated Radiation and Nuclear Science, Kyoto University

INTRODUCTION:

Though sulfide deposition-precipitation (SDP) method was a kind of new DP method, it was a very unique method and different from DP on several points such as preparation pH. However, until now, the structure of gold sulfide as a precursor synthesized by the SDP method was unknown.

On the other hand, Mössbauer effect (recoilless nuclear resonance) is the phenomenon of resonant absorption of γ -radiation, emitted at the radioactive decay of a nucleus in a radioactive material, which act as absorber. This method is widely used in material research that contains iron (^{57}Fe) and tin (^{119}Sn), which are easy to obtain radioactive isotopes that are radiation sources. However, ^{197}Au Mössbauer spectroscopy has not been widely used because radiation source, ^{197}Pt has short half-life.

The purpose of this study was to estimate the Debye temperature derived from recoil-free fraction in ^{197}Au Mössbauer spectroscopy for the precursor of heterogeneous gold catalysts by SDP method.

EXPERIMENTS:

Gold sulfide (Au_2S_x) and activated carbon supported gold sulfide were synthesized by the similar SDP method already reported[1]. ^{197}Au Mössbauer spectra were measured at Kyoto University Research Institute of Nuclear Science. The ^{197}Pt isotope ($T_{1/2} = 18.3$ h), γ -ray source feeding the 77.3 keV Mössbauer transition of ^{197}Au , was prepared by neutron irradiation of isotopically enriched ^{196}Pt metal at the Kyoto University Reactor. The measurement temperature was 14 - 20 K, and the measurement was performed by the transmission method.

RESULTS:

The ^{197}Au Mössbauer spectra for gold foil (standard) and precursor of supported gold cluster catalysts were measured. These spectra were normalized by the content of gold (n) in measured sample. Each area (A) of normalized spectrum was calculated. There is a following relationship between recoil-free fraction (f) and area;

$$f = a A/n \quad (\text{eq.1})$$

where "a" is proportional constant in this measurement equipment. On the other hand, equation of recoil-free fraction is as follows;

$$f = \exp \left\{ -\frac{6E_R}{k_B\theta_D} \left[\frac{1}{4} + \left(\frac{T}{\theta_D} \right)^2 \int_0^{\frac{\theta_D}{T}} \frac{x dx}{e^x - 1} \right] \right\} \quad (\text{eq.2})$$

where k_B is Boltzmann constant, E_R is recoil energy, T is measurement temperature and θ_D is Debye temperature. Variations in the recoil-free fraction ($\ln f$) of ^{197}Au Mössbauer spectrum as a function of Debye temperature derived from eq.2 were shown in Fig.1. Though Debye temperature for bulk gold was 165K, we estimated "a" in eq.1 from eq.2, and roughly estimated θ_D for the precursor from area and eq.2. It was turned out that $\theta_{D\text{-precursor}}$ was around 80 K. This θ_D was quite low but appropriate from the standpoint of precursor of gold cluster catalysts.

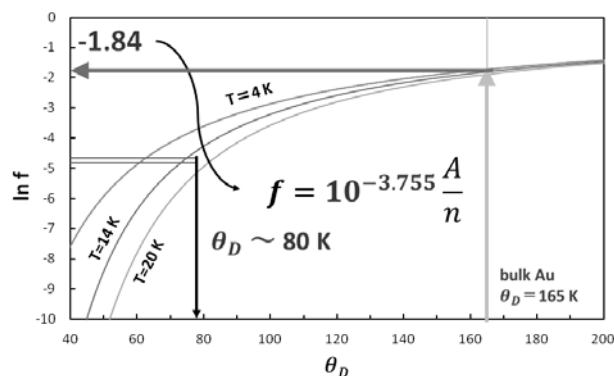


Fig.1. Variations in the recoil-free fraction ($\ln f$) of ^{197}Au Mössbauer spectrum as a function of Debye temperature derived from eq.2.

REFERENCE:

[1] H. Ohashi *et al.*, "Method for dispersing and immobilizing gold fine particles and material obtained thereby", Patent No. 5010.

PR7-7 Recoilless Fraction on ^{197}Au Mossbauer Spectroscopy

Yasuhiro KOBAYASHI

*Institute for Integrated Radiation and Nuclear Science,
Kyoto University*

INTRODUCTION: As a study of new materials, we are conducting Mössbauer spectroscopy of Au-supported catalysts. In the measurements, we noticed the samples in which the absorption intensity of the Mössbauer spectrum was small even though the amounts of Au in the samples were sufficient. This result indicates that the recoilless fraction is small, which is the probability of the Mössbauer absorption. In the case of nanoparticles, the recoilless fraction depends on the size of the particles. It could be the technique to measure the size of small nanoparticles that cannot be observed with an electron microscope.

Measuring the absolute amount of recoilless fraction is difficult due to the background fluctuations in the ^{197}Au Mössbauer measurement. Therefore, we investigated a method for estimating the Debye temperature from the temperature dependence of the spectral absorption intensity and confirmed its validity with pure Au foil.

The following equation describes the recoilless fraction f using the Debye model [1].

$$f = \exp \left[-\frac{3E_R}{2k\theta_D} \left\{ 1 + 4 \left(\frac{T}{\theta_D} \right)^2 \int_0^{\theta_D/T} \frac{udu}{e^u - 1} \right\} \right]$$

Here, T is the temperature, θ_D is the Debye temperature, and E_R is the recoil energy.

EXPERIMENTS: ^{197}Au Mössbauer measurement was conducted using a constant-acceleration spectrometer with a NaI scintillation counter. The ^{197}Au γ -ray source (77.3 keV) was obtained from ^{197}Pt (half-life; 18.3 hours) generated by irradiation of neutron to 98%-enriched ^{196}Pt metal foil using KUR. The γ -ray source and samples were cooled to the same temperatures using a helium refrigerator. The thickness of the Au foil (sample) was 20 μm . The isomer shift value of a gold foil was referenced to 0 mm/s.

RESULTS: Figure 1 shows the Mössbauer spectra at each temperature. The absorption areas on the spectra decrease at higher temperatures, indicating that the recoilless fraction decreases. Figure 2 shows the temperature dependence of the absorption area on the Mössbauer spectra. The areas are normalized by the value at 20K. The solid line is the calculated value from the equation. The absorption areas are proportional to the product of the recoilless fraction of the γ -ray source and the absorber. The Debye temperature of the γ -ray source is 270K, which is the Debye temperature of platinum metal. And the Debye temperature of the absorber is 164K from gold metal.

The observed absorption areas are in good agreement with the calculated curves. The observed area and the calculated value are normalized by the value of 20K, and no other corrections are made.

From this result, we found that the measurements of the temperature dependence of the absorption area are adequate for measuring the Debye temperature of the sample and are also helpful for the study of nanoparticles. In the future, we plan to measure temperature changes in various samples.

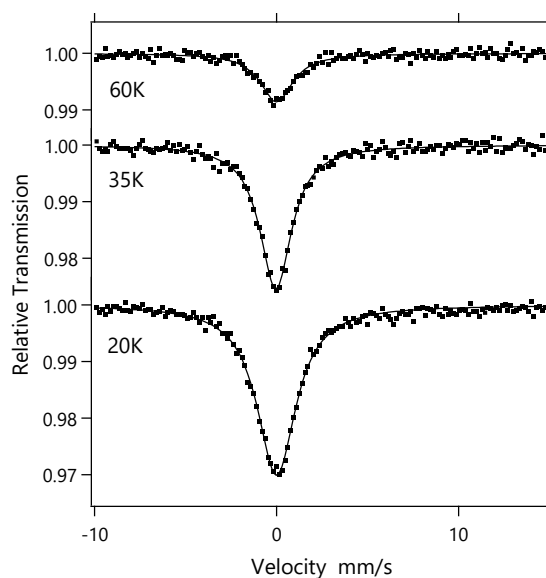


Fig. 1 The ^{197}Au Mössbauer spectra of Au foil at various temperatures.

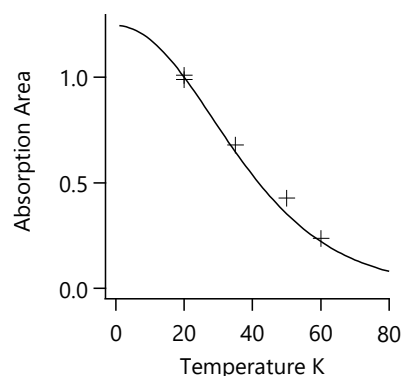


Fig. 2 Temperature dependence of the absorption area on the Mössbauer spectra. The markers are the observed absorption areas (normalized by the value at 20K), and the solid line is the calculated value.

REFERENCES:

[1] Gunther K. Wertheim, *Mössbauer Effect: Principles and Applications* (Academic Press, New York, 1964).

PR7-8 ^{61}Ni Mössbauer Spectroscopy for Supramolecular Bridging Cyanide Complexes

Takafumi KITAZAWA^{1,2}, Kosuke KITASE¹, Daiki UEDA¹, Daichi FUJIMOTO¹, Shunsuke ARAI¹, Yasuhiro KOBAYASHI³, Shinji KITAO³, Takumi KUBOTA⁴ and Makoto SETO³

¹Faculty of Science, Toho University

²Research Centre for Materials with Integrated Properties, Toho University

³Institute for Integrated Radiation and Nuclear Science, Kyoto University

⁴Agency for Health, Safety and Environment, Kyoto University

INTRODUCTION: The Mössbauer Effect has been found for about 100 nuclear transitions in some 80 nuclides in nearly fifty elements. The technique is a very valuable and helpful tool to the material sciences linking to molecular magnetisms. It is well-known that 3-d block transition metal complexes with d^4 - d^7 configuration in an octahedral crystal field have a possibility of SCO between the low spin (LS) and the high spin (HS) state. Octahedral iron(II) SCO systems with $3d^6$ can be transitioned between the diamagnetic (t_{2g}^6) and the paramagnetic ($t_{2g}^4(e_g)^2$) configuration. Coordination polymers with bistable systems between the LS and the HS states, usually triggered by external stimuli, such as temperature, light, pressure and guest molecules, are a class of potential candidates for smart materials. As the very important history of SCO researches of the Hofmann-like coordination polymers, the SCO in $\text{Fe}^{\text{II}}(\text{pyridine})_2\text{Ni}(\text{CN})_4$ was found using ^{57}Fe Mössbauer spectroscopy and SQUID measurements in 1996 [1], SCO supramolecular Hofmann-like metal-organic frameworks containing 2D layers and 3D structures, with octahedral iron(II) ions linked by cyanidometallates along the in-plane directions, have been investigated thoroughly for the development of interesting SCO materials in order to obtain potential applications in smart materials [2-7]. Ni(II) ions states are associated with Fe(II) ions state. Now we have carried out ^{61}Ni Mössbauer spectroscopy for three Hofmann type SCO compounds which act as different spin transition temperatures and behaviors including LS spin and HS spin ratios; $\text{Fe}(\text{pyridine})_2\text{Ni}(\text{CN})_4$, $\text{Fe}(3\text{-Methyl-py})_2\text{Ni}(\text{CN})_4$, and $\text{Fe}(3\text{-Cl-py})_2\text{Ni}(\text{CN})_4$, and mononuclear $\text{K}_2[\text{Ni}(\text{CN})_4]$.

EXPERIMENTS: We freshly synthesized $\text{Fe}(\text{pyridine})_2\text{Ni}(\text{CN})_4$, $\text{Fe}(3\text{-Methyl-py})_2\text{Ni}(\text{CN})_4$, and $\text{Fe}(3\text{-Cl-py})_2\text{Ni}(\text{CN})_4$, according to the applied methods [1,5-7] and mononuclear $\text{K}_2[\text{Ni}(\text{CN})_4]$.

^{61}Ni Mössbauer source production associated with $^{62}\text{Ni}(\gamma, p)^{61}\text{Co}$ was done using activation with Bremsstrahlung from the Electron beam of the KURNS-LINAC. ^{61}Ni Mössbauer measurements were carried out conventional methods, Since the half-life of ^{61}Co is about 100 minutes, about three hours measurements were done for one cycle. For one SCO compound sample, three times cycles are carried out in order to get

suitable Mossbaer spectra. All spectra were obtained at 16 K. Ni-14at%V alloy was used for characterizations of velocities.

RESULTS: As shown in Fig. 1, ^{61}Ni Mössbauer spectra of three SCO compounds with MOF(Metal Organic Framework) were found for the first time at 16K.

The obtained Mössbauer parameters have relationship with the square planar crystal field of $[\text{Ni}(\text{CN})_4]_2$ units. The parameters for three SCO compounds are slightly different due to slightly different Ni(II) environments, indicating environments of Ni(II) ions are associated with those of Fe(II) ions.

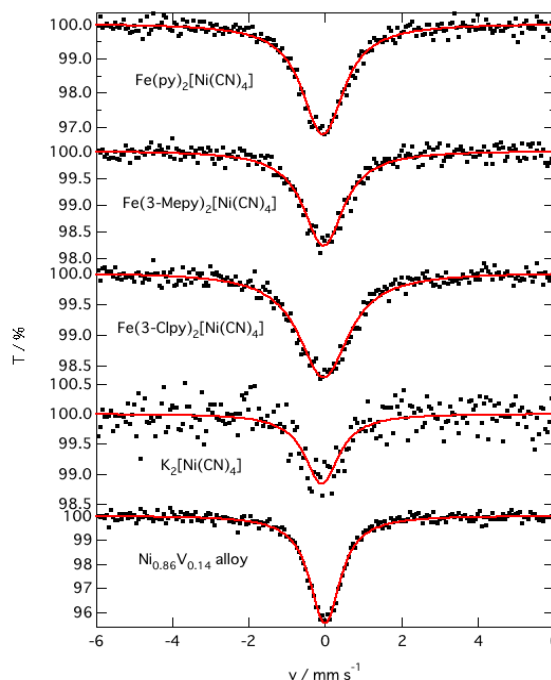


Fig.1 ^{61}Ni Mössbauer Spectroscopy for Supramolecular Bridging Cyanide Complexes.

REFERENCES:

- [1] T. Kitazawa, Y. Gomi, M. Takahashi, M. Takeda, M. Enomoto, A. Miyazaki, T. Enoki, *J. Mater. Chem.* 1996, 6(1) 119-121, DOI:10.1039/JM9960600119.
- [2] T. Kitazawa, Synthesis and Applications of New Spin Crossover Compounds. *Crystals* 2019, 9(8), 382; DOI:10.3390/cryst9080382.
- [3] K. Kitase, D. Akahoshi and T. Kitazawa, *Inorg. Chem.*, 60, 7, 4717-4722 (2021).
- [4] K. Kitase, T. Kitazawa, *Dalton. Trans.*, 49, 12210-12214 (2020). (Back Cover)
- [5] M. Gábor, T. Guillon, N. Moussa, L.Rechignat, T. Kitazawa, M. Nardone, B. Azzedine, *Chem. Phys. Lett.* 2006, 423(1-3), 152-156.
- [6] Kitazawa, T.; Eguchi, M.; Takeda, M; *Mol. Cryst. Liq. Cryst. Sci. Tech. A*, 2000, 341, 527-532 DOI:10.1080/10587250008026193.
- [7] T. Kitazawa, Mi. Takahashi, Ma. Takahashi, M. Enomoto, A. Miyazaki, T. Enoki, M. Takeda, *J. Radio-anal. Nucl. Chem.* 1999, 239(2), 285-290. DOI:10.1007/BF02349498.

PR7-9 Mössbauer spectroscopy of a perovskite-type iron oxide $\text{Ba}_{2/3}\text{La}_{1/3}\text{FeO}_3$

M. Onose^{1,2}, H. Takahashi¹, R. Takahashi³, H. Wadati^{3,4}, S. Kitao⁵, M. Seto⁵, and S. Ishiwata¹

¹Division of Materials Physics, Graduate School of Engineering Science, Osaka University

²Department of Applied Physics, the University of Tokyo

³Department of Material Science, Graduate School of Science, University of Hyogo

⁴Institute of Laser Engineering, Osaka University

⁵Institute for Integrated Radiation and Nuclear Science, Kyoto University

INTRODUCTION: Spin and charge ordering in transition-metal oxides manifests itself as an emergent collective phenomenon of strongly correlated electrons. For example, a perovskite-type iron oxide $\text{Sr}_{2/3}\text{La}_{1/3}\text{FeO}_3$ is known to show a characteristic spin-charge ordering (SCO) as shown in Fig. 1, where six-fold collinear spin ordering and three-fold charge ordering as $3\text{Fe}^{3.67+} \rightarrow 2\text{Fe}^{3+} + \text{Fe}^{5+}$ are coupled with each other[1,2]. This spin/charge ordering ranges from $x = 0$ to $x = 0.75$ in its Ba-substituted system $(\text{Sr}_{1-x}\text{Ba}_x)_{2/3}\text{La}_{1/3}\text{FeO}_3$, whereas our previous neutron diffraction experiments for $x = 1$ suggests a spin-charge decoupling: whereas the magnetic structure of the ground state remains to be the same as that of the SCO phase, an unexpected G-type AFM phase appears as the high-temperature phase. To further clarify the existence or absence of charge disproportionation for $x = 1$, we performed Mössbauer spectroscopy measurements.

EXPERIMENTS: A polycrystalline sample of $x = 1$ was obtained by high-pressure synthesis. The ^{57}Fe Mössbauer spectra were measured with a ^{57}Co source in Rh. The velocity was calibrated with $\alpha\text{-Fe}$. Fits to the Mössbauer spectra were performed by the least-squares method assuming Lorentzian peaks.

RESULTS: As shown in Fig. 2, the spectra in the paramagnetic phase ($180\text{K} \leq T \leq 293\text{K}$) can be well fitted by quadrupole-split doublets for $\text{Fe}^{3.67+}$, and those below 140 K by the superposition of two sextets corresponding to Fe^{3+} and Fe^{5+} , indicating the emergence of the SCO phase along with our previous neutron diffraction measurements. Although the spectra at $T = 160\text{K}$ in the G-AFM phase are significantly broadened making it difficult to obtain a satisfactory fitting, the asymmetric spectral shape, i.e., an asymmetric distribution of isomer shift, suggests the development of incoherent charge ordering or the slowing down of charge fluctuation as

$3\text{Fe}^{3.67+} \rightleftharpoons 2\text{Fe}^{3+} + \text{Fe}^{5+}$. The hyperfine field for $x = 1$ are comparable with the previous study of $x = 0$ [3], implying that they share the same SCO phase as a ground state. On the other hand, isomer shift (IS) for $x = 1$ is systematically larger than that for $x = 0$ by about 0.01 mm/s. This difference in IS is most likely due to the change in the bonding state of Fe-O, considering the IS of the related Fe^{4+} compounds SrFeO_3 [4] and BaFeO_3 [5].

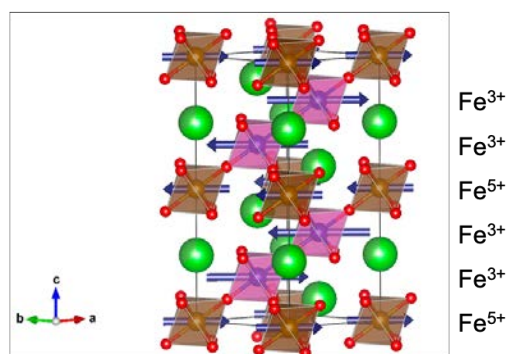


Fig. 1. Spin-charge ordered phase of $\text{Sr}_{2/3}\text{La}_{1/3}\text{FeO}_3$.

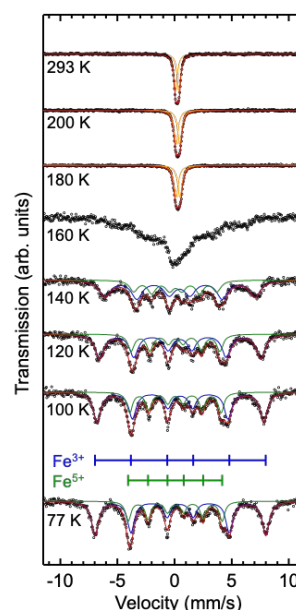


Fig. 2. Temperature dependence of the Mössbauer spectra for $\text{Ba}_{2/3}\text{La}_{1/3}\text{FeO}_3$ with the fitting curves of Lorentzian functions.

REFERENCES:

- [1] P. D. Battle *et al.*, *J. Solid State Chem.* **84**, 271 (1990).
- [2] J. Q. Li *et al.*, *Phys. Rev. Lett.* **79**, 297 (1997).
- [3] J. Blasco *et al.*, *Phys. Rev. B* **98**, 104422 (2018).
- [4] P. Adler *et al.*, *Phys. Rev. B* **73**, 094451 (2006).
- [5] N. Hayashi *et al.*, *Angew. Chem. Int. Ed.* **50**, 12547 (2011).

PR7-10 Research on magnetism in a novel Kondo Lattice III

Y. Kamihara, Z. Liu, T. Shimura, S. Kitao¹, and M. Seto¹

Department of Applied Physics and Physico-Informatics,
Faculty of Science and Technology, Keio University

¹Institute for Integrated Radiation and Nuclear Science,
Kyoto University

The compounds with a 1:2:2 compositional ratio (so-called "122 compounds") are attractive for thermoelectric materials and topological conductor with spontaneous magnetic moments. [1-3] In 2018, high quality polycrystalline samples of EuSn_2As_2 have been reported using a new synthesis technique. [4, 5] In the report, we prepared a polycrystalline sample of EuSn_2P_2 according to the similar process to that of EuSn_2As_2 . Theoretical magnetic phases of Eu sub lattice are calculated as ferromagnetic along to (a , b) axis and antiferromagnetic along to c axis. The magnetic phases are dominated by s - f interaction between Eu 4f electrons via itinerant electrons.

Gui *et al.* reported that a Neel temperature of the Eu sublattice was about 30 K in EuSn_2P_2 . [2] In the polycrystalline sample, Gui *et al.* also reported that antiferromagnetic phase with spontaneous magnetic moments $\sim 6 \mu_B$ at 2 K under 5 tesla. The reported spontaneous magnetic moments were smaller than those of theoretical Eu^{2+} ions with spontaneous magnetic moments $\sim 7 \mu_B$. A possible mechanism, which should explain the difference between experimental and theoretical magnetic moments of Eu^{2+} , is controversial. In this report, we demonstrate element-specific internal magnetic fields measurement for the polycrystalline EuSn_2P_2 using Mössbauer spectroscopy.

EXPERIMENTS: According to our previous report, polycrystalline samples of EuSn_2P_2 were prepared from Eu ingots and Sn-P pellets via a liquid phase reaction in carbon crucibles within evacuated silica tubes. [4] X-ray diffraction measurements at room temperature (RT) were performed in order to characterize the crystallographic phases of powdered sample of as-grown EuSn_2P_2 . In this research, we have measured ^{151}Eu and ^{119}Sn Mössbauer spectra for polycrystalline EuSn_2P_2 using conventional optical setting. Both of ^{151}Eu and ^{119}Sn Mössbauer spectra demonstrates magnetic splitting at low temperatures. The spectra were fitted to Lorentzian line shapes using the MossWinn [6, 7] Program.

RESULTS: Figure 1 shows temperature dependence of ^{151}Eu Mössbauer spectra observed for our polycrystalline sample. At temperature (T) = 298 K, there are apparent two structures, which are due to the emission and absorption of the gamma ray in the sample.

The structures are assigned for two valent states of Eu ions in EuSn_2P_2 ; i.e. a mixed valent state of Eu ions. The mixed valent state is similar to that observed for Eu ions in EuSn_2As_2 . [6]

At $T = 15$ K, a splitting of the lower structure is clearly

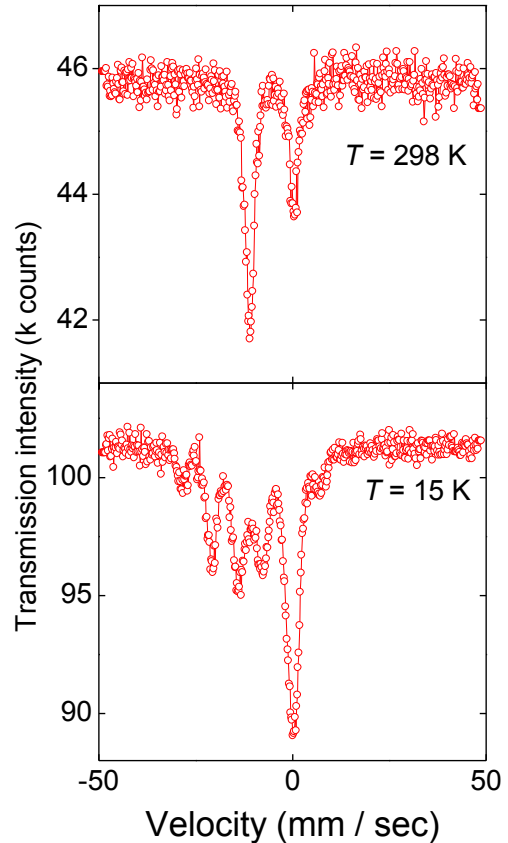


Fig. 1. ^{151}Eu Mössbauer spectra for EuSn_2P_2 at temperatures (T) = 15 K and 298 K.

observed. The splitting is mainly due to an existence of finite internal magnetic field.

In a future study, we will demonstrate quantitative analysis on element specific internal magnetic fields, spontaneous magnetic moments, isomer shifts, a portion of mixed valent state, and Debye temperature of EuSn_2P_2 .

These future study will verify bulk properties on the possible magnetic topological conductors, EuSn_2Pn_2 ($\text{Pn} = \text{P}, \text{As}$), in which the Eu ions exhibit the Kondo lattices.

REFERENCES:

- [1] M. Q. Arguilla, *et al.*, Inorg. Chem. Front. 4, 378 (2017).
- [2] X. Gui, *et al.*, ACS cent. Sci. 5, 900 (2019).
- [3] G. M. Pierantozzi, *et al.*, Proc. Natl. Acad. Sci. 119, e2116575119 (2022).
- [4] R. Sakagami, *et al.*, Mater. Sci. Tech. Jpn. 55, 72 (2018) in Japanese.
- [5] R. Sakagami, *et al.*, J. J. Appl. Phys. 60, 035511 (2021).
- [6] R. Sakagami, Ph. D thesis, Keio University, 2021. Synthesis and transport properties of van der Waals-type quasi-two-dimensional pnictide, EuSn_2As_2
- [7] Z. Klencsar: MossWinn Program, Budapest, 2001 [<http://www.mosswinn.com/>].

PR7-11 Optimization for the energy standard material for Mössbauer spectroscopy

R. Masuda, S. Kitao¹, Y. Kobayashi¹, M. Kurokuzu¹, T. Fujihara¹, and M. Seto¹

Graduate School of Science and Technology, Hirosaki University

¹*Institute for Integrated Radiation and Nuclear Science, Kyoto University*

INTRODUCTION: Mössbauer spectroscopy is usually known as a powerful method for the analysis of iron compounds. In fact, most of Mössbauer experiments has been performed using ⁵⁷Fe nuclide, although the other nuclides are also available in Mössbauer spectroscopy, in principle. This is because there is a critical problem in the preparation of the γ -ray source; we can purchase ⁵⁷Co for γ -ray source of ⁵⁷Fe Mössbauer spectroscopy, but we cannot do the corresponding radioactive isotopes for γ -ray source for Mössbauer spectroscopy using various nuclide. This problem can be overcome by making the isotopes by a nuclear reactor or an accelerator. KURNS has all of them and is actually the most active research institute for Mössbauer spectroscopy using various nuclides.

Recently, we are focused on the Mössbauer spectroscopy using rare-earth nuclides. The 4f electrons causes various electronic states, such as Kondo state. One of nuclides available for Mössbauer spectroscopy is ¹⁵¹Eu. Mössbauer spectroscopy using this nuclide is usually used performed with ¹⁵¹SmF₃ at room temperature because the recoilless fraction, the probability of Mössbauer effect, is reasonable at room temperature. However, recoilless fraction always increases as the temperature decreases. [1] Fig. 1 shows the temperature-dependence of the recoilless fraction of ¹⁵¹EuF₃, which is the decay product after the β -decay of ¹⁵¹SmF₃. The recoilless fraction is around 0.6 at room temperature, but it reaches around 0.9 at 10 K. This predicts further efficient measurement with 1.5 times deeper absorption by cooling the source material. However, there is another requisite; it should not have hyperfine splitting even at low temperature, although rare-earth element often shows magnetic order which induces nuclear Zeeman splitting and sometimes structural change from room temperature. Therefore, we measured Mössbauer spectra of EuF₃ at low temperature to certify no hyperfine splitting for the improvement of the efficiency of ¹⁵¹Eu Mössbauer spectroscopy.

EXPERIMENTS: The sample was non-enriched EuF₃ purchased from Wako pure chemical industry. The sample was shaped to the pellet with the cross section of 20 mm ϕ and the thickness of 25.3 mg EuF₃/cm². The Mössbauer spectroscopy was performed at Tracer Laboratory at KURNS. The γ -ray source was ¹⁵¹SmF₃ and the transmitted γ -rays after the cooled EuF₃ sample was detected by Xe proportional counter.

RESULTS: Fig. 2 shows the ¹⁵¹Eu Mössbauer spectra at some temperatures. No evidence of hyperfine structure is observed even at 10 K. Furthermore, the velocity values at absorption are equal in experimental error, about 0.05 mm/s for all temperatures. This is also reasonable even when we consider the second order Doppler shift, the thermal effect to the velocity value at absorption. The shift is calculated to be 0.057 mm/s at maximum in our case and similar to the experimental error. In the case of ¹⁵¹Eu, the isomer shift, the effect of valence state, is quite larger than this error; the difference between the isomer shift of Eu³⁺ compounds and those of Eu²⁺ ones, are typically 10 mm/s. Therefore, we can discuss the valence without any special consideration of the effect of second order Doppler shift at EuF₃.

This result suggests that the efficiency of ¹⁵¹Eu Mössbauer spectroscopy can be improved by cooling not only at Mössbauer spectroscopy with conventional radioactive γ -ray source, but also that with synchrotron radiation.

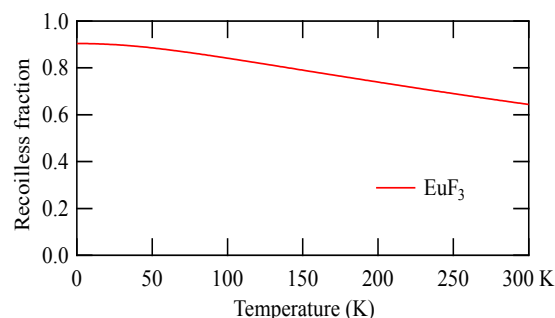


Fig. 1. Calculated Recoilless fraction of Mössbauer effect for ¹⁵¹Eu nuclear resonance at EuF₃.

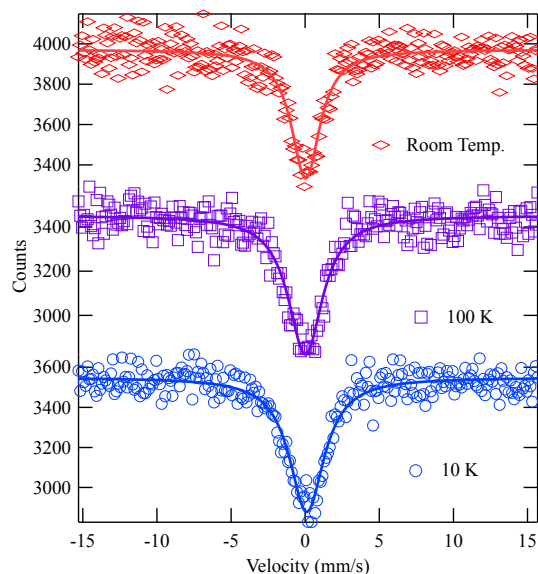


Fig. 2. ¹⁵¹Eu Mössbauer spectra of EuF₃ at some temperatures.

REFERENCES:

[1] N. N. Greenwood and T. C. Gibb, Mössbauer Spectroscopy (Chapman and Hall Ltd, London, 1971).

PR7-12 Development of ^{180}Hf Mössbauer Spectroscopy

S. Kitao¹, Y. Kobayashi¹, M. Kurokuzu¹, T. Kubota², H. Tajima³, T. Fujihara³, H. Yamashita³, R. Masuda⁴, and M. Seto¹

¹Institute for Integrated Radiation and Nuclear Science, Kyoto University

²Agency for Health, Safety, and Environment, Kyoto University

³Graduate School of Science, Kyoto University

⁴Faculty of Science and Technology, Hirosaki University

INTRODUCTION:

The Mössbauer spectroscopy is one of the most powerful methods to investigate electronic states and magnetic properties by extracting the information of a specific isotope. Even though more than one hundred of Mössbauer energy levels are known, Mössbauer spectroscopy in general is performed for quite limited isotopes, such as ^{57}Fe and ^{119}Sn . In order to promote studies for less-common Mössbauer isotopes, we have been developing practical methods for short-lived Mössbauer sources by neutron irradiation at Kyoto University Reactor (KUR). Moreover, some short-lived isotopes can be complementarily produced by high-energy γ -ray irradiation converted from electron beam using the electron linear accelerator (KURNS-LINAC). We have already developed practical preparation methods of the Mössbauer sources for various isotopes (source nuclides in parentheses): ^{61}Ni (^{61}Co), ^{125}Te (^{125m}Te), ^{129}I (^{129}Te , ^{129m}Te), ^{161}Dy (^{161}Tb), ^{166}Er (^{166}Ho), ^{169}Tm (^{169}Er), ^{170}Yb (^{170}Tm), ^{197}Au (^{197}Pt), etc.

In this research, a new attempt for ^{180}Hf Mössbauer spectroscopy is described. Hf has several Mössbauer isotopes and energy levels: ^{176}Hf (88.36 keV), ^{177}Hf (112.97 keV), ^{178}Hf (93.2 keV), ^{180}Hf (93.33 keV). However, all of these levels have high γ -ray energy of about 100 keV and their parent isotopes have short half-lives[1]. Because of these disadvantages, Hf Mössbauer spectroscopy have not been studied actively so far. Hf is an important element for some industrial applications and material sciences. Therefore, the improvement of the methods for Hf Mössbauer spectroscopy is necessary to become a useful technique to investigate Hf compounds.

EXPERIMENTS AND RESULTS:

Among the Hf Mössbauer levels, an attempt for the 93.3 keV level of ^{180}Hf has been studied. By neutron irradiation of ^{179}Hf , ^{180m}Hf with a half-life of 5.5 hours is produced[2,3]. Since a natural Hf contains ^{179}Hf with an abundance of 13.6 %, natural Hf was used for this experiment. As a candidate of the single-line material, HfC is tried as a source material. HfC was pelletized with Al powder and rapped with Al foil for the neutron irradiation. The irradiation was performed at the pneumatic tube(Pn) of KUR for 4 hours at 1MW operation or 1 hour at 5MW. In order to reduce shorter lived by-product, the irradiated source has used after waiting for a few hours from the end of irradiation. Since the recoilless fraction of Möss-

bauer isotope with high-energy level is low at high temperature, the sample and the source are cooled at the temperature of about 22 K. The γ -rays with the energy of 93.3 keV have been measured by a CeBr_3 scintillation

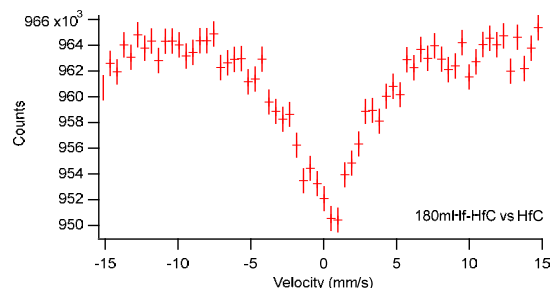


Fig. 1. ^{180}Hf -Mössbauer spectrum of HfC using ^{180m}Hf source in HfC at 22K.

detector. The spectra were measured for about half a day. The observed Mössbauer spectrum of HfC absorber using HfC source is shown in Fig. 1. The Mössbauer absorption spectrum has been successfully observed. Since the line shape is almost single line, ^{180}Hf Mössbauer spectroscopy will be able to be performed to some extent.

Figure 2 shows Mössbauer spectrum of HfO_2 absorber using HfC source. The spectrum is apparently broader than HfC absorber due to the quadrupole splitting of HfO_2 .

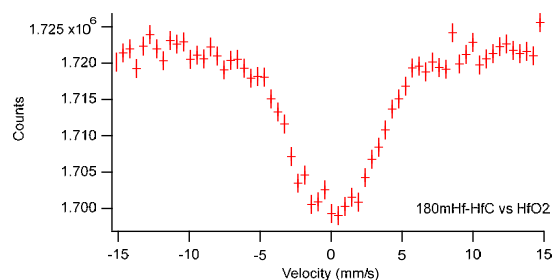


Fig. 2. ^{180}Hf -Mössbauer spectrum of HfO_2 using ^{180m}Hf source in HfC at 22K.

In summary, it is successfully confirmed that ^{180}Hf Mössbauer spectroscopy can be performed by a ^{180m}Hf source obtained by neutron irradiation of natural Hf. However, further improvement of the source material and measurement efficiency must be required for a practical spectroscopy.

REFERENCES:

- [1] "Mössbauer Spectroscopy" N. N. Greenwood and T. C. Gibb (Chapman and Hall, London, 1971).
- [2] E. Gerdau, H. J. Körner, J. Lerch, P. Steiner, Z. Naturforsch. **21 a**, 941(1966).
- [3] R. E. Snyder, J. W. Ross, D. St P. Bunbury, J. Phys. C: Sol. Stat. Phys. **1**, 1662(1968).

PR7-13 Experimental Preliminary Approach on the Precipitation Mechanism of Banded Iron Formation (BIF)

K. Yonezu, H. Hirano¹, K. Hongo¹, Y. Kobayashi² and T. Yokoyama³

Department of Earth Resources Engineering, Faculty of Engineering, Kyushu University

¹*Department of Earth Resources Engineering, Graduate School of Engineering, Kyushu University.*

²*Institute for Integrated Radiation and Nuclear Science, Kyoto University*

³*Department of Chemistry, Faculty of Sciences, Kyushu University*

INTRODUCTION: Banded Iron Formation (BIF) is chemically precipitated sedimentary rock at Precambrian age. Currently iron resource widely used in our industries largely depends on BIF. BIF was formed by seafloor hydrothermal activity. In addition, the hydrothermal water, anoxic water was mixed with oxic seawater (e.g., Otake and Otomo, 2021). However, there are many mysteries on the formation mechanism. One of the biggest issue is the alternation of iron mineral and silicate (+carbonate) minerals. Therefore, this study aims to understand the formation mechanism, especially redox condition during the formation of BIF.

EXPERIMENTS: The samples used here were collected from operating geothermal power plant or prepared by the rapid pH change of iron/silica bearing solutions. Former samples are so called silica scale, and those were analyzed by XRF and NMR. Latter samples were collected by filtration using 0.45 μ m and analyzed by mainly XRD. Precipitation percentage of iron and silica were also determined by ICP-AES using the difference before and after precipitation.

The precipitation experiments were carried out using the fixed volume (250ml) of aqueous solutions to limit the dissolved oxygen concentration. Once the dissolved oxygen was consumed to form iron bearing precipitates, no atmospheric oxygen affected in the system. Therefore, as increasing in ferrous ion in the system, more dissolved oxygen was consumed to create more anoxic condition during the experiments (reaction time was 15 minutes).

RESULTS: Five of silica scale samples were chemically analyzed. Those were directly precipitated from geothermal water, model of anoxic hydrothermal water without mixing by oxic aqueous solutions. Iron concentration in geothermal water is below detection limits of ICP-AES (less than 0.01 ppm), while iron concentration as Fe₂O₃ in silica scale were up to 15% (Tab. 1). This fact suggested that iron is specifically concentrated in silica scale. The concentration mechanism is still in discussion, but further Mossbauer spectroscopy strongly help understanding the precipitation mechanism due to amorphous form of silica scale. At least, some of aluminum precipitated as 6-coordination by NMR, suggesting that smectite group mineral precursor was formed.

Tab. 1. Chemical composition of silica scale used in this study.

	Unit	Sample 1	Sample 2	Sample 3	Sample 4	Sample 5
H2O(-)	%	0.0	5.4	2.5	3.8	0.9
H2O(+)	%	15.5	8.3	7.6	9.2	8.6
Fe ₂ O ₃	%	0.2	12.0	12.3	4.8	15.6
Al ₂ O ₃	%	12.9	7.0	6.6	10.5	9.3
Na ₂ O	%	1.6	0.8	0.6	1.4	1.4
K ₂ O	%	1.8	0.7	0.3	1.2	1.2
CaO	%	4.5	2.5	1.4	2.3	3.7
MgO	%	0.4	10.5	18.9	7.0	1.7
SiO ₂	%	75.3	55.6	49.1	70.2	67.3

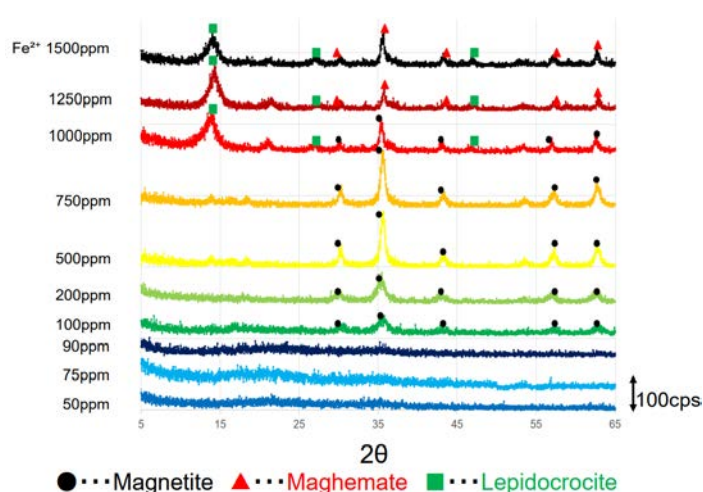


Fig. 1. XRD patterns of iron precipitates obtained from various initial ferrous concentration.

As shown in Fig. 1, different initial concentration of ferrous ion led to the different mineralogy of iron bearing precipitates. The monitored dissolved oxygen was almost zero when initial ferrous ion was more than 100 ppm. At the initial ferrous ion greater than 100 ppm, some of crystallized iron bearing minerals could be observed, while only amorphous phase precipitates (iron hydroxide) were collected less than 90 ppm initial ferrous ion conditions.

Crystallized iron bearing mineral can be further identified as magnetite, maghemite and lepidocrocite. Magnetite is dominant at 100-1000 ppm of initial ferrous ion, while maghemite is dominant at above 1250 ppm. In addition, lepidocrocite could be formed at above 1000 ppm of initial ferrous ion together with magnetite or maghemite. In order to fully understand the iron speciation of the precipitates, Mossbauer spectroscopy is powerful tool.

REFERENCES:

- [1] T. Otake and Y. Otomo, Shigen-Chishitsu, **71** (2021) 57-73.

I-2. COLLABORATION RESEARCHES

- 1. Slow Neutron Physics and Neutron Scattering*
- 2. Nuclear Physics and Nuclear Data*
- 4. Material Science and Radiation Effects*
- 5. Geochemistry and Environmental Science*
- 6. Life Science and Medical Science*
- 7. Neutron Capture Therapy*
- 8. Neutron Radiography and Radiation Application*
- 9. TRU and Nuclear Chemistry*
- 10. Health Physics and Waste Management*
- 12. Others*

CO1-1 Current Status of Versatile Compact Neutron Diffractometer (VCND) on the B-3 Beam Port of KUR, 2021

K. Mori¹, R. Okumura², H. Yoshino², K. Iwase³

¹*Institute of Materials Structure Science (IMSS), High Energy Accelerator Research Organization (KEK)*

²*Institute for Integrated Radiation and Nuclear Science, Kyoto University (KURNS)*

³*Department of Materials and Engineering, Ibaraki University*

INTRODUCTION: Neutron diffraction is a powerful tool to precisely determine the positions of light elements (H, Li, etc.) in solids. This is the main reason why neutron powder diffractometers are critical for structural investigations of energy storage materials such as rechargeable lithium-ion batteries and hydrogen-absorbing materials. The B-3 beam port of Kyoto University Research Reactor (KUR) had long been used as a four-circle single-crystal neutron diffractometer (4CND). For the last decade, however, the 4CND was so old that its research activity on neutron science was quite low. Nowadays, the versatile compact neutron diffractometer (VCND) has been installed instead of the 4CND, as shown in Fig. 1 [1]. The neutron wavelength, λ , which is monochromatized by the (220) plane of a Cu single crystal (i.e., Cu monochromator), is 1.0 Å. To cover the detector area of $6^\circ \leq 2\theta \leq 130^\circ$, twenty-five ³He tube detectors (1/2 inch in diameter) are used, where 2θ is the scattering angle. A detector bank including twenty-five ³He tube detectors is placed on the arm of the HUBER-440 goniometer. The distance from the Cu monochromator to the sample is approximately 2 m, and the distance from the sample to the detector is 1.2 m.

CRYSTAL STRUCTURE ANALYSIS: Aragonite is one of the crystal forms of calcium carbonate (CaCO₃). For biominerals such as shells, eggshells, pearls, and corals, aragonite plays an important role in their mechanical properties [2]. The crystal structure of the synthetic aragonite can be described by an orthorhombic system (space group *Pnma*). In Fig. 2, an excellent fit was obtained between the observed and calculated intensities (where $R_{wp} = 14.992\%$ and $S = 3.4488$). It is worth noting that the background intensities were omitted from the ND data. The values of a , b , and c were estimated to be 5.739(3), 4.962(2), and 7.968(4) Å, respectively. The atomic positions (x, y, z) and isotropic atomic displacements (B_{iso}) for each element were precisely determined as follows: Ca (0.236(3), 1/4, 0.417(2)) and $B_{iso}(\text{Ca}) = 0.67(38) \text{ \AA}^2$ in the 4c site; C (0.086(3), 1/4, 0.7619(14)) and $B_{iso}(\text{C}) = 0.21(29) \text{ \AA}^2$ in the 4c site; O1 (0.096(3), 1/4, 0.9247(18)) and $B_{iso}(\text{O1}) = 0.48(27) \text{ \AA}^2$ in the 4c site; and O2 (0.087(3), 0.477(2), 0.6821(12)) and $B_{iso}(\text{O2}) = 0.77(22) \text{ \AA}^2$ in the 8d site.

REFERENCES

1. K. Mori *et al.*, *JPS Conference Proceedings*, 33 (2021) 011093.
2. K. Iwase *et al.*, *J. Phys. Soc. Jpn. Suppl. A*, 70 (2001) 374.

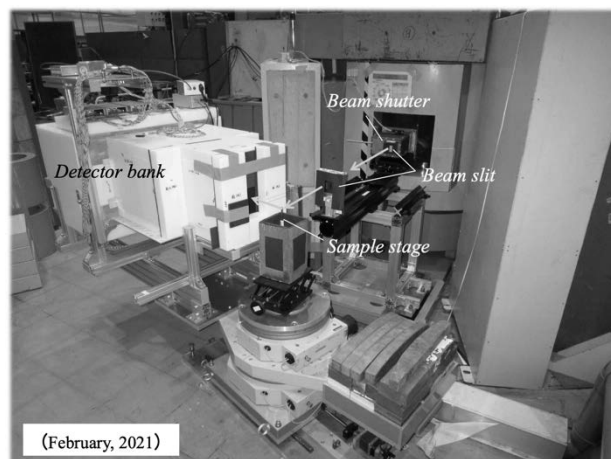


Fig. 1. Versatile compact neutron diffractometer (VCND) installed at the B-3 beam port of Kyoto University Research Reactor (KUR) [1].

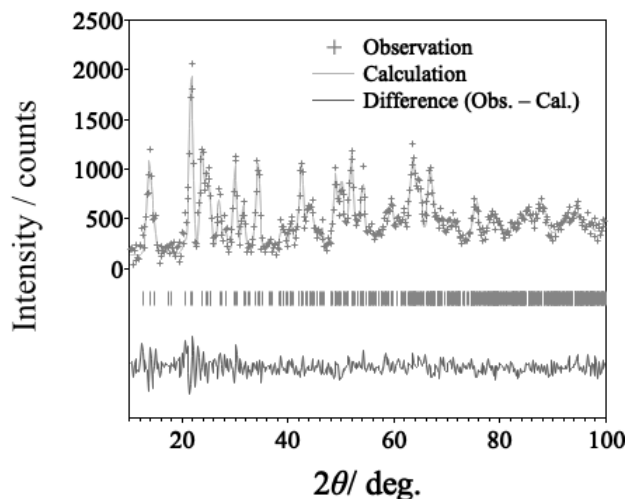


Fig. 2. Rietveld refinement using ND data for synthetic aragonite (CaCO₃) at room temperature.

CO1-2 Towards to mass production of high- m neutron focusing supermirrors

M. Hino¹, T. Hosobata², H. Endo³, F. Funama⁴, M. Takeda², Y. Yamagata², T. Oda⁵, H. Yoshinaga¹

¹*Institute for Integrated Radiation and Nuclear Science, Kyoto University (KURNS), Japan*

²*RAP, RIKEN, Japan*

³*IMSS, KEK, Japan*

⁴*Dept., Nucl. Eng., Kyoto University, Japan*

⁵*ISSP, University of Tokyo, Japan*

INTRODUCTION: Progress of neutron optical devices is very significant. We have established fabrication method for aspherical focusing supermirror with metal substrate [1-3]. The metallic substrate is robust and ductile, to which able to fabricate steeply curved surface with high form accuracy. It is also applicable to use under high radiation irradiation and high-temperature filed, even at a place close to the neutron target and moderator. Furthermore, it is possible to fabricate a large focusing mirror by combining multiple segmented mirrors with mechanical fastening entailing the usage of screw holes and fixture tabs. We have solved the problem of required surface roughness for neutron mirror. The roughness should be smaller than 0.3 nm for high- m supermirror coating. Here m is the maximum critical angle of the mirror in units of critical angle of natural nickel. By using electroless nickel-phosphorus (Ni-P) plating, we overcame the problem and are establishing fabrication process for aspherical focusing supermirror. There is still a problem of peeling off for high- m supermirror coating on metal substrate with steep curvature. It is also important to improve reflectivity of the supermirror. In this study, we report a status of mass production for high- m neutron focusing supermirrors.

EXPERIMENTS: We fabricated ellipsoidal metallic substrates with the Ni-P plating, based on the technology using ultrahigh precision cutting with correction processing, followed by mechanical precision polishing. The first precise manufacturing was conducted at a CNC machine for development of neutron optical devices at workshop of the KURNS. The ultra-precise manufacturing, polishing and cleaning of the metallic substrate were conducted at RIKEN. The supermirror coating was conducted with ion beam sputtering machine at the KURNS (KUR-IBS) [4]. Figure 1 shows the photograph of ellipsoidal supermirror deposited on the latest lot (LOT-23) and silicon substrates. The semi-major and semi-minor axes of the ellipsoidal supermirror were 1250 mm and 65.4 mm, respectively. The acceptable angle of the minor axis arc of the ellipsoidal supermirror is 20 degree. In this study, we had to reconfirm the importance of the cleaning process and storage period because many failures were made in depositing on a substrate with a long storage period. Eventually, we have fabricated $m=6$ NiC/Ti(C) supermirrors in which effective number of layers was 9750, where the half of the layers were very thin carbon interlayers. The thickness of interlayer is constant and

approximately a few sub-nanometers. In the point of view of the reflectivity performance, the effective number of periodic layers is 4875. The neutron experiments were conducted at the BL06 (VIN ROSE) beam port at J-PARC MLF.

RESULTS: Figure 2 shows reflectivity profiles of neutrons by the $m=6$ NiC/Ti (C) supermirror deposited on the monitor mirror (silicon substrate). The measurement was conducted by four incident angles, 0.8, 1.6, 3.2 and 4.8 degrees. By adding very thin carbon interlayer between NiC and Ti layers, we have realized $m=6$ supermirror with high reflectivity. Here the number of effective layers, 4875, is not so many enough for $m=6$ supermirror, and there is still room for improvement of reflectivity of the supermirror. Noting that it is not reflectivity of ellipsoidal supermirror. The evaluation of ellipsoidal supermirror is now analyzing.



Fig. 1. The photograph of LOT-23 ellipsoidal supermirrors with two monitor mirrors.

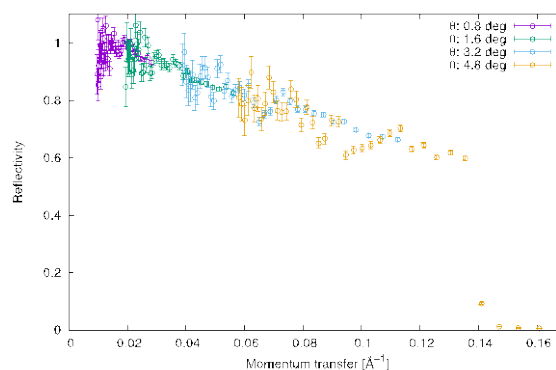


Fig. 2. The measured reflectivity of $m=6$ NiC/Ti (C) supermirror deposited on a monitor mirror (silicon substrate).

REFERENCES:

- [1] J.Guo, *et al.*, Optics Express 22(2014) 063108.
- [2] T.Hosobata, *et al.*, Optics Express 25(2017) 20012.
- [3] T.Hosobata, *et al.*, Optics Express 27(2019)26807.
- [4] M.Hino, *et al.*, Nucl. Instr. and Meth., **797**(2015) 265.

CO1-3 Development of multilayer mirrors for neutron interferometer

M. Kitaguchi, T. Fujiie¹, and M. Hino²

KMI, Nagoya University

¹Graduate School of Science, Nagoya University

²Institute for Integrated Radiation and Nuclear Science, Kyoto University

INTRODUCTION: Neutron interferometry is a powerful technique for studying fundamental physics. Numerous interesting experiments [1] have been performed since the first successful test of a single-crystal neutron interferometer [2]. However, the single-crystal interferometer is inherently not able to deal with a neutron that has a wavelength longer than twice its lattice constant. In order to investigate problems of fundamental physics, including tests of quantum measurement theories and searches for non-Newtonian effects of gravitation, the interferometry of cold neutrons is extremely important, since the sensitivity of interferometer for small interaction increases with the neutron wavelength. A large scale of interferometer also has the advantage to increase the sensitivity to small interactions.

One of the solutions is an interferometer using neutron multilayer mirrors [3]. We succeeded in developing a multilayer interferometer for cold neutrons in which two paths are completely separated for the first time using wide-gap etalons [4]. We can easily control parameters such as Bragg angle, reflectivity, and Bragg peak width by selecting the deposited material and tuning the bilayer thickness and the number of layers.

We have started the development of multilayer interferometer at the beamline 05 NOP in MLF. From 2019, we are continuing the experiments with etalons with monochromatic mirrors in order to demonstrate the performance of the interferometer. Figure 1 shows the interference fringes with etalons according to time-of-flight. The phase of interferogram depends on the wavelength of neutrons. We are testing the practical application of the interferometer. Neutron coherence scattering length of the material can be measured by inserting the sample into a path of the interferometer. The results of the trial measurements were consistent with the literature values.

Because the mirrors have narrow bandwidth of the neutron reflectivity, the number of neutrons contributing to the interference is limited. When the neutron supermirrors whose lattice constants vary gradually are utilized in the interferometer, the effective range of neutron wavelength can be broadened to be applicable to a pulsed source. In addition, the wavelength dependence of the interactions can be measured simultaneously by using pulsed neutrons.

EXPERIMENTS AND RESULTS: We are trying to fabricate the neutron mirrors with wide band for the interferometer by using Ion Beam Sputtering facility in KURNS. The mirrors should have the wide and smooth top of the reflectivity with the range of momentum trans-

fer from 0.4 nm^{-1} to 1.0 nm^{-1} . Especially, half mirrors with the wide range of neutron wavelength are needed for the interferometer. We tried to make the half mirrors and to measure the reflectivity at MINE2 in JRR3. Figure 2 shows the reflectivity of the half mirrors on the fused silica substrates. Neutron wavelength was 0.88 nm and the bandwidth of the beam was 2.7% of the wavelength. Mirrors with more uniform reflectivity were created. We are continuing the development of the mirrors for the neutron interferometer.

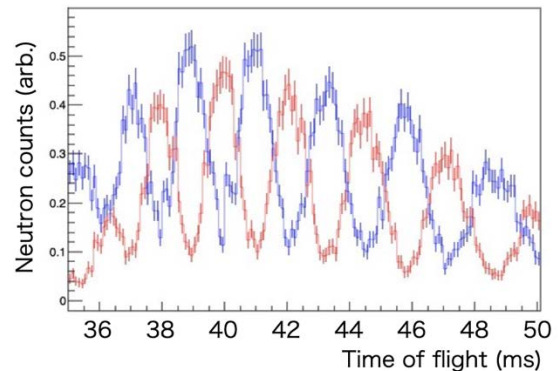


Fig. 1. Interference fringes with multilayer mirrors for pulsed neutrons. The contrast was improved.

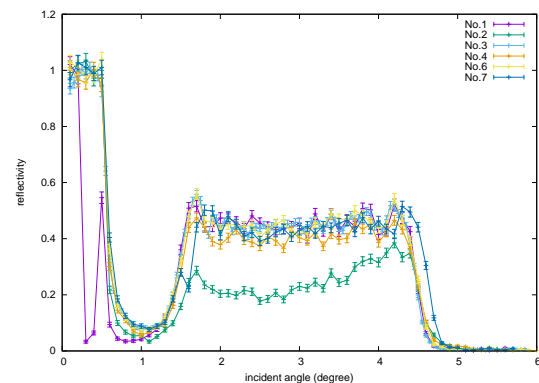


Fig. 2. Reflectivity of the half mirror with wide band of neutron wavelength. Colors represent the sample ID.

REFERENCES:

- [1] H. Rauch and S. Werner, Neutron Interferometry Oxford University Press, Oxford, 2000;
- [2] J. Byrne, Neutron, Nuclei and Matter Institute of Physics Publishing, London, 1994, Chap. 7;
- [3] Mater Wave Interferometry, edited by G. Badurek, H. Rauch, and A. Zeilinger North-Holland, Amsterdam, 1988.
- [4] H. Rauch, W. Treimer, and U. Bonse, Phys. Lett. 47A, 369 (1974).
- [5] M. Kitaguchi, *et al.*, Phys. Rev. A 67, 033609 (2003).
- [6] Y. Seki, *et al.*, J. Phys. Soc. Jpn. 79, 124201 (2010).

CO1-4 Development of high-resolution cold/ultracold neutron detectors using nuclear emulsion

N. Naganawa, M. Kimura^{1,2}, J. Yoshida³, M. Hino⁴, K. Hirota⁵, H. Kawahara⁶, M. Kitaguchi^{6,7}, K. Mishima^{5,8}, A. Muneem³, N. Muto⁶, and A. Umemoto^{6,9}

*Institute of Materials and Systems for Sustainability,
Nagoya University,*

¹*Nagoya Proton Therapy Center, Nagoya City University
West Medical Center*

²*Graduate School of Medical Sciences, Nagoya City
University*

³*High Energy Nuclear Physics Laboratory, Cluster for
Pioneering Research, RIKEN*

⁴*Institute for Integrated Radiation and Nuclear Science,
Kyoto University*

⁵*High Energy Accelerator Research Organization (KEK)*

⁶*Graduate School of Science, Nagoya University*

⁷*Kobayashi-Maskawa Institute for Origin of Particles
and the Universe (KMI), Nagoya University*

⁸*J-PARC Center*

⁹*Division of Physics, University of Tsukuba*

INTRODUCTION: Nuclear emulsion is a 3D-tracking detector for charged particles with a submicron resolution. It consists of silver halide crystals with diameter of several ten – several hundred nm. It works as a slow neutron detector by combining it with nuclides which absorb neutrons and emit charged particles. A cold/ultracold neutron detector with spatial resolution less than 100 nm has been developed by combining nuclear emulsion with a thin converter layer including ^{10}B [1]. An experiment (Experiment 1) was conducted at PF2, Institut Laue-Langevin (ILL) in order to obtain a spatial distribution of UCNs in the Earth's gravitational field using a detector fabricated by coating a nuclear emulsion on a converter layer sputtered by an ion beam sputtering system (KUR-IBS) in KURRI[2]. Nuclear emulsion can also be used for fundamental studies of radiology such as that of proton boron capture therapy (PBCT)[3]. A related experiment (Experiment 2) was conducted at CN-3 beam line. Studies for applications of emulsion detectors to neutron imaging are going on[4,5]. Also applications of fluorescent nuclear track detectors (FNTD) [9] to neutron imaging has been studied in parallel. An experiment with the latter detector (Experiment 3) was conducted at CN-3.

Experiment 1: Layers of $^{10}\text{B}_4\text{C}$ (200 nm)-NiC-C were sputtered on double-side-polished Si plates with thickness of 500 μm with KUR-IBS and were coated with 10 μm -thick fine-grained nuclear emulsion[6] at Nagoya University. They were exposed to UCNs of 9.5 m/s at the downstream of a mirror-absorber system of the qBOUNCE experiment[7] which is in a similar configuration as described in the Ref. [8] with keeping the gap between the mirror and the absorber 24 μm . The number of arrived UCNs at the fiducial area (6.5 cm \times 24 μm) of one of the detector was 1.1×10^4 . The detector was developed and tracks of α -particles and ^7Li from neutron absorptions that are in the angle acceptance of $\theta < 0.9$ rad were read out by an automatic track readout system at Nagoya University. The acceptance guarantees the spatial

resolution of the absorption points less than 100 nm.

Results: The number of the tracks read out from the fiducial area was 1674, which was reasonable considering the detection efficiency[1] and the fraction of tracks to be found in the angle acceptance. Analyses will be continued and a final spatial distribution will be obtained.

Experiment 2: The sample consists of fine-grained emulsion and a 16 μm thick polyvinyl alcohol sheet immersed in sodium tetrachloride solution. The sheet contains natural boron of 31 $\mu\text{g}/\text{cm}^2$. The sample was exposed to 20 meV neutrons at the CN3 beamline. The beam density was $5 \times 10^8 \text{ cm}^{-2}$. The exposed film was developed and observed under an epi-illumination optical microscope.

Results: The track density of α and ^7Li produced from $^{10}\text{B}(n, \alpha)^7\text{Li}$ reaction was expected to be $1 \times 10^6 \text{ cm}^{-2}$ from the amount of sodium tetrachloride and the reaction cross section. The number of observed tracks was $(1.3 \pm 0.1) \times 10^6 \text{ cm}^{-2}$, which is approximately consistent with the expectation. Furthermore, the number of silver grains along the observed tracks was counted manually. It showed a bimodal distribution reflecting the difference in energy deposition. We can extract α tracks produced in the proton boron capture reactions by counting the silver grains in a track.

Experiment 3: A sample of a neutron imaging device that combines an FNTD and a $^{10}\text{B}_4\text{C}$ (200 nm)-NiC-C film was created to study the fundamental characteristics of the detector. The FNTD is a single crystal of aluminum oxide doped with carbon and magnesium. It records tracks of ions, and the tracks are observed as fluorescence features against the background under a confocal laser microscope with a resolution of sub-micrometers. This detector can be reused repeatedly because UV laser irradiation can erase the recorded tracks. The sample was irradiated with the neutron beam for 10^4 sec under one megawatt thermal power of the reactor and recorded the tracks of neutron capture events from the $^{10}\text{B}_4\text{C}$ -converter and background γ -ray. The authors are tuning the UV laser conditions for the track erasure.

REFERENCES:

- [1] N. Naganawa *et al.*, Eur. Phys. J. C. 78 (2018) 959.
- [2] M. Hino *et al.*, Nucl. Instrum. Methods Phys. Res. A 797, 265–270 (2015).
- [3] D.-K. Yoon, N. Naganawa, M. Kimura *et al.*, Appl. Phys. Lett. 115 (2019) 223701.
- [4] K. Hirota *et al.*, J. Imaging (2021) 7, 4.
- [5] A. Muneem *et al.*, Research Square, 966133 (2021).
- [6] T. Asada *et al.*, Prog. Theor. Exp. Phys. 2017.6 (2017) 063H01.
- [7] H. Abele *et al.*, Nucl. Phys. A 827, 593c–595c (2009).
- [8] N. Muto *et al.*, arXiv:2201.04346 (2022).
- [9] M. Akselrod and J. Kouwenberg, Radiation Measurements 117 (2018) 35–51.

CO1-5 Development of a Spin Analyzer for Ultra-Cold Neutron

S. Kawasaki, T. Higuchi¹, S. Imajo¹, M. Kitaguchi², H. Akatsuka², K. Mishima⁴, and M. Hino³

Institute of Particle and Nuclear Study, KEK

¹*Research Center for Nuclear Physics, Osaka University*

²*Graduate School of Science, Nagoya University*

³*Institute of Material Structure Science, KEK*

⁴*Institute for Integrated Radiation and Nuclear Science, Kyoto University*

INTRODUCTION: Existence of non-zero permanent electric dipole moments (EDM) of the fundamental particles violates time reversal symmetry. Under CPT conservation, T violation implies CP violation. Thus, a precise measurement of an EDM may reveal the origin of matter dominant universe. The TUCAN (TRIUMF Ultra-Cold Advanced Neutron source) collaboration aims to measure a neutron EDM with a sensitivity of 10^{-27} ecm, which is more than one order better sensitivity than the current best measurement.

The neutron EDM is measured by the precise measurement of spin precession frequency of neutrons. Ultra-Cold Neutrons, whose kinetic energy is less than a few 100 neV, is used for the measurement. One of the key components of the measurement is a spin analyzer of the UCN. Since the kinetic energy of an UCN is so low that magnetic potential can be used as a spin filter. When iron, which has a large saturation magnetization of 2.2 T, is used for the spin filter, the effective potential V_{eff} is

$$V_{eff} = V_{Fe} \mp |\mu| \cdot |B| = 90 \text{ neV, or } 330 \text{ neV}$$

Where $V_{Fe} = 210 \text{ neV}$ is the Fermi potential of the iron, $\mu = 60 \text{ neV/T}$ is the magnetic moment of the neutron, and $B = 2.2 \text{ T}$. Only one spin state of UCNs with kinetic energies between 90 neV to 330 neV can transmit the iron magnetic potential. Therefore, magnetized iron functions as an UCN spin filter. In order to reduce UCN absorption, the iron should be as thin as an order of 100 nm.

EXPERIMENTS: The thin iron films are prepared by ion beam sputtering facility at the Institute for Integrated Radiation and Nuclear Science, Kyoto University (KURNS). We produced thin iron films with thicknesses of 30, 50, and 90 nm on Al foils and Si substrates.

Magnetic properties of the samples were measured by a vibrating sample magnetometer at KURNS. Samples on the Si substrates were also characterized by the cold neutron reflectometry. The measurements were carried out at the J-PARC/BL05. Polarized cold neutron beam was incident on the sample and the reflectivity was measured. A spin-flipper was used to change the spin state of the incident neutrons.

RESULTS: Figure 1 shows the magnetization curves of the samples. The iron films are fully saturated by the magnetic field of 12 kA/m for the samples on the Al foils and 4 kA/m for those on the Si substrates.

Figure 2 shows the reflectivity of the iron film with 90 nm thickness on the Si substrate. The reflectivity depends

on the momentum transfer of the reflected neutrons. The polarization of the incident neutron beam was evaluated by another experiment. From the fitting, the critical momentum transfer was extracted. This is translated to the effective potential of the samples 328 neV for the one spin state and 65 neV for the other spin state. This means the iron film has ability to select spin state for the UCNs in an energy range of 65 – 328 neV. This result is very promising for the development of the spin analyzer for UCN. We plan to evaluate the samples using UCNs in the spring 2022.

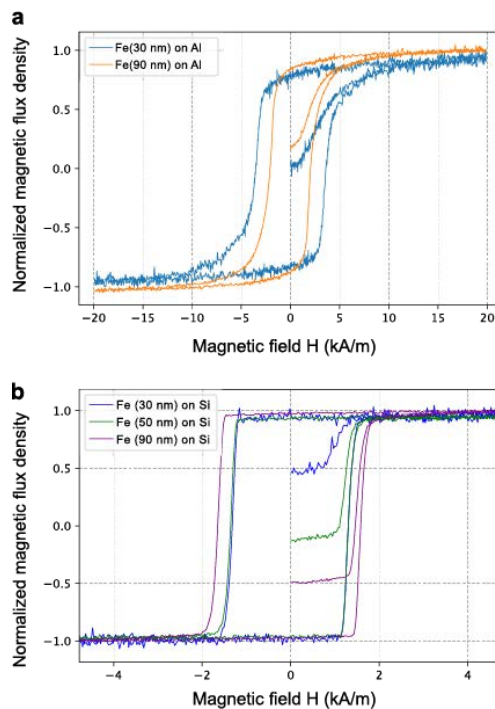


Fig. 1. Magnetization curves of iron films on Al foils (a) and on Si substrates (b). Figure from [1]

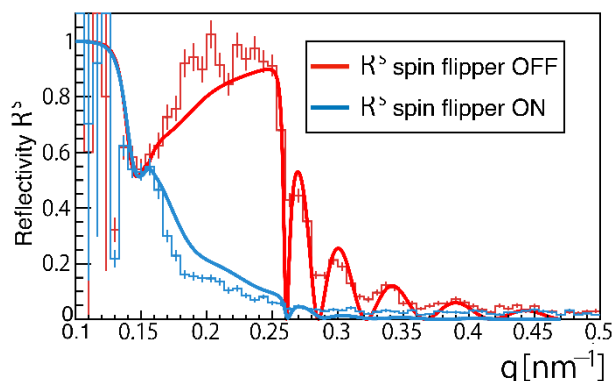


Fig. 2. Neutron reflectivity Red shows the data with spin flipper OFF and Blue shows the data with spin flipper ON. Solid lines are indicates fit result. Figure from [1]

REFERENCES:

[1] H. Akatsuka, M. Hino for the TUCAN Collaboration, JPS Conference Proceedings of SPIN2021, accepted.

CO2-1 Measurement of Energy Resokution in the KURNS-LINAC Pulsed Neutron Facility[2]

T. Sano, Y. Matuo, Y. Takahashi¹, K. Terada¹, H. Yashima¹ and J. Hori¹

Atomic Energy Research Institute, Kindai University
¹Institute for Integrated Radiation and Nuclear Science,
 Kyoto University

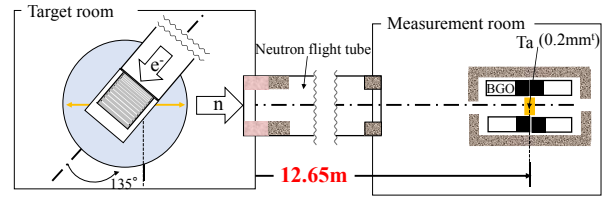


Figure 1 Experimental geometry

Table 1 KURNS-LINAC operational condition in this study.

Run No.	Frequency (Hz)	Beam pulse width (μsec)	Beam current (μA)
1	50	4	20.5
2	50	1	20.5
3	50	0.1	17.5
4	50	0.033	5.6

RESULTS:

Obtained energy resolutions in this experiment are shown in Fig.2 [2]. The energy resolutions with the beam pulse width of 4 μsec are depended on the incoming neutron energy to the sample, clearly. On the other hand, When the pulse width is shorter than 100 ns, the energy resolution shows a constant value. This indicates that as the pulse width increases, the pulse width component is dominant, whereas as the pulse width decreases, the contribution of neutron moderation by the moderator is dominant.

INTRODUCTION: The electron linear accelerator at the Research Reactor Institute, Kyoto University (KURRI-LINAC) had been originally established in 1965 by the High Voltage Engineering Co., USA and started as a 23 MeV machine. In 1971, the machine power had been increased to 46 MeV. The KURRI-linac has two different operation pulse modes. One is a long mode with a maximum repetition rate of 120 Hz, a pulse width of 0.1–4.0 μs and a peak current of about 0.5 A for the measurement at low energies below 10 eV. Another is a short mode with a maximum repetition rate of 300 Hz, a pulse width of 2–100 ns and a peak current of about 5 A for the measurement at high energies above 1 eV. It is worth noting that the peak current of short mode is ten times as large as that of long mode. In measurements of nuclear data, a water-cooled tantalum (Ta) target as a photo-neutron target and a light water moderator are used. There are two kinds of the moderator. One is a water tank type and another is an octagonal shape moderator called “pac-man type”. In order to measure accurate nuclear data, it is very important to evaluate the energy resolution ($\Delta E/E$) of a moderator. For example, the energy resolution for pac-man type moderator had been calculated about 0.7 % between energy range of 0.1eV from 10keV [1]. However, measurement and detail evaluation of energy resolutions for the tank type moderator has not carried out in KURRI-LINAC. Furthermore, the relationship between energy resolution and beam pulse width is not discussed in Reference [1].

In this study, the energy resolutions of neutron flux from a tank type moderator were obtained using the TOF technic in 4 operational mode with different pulse width.

EXPERIMENTS: In this study, the energy resolution of KURNS-LINAC was obtained by transmitted neutron flux via ^{181}Ta sample. In order to measure the transmitted neutron flux, a cylindrical moderator tanks which have 19 cm diameter and 30cm height was installed at the target room. The tanks were filled with light water.

We used the neutron at “12 m room” which is located on 135 deg. axis from the electron beam line. The flight path of neutron flux between the ^{181}Ta sample which has 0.2 mm thickness and the moderator was 12.65 m as shown in Fig.1. The transmitted neutron flux was measured by TOF technic with 12 BGO detectors. In order to obtain the relationship between neutron beam pulse width and energy resolution, the KURNS-LINAC was operated under 4 different conditions as shown in Table 1. The beam frequency was adjusted to 50 Hz and the pulse width were about 4 μsec – 0.033 μsec (nominal value).

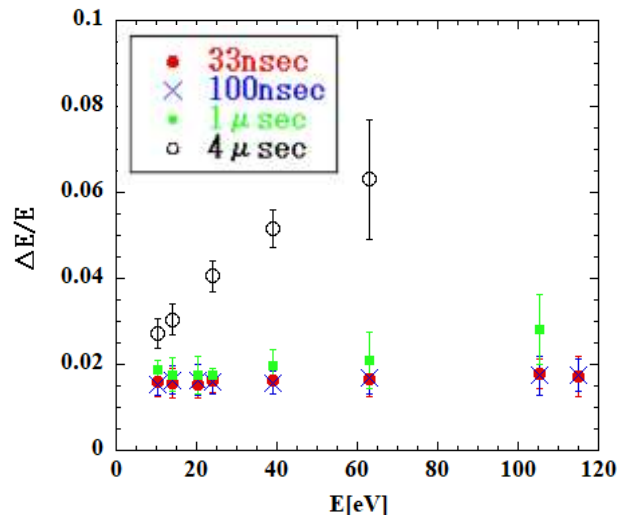


Figure 2 Results of Energy Resolutions

REFERENCES:

- [1] T. Sano, *et al.*, EPJ web of conference, Vol.146, 03031(2017).
- [2] Y. Matsuo, *et al.*, AESJ 2022 spring meeting, 2A07, (2022)

CO2-2 Measurements of Thermal-Neutron Capture Cross-Section of the $^{237}\text{Np}(n, \gamma)$ Reaction with TC-Pn in KUR

S. Nakamura¹, S. Endo¹, A. Kimura¹, Y. Shibahara²

¹Japan Atomic Energy Agency

²Institute for Integrated Radiation and Nuclear Science, Kyoto University

INTRODUCTION: In terms of nuclear transmutation studies with neutrons of minor actinides contained in nuclear wastes, accurate neutron capture cross sections are required to obtain transmutation rates. The present work selected ^{237}Np nuclide among minor actinides because ^{237}Np causes long-term radio-toxicity in nuclear waste management due to a long half-life of 2.14×10^6 years.[1] When examining the situation of thermal-neutron capture cross-section (σ_0) of ^{237}Np , there have been discrepancies in reported data even in recent year as shown in **Figure 1**. Previous study [2] has demonstrated that the σ_0 can be measured using the graphite thermal column equipment (TC-Pn) installed in KUR. Consequently, the present work aimed to measure the σ_0 of ^{237}Np by an activation method using a well-thermalized neutron field in the TC-Pn.

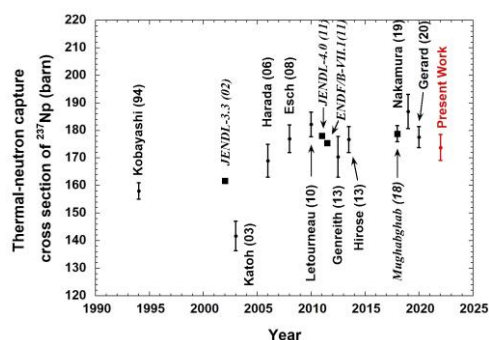


Fig.1 Situation of past reported data for the σ_0 of ^{237}Np .

EXPERIMENTS: Nitric acid solutions of ^{237}Np equivalent to 950 Bq and 370 Bq were dropped onto glass micro filters and dried with an infrared lamp. To monitor neutron flux components, flux monitor sets of Au/Al wire, Co, Sc, Mo and Ta foils were put around each Np sample as shown in **Figure 2**. A set of the ^{237}Np sample and flux monitors was used as a ^{237}Np target; two ^{237}Np targets were prepared. The targets were set separately at the upper edge of polyethylene capsules. Two dummy capsules were transferred to the TC-Pn in advance, and then the capsule containing ^{237}Np target was subsequently transferred so that the target would be exposed to the well-thermalized neutron field in TC-Pn. irradiated for 30 minutes in 1-MW power operation. The similar irradiation was performed on the second ^{237}Np target. After irradiations, the ^{237}Np samples and flux monitors were enclosed in a vinyl bag one by one, and then γ rays emitted from the samples and monitors were measured with a

high-purity Ge detector. The sample was placed at a distance of 100 mm from the front surface of the Ge detector. The gamma-ray peak efficiencies of the Ge detector were obtained with a mixed source. In the process of γ -ray measurements, we found that the radiation equilibrium was lost in the ^{237}Np samples. Hence, the amount of ^{238}Np was firstly measured; then the irradiated ^{237}Np samples were stored during a period of 11 half-lives of ^{233}Pa until radiation equilibrium would be maintained again. After that, the ^{237}Np samples were re-quantified with radiation equilibrium.

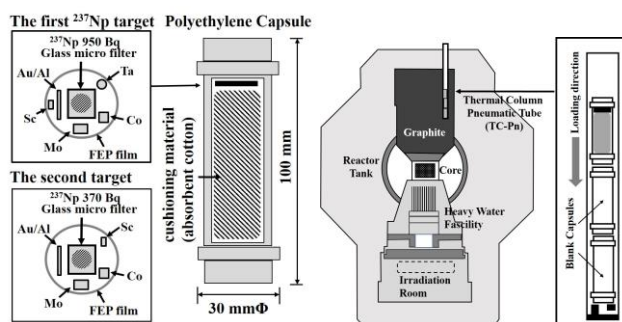


Fig.2 ^{237}Np targets and partial plane structure of KUR.

ANALYSIS: The reaction rates of neutron flux monitors were obtained from their γ -ray yields. With these reaction rates, the thermal-neutron flux component was derived on the basis of *Westcott's* convention [3], and found to be $(5.69 \pm 0.09) \times 10^{10}$ n/cm²/sec. The ^{237}Np samples were re-quantified using 312-keV γ rays emitted from ^{233}Pa in radiative equilibrium with ^{237}Np . The reaction rate of ^{237}Np was obtained with the sample amount, γ -ray yields given by ^{238}Np and experimental conditions.

RESULTS: The thermal-neutron capture cross section σ_0 was derived straightforward by dividing the reaction rate of ^{237}Np by the thermal-neutron flux component, and found to be 173.7 ± 4.8 barn in the first irradiation and 174.0 ± 5.1 barn in the second irradiation. By taking a weighted average of these results, the σ_0 was finally obtained as 173.8 ± 4.7 barn [4]. The present result was in agreement with the reported data given by a time-of-flight method [5, 6] within a limit of uncertainty.

REFERENCES:

- [1] R.B. Firestone *et al.*, Table of Isotopes, 8th ed. (1998).
- [2] S. Nakamura *et al.* *J. Nucl. Sci. Technol.* 2021; **58**(10): 1061.
- [3] C.H. Westcott *et al.* "Proc.2nd Int. Conf. Peaceful Use of Atomic Energy; Geneva", 1958; **16**: 70.
- [4] S. Nakamura *et al.* *J. Nucl. Sci. Technol.* (to be published.)
- [5] K. Hirose *et al.* *J. Nucl. Sci. Technol.* 2013; **50**: 188.
- [6] G. Rovira *et al.* *J. Nucl. Sci. Technol.* 2020; **57**: 24.

CO2-3 β -decay spectroscopy of rare fission products with a 4π clover detector using an Isotope Separator On-Line KUR-ISOL

S. Sakakibara¹, Y. Irie², T. Yamaguchi²,
T. Miyazawa², M. Shibata³ and A. Taniguchi⁴

¹School of Engineering, Nagoya University

²Graduate School of Engineering, Nagoya University

³Radioisotope Research Center, Nagoya University

⁴Institute for Integrated Radiation and Nuclear Science, Kyoto University

INTRODUCTION: The decay data of the fission products are important for the decay heat evaluation and also structure of neutron-rich nuclei. Many neutron-rich nuclei with mass numbers near 150 do not have detailed decay schemes because of their short half-lives and low fission yields. The nucleus of ^{155}Pr was proposed to have a half-life of 1.49 s by Wu *et al.* [1] and a level scheme of the daughter nucleus ^{155}Nd was reported by Hwang *et al.* using spontaneous fission of ^{252}Cf [2], but, no decay γ -rays have been reported. Based on the experimental results of $^{153,154}\text{Pr}$ in the last year and the expected yields of an on-line mass separator KUR-ISOL, the observation of the γ -rays in the β decay of ^{155}Pr are expected. In this year, to identify γ rays in the β decay of ^{155}Pr , β - γ coincidence measurements were carried out using a high-efficiency clover detector coupled with β -ray detectors. The clover detector has four large Ge crystals with a diameter of 80 mm and a length of 90 mm arranged in the shape of a four-leaf clover around a through hole with a diameter of 15 mm. The β -ray detectors to set in the through hole of the clover detector developed by Ishikawa [3] were modified.

EXPERIMENTS: 72 mg of 93% enriched $^{235}\text{UF}_4$ target was inserted at the through-hole facility in Kyoto University Reactor. The nuclei of interest were produced by thermal neutron-induced fission of ^{235}U . The nuclei of interests were transported by He- N_2 gas jets and ionized in a thermal ionization ion source. The mass-separated radioactive beams were collected on a thin Mylar tape and periodically transported to the center of the detector by a computer-controlled tape transport system, and were measured by the detectors. Two identical β -ray detectors were made of plastic scintillators 105 mm long, 12.6 mm wide, and 1 mm thick, contacted with a semi-cylindrical light guide with a radius of 6.5 mm, and set in a through-hole in the clover detector. A 3×3 mm² MPPC (Multi-Pixel Photon Counter) module C13367 made by Hamamatsu Photonics was mounted on the end of each light guide. The whole of the detectors was shielded with 10 cm thick lead bricks and 10 cm thick boron-doped polyethylene bricks outside them to reduce background neutrons and γ rays. Data were recorded on APV8008 and APV8016 DSP data acquisition systems made by Techno AP Corporation. The nucleus ^{155}Pr was measured in two modes of collection-measurement time sequence, those are 2.5 s - 2.5 s and 5 s - 5 s, for 16.5 h and 11 h, respectively. Prior to the measurements, ^{94}Rb , ^{94}Sr , ^{94}Y ,

and ^{146}La were measured to evaluate the performance of the β -ray detectors.

RESULTS and DISCUSSION: The coincidence efficiency of the β -ray detectors was determined from the ratio of the γ -ray peak areas of the coincidence spectra to those of single spectra about the four nuclides. The efficiency of the detector was about over 20% for the energy of β ray above 2 MeV.

To identify the γ rays in the decay of ^{155}Pr , the γ rays and Nd KX-rays and their decay properties, and coincidence relations between KX rays and γ rays were analyzed. The coincidence time was set to 500 ns. The measured β - γ coincidence spectrum is shown in Fig.1. In the spectrum, the background radiation such as the γ ray in the decay of ^{41}Ar produce with $^{40}\text{Ar}(n, \gamma)$ reaction in the reactor room were reduced effectively. The γ rays in the decay of ^{155}Nd and ^{155}Pm were clearly observed in the spectrum. The seven γ -rays and an excited level were newly assigned in the decay scheme of ^{155}Nd , but unfortunately, any γ rays in the decay of ^{155}Pr were not observed. If γ rays have high multipolarity, the Nd KX-rays should be observed and they should decay with the proposed half-life [2]. So, the decay properties of KX-ray region were analyzed with the spectrum-multi-scaling analysis, but the corresponding energy region of Nd KX-ray did not decay with half-life of about 1.5 s.

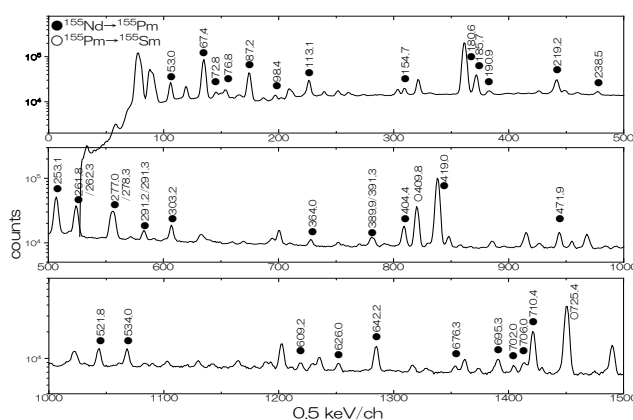


Fig. 1. A β - γ coincidence spectrum for the mass-separated beam of $A=155$.

The reason why ^{155}Pr could not be observed is the shorter half-life than the reported value [1], the low fission yield than the reference [4], or both. To identify the γ rays, it is necessary to rearrange the measuring setup including the tape transport system.

REFERENCES:

- [1] J. Wu *et al.*, Phys. Rev. Lett. 118, 072701 (2017).
- [2] J. K. Hwang *et al.*, Phys. Rev. C78, 014309 (2008).
- [3] Y. Ishikawa, Graduate School of Engineering, Nagoya University, master's thesis (2021).
- [4] <https://www.ndc.jaea.go.jp/cgi-bin/FPYfig>.

CO2-4 Development of a current-mode ^3He gas neutron detectors for BNCT

T. Matsumoto, A. Masuda, S. Manabe, H. Harano, J. Hori¹, K. Terada¹

National Metrology Institute of Japan, National Institute of Advanced Industrial Science and Technology

¹ KURNS

INTRODUCTION: In the present study, we have developed a current-mode neutron detector [1] that can be used in intense neutron fields such as boron neutron capture therapy (BNCT) fields. It is necessary to measure the neutron flux for a large dynamic range because of connection between a BNCT field in a hospital and a neutron calibration field in the National Institute of Advanced Industrial Science and Technology (AIST). The difference of neutron fluxes between the BNCT field and the calibration field is more than 5 orders of magnitude. We have developed a new ^3He gas detector (proportional counter or ionization chamber) with the current mode. The current mode gas detector is expected to be high radiation resistance in comparison with a photo-multiplier tube in the scintillation detector. However, subtraction of gamma-ray component is a problem that need to be overcome in the current-mode neutron detector. In the present study, we experimentally verify the gamma-ray subtraction method in the current-mode ^3He gas detector using ^3He proportional counters with 4 different gas pressures.

EXPERIMENTS: A collimated neutron beam with 30-mm diameter was obtained by the photo neutron reaction using a tantalum target with a water moderator at the KURNS Linac [2]. Figure 1 shows the experimental setup. In the experiments, we used ^3He proportional counters with nominal ^3He gas pressures of 4, 0.2, 0.02 and 0.002 atm (Reuter Stokes RS-P4-0806-275, RS-P5-0806-221, RS-P5-0806-220 and RS-P5-0806-222). All counters have total gas pressure with 6 atm and partial pressure of Kr with 2 atm. The ^4He gas was used as other gas in the counters with 0.2, 0.02 and 0.002 atm. Each ^3He proportional counter was set at approximately 12 m away from the target. The ^3He proportional counters were measured by means of the time-of-flight (TOF) method. The measurements were performed for both pulse and current modes. In the pulse mode, signals from the ^3He proportional counter were obtained using a pre-amplifier (ORTEC 142PC) and main amplifier (ORTEC 570). In the current mode, the signals were obtained using a current integrator (ORTEC 439). Finally, TOF data were extracted using a multi-stop time to digital converter and a multi-channel analyzer (Fast Com Tec MPA3).

RESULTS: Figure 2 shows results of output count rates for pulse and current modes. The count rates for the linac experiments were normalized using counts obtained from a BF_3 proportional counter used as a neutron monitor. In the case of current mode, the count rate is proportional to the electric current obtained from the counter. In the pulse mode, signals due to only neutrons are obtained by setting

regions of interest in the pulse height and TOF spectra. On the other hand, gamma-ray component is included in the current mode. Especially, the gamma flash from the target is dominant. Gamma-ray component is extracted from different of slopes for the pulse and current modes in the linac experiments in Figure 2. In Figure 2, results obtained from measurements at a thermal neutron field at AIST are also included. In this case, the slope of results of pulse mode in the linac experiments are similar to those of current mode in the AIST experiments, because the gamma-ray component in the AIST thermal neutron field is considerably smaller than the gamma flash. It was confirmed that the neutron-gamma discrimination in the current-mode ^3He gas detector is available using a pair of ^3He and ^4He gas detector. To evaluate measurement uncertainty, we will improve further the experimental evaluation of electrical noise and gamma-ray background. Especially, the evaluation of electrical noise is very important in accelerator facilities.

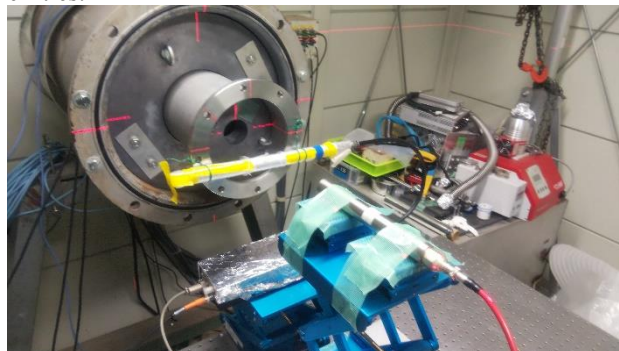


Fig. 1. Experimental setup for the ^3He gas detector. The detector was set at approximately 12 m away from the target.

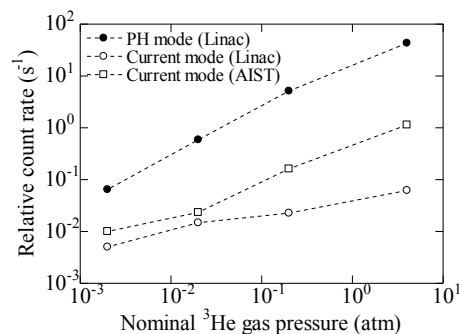


Fig. 2. Outputs from 4 ^3He proportional counters in the pulse and current modes.

REFERENCES:

- [1] T. Matsumoto *et al.*, Radiat. Prot. Dosim. 188 (1), 117 (2020).
- [2] K. Kobayashi *et al.*, Annu. Rep. Res. Reactorinst. Kyoto Univ. 22, 142 (1989).

This work was supported by JSPS KAKENHI (21H03755 and 19K12638).

CO2-5 Quantitation of Gamma Ray Emission from Capture Reaction of Uranium-238 (3)

Y. Nauchi, J. Hori¹, K. Terada¹, and T. Sano²

Central Re-search Institute of Electric Power Industry

¹Kyoto University Institute for Integrated Radiation and Nuclear Science

²Atomic Energy Research Institute, Kindai University

INTRODUCTION:

In a reactor core, γ rays are radiated by some kinds of neutron induced reactions such as the fission, capture, inelastic scattering, etc. Accordingly, γ ray spectroscopy is potentially useful to identify and quantify those reactions. Focusing on that, one of the authors has studied γ ray spectroscopy for Kyoto University Critical Assembly (KUCA) [1]. In KUCA, the uranium fuel of 93 wt% ^{235}U enrichment is scheduled to be alternated to the fuel with lower enrichment (LEU). By the reduction of the enrichment, the reactions of ^{238}U would be more significant in the core. In order to quantify the capture reaction rates of ^{238}U , we need neutron induced γ ray emission data. For the reason, prompt γ ray spectrum measurements have been conducted for uranium metallic samples irradiated by neutrons of white spectrum at the LINAC facility [1,2].

EXPERIMENTS:

The outline of the γ ray spectroscopy is as same as the previous studies [1,2], where the $^{238}\text{U}(n,\gamma)$ γ ray was measured with a HP-Ge detector and the pulse height (PH) and the time after the beam pulse incident on the tungsten target (TOF) were stored event by event. Then we can see the PH spectrum for a specific neutron energy. In 2020, PH had been shifted for resonance energy neutrons by extending the pulse width from 1 to 3 μs [2]. In this year, the relation between the pulse width and the spectrum gain was carefully checked. By inserting lead sheet with 6 mm thickness in the neutron beam duct, the spectrum shift was prevented as shown in Fig. 1. Thanks to the extension of the pulse width and the increment of currents, the statistical error in the spectra was reduced.

In order to calibrate the TOF data, we measured TOF for a ^{10}B sample while the source neutron was filtered with Cd, In, Ag, and Co plates. For the uranium sample, PH and TOF spectra were also measured with and without the plates. Those spectra are shown in Fig. 2. The filtered spectrum for uranium sample was often used to evaluate background events. In the TOF range greater than 8000, there is a difference between the spectra of filtered and non-filtered conditions. Those might be due to emission of γ rays from fission products (FPs) with half-lives longer than beam periods (20 ms). FPs are generated by fission of ^{235}U or ^{238}U in the sample. Then we should consider subtracting component from the spectra in Fig.1. Some bumps in spectra for thermal neutrons in Fig. 1 are due to such FP γ rays.

For quantification of γ ray emission per capture, its reaction rate should be known. For that, the pulse height weighting method is useful with calculated response function R. Compared to HP-Ge, response cal-

ulation is easier for scintillators. Then we measured $^{238}\text{U}(n,\gamma)$ γ rays with a BGO of 7.56 cm ϕ x 7.56 cm. The spectra are shown in Fig. 3. For all incident neutron energies, structures related to $^{238}\text{U}(n,\gamma)$ 4060 keV γ rays appear as well as $^{56}\text{Fe}(n,\gamma)$ components. We shall estimate the response and try to deduce the reaction rates from these data.

REFERENCES:

- [1] Y. Nauchi *et al.*, KURNS prog.rep.2019, CO3-3.
- [2] Y. Nauchi *et al.*, KURNS prog.rep.2019, CO2-2.
- [3] Y. Nauchi *et al.*, KURNS prog.rep.2020, CO2-1.

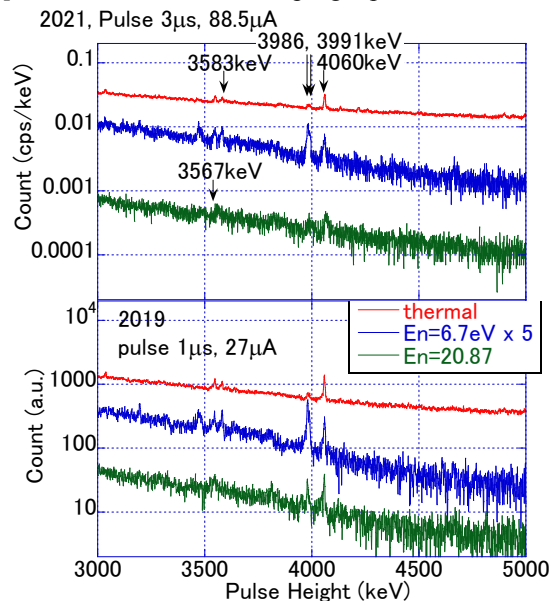


Fig. 1. Comparison of pulse height spectrum for different pulse width.

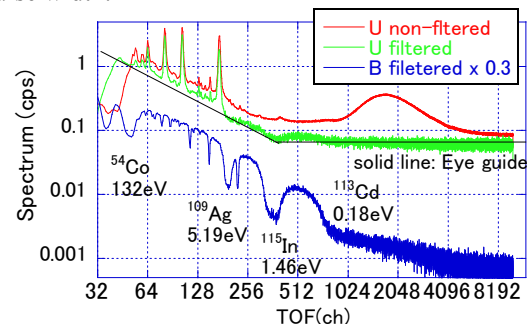


Fig. 2 Filtered TOF spectrum for Background Estimation.

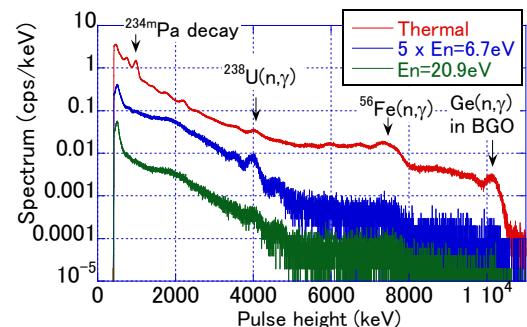


Fig. 3 gamma ray spectrum measured with BGO.

CO2-6 Development of a neutron scintillator for a compact NRTA system (Part 2)

J. Lee¹, K. Hironaka¹, F. Ito¹, T. Takahashi¹, M. Koizumi¹, J. Hori², and K. Terada²

¹*Integrated Support Center for Nuclear Nonproliferation and Nuclear Security, Japan Atomic Energy Agency*

²*Institute for Integrated Radiation and Nuclear Science, Kyoto University*

INTRODUCTION: The Japan Atomic Energy Agency (JAEA) is conducting research and development of active neutron NDA techniques [1] for nuclear nonproliferation and security. As a part of these projects, technology developments for a compact neutron resonance transmission analysis (NRTA) [2] system using a laser-driven neutron source (LDNS) was performed [3]. Using an extremely short pulse laser (~ps), an LDNS can provide short-pulsed fast neutrons (~ns) [4]. This is potentially useful to perform high resolution NRTA measurements (neutron time-of-flight (TOF) measurements) with a short flight path.

In experiments of NRTA, one of the origins of background is the emission of 2.2-MeV gamma rays of $^1\text{H}(n, \gamma)^2\text{H}$ reaction in a moderator for pulse neutron generation. The 2.2-MeV gamma-ray emission decreases exponentially just after a neutron pulse generation with a decay time of few hundreds μs . In a measurement using short flight path, therefore, the background overlaps neutron resonance dips of a spectrum, resulting in decline of sensitivity of the NRTA system. To overcome the problem, we developed a multi-layer ^6Li glass scintillation (MLS) detector [5] that has low sensitivity to high energy gamma rays.

In the previous experiment [5], we compared the performance of an MLS detector (total ^6Li thickness: 0.5 cm) and a conventional ^6Li glass scintillation detector (^6Li thickness: 1.0 cm). Influence of the 2.2-MeV gamma ray in TOF spectra ($<100 \mu\text{s}$) were examined. From the study, we concluded that the MLS detector could reduce the sensitivity to 2.2 MeV gamma rays.

Based on the previous results [5], we manufactured a new and upgraded MLS detector. The total thickness of ^6Li glass was increased to 1.5 cm to achieve better neutron detection efficiency. Another photomultiplier tube (PMT) was introduced to eliminate noise signals by using the coincidence technique. The performance of the new MLS detector was tested at the Kyoto University Institute for Integrated Radiation and Nuclear Science – Linear Accelerator (KURNS-LINAC). Neutron transmission spectra were measured varying the thicknesses of resonance samples.

EXPERIMENT AND RESULT: A performance test of the MLS detector was performed at the 12 m TOF measurement room of the KURNS-LINAC. Pulsed electron beams of about 30 MeV were used for the pulsed fast neutron generation with a repetition rate of 50 Hz, pulse width of 100 ns, and average current of about 18 μA . To slow down the fast neutrons, a water tank (20 cm in di-

ameter and 30 cm in height) was used as a neutron moderator. A Pb-shadow bar (5 cm in diameter and 20 cm in length) was placed in front of the entrance of the neutron flight tube to reduce the gamma-flash. As the resonance sample, the three indium (In) samples of different thicknesses (0.02, 0.05, and 0.1 mm) were used. To estimate the background level, 0.7-mm thick silver, 0.5-mm thick tantalum, and 1.0-mm thick cadmium were used as the black resonance filters. In the present experiment, the output signals from the MLS detector were processed using a 0.5-GS/s flash waveform digitizer (CAEN V1730) and then transferred to a computer.

Fig. 1 shows the TOF spectra of the three In samples with the resonance filters. The three 1.46 eV resonance peaks of ^{115}In were clearly observed from the TOF spectra obtained by the MLS detector. At present, we have been analyzing the obtained TOF spectra for NRTA.

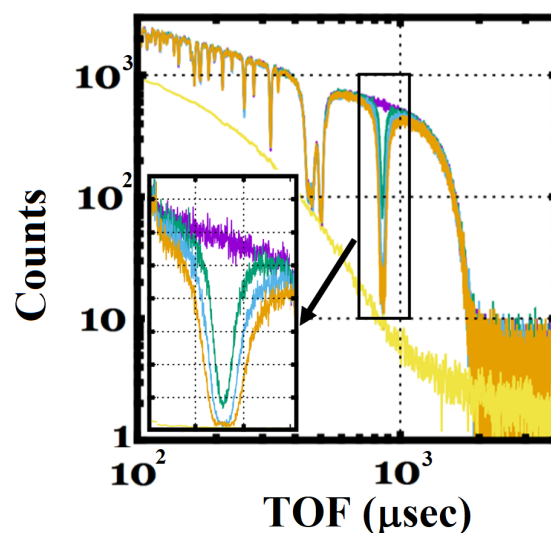


Fig. 1 TOF spectra obtained by the MLS detector.

ACKNOWLEDGEMENTS: This research was implemented under the subsidy for “promotion of strengthening nuclear security and the like” of the MEXT (the Ministry of Education, Culture, Sports, Science, and Technology of the Japanese government).

REFERENCES:

- [1] M. Koizumi *et al.*, Proc. of INMM & ESARDA Meeting 2021, #201.
- [2] P. Schillebeeckx *et al.*, Nuclear Data Sheets, 113, p3054-3100 (2012).
- [3] J. Lee *et al.*, Proc. of INMM & ESARDA Meeting 2021, #119.
- [4] K. Tanaka *et al.*, Proc. on 2019 IEEE NSS/MIC, DOI: 10.1109/NSS/MIC42101.2019.9059945 (2019).
- [5] F. Ito *et al.*, KURNS Progress Report 2020, CO2-6 (2021).

CO2-7 Neutron induced fission cross section measurement of ^{233}U

J. Hori¹, T. Sano², K. Terada¹, Y. Takahashi¹, and H. Yashima¹

¹Institute for Integrated Radiation and Nuclear Science, Kyoto University

²Atomic Energy Research Institute, Kindai University

INTRODUCTION:

The thorium based nuclear fuel cycle has many advantages with respect to the reduction of the risk of proliferation of fissile material and the reduction of buildup of long-lived higher actinides. In the previous works, we have already finished the neutron capture cross section measurement of ^{232}Th [1, 2]. Uranium-233 is the main fuel in the thorium fuel cycle, and its fission reaction plays an important role in the reactor system. Therefore, it is necessary to improve the accuracy of nuclear data associated with the neutron induced fission cross sections of ^{233}U for the feasibility study of the thorium nuclear system. We carried out the neutron induced fission cross-section measurement of ^{233}U .

EXPERIMENTS:

The experiment was performed with the time-of-flight (TOF) method at the 46-MeV electron linear accelerator in Institute for Integral Radiation and Nuclear Science, Kyoto University. Pulsed neutrons were produced from a water-cooled Ta target in a water tank as a neutron moderator. The flight path used in the experiment is in the direction of 135 degrees to the electron beam. The pulsed neutron beam was collimated to 30 mm in diameter. The ^{233}U sample was electrodeposited on a stainless steel plate with an active spot of 20 mm in diameter. The sample deposits of ^{233}U was set in a back-to back (BTB) type double fission chamber [3] which was used as a fission products detector. The distance between the electrode and the deposit layer is 8 mm. The BTB chamber is filled with a mixed gas of Ar and CO_2 at a pressure of 1 atm.

The ^{233}U sample in the BTB chamber was placed at 10.2 m from the Ta target in the TOF beam line. Fission events were detected via the energy deposited in the gas by the fission fragments produced in very thin layer of fissile material. Output signals from the chamber were stored in the Yokogawa's WE7562 multi-channel analyzer as the two dimensional data of pulse-height (PH) and TOF.

The linac was operated with two different conditions. One is for the low-energy experiment below 1 eV with a repetition rate of 50 Hz and the other is for the high energy experiment with a repetition rate of 200 Hz, respectively. In the high energy experiment, a Cd sheet of 0.5 mm in thickness was inserted into the TOF beam line to suppress overlap of thermal neutrons from the previous pulses due to the high frequency of the linac operation. A beam width and an electron energy were 100 ns and about 30 MeV., respectively.

To obtain the neutron flux at the sample position, neutrons were also measured by using a ^6Li -glass detector

directly. The efficiencies of the ^6Li -glass detector were provisionally estimated by using the $^6\text{Li}(n,\alpha)$ standard cross sections and the nominal thickness of scintillator. The energy calibration of the TOF neutron beam and the determination of background were performed in the additional experiment with the well-known resonance energies of 1.457 eV of In, 5.19 eV of Ag, 132 eV of Co, and 336 eV of Mn.

RESULTS:

Making use of the BTB chamber and the TOF method, the neutron-induced fission cross sections of ^{233}U were obtained relative to the $^6\text{Li}(n,\alpha)$ standard cross section at the energies from 0.002 eV to 1 keV. The relative cross sections were normalized to the reference value of 531.5 b at 0.0253 eV in the JENDL-4.0[4]. Figure 1 shows the comparison of the preliminary results with the evaluated values in JENDL-4.0.

The evaluated data in JENDL-4.0 show general agreement with the present results in the resonance region below 10 eV, although the evaluated data are considerably higher than the present results in high energy region.

We will try to derive the final results from the detail analysis on the detection efficiencies of ^6Li -glass detector.

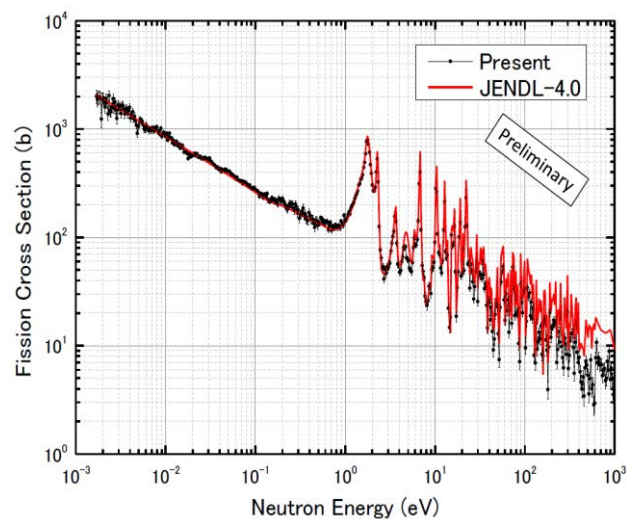


Fig.1 Comparison of the experimental fission cross sections of ^{233}U with the evaluated values in JENDL-4.0.

ACKNOWLEDGEMENT:

A part of the present study was supported by CHUBU Electric Power Co., Inc.

REFERENCES:

- [1] J. Hori *et al.*, *Proc. of PHYSOR2014*, Kyoto, Japan, Sep.28-Oct.3, 2014, 1127788 (CD-ROM).
- [2] J. Lee *et al.*, *Energy Procedia*, **131**, 306-311 (2017).
- [3] K. Kobayashi *et al.*, *J. Nucl. Sci. Technol.*, **36**, 20 (1999).
- [4] K. Shibata *et al.*, *J. Nucl. Sci. Technol.*, **48**, 1-30 (2011).

CO3-1 Subcriticality measurement by using a small neutron detector (3)

T. Misawa¹, Y. Kitamura¹, T. Takahashi¹, A. Yasui², and S.Okazaki²

¹Inst. Integrated Radiation and Nucl. Sci., Kyoto Univ.

²Graduate school of Energy Science, Kyoto Univ.

INTRODUCTION: In the fuel debris removal process of Fukushima Daiichi nuclear power plant, subcriticality monitoring system should be equipped to prevent criticality accident. For this purpose, International Research Institute for nuclear Decommissioning (IRID) is developing criticality control techniques for fuel debris removal based on neutron noise analysis using Feynman-alpha method or Rossi-alpha method. Prototype of the sub-criticality monitoring system was tested to verify applicability on various sub-criticality measurement conditions.

For this measurement, a small neutron detector based on a SiC with boron coated film is one of the candidates at Fukushima because of its toughness against gamma-ray and neutron radiation exposure and low detection efficiency for gamma-ray. We are also developing a data transfer system from this SiC neutron detector to data acquisition system which is placed at outside of a reactor vessel by a specially designed optical fiber with high resistance against radiation. In this research, we used this new data transfer system to measure subcriticality.

EXPERIMENTS: Experiment was carried out at KUCA solid moderated core, B-core, as shown in Fig.1 whose fuel assemblies were 3/8”p36EU with relatively soft neutron spectrum. The fuel coupon plates were sandwiched with polyethylene plates and assemblies were surrounded by polyethylene reflector to simulate water. This core was in subcritical state with low subcriticality with Cf-252 neutron source inserted in a fuel assembly. Data transfer system is illustrated in Fig.2. Boron-lined neutron detector was inserted in a periphery fuel region whose neutron detection analog signal was transfer pre-amplifier and then a data sender system by a co-axial cable. In the data sender system, analog signal was changed to optical digital signal and it was transferred to the data receiver system located at outside of the reactor room by a thin and long quartz optical fiber cable. Then digital data was changed to analog data in the data receiver system and finally neutron detection time whose time bin was 1 micro-second was transferred to PC by USB cable and stored in PC.

DATA ANALYSIS: Neutron detection time stamp data stored in PC whose time unit was $1 \mu s$ were analyzed by the neutron noise analysis methods, Feynman-alpha

method and Rossi-alpha method.

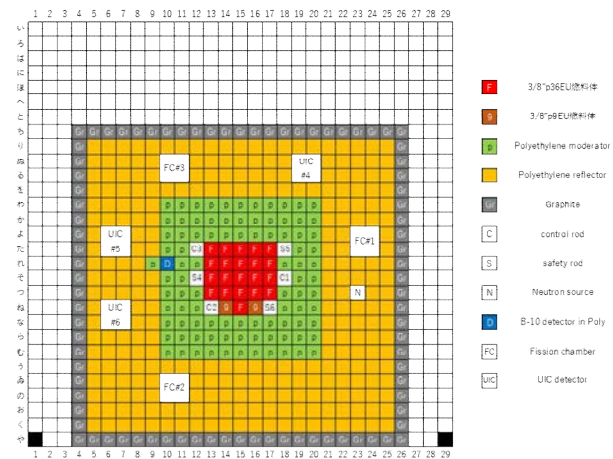


Fig.1 Core configuration.

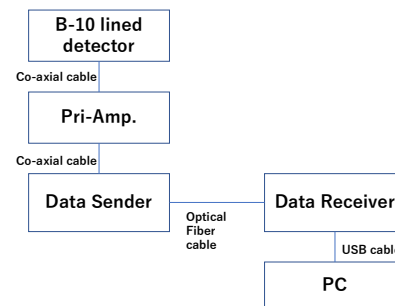


Fig.2 Data transfer system.

Table 1 Experimental results.

Subcriticality (%dk/k)	Calculated Alpha (s ⁻¹)	Experimental Alpha (s ⁻¹)
1.08	382	405 ± 2
1.38	442	468 ± 2
1.60	487	511 ± 2
1.90	547	590 ± 2
2.11	588	656 ± 2

RESULTS: Results of Feynman-alpha method are shown in Table 1, where prompt neutron decay constants (alpha value) in various subcriticalities are listed. It is found that alpha value is close to calculated values in near critical state.

We continue to develop this data transfer system based of optical fiber combined with a SiC neutron detector for future usage.

CO3-2 Reactor Noise Power-Spectral Analysis for a Graphite-Moderated and -Reflected Core (III)

A. Sakon, K. Hashimoto, T. Sano,
 K. Nakajima¹, T. Kanda¹, M. Goto¹, Y. Fukaya², S. Okita²,
 N. Fujimoto³, and Y. Takahashi⁴

Kindai University Atomic Energy Research Institute
¹Graduate School of Science and Engineering, Kindai University

²Sector of Fast Reactor and Advanced Reactor Research and Development, Japan Atomic Energy Agency

³Faculty of Engineering, Kyushu University

⁴Institute for Integrated Radiation and Nuclear Science, Kyoto University

INTRODUCTION: In the last study, a neutron detector located about 55 cm away of fuel assembly measured the auto power spectral density. However, the prompt neutron decay constants obtained by this detector was different from that of other detectors. The objective of this study is experimental study of reactor noise analysis by the power spectrum method using neutron detector placed outside reactor core.

EXPERIMENTS: The core configuration is shown in Fig. 1. “F” is test zone fuel assembly. “D” is a driver fuel assembly. “G” is graphite reflector. Yellow cell is polyethylene reflector. “1” to “6” are BF₃ proportional neutron counter positions. The dimensions these counters are 1.0 in. diameter and 15.47 in. length. The distance from core region to detector positions “1” and “2” are about 15cm, that to detector position “3” is about 20cm, that to detector position “4” is 35cm, that to detector position “5” is 55cm, that to detector position “6” is about 75cm.

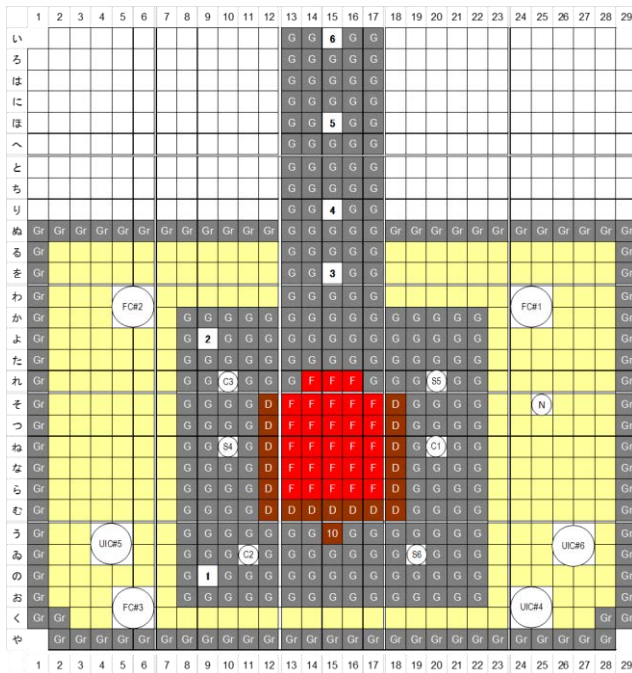


Fig. 1 Core configuration.
 (B7/4”G2/8”p8EU(3)+3/8”p38EU)

Reactor noise analysis by power spectrum method was performed in the critical state of suitable reactor power for each detector position. The reactor power during measurement was adjusted so that the count rate of each detector was about 3,000[cps].

RESULTS: The auto power spectral densities and cross power densities by detector position “3” to “6” are shown in Fig. 2 and Fig. 3. These figures also include least squares fits of a conventional formula [1] to the spectral densities to determine the prompt neutron decay constant α_0 ($\beta_{\text{eff}}/\Lambda$), where the fitting was confined to a frequency range from 2.5 to 100 Hz or 2.5 to 50 Hz. The prompt neutron decay constant obtained by the detectors “3” and “4” were the same within the error range. However, the decay constant obtained by detector “5” and “6” were very different. In the future, it is necessary to improve the fitting formula and reexamine the analysis frequency range of power spectrum method.

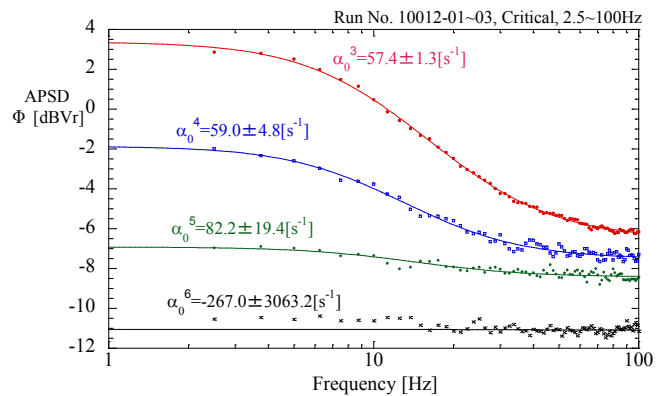


Fig. 2 Auto power spectral densities.
 (Detector “3” to “6”)

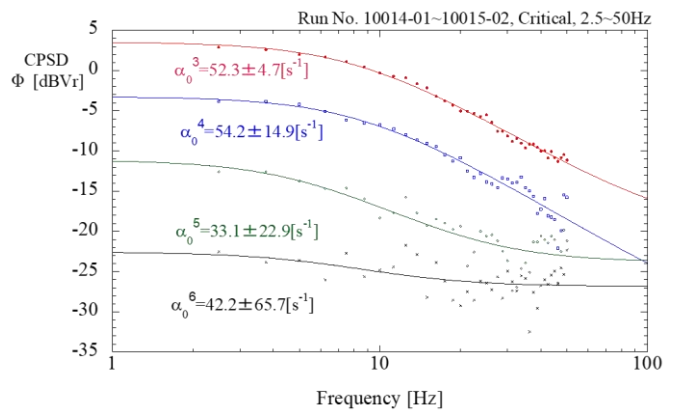


Fig. 3 Cross power spectral densities.
 (Detector position “3” to “6”)

REFERENCES:

[1] M. M. R. Williams, Random Processes in Nuclear Reactors, (Pergamon Press, Oxford,1974), section 3.6.

CO3-3 Reactor Physics Experiment in a Graphite Moderation System for HTGR (III)

Y. Fukaya, S. Okita, S. Kanda¹, M. Goto¹, K. Nakajima¹, A. Sakon¹, T. Sano¹, K. Hashimoto¹, Y. Takahashi² and H. Unesaki²

Sector of Fast Reactor and Advanced Reactor Research and Development, Japan Atomic Energy Agency
¹*Kindai University Atomic Energy Research Institute*
²*Institute for Integrated Radiation and Nuclear Science, Kyoto University*

INTRODUCTION: The Japan Atomic Energy Agency (JAEA) started the Research and Development (R&D) to improve nuclear prediction techniques for High Temperature Gas-cooled Reactors (HTGRs) in 2018. The objectives are to introduce the generalized bias factor method to avoid full mock-up experiment for the first commercial HTGR and to improve neutron instrumentation system by virtue of the particular characteristics due to a graphite moderation system. For this end, we composed B7/4”G2/8”p8EU(3)+3/8”p38EU in the B-rack of Kyoto University Critical Assembly (KUCA) in 2021.

EXPERIMENTS: The core configuration is shown in Fig.1. The objective is to cover the characteristics of commercial HTGR with relatively high enriched fuel. The Gas Turbine High Temperature Reactor 300 (GTHTR300) employs 14wt% enriched uranium fuel to achieve high burn-up of 120GWd/t. The core of B7/4”G2/8”p8EUNU+3/8”p38EU composed in 2018 has the fuel assembly averaged enrichment of which is 5.41wt% to realize a characteristics of High Temperature Engineering Test Reactor (HTTR). The characteristics of GTHTR300 are expected to be evaluated by the interpolation of the characteristics of the two cores from the viewpoint of generalized bias factor method because the present core is composed of only highly enriched uranium plate.

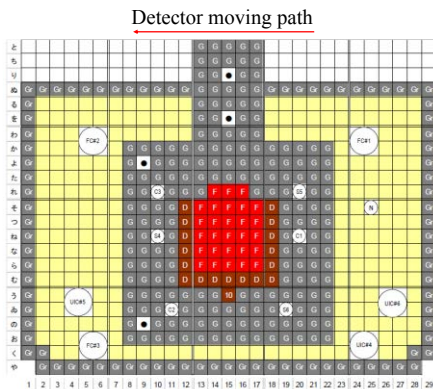


Fig. 1 Core configuration.

To demonstrate the power distribution measurement system from ex-core detector which have been developed by JAEA[1], not only a noise analysis, which was performed by the detector expressed by a dot mark in Fig. 1, but also neutron detector signals measurement by a moving

detector as shown in Fig. 2 were performed.



Fig.2 Moving detector system.

RESULTS: The spectrum of the core is compared with that of GTHTR300 in Fig.3. The Maxwell peak is successfully realized and close sensitivity is expected.

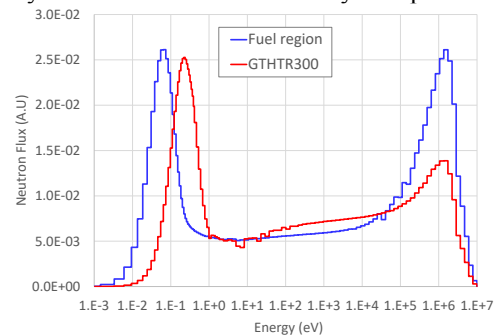


Fig.3 Neutron spectrum.

The moving detector system is expected to demonstrate a power distribution measurement from ex-core detector. By virtue of a long neutron flight path of a graphite moderation system, the power distribution can be evaluated by inverse analysis with measurement data by moving detector system. The feasibility was already proved by a numerical simulation in HTTR geometry [1]. The detector signals along with the moving path illustrated in Fig.1 are shown in Fig. 4. The detector moves 1m stroke by 87 sec. The expected detector signals were obtained compared with calculation result by MVP code.

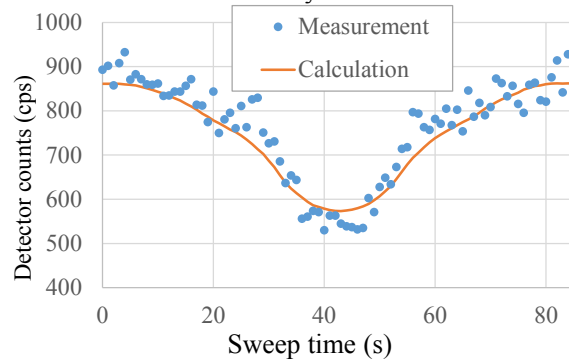


Fig.4 Neutron detector signals

Reference:

[1] Y. Fukaya, S. Okita, S. Nakagawa, *et al.*, “Computed tomography neutron detector system to observe power distribution in a core with long neutron flight path,” *Ann. Nucl. Energy* 168, pp.108911_1-108911_7,(2022).

CO3-4 Measurement of fundamental characteristics of nuclear reactor at KUCA (VII)

Y. Kitamura¹, T. Misawa¹, Y. Takahashi¹, M. Nakano^{2,3},
Y. Hayashi^{2,4}, Y. Morimoto^{2,5}

¹Institute for Integrated Radiation and Nuclear Science,
Kyoto University

²International Research Institute for Nuclear Decommissioning

³Mitsubishi Heavy Industries

⁴Toshiba Energy Systems & Solutions Corporation

⁵Hitachi-GE Nuclear Energy, Ltd.

ACKNOWLEDGEMENTS: The authors This work is a part of “Development of Safety System (Liquid/Gas System, Technologies for Criticality Control” project supported by the Ministry of Economy, Trade and Industry (METI). The authors would like to express their deep thanks to Mrs. S. Wada^{2, 3}, M. Shimizu^{2, 3} and H. Yazawa^{2, 3} for their helps in performing the KUCA experiment.

INTRODUCTION: The reactor noise methods can measure the subcriticality without additional instruments. International Research Institute for Nuclear Decommissioning (IRID) is developing the monitoring subcriticality system based on the reactor noise methods using the Feynman-alpha method. A prototype system was developed using B-10 neutron detectors [1]. The system is required with radiation hardness. We, IRID, picked up the corona detectors and multi-cell detector as the candidate detectors with radiation hardness.

For this measurement, the applicability of the monitoring subcriticality systems with corona counters with B-10 or He-3 and a multi-cell He-3 detector are verified.

EXPERIMENTS: Experiment was carried out at KUCA solid moderated core, B-core, as shown in Fig.1 whose fuel assembly was 3/8”p32EU. We measured some cores that changed number of the fuel assemblies, in order to simulate shallow/deep subcriticality and situation of high neutron count-rate. This core was aimed to compare the porotype system with B-10 detectors used in past experiments. In Fig.1, D1 is mean a corona He-3 detector, D2 is mean a corona B-10 detector, and D3 is mean a multi-cell He-3 detector.

RESULTS: As shown in Fig. 2, the testing systems can measure the available time-list data for the Feynman-alpha method. The comparison of k-effective evaluated by time-list data of each system is shown in Fig. 3. These results those k-effective are higher than 0.95 are good agreement with reference k-effective simulated by the MVP code with JENDL-4. The results in the deep subcriticality less than 0.7 of k-effective are agreement with 10% error.

The test results showed that the testing systems are feasible to measure the subcriticality.

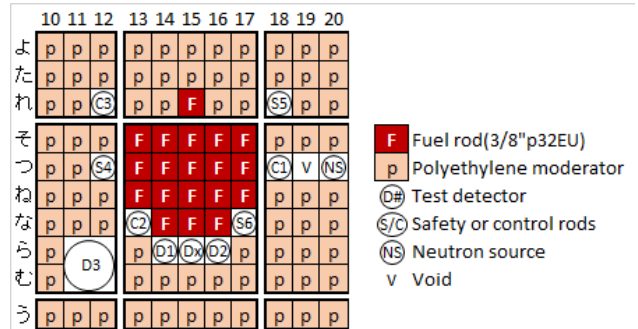


Fig. 1 Core configuration.

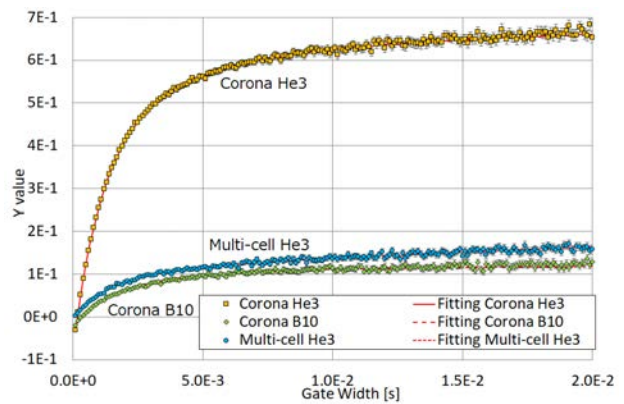


Fig. 2 Example of Feynman-Y value & curve.

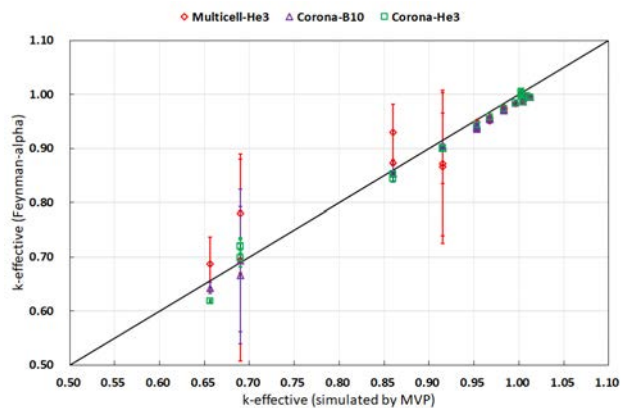


Fig. 3 Comparison of k-effective.

REFERENCES:

[1] S. Wada *et al.*, *Proc. of ICNC2019*, Paris France, Sep. 15-20 (2019).

CO3-5 Verification of a method to estimate reactivity in a deep subcritical state

Y. Yamane, S. Araki, Y. Kitamura¹, T. Misawa¹

Japan Atomic Energy Agency

¹Institute for Integrated Radiation and Nuclear Science, Kyoto University

INTRODUCTION: The estimation of reactivity of an amount of unknown fissile material is one of important issues in the field of criticality safety.

JAEA has been theoretically developing a method to estimate the reactivity from neutron count rate alone[1-2]. The method is based on a newly developed equation of power in quasi-steady state after prompt jump/drop of power due to reactivity and/or neutron source change.

The purpose of the experiment is to obtain the experimental data for the verification and validation of the developed method. This time, the data were obtained for deep subcritical states around $k_{eff} = 0.95$, which is a threshold value for a subcritical condition in a numerical analysis.

EXPERIMENTS: A subcritical experiment was done with the basic critical core configuration known as 3/8” p36EU of A-core. The Am-Be was used as the external neutron source.

³He detectors were used. Figure 1 shows the core configuration and the position of Am-Be neutron source.

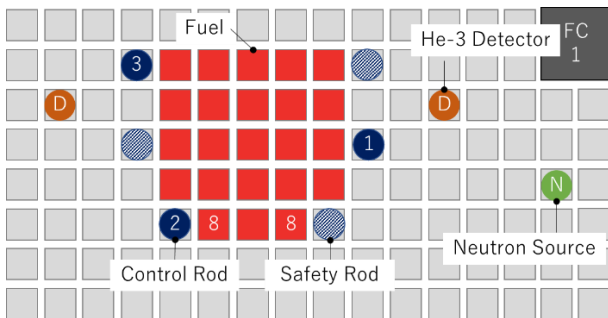


Fig. 1. Configuration of fuels and devices in A-core.

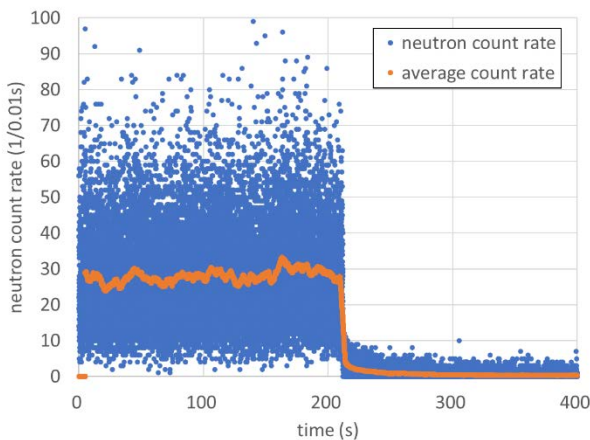


Fig. 2. Neutron count rate data. Blue circle shows neutron counts per 0.01s and orange circle shows a profile of averaged one.

For the first several hundred seconds, as shown in Fig.2, the system was kept under a subcritical steady state. Then a negative reactivity was inserted by dropping control rods, C1-C3, safety rods, S4-S6, and/or Center Core. The achieved k_{eff} is shown in Table1. 6 rods were dropped for 0.97, Center Core for 0.95 and the rods and CC for 0.93. Those k_{eff} values were roughly estimated by summing up the reactivity worth of each device.

After that, neutron count rate decreased and the measurement was terminated after several hundred seconds or more.

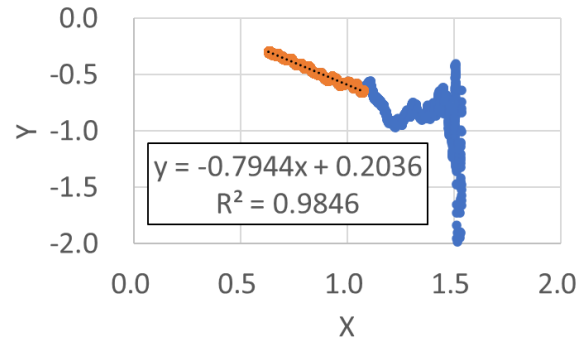


Fig. 3. Linear fitting to the points (X, Y) calculated from the neutron count rate data shown in Fig. 2.

RESULTS: Reactivity value was estimated following the procedure described in [2], in which the neutron count rate data from the detector far from the neutron source was chosen and treated. The points $(X(t), Y(t))$ were calculated from the neutron count rate data and its slope value, $a = -0.794$, was estimated by linear fitting as shown in Fig. 3. Then the reactivity value was calculated as follows;

$$\rho_{\$} = \frac{1}{(1/a + 1)} = -3.9$$

The estimated value obtained by preparatory calculation with the new method was summarized in Table 1. The difference between the reference value and estimated one is up to 12%. It shows the applicability of the new method to deep subcritical state, and more detailed analysis is needed to quantify its degree of accuracy.

Table 1. The experimental condition and estimated reactivity value by applying the new method.

operation	keff	reactivity		
		reference (\$)	estimated(\$)	difference(%)
drop C1-S6	0.97	-4.1	-3.9	-5.4
drop CC	0.95	-8.1	-9	12
drop all	0.93	-12	-12	-5

REFERENCES:

[1] Y. Yamane, J. Nucl. Sci. Technol. Vol.57(8), 926-931 (2020).

[2] Y. Yamane, J. Nucl. Sci. Technol.

<https://doi.org/10.1080/00223131.2022.2053221> (2022).

CO3-6 Basic Experiment on Reactor Power Distribution Reconstruction by Ex-core Neutron Detectors

T. Sano, A. Sakon¹, K. Nakajima¹, M. Goto¹, T. Kanda¹,
K. Hashimoto¹, Y. Takahashi², C. H. Peyon²

Atomic Energy Research Institute, Kindai University
¹Graduate School of Science and Engineering, Kindai University
²Institute for Integrated Radiation and Nuclear Science, Kyoto University

INTRODUCTION: We are developing an in-core power distribution estimation method (PHOEBE) using ex-core neutron detectors to reduce the cost and improve the maintainability of nuclear instrumentation in small reactors as a distributed power source [1]. Theoretical and numerical examinations were initially studied with the experimental demonstration conducted at UTR-KINKI [2]. The demonstration was conducted with a simple core. Hence, more complex experiment geometry is required to evaluate the power distribution of the core inner region for the experimental demonstration of PHOEBE. In this study, a new core was constructed at KUACA and tested to confirm the effectiveness of PHOEBE.

EXPERIMENTAL GEOMETRY: Figure 1 shows a configuration of fuel element in this experiment. A unit cell consisted of one 1/16" EU plate, two 1/8" PE plate and one 1/4" graphite plate. The fuel element had 30- or 14-unit cells and graphite reflectors. Figure 2 shows the experimental core layer. 31 fuel elements were loaded into the core and 3 control rods, 3 safety rods, graphite reflectors elements were installed. In addition, 8 eight neutron detector systems (ERYNGII), which can efficiently measure epi-thermal neutrons as shown in Fig. 3, were inserted for this experiment.

RESULTS: Table 1 shows the measured neutronics characteristics. The all characteristics were satisfied with the KUACA regulations. In this core, the power distribution was distorted by control rod manipulation or special fuel element, and the epi-thermal neutron flux were measured by ERINGII. As a result, the validity of PHOEBE was confirmed.

REFERENCES:

- [1] R. Kimura, *et. al.*, Nucl. Sci. Eng. 2020; 195(12), pp1279-1290.
- [2] R. Kimura, *et. al.*, AESJ 2021 Fall Meeting, 2109, (2021).

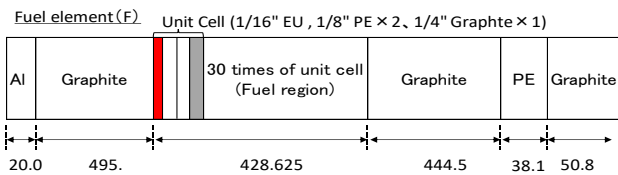


Figure 1 Configuration of fuel element.

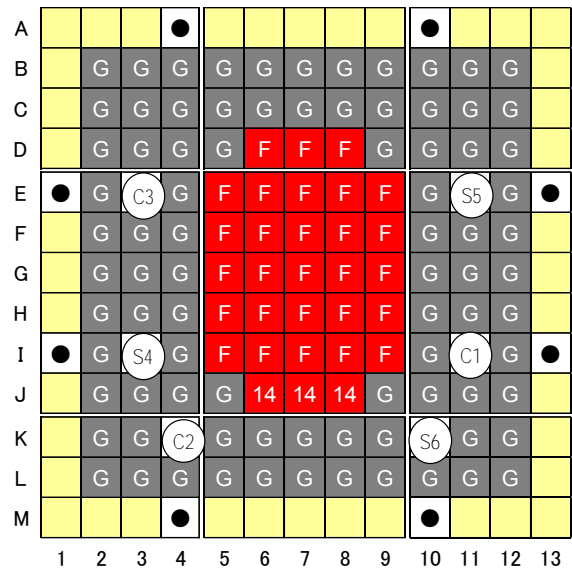


Figure 2 Experimental core.

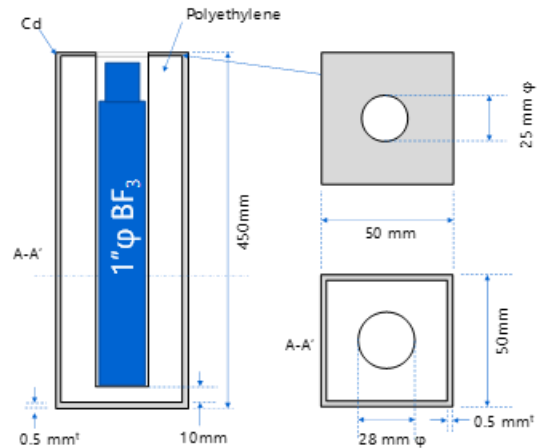


Figure 3 Schematic diagram of neutron detector system. (ERYNGII)

Table 1 Measured neutronics characteristics.

Neutronics Characteristics	Char-acteristics	Measured	KUCA Regulation
Excess reactivity (%dk/k)		0.154	< 0.35
Max. reactivity insertion rate (%dk/k/sec)		0.007 C3:830mm-730mm	< 0.02
Rod worth (%dk/k)	C1	0.599	Max. worth < 1/3 of total worth
	C2	0.422	
	C3	0.654	
Center core worth (%dk/k)	Total	(0.599+0.422+0.654)x2=3.350	Total worth > Excess + 1 %dk/k
Center core worth (%dk/k)		3.325	> 1%dk/k

CO3-7 Measurement of Neutronics Characteristics for Th loaded core at KUCA (III)

T. Sano, T. Kanda¹, J. Hori², Y. Takahashi², K. Terada², H. Yashima², and H. Unesaki²

Atomic Energy Research Institute, Kindai University

¹Graduate School of Science and Engineering, Kindai University

²Institute for Integrated Radiation and Nuclear Science, Kyoto University

INTRODUCTION:

In engineering discussions of the feasibility of new reactor systems, it is necessary to evaluate the impact of the fuels and materials for the neutronics characteristics such as criticality, conversion rate, and fuel balance. In order to develop of Thorium (Th) nuclear system, critical experiments on Th loaded cores using the KUCA with solid moderator core have been systematically carried out to perform neutronics characteristics measurements of Th loaded thermal neutron systems and integral evaluation of Th cross sections [1]. In order to perform nuclear design for Th loaded reactors, it is important to validate U-233 nuclear data. In order to perform an integral validation of U-233 fission cross section, measurements of sample reactivity worth in KUCA solid moderated core were carried out.

EXPERIMENTS:

In this experiment, two types of fuel element were loaded into the KUCA solid moderated core. Figure 1 shows composition of a fuel element “F” and a special fuel element “S”. The fuel element “F” was consisted of 31 unit cells and sandwiched by a upper and a lower polyethylene reflector. The unit cell has one enriched uranium plates of 0.159 mm (1/16 in.) thickness, three polyethylene plates of 0.318 mm (1/8 in.) thickness. The fuel element “S” was consisted of 30 unit cells and one sample case made of aluminum. The geometry of sample case has 50.8 mm × 50.8 mm × 11.11 mm (7/16 in.).

A sample plate was made of U₃O₈-Al and the amount of U-233 in a plate was about 0.09 g. The U-233 enrichment was 99.4 wt% [2]. The geometry of a plate was 12.66 mm × 12.68 mm × 1.08 mm¹ and has a round chamfering (R = 3 mm). 9 plates of U-233 sample were set into a aluminum sample case. Figure 2 shows a core configuration of this experiment. The experimental core has 24 fuel elements “F” and one special fuel element “S”. The C1 – C3 are control rods and the S4 – S6 are safety rods.

RESULTS:

The sample reactivity value was defined as the difference of excess reactivity between the core with the aluminum case installed the U-233 sample plates and the core with the aluminum case without the samples. The excess reactivity measurements were carried out by the positive period method. In each measurement, the C2 and C3 control rods were set to the upper limit (U.L.) and the C1 control

rod was adjusted to the critical position. And the C1 control rod was drawn out to the U.L. from the critical position and the reactivity was inserted into the core. As the result, the excess reactivity with and without U-233 sample were 0.1003 ± 0.0032 %dk/k and 0.0649 ± 0.0014 %dk/k [2]. Therefore, the sample worth was obtained as 0.0354 ± 0.0015 %dk/k [2].

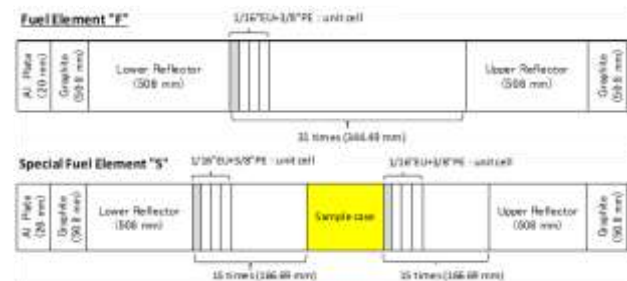


Figure 1. Configuration of a fuel element “F” and “S”.

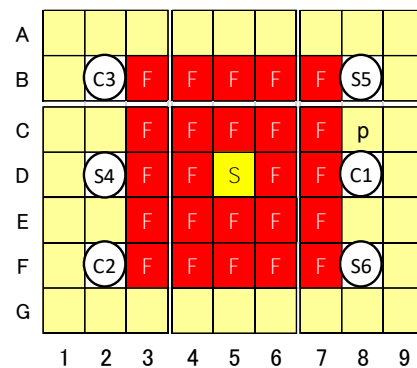


Figure 2 Core configuration.

ARKNOWLEDGEMENT:

A part of the present study was supported by CHUBU Electric Power Co., Inc.

REFERENCES:

- [1] T. Sano, *et. al.*, Proc on PHYSOR2020, Cambridge, UK, Mar.29th – April 2nd, (2020).
- [2] T. Sano, *et. al.*, Abstract of AESJ 2021 Fall meeting, Online, 1F14, (2021).

CO3-8 Subcriticality measurement by using a small neutron detector (4)

T. Misawa, Y. Kitamura and T. Takahashi

*Institute for Integrated Radiation and Nuclear Science,
Kyoto University*

INTRODUCTION: Subcriticality monitoring system has to be used to detect criticality approach for each step of debris removal in Fukushima Daiichi nuclear power plant. For this purpose, International Research Institute for nuclear Decommissioning (IRID) is developing criticality control techniques for fuel debris removal based on neutron noise analysis using Feynman-alpha method. A prototype of the sub-criticality monitoring system was tested to verify applicability on various sub-criticality measurement conditions.

For this measurement, a small neutron detector based on a SiC with boron coated film is one of the candidates at Fukushima because of its toughness against gamma-ray and neutron radiation exposure and low detection efficiency for gamma-ray. We are also developing a data transfer system from this SiC neutron detector to data acquisition system which is placed at outside of a reactor vessel by a specially designed optical fiber with high resistance against radiation. In this research, we used this new data transfer system to confirm the availability for subcriticality measurement.

EXPERIMENTS: Experiment was carried out at KUCA solid moderated core, B-core whose fuel assemblies were 3/8"p36EU. Data transfer system is illustrated in Fig.1. Boron-lined neutron detector was inserted in a periphery fuel region whose neutron detection analog signal was transfer pre-amplifier and then a data sender system by a co-axial cable. In the data sender system, analog signal was changed to optical digital signal and it was transferred to the data receiver system located at outside of the reactor room by a thin and long quartz optical fiber cable. Then digital data was changed to analog data in the data receiver system and finally neutron detection time whose time bin was 1 micro-second was transferred to PC by USB cable and stored in PC.

In the previous year experiments, unexpected noise signal sometimes appeared, for example once in 5 minute, in accumulated data, which cause inaccurate subcriticality results. This unexpected data transfer may be caused from data transfer system, however, we cannot clear up this phenomena up to the present time.

To remove those unexpected noise signal, we divided time stamp data into several part, and each time period

data was analyzed by the neutron noise analysis methods, Feynman-alpha method and Rossi-alpha method. Then, we compared those results to confirm existence of noise signal.

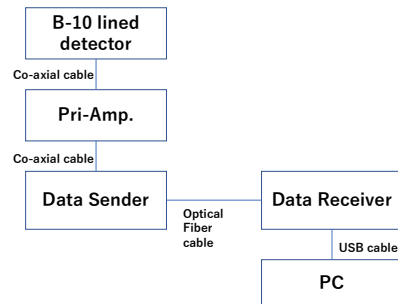


Fig.1 Data transfer system.

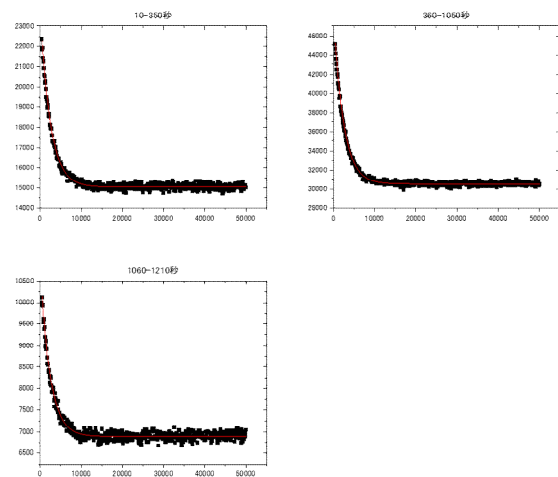


Fig.2 Rossi-alpha results by dividing time stamp data.

RESULTS: The results are shown in Fig. 2 for Rossi-alpha method after removing unexpected time stamp data. By using this data dividing technique, it is possible to remove unexpected noise signal data.

We continue to improve this data transfer system based of optical fiber combined with a SiC neutron detector for future usage.

CO3-9 Measurement of Validation Data for Kinetics Parameter and Reactor Kinetics

Y. Nauchi, S. Sato, Y. Takahashi¹, H. Unesaki¹, Y. Kitamura¹

Central Research Institute of Electric Power Industry
¹Institute for Integrated Radiation and Nuclear Science,
 Kyoto University

INTRODUCTION: Precise estimation of the reactor kinetics is essential for the nuclear safety. In CRIEPI, continuous energy Monte Carlo (MC) method has been studied to estimate the point kinetics parameters in a critical condition [1, 2] and reactor periods [3]. Besides, time dependent neutron transport calculation techniques are now under development [4, 5]. In order to validate those calculations, comprehensive data sets of reactor kinetics were measured in A3/8²p36EU(3) core.

RESPONSE FOR STEP REACTIVITY INSERTION: Positive and negative reactivities were inserted stepwisely by moving C1 rod and time variation of power was measured as shown in Fig. 1 (left). The reactivity range was from -46 to 51 pcm. The asymptotic period given by the flux a few hundred seconds after the insertion shall be used to validate whether the effective delayed neutron fraction repartition per precursor family, $\beta_{eff,i}$, relates the measured periods to the calculated static reactivities [1,2]. The transient phase from the prompt jump to the asymptotic behavior is also useful to validate time dependent calculation. For that, the prompt jump behavior was focused by raising the initial critical power (Fig. 1, right).

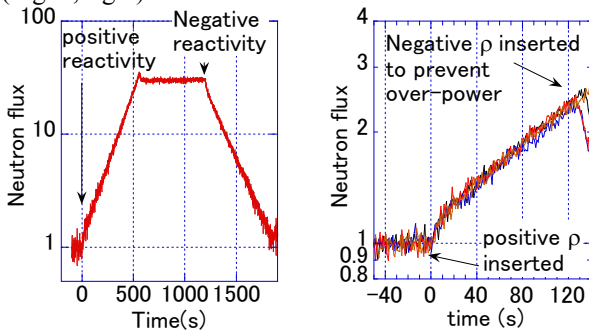


Fig.1 Response to positive & negative step reactivity insertion (left). Focusing on prompt jump (right).

EFFECT OF REACTIVITY INSERTION RATE:

Reactivity insertion rate is also important for kinetics behavior of a core. In this work, we attained criticality by adjusting the C1 rod position (688 mm) while C2 and C3 rods were withdrawn. Then the C1 rod was fully inserted from time 0 second by 1) dropping and by 2) continuous down with speed of -8.013 mm/s. Neutron flux decrement with time was measured three times for both the insertion conditions. The results are shown in Fig. 2. In the rod drop measurements, the negative reactivity was measured -404, -392, -394 pcm for the case 1, 2, 3, respectively. The time dependent neutron flux of case 2 and 3 are similar and that of case 1 is bit different. Due to the instant insertion of the negative reactivity, negative

prompt jump was observed. Whereas in the continuous down case, the time dependent neutron flux of the three cases is similar each other and that is very credible as the validation data. According to the worth curve of C1 rod and the insertion speed, the negative reactivity of -392 pcm is given within 34.5 s. After 35 s, the flux by the continuous down of C1 rod approaches to that by the rod drop test. These data shall be applied to validate the time dependent MC calculation.

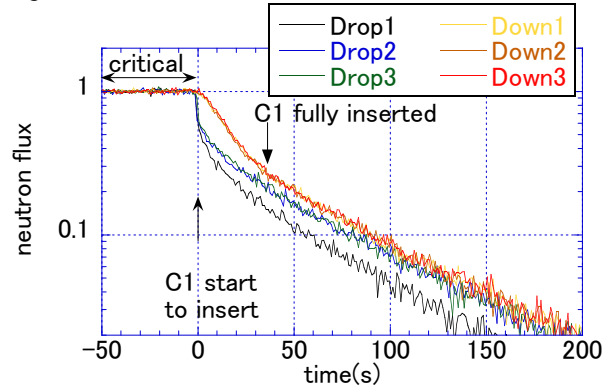


Fig. 2 Neutron flux decrement by C1 rod insertion.

VARIANCE TO MEAN METHOD: For the validation of the generation time Λ , measurement of α eigenvalue is useful. For that, the Feynman - α measurement was done with a conventional method. The neutron count rate in FC #2 and #3 were measured with dwell time of 0.1 ms and the Y value and α were preliminary evaluated without correction for dead time of detectors. β_{eff} and Λ are calculated with enhanced MCNP-5.1.30 with the AcelibJ40 library. The reactivity ρ is given based on the rod worth curve based on $\beta_{eff,ij}$ by MCNP calculation [1,2]. Then the calculated α is given as $\alpha = (\beta_{eff} - \rho) / \Lambda$. The measured and calculated α s are compared in Table 1. The C/E ranges from 0.985 to 1.126. We shall investigate the influences of the dead time and spatial higher-mode flux to make C/E more credible.

Table 1: Measured and calculated α eigenvalue.

Reactivity (pcm)	Measured α (s ⁻¹) by FC#2	C/E	Measured α (s ⁻¹) by FC#3	C/E
-329	214.09	1.040	225.92	0.985
-144	171.44	1.084	174.46	1.065
-72	161.23	1.065	152.93	1.122
0	139.64	1.126	155.08	1.014

ACKNOWLEDGEMENT: The authors are so honored to have been a part of the historical moment when the Run No. of KUCA reaches 10,000 since its commencement in 1974.

REFERENCES:

- [1] Y. Nauchi *et al.*, *JNST*47(11)977-990, 2010.
- [2] A. Zoia *et al.*, *ANE*96 377-388, 2016.
- [3] Y. Nauchi *et al.*, *ANE*162 108486, 2021.
- [4] Y. Nauchi, *JNST*56(11)996-1005, 2019.
- [5] Y. Nauchi, Proc. M&C2021, Oct.3-7, 2021.

CO3-10 Basic Research for Sophistication of High-power Reactor Noise Analysis (IV)

S. Hohara¹, T. Sano¹, A. Sakon¹, K. Nakajima², K. Hashimoto¹

¹Atomic Energy Research Institute, Kindai University
²Graduate School of Science and Engineering, Kindai University

INTRODUCTION: Reactor noise for high-power reactors were actively measured in the 1960's and 1970's. The major focuses of those researches were for the abnormality diagnosis or the output stabilization diagnosis, and almost researchers were in the field of system control engineering or instrumentation engineering. High-power reactor noise measurements for dynamics' analysis of reactivity change, reactivity feedback or reactor characteristics itself were few in the time (1960's and 1970's), because of the powerless measurement system. In this research, we plan to measure KUR's output with present-day measurement system and plan to analyze with several analysis methods. The results of this work will supply some knowledges and technics in the aspect of sophistication of reactor noise analysis or simulation methods.

In this year, we tried to measure the reactor nuclide noise of the critical state KUR core via a 1-inch ³He counters at CN-1 port focused on epi-thermal neutrons. The experimental work was done on 25th November 2021. As the result of the experiment, a result looks like the nuclear reactor noise was observed in 1MW critical state.

EXPERIMENTS:

In this experiment, the output signal of the ³He counters (LND 25291 × 3) were put into Spectro Scopy AMPs (2022: Canberra and 590A: ORTEC), and the output of the SSAs were measured with a time-series measurement system (HSMCA4106_LC: ANSeeN Inc.). A schematic view of the measurement is shown in Fig.1, and the counter installation overview is shown in Pic.1.

As you can find in Pic.1, the neutrons from the KUR core were measured with ³He counters via a 5-mm thickness B₄C sheet.

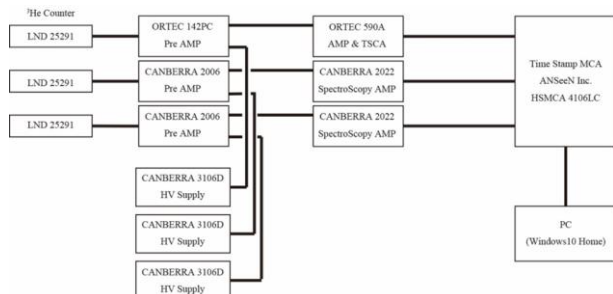
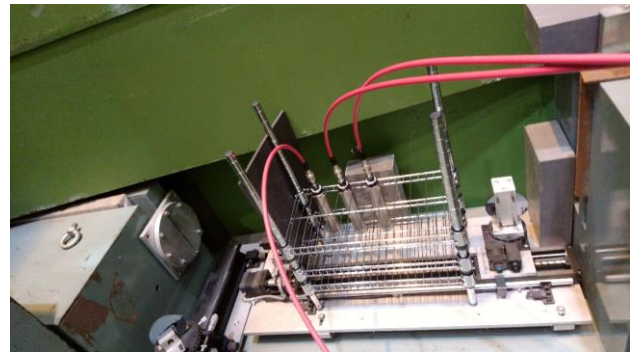


Fig. 1. Schematic view of the measurement.

The experimental condition is shown in Table.1. The reactor Power was set in 1MW. The measurement time was

8,000 sec.



Pic. 1. An overview of the counter installation

Table 1. Experimental condition

Reactor Power [W]	Measurement Time [sec]	Count Rate [cps]
1M	8,000	620 - 660 (#1) 210 - 230 (#2) 560 - 600 (#3)

RESULTS:

The measurement results were analyzed by Feynman- α / bunching method, Rossi- α method and Covariance to Mean Ratio method.

As a result of the Feynman- α analysis, plot shapes like Feynman's theoretical formula were not obtained, because of the gradually increasing of the KUR power.

As a result of the Rossi- α analysis, plot shapes like Orndoff's theoretical formula were obtained on the 3 counters' results. As a result of the Covariance to mean ratio analysis, plot shapes like Feynman's theoretical formula were obtained, however the Y values were extremely small.

An analysis result example of the Rossi- α analysis is shown in Fig.3. The result of this work show that the neutron energy selection may improve the sensitivity of the reactor nuclide-noise measurements for the light water moderation reactor.

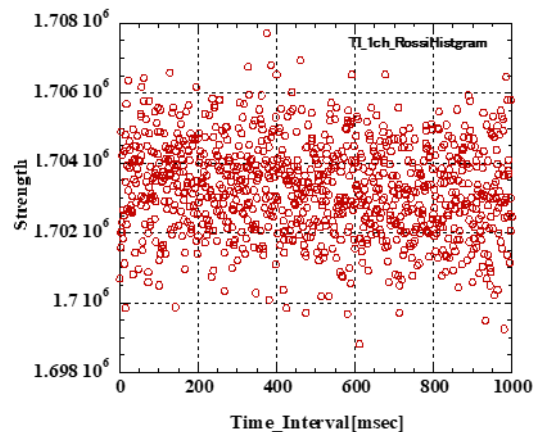


Fig. 2. A result example of Rossi- α analysis

CO3-11 Development of Faster Measurement Method of High Neutron Flux with SPND

C. H. Pyeon and R. Okumura

*Institute for Integrated Radiation and Nuclear Science,
Kyoto University*

INTRODUCTION: To safely control the reactor, monitoring neutron flux inside the reactor is necessary. Therefore, a reliable technology is needed to measure neutrons of high intensity, as in the reactor. Self-powered neutron detectors (SPNDs) are available as detectors to perform the measurement. The SPND is possible to obtain information on neutron flux by measuring the current signal generated with the use of activation of emitter material (Rh, V, Co etc.). In the detection principle, the response time of the detector is determined by the time constant of activation decay, which makes it difficult to respond quickly. In this study, we will explore a method to speed up the response of SPND by digital data processing.

EXPERIMENTS: Since the self-output neutron detector requires high neutron intensity, neutron measurements were conducted in the inclined irradiation borehole (SLY) of the Kyoto University research Reactor (KUR), which allows measurements to be made close to the reactor core in this test. The preliminary measurement was performed with the detector inserted during 1 MW operation, and the next measurements of output power were carried out at the KUR operation ranging between 1 and 5 MW. The detector was a self-output neutron detector using rhodium (Rh) as the detector. The output of the self-output neutron detector was measured using a pico-ampere-meter.

RESULTS: Figure 1 plots the current from the SPND versus time versus the linear output meter of the furnace; the output of the SPND at 1 MW output was about 5 nA the response time of the detector after insertion into the SLY was about 300 s. The response time is due to the decay constants of the activation products of ^{113}Rh , ^{114}Rh and $^{114\text{m}}\text{Rh}$, of 40 s and 4.4 min. When the output was changed from 1 MW to 5 MW, the maximum current

value from the SPND was 24 nA at 5 MW.

To accurately examine the time response of the SPND, we examined the time variation after the detector was pulled out from the SLY. The results of exponential fitting to the time variation are shown in Figure 2. Figure 2 indicates that the time variation is confirmed to be reproduced by adding the two exponential curves together. The time constants of the response were 41 s and 4.3 min, respectively. The ratio of the current values derived from ^{104}Rh and $^{104\text{m}}\text{Rh}$ was 1:0.07. Using the parameters, we will investigate a useful way to estimate the output of SPNDs more quickly.

In this study, we considered the method to estimate the output from the activation equation. The activation equation can be expressed by Eqs. (1) and (2) as follows:

$$N_{\text{Rh}^{104}} = -\lambda_{\text{Rh}^{104}} N_{\text{Rh}^{104}} + \lambda_{\text{Rh}^{104\text{m}}} N_{\text{Rh}^{104\text{m}}} + N_{\text{Rh}^{102}} \sigma f \quad (1)$$

$$N_{\text{Rh}^{104\text{m}}} = -\lambda_{\text{Rh}^{104\text{m}}} N_{\text{Rh}^{104\text{m}}} + N_{\text{Rh}^{102}} \sigma f \quad (2)$$

where σ is the activation cross section, f the neutron flux, and N the number of atoms.

The two equations are different from each other, and the filtered neutron fluxes are plotted in Figure 3. The filtered result were found to respond faster than the raw measurement result.

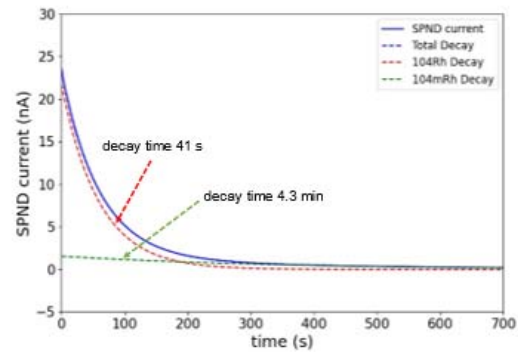


Fig. 2 Plot focused on SPND current decay after the detector pulled out from SLY. The decay curve was fitted with the two exponential curves.

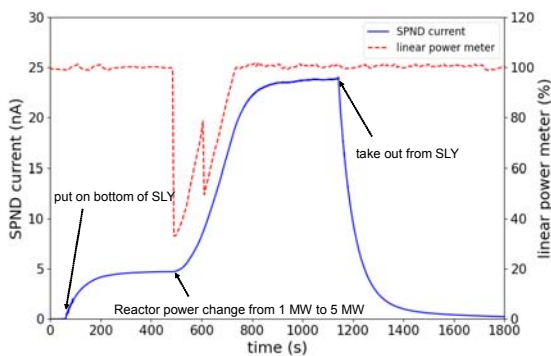


Fig. 1 Plot of SPND measured current and linear power meter ratio via time.

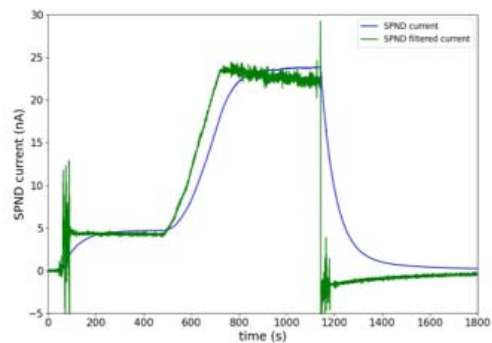


Fig. 3 Comparison between the raw SPND current and the filtered one.

CO4-1 Characterization of Additive Aggregation in Lubricant using Small-Angle X-ray Scattering

Y. Oba, M. Hino¹, R. Motokawa, N. Adachi², Y. Todaka², R. Inoue¹, and M. Sugiyama¹

Materials Sciences Research Center, Japan Atomic Energy Agency

¹Institute for Integrated Radiation and Nuclear Science, Kyoto University

²Department of Mechanical Engineering, Graduate School of Engineering, Toyohashi University of Technology

INTRODUCTION: In lubricants, nanostructures of additives are closely related to their lubrication properties. Although small-angle scattering is a promising means to characterize such nanostructures [1,2], it is not commonly used in the field of tribology. While small-angle neutron scattering (SANS) has been conducted in those previous studies, we have recently examined the application of small-angle X-ray scattering (SAXS) to the characterization of the additives in the lubricants [3]. The results show that SAXS is useful for the observation of the additives. While SANS can precisely analyze the nanostructures using contrast matching and variation techniques with deuterated samples, SAXS can provide easy access to experiments. However, a part of samples shows very weak scattering. Therefore, in this study, denser samples are measured to discuss the detail of the nanostructures of the additives.

EXPERIMENTS: SAXS measurements were performed using the in-house SAXS instrument with Mo $K\alpha$ radiation. Scattering patterns were obtained using a two-dimensional detector (PILATUS 100k) equipped with a 1000 μm -thick silicon sensor. The path of X-ray between the entrance slit and up to the detector including the sample area was in vacuum to eliminate background scattering from air and vacuum windows. Oleic acid (OA) and oleyl acid phosphate (OLAP) were chosen as the additive and poly- α -olefin (PAO) as base oil. In our previous study, we measured 5 mass% OA and 1 mass% OLAP dispersed in PAO [3]. In the current study, 20 mass% OA and 10 mass% OLAP in PAO were measured. The samples were sealed in sample cells with the optical path length of 10 mm. Two samples-to-detector distances (SDD), 0.4 and 1.8 m, were used to cover wide q range, where q is the magnitude of the scattering vector. The measurement times are 1 hour and 5 hours for 0.4 m and 1.8 m conditions, respectively.

RESULTS: Fig. 1 shows the SAXS profiles of 20 mass% OA in PAO, 10 mass% OLAP in PAO, and pure PAO. Based on our previous report [3], a peak at around $q = 4.5 \text{ nm}^{-1}$ reflects the nanostructures in PAO. Both OA and OLAP show additional scattering compared to PAO. Therefore, we successfully observe the nanostructures of these additives using SAXS. Compared to our previous

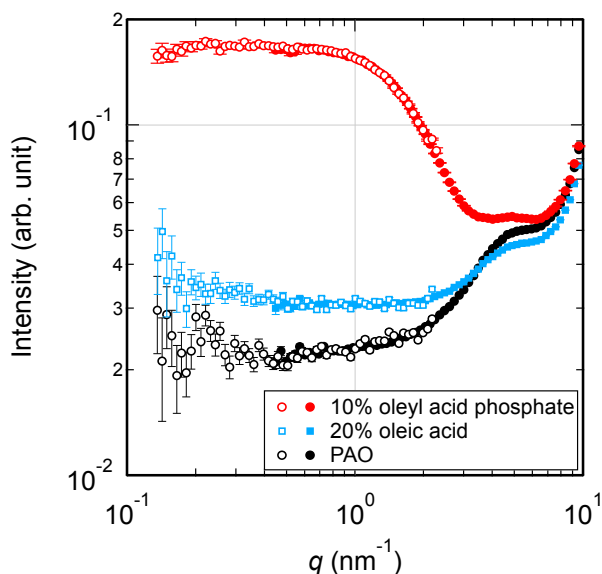


Fig. 1. SAXS profiles of 20 mass% OA in PAO, 10 mass% OLAP in PAO, and pure PAO. Open and filled symbols indicate the profiles obtained using SDD = 1.8 and 0.4 m, respectively.

study, OA indicates significant scattering. This is attributed to the denser concentration of 20 mass%. In the q range higher than 3.4 nm^{-1} , the scattering intensity of PAO exceeds that of 20 mass% OA in PAO. This is probably due to the partial specific volume of OA.

Fig. 1 also shows that the SAXS profile of 10 mass% OLAP has a significant shoulder in the q range lower than about 2.5 nm^{-1} . This feature corresponds to the gyration radius of about 0.7–0.8 nm and larger than the size of a single OLAP molecule [4]. Hence, OLAP probably forms aggregate in PAO.

These result will promote further development of advanced lubricants in conjunction with the nanostructural characterization by SAXS.

ACKNOWLEDGMENTS: A part of this work was supported by JST "Collaborative Research Based on Industrial Demand" Grand Number JPMJSK1511, Japan.

REFERENCES:

- [1] M. J. Covitch *et al.*, Adv. Chem. Eng. Sci., **5** (2015) 134-151.
- [2] M. T. Savoji *et al.*, Ind. Eng. Chem. Res., **57** (2018) 1840-1850.
- [3] Y. Oba *et al.*, KURNS Progress report 2019, (2020) 148.
- [4] Y. Oba *et al.*, Chem. Lett. **49**, (2020) 823.

CO4-2 Radiation Tolerance of SiC p+n Junction-Diodes for Beam Monitor Applications

T. Kishishita, M. Hagiwara¹, M. M. Tanaka, H. Yashima², R. Kosugi³

High Energy Accelerator Research Organization, KEK
¹National Institutes for Quantum Science and Technology

²Institute for Integrated Radiation and Nuclear Science, Kyoto University

³National Institute of Advanced Industrial Science and Technology

INTRODUCTION: Silicon carbide (SiC) has been considered as a potential alternative to Si for the manufacture of dosimeters, spectrometers, and charge particle detectors in high energy physics experiments, by virtue of its operation capability in strong radiation and/or high-temperature environments. To take advantage of such properties for future radiation detectors with a comparable size of silicon, we firstly investigated the influence of the bulk defects on the radiation sensor characteristics, by irradiating neutrons at Institute for Integrated Radiation and Nuclear Science, Kyoto University.

EXPERIMENTS: The reverse blocking characteristics is a primary concern of the radiation effects. The radiation-induced effects are generally divided into bulk and surface defects. The formers are caused by the displacement of crystal atoms, introducing to the increase of the leakage current and degraded reverse blocking characteristics. The latter include all effects in the covering dielectrics and the interface region. Since the bulk damage caused by the elastic nuclear scattering of the lattice nuclei has a profound effect in our device, we irradiated neutrons to pixelized diodes under unbiased conditions. The irradiation test was conducted by putting the samples at the Kyoto University nuclear reactor core. After disassembling of the samples, we carried out measurements of the leakage current and compared with those of the pre-irradiation samples.

RESULTS: The typical I-V characteristics before irradiation are shown in Figure 1. The leakage current shows a device-to-device dependence and are distributed between 1~8 nA at a reverse bias of 1 kV (corresponding to leakage current density of 10~83 nA/cm²). The fundamental reason of the distribution is beyond comprehension, however, the bulk defects in the crystal are the natural interpretation. Figure 2 shows the typical leakage currents after irradiation. Compared with Fig. 1, the bulk leakage current in reverse bias is not increased after neutron irradiation of 1.63×10^{13} n_{eq}/cm² fluence, except the pixel-to-pixel dependence and data fluctuation due to the different sampling time settings. The reverse blocking property was also retained up to 3 kV. Irradiation tests at higher fluences are severe with the current device struc-

ture due to the radioactivation of the metals. We note that the 1 MeV neutrons have the same efficiency in the detector degradation as 24 GeV protons at a comparable neutron equivalent fluence. The theoretical nonionizing energy loss (NIEL) calculation performed on SiC can be found in Lee et al. [1]. The primary radiation defects produced by single particles (protons and pions) or gamma-rays were not evaluated in this measurement, however, the number of primary defects is reported as low as that of diamond. Thus, we conclude that the bulk defects introduced by irradiation at the 10^{13} neutron equivalent fluence is ignorable, in agreement with the previous studies on neutron-irradiated pn devices [2, 3].

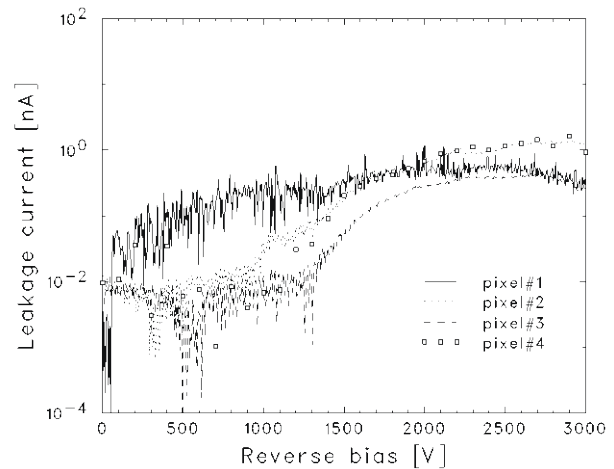


Fig. 1. Typical reverse blocking characteristics of the fabricated pixel diodes.

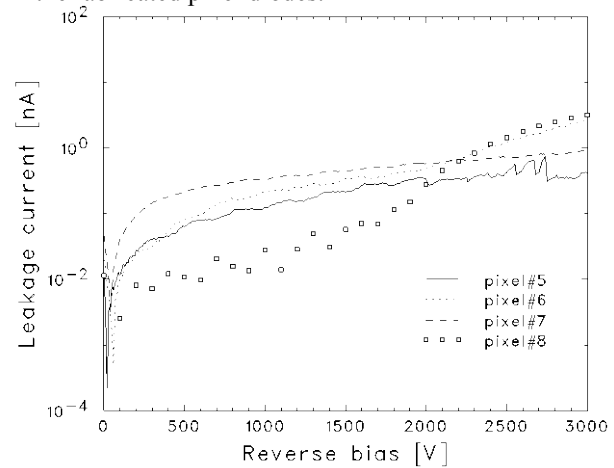


Fig. 2. Typical reverse blocking characteristics after 1 MeV neutron irradiation of 1.63×10^{13} n_{eq}/cm².

REFERENCES:

- [1] K. K. Lee *et al.*, Nucl. Instrum. Methods Phys. Res. B, vol.210, pp.489-494, 2003.
- [2] F. Moscatelli *et al.*, IEEE Trans. Nucl. Sci., vol.53, pp.1557--1563, 2006.
- [3] J. M. Rafi *et al.*, IEEE Trans. Nucl. Sci., vol.67, pp.2481--2489, 2020.

CO4-3 TDPAC Spectra of the $^{111}\text{Cd}(\leftarrow^{111\text{m}}\text{Cd})$ and $^{117}\text{In}(\leftarrow^{117}\text{Cd})$ Probes in CdIn_2O_4

W. Sato, S. Komatsuda¹, A. Taniguchi², M. Tanigaki², and Y. Ohkubo²

Institute of Science and Engineering, Kanazawa University

¹*Institute of Human and Social Sciences, Kanazawa University*

²*Institute for Integrated Radiation and Nuclear Science, Kyoto University*

INTRODUCTION: Ternary spinel oxides exhibit various physical properties depending on the constituent metal elements and on their distribution between the tetrahedral A site and octahedral B site. Among various metal elements, it is known that Cd^{2+} is likely to occupy the A site forming normal spinel with divalent ions and trivalent ions on the A and B sites, respectively. In our recent time-differential perturbed angular correlation (TDPAC) experiments on Cd spinel compounds such as CdFe_2O_4 and CdIn_2O_4 , we noticed unexpected phenomenon that the directional anisotropy of the cascade γ rays emitted from the $^{111}\text{Cd}(\leftarrow^{111\text{m}}\text{Cd})$ probe shows exponential-like relaxation as if the nuclear spin would experience dynamic perturbation from the extranuclear field [1,2]. If the attenuation of the anisotropy arises from dynamic perturbation, we can expect temperature dependence of the relaxation constant λ as in the following expression of the time-differential perturbation factor $G_{22}(t)$ as a function of the time interval t between the cascade γ -ray emission:

$$G_{22}(t) = \exp(-\lambda t). \quad (1)$$

In order to provide insight into the phenomenon, we have obtained high temperature TDPAC spectra for CdIn_2O_4 , using two different probes $^{111}\text{Cd}(\leftarrow^{111\text{m}}\text{Cd})$ and $^{117}\text{In}(\leftarrow^{117}\text{Cd})$. Here, a preliminary result is reported.

EXPERIMENTS: Neutron irradiation was performed for cadmium oxide (CdO) enriched with ^{110}Cd and ^{116}Cd in Kyoto University Reactor to produce radioactive $^{111\text{m}}\text{Cd}$ and ^{117}Cd , respectively, by neutron capture reactions. Each of the radioactive $\text{Cd}(^{111\text{m}}\text{Cd})\text{O}$ and $\text{Cd}(^{117}\text{Cd})\text{O}$ powders was separately mixed well with stoichiometric amounts of CdO and In_2O_3 in an agate mortar. The mixtures were then pressed into disks and sintered in air at 1373 K for 45 min.

TDPAC measurements were carried out for the $^{111}\text{Cd}(\leftarrow^{111\text{m}}\text{Cd})$ and $^{117}\text{In}(\leftarrow^{117}\text{Cd})$ probes with the intermediate states of $I = 5/2$ and $3/2$ having half-lives of 85.0 and 54.6 ns, respectively. In the present work, we obtained the perturbed angular correlation as a function of the time interval of the cascade γ -ray emissions by the following expression:

$$A_{22}G_{22}(t) = \frac{2[N(\pi, t) - N(\pi/2, t)]}{N(\pi, t) + 2N(\pi/2, t)}, \quad (2)$$

where A_{22} denotes the angular correlation coefficient and $N(\theta, t)$ stands for the number of the delayed coincidence events observed at an angle θ . The measurements were performed at 973 K.

RESULTS: The TDPAC spectra of $^{111}\text{Cd}(\leftarrow^{111\text{m}}\text{Cd})$ and $^{117}\text{In}(\leftarrow^{117}\text{Cd})$ in CdIn_2O_4 are shown in Fig. 1. The spectrum of $^{111}\text{Cd}(\leftarrow^{111\text{m}}\text{Cd})$ (Fig. 1(a)) exhibits a relaxing trend in the directional anisotropy, which is similar to the spectra observed at room temperature and 77 K [1]. However, the relaxation time seems a little longer for the present spectrum. This slight temperature dependence may suggest that the motion of charges surrounding the probe is thermally activated at the present high temperature. The spectrum of $^{117}\text{In}(\leftarrow^{117}\text{Cd})$ also shows gradual attenuation of the directional anisotropy. It should be noted that the probe nuclei having interaction with the extranuclear fields are of different elements, Cd and In. Thus, the present observation demonstrates that the probes of different elements are perturbed in the same way and show similar spectral patterns. In order to clarify the cause of the spectral attenuation, detailed temperature dependence needs to be investigated.

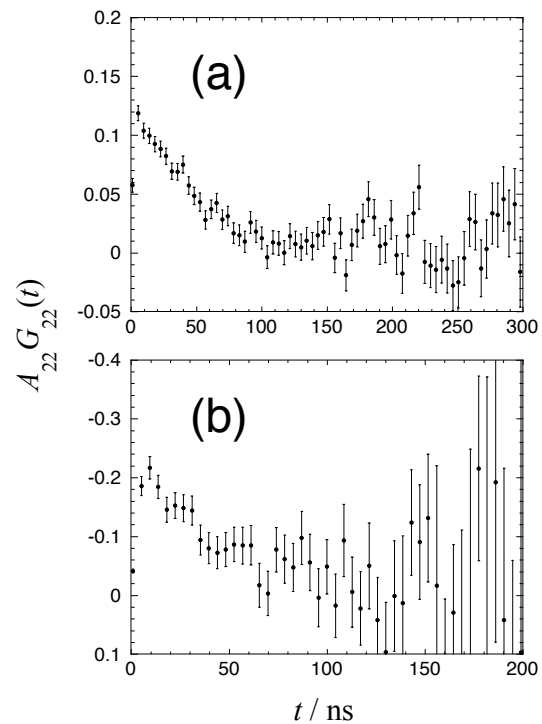


Fig. 1. TDPAC spectra (a) of $^{111}\text{Cd}(\leftarrow^{111\text{m}}\text{Cd})$ and (b) of $^{117}\text{In}(\leftarrow^{117}\text{Cd})$ in CdIn_2O_4 measured at 973 K.

REFERENCES:

- [1] W. Sato *et al.*, J. Radioanal. Nucl. Chem., **316** (2018) 1289-1293.
- [2] W. Sato *et al.*, KURNS Prog. Rep., **2020** (2021) 113.

CO4-4 Synthesis of metal nanocomplexes in water solution by γ -ray and electron irradiation reduction

F. Hori, K. Zhu, T. Yamada, T. Matsui¹, N. Taguchi², S. Tanaka² and Q. Xu³

Dept. of Engineering, Osaka Prefecture University

¹Center for Advanced Education of Entrepreneurship and Innovation, Osaka Prefecture University

²AIST, Kansai Center

³KURNS

INTRODUCTION: It is known that metal nanoparticles (NPs) have some specific properties, which are not appeared in bulk materials such as catalytic activities, magnetic properties, electric conductivity and light absorption. These properties depend on its size, shape, structure, chemical composition and so on. In general, metal nanoparticles can be produced by various top-down and bottom-up methods. Above all, chemically synthesizing as bottom-up method can control the size and shape of it. However, it is not easy to fabricate multi elemental alloy NPs controlling with their structure. Almost fabrication method of NPs with commercially is based on equilibrium chemical reaction in ionic solution with reduction additive. We have been studying to synthesize various metal NPs by non-equilibrium reaction method that is reduction reactions induced by ultrasonic, solution plasma, electron beam, ion beam and gamma-ray irradiation into aqueous solution [1]. Recently, by using this radiation reduction method, we have been trying to synthesize metal nanocomposites. In this study, we have studied the fine structure of nanoparticles synthesized by electron and gamma-ray irradiation reduction in water solutions including multiple metal ions.

EXPERIMENTS:

Aqueous solutions with various ternary combination of a given concentration of metal complexes ((CH₃COO)₂Cu·H₂O), AgNO₃, NiCl, Na[AuCl₄] and PdCl₂NaCl₃H₂O with an additive of polyvinyl (PVP) and 8.5 vol% ethylene glycol were prepared. The ratio of all ions concentration was adjusted to the ratio of 0.5 to 2.0 in the solution. The solution was argon gas purged and sealed into polystyrene vessels. They were irradiated at about 300 K with 1.17 and 1.33 MeV gamma-rays from ⁶⁰Co radio active source at gamma irradiation facility in KURRI, Kyoto University. The total dose was fixed to 10 kGy with the dose rate of 1.0 kGy/h. Also, same solutions were irradiated 8 MeV electron with total dose of 10kGy in about 60 sec by linear accelerator at same facility. After irradiation, the samples were measured for UV-vis absorption spectra. The structures for all colloidal products were examined by X-ray absorption fine structure (EXAFS) and X-ray photoelectron spectroscopy (XPS) at

KEK-PF BL-27, X-ray diffraction and transmission electron microscope.

RESULTS:

Fig. 1 shows the TEM image of nanoparticles synthesized by electron and gamma-ray irradiation reduction methods in the solution including Ag, Au, Cu and Ni ions. As is seen in these figures, the size of nanoparticles are clearly different. This is because the higher reduction rate of electron irradiation than that of gamma-ray irradiation. This result is in good agreement with the result of correlation of particle size produced by irradiation with different irradiation reduction rates [2].

Fig. 2 shows the EXAFS spectra of synthesized nanoparticles in a AgAuCu ternary solution after electron and gamma-ray irradiation reduction. In case of electron irradiation, only one peak appeared but double peaks appeared in case of gamma-ray irradiation. These peaks originated from Cu-O and Cu-Cu metal combinations mainly. It found that the main products are Cu-oxide in case of electron irradiation, and Cu-metal alloy nanocomposites in case of gamma-ray irradiation.

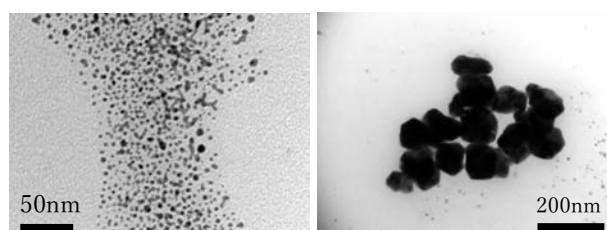


Fig. 1. TEM images of products in a Ag, Au and Cu ions solution synthesized by (a) electron irradiation and (b) gamma-ray irradiation.

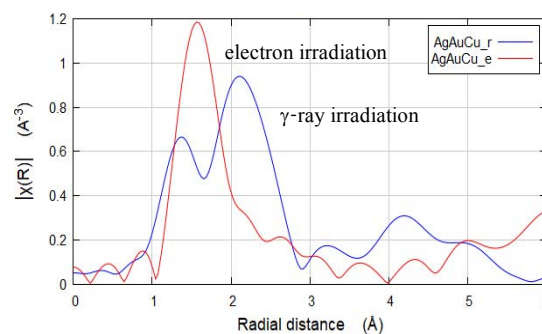


Fig. 2 EXAFS spectra of electron and gamma-ray irradiation reduction solutions including Ag, Au and Cu Au ions.

REFERENCE:

- [1] N. Taguchi *et al.*, Rad. Phys. Chem. 78, (2009) 1049-1053.
- [2] N. Maeda *et al.*, Mater. Res. Soc. Symp. Proc. Vol. 900E.

CO4-5 Hydrogen trapping behavior at vacancy in Fe-Al alloy with electron irradiation

F. Hori, H. Otomo, H. Obayashi, Y. Morikuni, K. Ohsawa¹,
Q. Xu², N. Abe², A. Iwase³ and K. Yasunaga³

Dept. of Quantum & Radiation Eng., Osaka Pref. Univ.

¹*Res. Inst. of Appl. Mech., Kyushu University*

²*KURNS*

³*Wakasa-wan Energy Research Center*

INTRODUCTION: Intermetallic compounds have good properties such as specific strength to weight ratio, oxidation resistance and strength in elevated temperature. In addition, some of them can be applied for hydrogen storage material by production of hydride such as Mg and Ni based compound alloys. On the other hand, it found that hydrogen absorption properties in some compound alloys. It is reported that novel Ni- based alloy including defect type free volume can be used as hydrogen permeation membranes to separate H₂ from CO₂ and other gases obtained from water. Also, first principle calculation result shows that not only one hydrogen atom but some number of hydrogen atoms possibly be trapped by a single vacancy in B2 ordered Fe-Al alloy. However, the interaction between vacancy and hydrogen atom in this type of Fe-Al alloy is not cleared yet. So far, we have been studied defects behavior introduced by various energetic electron and ions irradiation. In this study, we have studied the interaction between hydrogen atom and non-equilibrium vacancies introduced by electron irradiation.

EXPERIMENTS: B2 ordered Fe-Al alloys were prepared by arc melting method in argon gas atmosphere. Sliced samples with the thickness of 0.5 mm were annealed at 1273 K for 20 h and cool down to 973 K slowly and then quenched into water. These specimens were irradiated with 8 MeV electron up to the fluence of 4×10^{18} /cm² at KURRI, Kyoto University. Irradiation was carried out at about 330 K with temperature controlling water cool system. Hydrogen was introduced for unirradiated and electron irradiated samples at 0.1 mA/cm² in a NH₄SCN solution bath added 0.001 mol/L H₂SO₄ by electro chemical method for 8 hours. These samples were examined by X-ray diffraction (XRD). Also, the thermal desorption spectroscopy (TDS) was measured with heating rate of 1 K/s.

RESULTS: Figure 1 shows the X-ray diffraction spectra of Fe-Al alloy before, after electron irradiation and hydrogen charged after irradiation. The movement of the Bragg peak of (211) plane to a slightly higher angle is considered to be due to the formation of point defects by electron irradiation. But this peak shift recovered after hydrogen introduction. This is considered to be due to hydrogen trapping at vacancy site. Figure 2 shows the TDS spectra for hydrogen introduced Fe-Al alloys with and without electron irradiation. This figure clearly shows that the amount of absorbed hydrogen after electron irradiation is larger than that without irradiation. In addition, a sharp peak appears at 650 K, which indicates the dissociation temperature of hydrogen atoms from the pores introduced by electron irradiation.

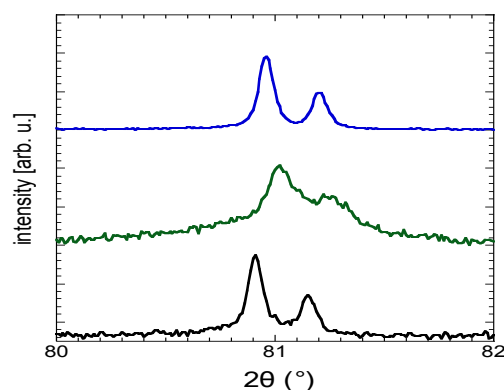


Fig. 1 XRD profiles of Fe-Al alloy before irradiation, after electron irradiation and hydrogen introduced after irradiation.

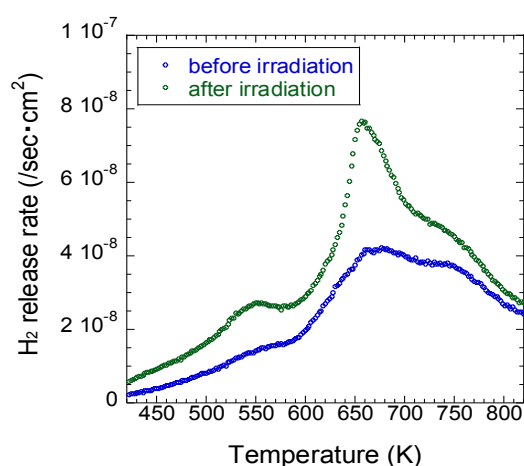


Fig. 2 TDS spectrum of hydrogen introduced into electron-irradiated and unirradiated Fe-Al alloy samples.

CO4-6 Study of resonant frequency change with irradiation dose of piezoelectric PZT element

M. Kobayashi, T. Miyachi, S. Takechi¹, Reo Kunimatsu¹, Ryo Sasaki¹, Masaya Danjohbara¹ and Haruki Oh'ishi¹

Planetary Exploration Research Center, Chiba Institute of Technology

¹*Graduate School of Engineering, Osaka City University*

INTRODUCTION: This study aims to establish an inexpensive method for dosimetry in high-dose environments. We consider changes in piezoelectric properties of piezoelectric elements due to irradiation for dosimetry in high-dose environments. For this purpose, the mechanism of radiation-induced change of piezoelectric properties has been investigated.

In a previous experiment conducted at NIRS/HIMAC, piezoelectric PZT elements were irradiated with 400 MeV/n Xe particles, and the decrease in the electromechanical coupling coefficient k was investigated [1]. As a result, it was found that k_r of the irradiated PZT element was $-0.35\%/kJ$, which is a phenomenon concerning the irradiation dose. In order to investigate what happens to piezoelectric elements due to irradiation, electron beam irradiation experiments have been conducted at KUR/LINAC. The effect of temperature, which was negligible in the Xe particle experiments, has been investigated and controlled in the experiments at KUR/LINAC.

EXPERIMENTS IN THE FISCAL YEAR 2021: The geometry of the PZT element that has been irradiated so far was changed from a cylindrical shape of $\phi 18 \text{ mm} \times t12 \text{ mm}$ to a disk shape of $\phi 18 \text{ mm} \times t1 \text{ mm}$. This shape satisfies the conditions of the approximate formula for determining k , and the evaluation of k value as an absolute value can now be performed instead of the evaluation of relative changes. Furthermore, the thickness of the electron-beam irradiation target was made thinner, which reduced the number of neutrons produced and thus met the objective of this experiment, which was to investigate the contribution of electron beams alone. The thinner target also improves the air-cooling effect during irradiation, and the temperature can be suppressed to a moderate value ($\leq 90^\circ\text{C}$) even with an electron dose of $4.8 \mu\text{A}$, whereas the irradiation current is about $1 \mu\text{A}$ for the conventional device, thus shortening the irradiation time from half a day to about one hour. This enabled us to shorten the irradiation time from half a day to about one hour, thereby improving the efficiency of the experiment.

In addition to such experimental setup, experiments were conducted to investigate the difference in response to electron irradiation between different types of PZT elements (soft PZT, high-temperature soft PZT, and high-temperature hard PZT), which are the specimens. The difference between the "soft" and "hard" materials is simply that the "soft" material is more or less distorted when a voltage is applied to it. The "high-temperature" materials are those that have a high Curie temperature at which they are completely depolarized. Table 1 summarizes the percentage change in k after electron irradiation

of each PZT. This is a summary of the experimental results using four samples for the soft material, three samples for the high-temperature soft material, and three samples for the high-temperature hard material. The k_t in the thickness direction of the high-temperature soft material is not shown due to measurement problems.

DISCUSSION: The mechanism of radiation-induced degradation on piezoelectric PZT element was discussed. However, the effect of depolarization caused by temperature rise due to irradiation is excluded. Radiation-induced degradation includes (1) migration of atoms in crystals, (2) conversion to other nuclides by nuclear reactions, (3) acceleration of chemical reactions such as cross-linking or oxidation (mainly in polymer materials), and (4) dielectric breakdown due to charge accumulation generated by ionizing effects (mainly in semiconductors). The change in the properties of PZT due to electron irradiation is considered to be dominated by (4). Analysis of gamma-ray spectra immediately after irradiation shows that the number of activated atoms is limited. It is noteworthy that k is larger in the high-temperature hard material. At first glance, this appears to be an increase in piezoelectricity, but it may be that the destruction of the domain walls inside the piezoelectric ceramics "softens" the entire element and increases electromechanical coupling coefficient k . In this case, the domain walls would be ionized by radiation. In this case, the domain walls may have been destroyed by the electric charge accumulated by ionization due to radiation. We would like to investigate this further in the future.

Table 1. Variation rate of coupling coefficient k per unit absorbed dose.

PZT type	$\Delta k_r [\%/kJ]$	$\Delta k_t [\%/kJ]$
Soft	-0.090 ± 0.013	-0.10 ± 0.059
High temp. soft	-0.087 ± 0.038	---
High temp. hard	$+0.13 \pm 0.081$	-0.050 ± 0.0061

REFERENCES:

- [1] S. Takechi *et al.*, Japanese Journal of Applied Physics 60 038003 (2021).
- [2] M. Kobayashi *et al.*, Japanese Journal of Applied Physics 53, 066602 (2014).
- [3] M. Kobayashi *et al.*, Japanese Journal of Applied Physics 52, 126604 (2013).

CO4-7 Concentration Dependence of Local Structures at Cd Sites in $\text{Cd}_x\text{Sr}_{1-x}\text{TiO}_3$ Studied by TDPAC Method

S. Komatsuda, W. Sato¹, A. Taniguchi², M. Tanigaki², and Y. Ohkubo²

Institute of Human and Social Sciences, Kanazawa University

¹*Institute of Science and Engineering, Kanazawa University*

²*Institute for Integrated Radiation and Nuclear Science, Kyoto University*

INTRODUCTION: Strontium titanate (SrTiO_3) is a cubic perovskite compound of ABO_3 type. Among ABO_3 perovskites, SrTiO_3 has a wide band gap values of 3.2 eV, and doping effect of SrTiO_3 -based materials is attracting much attention. It is known from many previous reports that chemical and physical properties of SrTiO_3 change depending on the kind of dopant ions and the surrounding local structures[1]. For a practical use of SrTiO_3 , it is necessary to obtain more microscopic information on various impurity sites. Therefore, we applied the time-differential perturbed angular correlation (TDPAC) method to study the local structures at impurity sites in SrTiO_3 . In our previous TDPAC study of SrTiO_3 doped with the $^{111}\text{Cd}(\leftarrow^{111}\text{In})$ probe, it is suggested that In dopants replace Sr^{2+} and Ti^{4+} in the lattice sites where defect exists in the vicinity of the probes. In order to obtain further information on the local fields at various impurity sites, we have thus performed TDPAC measurements for SrTiO_3 with $^{111}\text{Cd}(\leftarrow^{111m}\text{Cd})$ probe, the same probe, but descended from a different parent nucleus. In order to uniformly introduce $^{111}\text{Cd}(\leftarrow^{111m}\text{Cd})$ probe in SrTiO_3 , we first studied local structure of the $^{111}\text{Cd}(\leftarrow^{111m}\text{Cd})$ in $\text{Cd}_x\text{Sr}_{1-x}\text{TiO}_3$ at various Cd concentration. We here report part of the result of TDPAC measurements for the $^{111}\text{Cd}(\leftarrow^{111m}\text{Cd})$ in $\text{Cd}_x\text{Sr}_{1-x}\text{TiO}_3$

EXPERIMENTS: Stoichiometric amount of SrCO_3 , CdCO_3 , and TiO_2 powders were mixed in the mortar. The powders were pressed into disks. For TDPAC measurements, about 3 mg of CdO enriched with ^{110}Cd was irradiated with thermal neutrons in Kyoto University Research Reactor, and radioactive ^{111m}Cd was generated by $^{110}\text{Cd}(n, \gamma)^{111m}\text{Cd}$ reaction. The neutron-irradiated CdO powder was dissolved in 6M HCl and added in droplets onto the pre-sintered $\text{Cd}_x\text{Sr}_{1-x}\text{TiO}_3$ disk. The disk was sintered in air at 1373 K for 90 min. The TDPAC measurement was carried out for the 151-245 keV cascade γ rays of $^{111}\text{Cd}(\leftarrow^{111m}\text{Cd})$ probe with the intermediate state of $I = 5/2$ having a half-life of 85.0 ns.

RESULTS: Figure 1 shows the TDPAC spectra of $^{111}\text{Cd}(\leftarrow^{111m}\text{Cd})$ (a) in $\text{Cd}_x\text{Sr}_{1-x}\text{TiO}_3$ ($x = 0.04$) and (b) in $\text{Cd}_x\text{Sr}_{1-x}\text{TiO}_3$ ($x = 0.06$) at room temperature. The directional anisotropy on the ordinate, $A_{22}G_{22}(t)$, was deduced with the following simple operation for delayed coincidence events of the cascade:

$$A_{22}G_{22}(t) = \frac{2[N(\pi, t) - N(\pi/2, t)]}{N(\pi, t) + 2N(\pi/2, t)} \quad (1)$$

Here, A_{22} denotes the angular correlation coefficient, $G_{22}(t)$ the time-differential perturbation factor as a function of the time interval, t , between the relevant cascade γ ray emissions, and $N(\theta, t)$ the number of the coincidence events observed at angle, θ . With respect to Fig. 1(a), the spectral pattern is damped. Because the dynamic perturbation should not be considered in a TDPAC measurement at room temperature, the spectral pattern was fitted with two static electric quadrupole frequencies which have large distribution widths ($\delta = 27(7)\%$, $82(12)\%$). These large values of distribution widths indicate local randomness at $^{111}\text{Cd}(\leftarrow^{111m}\text{Cd})$ probe sites in $\text{Cd}_x\text{Sr}_{1-x}\text{TiO}_3$. On the other hand, the spectrum in Fig. 1(b) can be reproduced by a fit with three unique quadrupole frequencies, which suggests that $^{111}\text{Cd}(\leftarrow^{111m}\text{Cd})$ probes occupied three specific lattice sites in $\text{Cd}_x\text{Sr}_{1-x}\text{TiO}_3$. These experimental results show that Cd ions dispersed into $\text{Cd}_x\text{Sr}_{1-x}\text{TiO}_3$ perovskite structure at atomic scale by increase of Cd ratio from $x = 0.04$ to $x = 0.06$. This concentration dependence of local structure at Cd site might be attributed to the change of lattice constant of $\text{Cd}_x\text{Sr}_{1-x}\text{TiO}_3$. For more information on this concentration dependence, investigations of lattice constants of $\text{Cd}_x\text{Sr}_{1-x}\text{TiO}_3$ perovskite are now in progress.

REFERENCE:

[1] C. M. Culbertson *et al.*, *Scientific Reports* **10** (2020) (3729(1)-3729(10)).

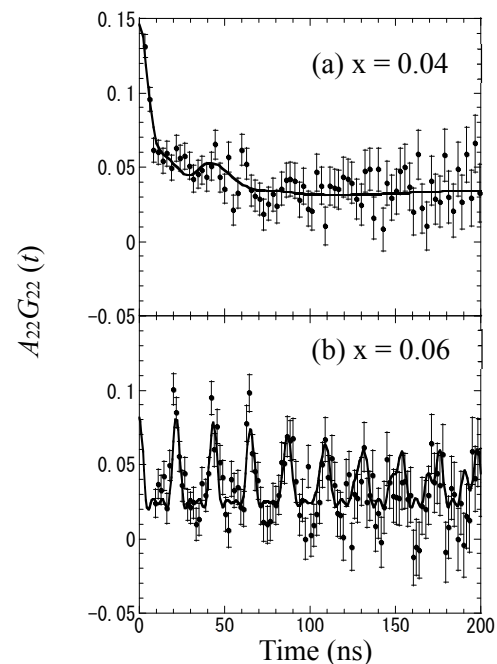


Fig. 1. TDPAC spectra of $^{111}\text{Cd}(\leftarrow^{111m}\text{Cd})$ (a) in $\text{Cd}_x\text{Sr}_{1-x}\text{TiO}_3$ ($x = 0.04$) and (b) in $\text{Cd}_x\text{Sr}_{1-x}\text{TiO}_3$ ($x = 0.06$) at room temperature.

CO4-8 Operation of Field Emission Image Sensor under Gamma-ray Irradiation

Y. Gotoh, Y. Neo¹, K. L. Zheng¹, M. Nagao², T. Okamoto³, N. Sato⁴

Graduate School of Engineering, Kyoto University

¹*Institute of Electronics, Shizuoka University*

²*National Institute of Advanced Industrial Science and Technology*

³*National Institute of Technology, Kisarazu College*

⁴*Institute for Integrated Radiation and Nuclear Science, Kyoto University*

INTRODUCTION: In decommissioning of Fukushima Daiichi Nuclear Power Plant, radiation tolerant image sensors are strongly demanded. We have been developing a vacuum-based image sensor, which is consisted of a matrix type field emitter array (FEA), a mesh electrode and a photoconductor film (field emission image sensor) [1]. The image sensor detected light signal even after the gamma-ray irradiation to the dose of 1 MGy. Operation of field emitters under gamma-ray irradiation was demonstrated and no significant change of the properties due to gamma-ray irradiation could not be detected [2]. However, imaging characteristics under gamma-ray irradiation has not yet been confirmed. In this study, variation of the photo-signal detection properties with and without gamma-ray irradiation was investigated.

EXPERIMENTS: The FEA used in the present study was fabricated at National Institute of Advanced Industrial Science and Technology [3], and possessed 1,024 hafnium carbide emitters. It should be stressed here that the FEA was not a matrix-type. Cadmium telluride/cadmium sulfide photo diode, which was originally developed as a solar cell was used as an anode (photoconductor) [4]. Antimony sulfide thin film was formed on the surface of the photoconductor. The FEA, mesh electrode and anode were installed in a vacuum vessel which was evacuated by a non-evaporable getter pump. Gamma-ray irradiation was performed at Cobalt-60 Gamma-ray Irradiation Facility, Institute for Integrated Radiation and Nuclear Science, Kyoto University. The vacuum vessel was settled in the irradiation room at the position 30 cm away from the gamma-ray source. An electric light was also settled in the irradiation room to illuminate the image sensor. The emitter was grounded and the gate was positively biased to extract the electrons. The mesh and the anode were also positively biased, typically 120 V and 10 V, respectively. After several measurements of anode current-gate voltage characteristics, operation of the image sensor was conducted. Giving a fixed voltage to the gate, the variation of the anode current was observed with and without light illumination under gamma-ray irradiation.

RESULTS: Figure 1 shows the variation of the anode current under gamma-ray irradiation. The estimated dose rate of irradiation was about 220 Gy h⁻¹, which is higher than that of irradiation observed in the primary contain-

ment vessel of Fukushima Daiichi Nuclear Power Plant [5]. The electric light was turned on and off every 10 seconds to confirm the capability of photo-signal detection. As is shown in Fig. 1, the anode current showed a step like variation, of which interval corresponded to the interval of the light illumination. From this figure, it is shown that the present device could detect photo-signal even under high dose rate gamma-ray irradiation. The intensity of illumination could not be evaluated in this study, so measurements with known intensity of illumination is necessary to estimate the property of the image sensor. Small signal would be attributed to the poor adjustment of the operating conditions of the image sensor. Deterioration of the antimony sulfide layer would be another reason. The device configuration was not fully optimized in the present study. Therefore, improvement of the device performance can be expected, optimizing the operating condition and device configuration.

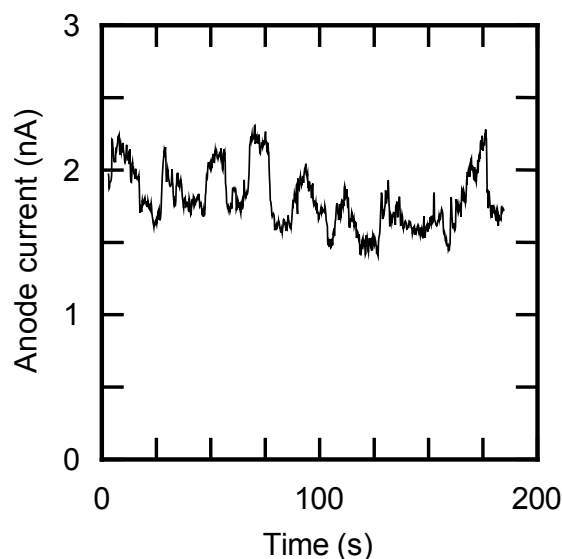


Figure 1. Variation of the anode current with and without light illumination under the gamma-ray irradiation.

REFERENCES:

- [1] Y. Gotoh *et al.*, IEEE Trans. ED **67** (2020) 1660-1665.
- [2] Y. Gotoh *et al.*, KURRI Progress Report 2018 (2018) CO4-3.
- [3] T. Sato *et al.*, J. Vac. Sci. Technol. B **21** (2003) 1589-1593.
- [4] T. Okamoto *et al.*, Jpn. J. Appl. Phys. **60** (2021) SBBF02.
- [5] Fukushima Daiichi Nuclear Power Plant, Investigation Results Inside Unit 2 PCV. Accessed: April 22, 2022. [Online]. Available: <https://www.meti.go.jp/earthquake/nuclear/decommissioning/committee/osensuitaisakuteam/2019/02/3-3-3.pdf>.

CO4-9 Radiochemical Research for the Advancement of $^{99}\text{Mo}/^{99\text{m}}\text{Tc}$ Generator by (n, γ) Method (4)

Y. Fujita, M. Seki, M. C. Ngo¹, T. M. D. Do¹, X. Hu¹,
Y. Yang¹, T. Takeuchi, H. Nakano, Y. Fujihara²,
H. Yoshinaga², K. Nishikata, T. Omori, J. Hori²,
T. Suzuki¹, H. Suematsu¹ and H. Ide

Department of JMTR, Japan Atomic Energy Agency

¹Graduate School of Engineering, Nagaoka University of
Technology

²Institute for Integrated Radiation and Nuclear Science,
Kyoto University

INTRODUCTION: The research and development (R&D) has been carried out to produce Molybdenum-99 (^{99}Mo) by the neutron activation method ((n, γ) method) from viewpoints such as nuclear security. In order to apply the (n, γ) method to the $^{99}\text{Mo}/^{99\text{m}}\text{Tc}$ generator, it is necessary to improve the properties of Alumina (Al_2O_3) used as Mo adsorbent. To date, we have evaluated the quality of the $^{99\text{m}}\text{Tc}$ solution obtained from the column packed with the developed Al_2O_3 specimens. However, the problem was that ^{99}Mo was desorbed in the solution[1]. In this work, we evaluated the quality of the $^{99\text{m}}\text{Tc}$ solution obtained by taking measures to reduce the desorption of ^{99}Mo . The measures are (1) application of dynamic adsorption, (2) increasing the concentration of the sodium molybdate solution (Mo solution), (3) reducing the amount of Mo added, (4) acid treatment of the alumina specimens, and (5) sufficient washing of the alumina specimens.

EXPERIMENTS: MoO_3 pellet pieces irradiated with Pn-2 were dissolved with 6M-NaOH aq. The Mo concentration of the solution was adjusted to about 330 g/L, and the pH was adjusted to 2 - 3 by adding concentrated hydrochloric acid. Four types of alumina specimen (D-201-300, V-V-300, V-B-300, Medical Alumina)[2] were prepared and immersed in hydrochloric acid at pH3 overnight for acid treatment. A fluororesin column (ID 9 mm \times 62 mm) whose shape was same as that built into a commercial $^{99}\text{Mo}/^{99\text{m}}\text{Tc}$ generator was filled with 2 g of each alumina specimen. The column was connected to a peristaltic pump and 0.2 mL of Mo solution was added to each column. Then, fifty milliliter of saline was flowed through the columns to wash thoroughly. After 24 hours, ten milliliter of saline was flowed through the columns to obtain $^{99\text{m}}\text{Tc}$ solutions as milking process. The eluate was collected as 1mL aliquots. The flow rate was approximately 40 mL/h. The milking was carried out for 2 days. The activities of obtained solution were measured by a gamma ray spectrometer.

RESULTS: The ^{99}Mo specific activity of the Mo solution was 13.1 MBq/g-Mo when the solution was added to the columns.

Table 1 shows the Mo adsorption capacities of each alumina specimen. The alumina specimens were subjected to

acid treatment, but the adsorption capacities didn't improve. About 90% or more of $^{99\text{m}}\text{Tc}$ was eluted with 4 mL of saline with the developed alumina specimen.

Table 1. Mo adsorption capacities of alumina specimen.

	D-201-300	V-V-300	V-B-300	Medical Alumina
Mo adsorption capacity (mg/g- Al_2O_3)	24.1	31.4	30.8	28.8

On the other hand, ^{99}Mo was contained in the $^{99\text{m}}\text{Tc}$ solutions eluted from the columns. In the Minimum Requirements for Radiopharmaceuticals of Japan (MRRP), the desorbed ^{99}Mo amount in $^{99\text{m}}\text{Tc}$ solution is specified using the $^{99}\text{Mo}/^{99\text{m}}\text{Tc}$ ratio as an index. The standard value is $^{99}\text{Mo}/^{99\text{m}}\text{Tc} \leq 0.015\%$. Fig.1 shows a comparison of the $^{99}\text{Mo}/^{99\text{m}}\text{Tc}$ ratio of the $^{99\text{m}}\text{Tc}$ solution in the present work and the previous work. In the ^{99}Mo desorption reduction measures, the acid treatment of alumina had no effect. However, due to the application of dynamic adsorption, increasing the concentration of Mo solution, and reducing the amount of Mo added, the $^{99}\text{Mo}/^{99\text{m}}\text{Tc}$ ratio was significantly improved and reduced by about 50%. Therefore, it was suggested that the application of dynamic adsorption, increasing the concentration of Mo solution and reducing the amount of Mo added are effective in improving the Mo desorption property.

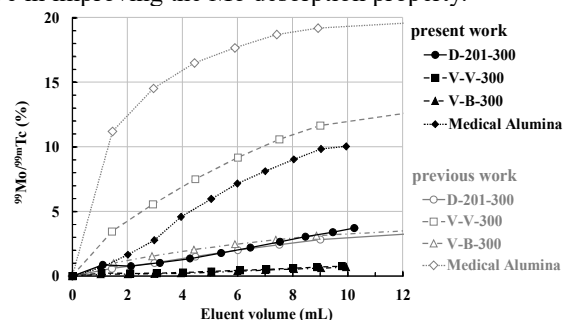


Fig. 1. Comparison of the $^{99}\text{Mo}/^{99\text{m}}\text{Tc}$ ratio of the $^{99\text{m}}\text{Tc}$ solution in the present work (dynamic adsorption) and the previous work (static adsorption) on day 1.

The pH standard value of the $^{99\text{m}}\text{Tc}$ solution is specified as pH 4.5 to 7.0. The pH of the $^{99\text{m}}\text{Tc}$ solution obtained from the developed alumina specimens deviated to the basic side.

In this work, the $^{99\text{m}}\text{Tc}$ solution didn't meet the MRRP, but it was suggested that the quality could be improved by changing the adsorption method and conditions. It is difficult to meet the MRRP with the current column shape. In the future, we will improve the quality of the $^{99\text{m}}\text{Tc}$ solution for practical use by optimizing the column shape and Mo adsorption conditions.

REFERENCES:

- [1] Y. Fujita *et al.*, J. Radioanal. Nucl. Chem. **327**(2021) 1355-1363.
- [2] Y. Suzuki *et al.*, Transactions of the Materials Research Society of Japan, **43**(2018)75-80.

CO4-10 The effect of ion irradiation on yttria stabilized zirconia (YSZ) single crystal substrates using a slow positron beam

T. Ozaki, H. Sakane¹, A. Yabuuchi² and A. Kinomura²

School of Engineering, Kwansai Gakuin University

¹ SHI-ATEX Co., Ltd.

² Institute for Integrated Radiation and Nuclear Science, Kyoto University

INTRODUCTION: The rare-earth (RE)-based cuprate superconductor REBa₂Cu₃O_y (REBCO) exhibits high-temperature superconductivity and is expected to be useful for magnetic coils. Critical current properties in applied magnetic fields are improved by introducing lattice defects using ion-irradiation techniques. Positrons are sensitive to vacancy-type defects, and they are useful for characterizing irradiation-induced defects. However, it is difficult to characterize irradiation-induced defects in GdBCO coated conductors (CCs), which were industrially produced with a roll-to-roll process because GdBCO CCs initially contain vacancy clusters, whose size is larger than that of the newly-formed defects induced by the irradiation [1]. In this study, yttria stabilized zirconia (YSZ), which is an oxidized material and almost the same density as GdBCO, single crystal substrates were irradiated with He ions at 600 keV or Au ions at 10 MeV, and then probed using a slow positron beam.

EXPERIMENTS: The YSZ single crystal substrates were irradiated with 600 keV He⁺ (< 2.0×10¹⁶ cm⁻²) or 10 MeV Au⁴⁺ (< 7.0×10¹³ cm⁻²) ions. The unirradiated and irradiated samples were probed by the KUR slow positron beam and the Doppler broadening of annihilation radiation (DBAR) spectra were acquired with incident positron energies E₊ = 9 keV. Figure 1 shows positron implantation profile. The sharpness of the DBAR spectra is evaluated by a value called the S-parameter, which becomes generally lower when positrons annihilate in a perfect lattice, and higher when positrons are trapped into vacancies [2].

RESULTS: Figure 2(a) and 2(b) show dose dependence of S-parameter for YSZ single crystals irradiated at 600 keV He⁺ and 10 MeV Au⁴⁺ ions, respectively. S-parameter is closely correlated to concentration and size of defects in a material. As shown in Fig. 2, S-parameters increases with increasing fluence up to 1.0×10¹⁶ cm⁻² for He-ion irradiation and 2.0×10¹³ cm⁻² for Au-ion irradiation, above which no significant increase can be observed. This indicates that almost all of the positrons are trapped at irradiation-induced vacancy-type defects in the samples with the saturated S-parameter value. The saturated S-parameter value of YSZ single crystal substrate irradiated at 10 MeV Au ions is larger than that of the one irradiated at 600 keV He ions. This could be because the size of irradiation defect produced by Au-ions is larger than that of the one produced by He-ions.

REFERENCES:

- [1] A. Yabuuchi *et al.*, Appl. Phys. Express, 13 (2020) 123004.
- [2] R. W. Siegel, Ann. Rev. Mater. Sci., 10 (1980) 393–425.

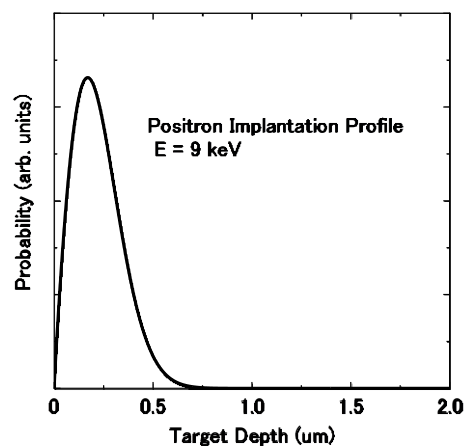


Fig. 1. Positron implantation profile in YSZ single crystal substrate.

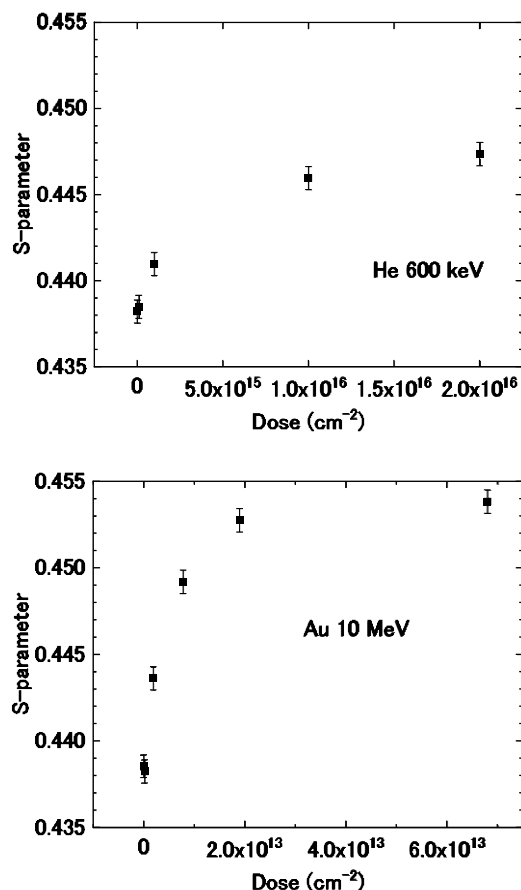


Fig. 2. Dose dependence of S-parameter for YSZ single crystal substrate irradiated at (a)600 keV He⁺ and (b)10 MeV Au⁴⁺ ions.

CO4-11 Study on formation mechanisms of low-fluence ion-irradiation induced damages on semiconductor surfaces

J. Yanagisawa, R. Shigesada, Q. Xu¹, A. Yabuuchi¹, K. Takamiya¹, and A. Kinomura¹

School of Engineering, The University of Shiga Prefecture

¹Institute for Integrated Radiation and Nuclear Science, Kyoto University

INTRODUCTION: To study the influences of ion irradiation induced damage on semiconductor surfaces at lower energies, we have prepared the plasma-exposed chips of the Si wafer as the samples. In the previous study using the oxygen plasma [1], we have observed almost no damages inside the sample surfaces. Because of the use of the oxygen, the Si surface was oxidized and the surface of the Si sample was covered with thin oxidized films. Therefore, the effect of the plasma treatment on Si substrate was not evaluated. In the present study, we have used the SF₆ gas to generate the plasma, and the effect of the damage induced during the etching of the Si surface was investigated by the S (line shape) parameter and the life-time measurement of the positron annihilation using the KUR slow positron beam system.

EXPERIMENTS: Chips of a Si (100) wafer with a size of about 18 mm × 18 mm were exposed to the RF (radio-frequency) plasma at a power of 5 W (#2, #3, #6, #7) or 40 W (#4, #5, #8, #9) with the oxygen gas pressure of 10 Pa (#2-#5) or 30 Pa (#6-#9) for 15 min. (#2, #4, #6, #8) or 30 min. (#3, #5, #7, #9). The sample of #1 was an untreated Si as a reference. For the measurement of the S parameters, slow positron beams at energies of 0 – 30 keV was used. Positron annihilation intensity at inter-lattice (I₁) with bound electrons and inside damages (I₂) with conduction electrons were obtained from the positron life-time spectra for each sample.

RESULTS: Fig. 1 shows the S parameters for the plasma treated, as well as untreated, Si wafer samples. In contrast to the oxygen plasma treated Si [1], S parameters

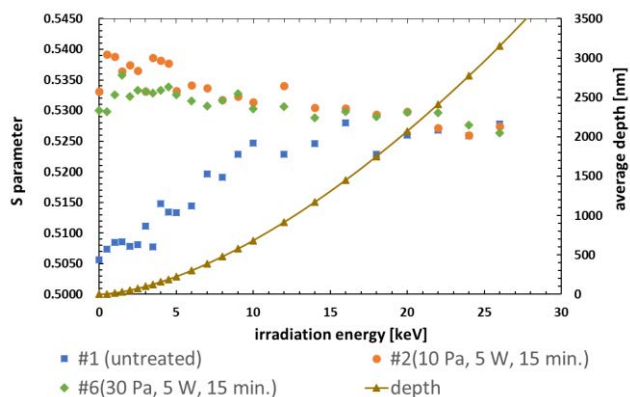


Fig. 1. S parameters for SF₆ plasma treated (#2, #6) and untreated (#1) Si wafer samples as a function of positron energy.

at lower positron energies for plasma treated Si were increased, showing that the damages were induced to the surface region of the Si wafer during the plasma etching using the SF₆ gas. The S parameter of #2 (SF₆ gas pressure of 10 Pa) was larger than #6 (that of 30 Pa), which is because of the larger ion energies inside plasma for lower gas ambient in which the collision between ions (and/or radicals) are reduced in the lower density plasma.

From the life-time measurement of the positron annihilation, the annihilation intensity of positrons at inter-lattice sites (I₁) and that at inside damages (I₂), such as vacancies and voids, can be obtained. The result is shown in Table 1. Although I₁ was far larger than I₂ for untreated Si (#1), as might be expected, the values of I₂ were increased to roughly about 6 - 7 times of that of I₁ after plasma treatment, indicating that the damages were surely induced by the plasma treatment used in the present study. For the sample #9, however, the value of I₂ was lower compared to other plasma-treated Si (#2 - #8). This might be because of the recovery of the induced damages due to the temperature-rise of the Si sample (*i.e.*, annealing effect) during the plasma treatment using the conditions of the plasma of higher RF power (40 W), higher SF₆ gas pressure (30 Pa), and longer process time (30 min.), used for #9.

Table 1. Annihilation intensities of positrons with electrons at inter-lattice (I₁) and inside damages (I₂).

sample	I ₁ [%]	I ₂ [%]
#1	93.27	6.728
#2	12.03	87.97
#3	14.64	85.36
#4	15.46	84.54
#5	11.94	88.06
#6	11.03	88.97
#7	12.89	87.11
#8	16.03	83.97
#9	19.82	80.18

CONCLUSION: After the SF₆-plasma treatment of Si wafer, damages of the etched surface was investigated using the method of the positron annihilations. It is found that both the value of the S parameter and the value of the annihilation intensity of positrons at inside damages were increased after the plasma treatment, indicating that damages, such as vacancies and voids, were induced inside the etched Si surfaces after the plasma treatment at conditions used in the present study.

REFERENCE:

[1] J. Yanagisawa, T. Furukawa, Q. Xu, A. Yabuuchi, K. Takamiya, and A. Kinomura, KURNS Progress Report 2020 (Kyoto University), CO4-6 (R2052).

CO4-12 Complex Structure of Ions Coordinated with Hydrophilic Polymer 22. Ionic Diffusion in Polymeric Structure Utilized by Polyiodide Ions. (3)

A. Kawaguchi and Y. Morimoto

KURNS

INTRODUCTION:

We have been investigating dynamical and interacted structures between iodine and polymers. Here, the term of "iodine" indicates not only simple I_2 , but polyiodide ions (I_n^{m-} , m, n : integer, $n > 1$, "Poly-Iod" mentioned below) as charged molecules, which suggest concealed potential and diverse availability. [1,2]

While "Poly-Iods" are composed of iodine as unique element, their structure (atomic distance and charge distribution in one molecule) and coordination behavior between "Poly-Iods" can be widely modified corresponding to their environment. Occasionally, dipole or distributed positive charge (σ -hole) on "Poly-Iods" can be localized corresponding to their bonds with other atoms or ions. Or, though iodine is a member of halogen, mono-iodide ion, I^+ , which does not belong to "Poly-Iods", can behave as single ion with positive charge. [3,4]

Such characteristic nature and ambiguity of iodine or "Poly-Iods" are also more emphasized in interaction with polymeric matrices or macromolecular environments. Experimental procedure for "iodine doping", which introduces "Poly-Iods" solved in solutions into the matrices advances through easy operation under normal pressure at room temperature. While various polymers (both natural and synthesized ones) can diffuse "Poly-Iods" into them and construct modified structure in which each matrix coordinates with "Poly-Iods", the structures as "iodine-doped" polymer often indicates paradoxical results as phenomena. For example, operation of "iodine doping" for polyamide-6 (PA6) introduces hardening and structuring as coordination of "Poly-Iods" with crystallite of PA6 or their re-orientation. On the other hand, simultaneously, operation also introduces softening or de-structuring as vanishing orientation or activation for ionic mobility. [5-7] Such paradoxical behaviors can be observed not only in PA6 matrix but also in other hydrophilic matrices such as poly vinyl-alcohol (PVA) or even in hydrophobic matrices. Furthermore, "Poly-Iods" even solved in aqueous solutions can interact with *hydrophobic* matrices. [8]

These paradoxical ambiguity indicated by "iodine-doping" process and following activity suggest that "Poly-Iods", which are surely charged molecules solved in aqueous solutions, may overcome division between hydrophilic and hydrophobic matrices restrictively.

DISCUSSION:

The most popular phenomenon as coordinated structure between "Poly-Iods" and polymer is "iodine-starch com-

plex"; it is explained as coordination of starch as aqueously solved polymer with I_3^- or I_5^- . [9] On the other hand, existence of I_5^- or hydrophobic structure of helix chain of starch in the complex is not considered sufficiently. And, besides such aqueously solved polymer as host matrices, structure and functionality in matrices like as PA6 or PVA, which are hydrophilic and but unsolvable, should be complicated. Additionally, comprehensive explanation or theory have not be suggested yet.

Modestly saying, however, explanation should be offered beyond common dogma which may not be often considered strictly in chemistry. While chemical structure of monomer unit along polymer chain should be one of important information, it does not wholly dominate and explain characterization and functionality of polymeric system where hierarchic structures exist inevitably. There can be suggested "hydrophilicity or dipole in hydrophobic matrix" or "(localized) hydrophobicity in hydrophilic polymer".

In such microscopic environment presented for diffusion, simultaneous achievement for both coordination to fix ions with host matrices and dynamic transfer of substances through them can be suggested. It also means that "hydrophilicity vs. hydrophobicity of polymer" or "softening vs. hardening of result composite" should be discussed considering hierarchic structures in polymers.

Such ambiguous discussion which deviates from ordinary chemistry might be required for dynamics and structure in polymeric matrices. [to be continued]

ACKNOWLEDGMENTS: Some parts of these discussion are suggested by experimental results researched with Dr. Gotoh (Shinshu Univ.) and his staff and partially funded by NEDO. [2]

REFERENCES:

- [1] patent. JPN-5444559 (2014).
- [2] "Projects for Practical Use from Innovation" sponsored by NEDO (2007-2009).
- [3] T.J. Marks & D.W. Kalina, "Extended Linear Chain Compounds" vol.1 ch.6., ed. J.S. Miller (Plenum Press, 1982).
- [4] T. Clark, *et.al.*, *J Mol. Model*, **13**, 291-296 (2007).
- [5] A. Kawaguchi, *Polymer*, **35**, 3797-3798 (1994).
- [6] KAWAGUCHI Akio, *et.al.*, *SPring-8 User Exp. Rep.* **5** (2000A), 354-354 (2000).
- [7] A. Kawaguchi, *Sens. & Act. B*, **73**, 174-178 (2001).
- [8] A. Kawaguchi, *Polym. Prep. Jpn.*, **62**, 5116-5117 (2013).
- [9] Rundle, R.E. and Baldwin, R.R., *J. Am. Chem. Soc.*, **65**, 554-558 (1943).

CO4-13 Demagnetization Measurement of Permanent Magnet Materials Against Neutron Irradiation

Y. Fuwa¹, Y. Kuriyama², Y. Iwashita², K. Takamiya², and T. Takayanagi¹

¹J-PARC Center, Japan Atomic Energy Agency

²Institute for Integrated Radiation and Nuclear Science, Kyoto University

INTRODUCTION: In recent years, energy-saving has become one of the most critical issues for developments in particle accelerator research. The range of applications of permanent magnets in accelerators is expanding to reduce energy consumption. In addition to rare earth magnets with large remanent magnetization, the use of inexpensive ferrite magnets has been proposed [1,2].

One of the problems associated with applying permanent magnets in particle accelerators is demagnetization caused by radiation. Many research groups conducted experiments to evaluate the demagnetization for undulators in synchrotron radiation facilities [3], but the data has many discrepancies [4]. In addition, there is a lack of data on radiation demagnetization for ferrite magnets. Therefore, a more precise analysis of the radiation demagnetization is required for accelerators targeting higher beam intensities. Experiments have been carried out using the irradiation facilities of the KUR.

EXPERIMENTS: In this study, magnet samples were irradiated with up to 3×10^{19} n/cm² neutrons using a Pneumatic transport tube (Pn-2), a hydraulic transport tube (Hyd), and a long-term irradiation plug (LI). The rate of radiation-induced demagnetization was evaluated by comparing the remanent magnetization of samples before and after the irradiation. To measure the magnetization of the samples, we prepared a rotating stage for magnet samples and a Helmholtz-like pickup coil. By rotating the sample in the pickup coil, the voltage is induced in the coil. The measured amplitude of the induced voltage corresponds to the magnetization of the sample. This method made it possible to evaluate the amount of magnetization more precisely and in a shorter time than with a Hall probe [5,6].

RESULT AND DISCUSSION: Ferrite magnets (Y30H) and neodymium magnets (N35H, N40) were used as samples in this experiment. Fig. 1 shows the measured demagnetization rate as a function of irradiated neutron fluence [7]. For the ferrite magnets, 10% demagnetization was observed at a neutron fluence of 3×10^{19} n/cm². For neodymium magnets, it was confirmed that large demagnetization was observed up to an irradiation dose of 10×10^{16} n/cm². Comparing the results of N35H and N40, the magnitude of demagnetization differs by approximately a factor of two for the same amount of neutron irradiation. These results suggest that one of the reasons for the variation of data in previous studies may be that the samples with different compositions were treated the same. The temperature of the sample at the time of irradiation may also affect the degree of demagnetization.

As a next plan, we plan to conduct experiments to systematically evaluate the effects of different material compositions and irradiation temperatures on demagnetization.

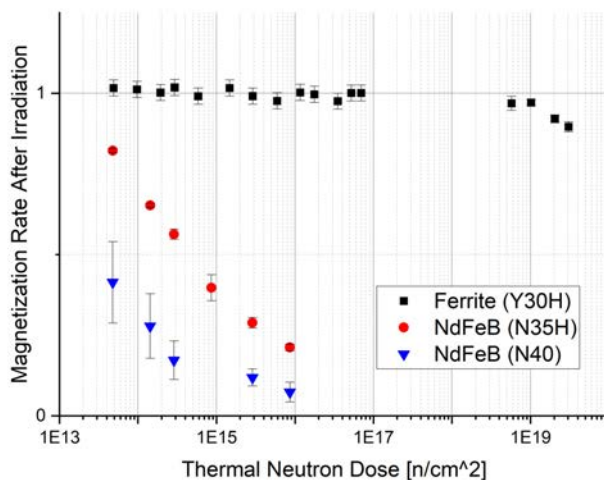


Fig. 1. Measured demagnetization rate for the samples of ferrite (Y30H), and neodymium magnets (N35H, N40).

REFERENCES:

- [1] Y. Fuwa and Y. Iwashita, "Performance evaluation of a klystron beam focusing system with anisotropic ferrite magnet", *Progress of Theoretical and Experimental Physics*, 2017, 023G01.
- [2] Y. Iwashita, M. Abe, T. Yako, Y. Fuwa and N. Terunuma, "Bipolar Correction Magnet With Permanent Magnets", *IEEE Transaction on Applied Superconductivity*, Vol. 30, No. 4, JUNE 2020, 4003703.
- [3] [7] T. Bizen and H. Kitamura, "Radiation-induced Demagnetization of Nd₂Fe₁₄B Magnets for Undulators" *Journal of JSSRR*, March 2004 Vol. 17 No. 2 pp. 53-58.
- [4] X.-M. Maréchal, T. Bizen, Y. Asano, and H. Kitamura, "65 MeV Neutron Irradiation of Nd-Fe-B Permanent magnets", *Proceedings of European Particle Accelerator Conference (EPAC) 2006, THPCH135*, pp. 3116-3118 (2006).
- [5] T. Yako, Y. Iwashita, M. Abe, T. Kurihara, M. Fukuda, M. Sato, T. Sugimura, Y. Fuwa, K. Takamiya, and Y. Inuma, "Measurement of Radiation Resistivity of Ferrite Permanent Magnets Irradiated by Neutrons", *Proceedings of the 16th Annual Meeting of Particle Accelerator Society of Japan*, 1003-1005 (2019).
- [6] Y. Fuwa, Y. Kuriyama, and Y. Iwashita, "Magnetization Measurement Scheme for Radiation Demagnetization Evaluation of Permanent Magnets", *Proceedings of the 18th Annual Meeting of Particle Accelerator Society of Japan*, 58-60 (2021).
- [7] Y. Fuwa, T. Takayanagi, Y. Kuriyama, Y. Iwashita, and K. Takamiya, "Radiation-Induced Demagnetization Measurement of Permanent Magnet Materials by Systematic Neutron Irradiation", *27th International Conference on Magnet Technology*, TUE-P10-115-05 (2021).

CO4-14 Evaluation of Deuterated Macromolecular Crowder by Small Angle X-ray Scattering and Dynamic Light Scattering

Y. Nagata¹, M. Sugiyama², R. Inoue², N. Sato², and K. Morishima²

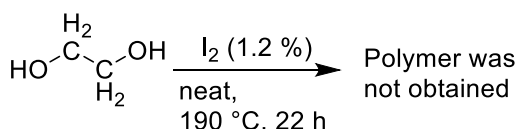
¹Institute for Chemical Reaction Design and Discovery, Hokkaido University

²Institute for Integrated Radiation and Nuclear Science, Kyoto University

INTRODUCTION: A wide variety of biomolecules exist at high concentrations in the living cells and are thought to have a significant effect on the structure and dynamics of proteins.¹⁻³ Usually, measurement experiments on protein solutions are performed using dilute solutions (1 mg/mL or less). However, there is a large difference from the actual concentration (200 to 400 mg/mL) in the living cell. Therefore, it is quite important to reproduce the intracellular environment by adding various compounds (so-called crowders to reproduce the intracellular crowded system) at high concentrations to measure protein structure and dynamics under realistic conditions, and polymer crowders have been studied.

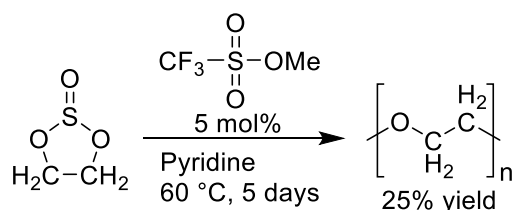
In this study, we focus on the preparation of polyethylene glycol (PEG) and deuterated PEG as macromolecular crowders to analyze their properties by small-angle X-ray scattering (SAXS) and dynamic light scattering (DLS) experiments.

EXPERIMENTS and RESULTS: Firstly, we have tried direct polymerization of 1,2-ethanediol in the presence of iodine according to the previous report. After the heating for 22 h at 190 °C, we obtained the corresponding oligomer products (up to 5 mers) and could not obtain H-PEG (Scheme 1).⁴



Scheme 1. Synthesis of a PEG from 1,2-ethanediol at 190 °C for 22 h.

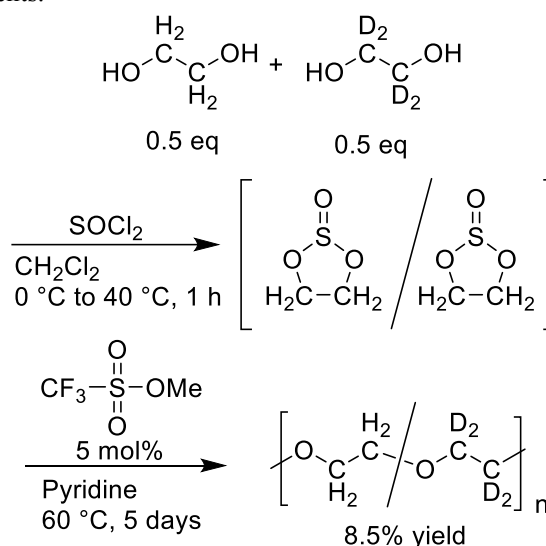
We then tried a polymerization of ethylene sulfite in the presence of methyl trifluoromethanesulfonate according to a report (Scheme 2).⁵



Scheme 2. Synthesis of PEG from ethylene sulfite at 60 °C for 5 days.

After 5 days at 60 °C, PEG was obtained at 25% yield. The number average molecular weight of the obtained PEG was estimated as 1140 (25.9 mers) based on the ¹H NMR analysis.

Subsequently, we tried to partially deuterated PEG, which is an important material for the contrast variation small-angle neutron scattering (SANS) measurements. 1,2-ethanediol and deuterated 1,2-ethanediol was converted to deuterated and non-deuterated 1,3,2-dioxathiolane 2-oxide, which were polymerized in the presence of methyl trifluoromethanesulfonate without purification (Scheme 3). We certainly obtained the partially deuterated PEG; however, the yield was insufficient (8.5%). Now we are optimizing the reaction conditions of this reaction to obtain partially deuterated PEGs with high yield to submit SAXS, DLS, and SANS experiments.



Scheme 3. Synthesis of a partially deuterated PEG from 1,3,2-dioxathiolane 2-oxide from 1,2-ethanediol and deuterated 1,2-ethanediol.

REFERENCES:

- [1] Minton, A. P. Implications of macromolecular crowding for protein assembly. *Curr. Opin. Struct. Biol.* **2000**, *10*, 34-39.
- [2] Ellis, R. J. Macromolecular crowding: an important but neglected aspect of the intracellular environment. *Curr. Opin. Struct. Biol.* **2001**, *11*, 114-119.
- [3] Ellis, R. J. Macromolecular crowding: obvious but underappreciated. *Trends Biochem. Sci.* **2001**, *26*, 597-604.
- [4] Schnabel, R. Synthesis of Deuterated Polyethylene Glycols. *J. Label. Compd. Radiopharm.* **1992**, *31*, 91-94.
- [5] Azuma, N.; Sanda, F.; Takata, T.; Endo, T. Effect of ring size on the cationic ring-opening polymerization of cyclic sulfites. *Macromol. Chem. Phys.* **1998**, *199*, 1785-1789.

CO4-15 TDPAC Measurement of $^{111}\text{Cd}(\rightarrow ^{111}\text{In})$ in Ultrafine Bubble Water

M. Tanigaki, D. Hayashi¹, Y. Ohkubo, A. Taniguchi, Y. Ueda², Y. Tokuda³

Institute for Integrated Radiation and Nuclear Science, Kyoto University

¹*Graduate School of Science, Kyoto University*

²*Research Institute for Sustainable Humanosphere, Kyoto University*

³*Department of Education, Shiga University*

INTRODUCTION: Ultrafine bubbles, the gaseous cavities with diameters less than one micrometer, have recently attracted much attention because of their multifunctionalities [1]. While applications of ultrafine bubbles are extended in a wide variety of fields, fundamental studies on ultrafine bubbles themselves are not well extended because of their small size, smaller than the wavelength of radiant rays.

As we have previously shown in the internal pressure measurement of Xe-ultrafine bubbles [2], the perturbed angular correlation measurement is a useful technique for the study of the ultrafine bubble.

This time, the time differential perturbed angular correlation (TDPAC) of $^{111}\text{Cd}(\rightarrow ^{111}\text{In})$ in the aqueous solution with ultrafine bubbles is performed for the study of the interface of ultrafine bubbles, which should be one of the essential origins of its multifunctionality.

EXPERIMENTS: Typical four-counter TDPAC measurements were performed for the 171-245 keV cascade in $^{111}\text{Cd}(\rightarrow ^{111}\text{In})$ in aqueous solutions of pH = 2, 10, and 14 with/without Oxygen-ultrafine bubbles. The average diameter and the density of the ultrafine bubbles in each sample were 314 nm and $1.03 \times 10^7/\text{mL}$, respectively. ^{111}In was obtained from Nihon Medi-Physics as the aqueous solution of $^{111}\text{InCl}_3$ at the pH of approximately 2. This ^{111}In solution was added to each aqueous solution sample, followed by the pH adjustments by the appropriate addition of NaOH or HCl. For comparison, aqueous samples without ultrafine bubbles were also prepared in the same way. The angular correlation term $A_{22}G_{22}(t)$ is given by the following equation,

$$A_{22}G_{22}(t) = \frac{2(N(180^\circ, t) - N(90^\circ, t))}{N(180^\circ, t) + 2N(90^\circ, t)}$$

where $N(90^\circ, t)$ and $N(180^\circ, t)$ are the counting numbers of the 171-245 keV γ - γ cascade at 90 and 180 degrees, respectively. Time-dependent term $G_{22}(t)$ for each sample was obtained by normalizing obtained $A_{22}G_{22}(t)$ by the

asymmetry parameter of 171-245 keV cascade in ^{111}Cd , $A_{22} = -0.18$.

RESULTS: Demille reported a long relaxation time in the cases that either low (up to pH = 3.5) or high (between pH = 13 and 14) pH region, and an initial drop to a minimum at 15 to 20 ns and at later times a slow relaxation similar to that observed at extreme pH values in pH = 3.5~13. This pH dependence is understood as the quadrupole interaction in the symmetrical complexes $[\text{In}(\text{H}_2\text{O})_6]^{3+}$ and $[\text{In}(\text{OH})_6]^{3-}$ in extreme pH values, and the formation of less symmetrical complexes and tumbling aggregations at intermediate pH values [3].

Observed $G_{22}(t)$ in the present study well reproduced the results reported by Demille, and the initial drop at 15 to 20 ns in $G_{22}(t)$ at pH = 10 was more significant in Oxygen-ultrafine bubble water (Fig. 1). This difference may be caused by the interactions between the In complexes and the ultrafine bubbles. More studies, such as the detailed pH dependence, are underway.

The present work is supported by JSPS KAKENHI Grant Number 18K03948 and 21K03854.

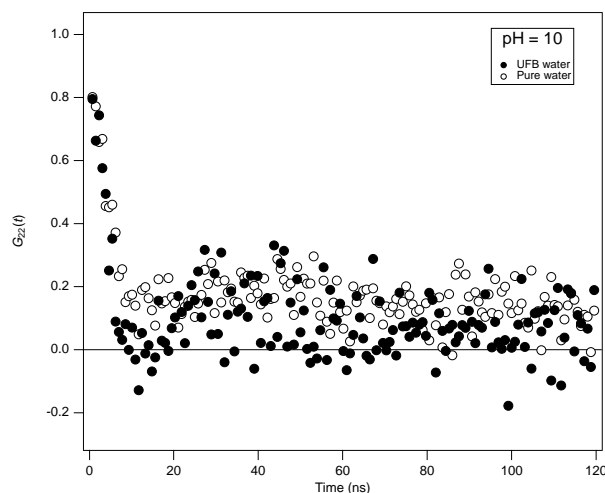


Fig. 1 TDPAC spectra of $^{111}\text{Cd}(\rightarrow ^{111}\text{In})$ in ultrafine bubble water and pure water at pH = 10.

REFERENCES:[1] E. G. Denis, The fine bubble breakthrough. <https://www.iso.org/news/2014/05/Ref1844.html>
[2] M. Tanigaki, T. Yamakura, Y. Ueda, A. Taniguchi, Y. Tokuda, and Y. Ohkubo, KURNS Progress Report 2018, p.31.

[3] G. R. Demille, D. L. Livesey, K. Mailer and S. P. Turner, Chemical Physics Letters, **44** (1976) 164-168.

CO4-16 Tritium release behavior from neutron-irradiated FLiNaK mixed with Ti powder

K. Katayama, K. Kubo, T. Ichikawa, A. Ipponsugi, M. Oya, T. Takeishi¹, and Y. Iinuma²

Department of Advanced Energy Engineering Science,
Kyushu University

¹Faculty of Engineering, Kyushu University

²Institute for Integrated Radiation and Nuclear
Science, Kyoto University

INTRODUCTION: In DT fusion reactors, understanding of tritium behavior is important from a viewpoint of safety. In the self-cooling liquid blanket concept tritium breeding material plays two important roles of tritium transport and heat transport. Tritium is produced in the breeding material by the nuclear reaction between neutrons and Li. Fluoride molten salts such as FLiNaBe and FLiBe are a promising liquid blanket material due to high stability at high temperatures, low reactivity with O₂ and H₂O, and low MHD pressure drop. Since fluoride molten salts have a low solubility for hydrogen isotopes, the produced tritium tends to release from the molten salt. This property means that tritium can be easily recovered from the molten salt but also a part of tritium is lost to the outside of cooling tubes by the permeation on the way to the tritium recovery system. For suppressing tritium loss by increasing effective solubility for tritium, the addition of Ti powder was proposed [1]. However, few studies on molten salt materials containing Ti powder have been performed. In order to control tritium safely and to design tritium recovery system, it is necessary to understand the fundamental behavior of tritium in the molten salt mixed with Ti powder. Since FLiNaBe and FLiBe contain highly toxic beryllium and is not easy to handle safely, FLiNaK is usually used as a simulated fluid. In this study, the solid state sample of FLiNaK mixed with Ti powder was irradiated by neutrons at Kyoto University Research Reactor, and tritium release behavior from the free surface of the molten salt by heating was observed in Kyushu University.

EXPERIMENTS: In the powders of LiF, NaF and KF were mixed in a Ni crucible under Ar atmosphere. The Ni crucible was put in the stainless-steel heating pot and repeatedly heated to 600 °C with Ar purging to remove impurity water vapor. The heating was repeated to homogenize the FLiNaK and the plateau region of temperature change was confirmed at at 454 °C which is melting point of FLiNaK. Ti powder was added to the part of FLiNaK with 2.5 wt% and it was heated with Ar purging. The prepared sample of FLiNaK was packed into quartz tubes in vacuum and it was installed into a polyethylene capsule. The thermal neutrons irradiation was performed by at pneumatic tube 2 (Pn-2) with the fluence of at Pneumatic Tube 2 (Pn-2) of the $1.7 \times 10^{15} \text{ cm}^{-2}$.

Tritium release experiment was carried out in Kyushu University. The schematic illustration of experimental apparatus is shown in Fig.1 The irradiated sample was

put in a Mo crucible and it was installed in the stainless-steel reaction tube. In order to melt the sample sufficiently, heating temperature was set to be to 600 °C or 700 °C with Ar purge. The chemical form of tritium released from the sample was expected to be TF and HT (T₂) and HTO (T₂O) and these were separately quantified. Details of the quantification method were described in Ref.2.

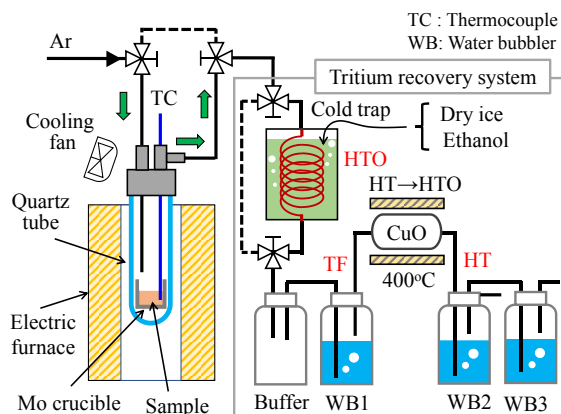


Fig.1 The schematic of experimental apparatus.

RESULTS: Fig.2 shows tritium desorption rate of HT and TF from neutron irradiated FLiNaK with 2.5 wt% Ti powder. It was found that most tritium was released as HT. A large difference was observed in the change of desorption rate between 600 °C and 700 °C. It can be said that the lower the temperature, the higher the tritium absorption capacity of Ti, so that the amount of tritium transferred to Ti in FLiNaK increased and the release from the free interface was suppressed. Since tritium desorption from Ti is took place with decreasing tritium concentration in FLiNaK, the decreasing of the desorption rate was slow at 600 °C. On the other hand, at 700 °C, the amount of tritium absorbed in Ti is small, and the concentration of tritium in FLiNaK decreased rapidly, and the decreasing of the desorption rate was fast.

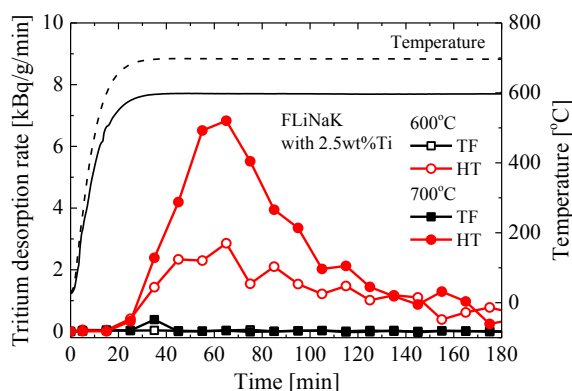


Fig.2 Tritium desorption rate at 600 °C and 700 °C from FLiNaK mixed with 2.5 wt% Ti.

REFERENCES:

- [1] A. Sagara, *et al.*, Fusion Eng. Des. 89 (2014) 2114.
- [2] K. Kubo, *et al.*, Fusion Eng. Des. 171 (2021) 112558.

CO4-17 Tritium recovery behavior for tritium breeder $\text{Li}_4\text{SiO}_4 - \text{Li}_2\text{TiO}_3$ biphasic material

Y. Oya¹, S. Hirata², Fei Sun³, Yongjin Feng⁴, Xiaoyu Wang⁴, Hailiang Wang⁵, M. Kobayashi⁶, Y. Iinuma⁷ and R. Okumura⁷

¹ Faculty of Science, Shizuoka University

² Graduate School of Integrated Science and Technology, Shizuoka University

³ School of Material Science and Engineering, Hefei University of Technology

⁴ Fusion Technology Research Division, Center for Fusion Science, Southwestern Institute of Physics

⁵ College of Physics, Sichuan University

⁶ National Institute for Fusion Science

⁷ Institute for Integrated Radiation and Nuclear Science, Kyoto University

INTRODUCTION: In the fusion blanket system, tritium (T) is produced by (n, α) reaction with lithium (Li). Li_2TiO_3 (LTO) and Li_4SiO_4 (LSO) are regarded as one of the promising solid breeder candidates. LTO has higher chemical stability, but the lithium density is not so high. On the contrary, LSO has higher Li density. Recently, LSO-LTO biphasic materials are proposed as advanced candidates to achieve high tritium breeder ratio (TBR) and quick T recovery at lower temperature by the combination of both LSO and LTO advantages. However, the T recovery performance was not well understood. In this study, LSO-LTO biphasic materials with various phase ratios were used and their tritium desorption behaviors after neutron irradiation was evaluated by T thermal desorption spectroscopy (T-TDS).

EXPERIMENTS: Three kinds of pebble samples with different phase rates, namely $\text{Li}_4\text{SiO}_4\text{-Li}_2\text{TiO}_3$ (LSO-LTO), $2\text{Li}_4\text{SiO}_4\text{-Li}_2\text{TiO}_3$ (2LSO-LTO) and $\text{Li}_4\text{SiO}_4\text{-}2\text{Li}_2\text{TiO}_3$ (LSO-2LTO) were fabricated at Southwestern Institute of Physics (SWIP) in China [1]. These samples were introduced in Kyoto University Research Reactor (KUR) to perform neutron irradiation. The thermal neutron flux was $5.50 \times 10^{12} \text{ n cm}^{-2} \text{ s}^{-1}$ and the fluence was reached to be $7.96 \times 10^{16} \text{ n cm}^{-2}$. After the neutron irradiation, T-TDS measurement was performed at Shizuoka University from R.T. to 1113 K with the heating rates of 5 - 30 K min^{-1} . After T-TDS, total T amount trapped by water bubbler was measured by a liquid scintillation counter.

RESULTS: Fig. 1 shows the T-TDS results. In this experiment, no HT was observed and almost all of T was released as HTO form. The major T desorption temperature was shifted toward lower temperature side as increasing the phase rate of LTO. For 2LSO-LTO sample, the T desorption was also observed at higher temperature

side, but as increasing the phase ratio of LTO, these desorption peaks were disappeared. This is conceivable that the grain size is become smaller as increasing the content of LTO, which would affect the tritium desorption due to shorter diffusion distance. Table 1 summarizes the lithium density and the amount of desorbed T with chemical form of HTO and HT. It was clear that most of T was released as water form (HTO). The largest T retention was observed for 2LSO-LTO, and as the phase ratio of LTO increased, T retention was reduced, which was consistent with Li density in the samples. In addition, by increasing the phase ratio of LTO, T release temperature were shifted toward lower temperature side, indicating to the easy T recovery. Comparing of T-TDS spectra for biphasic LSO-LTO ceramic with monophasic LSO or LTO, the shape of TDS spectra was close to that for LTO as increasing the phase rate of LTO. As the phase ratio of LSO was increased, T-TDS spectra was consistent with that for monophasic LSO. [2,3] Therefore, it was concluded that LSO-LTO biphasic materials with the phase ratio of 1 : 1 has higher T recovery performance at lower temperature and good mechanical property.

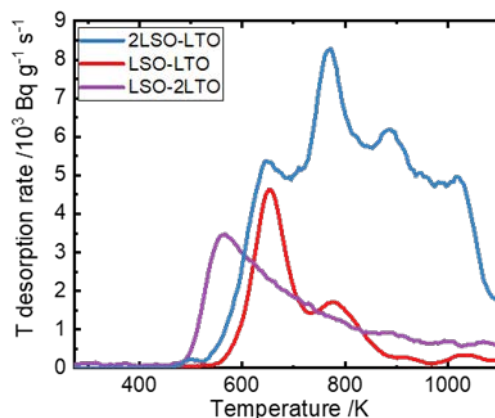


Fig. 1 T-TDS spectra of 2LSO-LTO, LSO-LTO and LSO-2LTO at 20 K min^{-1} .

Table 1 Li density and the amount of desorbed tritium.

Sample	Li density (g cm^{-3})	HTO (MBq g^{-1})	HT (MBq g^{-1})
2LSO-LTO	0.44	8.63	0.21
LSO-LTO	0.39	4.37	0.28
LSO-2LTO	0.35	3.27	0.12

REFERENCES:

- [1] C. Dang *et al.*, J. Nucl. Mater. 500 (2018) 265-269.
- [2] Qilai Zhou *et al.*, J. Nucl. Mater. 522 (2019) 286-293.
- [3] Q. Qi *et al.*, J. Nucl. Mater. 539 (2020) 152330.

CO4-18 Vacancy migration energy in CrFeCoNi medium-entropy alloy

H. Araki, K. Sugita, M. Mizuno, A. Yabuuchi¹ and A. Kinomura¹

Graduate School of Engineering, Osaka University

¹Institute for Integrated Radiation and Nuclear Science, Kyoto University

INTRODUCTION: Tsai *et al.* [1] originally proposed the concept of sluggish diffusion, based on a positive correlation between the activation energies for atomic diffusion, which are normalized by the melting temperature, T_m , and the number of constituent elements in the CrMnFeCoNi high-entropy alloy (HEA) and its subsystems. However, the reason for the sluggishness of diffusion is not quite clear.

In the CrMnFeCoNi HEA and its subsystems at high temperatures, atomic diffusion is expected to proceed via a vacancy mechanism because they are substitutional solid solutions. Therefore, vacancy formation and migration energies in the CrMnFeCoNi HEA and its subsystems are important indexes for understanding the sluggish diffusion. In this work we have evaluated the vacancy migration energy in CrFeCoNi medium-entropy alloy by observing the vacancy migration and annihilation behavior during an annealing process after electron irradiation, with the use of the positron lifetime spectroscopy.

EXPERIMENTS: An arc-melted ingot of CrFeCoNi alloy was homogenized at 1373 K for 24 h under argon atmosphere, and cut into 10 mm × 10 mm × 0.5 mm plates. The plates were polished and then sealed in silica tubes. Solution heat treatment was carried out for 1 h at 1373 K and the samples were quenched in water. Their X-ray diffraction analysis shows that all the samples are composed of single phase with a fcc structure. Then, the samples were irradiated in water with 8 MeV electrons at a fluence of approximately, $1 \times 10^{22} \text{ e}^- \text{ m}^{-2}$ below 358 K using the electron linear accelerator at the Institute for Integrated Radiation and Nuclear Science, Kyoto University. The irradiated samples were isochronally annealed in a temperature range from 373 to 673 K. The temperature step during the isochronal annealing was 25 K and the duration of exposure to each temperature was 1 h.

The positron lifetime measurements were made at 297–299 K using a fast-fast timing coincidence system with a time resolution (FWHM) of 180–183 ps.

RESULTS: Before the electron irradiation the positron lifetime spectrum for the solution-treated alloys was represented by only one component of 108 ps, which is approximately equal to the values calculated for the defect-free constituent pure metals. This indicates that positrons annihilate in the bulk for the solution-treated alloy sample. After electron irradiation, the mean positron lifetime was increased to 133 ps. The analysis of positron lifetime spectra for the as-irradiated sample shows that many positrons are trapped and annihilate in the monovacancies introduced by electron irradiation, because the lifetime component, τ_2 , of trapped positrons was 180 ps,

which is in agreement with the experimental values for monovacancies in the constituent pure metals. Assuming that the specific trapping rate of monovacancies, μ_v , is 10^{15} s^{-1} , the vacancy concentration in the as-irradiated sample is of the order of a few atomic parts per million.

Fig.1 shows the change in the vacancy concentration during the isochronal annealing of the irradiated sample, which was evaluated on the basis of the two- or three-component analyses for the positron lifetime spectra. In the temperature range where dislocations and monovacancies are expected to coexist, the positron lifetime spectra were analyzed on the assumption that the positron lifetime component of dislocation is 150 ps. As shown in Fig.1, the vacancy concentration decreases with annealing temperature, because the vacancies introduced by electron irradiation gradually disappear as the vacancies become mobile during the isochronal annealing. The decrease in the vacancy concentration was theoretically analyzed on the basis of Dryzek *et al.*'s model for isothermal annealing [2].

Assuming that the vacancy migration energy is constant over the whole temperature range, there remains a few discrepancies between the theoretical fitting model and the experimental data, as shown in Fig.1. The positron lifetime measurements indicate that dislocation loop components are detected in addition to vacancies at high temperatures, suggesting that the vacancy migration process is easily influenced by the presence of dislocations. Therefore, we assumed two-component vacancy migration energies (H_m^L , H_m^H) and optimized their values to fit the experimental data. The value of H_m^L obtained in the low temperature range is 0.92 eV, which is nearly equal to 0.93 eV of vacancy migration energy in CrMnFeCoNi [3].

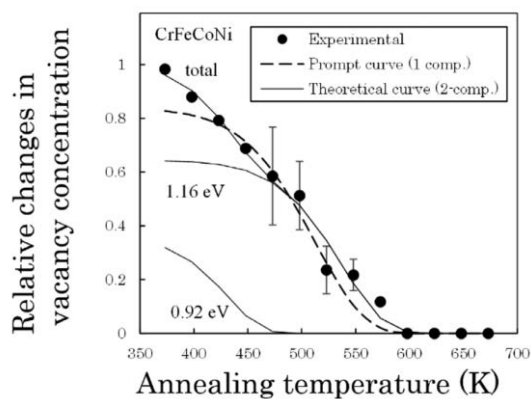


Fig. 1 The relative changes in vacancy concentration obtained from experiments and theoretical calculations.

REFERENCES:

- [1] K. Y. Tsai, M. H. Tsai and J. W. Yeh, *Acta Mater.*, **61** (2013) 4887.
- [2] J. Dryzek, C. Wesseling, E. Dryzek and B. Cleff, *Mater. Lett.*, **21** (1994) 209.
- [3] K. Sugita, R. Ogawa, M. Mizuno, H. Araki and A. Yabuuchi, *Scripta Materialia*, **208** (2022) 114339.

CO4-19 A study on destruction of cesium aluminosilicate compounds by gamma irradiation (3)

H. Ohashi, R. Tawatari, T. Saito¹

Faculty of Symbiotic Systems Science, Fukushima University

¹KURNS

INTRODUCTION: Pollucite which is one of cesium aluminosilicate compounds have attracted attention as a final storage material of ¹³⁴Cs and ¹³⁷Cs. Pollucite is able to synthesized by hydrothermal method in low temperature below 300°C [1]. Pollucite has various properties that favor the immobilization of Cs ions.

However, the damage to the aluminosilicate framework by radiation decay is concerned because it contains ¹³⁴Cs and ¹³⁷Cs. It has been reported that the effect of β -ray emission and nuclide conversion by β -decay of ¹³⁷Cs on aluminosilicate framework is minor [2, 3]. On the other hand, there are few reports of effects by gamma rays on pollucite framework. Therefore, we examined the effect of gamma radiation on the aluminosilicate framework of Pollucite.

EXPERIMENTS: Potassium aluminate, potassium metasilicate and cesium chloride were dissolved in potassium hydroxide solution. The solution was placed in a Teflon inner cylinder pressure container. Pollucite was synthesized by hydrothermal method, holding the container at 180°C for 48 hours. The resulting precipitate was washed by distilled water. Thereafter, each solid was collected by filtration and dried at 110 °C for 12 hours or more. After that, each dried solid was stirred and washed using 0.1 mol dm⁻³ HCl and NH₄Cl for a day, respectively.

The powder samples were characterized by XRD, and gamma-irradiated at 0 and 100 kGy by ⁶⁰Co source. The leaching test by PCT-A method [4] was carried out to evaluate the change of Cs retention performance by framework damage. Concentration of cesium in solution leached was estimated by Ge Semiconductor Detector and atomic absorption spectrophotometry

RESULTS: All the XRD patterns of powders prepared were demonstrated that they were pollucite, and all the patterns showed that they contained only single-phase pollucite. The leaktests have been studied and we estimated that amount of leached cesium from samples with and without ⁶⁰Co-irradiation were over 10 ppm Cs. It was quite higher than those measured by other researchers[5]. Then, each dried solid was washed using 0.1 mol dm⁻³ HCl and NH₄Cl. The results for leaktests were shown in Table 1. The concentration of cesium ions leaked from pollucite was 10-15 ppm Cs. It was comparable with that at last year. The reason why the cesium ion concentration decreased by washing was due to the excessive adsorption of cesium ions on the sample surface. The washing process has proved to be very important in preparing the final disposal material.

In our previous study, the irradiated pollucite sample showed little difference from the non-irradiated one in the amount of leached cesium. There were no effects of γ -ray on the aluminosilicate framework of pollucite in these experiments.

Table 1 Results for PCT-A-like leaktest.

sample	T (°C)	t / hr	Leakage rate	Method
Fukushima polluted soil	90	40	0.126%	Ge Semiconductor Detector
Pollucite	90	40	0.034%	AAS

REFERENCES:

- [1] Y. Yokomori *et al.*, *Sci. Rep.*, **4** (2014), 4195
- [2] J. Fortner *et al.*, Argonne National Laboratory, Argonne, Illinois 60439 (2001).
- [3] N. J. Hess *et al.*, *J. Nucl. Mater.*, **281** (2000), 22-33.
- [4] ASTM C 1285-02 (2008).
- [5] Z. Jing *et al.*, *J. Hazard. Mater.*, **306** (2016), 220–229.

CO4-20 Study on HPLC Elution Behavior of Heavy Lanthanide Metallofullerenes

K. Akiyama¹, S. Nishimura¹, T. Kuroda¹, K. Takamiya², and S. Kubuki¹

¹Department of Chemistry, Tokyo Metropolitan University
²Institute for Integrated Radiation and Nuclear Science, Kyoto University

INTRODUCTION: Metallofullerene (EMF) is a clathrate compound encapsulating metal atom in fullerene molecule. Lanthanide (Ln) EMFs: Ln@C₈₂ have two or three charge transferred electrons on the C₈₂ cage from the encapsulated Ln atom, and their electronic states reflecting the number of charge transfer electrons [1]. From the view point of inorganic chemistry, It is interesting to know that the effect of the electronic state for a series of the encapsulated 10 lanthanide elements (La, Ce, Pr, Nd, Gd, Tb, Dy, Ho, Er, Lu) with the electronic states of (Ln³⁺)@(C₈₂³⁻) on the electronic state of the Ln@C₈₂ molecule from the difference in interaction with pyrenyl stationary phase. So far, we have made clear the retention time in the pyrenyl stationary phase for five types of Ln@C₈₂ from La to Gd by the thermal neutron activation method. On the other hand, the HPLC retention time of Ln@C₈₂ with heavy lanthanide elements have not been obtained because the half-life of the radio nuclide produced by thermal neutron irradiation such as Dy and Er is very short, and the interference by the production of Ln₂@C₈₂ and Ln₂C₂@C₈₀, whose production rate increase competitively with Ln@C₈₂ as the increase of the atomic number of Ln. In this study, we used already purified Ln@C₈₂ of heavy lanthanide by HPLC column of a 5PBB for the neutron activation and developed at three different temperature using newly developed column cooler to obtained detailed HPLC retention time of these Ln@C₈₂s.

EXPERIMENTS: The Ln@C₈₂ (Ln = La, Pr, Dy, Ho, Er) studied in this work was produced by the arc discharge method (DC 60 A) at 50 kPa under He atmosphere. The MF component was extracted from the crude fullerene extract obtained by arc discharged soot by an oxidation method using TiCl₄ [2]. After that, the extracts were injected into a HPLC column of 5PBB (eluent: toluene, flow rate: 6.0 ml/min) for the isolation of Ln@C₈₂s. These isolated Ln@C₈₂ were separately sealed into polyethylene vial and activated by a thermal neutron in the KUR of the Institute for Integrated Radiation and Nuclear Science, Kyoto university. After the irradiation, these samples were mixed and developed into a Buckyprep column (eluent: toluene) with a flow rate of 3.2 mL/min at 20 °C (room temperature), 0 °C, and -10 °C to obtain the radiochromatogram.

RESULTS: Figure 1 shows the radiochromatogram of Ln@C₈₂ obtained at 20 °C, 0 °C, and -10 °C together with HPLC chromatogram monitored by UV absorption. For each temperature, elution peak of Ln@C₈₂ was observed

around 60 min., 75 min., and 85 min., respectively. Some data, such as Pr, were found to be not enough statistics. However, we have succeeded to obtain relatively good chromatogram for some of the targeted heavy lanthanide metallofullerenes. In the near future, improvements such as increasing the sample weight will be attempted to acquire data in addition to heavy lanthanoids, such as Ce, Nd, Tb, and Lu, for which data has not been acquired in this time.

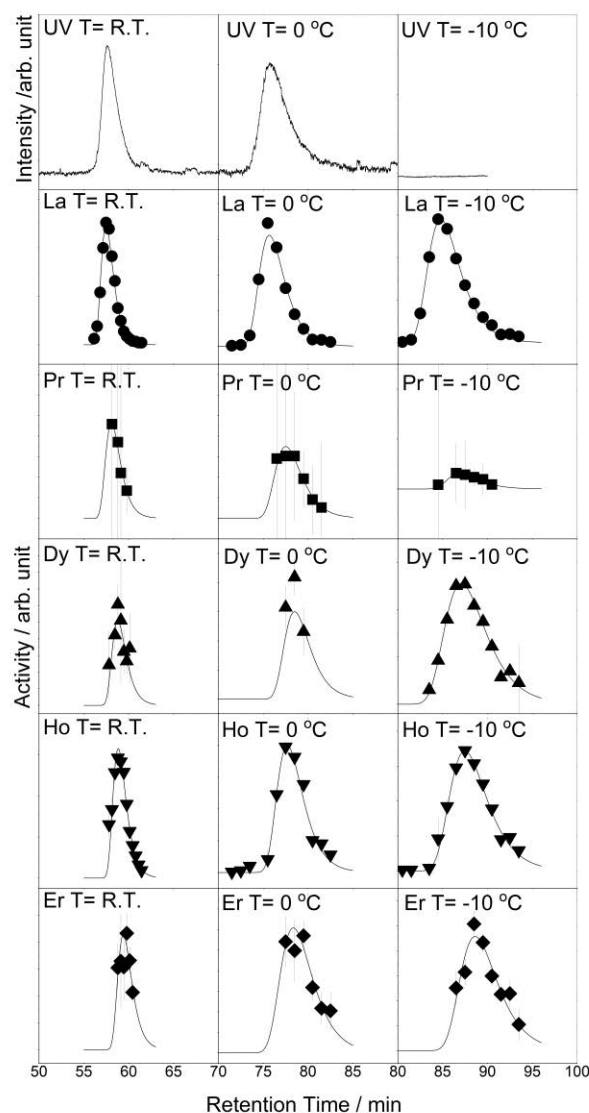


Fig. 1. Radiochromatogram of studied Ln@C₈₂ obtained at 20 °C, 0 °C, and -10 °C, respectively. Solid lines of radiochromatogram in this figure indicates the result of least square fit of the data.

REFERENCES:

- [1] H. Shinohara, Rep. Prog. Phys. **63** (2000) 843-892.
- [2] K. Akiyama *et al.*, J. Am. Chem. Soc., **134** (2012) 9762-9767.

CO4-21 Glass compositional dependence of radiophotoluminescence in Cu-doped aluminoborosilicate glass

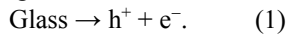
Y. Nishi, A. Kinomura¹, T. Saito¹, A. Okada², T. Wakasugi², K. Kadono²

Graduate School of Science and Technology,
Kyoto Institute of Technology

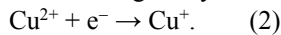
¹Institute for Integrated Radiation and Nuclear Science,
Kyoto University

²Faculty of Materials Science and Engineering,
Kyoto Institute of Technology.

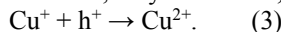
INTRODUCTION: Radiophotoluminescence (RPL) is an emission from luminescent centers that are generated in materials by exposure to ionizing radiation. Recently, we have reported that Cu-doped aluminoborosilicate and silica glasses exhibit prominent RPL [1, 2]. The RPL mechanism of these glasses are explained as follows. First, ionizing radiation generates electron-hole pairs in the Cu-doped glasses,



Then, the electrons are trapped at Cu^{2+} ions, and the Cu^{2+} ions are converted to Cu^+ ions, which emit bright luminescence in the visible region by UV excitation,



The reverse reaction, in which Cu^+ ions trap holes and are converted to Cu^{2+} ions, may also occur,



This reaction (3) reduces the RPL centers. Therefore, in the Cu-doped glasses, the RPL is induced by the progress of reaction (2). In this RPL mechanism, the concentration ratio of Cu^+ and Cu^{2+} ions, and the concentration of Cu^+ ions in glasses are important to observe remarkable RPL. The amount of Cu^+ ions should be less than that of Cu^{2+} ions, and it is better that the concentration of Cu^+ ions is as low as possible. It is well known that the concentration ratio of Cu^+ and Cu^{2+} ions are strongly dependent on the components and compositions, and the preparation conditions of glasses. Thus, we have investigated the relationship between the RPL behaviors, and the glass systems and compositions. Here, we present a new composition of the aluminoborosilicate glass which exhibits more prominent RPL than the previously reported one [1].

EXPERIMENTS: The compositions of the prepared glasses are $25\text{Na}_2\text{O} \cdot 25\text{Al}_2\text{O}_3 \cdot 10\text{B}_2\text{O}_3 \cdot 40\text{SiO}_2$ (mol%) (ABS25) and $30\text{Na}_2\text{O} \cdot 20\text{Al}_2\text{O}_3 \cdot 10\text{B}_2\text{O}_3 \cdot 40\text{SiO}_2$ (ABS30); the former is the composition previously reported [1] and the latter is a new composition. The concentration of copper incorporated into these glasses was 5 mmol% of Cu to 100 mol% of the host glasses. Obtained glasses were cut to 1.0 mm in thickness and both sides were optically polished.

X-ray and γ -ray irradiations of the glasses were performed using an X-ray fluorescence spectrometer equipped with an X-ray source with a Rh target, and the ^{60}Co gamma-ray irradiation facility in the Institute for Integrated Radiation and Nuclear Science, Kyoto Univer-

sity, respectively. Both irradiations were performed at room temperature.

RESULTS:

Figure 1 shows the emission spectra of the Cu-doped glasses before and after the X-ray irradiation. Before the irradiation, a weak emission assigned to the transition from $3d^9 4s^1$ to $3d^{10}$ of Cu^+ is observed for the ABS25 glass whereas the emission is hardly detected for the ABS30 glass. This means that the ABS30 glass contains almost no Cu^+ ions whereas some amount of copper ions in the ABS25 glass present as Cu^+ ions [1]. This is due to the difference in the basicity of glass; in the glasses of higher basicity, the redox equilibrium between Cu^{2+} and Cu^+ ions shifts to the oxidation side, i.e., the side of Cu^{2+} . After the irradiation, the intensity of the emission remarkably increased. The emission intensity of the ABS30 glass after the irradiation is almost the same as that of the ABS25 glass. Therefore, the ABS30 glass is a material that exhibits a more prominent RPL behavior.

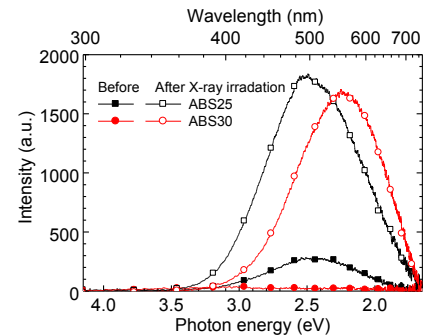


Figure 1 Luminescence spectra of Cu-doped aluminoborosilicate glasses before and after X-ray irradiation.

In order to investigate the relationship between the luminescence intensity and the irradiation dose, the Cu-doped ABS30 were exposed to various doses of γ rays. Figure 2 shows the dependence of RPL intensity on the γ -ray irradiation dose. The RPL intensity increased even at 10 Gy or less. The inset show that the RPL intensity proportionally increased with the γ -ray dose until about 300 Gy and then tended to be deviated from the proportionality. This value is much higher than that reported for the Ag-activated aluminophosphate glasses used for personal dosimeters.

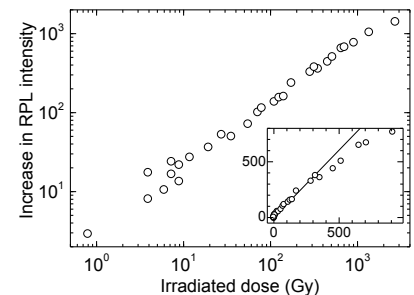


Figure 2 Dependence of RPL intensity of Cu-doped ABS30 glass on irradiation dose after exposure to ^{60}Co γ -rays. Irradiation dose is represented as absorption dose for water.

In conclusion, the Cu-doped aluminoborosilicate glass is promising for dosimeters used in environments under the relatively high irradiation doses.

REFERENCE:

- [1] H. Hashikawa, *et al.*, *J. Am. Cer. Soc.*, **102**(4), 1642-1651 (2019).
- [2] Y. Takada, *et al.*, *AIP Adv.*, **11**(3), 035208 (2021).

CO4-22 Formation of radiation defects on tungsten and their influence on effect of hydrogen isotope retention

K. Tokunaga, M. Matsuyama¹, M. Hasegawa,
K. Nakamura and Q. Xu²

Research Institute for Applied Mechanics, Kyushu University

¹*Hydrogen Isotope Research Center, University of Toyama*

²*Institute for Integrated Radiation and Nuclear Science, Kyoto University*

INTRODUCTION: It is of a great importance to clarify phenomena of implantation, retention, diffusion and permeation of tritium (T) on surface of the armor materials of the first wall/blanket and the divertor on fusion device from a viewpoint of precise control of fuel particles, reduction of tritium inventory and safe waste management of materials contaminated with tritium. Refractory metals such as tungsten (W) is potential candidate for the armor of the first wall and the divertor plate of the fusion reactor because of its low erosion yield and good thermal properties. The armor material will be subjected to heavy thermal loads in the steady state or transient mode combined with high energy neutron irradiation that will cause serious material degradation. In addition, high energy runaway electrons would bombard the armor materials along the equatorial plane in fusion device. It is considered that these cause radiation damage and enhance tritium retention. In the present works, T exposure experiments have been carried out on W samples which were irradiated by high energy electrons to investigate effects of high energy electrons irradiation on microstructure and tritium retention of W. In this fiscal year, pure W and recrystallized W were irradiated by high energy electron beam. Before and after that, positron annihilation experiment was carried out to identify the radiation defect. In addition, EBSD (Electron Back Scatter Diffraction Patterns) analyses has been carried out on the specimens before and after the electrons irradiation. Tritium exposure experiments have been carried out using a tritium (T) exposure device.

EXPERIMENTS: W samples used were ITER specification W (ALMT-grade) (SR-W) and its recrystallized W (RC-W). The SR-W was fabricated via a powder metallurgical route including cold isostatic pressing, sintering, hot rolling, and heat treating to relieve the residual stresses. Some of the machined SR specimens were subjected to a full recrystallization treatment at 2000 °C for 1 hr in vacuum. Sizes of the specimens were 10 mm x 10 mm x 1mm (10 mm x 10 mm : ND-TD). The surface of the both samples were polished to be mirrored. High energy electrons irradiation has been carried out using LINAC in Institute for Integrated Radiation and Nuclear Science, Kyoto University. An peak energy of electron irradiated was 8 MeV and DPA was 5.8×10^{-3} . Temperature during the irradiation was measured by thermocou-

ples which was contacted with a backside of the W samples. Before and after that, positron annihilation experiment was carried out to identify the radiation defect. In addition, a high energy ion irradiation experiment has started to carry out. The sample surface was irradiated by 2.5 MeV Fe ions with a fluence of 5×10^{18} ions/m² at RT. T exposure experiments have been carried out using a T exposure device in University of Toyama. Pressure of the T gas was 1.3 kPa and T exposure was kept for 4 h at 100 °C. T concentration in the gas was about 5 %. After the exposure to T gas, T amount retained in surface layers of the sample was evaluated by imaging plate (IP) measurements and β -ray-induced X-ray spectrometry (BIXS).

RESULTS: In the condition of 8 MeV electrons irradiation, the electron beams go through in 1 mm thickness W sample. On the other hands, damage by the Fe ion beam irradiation is very thin surface layer (a few μm). However, DPA of the damage area of the Fe ions irradiation is larger than that of the electron irradiation. Figure 1 shows the result of the IP measurement. The amount of T of the specimen surfaces evaluated by comparison with the standard samples is shown as Figure 2. These results indicate that the amount of T of the specimens irradiated by the electron and the Fe ion beams increases comparing with un-irradiated specimens. Quantitative evaluation is currently underway.

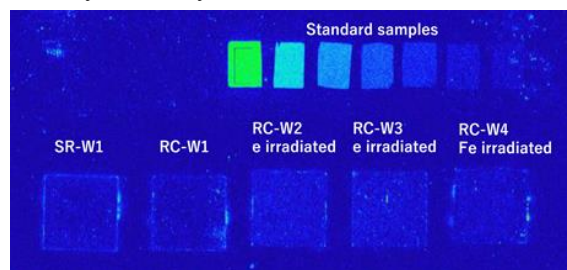


Figure 1 Result of IP measurement.

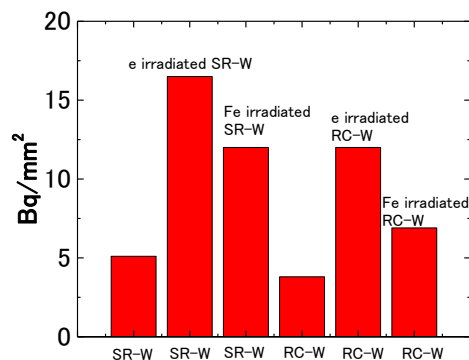


Figure 2 Amount of tritium on before and after electron and Fe ion irradiation measured by IP measurement. SR-W and RC-W are stress relief and recrystallized state, respectively.

CO4-23 Neutron irradiation tests for ITER plasma diagnostics

M. Ishikawa, T. Ushiki, E. Yatsuka, T. Yokozuka, H. Murakami, T. Kikuchi, K. Nojiri and T. Hatae

National Institutes for Quantum Science and Technology

INTRODUCTION: ITER [1] is being built in France by international cooperation. This study focuses on neutron irradiation effects on optical elements used in Diagnostics for ITER. Expected 1 MeV Silicon equivalent fluence is 10^{12} - 10^{15} n/cm² depending on locations of components. In order to investigate the effect of such high fluence on the actual components in a short time, neutron irradiation was performed using the slant exposure tube and the pneumatic tubes of the KUR. This report mainly presents, (1) effect of neutron irradiation of Silicon (Si) which is candidate material for optical lens of Infrared Thermography (IRTh) system and (2) briefly summarize the test results for the Edge Thomson Scattering system (ETS).

(1) Irradiation Tests of Si for Optical Lens of IRTh

IRTh will use Si lens in the ITER environment. Recent gamma-ray irradiation tests conducted by the authors show that the transmittance of Si is not significantly degraded by gamma-ray irradiation. However, some studies suggest that strong neutron irradiation induce several absorption bands in the wavelength range of IRTh (1.5 μ m-4.5 μ m) [2]. This study investigated threshold value of the total neutron dose for keeping transmittance of Si.

EXPERIMENTS: The slant exposure tube and pneumatic transportation facility was used for irradiation test of Si samples. In this test, several Si samples were irradiated in several neutron fluence up to 1.0×10^{17} (n/cm²).

RESULTS: Figure 1 shows the irradiation test result of Si samples. As shown in Figure 1, the two fatal absorption bands (near-edge (less than 1.2 μ m) and 1.78 μ m) were induced by neutron irradiation. Figure 2 shows dependence of transmittance degradation of Si on neutron fluence. Absorption of near-edge (1.2 μ m) and 1.78 μ m exponentially increased from neutron fluence of 5.0×10^{15} (n/cm²). Judging by these results, the author concluded that Si lens unit can survive in ITER environment if neutron fluence at the location of lens unit can be decreased to about 2.5×10^{15} (n/cm²) by shielding design. This value can be easily achieved by shielding of 20 cm-thick Boron carbide.

(2) Irradiation Tests of Optical Fibers of ETS

EXPERIMENTS: An optical fiber (hydrogen loaded fiber) that transmits the signal light of ETS was irradiated up to 9×10^{14} cm⁻² for fast neutron and 8×10^{15} cm⁻² for thermal neutron, which is equivalent to the 20-year cumulative fluence of the most severely irradiated areas of fibers of ETS in ITER. The performance deterioration due to neutron irradiation was investigated by comparing the wavelength dependence of transmitted signal before and after irradiation.

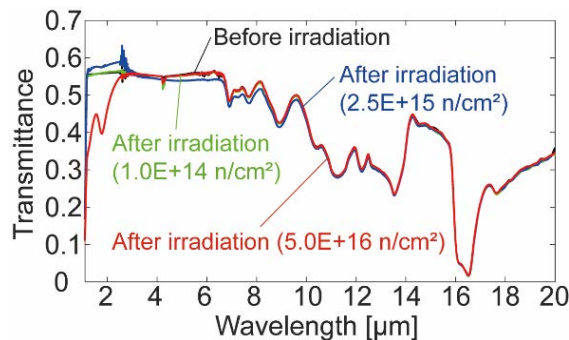


Fig. 1: Irradiation test result of Si samples.

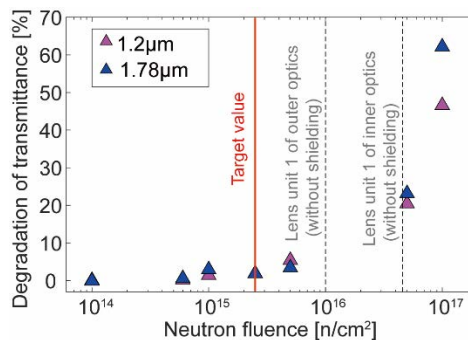


Fig. 2: Dependence of transmittance degradation of Si on neutron fluence.

RESULTS: Wavelength dependences of the signal before and after irradiation were compared. When normalized by the signal intensity of 743 nm, which was the peak value, the wavelength dependence of the signal was almost unchanged before and after neutron irradiation. It is unlikely that the transmittance was uniformly deteriorated in a wide wavelength range. This result indicates that it is highly possible that the spectral transmittance is not deteriorated by neutron irradiation in ITER.

ON GOING INVESTIGATIONS AND PROSPECTS:

The neutron irradiation test of grass materials (KU-1, KUVI) which will be used as vacuum window of Divertor Impurity Monitor was performed and the effect of the neutron irradiation on spectral transmittance is being investigated.

The preamplifier of Microfission Chamber (MFC) amplifies and converts the weak signal from the MFC detector into a noise tolerant strong output. The preamplifier will be installed in the port cell area and maximum neutron flux at the installation position of the preamplifier could become about 2.0×10^6 n/cm²s. However, the effects on neutrons have not been evaluated yet. Therefore, in order to evaluate how much neutron shielding is needed neutron irradiation tests on the preamplifiers will be conducted in 2022

REFERENCES:

- [1] B. Bigot, Fusion Eng. Des., **146**, 124 (2019).
- [2] L. J. Cheng and J. C. Corelli, Phys. Rev. **152**, No.2, 761-774 (1966).

CO4-24 Vacancy Formation by Al Doping in β -FeSi₂ Studied by a Reactor-Based Slow Positron Beam

A. Yabuuchi

*Institute for Integrated Radiation and Nuclear Science,
Kyoto University*

INTRODUCTION: β -FeSi₂ is expected as an environmentally friendly infrared luminescent material. However, further enhancement of luminescence intensity is desired for practical use. Doping of β -FeSi₂ with Al atoms which substitute Si sites has been reported to enhance the luminescence intensity [1]. The enhancement of luminescence intensity was considered to result from the filling of Si vacancies with Al atoms. In this study, defects in β -FeSi₂ thin films doped with Al atoms occupying Si sites and Mn atoms occupying Fe sites were investigated with a slow positron beam.

EXPERIMENTS: Undoped, Al-doped, and Mn-doped β -FeSi₂ films were prepared by the ion-beam synthesis method [1]. Each sample is expected to have a β -FeSi₂ layer with a thickness of around 60 nm on the surface of the Si substrate. These samples were probed by a slow positron beam at the Kyoto University Research Reactor [2]. The Doppler broadening of annihilation radiation (DBAR) spectra were acquired. All samples were treated with dilute hydrofluoric acid to remove oxide films before measurement. The shape of the obtained DBAR spectra was characterized in terms of the S -parameter [3], which depends on the fraction of positron annihilation with low momentum electrons.

RESULTS: Figure 1 shows S -parameters as a function of incident positron energy for each sample. The Al-doped sample shows an increase in S -parameters. This indicates that Al doping leads to the formation of vacancies. Figure 2 shows the positron implantation profile when positrons are implanted into β -FeSi₂ with an energy of 3 keV. The incident positron energy was fixed at 3 keV to probe the β -FeSi₂ layer formed on the Si substrate surface of each sample, and the coincidence DBAR spectra were acquired. Figure 3 shows the coincidence DBAR spectra of each sample normalized by that of the reference sample (Si), called the ratio curves. The peak around $11 \times 10^{-3} m_0 c$ is reduced in the Al-doped sample, indicating that the spectral shape is closer to that of Si. This means that the vacancies contained in the Al-doped sample are Fe vacancies. Contrary to the previously considered hypothesis, Al-doping was found to result in the formation of Fe vacancies.

REFERENCES:

- [1] Y. Terai and Y. Maeda, Appl. Phys. Lett., **84** (2004) 903.
- [2] A. Yabuuchi, Nucl. Instrum. Method Phys. Res., Sect. B **513** (2022) 44.
- [3] F. Tuomisto and I. Makkonen, Rev. Mod. Phys. **85** (2013) 1583.

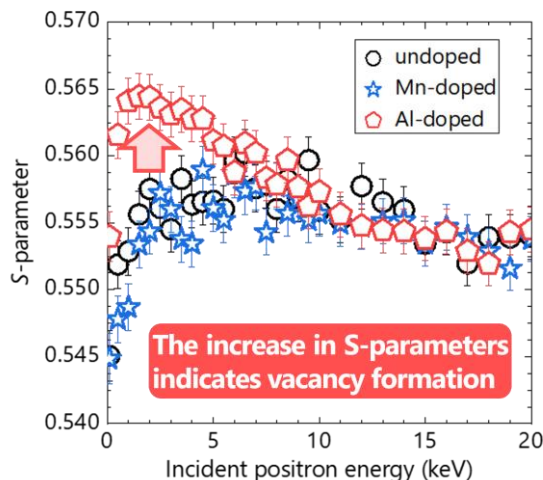


Fig. 1. S -parameters as a function of incident positron energy for each sample.

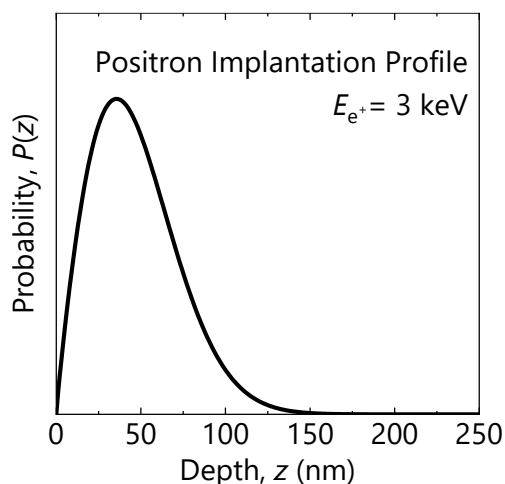


Fig. 2. Implantation profile of positrons implanted into β -FeSi₂ with an energy of 3 keV.

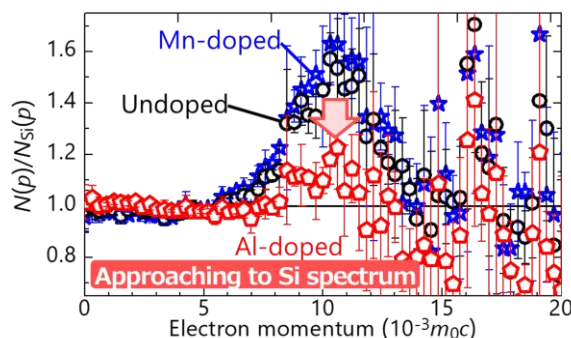


Fig. 3. Coincidence DBAR spectra obtained for each sample at incident positron energy of 3 keV. Each spectrum is normalized by that of Si.

CO4-25 Change in Fe valence state of Fe and Ni substituted Li_2MnO_3 positive electrode material during different charge and discharge depths by ^{57}Fe Mössbauer spectroscopy

M. Tabuchi and Y. Kobayashi¹

National Institute of Advanced Industrial Science and Technology (AIST)

¹Kyoto University Institute for Integrated Radiation and Nuclear Science

INTRODUCTION: The Fe and Ni substituted Li_2MnO_3 (present composition: $\text{Li}_{1+x}(\text{Fe}_y\text{Ni}_{0.3-y}\text{Mn}_{0.7})_{1-x}\text{O}_2$, $0 < x < 1/3$) is an attractive positive electrode material for next-generation and large-scale lithium-ion battery (LIB) [1]. To use it for LIB to the electric vehicle (EV), minimizing Ni content and utilizing Fe as redox center are necessary to avoid the risk of depletion for Ni source.

To accomplish above subject, understanding Fe valence change during different charge and discharge depths is needed by ^{57}Fe Mössbauer spectroscopy.

EXPERIMENTS: The sample was prepared by coprecipitation-calcination method. Water-soluble Fe, Ni and Mn salts dissolved in distilled water and dripped into NaOH solution at +20°C for 2-3 h. The coprecipitate was aged and oxidized by bubbling with O_2 flow for 2 days. The product was washed with distilled water and then was filtered. It mixed with Li_2CO_3 ($\text{Li}/(\text{Fe}+\text{Ni}+\text{Mn})=2$) into distilled water to make homogeneous slurry. The dried slurry was used as a precursor. The precursor was powdered using vibration mill and then was calcined at 650 °C for 5h in air. The product was milled again and calcined at 850 ($y=0.15$ and 0.20) or 900 °C ($y=0.10$) for 5h in air or N_2 flow. After each calcination, the product was washed with distilled water and then continue to the filtration and drying processes.

The samples were characterized by X-ray diffraction (XRD), chemical analysis and half-cell tests. The lithium metal and 1.5 M LiPF_6 EC-DMC (3:7) used as anode and electrolyte, respectively. The velocity axis of ^{57}Fe Mössbauer spectra was calibrated by α -Fe.

RESULTS: The XRD patterns for all samples can be indexed by monoclinic Li_2MnO_3 -type structure ($C2/m$). The crystallographic parameters depend on calcination atmospheres even at same transition metal (TM) ratio; the lattice parameters and volume and sum of TM occupancy (g_{total}) for the sample calcined in N_2 were larger than those for the sample calcined in air. The elemental analysis data showed that nominal Fe:Ni:Mn ratio was kept after preparation and the $\text{Li}/(\text{Fe}+\text{Ni}+\text{Mn})$ ratio for the sample calcined in N_2 was smaller than that for the sample calcined in air. These results mean that at least one of TM ions in sample calcined in N_2 was reduced. Fe valence state was checked by ^{57}Fe Mössbauer spectroscopy for the sample with $y=0.15$. The area fraction of minor $\text{Fe}^{3.5+}$ or Fe^{4+} component for the sample calcined in N_2 was smaller than that for the sample calcined in air. Therefore, Fe valence state is responsible for the calcination atmosphere.

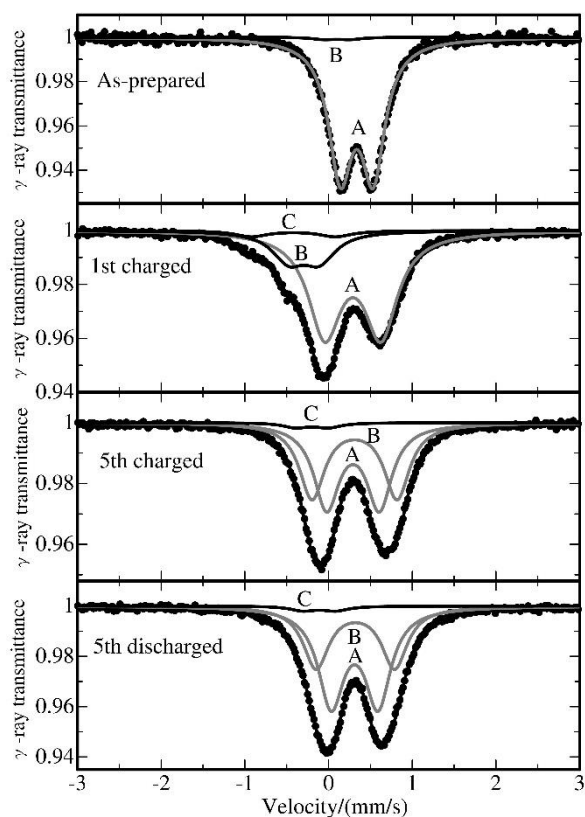


Fig. 1 ^{57}Fe Mössbauer spectra for $\text{Li}_{1+x}(\text{Fe}_{0.15}\text{Ni}_{0.15}\text{Mn}_{0.7})_{1-x}\text{O}_2$ ($0 < x < 1/3$) calcined in N_2 . Gray symmetric doublet corresponds to high-spin trivalent iron.

Fig. 1 depicts change in Fe valence state during different charge and discharge depths for $\text{Li}_{1+x}(\text{Fe}_{0.15}\text{Ni}_{0.15}\text{Mn}_{0.7})_{1-x}\text{O}_2$ ($0 < x < 1/3$) calcined in N_2 atmosphere. On 1st charging, pentavalent Fe components (B and C) [2] were observed with trivalent one (A), indicating that Fe^{3+} to Fe^{5+} oxidation behavior was detected. The area fraction of pentavalent Fe component is drastically reduced at the end of charging (5th charging), meaning that most Fe ion is trivalent state. Almost same spectrum was obtained at 5th discharged state. The results show that the trivalent iron was utilized on initial Li-extraction process. Therefore, suppress of pentavalent iron reduction until the end of charging is necessary to improve its electrochemical performance.

REFERENCES:

- [1] M. Tabuchi *et al.*, J. Power Sources, **196** (2011) 3611-3622.
- [2] G. Demazeau *et al.*, Mat. Res. Bull., **16** (1981) 1465-1472.

CO4-26 Evaluation of Structural Vacancies for Semiconducting Quasicrystal Approximant Al-Si-Ru by Positron Annihilation Spectroscopy

K. Kitahara¹, K. Kimura¹, A. Kinomura², Q. Xu²,
N. Oshima³, Y. Ohta⁴, I. Kanazawa⁴

¹Department of Advanced Materials Science, The University of Tokyo

²KURNS

³National Institute of Advanced Industrial Science and Technology

⁴Department of Physics, Tokyo Gakugei University

INTRODUCTION: One interesting feature of many exotic physical properties of Al-based quasicrystals is tendency to show high electrical resistivities and negative temperature coefficients[1]. The physical origin of these anomalous properties has not been satisfactorily explained so far. Semiconducting quasicrystals have attracted attention, not only from the perspective of the academic field, but also from the standpoint of application to thermoelectric materials to realize a direct conversion between the thermal and electrical energies. Kimura et al.[2] have shown that the vacant centers of the Al-based icosahedral clusters plays an important role for stabilities and chemical bonding nature of clusters. The various experimental results[3-5] support that the structural vacancy of the icosahedral clusters plays an important role in the bonding nature and electronic transport properties in Al-based quasicrystals and approximants. Recently Kimura and coworkers[6] have discovered the semiconducting-like quasicrystal approximant of Al-Si-Ru. It is of significance to study the semiconducting Al-Si-Ru quasicrystal approximant from the standpoint of structural vacancies. Positron annihilation method is powerful one for detecting structural vacancies of icosahedral quasicrystals[7]. In this study, we have estimated structural vacancies of the semiconducting quasicrystal approximant of Al-Si-Ru by means of positron annihilation methods.

EXPERIMENTS :

Bulk samples of 1/0-Al-Si-Ru and χ phase Al-Si-Ru were sealed in a quartz tube and annealed for 1 week at 1000 C and annealed for 1 week at 927 C, respectively. The phase characterization was performed by X-ray diffraction. The Doppler broadening spectra were measured using a slow variable mono-energetic positron beam. CDB measurements were performed with a collinear setup of two Ge detectors.

RESULTS and DISCUSSIONS:

Figure 1 shows X-ray diffraction patterns of C-phase $\text{Al}_{69}\text{Si}_{17.5}\text{Ru}_{23.5}$ (from up, C0, C2, C5, C9) and a diffraction pattern of the model of approximate 1/0 Al-Si-Ru (down). By using the slow positron beam, we have estimated the change in S-parameter with positron-incident energies in C-phase $\text{Al}_{69}\text{Si}_{17.5}\text{Ru}_{23.5}$ (semiconduction approximate) and χ phase $\text{Al}_{66}\text{Si}_{15}\text{Ru}_{19}$. In both materials, S-parameter increases remarkably from ~ 0 to ~ 1 keV. This

means that density of structural vacancies of C-phase Al-Si-Ru is comparable with that of χ phase Al-Si-Ru. Comparing with other experiment results[5,8], densities of structural vacancies of C-phase Al-Si-Ru and χ phase Al-Si-Ru are comparable with those of $1/1\text{Al}_{73}\text{Re}_{17}\text{Si}_{10}$ [5] and $1/0\text{AlPdRu}$ [8]. Taking account of the previous studies[5,9], densities of structural vacancies of C-phase Al-Si-Ru and χ phase Al-Si-Ru are estimated to be order of 10^{20} cm^{-3} . Then we have done the coincidence Doppler broadening(CDB) spectra of C-phase Al-Si-Ru and χ phase Al-Si-Ru.

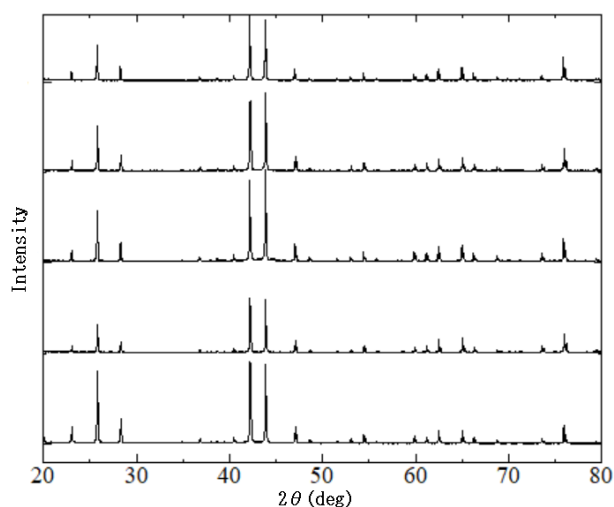


Figure 1: X-ray diffraction patterns of C-phase $\text{Al}_{69}\text{Si}_{17.5}\text{Ru}_{23.5}$ and the model of 1/0 Al-Si-Ru (from up to down).

Experimental results suggested strongly that the trapping sites of C-phase and χ phase seem to be similar. The present study shows that there exist deformed Mackay clusters[10] with vacant centers in semiconducting C-phase Al-Si-Ru.

REFERENCES:

- [1] K. Kimura and S. Takeuchi, in Quasicrystals: The State of Art, 2nd ed., D.P. Divincenzo and P.J. Steinhart, eds., World Scientific, Singapore, 1999, pp.325-309.
- [2] K. Kimura et al., J. Solid State Chem. 133(1997)302.
- [3] K. Sato et al., Phys. Rev. B 59(1999)6712.
- [4] K. Kirihara et al., Phys. Rev. Lett. 85(2000)3468.
- [5] K. Yamada et al., Phil. Mag. 98(2018)107.
- [6] Y. Iwasaki et al., Phys. Rev. Mater. 3(2019)61601.
- [7] I. Kanazawa et al., Phys. Rev. Lett. 79(1997)2269.
- [8] M. Nakajima et al. in preparing.
- [9] K. Sato et al., Appl. Surf. Sci. 194(2002)155.
- [10] R. Simura et al., Mater. Trans. 58(2017)1101.

CO4-27 Effect of gamma radiation on ultra-micro structure of hardwood cell-wall

K. Murata, Y. Imataki, M. Nakamura, T. Saito¹

Graduate School of Agriculture, Kyoto University

¹Institute for Integrated Radiation and Nuclear Science, Kyoto University

INTRODUCTION: Space-wood project (LignoStella project) is performed by Kyoto University collaborating with Sumitomo forestry Co Ltd in order to challenge to use wood-material in outer space. Firstly, possibility to use wood material in outer space has to be confirmed because a small wooden artificial satellite is going to launch until 2023. Space exposure test of wood specimen started on ExBAS at ISS in March 4, 2020. The wood specimen is going to be exposed until Dec. 2020. They will be affected by atomic oxygen and cosmic ray. In this study, effect of gamma-ray irradiation on cell-wall of wood material was studied on the ground in parallel with the exposure tests in outer space.

EXPERIMENTS: The sample was Honoki (*Magnolia obovate*), which is 100 mm (length) × 10 mm (radial) × 2 mm (tangential) in size. They were conditioned in 20 °C and 60%RH for a few weeks before the dose test. They were irradiated for 5 hours, and four types of dose was performed, which is 30 kGy, 3 kGy, 1kGy and 0.1 kGy. Before and after irradiation, bending test was performed to obtain Young's modulus in 3 point bending test until 5 N. After irradiation, ultra-micro structure of cell wall was observed using a small angle X-ray scattering analysis (SAXS) (Rigaku, Nano-viewer). The camera distance was 1000 mm and X-ray scattering (wave length 0.154 nm) was recorded by 2-dimensional detector (PI-LATUS 100K). Diameters of particle or pore and fractal dimension, distance between crystals were measured using scattering profiles.

RESULTS: As shown in Fig. 1, density of wood specimen of 30 kGy dose decreased by approximately 1 kg/m³ more than other dose specimens. Young's modulus of wood specimen of 30 kGy dose changed by gamma irradiation, but other specimen did not change even if density

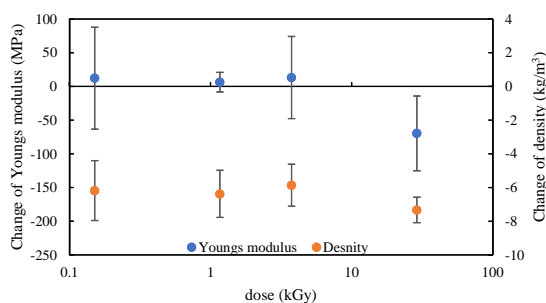


Fig. 1. Change of specific Young's modulus and density by gamma irradiation.

decreased. As shown in Fig. 2, fractal dimensions did not change by irradiation. We think that mass fractal dimension show density of electron in cell-wall matrix, and meso-pore in cell-wall may not change by irradiation. As shown in Fig. 3, diameters of particle or pore were obtained using Guinier plot. The size was similar to diameter of cellulose micro fibril (CMF), so we determine that the particle is CMF. Diameters of CMF decreased slightly by irradiation. As shown in Fig. 4, distances of CMF were obtained using Krathy plot. The change in distance was similar to that of the diameter. But, we can not understand why Young's modulus and density of 30 kGy decreased more than other species.

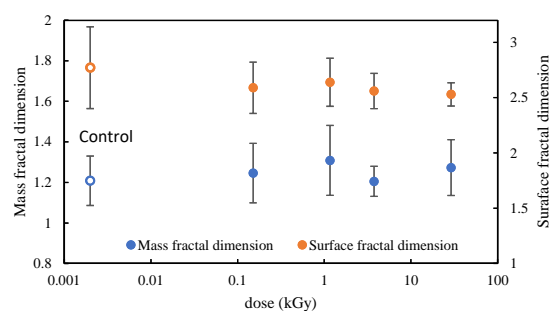


Fig. 2. Change of fractal dimension by gamma irradiation.

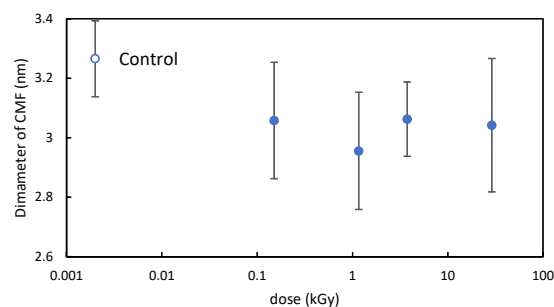


Fig. 3. Change of diameter of CMF by gamma irradiation.

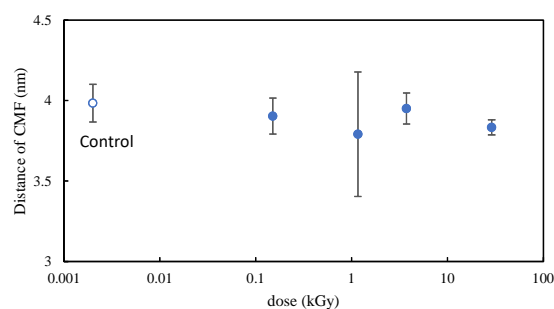


Fig. 4. Change of distance of CMF by gamma irradiation.

CO5-1 Trace elements, halogen, and Ar-Ar/I-Xe analyses of the Hayabusa2 returned samples

R. Okazaki¹, S. Sekimoto², N. Shirai³, N. Iwata⁴, and Y. N. Miura⁵

¹*Department of Earth and Planetary Sciences, Kyushu University*

²*KURNS*

³*Department of Chemistry, Tokyo Metropolitan University*

⁴*Faculty of Science, Yamagata University*

⁵*Earthquake Research Institute, University of Tokyo*

INTRODUCTION: The spacecraft Hayabusa2 brought back the surface and sub-surface materials from the C-type near-Earth asteroid (162173) Ryugu [1]. The Ryugu samples were allocated to the volatile sub-team, which is one of the Hayabusa2 initial analysis sub-teams [2]. As part of the volatile team's studies, we conducted combination analyses of the neutron-irradiated Ryugu samples to determine the abundances of minor/trace elements by Instrumental Neutron Activation Analysis (INAA), Ar-Ar and I-Xe ages, and the halogen abundances. Prior to the neutron-irradiation, Fourier-Transform Infrared (FT-IR) spectroscopy, Field-Emission Scanning Electron Microscope (FE-SEM) observation, and Secondary Ion Mass Spectrometry (SIMS) analysis were carried out [3]. Measurements of the native volatile compositions such as noble gas and nitrogen isotopes were also carried out using different grains of the Ryugu samples [4, 5]. These analytical results provided important information about the evolution history of the primitive bodies in the early solar system.

EXPERIMENTS: In advance of the Hayabusa2 sample analyses, the rehearsal was conducted in July 2021 using meteorite samples (Allende, Murchison, Bjurböle, and Shallowater) and our standard samples (JB-1, BHVO-2, DTS-2b, MMhb1, orthoclase, and wollastonite). For short-lived nuclide measurements, NaCl and CaCO₃ standards were also prepared. Each of the samples was encapsulated in diamond dishes sealed with polyester tape. The samples in the diamond dishes were first subjected to the Pn3 irradiation for gamma ray measurements of short-lived nuclide measurement (project #: R3038, PI: N.S.). Prior to the Hydro irradiation, the polyester tapes were removed from the diamond dishes. Each of the diamond dishes was wrapped with pure aluminum foil and encapsulated in the Hydro irradiation capsules for long-live nuclide measurement and conversion of halogens and potassium to noble gases (project #: R3127, PI: Y.N.M.).

In June 2021, the Hayabusa2 samples (typically 0.8 mm-sized individual grains) were allocated to the volatile sub-team. Each of them was pressed onto pure Cu disks and pelletized. The pelletized samples were studied by the FT-IR, FE-SEM, and SIMS analyses prior to the INAA and noble gas analyses. After the SIMS analysis, each of the pelletized samples was removed from the Cu disks to collect in the diamond disk containers. Each of

the samples in the diamond container was measured for short-lived nuclides (project #: R3038, PI: N.S.), and then subjected to the Hydro irradiation (project #: R3121, PI: N.I.). As in the rehearsal, the meteorite samples and the standard samples were also analyzed in the same way as the Hayabusa2 samples.

REUSLTS and DISCUSSION: In the rehearsal, short-lived nuclides (²⁴Na, ²⁷Mg, ²⁸Al, ³⁸Cl, ⁴⁹Ca, ⁵¹Ti, ⁵²V and ⁵⁶Mn) were determined for Allende and Murchison samples by gamma-ray measurements. Noble gas isotopes were measured for the mineral standard samples. These results of the rehearsal confirmed the validity of our measurement procedures.

The Hayabusa2 samples were irradiated in the Hydro irradiation term of Oct. 2021. One month later, the irradiated samples were removed from the irradiation capsule, and it was found that the irradiation capsule had been flooded by reactor cooling water during the irradiation. The Al foils that wrapped the sample-containing disks became gray, cloudy and hardened (Fig. 1). The samples were carefully recovered from the disks, and long-lived nuclides (⁴⁶Sc, ⁵¹Cr, ⁵⁸Co, ⁵⁹Fe, ⁶⁰Co, ⁶⁵Zn, ⁷⁵Se, ¹⁵²Eu and ¹⁹²Ir) were measured.

After the gamma ray measurements, only small amounts of the samples were transferred to Kyushu Univ., enough to ensure that no radioactivity was detected. The effects of alteration due to the exposure to water are being evaluated based on the noble gas compositions of the standard and meteorite samples.



Fig. 1. Recovered diamond dishes after the Hydro irradiation.

REFERENCES:

- [1] Tsuda *et al.*, *Acta Astronaut.*, **171** (2020) 42-54.
- [2] Tachibana *et al.*, *Hayabusa Symposium 2021* (2021) abstract #S1-3.
- [3] Okazaki *et al.*, *Hayabusa Symposium 2021* (2021) abstract #S1-7.
- [4] Okazaki *et al.*, *53rd Lunar and Planetary Science Conference* (2021) abstract #1348.
- [5] Byrne *et al.*, *53rd Lunar and Planetary Science Conference* (2021) abstract #2096.

CO5-2 Track observation in muscovite irradiated by ^{252}Cf and ^{241}Am sources

N. Hasebe, T. Nakashima¹, K. Miura¹, U. Uyangaa¹, G. Shuukhaaz¹, K. Oohashi², S. Akutsu², Y. Iinuma³, and K. Takamiya³

Institute of Nature and Environmental Technology, Kanazawa University

¹*Graduate School of Natural Science and Technology, Kanazawa University*

²*Graduate School of Science and Technology for Innovation, Yamaguchi University*

³*Institute for Integrated Radiation and Nuclear Science, Kyoto University*

INTRODUCTION: Uranium or thorium emit alpha particles and U,Th/He or U/Pb datings is applied to geological samples. When parent atoms emit alpha particles, these parent atoms recoil in accordance with the law of momentum conservation and leave disordered parts in crystal structure. When chemically etched, these disordered parts are selectively dissolved and leave tracks, which are known as alpha recoil tracks (ARTs), on the etched surface of geological samples (Fleischer, 2003). Compared to the fission tracks, which are formed by the travel of ionized particles with more energy than recoiling, ARTs are expected to be small and thus less commonly used in Geology. To establish ART dating, knowledge on their appearance under particular sample treatment and observation equipment is necessary. Here in this study, we tried to create artificial ARTs by ^{252}Cf (Hashimoto et al., 1989) and ^{241}Am sources.

EXPERIMENT: Mica samples with clear cleavage is used as an ART recorder. Uranium and thorium concentrations of the mica are measured by the LA-ICPMS beforehand, and the results was under the detection limit. However, when etched with 48% HF for 2h at 32°C, two types of tracks are observed (Figure 1). One is the size of about 10µm in diameter and deep, the others show variety of size and shallow, almost invisible. Therefore mica sheets were first annealed at 600°C for 5 hours then irradiated under the vacuum by ^{252}Cf and ^{241}Am sources at the Cf facility, KUR.

RESULTS: Because ^{252}Cf sources (200MBq and 1MBq were available) are rather strong and accompany by spontaneous fission, the resultant irradiated mica had so many fission tracks and they made the observation of ART difficult. When the cover of 200MBq ^{252}Cf source was tested as a irradiation source, the strength of activity was fine, but the distribution was heterogeneous, again not suitable for experiment. When ^{241}Am source (around 200kBq) was tested, the number of tracks on the mica surface was increased against time (Figure 2), and indicate that ^{241}Am source is capable of giving artificial ART on crystals. Hereafter, after investigating the registration efficiency on the mica sheet, we will irradiate other minerals to see shape and registration efficiency of ART therein. Then we plan to apply ART dating to un-

known geological samples.

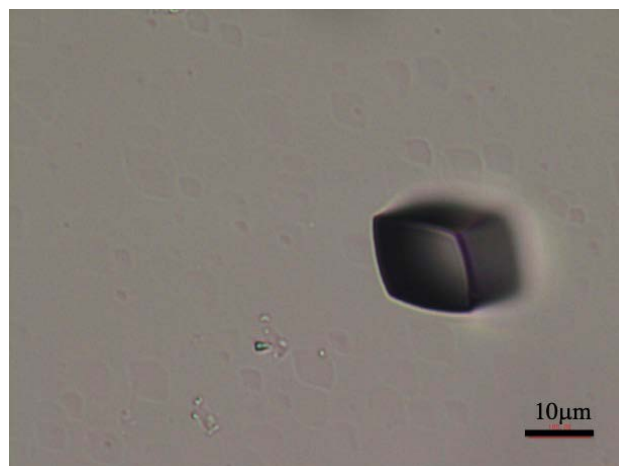


Fig. 1. Microscopy photo of mica after etching without annealing nor artificial irradiation.

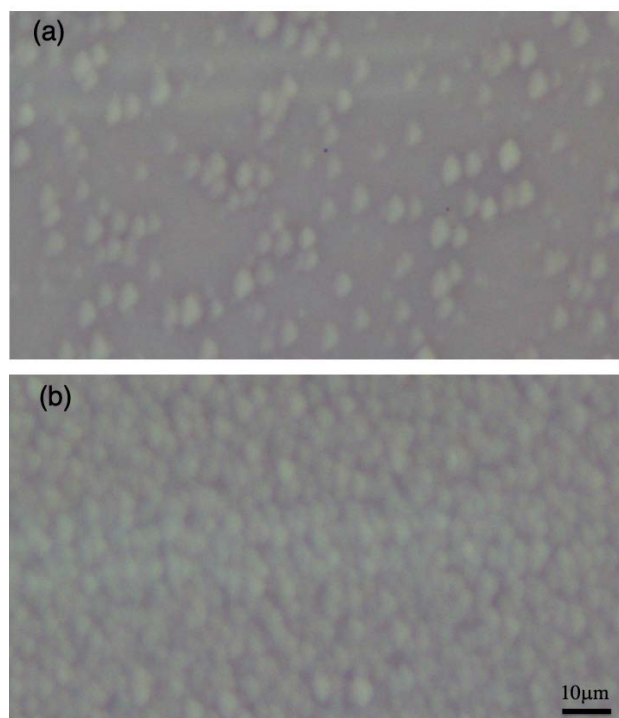


Fig. 2. Phase contrast microscopy photo of mica after annealing, irradiation and etching. (a) after 12h irradiation. (b) after one week irradiation

REFERENCES:

- [1] Fleischer, R.L. Geoch. Cosmoch. Acta 67, 4769-4774 (2003).
- [2] Hashimoto, T., et al, Nuclear Tracks, 4, 263-269 (1980).

CO5-3 Volcanic and Tectonic History of Philippine Sea Plate (South of Japan) Revealed by $^{40}\text{Ar}/^{39}\text{Ar}$ Dating Technique

O. Ishizuka, S. Sekimoto¹, R. Okumura¹, H. Yoshinaga¹,
Y. Iinuma¹, T. Fujii²

Geological Survey of Japan, AIST

¹*Institute for Integrated Radiation and Nuclear Science,
Kyoto University*

²*Graduate School of Engineering, Osaka University*

INTRODUCTION:

Robust tectonic reconstruction of Philippine Sea Plate evolution for the period immediately before and after subduction initiation at ~52 Ma along the western Pacific margin is prerequisite to understand cause of subduction initiation and test competing hypotheses for subduction initiation such as spontaneous or induced nucleation (e.g., Stern, 2004). Since gravitational instability between the neighboring plates is thought to be a critical factor for subduction initiation (e.g., Leng and Gurnis 2015), it is important to understand the age, origin and crustal structure of the overriding plate.

In this study we have investigated magmatism in the oldest part of the Philippine Sea Plate to 1) reveal for the first time the age and origin of Kita-Daito Basin and the intervening Daito Ridge Group; 2) understand origin of Eocene magmatism widely distributed in and around the Daito Ridge Group. The outcome of these studies will assist in understanding the time sequence of magmatic and tectonic events which took place within a relatively short period around 45-52 Ma, i.e., during and after subduction initiation along the Pacific margin.

EXPERIMENTS: Ages of the igneous rocks were determined using the $^{40}\text{Ar}/^{39}\text{Ar}$ dating facility at the Geological Survey of Japan/AIST. 10-15 mg of phenocryst-free groundmass, crushed and sieved to 250 – 500 μm in size, was analyzed using a stepwise heating procedure. The samples were treated in 6N HCl for 30 minutes at 95°C with stirring to remove any alteration products (clays and carbonates) present in interstitial spaces. After this treatment, samples were examined under a microscope. Sample irradiation was done either at the Kyoto University Reactor (KUR). The neutron irradiation was performed for 10 h at the hydro-irradiation port under 1 MW operation, where thermal and fast neutron fluxes are 1.6×10^{13} and 7.8×10^{12} n/cm² s, respectively, or for 2 h under 5 MW operation, where thermal and fast neutron fluxes are 8.15×10^{13} and 3.93×10^{13} n/cm² s respectively. Argon isotopes were measured in a peak-jumping mode on an IsotopX NGX noble gas mass spectrometer fitted with a Hamamatsu Photonics R4146 secondary electron multiplier.

RESULTS: 9 samples have been dated by the laser-heating $^{40}\text{Ar}/^{39}\text{Ar}$ dating technique. Andesitic rocks from the basin floor of the Kita-Daito Basin show age range between 41.04 and 46.11 Ma. Andesites and basalts from the Northern Philippine Sea Seamounts gave age range between 42.10 and 46.29 Ma. Dioritic samples from the KPR–Daito Ridge intersection were dated on biotite separates by stepwise heating analysis. For the sample 6K1438R11, duplicate analyses gave consistent plateau ages of 48.1 ± 0.4 Ma and 47.66 ± 0.14 Ma. Porphyritic andesite from the southeastern part of the Oki-Daito Ridge returned slightly disturbed age spectrum with increasing ages with increasing laser output (i.e., temperature). 13 steps at higher temperature steps give indistinguishable ages with a weighted average of 109.30 ± 0.20 Ma.

SUMMARY:

1) Eocene andesitic magmatism (Northern Philippine Sea volcanics) has been discovered in and around the Kita-Daito Basin. $^{40}\text{Ar}/^{39}\text{Ar}$ and zircon U-Pb dating results of these igneous rocks indicate that the andesitic rocks formed mainly between 45 and 42 Ma.

2) The results of this study strongly imply that the Kita-Daito Basin postdate subduction initiation of the western margin of the Pacific Plate to form Izu-Bonin-Mariana arc.

3)

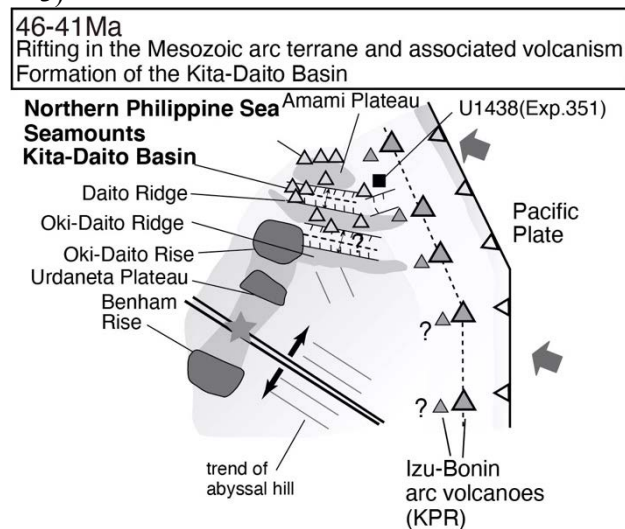


Fig. 1. Schematic tectonic history for the northern part of the Philippine Sea Plate (Ishizuka et al., 2022).

REFERENCES:

[1] O. Ishizuka *et al.*, *Geochem. Geophys. Geosyst.*, **23**, e2021GC010242. (2022)115-120.

CO5-4 Determination of Mercury content using INAA

N. Shirai¹ and S. Sekimoto²

¹Department of Chemistry, Tokyo Metropolitan University

²Institute for Integrated Radiation and Nuclear Science, Kyoto University

INTRODUCTION: Mercury is cosmochemically classified as a highly volatile element based on its condensation temperature, meaning that Hg is supposed to have condensed at a relatively low temperature from the hot solar nebular gas in the early solar system [1]. Elemental abundance of Hg can potentially be used as cosmo-thermometers. Geochemically, Hg is classified as a chalcophile element. Mercury provides us information about the mantle-core differentiation including core formation [e.g., 2]. There is a paucity of accurate Hg values in cosmochemical and geochemical samples due to the potential loss of Hg during analysis. It has been known that sample is easily contaminated with Hg in analytical laboratories, which could explain the extremely large variations of observed in meteorite samples [3]. Among the analytical procedure, INAA is suitable for the determination of Hg due to the non-destructive method. In INAA, two isotopes (¹⁹⁷Hg and ²⁰³Hg) were usually used. The 77.4 keV peak of ¹⁹⁷Hg could not be detected by INAA. Although the 279.2 keV peak of ²⁰³Hg could be detected, there is possibility of spectral interferences from Se and Ta. In this study, Hg abundances of environmental samples with having different Hg/Se ratios were determined by INAA, and the accuracy of the obtained values was evaluated.

EXPERIMENTS: JSAC 0601-2 (plastic), JSAC 0602-2 (plastic) and NIES No.5 (human hair), No.9 (sargasso) and No.13 (human hair) was used in this study. Mercury abundances for the four reference standard materials (JSAC 0601-2, 0602-2, NIES No.5 and NIES No.13) were reported as certified value, while reference value was reported for NIES No. 9. These samples weighing 20 – 40 mg were sealed in high pure polyethylene bag. Single element standard solutions for atomic absorption analysis were used for Se and Ta to confirm spectral interferences from these two elements. These standard samples were prepared by dropping known concentration solution of these elements on the three sheets of filter papers. Samples were irradiated for 1 h at the pn-2 of KURRI, whose thermal and fast neutron fluxes are 5.6×10^{12} and $1.2 \times 10^{12} \text{ cm}^{-2}\text{s}^{-1}$, respectively. After irradiation, samples were measured for gamma-rays several times with different cooling intervals.

RESULTS : The 279 keV peaks for all samples were detected. As the ⁷⁵Se and ¹⁸²Ta peaks interfere with the ²⁰³Hg peak at 279.2 keV and correction must be performed. The ¹⁸²Ta peaks for all samples analyzed in this study could not be detected. In this study, we estimated the ratio of the intensity of the gamma-ray peak of 264.7 keV to the 279.5 keV peak using a standard sample for Se. This ratio was applied to the 264.7 keV peak of the sam-

ple, and the intensity of the gamma-ray peak of 279.5 keV of ⁷⁵Se was subtracted from the those of 279.2 keV peak of ²⁰³Hg. The 264.7 keV peak of ⁷⁵Se could not be detected in JSAC 0601-2 (plastic), JSAC 0602-2 (plastic), and No.9 (sargasso), and the correction of spectral interference from Se was not made. For other elements, Se abundances were calculated by using a reference sample for Se, and the correction was performed. Among the samples analyzed in this study, JSAC 6020-2 has the highest Hg content, and the degrees of spectral interferences from ⁷⁵Se and ¹⁸²Ta were negligible. Thus, this sample was used as a reference standard for the determination of Hg. Analytical results were shown in Table 1, where certified values for Hg and Se are shown for comparison. Our Se values for NIES No. 5 and No. 13 are in good agreement with certified values. Our Hg value for JSAC 0601-2 was consistent with the certified value. However, differences in Hg values between our data and certified value were observed for the other three samples (NIES No. 5, No. 9, and No. 13). For NIES No. 9, no gamma-ray peaks for Se and Ta could be detected, and a correction was not performed. Our value was about eight times higher than the certified value. Contributions of spectral interferences from Se were about 5-6% for NIES No. 5 and 6-8% for NIES No. 13. Our values for NIES No. 5 and No. 13 were 25% and 13% higher than certified values, respectively. Although it is recommended that the minimum sample weight for NIES No. 5, No. 9, and No. 13 are 200, 400, and 120 mg, sample weights for these samples were 20 to 40 mg in this study. Differences between our data and certified values may be explained by sample heterogeneity. We need to confirm whether there is heterogeneity at the level of several ten mg of the sample by analyzing these samples with different weights.

Table 1. Analytical result for the four reference standard materials.

Reference material	Hg (ppm)		Se (ppm)	
	This work	Certified value	This work	Certified value
JSAC 0601-2 Plastic	1.30±0.05	1.3±0.1	n.d.	
NIES No.5 Human hair	5.49±0.17	4.4±0.4	1.50±0.16	1.4
NIES No.13 Human hair	4.97±0.13	4.4±0.4	1.84±0.10	1.79±0.17
NIES No.9 Sargasso	0.324±0.030	0.04	n.d.	

REFERENCES:

- [1] K. Lodders, *Astrophys. J.*, **591** (2003) 1220-1247.
- [2] D. Canil *et al.*, *Chem. Geol.*, **396** (2015) 134-142.
- [3] D. S. Lauretta *et al.*, *Earth Planet. Sci. Lett.* **171** (1999) 35-47.

CO5-5 Basic research on the trace elements analysis of airborne dust in the environment by INAA & PIXE

N. Hagura^{1,2}, T. Matsui¹, T. Uchiyama², H. Matsuura^{1,2}

¹ Nuclear Safety Engineering, Science and Engineering, Tokyo City University

² Atomic Energy Research Laboratory, Science and Engineering, Tokyo City University

INTRODUCTION: Compared to a few decades ago, when air pollution was a serious social problem, environmental standards are now properly defined and rarely cause negative influence on the human body. On the other hand, since the distribution of substances in the environment is known to have a large degree of variation, it is important to continuously sample and analyze the dynamics of elements over a long period of time.

The Atomic Energy Research Laboratory of Tokyo City University (TCU-AERL) operated the Musashi reactor until 1989 and has been conducting research using neutrons, including instrumental neutron activation analysis (INAA). Although now it is in the decommissioning phase, the facility is still in operation as a facility for conducting experiments using RI. In 2018, a 1.7 MV Pelletron tandem accelerator (TCU-Tandem) was installed to conduct trace element analysis using Particle Induced X-ray Emission (PIXE) [1]. As it becomes increasingly difficult to conduct experiments using research reactors, the advancement of analytical methods using accelerator ion beams is considered to be an effective. With the development of accelerator neutron sources also progressing, the realization of accelerator-based neutron activation analysis methods is also being considered.

We believe that the idea of combining ion beam analysis and neutron activation analysis may be effective as an analytical method for environmental samples that require analysis of a large number of samples in a short period of time.

In this study, we measured airborne dusts sampled at the TCU-AERL, where sampling has been ongoing since 2002 [2]. During the years since 2011, we have been studying the decay of radiocesium (Cs-137) and changes in its chemical form using another analytical method [3, 4].

EXPERIMENTS: We use a high volume air sampler (Shibata Scientific Technology LTD., HV-1000F, filter: ADVANTEC, QR-100 (collection efficiency: 99.99% for 0.3 μm particles)) with an inhalation flow rate of 700 L min^{-1} . The radioactivity of the filter that has collected dust is measured by a high-purity germanium semiconductor detector, and a part of the filter was stored for neutron activation analysis.

Irradiation was performed at the research reactor KUR at the Institute for Integrated Radiation and Nuclear Science, Kyoto University, between the July and August with four machine times in FY2021. The irradiation conditions are shown in Table 1. The measurement of radioactivity of short half-life nuclides was carried out using the HP-Ge semiconductor detector of the hot laboratory of KUR.

And long and medium-lived nuclides, after cooling for one or two weeks, transported to the TCU-AERL, and was measured by a HP-Ge semiconductor detector. JLK-1 was used as a comparative standard substance.

Table 1. Irradiation conditions.

Irradiation			Operating power	Thermal neutron flux
date	time	position		
2021/7/6	60 min	Pn-2	1 MW	5.5×10^{12} n/cm ² /sec
2021/7/27	30 sec	Pn-3		4.7×10^{12} n/cm ² /sec
2021/8/3	60 min	Pn-2		5.5×10^{12} n/cm ² /sec
2021/8/24	30 sec	Pn-3		4.7×10^{12} n/cm ² /sec

RESULTS: In FY2021, 24 samples sampled between 2014 and 2019 were measured. We plan to organize the data together with the results of past measurements. In addition, PIXE analysis is being conducted at TCU-Tandem. Fig. 1 shows an example of the results of PIXE analysis for mainly light elements in vacuum. In addition, we are now adjusting the beamline for PIXE measurement in air in order to measure more samples efficiently.

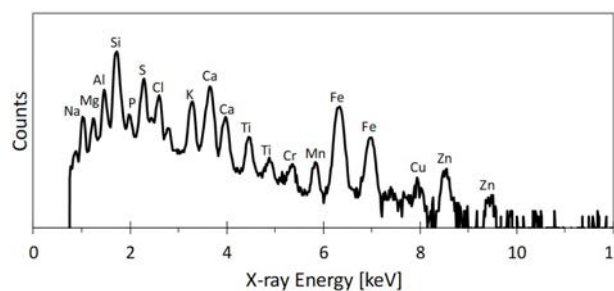


Fig. 1. An example of PIXE Spectra measured by PIXE beam line of TCU-Tandem.



Fig. 2. In-air PIXE analysis system at TCU-Tandem.

REFERENCES:

- [1] N. Hagura, *et al.*, Transactions of the Atomic Energy Society of Japan, 17 (3-4), pp. 111-117 (2018).
- [2] K. Hirose, *et al.*, Atmospheric Environment, 38 (38), pp. 6601-6608 (2004).
- [3] K. Nakamachi, *et al.*, Bunseki Kagaku, 64 (8) pp. 589-594 (2015).
- [4] N. Hagura, *et al.*, Bunseki Kagaku, 66 (3), pp. 201-204 (2017).

CO5-6 Long term change in soil elements of the atmospheric coarse particle observed at Sakai,Osaka

Norio Ito, Akira Mizohata, Yuto Iimura¹, Hisao Yoshinaga¹

Radiation Research Center, Osaka Prefecture University,

¹ Institute for Integrated Radiation and Nuclear Science, Kyoto University

Atmospheric aerosols, which are particles suspended in the atmosphere, have a particle size of 0.001 to 100 μm (radius when spherical) and have various chemical compositions. The particle size and chemical composition vary depending on where and how it was made. The fine particles of which particle size is smaller than 2 μm are almost made from the combustion process and through some chemical reactions of gaseous matters. Coarse particles of which size are larger than 2 μm are almost naturally derived particles such as soil particles and sea salt particles and particles made by physical fracture. Fine particles that enter the respiratory tract can affect the health. For the indirect effect of coarse particle, cloud formation and solar scattering, coarse particles contribute to the some factors on which a climate changes. Consequently, coarse particles do not have much direct health effects, but they can have a greater impact on humankind by their effecting on the climate.

Our observations of the aerosols at Sakai show that the change in atmospheric aerosol concentration observed in Sakai City since 1995 has been decreased for both fine and coarse particles. The decreasing tendency of fine particles was caused by the decrease of particles derived from anthropogenic sources due to environmental measures, but the decreasing tendency of coarse particles is unlikely to decrease due to environmental measures, and it is due to changes in the natural environment including land use. Coarse particles are greatly influenced by soil particles which are affected by soil particles from a wide area as well as around the observation point and also affected by areas more than 2000 km away, such as yellow sand particles from China land. We will evaluate how much the effect is near the observation point or far away (from China land). In this

report, we focus on the concentration change in aluminum (Al) and calcium (Ca), which are the main components of soil particles that occupy the main part of coarse particles, and have estimated the factors that cause the reduction of coarse particles.

We have collected the coarse particle (> 2 μm) in 5 particle size ranges (>11, 7.0-11, 4.7-7.0, 3.3-4.7, 2.1-3.3 μm) using Andersen sampler and analyzed the elemental composition concentration in each particle size range by neutron activation analysis. From the results of Al and Ca concentrations, we found the following.

1) The concentration of coarse particles have decreased (1995-2020) and also the main components Al and Ca tended to decrease. (Fig.1)

2) However, there was no clear decrease in the concentrations of Al and Ca in the particle size range with the largest particle size (> 11 μm), in which range the influence of the vicinity was large, but the concentrations of Al and Ca in the particle size range below this range have clear decrease trend.

From the above, we have concluded that the ratio of Al and Ca to silicon (Si), which is the main component of soil in the neighboring soil particles, might changed (Si cannot be analyzed by neutron activation analysis). This change in composition might be caused by the effect of changes in the properties of soil particles from the surrounding area. Because the concentration of coarse particles in March and April is not clearly decreasing compared to other periods, this shows that the influence of soil particles from mainly China land, which has a large impact during this period, has not decreased much. From this results, we have estimated that the influence of soil from the surrounding area might be changed by the land use and changes in rolled up soil particles due to changes in traffic volume.

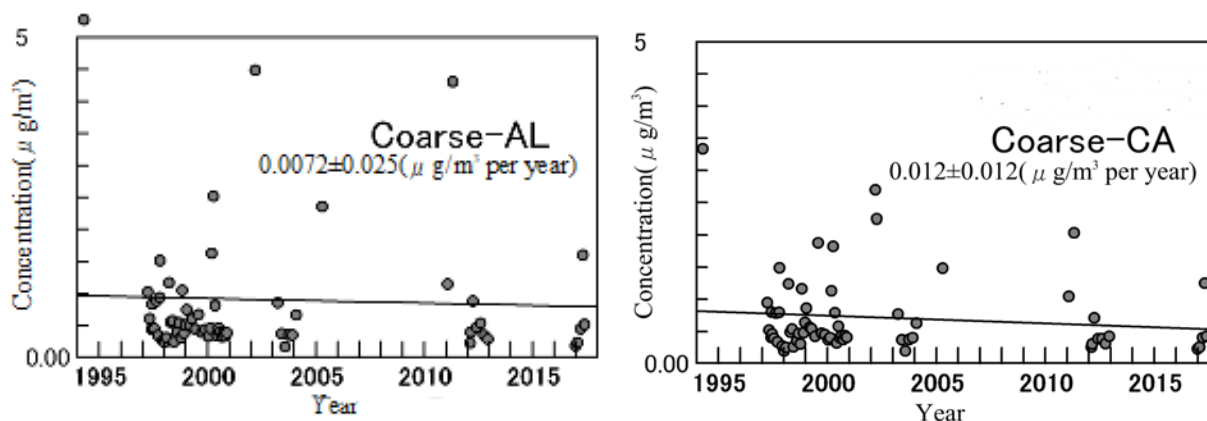


Fig.1 Long term (1995-2020) change in concentration of Al and Ca in the atmospheric coarse particle (>2 μm).

CO5-7 Eoarchean gneisses and their thermal histories

H. Hyodo¹, K. Sato^{1,2,3}, H. Kumagai³ and K. Takamiya⁴

¹ Institute of Frontier Science and Technology,
Okayama University of Science

² Department of Liberal Arts for Career Development,
Sakura no Seibo Junior College

³ Submarine Resources Research Center, Japan Agency
for Marine-Earth Science and Technology

⁴ Institute for Integrated Radiation and Nuclear Science,
Kyoto University

INTRODUCTION: The Canadian Shield has the oldest rocks; Acasta gneiss in the Northwest territory, and orthogneiss in the Saglek Block in the Labrador; both showing U-Pb age of c.a. 4.0 Ga [1]. We have already reported ⁴⁰Ar/³⁹Ar age results on zircons and potassic minerals [2]. Acasta gneiss results are consistent among all the minerals, giving 1.9-2.0 Ga ages of Wopmay orogen, whereas only Labrador zircon showed ages older than 4.0 Ga. Recent study [3] indicated that the part of Greenland possibly belonged to Rae Province which recorded c.a. 1.9 Ga event. These results suggest that the Labrador zircon somehow might have preserved the 4.0 Ga age. Zircon does not contain potassium, but it normally has many little inclusions. The age might originate from these inclusions with some potassium. We analyzed the gas release pattern of the Labrador and Acasta zircons, and compared the diffusion characteristics of the zircons.

EXPERIMENTS: Rock samples were sieved in #25-100 mesh. After ultrasonic cleaning in distilled water, single mineral grains were separated by handpicking. The mineral grains were irradiated using the hydraulic facility of KUR for 47 hours at 1 MW, and subsequently 6 hours at 5MW. The total neutron flux was monitored by 3gr hornblende age standard [4], irradiated in the same sample holder. In the same batch, CaSi₂ and KAlSi₃O₈ salts were used for interfering isotope correction. A typical J-value was $(1.183 \pm 0.090) \times 10^{-2}$. In stepwise heating experiment, the minerals were heated under defocused laser beam, and temperature of sub-millimeter grains was measured using infrared thermometer of which spatial resolution is 0.3 mm in diameter with a precision of 5 degrees. A feedback circuit for relatively long time-lag heating control is used not to overshoot the programmed temperature. Zircon has relatively high melting point, and a near-infrared laser was used for final fusion. Argon isotopes were measured using a mass spectrometer with mass resolution of approximately 400, allowing to separate hydrocarbon from ³⁹Ar and other argon isotopes.

RESULTS AND DISCUSSIONS: An example of argon release pattern of step heating results from a Labrador zircon grain is illustrated in Fig.1. The ⁴⁰Ar fraction at the highest temperature over 1400 degrees has a small error, giving a ⁴⁰Ar/³⁹Ar ratio of Eoarchean age (> 4.0 Ga). The

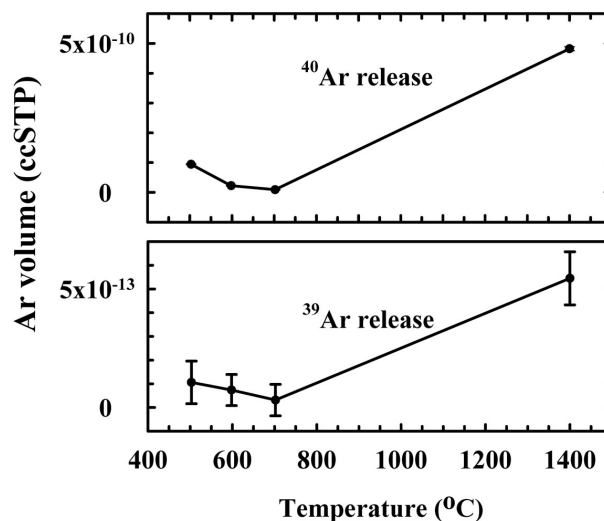


Fig. 1. ⁴⁰Ar/³⁹Ar release pattern during step heating of a Labrador zircon grain. The experimental error in ⁴⁰Ar analyses is very small while ³⁹Ar error is moderately large due to its small amount. The highest temperature step gave older than 4.0 Ga.

K-Ar and ⁴⁰Ar/³⁹Ar ages in Labrador area generally show c.a. 1.9 Ga. The results from Acasta gneiss showed that ⁴⁰Ar/³⁹Ar step ages of zircons are close to the and the U-Pb age of apatite (c.a. 1.9 Ga) [5]. Comparison of these results suggests that potassium carrier in the Labrador zircon did not experience the 1.9 Ga overprint event. In argon geochronology, presence of excess argon cannot be excluded in metamorphic rocks. In this case, the very high extraction temperature may play a key role to distinguish between the nearly-true age and excess age. The Labrador hornblende and biotite data do not suggest excess ages, and Wopmay orogen seems to have overprinted the Acasta zircon as well as hornblende and biotite. If we assume excess argon only in the Labrador zircon, we need to assume a special conditions to create excess argon only in the zircon at very high temperature. This may be clarified in view from P-T condition analyses in metamorphic petrology.

REFERENCES:

- [1] T. Komiya, *et al. Geoscience Frontiers* **8** (2017) 355-385.
- [2] H. Hyodo, K. Sato, H. Kumagai and K. Takamiya, *KURNS Progress Report 2019 CO5-7*.
- [3] K. Thrane, *Precambrian Research* **357** (2021) 106139.
- [4] J.C. Roddick, *Geochim. Cosmochim. Acta* **47** (1983) 887-898.
- [5] Y. Sano, *et al. Geochimica Cosmochimica Acta* **63** (1999) 899-905.

CO5-8 Absorption of alkali metal ions by white radish sprouts (III)

M. Yanaga, H. Nomura¹, K. Yamazawa¹, H. Yoshinaga²,
R. Okumura² and Y. Iinuma²

*Center for Radioscience Education and Research,
Faculty of Science, Shizuoka University*

¹*Department of Chemistry, Faculty of Science, Shizuoka
University*

²*KURNS*

INTRODUCTION: Previously, we reported that the absorption of radioactive cesium ions from contaminated soil into rice plants increased by adding stable cesium ions to irrigation water and that the possibility that the cesium ions added were replaced with radioactive cesium ions in soil [1, 2]. However, we also noted addition of excess amount of stable cesium caused an obstacle to growth of rice plant [3].

Therefore, in the present study, we examined the removal of radioactive cesium from soil through chemical treatment with various kinds of alkali ion solutions. At first, two types of soil, kuroboku soil (Andsols) and vermiculite were contaminated artificially to understand the distribution and behavior of radioactive cesium in soil and to provide insights into removal methods. Second, the effect of decontamination with alkaline ions on the growth of plants was investigated. In investigation of the behavior of trace elements in white radish sprouts, simulated decontamination with alkaline ions was performed on the soil containing no radioactive cesium and examined.

EXPERIMENTS: ¹³⁷Cs removal from soil A sample (30 g) of commercially obtained vermiculite or kuroboku soil was placed in a metal mesh, immersed in 300 mL of aq. ¹³⁷Cs (116 Bq) solution for one day, then removed from the solution and dried. After that, 100 mL of 0.140 mol/L KCl, RbCl or CsCl solution were added to a beaker containing the contaminated soil and the mixture was stirred. After stirring, the beaker of soil and solution was allowed to stand for 10 minutes, then, each soil was washed with pure water once or twice. The same treatments were applied to soil that was not contaminated with radioactive cesium.

Materials and Method The dried each soil mentioned above was placed in a plastic pot, wetted with pure water and 1.0 g of radish sprouts seeds were sown on it. After germination, Hyponex diluted 2000 times was added as liquid fertilizer. After that, they were cultivated for 14 days while giving only pure water as appropriate. White radish sprouts cultivated in soil without radioactive cesium were subjected to INAA.

INAA The samples in polyethylene capsules were irradiated in Pn-3 for 90 seconds and in Pn-2 for 4 hours, for short and long irradiation, respectively. As comparative standards, the certified NIST Standard Reference Material 1577b Bovine Liver as well as elemental

standard for Cs was used. The γ -ray spectroscopic measurements with an HPGe detector were performed repeatedly for the short-irradiated samples: the first measurements for 120 – 900 seconds after decay time of 5 - 15 minutes and the second one for 250 - 1200 seconds after 60 - 150 minutes. The long-irradiated samples were measured for 1 - 24 hours after an adequate cooling time (15 - 60 days).

RESULTS: When KCl solution was used as a decontamination agent, no growth disorder of white radish sprouts was observed. When a CsCl solution was used as a decontamination agent, radish sprouts cultivated in kuroboku soil that had not been washed with pure water after decontamination showed significant growth disorders. On the other hand, the growth disorder of radish sprouts cultivated with vermiculite was not so remarkable. This indicates that cesium ions are retained in kuroboku soil in a form that is easily absorbed by plants. When the RbCl solution was used as the decontamination agent, a slight growth disorder was observed for kuroboku soil that were not washed with pure water.

The decontamination effect estimated from the radioactive cesium absorbed by white radish sprouts was hardly observed in the KCl solution. As same as our previous report, the CsCl solution was able to remove some radioactive cesium from both kuroboku soil and vermiculite. On the other hand, although the RbCl solution had a low effect of removing cesium in vermiculite, a remarkable decontamination effect could be observed on kuroboku soil.

The concentration of trace elements in radish sprouts cultivated in soil after decontamination with RbCl is described. Even when cultivated in soil washed with pure water after decontamination treatment, the concentration of rubidium ions absorbed by radish sprouts was high. However, no abnormality was found in the concentrations of essential elements such as potassium and manganese. Just as there was no apparent growth disorder. Considering that the actual field soil is a mixture of kuroboku soil and clay minerals, it is necessary to consider the use of Rb ions, which are highly effective in decontaminating kuroboku soil.

REFERENCES:

- [1] M. Yanaga *et al.*, NMCC ANNUAL REPORT, 22 (2015)185-190.
- [2] M. Yanaga *et al.*, NMCC ANNUAL REPORT, 23 (2016)172-179.
- [3] M. Yanaga *et al.*, KURNS Progress Report 2018 (2019)CO5-10.

CO5-9 SEM-EDS analysis of fine particles produced from model debris, (U,Zr)O₂, by laser ablation for decommissioning of Fukushima Daiichi Nuclear Power Plant

A. Toyoshima, K. Takamiya¹ and H. Furutani²

Institute for Radiation Sciences, Osaka University

¹*Institute for Integrated Radiation and Nuclear Science, Kyoto University*

²*Center for Scientific Instrument Renovation and Manufacturing Support, Osaka University*

INTRODUCTION: Recently, first preliminary removal of the fuel debris remaining in Fukushima Daiichi Nuclear Power Plant (1F) is just trying to be started. In the removal, however, fine particles containing alpha emitters such as ²³⁵U and ²³⁹Pu are concerned to be generated in cutting the debris. We are therefore developing a novel real-time detection method of the scattered fine particles using Aerosol Time-Of-Flight Mass Spectrometer (ATOFMS) which can measure the particle size and can identify chemical composition and contained isotopes for each particle floated in carrier gas. At present, we are fabricating an enlargement and condensation apparatus to increase the detection sensitivity of ATOFMS by enlarging non-measurable tiny particles with ATOFMS to measurable-sized ones. The present study aims at evaluating influence of the enlargement and condensation of fine particles to detection sensitivity of ATOFMS by its surface observation. Here we carried out SEM-EDS measurement of modeled fine particles containing ²³⁸U without condensation.

EXPERIMENTS: Fine particles were prepared from (U,Zr)O₂ pellets as well as a ZrO₂ one by laser ablation. The pellets had different U/Zr ratios. Laser power was 20-30 kW. In a closed chamber, the pellet was irradiated by the laser. The generated fine particles were swept out of the chamber by carrier gas of dried air and were collected on a carbon tape in an impactor connected with a thin tubing. SEM-EDS measurement of the collected samples was carried out after the transportation of these to KURRI. Energy of bombarded electrons was 10 kV or 15 kV. SEM images and X-ray spectra of the samples were taken for a few tens of fine particles found on the carbon tapes.

RESULTS: In Fig. 1, a SEM image of the fine particles from the ZrO₂ pellets were demonstrated as an example. Many of tiny particles with a diameter of less than one micrometer and a few of larger particles were observed. We also analyzed the fine particle by EDS. An example is the particle in Fig. 1, in which analyzed point is depicted by a cross symbol. In Fig. 2, observed spectrum is showed. Characteristic X-rays of C, O, Y, and Zr are seen. Zr and O peaks from ZrO₂ are clearly observed. Because the commercially available ZrO₂ pellets used contains 8mol% Y₂O₃, the x-ray of Y is also detected. C is from the carbon tape as a support. For other fine particle samples prepared from (U,Zr)O₂, results are under analysis.

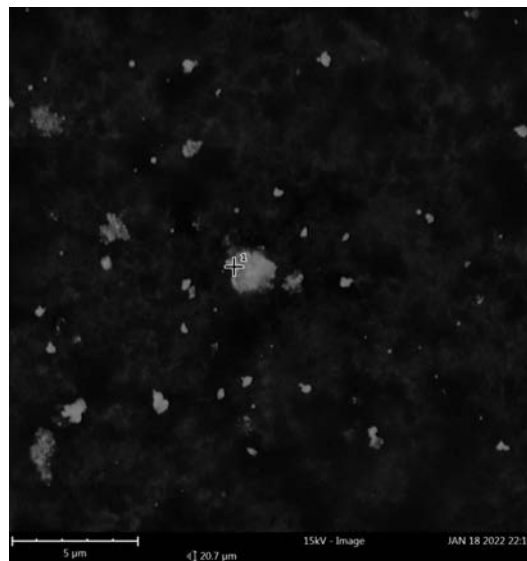


Fig. 1. SEM image of fine particles prepared from ZrO₂ pellet by laser ablation.

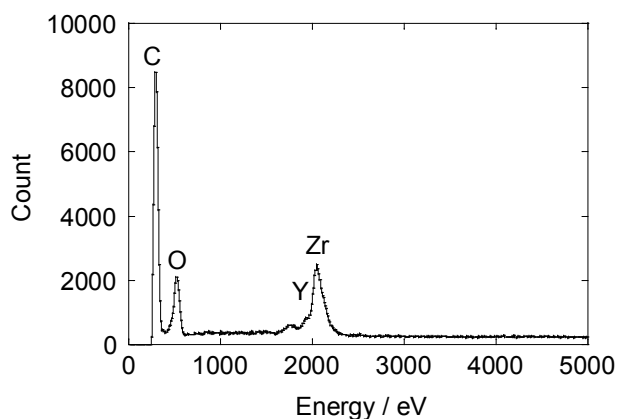


Fig. 2. EDS spectrum of fine particles prepared from ZrO₂ pellet by laser ablation.

CO5-10 ^{40}Ar - ^{39}Ar Dating of Extraterrestrial Materials in KURNS

N. Iwata, S. Sekimoto¹, R. Okazaki² and Y. N. Miura³

Faculty of Science, Yamagata University

¹*Institute for Integrated Radiation and Nuclear Science, Kyoto University*

²*Department of Earth and Planetary Sciences, Kyushu University*

³*Earthquake Research Institute, University of Tokyo*

INTRODUCTION: Radiometric dating is useful tool for unveiling formation and evolution process of planetary material. ^{40}Ar - ^{39}Ar method is invaluable to date the timing of heating events on planetesimals and asteroids (e.g. Swindle et al. (2014) [1]). Especially, ^{40}Ar - ^{39}Ar dating method with laser heating technique is suitable for small amount sample (e.g. Kelley, 1995 [2] and Hyodo, 2008 [3]).

For example, tiny material returned from asteroid 25143 Itokawa is dated using laser heating ^{40}Ar - ^{39}Ar dating method by Park et al. (2015) [4] and Jourdan et al. (2017) [5]. These ages indicate the timing of catastrophic events which occurred on Itokawa's precursor body. Combining the ^{40}Ar - ^{39}Ar ages and other chronological data, Terada et al. (2018) [6] overviewed the time evolution of the Itokawa asteroid. Successor to earlier works, ^{40}Ar - ^{39}Ar dating of material that recovered from asteroid 162173 Ryugu and other extraterrestrial materials have been carried out using KUR (project #R3007, PI: RO, [7]).

To implement of dating of extraterrestrial material by ^{40}Ar - ^{39}Ar method, we will develop a system which includes laser-heating gas extraction and gas purification line in KURNS (Fig. 1).

EXPERIMENTS: Dr. R. Okazaki of Kyushu University designed the system. A continuous Nd-YAG laser (~60 W) extract gas from neutron irradiated sample. The extracted gas is purified using a SORB-AC getter pump in purification part. After the purification of extracted gas, argon isotope ratios in the gases are analyzed by using an on-line connected quadrupole mass spectrometer. Alternatively, purified gases are encapsulated into metal gas trap, and are transported to laboratories of noble gas analysis (e.g. Kyushu University). Then, argon isotope of the gas is analyzed using a high sensitivity mass spectrometer. Whole of the extraction and purification parts will be evacuated by an oil rotary pump, two turbo molecular pumps and an ion pump to ultra-high vacuum condition.

RESULTS: We have continued assembling of the gas extraction and purification system in KURNS in FY2021. We could evacuate the extraction and purification parts using oil rotary pump. Unfortunately, the construction work was not finished due to influence of epidemic prevention of COVID-19. We are going to continue setting the system up during FY2022.

REFERENCES:

- [1] T. D. Swindle *et al.*, in *Advances in $^{40}\text{Ar}/^{39}\text{Ar}$ Dating: from Archaeology to Planetary Sciences*, edited by Jourdan, Mark, Verati (Geol. Soc., London, Spec. Pub. **378**, 2014) 333-347.
- [2] S. P. Kelley, in *Microprobe techniques in the earth sciences*, edited by Potts, Bowles, Reed, Cave (Chapman & Hall, London, 1995) 327-358.
- [3] H. Hyodo., *Gondwana Res.* **14** (2008) 609-616.
- [4] J. Park *et al.*, *Meteorit. and Planet. Sci.*, **50** (2015) 2087-2098.
- [5] F. Jourdan *et al.*, *Geology*, **45** (2017) 819-822.
- [6] K. Terada *et al.*, *Sci. Rep.*, **8** (2018) #11806.
- [7] R. Okazaki *et al.*, *Hayabusa 2021 Symposium (2021) abstract #S1-7.*

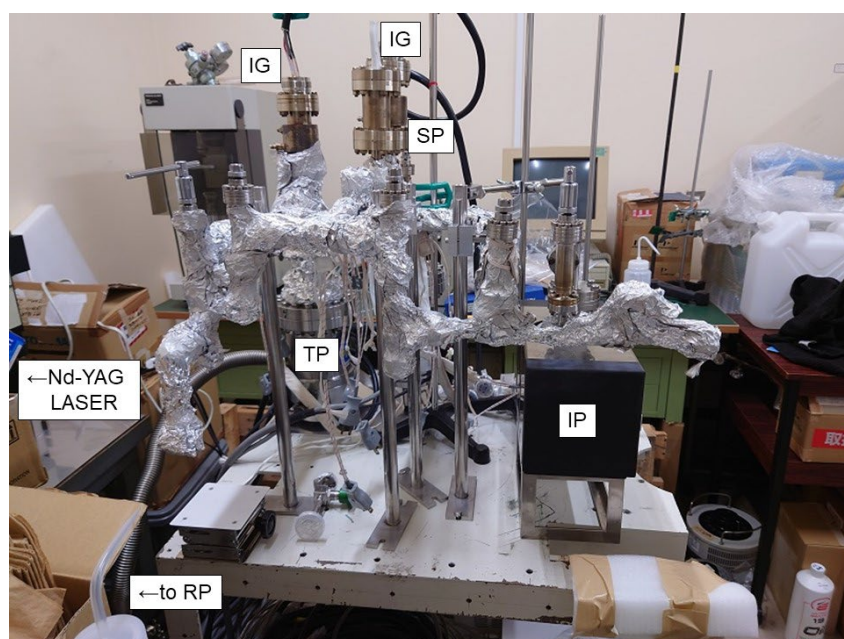


Fig. 1. View of gas extraction and purification line at KURNS. RP, TP, IP, SP and IG respectively denotes oil rotary pump, turbo molecular pump, ion pump, SORB-AC getter pump and ion gauge.

CO5-11 Ar-Ar and I-Xe Dating for Meteorites and the Hayabusa2 Returned Samples

Y. N. Miura, N. Iwata¹, R. Okazaki² and S. Sekimoto³

Earthquake Research Institute, University of Tokyo

¹ *Faculty of Science, Yamagata University*

² *Department of Earth and Planetary Sciences, Kyushu University*

³ *KURNS*

INTRODUCTION: Extra-terrestrial materials, such as meteorites, micrometeorites, and samples collected by asteroid/planet explorations, provide a variety of information for understanding the origin and evolution of the solar system. In particular, age determination gives us direct knowledge about thermal histories as well as timing of the events occurred in solar nebular and on the parent bodies. Ar-Ar and I-Xe ages usually, but not always, correspond to aqueous alteration and/or thermal events due to metamorphism/meteoroid impacts suffered on the parent body, and the parent body formation, respectively [e.g., 1, 2]. Despite of their importance, Ar-Ar and I-Xe dating is performed at limited laboratories because they require technique involving neutron irradiation and isotope measurements of the radioactive materials. In order to conduct Ar-Ar and I-Xe dating for extra-terrestrial samples, we attempt to establish the analytical protocol and apparatus. A system for gas extraction, purification, and measurements is being constructed at KURNS.

EXPERIMENTS: (i) Hayabusa2, a mission operated by the Japan Aerospace Exploration Agency (JAXA), returned samples from the C-type near Earth asteroid (162173) Ryugu. Small grain samples (typically 0.8 mm in size) were distributed to us (PI. R. Okazaki) for Ar-Ar and I-Xe dating. Prior to analyses of the Hayabusa2 samples, advanced experiments were performed. One of the experiments were conducted in July 2021. Two meteorites (Allende and Murchison) and terrestrial rocks and minerals were subjected to hydro irradiation as standard and interference-monitor samples. Individual samples were put in a hole of the diamond dish, which were wrapped with Al foil and stored in a Hydro irradiation capsule. In October 2021, returned Ryugu samples set on diamond dishes were irradiated (R3038; R3007) [3].

(ii) In Ar-Ar and I-Xe dating, isotope measurements of Ar and Xe for samples after neutron irradiation are necessary. For quicker and easier operation of Ar-Ar dating, we are constructing an apparatus for gas extraction, purification, and Ar isotope analyses. It needs ultra-high vacuum state and is composed of an Nd-YAG laser, a SORB-AC getter, vacuum gauges, and vacuum pumps (a mass spectrometer has not connected yet). Gases are extracted from samples by laser heating. Extracted gases are purified by the getter. And then, gases are planned to be (a) measured on-site with a quadrupole mass spectrometer (QMS) and/or (b) stored in bottles and measured with a high sensitivity sector-type mass spectrometer at Kyushu University. Va-

lidity of QMS was reported for K-Ar dating [e.g., 4-6]. In situ Ar-Ar dating using the laser heating and Ar measurements by a QMS at KURNS can avoid transportation of irradiated samples. We are examining the sensitivity, background level and availability of the QMS at the Univ. of Tokyo.

RESULTS: (i) The samples were first studied for short lived nuclides by Dr. Shirai and co-investigators. Then, the samples were irradiated, cooled, isolated from the dishes and transported to Kyushu University to measure noble gases (including Ar and Xe) with the sector-type mass spectrometer. The results are being analyzed in detail.

(ii) Most of the line components were assembled and evacuated at KURNS. The heating examination for the laser has not been done. The QMS that is planned to be connected to the line at KURNS was installed into the ultra-high vacuum system at the Univ. of Tokyo (Fig. 1) for performance tests. Because the amounts of Ar released from irradiated samples are generally small, low background conditions are required. To examine analytical procedures and to determine the sensitivity and the precision of isotopic ratios, quantitative amounts of air, $\leq 7 \times 10^{-6}$ cm³STP for ⁴⁰Ar, were introduced into the QMS. Suitable sample amounts and heating temperature steps will be discussed based on the results from these experiments.



Fig. 1. The QMS is connected to the ultra-high vacuum line.

REFERENCES:

- [1] D. S. Lauretta and H. Y. McSween, *Meteorites and the Early Solar System II* (Space Science Series, Univ. of Arizona Press) (2006).
- [2] A. Longobardo, *Sample Return Missions: The Last Frontier of Solar System Exploration* (Elsevier) (2021).
- [3] R. Okazaki *et al.*, *Hayabusa Symposium 2021* (2021) abstract #S1-7.
- [4] B. Schneider *et al.*, *Quaternary Geochronology*, **4** (2009) 508-516.
- [5] Y. Cho *et al.*, *Planet. Space Sci.*, **128** (2016) 14-29.
- [6] Y. Cho and B. A. Cohen, *Rap. Comm. Mass Spectrometry*, **32** (2018) 1755-1765.

CO5-12 Neutron Activation Analysis of cosmo- and geo-chemical samples

M. Ebihara, Y. Hidaka¹, T. Taisei¹, N. Shirai¹, S. Sekimoto²

Department of Earth Sciences, Waseda University

¹*Department of Chemistry, Tokyo Metropolitan University*

²*Institute for Integrated Radiation and Nuclear Science, Kyoto University*

INTRODUCTION: Halogen elements are a group of the elements belonging to group 17 in a periodic table of the elements, consisting of fluorine (F), chlorine (Cl), bromine (Br) and iodine (I) as stable elements. Geochemically, halogens behave with relatively high volatility and incompatibility with silicates. Therefore, halogens are relatively abundant in several reservoirs in the outer layer of the earth such as sea water, oceanic sediments and crustal materials. Cosmochemically, halogens are grouped into moderately volatile (for F and Cl) and highly volatile elements (for Br and I). However, their behavior in the early solar system is not well understood even at present. A major reason for making difficult in understanding the cosmochemical behavior of halogens is the lack of reliable data of halogen contents in bulk meteorite samples. A main goal of this study is to obtain reliable halogen content data for chondritic meteorites, especially carbonaceous chondrites for better understanding of the halogen behavior when our solar system formed. Before reaching this goal, we determined halogen contents in geochemical reference samples to establish the analytical procedure applicable to meteorite samples. Contents of the three halogens were determined by radiochemical neutron activation analysis (RNAA).

EXPERIMENTS: Two geochemical reference samples of about 200 to 300 mg each in clean plastic vials and reference standard samples of the three halogens were irradiated with neutrons for 10 min with a thermal neutron flux of $1 \times 10^{13} \text{ cm}^{-2} \text{ s}^{-1}$ in the Pn-3 irradiation tube. After the irradiation, the samples were subjected to radiochemical separation of the three halogens. The radiochemical procedure used was essentially the same as previously described ([1], [2]) and are briefly summarized in the following. Each meteorite specimen was alkaline-fused with sodium hydroxide. The resulting fusion cake was disaggregated with water and the supernatant fractions was recovered by centrifugation. After neutralizing with nitric acid, I was precipitated as palladium iodide, which was immediately measured for a 423 keV gamma-ray emitted by ¹²⁸I whose half life is 27 min. From the supernatant, silver chloride and silver bromide precipitates were recovered by adding silver nitrate solution. Gamma-rays of ³⁸Cl (half-life: 30 min) and ⁸²Br (half-life: 35 h) were measured just after the measurement of ¹²⁸I and on the following days, respectively. After completion of all gamma-ray measurements, the palla-

dium iodide and silver chloride-bromide mixture precipitates were reactivated for determining chemical yields.

RESULTS: Some preliminary results are summarized in Table 1. Errors quoted are uncertainties due to counting statistics (one standard deviation) in gamma spectrometry.

Table 1 Analytical results (in $\mu\text{g/g}$) of three halogens.

sample	Cl		Br		I	
AGV-2	76.5	± 3.2	0.085	± 0.006	0.023	± 0.005
<i>lit. 1</i>	72.5	± 2.7	0.101	± 0.007	0.197	± 0.038
BCR-2	100	± 2.2	0.121	± 0.009	0.048	± 0.018
<i>lit. 1</i>	112	± 1	0.144	± 0.008	0.082	± 0.022
BHVO-2	97	± 3.4	0.253	± 0.017	0.081	± 0.008
<i>lit. 1</i>	104	± 4	0.240	± 0.013	0.307	± 0.050
GSP-2	336	± 14	0.067	± 0.010	0.011	± 0.007
<i>lit. 1</i>	363	± 29	0.117	± 0.020	0.075	± 0.018
GSR-1	126	± 4	0.120	± 0.024	0.012	± 0.005
<i>lit. 2</i>	116	± 10	0.58	± 0.07		
GSR-2	38.9	± 3.6	0.021	± 0.013	0.011	± 0.005
<i>lit. 2</i>	49.1	± 5.6	0.17	± 0.01	0.004	± 0.003
GSR-5	37.2	± 1.5	0.238	± 0.014	0.249	± 0.014
<i>lit. 2</i>	49.7	± 5.4	0.51	± 0.02	0.14	± 0.01
GSD-7a	43.4	± 7.1	0.813	± 0.045	0.471	± 0.016
<i>lit. 2</i>	39.0	± 6.5	1.05	± 0.11	0.38	± 0.04
GSD-11	320	± 12	1.41	± 0.05	2.56	± 0.08
<i>lit. 2</i>	276	± 13	1.88	± 0.10	1.86	± 0.10
JR-3	139	± 9	0.549	± 0.023	0.469	± 0.023
<i>lit. 3</i>	134	± 12	0.577	± 0.045	0.482	± 0.037

lit. 1: [3], *lit. 2:* [4], *lit. 3:* [2] ("*lit.*" denotes literature)

Data in *lit. 1* and *lit. 3* were obtained by RNAA using the same analytical procedure as used in this study. Data of *lit. 3* were obtained by ICP-MS. In Comparison with literature values, the following features can be seen; (i) (for Cl) literature data and our data are all consistent, (ii) (for Br) all data of *lit. 2* are systematically lower than ours, (iii) (for I) all data of *lit. 1* are systematically higher than ours, while some of *lit. 2* are lower than ours, (iv) (for three halogens) data of *lit. 3* and ours are consistent. We have repeatedly analyzed reference samples including those listed in Table 1 to critically evaluate the literature values. Outcomes will be submitted to scientific journals in near future.

REFERENCES:

- [1] M. Ebihara *et al.*, J. Radioanal. Nucl. Chem., **216** (1997) 107-112.
- [2] S. Sekimoto and M. Ebihara, Anal. Chem., **85** (2013), 6336-6341.
- [3] S. Sekimoto and M. Ebihara, Geostand. Geoanal. Res., **41** (2017) 213-219.
- [4] T. He *et al.*, Anal. Chem., **91** (2019) 8109-8114.

CO5-13 Collisional histories of the LL chondrite parent body revealed by $^{40}\text{Ar}/^{39}\text{Ar}$ dating

H. Sumino, A. Takenouchi¹, K. Arai², J. Ren, M. Koike³, R. Okumura⁴, Y. Inuma⁴, H. Yoshinaga⁴ and S. Sekimoto⁴

Graduate School of Arts and Sciences, University of Tokyo

¹*Kyoto University Museum, Kyoto University*

²*Graduate School of Science, University of Tokyo*

³*Graduate School of Advanced Science and Engineering, Hiroshima University*

⁴*Institute for Integrated Radiation and Nuclear Science, Kyoto University*

INTRODUCTION: A collisional event is a fundamental process of evolving and disrupting asteroidal bodies in the solar system. Because collisions induce shock metamorphism in meteorites, we can reveal a history of asteroidal evolution/destruction by examining shocked meteorites. Ordinary chondrites, the most abundant meteorites reported, record complex collisional histories on their parent bodies, particularly in the “early” solar system. Although LL chondrites are less investigated than H and L chondrites, certain authors suggested that LL chondrite parent body(ies) underwent a shock event before 4.5 Ga and a major shock event at 4.2 Ga [e.g., 1,2].

For discussions on such collisional histories, $^{40}\text{Ar}/^{39}\text{Ar}$ ages have been commonly adopted to examine collisional ages. The high diffusion rate of Ar leads to loss of radiometric Ar during shock heating [e.g., 3]. On the other hand, some shock events are accompanied by postshock heating so weak (e.g., Fritz et al., 2017; Gillet & El Goresy, 2013; Sharp & Decarli, 2006; Stöckler et al., 1991, 2018) that a resetting of $^{40}\text{Ar}/^{39}\text{Ar}$ ages is not always attained, and resistance against resetting depends on shock textures [e.g., 4]. Moreover, certain meteorites may have experienced multiple shock events, and possibly aliquots from the same meteorites having different petrological textures yield distinct $^{40}\text{Ar}/^{39}\text{Ar}$ ages. Therefore, when we conduct $^{40}\text{Ar}/^{39}\text{Ar}$ chronological analysis to determine collisional ages, we should carefully observe shock textures and use the same aliquot for $^{40}\text{Ar}/^{39}\text{Ar}$ analysis. However, the number of such chronological–petrological studies is still limited [e.g., 5], and relations between shock ages and collisional events are unclear, except for a major shock event at 0.5 Ga on the L chondrite parent body. To explain such collisional histories, including a time transition of impact scales, we require a chronological–petrological study of multiple meteorites. In this study, we focused on an LL chondrite and performed $^{40}\text{Ar}/^{39}\text{Ar}$ chronological–petrological analyses of an LL 6 brecciated chondrite to delineate the collisional history of the LL chondrite parent body.

EXPERIMENTS: The samples of 5-50 mg each and standards for neutron fluence were wrapped with aluminum foil and put in aluminum capsules of $\phi 10$ mm x

30 mm. The capsules were irradiated with neutrons in KUR. After the irradiation, the samples were sent to the University of Tokyo. The samples were loaded into an ultrahigh-vacuum, noble gas extraction, purification, and separation line. Argon was extracted from the samples by heating up to 1800°C, purified with hot titanium-zirconium getters, separated into each noble gas with temperature-controlled cold traps, and then determined their isotope compositions with a noble gas mass spectrometer [6,7]. The fast neutron flux was estimated as $(1.0\text{--}1.2) \times 10^{18}$ neutrons cm^{-2} , from the production of ^{39}Ar from ^{39}K in the Hb3gr hornblende standard in which K contents have been determined by [8].

RESULTS: Petrological observations revealed that NWA 2139 experienced at least five impact events, including at least two brecciation events, and two shock-induced heating events inducing silicate darkening and healing cracks, and one weak shock event inducing thin shock veins. $^{40}\text{Ar}/^{39}\text{Ar}$ analysis demonstrated that four aliquots of NWA 2139 provided a mini-plateau age of 4.17 ± 0.10 Ga in high-temperature fractions. One aliquot shows a partial degassing event at <3.9 Ga. The heating event at 4.17 ± 0.10 Ga induced the recrystallization of the thick veins and healing cracks in NWA 2139, which is the major heating event on the LL chondrite parent body, as reported in other LL chondrites [e.g., 1,2]. Silicate darkening, thick shock vein formation, and two brecciations occurred before the major heating event at 4.17 ± 0.10 Ga, whereas the thin shock vein formed after the heating event. The LL parent body might have been broken up by 1.7 Ga, based on studies of probably from 4.2 to 3.8–3.9 Ga. No brecciation occurred after 4.2 Ga, and many other LL chondrites, including NWA 2139, did not experience a strong shock event within 1.5–1.7 Ga reported for Itokawa particles and the Chelyabinsk meteorite. Moreover, the heating event at 4.2 Ga is a common event in multiple LL chondrites.

REFERENCES:

- [1] E. T. Dixon *et al.*, *Geochim. Cosmochim. Acta*, **68** (2004), 3779-3790.
- [2] J. M. Friedrich *et al.*, *Geochim. Cosmochim. Acta*, **139** (2014), 83-97.
- [3] T. D. Swindle *et al.*, *Geol. Soc. London Spec. Pub.* **378** (2014), 333-347.
- [4] J. Kunz *et al.*, *Meteor. Planet. Sci.* **32** (1997), 647-670.
- [5] J. R. Weirich *et al.*, *Meteor. Planet. Sci.* **45** (2011), 1868-1888.
- [6] N. Ebisawa *et al.*, *J. Mass Spectrom. Soc. Jpn.* **52** (2004) 219-229.
- [7] M. Kobayashi *et al.*, *Chem. Geol.* **582** (2021), 120420.
- [8] J. C. Roddick, *Geochim. Cosmochim. Acta* **47** (1983), 887-898.

CO5-14 Application of the Single Comparator Method to Photon Activation Analysis at KURNS

Md. S. Reza and Y. Oura

Graduate School of Science, Tokyo Metropolitan University

INTRODUCTION: Instrumental photon activation analysis (IPAA) is multielemental and nondestructive analytical method like instrumental neutron activation analysis (INAA). Comparative method is generally used for determination of elemental contents in IPAA. In INAA, k_0 method, which was developed based on a single comparator method, as well as comparative method is used. A single comparator method and k_0 method can determine all elemental contents by using only single element comparator. But there are no reports on determination by the single comparator method in IPAA as far as we know. So, we have applied single comparator method to IPAA at the Research Center for Electron Photon Science (ELPH), Tohoku University using photoreaction yield ratios obtained by Oura et al.[1] at ELPH. Since neutron spectrum is unique to each irradiation position in a reactor, its correction is essential in k_0 -INAA. However, energy spectrum of the bremsstrahlung from any electron accelerator should be nearly identical for the same acceleration energy of the electrons and the same converter material. There must be no need to correct the energy spectrum as for the k_0 -INAA. That is, the yield ratios by Oura et al. should be also used to perform IPAA in any institution. In this study, the single comparator method was performed on various reference standard samples at the electron accelerator at the Institute for Integrated Radiation and Nuclear Science, Kyoto University (KURNS) other than ELPH.

EXPERIMENTS: Several geochemical and environmental reference samples, which were same as those analyzed at ELPH, in an Al foil container were irradiated with stainless steel (SUS) foil fluence monitors by bremsstrahlung with $E_0 = 33.3$ MeV from an electron LINAC at KURNS under air-cooling for 6 hours. The bremsstrahlung was produced by a Pt convertor (2-mm thick x 2 pieces). After irradiation, samples were transferred to a new Al foil container. Then, γ -rays in samples were measured by a Ge detector calibrated with ^{152}Eu and ^{182}Ta sources. Samples were placed at approximately 10-20 cm from the Ge detector to reduce true coincidence.

The determination calculation was performed using the single comparator method. In this study, Ni was used as the comparator, and the elemental mass fraction was calculated using Equation (1),

$$C = \frac{M_x \times r_{Ni}}{M_{Ni} \times r_x} \times \frac{A_x}{A_{Ni}/w_{Ni}} \times \frac{\sigma_{Ni}}{\sigma_x} \times \frac{1 - e^{-\lambda_x t}}{1 - e^{-\lambda_{Ni} t}} \div W \quad (1)$$

where C is the elemental mass fraction, A is the induced radioactivity at the end of the irradiation period, W is the sample mass, w is mass of an element, M is the atomic

weight, r is the isotopic abundance, σ is the reaction yield, λ is the decay constant, and t is the irradiation time. The suffixes 'x' and 'Ni' express the parameter for the sample and Ni monitor, respectively. The reaction yield ratios (σ_x/σ_{Ni}) were taken from Oura et al.[1] The specific activity of ^{57}Ni (A_{Ni}/w_{Ni}) at the position of each sample position was calculated using an interpolation of ^{57}Ni activities in SUS foils using a function determined by the least squares method.

RESULTS: Ratios of determination values to literature values (certified or recommended values) for determined elements are shown in Fig.1 with analytical results obtained at ELPH, where yield ratios used in the single comparator method were determined at. Determination values obtained at ELPH expressed by open symbols were consistent with literature values within $\pm 10\%$ for almost elements, and some results were within $\pm 20\%$. The results obtained at KURNS expressed by closed symbols, which is a different facility from the one where reaction yield ratios were determined, were also consistent with literature values like the result at ELPH. It is concluded that the single comparator method using reaction yield ratios obtained with the LINAC at ELPH [1] can generally be applied to IPAA using any accelerators.

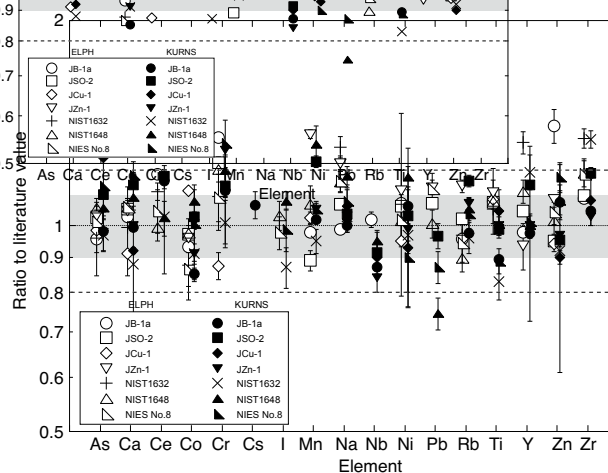


Fig. 1. Comparison between mass fractions determined in 7 kinds of reference samples and their literature values. The irradiation energy was $E_0 = 33.3$ MeV. The shaded area and dotted lines express the range of $\pm 10\%$ of the literature value and $\pm 20\%$ of the literature value, respectively.

REFERENCES:

[1] Y. Oura *et al.*, ELPH Annual Report 2017 (2018), 115-120.

CO5-15 Distribution of radiocesium in forestry area in Fukushima

T. Ohta, S. Fukutani¹, T. Kubota², R. Takeo, Y. Mahara³

Department of Nuclear, Nagaoka University of Technology

¹Institute for Integrated Radiation and Nuclear Science, Kyoto University

²Agency for Health, Safety and Environment, Kyoto University

³Kyoto University

INTRODUCTION: Vast forest was markedly contaminated by radioactive plums containing radiocesium in the wide range of the eastern part of Japan in 2011 [1–4]. As forests have an important role in preventing landslides and maintaining the ecological and hydrological system, the destructive forest should be avoided and an appropriately managed tree-felling should be conducted. It is necessary to know the environmental dynamics of radiocesium in forest to keep the forestry vividly.

In our previous field study [1], most of the radiocesium in the tree rings was directly absorbed by the atmospheric direct uptake via the bark and leaves rather than by roots. The chemical form of radiocesium on the leaves and bark would have been a mixture of water-soluble and insoluble forms. Another our previous study [2] demonstrated that the effluence rate of radiocesium (¹³⁷Cs) obtained from dissolved assay experiments on the trunks of *Cryptomeria japonica*, indicating that the radiocesium in the trees was mainly water-soluble.

As radiocesium in tree may be absorbed from the roots in the future, it is important to know how much dissolved radiocesium is released from the soil. In this study, sequential-extraction experiment of radiocesium was attempted to the surface soil 10 years after the accident, and compare the distribution ratio of the radiocesium in the soils: 2 years after the accident and 10 years after the accident.

EXPERIMENTS:

We extracted ¹³⁷Cs from the surface soil sample from the Fukushima. The soil of depths of 0–2.5 cm was well mixed and the samples were used in the sequential-extraction experiment [4]. A ratio of solution to sample of 5 (v/w) was used for extraction in each step. After each fraction was stored into a U-8 vessel, ¹³⁷Cs was measured by gamma-ray spectrometry.

Furthermore, we measured radiocesium in tree ring of *Cryptomeria Japonica* in the Fukushima. Detailed pre-treatment of the tree-ring and measurement of the radiocesium in the samples are described by our previous study[1].

RESULTS: As shown in Fig. 1, the sequentially chemical fractionations of ¹³⁷Cs in the soil indicate that most part of ¹³⁷Cs were insoluble 2 years after the accident.

After 10 years later from the accident, ¹³⁷Cs was strongly fixed in the mineral of the soil, ¹³⁷Cs in the water soluble fraction and ion exchange fraction decreased (Fig. 2).

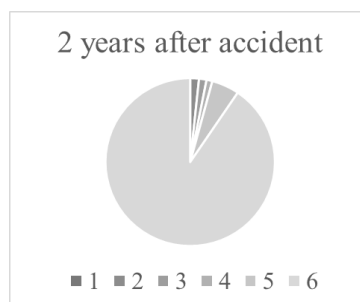


Fig. 1 Distribution of ¹³⁷Cs in the surface soil collected at the Fukushima [4].

*1: ultrapure water, F: 1 M of NaAc, F: 1-M NaAc-HAc (pH 5), 4: 0.04-M NH₂OH · HCl in 25 % (v/v) HAc (pH 2), 5: 30 % H₂O₂ (with HNO₃, pH 2), 1.8-M NH₄Ac in 11 % HNO₃(v/v), 6: Residual



Fig. 2 Distribution of ¹³⁷Cs in the surface soil collected at the Fukushima.

*1: ultrapure water, 2: 1 M of NaAc, 3: Residual

Furthermore, concentrations of the tree ring were less than 50Bq/kg collected in 2014. We compared that the concentration of the tree ring at the same sampling site, the concentration of radiocesium did not increase from 2012 to 2014. We concluded that the radiocesium was not absorbed from the root effectively.

REFERENCES:

- [1] Y. Mahara *et al.*, Sci. Rep., **4** (2014) Article number 7121.
- [2] T. Ohta *et al.*, J. Radioanal. Nucl. Chem., **310** (2016) 109-115.
- [3] Y. Mahara *et al.*, Sci. Rep., **11** (2021) Article number 8404.
- [4] T. Ohta *et al.*, Radiological Issues for Fukushima's Revitalized Future, edited by T. Takahasi (Springer, 2016) 13-24.

CO5-16 Determination of Abundance of Rare Metal Elements in Seafloor Hydrothermal Ore Deposits by INAA Techniques-8: Cross check with ICP-QMS analysis (2)

J. Ishibashi, Y. Inoue¹, K. Yonezu², T. Nozaki³, Y. Takaya⁴, R. Okumura⁵, Y. Inuma⁵, H. Yoshinaga⁵ and K. Takamiya⁵

Ocean-bottom Exploration Center, Kobe University

¹*Department of Earth and Planetary Sciences, School of Science, Kyushu University*

²*Department of Earth Resources Engineering, Faculty of Engineering, Kyushu University*

³*Submarine Resources Research Center, Research Institute for Marine Resources Utilization, Japan Agency for Marine-Earth Science and Technology (JAMSTEC)*

⁴*Department of Systems Innovation, School of Engineering, The University of Tokyo*

⁵*Institute for Integrated Radiation and Nuclear Science, Kyoto University*

INTRODUCTION: Instrumental neutron activation analysis (INAA) has several advantages for geochemical tools to provide useful information for mineral exploration. INAA enables highly sensitive multi-element analysis without geochemical pretreatment. We have conducted studies using mineralized samples collected from seafloor hydrothermal fields, with a view to extend the range of application of this technique. Here we report a result of cross check with inductively coupled plasma quadrupole mass spectrometry (ICP-QMS analysis).

EXPERIMENTS: Sulfide deposit and metalliferous sediment collected from an active seafloor hydrothermal field in a seamount in Izu-Bonin Arc were provided for cross check analysis. In total 29 samples were selected to examine analytical accuracy in wide range of concentrations, and aliquots for INAA and ICP-QMS analysis were split from the same powdered sample.

INAA analysis was conducted by two runs. For short life nuclides, powdered samples of 10-20 mg were irradiated at Pn-3 (thermal neutron flux = 4.68×10^{12} n/cm²/sec) for 30 seconds, and the gamma ray activity was measured for 3 minutes after adequate cooling time (3~15 minutes). For long life nuclides, powdered samples of 10-20 mg were irradiated at Pn-2 (thermal neutron flux = 5.50×10^{12} n/cm²/sec) for 30 minutes, and the gamma ray activity was measured for 15 minutes after adequate cooling time (~30 hours).

ICP-QMS analysis followed the procedure reported in the previous study [1]. Powdered samples of ca. 50 mg were dissolved by HNO₃-HClO₄-HF digestion in Teflon PFA screw-cap beakers, then heated overnight on a hot plate at 110 °C. The digested samples were progressively evaporated at 110 °C for more than 12 h, 130 °C for 3 h and 160 °C until dryness. The residue was dissolved in 5 mL Milli-Q de-ionized water combined with 4 mL HNO₃ and 1 mL HCl, then further diluted to 1:100 by mass (total dilution factor ca. 20,000) before introduction into the ICP-QMS (Agilent 7500ce).

RESULTS: Content of nine elements (Al, Mn, Cu, Zn, Ba, Na, As, Sb and Au) determined by INAA is plotted against that by ICP-QMS analysis (Fig. 1). Contents determined by two analytical techniques basically well agreed, except for the case that determination of some specific elements was difficult due to extremely low content. Disagreement in Ba content for Ba-rich ore sample is caused by incomplete dissolution during the chemical treatment for ICP-QMS analysis [1]. Accuracy of INAA was confirmed for determination of metal elements in adequate content ranges such as Zn (>1%), Cu (>1000 ppm), As (>100ppm), Sb (>100ppm) and Au (>1 ppm). Determination of Al in low contents below 1000 ppm showed rather poor accuracy by INAA probably due to short irradiation time to inhibit back ground.

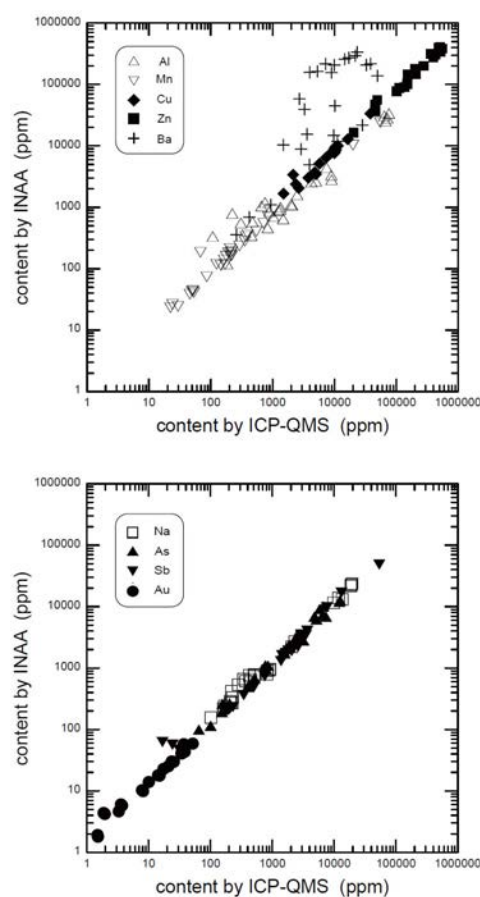


Fig. 1. Result of cross check analyses between ICP-QMS and INAA for sulfide deposit and metalliferous sediment (Upper: short lived nuclides, Lower: long lived nuclides). Note that both axes are in logarithm scale.

REFERENCES:

[1] Nozaki *et al.*, *Sci. Rep.*, **11**, 8809 (2021).

CO5-17 Neutron activation analysis of carbonate reference materials: coral (JCp-1) and giant clam (JCt-1)

S. Sekimoto, Y. Homura^a, V.D. Ho¹, M. Inagaki, N. Shirai², T. Ohtsuki

Institute for Integrated Radiation and Nuclear Science, Kyoto University

¹*Nuclear Research Institute, Vietnam Atomic Energy Institute*

²*Department of Chemistry, Tokyo Metropolitan University*

^a*Present address: Novaltis Farma*

INTRODUCTION: Geochemists are often interested in the abundance of halogen elements in geochemical materials such as crustal rocks, mantle materials, and meteorite samples, because halogens play an important role in investigating the petrogenesis of such materials and assist in tracing their origins and/or precursor materials [1-3]. In our previous work, radiochemical neutron activation analysis (RNAA) was refined to accurately determine even trace amounts of halogens (chlorine, bromine, and iodine) in sedimentary rock reference samples [4]. Subsequently, U.S. Geological Survey (USGS) geochemical reference materials were subjected to RNAA, and the data obtained were compared with literature data [5]. The two kinds of carbonate reference materials investigated here, JCp-1 (Coral) and JCt-1 (Giant Clam), are prepared by the Geological Survey of Japan/National Institute of Advanced Industrial Science and Technology (GSJ/AIST), and the concentrations of many major and a few trace elements in these materials have been determined [6-8]. Data about the halogen contents in these materials is expected to significantly contribute to a better understanding of the chemistry of seawater and the marine environment, since halogens (especially iodine) are known to be extremely useful in investigating the geochemical circulation of terrestrial materials [9]. However, to our knowledge, there is not much data on the halogen contents of these carbonate materials.

The present study aims to use RNAA and instrumental NAA (INAA) to determine trace amounts of three halogens in JCp-1 and JCt-1, together with other elements. Based on the halogen data, the differences between the two carbonate reference materials is investigated.

RESULTS: To probe the utility of the halogen data in interpreting geochemical formations, we have compared the halogen contents in these two carbonate materials with those in nine sedimentary rock materials (RNAA was used to determine the halogen content in all cases [4]). The ratios for I/Cl and Br/Cl in all these materials were calculated and are shown in Fig 1. Here, the sedimentary rocks are classified into two groups (the rocks in seawater and those in inland water). The ratios corresponding to sedimentary rocks in seawater (denoted by closed triangles) tend to be lower than the ratios for the sedimentary rocks in inland water (closed circles). This can be attributed to the fact that sedimentary rocks in

seawater are affected to a greater extent by the high chlorine content in seawater. Since the two carbonate materials, coral and clam, are both found in seawater, it is reasonable that JCp-1 and JCt-1 exhibit lower ratios than the four sedimentary rocks in inland water. The ratio of I/Cl for JCt-1 is lower than those for the five sedimentary rocks in seawater, as well as lower than that for JCp-1 by more than one order of magnitude, suggesting that iodine may have been fractionated from Br during the process of formation of JCt-1.

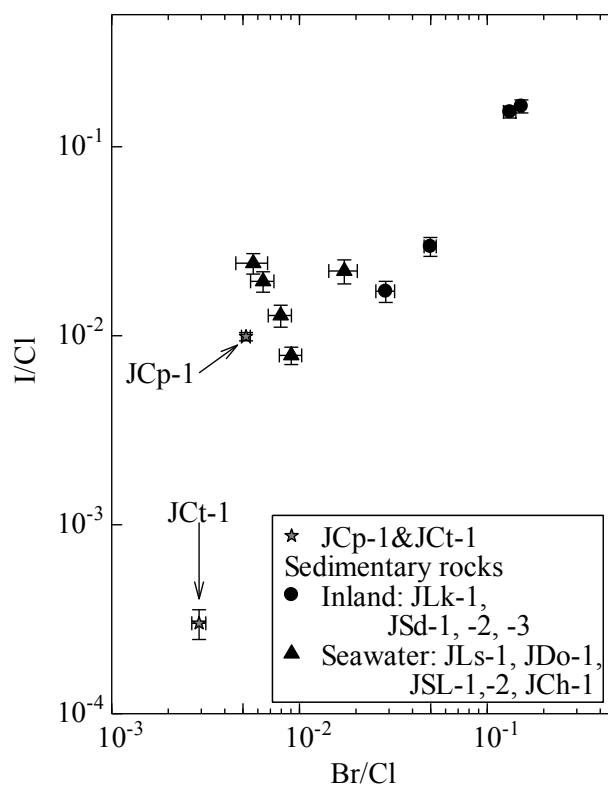


Fig. 1 I/Cl vs. Br/Cl ratios for JCp-1, JCt-1 and sedimentary rocks.

REFERENCES:

- [1] MA Kndrick *et al.*, *Geochim. Cosmochim. Acta (GCA)* **235** (2018) 285-304.
- [2] L. Hughes *et al.*, *GCA* **243** (2018) 1-23.
- [3] DE Harlov *et al.*, *The Role of Halogens in Terrestrial and Extraterrestrial Geochemical Processes* Springer Geochemistry, Gewerbestrasse, Switzerland (2018).
- [4] S. Sekimoto *et al.*, *Anal. Chem.* **85** (2013) 6336-6341.
- [5] S. Sekimoto *et al.*, *Geostand. Geoanal. Res.* **41** (2017) 213-219.
- [6] S. Aizawa, *J. Radioanal. Nucl. Chem.* **278** (2008) 349-352.
- [7] M. Inoue *et al.*, *Geostand. Geoanal. Res.* **28** (2004) 411-416.
- [8] T. Okai *et al.*, *Chikyuu Kagaku* **38** (2004) 281-286.
- [9] B. Deruelle *et al.*, *Earth Planet. Sci. Lett.* **108** (1992) 217-227.

CO6-1 Contribution of indirect actions to cell lethality in mixed neutron and BPA irradiation

R. Hirayama, Y. Sanada¹, A. Uzawa, M. Suzuki¹, S. Masunaga¹ and S. Hasegawa

National Institutes for Quantum Science and Technology
¹ Institute for Integrated Radiation and Nuclear Science,
Kyoto University

INTRODUCTION: Excellent dose distribution in a cell of neutron capture reaction of boron atom induces high relative biological effectiveness. These phenomena are commonly assumed to be an interaction between cells and low energy heavy particles (α and Li) resulting from the boron atom fissions in the cells. However, there has been little study done concerning the action of the particles on living cells. We have investigated contributions of indirect actions of radiation in cell killing by heavy ions with radical scavenger that selectively reduces the indirect action [1].

Therefore, it is important that how these mechanisms can be made to clear through a thorough basic research in boron neutron capture therapy is urgently discussed. The main object of this year is to make clear the contribution of indirect action of neutron beam to cell killing using mammalian cells.

EXPERIMENTS: We used HSGc-C5 (JCRB1070, here after call as HSG) cells. HSG cells were grown in Eagle's minimum essential medium supplemented with 10% fetal bovine serum and antibiotics (100 U/ml penicillin and 100 μ g/ml streptomycin) under humidified air with 5% CO₂ at 37°C. The cells were suspended at a density of about 3×10^5 cells/ml. The cells in Polypropylene tubes were irradiated at the remodeled heavy water facility at the KURRI.

Total fluencies of thermal neutron, epithermal neutron and fast neutron were measured by means of gold foil activation analysis. The gamma ray dose including secondary gamma rays was measured with a thermo luminescence dosimeter. Boron concentrations in the cells were taken to be equivalent to those in the medium as reported previously [2].

Three hours prior to irradiation, cells are treated with 25 μ g/ml BPA.

After irradiation, cells were seeded in triplicate onto 100 mm (Φ) culture dishes at densities to give approximately 100 colonies per dish. After 14 days of incubation, the colonies were fixed with 10 % formalin solution and stained with 1 % methylene blue in water. Colonies consisting of more than 50 surviving cells were scored.

The contribution of indirect action on cell killing can be estimated from the maximum degree of protection by dimethylsulfoxide (DMSO) [1], which suppresses indirect action by quenching OH radicals without affecting the direct action of neutron beam on cell killing.

RESULTS: The surviving fractions of HSG cells irradiated with 0.335 Gy dose initially increased with in-

creasing DMSO concentration and then plateaued at higher concentrations (Fig.1A). Degrees of protection (DP: $(\ln SF_0 - \ln SF_x) / \ln SF_0$) defined was calculated and plotted as a function of the DMSO concentration (Fig. 1B). Since the curve were upper concave in nature, DP curve was approached saturation as the concentration of DMSO increased. The maximum DP (i.e., saturation level) for DMSO concentrations was 0.30. Namely, the OH radical-mediated indirect action contributions to cell killing by neutron beam was 30%.

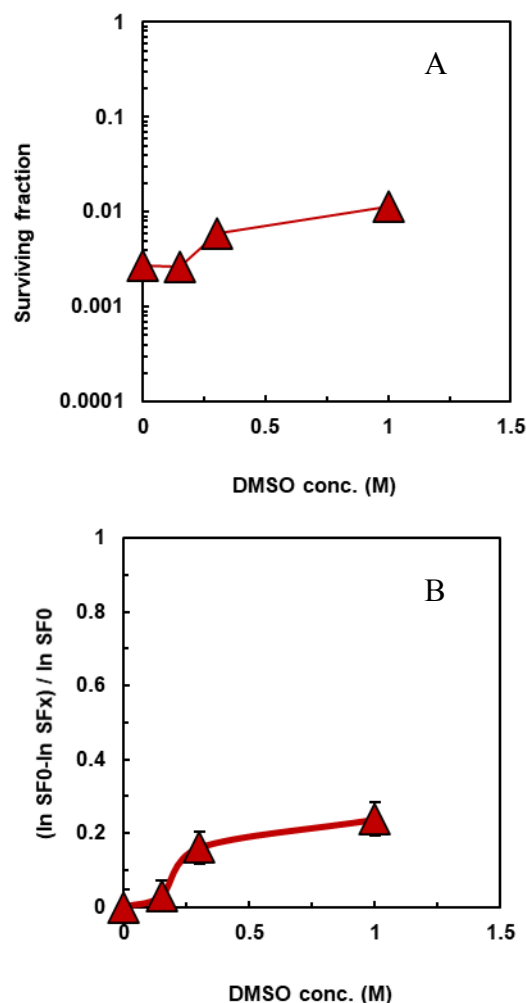


Fig. 1. Effects of DMSO on the survival of HSG cells after exposure to neutron beam. (A) HSG cell survival irradiated with neutron beam in the presence of various concentration of DMSO. (B) Degrees of protections were determined from panel A. The curve was fitted by MichaelisMenten kinetics. The error bars represent the standard errors.

REFERENCES:

- [1] R. Hirayama *et al.*, Radiat. Res., **171** (2009) 212-218.
- [2] Y. Sakurai and T. Kobayashi, Nucl. Instrum. Methods Phys. Res. Sect. A., **453** (2000) 569-596.

CO6-2 The tumor invasion enhanced by the conditioned-medium after X-rays via EGFR pathway

H. Yasui¹, M. Eitaki¹, Y. Sanada², S. Masunaga², and O. Inanami¹

¹Laboratory of Radiation Biology, Faculty of Veterinary Medicine, Hokkaido University

²Particle Radiation Biology, Division of Radiation Life Science, Institute for Integrated Radiation and Nuclear Science, Kyoto University

INTRODUCTION: In cancer studies, it has been suggested that irradiation sometimes enhances invasion of tumor cells. Although there are many studies that estimate effects of direct irradiation on tumor cell invasiveness, not so many reports did bystander effects of irradiated tumor cell conditioned medium (CM) on it. Furthermore, the same effect of high LET radiation therapy such as boron neutron capture reaction (BNCT) has not been reported. In this study, we conducted the experiments to examine effects of X-irradiated tumor cell CM on cellular invasiveness in breast cancer and lung cancer-derived cells, prior to BNCT challenge. In 2018 and 2019, using human breast adenocarcinoma MDA-MB-231 cells and human lung adenocarcinoma A549 cells, we reported the X-ray irradiated cell-derived CM promotes cell infiltration ability even if taken into consideration cell proliferation activity and Epidermal growth factor (EGF) acts as a bystander factor to promote the cell invasion ability. [3, 4]. In this year, we examined the effect of EGF suppression on the invasiveness and MMP activity of CM-treated MDA-MB-231 cells.

EXPERIMENTS:

[Western blotting] Cells were treated with CM containing 10% FBS (CM/10 % FBS) for 0, 0.5, 1, 3 or 6 h. When cells were co-treated with AG1478, an EGFR tyrosine kinase inhibitor, they were pre-treated with 500 nM AG1478 for 10 min before treatment of CM/10 % FBS. After the treatment, cells were collected and lysed. Proteins were separated by SDS-PAGE and transferred onto nitrocellulose membranes. The membranes were probed with anti-EGFR, anti-pEGFR. After being probed with HRP-conjugated secondary antibodies, bound antibodies were detected with Western Lightning™ Chemiluminescence Reagent Plus kit (Perkin Elmer Life Sciences, Boston, MA, USA).

[In situ gelatin zymography] On cover glasses were covered with 0.178% gelatin and 0.022% fluorescein-conjugated gelatin, cells (2×10^5) were suspended in RPMI 1640/10% FBS and seeded. The cells were cultured for 6 hours to adhere to gelatin, the medium was replaced with CM / 10% FBS and the cells were cultured for an additional 18 hours. Cells on the cover glass were fixed with 3.7% paraformaldehyde and permeabilized with 0.5% Triton X-100. F-actin was stained with PBS containing 1% Alexa Fluor 488 phalloidin, and nuclei were further stained with PBS containing 300 nM DAPI. The fluorescence image was taken using an LSM 700

confocal microscope.

RESULTS: To investigate whether X-ray-irradiated cell-derived CM, which has been suggested to increase EGF, promotes cell infiltration through EGFR, the effect of AG1478 on EGFR phosphorylation. EGFR phosphorylation at 3 h of CM treatment was increased in 4 Gy CM treated cells compared to 0 Gy CM treated cells, and this increase was clearly suppressed by AG1478 treatment (Fig. 1A). Furthermore, Cell invasion capacity was increased in 4 Gy CM treated cells, and this increase was significantly suppressed by AG1478 treatment (Fig. 1B). These results suggest that X-ray-irradiated cell-derived CM promotes cell infiltration ability via EGFR. Next, we considered that EGF in CM derived from X-irradiated cells might promote the degradation ability of extracellular matrix via EGFR and examined it by in situ gelatin zymography. As shown in Fig. 2, the gelatin decomposition area per cell was significantly increased in the 4 Gy CM-treated cells. Furthermore, this increase was significantly suppressed by AG1478 treatment. These results suggest that X-ray-irradiated cell-derived CM promotes extracellular matrix resolution via EGFR.

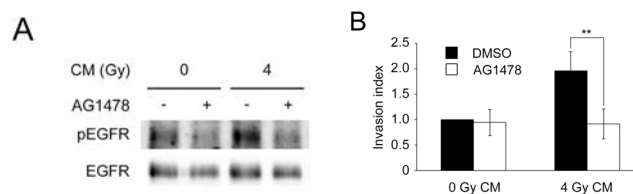


Fig. 1. Involvement of EGFR in promoting cell infiltration induced by X-irradiated cell-derived CM.

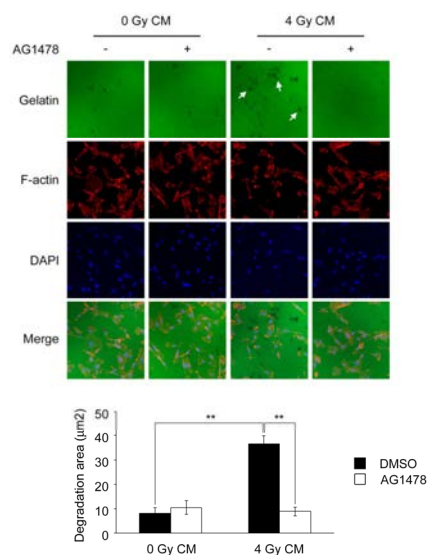


Fig. 2. Effect of CM on the degradation ability of extracellular matrix.

REFERENCES:

- [1] H. Yasui *et al.*, KURNS Progress Report 2018, PR8-7.
- [2] H. Yasui *et al.*, KURNS Progress Report 2019, PR6-8.

CO6-3 Physicochemical analysis of protein ILEI, which reduces amyloid- β protein production

E. Hibino^{1,2}, K. Morishima³, R. Inoue³, M. Sugiyama³,
and M. Nishimura¹

¹*Molecular Neuroscience Research Center, Shiga University of Medical Science*

²*Graduate School of Pharmaceutical Sciences, Nagoya University*

³*Institute for Integrated Radiation and Nuclear Science, Kyoto University*

INTRODUCTION: Although the number of patients with Alzheimer's disease in Japan continues to increase, no effective disease-modifying drugs have been developed until now. Alzheimer's disease is hypothesized to be caused by the excessive accumulation of amyloid- β protein ($A\beta$) in the brain, and we have previously discovered that the secreted protein ILEI reduces $A\beta$ production by a specific pathway [1]. After secreted extracellularly, ILEI binds to the extracellular region of presenilin-1, one of the components of the γ -secretase complex. Although the details are currently unknown, this binding promotes nonspecific proteolysis of the $A\beta$ precursor protein, the substrate of γ -secretase, and suppresses $A\beta$ production. However, the structural mechanisms involved in the binding are still unknown. More recently, the X-ray crystal structures of monomeric and dimeric forms of ILEI have been reported [2], but the relationship between the monomeric and dimeric forms and their functions is not clear. These structural aspects are critical issues for Alzheimer's disease drug development.

The objective of this study is to clarify the relationship of ILEI dimers to the inhibitory function of $A\beta$ production and to elucidate the molecular mechanism of ILEI.

EXPERIMENTS: The wild-type and C185A mutant of ILEI (55-227)-His was produced in an *E. coli* expression system and purified by Ni-NTA resin and size exclusion chromatography (SEC). SDS-PAGE and SEC in the non-reducing state confirm that they are a single band and a single peak, respectively. To compare the properties of wild-type and mutant forms, they were analyzed by analytical ultracentrifuge (AUC). The measurement temperature was 25°C and the rotational speeds were 60,000 rpm. To evaluate the function of $A\beta$ production, plasmids encoding APP-CTF and control vectors or plasmids encoding ILEI (wild-type or C185A mutant) were co-transfected into ILEI knock-out HEK293 cells, and the supernatant was quantified using an ELISA kit (Human Amyloid β (1-40) Assay Kit, IBL).

RESULTS: One of the functions of ILEI is oncogenesis, which is reported to be inhibited by the replacement of Cys185 with Ala [2]. We thus identified differences in physical properties to clarify the relationship between the C185A mutation and the inhibitory function of $A\beta$ production.

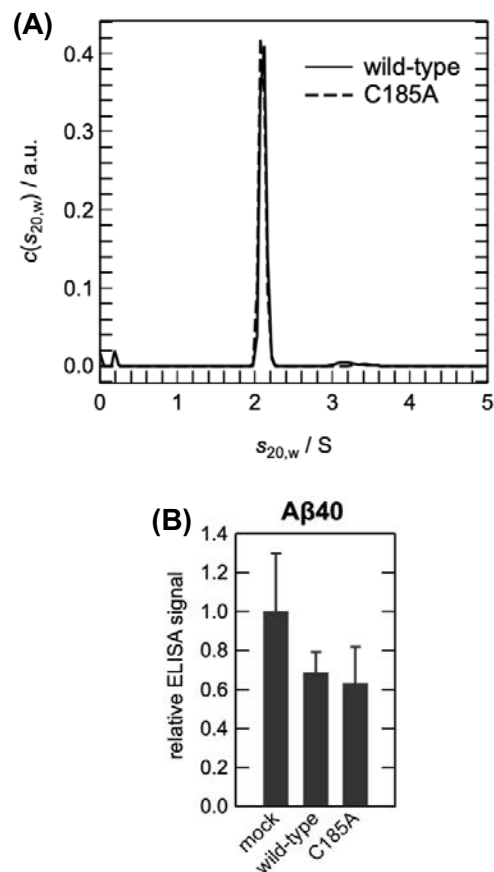


Fig. 1 **A**, Results obtained from analytical ultracentrifugation for wild-type and C185A mutant of ILEI. **B**, Quantitation of $A\beta$ 40 by ELISA.

First, the configuration of the wild-type and C185A mutants was analyzed by AUC, but no significant differences were observed (Fig. 1A). In addition, the amount of $A\beta$ was quantified by ELISA to analyze the inhibitory function of $A\beta$ production. As a result, it was found that C185A has the same ability to inhibit $A\beta$ production as wild-type (Fig. 1B). These results mean that the inhibitory function of ILEI in the production of $A\beta$ and oncogenesis were found to be exhibited by completely different mechanisms. This is an important finding for the development of ILEI-based drugs for Alzheimer's disease.

REFERENCES:

- [1] H. Hasegawa, L. Liu, I. Tooyama, S. Murayama and M. Nishimura, *Nat. Commun.*, **5** (2014) 3917.
- [2] M. Kral, C. Klimek, B. Kutay, G. Timelthaler, T. Lendl, B. Neuditschko, C. Gerner, M. Sibilica and A. Csizsar, *The FEBS Journal*, **284** (2017) 3484–3505.

CO6-4 Solution scattering approach for dynamics of Lys48-linked tri-ubiquitin chain

M. Yagi-Utsumi, M. Hiranyakorn, K. Kato, A. Okuda¹, K. Morishima¹, R. Inoue¹, and M. Sugiyama¹
Exploratory Research Center for Life and Living Systems (ExCELLS) and Institute for Molecular Science (IMS), National Institutes of Natural Sciences
¹*Institute for Integrated Radiation and Nuclear Science, Kyoto University*

INTRODUCTION: Ubiquitin (Ub) molecules can be enzymatically connected through a specific isopeptide linkage, thereby mediating various cellular processes by binding to Ub-interacting proteins through their hydrophobic surfaces. The Lys48-linked Ub chains, which serve as tags for proteasomal degradation, undergo conformational interconversions between open and closed states, in which the hydrophobic surfaces are exposed and shielded, respectively. Previously, we provided a quantitative view of such dynamic processes of Lys48-linked triUb chain in solution [1]. The native and cyclic forms of Ub chains are prepared with isotope labeling by in vitro enzymatic reactions. Our comparative NMR analyses using monomeric Ub and cyclic diUb as reference molecules enabled the quantification of populations of the open and closed states for each Ub unit of the native Ub chains (Fig. 1). The data indicated that the most distal Ub unit in the Ub chains was the most apt to expose its hydrophobic surface, suggesting its preferential involvement in interactions with the Ub-recognizing proteins. We also demonstrated that a mutational modification of the distal end of the Ub chain could remotely affect the solvent exposure of the hydrophobic surfaces of the other Ub units.

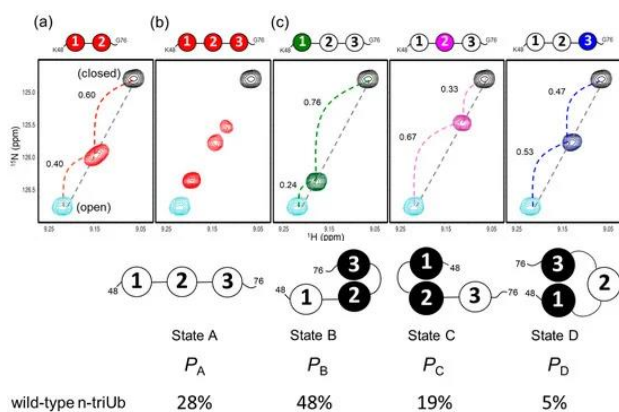


Fig. 1. (Upper) ¹H-¹⁵N HSQC peaks originating from Val70 of (a) uniformly ¹⁵N-labeled diUb (red), (b) uniformly ¹⁵N-labeled triUb (red), (c) unit-selectively ¹⁵N-labeled triUb chains at the distal Ub1 (green), the middle Ub2 (magenta) and the proximal Ub3 (blue). (Lower) Cartoon model of the conformational equilibrium of n-triUb. The populations of states A, B, C, and D of n-triUb are denoted as P_A , P_B , P_C , and P_D , respectively.

Small-angle neutron scattering (SANS) and small-angle X-ray scattering (SAXS) are powerful techniques for the structural characterization of biomolecular complexes. In particular, neutron spin echo (NSE) measurement enables a direct observation of coupled internal protein dynamics. Here, we attempted to elucidate the time scale of the transit domain motions of the Lys48-linked triUb chain as a feasibility study of NES collaborated with SAXS and molecular dynamics (MD) simulation.

EXPERIMENTS: We prepared the Lys48-linked triUb in D₂O solution (5mL, 10mg/ml). We had measured NSE of Lys48-linked triUb at NCNR, NIST. We also performed SEC-SAXS of Lys48-linked triUb chain using the laboratory-based SAXS instruments (NANOPIX, Rigaku).

RESULTS: We firstly performed SEC-SAXS of Lys48-linked triUb chain. As shown in Fig. 2, the experimental SAXS profile (blue marks) showed disagreement with that calculated one (red line) from crystallographic data (State D in Fig. 1). This result strongly supported that the dynamical conformational interconversions revealed by NMR experiments were also observed in SAXS data. Then, we measured NSE of Lys48-linked triUb at the two temperatures of 10 and 42 degrees. An incident neutron wavelength of 6 and 8 angstroms was used to cover fourier times up to 20 ns in a q-range from 0.06 to 0.22 inverse angstroms. Intermediate scattering functions for both states were successfully obtained. The effective diffusion constants (D_{eff}) were obtained by exponential fittings at each q. D_{eff} should include translational and rotational diffusion as well as internal domain motions. The experimentally obtained D_{eff} s are consistent with the MD simulation derived ones at 10 degrees. Based on these results, the contribution of the internal motions can be estimated. The analysis on the temperature dependence of the internal dynamics is on progress. We are trying to analyze the NSE data combined with computational analysis to observe the functional domain motions of Lys48-linked triUb.

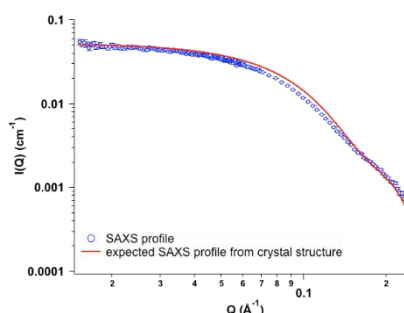


Fig. 2. SAXS of Lys48-linked triUb. Blue marks and red line show experimental and calculated data, respectively.

REFERENCE:

[1] M. Hiranyakorn *et al.*, *Int. J. Mol. Sci.* **21**, 5351 (2020). DOI: 10.3390/ijms21155351.

CO6-5 Radioresistance Mechanisms Acquired by Adaptive Evolution and their Evolutionary Mechanisms II

T. Saito

*Institute for Integrated Radiation and Nuclear Science,
Kyoto University*

INTRODUCTION: In nature, organisms have evolved diversely by adapting to various environmental conditions, some of which can survive in extremely severe environments. Elucidating the mechanisms by which organisms adapt to such severe environmental conditions can provide meaningful information on evolution and biological diversity. Some bacteria, known as radioresistant bacteria, demonstrate extreme resistance to ionizing radiation [1]. The extreme resistance mechanism of these bacteria to ionizing radiation is an interesting area of research from the standpoint of adaptive mechanisms employed by organisms in nature. In order to elucidate the mechanisms of radioresistance in these organisms, their biological defense mechanisms against external stress must be investigated at the molecular level. However, studies on naturally-occurring radioresistant organisms are particularly challenging owing to the limited knowledge of their genetic and biochemical properties. Therefore, in this study, radioresistant *Escherichia coli*, the wild-type genetic and biochemical characteristics of which have been elucidated in detail, were generated by an adaptive evolution experiment using gamma rays as the selective pressure, and the characteristics of the evolved radioresistant *E. coli* were compared with those of the wild-type. A previous reports of this study described the generation of radioresistant *E. coli* with a 7.9-fold resistance compared with that of wild-type *E. coli* [2, 3]. A significant increase in the expression of genes involved in SOS response, response to stimulus, DNA repair, and DNA metabolism (described as anti-stress genes in the text) in radioresistant *E. coli* compared with wild-type *E. coli* under constitutive conditions was observed. This report describes differences in gene expression status between wild-type and radioresistant *E. coli* following gamma irradiation.

EXPERIMENTS: Gamma irradiation and RNA sequencing: Wild-type and radioresistant *E. coli* cells were grown in LB medium at 37°C and 200 rpm to the early log phase. Twenty milliliters of the culture medium was centrifuged at 2000 × *g* at 20°C for 20 min. The supernatant was removed, and the pellet was suspended in 5 mL of PBS (–). Wild-type and radioresistant *E. coli* cell suspensions were irradiated with gamma rays at a 33% survival dose (65 Gy and 420 Gy, respectively) at a dose rate of 22 Gy/min at 20 ± 3°C. The irradiated *E. coli* cell suspension

was added to 200 mL of LB medium and incubated at 37°C and 200 rpm for 2 h. The resulting *E. coli* cell suspension was centrifuged at 4000 × *g* at 4°C for 10 min, and the supernatant was removed to obtain a pellet. Total RNA extraction from the resulting pellet and RNA sequencing were performed according to previously reported methods [3].

Analysis of gene expression status: In the analysis, gene expression data with “fragments per kilobase of exon per million reads mapped” values less than 1 for all samples from the two groups compared were filtered out to eliminate noise data. Genes differentially expressed in radioresistant *E. coli* compared with those in wild-type *E. coli* were identified by Welch's t-test and correction for multiple testing using the Benjamini and Hochberg method (BH method) [4]. In addition, Gene Ontology (GO) analysis for the differentially expressed genes (DEGs) in radioresistant *E. coli* was performed using the Database for Annotation, Visualization and Integrated Discovery bioinformatics resources ver.6.8.

Statistical analysis: Welch's t-test and BH method were used to identify DEGs among many genes, and a q-value of less than 0.05 was considered statistically significant. The Expression Analysis Systematic Explorer score was used to test for significance in the GO analysis, and a P-value of less than 0.05 was considered statistically significant [5].

RESULTS: No significant differences were observed in anti-stress gene expression between the non-irradiated and gamma-irradiated wild-type *E. coli*. In contrast, comparing non-irradiated and gamma-irradiated radioresistant *E. coli*, the expression levels of anti-stress genes were significantly increased in gamma-irradiated radioresistant *E. coli*. Furthermore, in a comparison between gamma-irradiated wild-type and gamma-irradiated radioresistant *E. coli*, the expression levels of anti-stress genes in the radioresistant *E. coli* were significantly higher than that in the wild-type *E. coli*. These results strongly suggest that the radiation induction of genes involved in cell recovery, DNA repair, cell survival, and stress response is involved in the mechanism of high radioresistance in the evolved radioresistant *E. coli*.

REFERENCES:

- [1] T. Saito, *Viva Origino*, **30** (2007) 85–92.
- [2] T. Saito, *KURNS ProgressReport 2019* (2020) 211.
- [3] T. Saito, *KURNS ProgressReport 2020* (2021) 162.
- [4] Y. Benjamini and Y. Hochberg, *J. R. Statist. Soc. B*, **57** (1995) 289–300.
- [5] D. W. Huang *et al.*, *Nat. Protoc.* **4** (2009) 44–57.

CO6-6 Oligomeric structural transition of HspB1 from Chinese hamster

N. Kurokawa, R. Midorikawa, M. Nakamura, K. Noguchi¹, K. Morishima², R. Inoue², M. Sugiyama² and M. Yohda

Department of Biotechnology and Life Science, Tokyo University of Agriculture and Technology

¹Instrumentation Analysis Center, Tokyo University of Agriculture and Technology

²Institute for Integrated Radiation and Nuclear Science, Kyoto University

INTRODUCTION: HspB1 is a mammalian small heat shock protein that is ubiquitously expressed in almost all tissues and involved in regulating many vital functions. Previously, we analyzed the oligomeric structure of HspB1 from CHO cells (CgHspB1) by size exclusion chromatography with multiangle light scattering (SEC-MALS) and small-angle X-ray scattering (SAXS). The results suggested that CgHspB1 has a 16-mer structure [1]. However, the molecular architecture of HspB1 is controversial. Recently, the crystal structure of human HspB1 was reported [2]. Twenty-four monomers form the oligomeric complex of human HspB1 in a spherical configuration. Each monomer is constructed of a structurally conserved α -crystallin domain exhibiting a 6-stranded beta-sandwich as previously described with mobile N- and C-termini. These results suggest the oligomeric structure of HspB1 changes with the conditions, such as temperature or concentration. This study examined the oligomeric structural change of CgHspB1 by sedimentation velocity analytical ultracentrifugation (SV-AUC).

EXPERIMENTS: Wild-type CgHspB1 and the phosphorylated mimics CgHspB1 and CgHspB1S15D were expressed in *E. coli* using a pET23b vector. They were purified by anion exchange chromatography using TOYOPEARL DEAE-650, RESOURCE Q column, and gel filtration chromatography using Superdex 200. The size of the oligomer structure under various temperature conditions was examined by analytical ultracentrifugation (AUC).

RESULTS: Figure 1 shows the SV-AUC results of CgHspB1 wild type (CgHspB1WT) depending on the temperature and concentration. At a low temperature of 4 °C, CgHspB1 exists as an 18-mer, probably a trimeric complex of hexamers. It is relatively unstable and partially dissociates into small oligomers, hexamers, and dodecamers. At elevated temperatures, the 24-mer was more stable than the 18-mer. The 24-mer is also in dynamic equilibrium with the dissociated oligomers in the hexameric unit. The hexamer further dissociates to dimers. Previously, we showed that a phosphorylation mimic mutant of CgHspB1 with the replacement of Ser15 with Asp (CgHspB1S15D) exhibited relatively lower oligomer stability and more remarkable chaperone activity than the wild type [1]. In AUC-SV, the CgHspB1S15D mutant showed almost identical results as CgHspB1WT. Although we expected to observe more

dissociated conformers in CgHspB1S15D at 40 °C, there was virtually no difference. To elucidate the role of the disulfide bond, we examined the effect of dithiothreitol (DTT) on the oligomer conformation of CgHspB1WT at 40 °C. At a low concentration of 0.05 mg/mL, the large oligomer of CgHspB1WT almost wholly dissociated into small oligomers. They seem to be dimers, hexamers, dodecamers, and 18-mers without DTT. In the presence of DTT, the proportion of dimers increased, suggesting that disulfide bonds between dimers partially stabilize hexamers.

CONCLUSION: Our results suggest the following conformational transition model. At a low temperature of 4 °C, CgHspB1 exists as an 18-mer, probably a trimeric complex of hexamers. It is relatively unstable and partially dissociates into small oligomers, hexamers, and dodecamers. At elevated temperatures, the 24-mer was more stable than the 18-mer. The 24-mer is also in dynamic equilibrium with the dissociated oligomers in the hexameric unit. The hexamer further dissociates to dimers. The disulfide bond between conserved cysteine residues seems to be partly responsible for stabilizing hexamers.

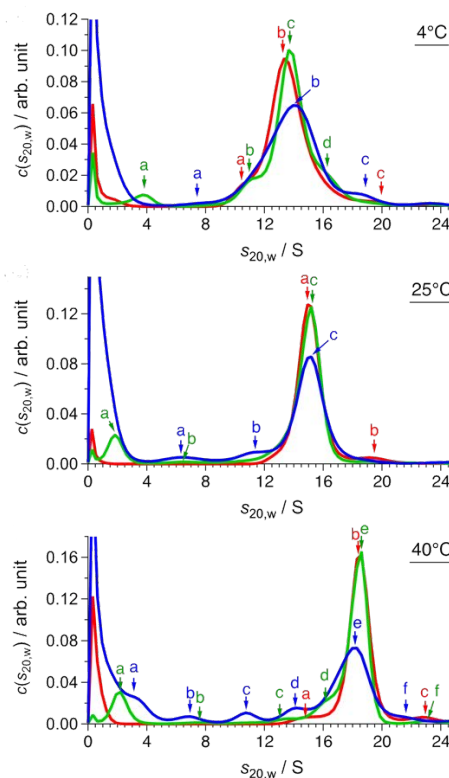


Fig. 1. SV-AUC results of CgHspB1 WT at 4 °C, 25 °C, and 40 °C. Red, green, and blue lines represent $c(s_{20,w})$ at 1.5 mg/mL, 0.5 mg/mL, and 0.1 mg/mL, respectively.

REFERENCES:

- [1] E. Sha *et al.*, FEBS Open Bio., 9 (2019) 1826–1834.
- [2] L. Nappi *et al.*, J. Clin. Invest. 130 (2020) 699–714.

CO6-7 Study of Ku recognition to a DNA DSB end induced by ionizing radiation

K. Akamatsu¹, N. Shikazono¹ and T. Saito²

¹*Institute of Quantum Life Science, National Institutes for Quantum and Radiological Science and Technology (QST)*

²*KURNS*

INTRODUCTION:

DNA lesions induced by ionizing radiation and chemicals can cause mutation and carcinogenesis. In particular, complex double strand break (DSB), having a few base lesions near the end, is believed to hardly be repaired. This damage would be induced around high-LET ionizing radiation tracks. In fact, evidence is found in the direct observation by AFM (atomic force microscopy) [1]. However, the reason why the complex DSBs are unreparable is unknown. A possible hypothesis is that a repair system by non-homologous end joining (NHEJ), initiated by recognition of DSB end by Ku70/80 heterodimer (Ku), is unsuccessful due to a complex DSB end. In this study we investigate the affinity of Ku-DSB complex and possible formation of Ku-DSB covalent cross-linking using a real DSB end induced by irradiation as well as a model DSB end. Abundant DNA fragments with DSB are needed for this study.

EXPERIMENTS:

•Sample preparation and irradiation

The supercoiled plasmid DNA was used as a sample for the study. The DNA was dissolved to be ~10 mg/mL in 0.2 M Tris-HCl buffer (pH 7.5) which is a cell-mimetic condition in relation to radical scavenging capacity. Eight microliters of the DNA solution were transferred to a glass plate (10 mm ϕ) under 100 % RH at r.t., and was irradiated with heavy ion beams at TIARA and HIMAC (QST), and ⁶⁰Co γ -rays (LET: ~0.3 keV/ μ m; KURNS) as a standard radiation source. Each of irradiated DNA samples was divided into a few aliquots and purified by ethanol precipitation, followed by being dried in vacuum. The dry samples were kept at -20°C until use.

•Isolation of linear-formed fragment from irradiated pUC19 by agarose gel electrophoresis

The irradiated DNA pellet was dissolved in 80 μ L of 0.5 x TBE buffer at pH 8 with loading dye solution. The DNA sample solution was applied to several wells on an agarose gel. After electrophoresis (25V, 18h at 4°C), one lane was cut out by a scalpel and was stained by ethidium bromide, which is used as a marker gel to isolate a band containing linear-formed fragment from the other lanes. The stained marker gel was reset on the original gel, and the bands containing the DNA with DSBs were collected using an illuminator equipped with a visible light excitation system. The obtained gel fragments were set into D-Tube Dialyzer to isolate the DNA fragments from the gel by electrophoresis (120V, 4°C, 1h).

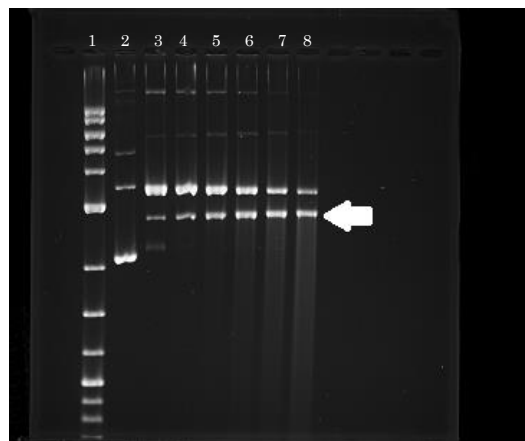


Fig. 1. The image of agarose gel electrophoresis of γ -irradiated pUC19. The gel was stained by ethidium bromide. Lane1: 0.1-10kbp 2-log ladder marker, lane2: non-irradiated control (supercoiled form), lane3: 1kGy, lane4: 2kGy, lane5: 3kGy, lane6: 5kGy, lane7: 7kGy, lane8: 10kGy. The arrow indicates linear formed DNA fragments. The upper bands than the arrow indicate those of the open circular DNA, induced by a single strand break formation on a supercoiled DNA.

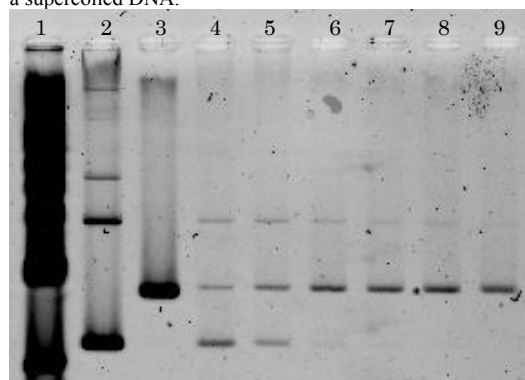


Fig. 2. The image of agarose gel electrophoresis of isolated linear-formed pUC19 fragments induced by γ -irradiation. The gel was stained by ethidium bromide. Lane1: 0.1-10kbp 2-log ladder marker, lane2: non-irradiated control, lane3: pUC19 digested by Sma I, lane4: 1kGy, lane5: 2kGy, lane6: 3kGy, lane7: 5kGy, lane8: 7kGy, lane9: 10kGy.

RESULTS AND DISCUSSION:

Figure 1 shows an agarose gel image of γ -irradiated pUC19, indicating that the original supercoiled DNA was successively changed to linear formed fragment via open circular form with increasing absorption dose. Figure 2 shows a gel image of samples after isolating linear-formed DNA. At a low dose, supercoiled DNA fragments fairly remain, whereas highly-fragmented DNA molecules may be contaminated at a high dose. Consequently, the optical dose at the present irradiation condition is around 3kGy. We have plans to use the isolated DNA substrates for the study of Ku-DSB interaction by means of e.g., electrophoretic mobility shift assay and slot-blot-ELISA.

REFERENCES:

- [1] T. Nakano, *et al.*, Proc.Natl.Acad.Sci.USA **119** (2022) e2119132119.

CO6-8 Estimation of trace elements in foods and amounts of intake of wild Japanese macaques

M. Fukushima¹, Y. Tsuji¹, Y. Iinuma²

¹Faculty of Sciences and Engineering, Ishinomaki Senshu University

²Institute for Integrated Radiation and Nuclear Science, Kyoto University

INTRODUCTION: It is important to obtain multi element levels in food samples of wild animals for their conservation. Several reports on behavior observation, nutritional analyses, and estimations of energy and protein intake for wild Japanese macaques (*Macaca fuscata*), endemic species in Japan, have been published [1-3]. Primates need trace elements in addition to basic nutritional terms (e.g., protein and energy) [4], but there have been less information on their intake of trace elements from natural food. Y. Tsuji collected food and feces of wild macaques inhabiting Kinkazan Island, Ishinomaki, Miyagi in 2004-2005. Kinkazan is isolated from main island about 0.7 km away, and there are no residents. Intake of trace elements can be estimated by subtracting amounts of elements in feces from those of food. Also, another approach for estimating intake of trace elements, enzymolysis was applied to food samples.

EXPERIMENTAL: Food samples included leaves, flowers, buds, seeds, barks, nuts of woody plants, seaweeds, shells, insects, leaves of herbaceous plants, and mushrooms. Samples were freeze dried without washing with water, and pulverized. Dried powder of nuts was then dry-ashed for 5.5 hours at 550°C. Feces were kept in 70% ethanol after the collection, and ashed for 2 hours at 600°C after drying ethanol at 60°C.

NAA was done by two different conditions according to nuclides for the interest. 1) One portion of samples was irradiated for 1-1.5 min in TcPn site. After 3 minutes decay, gamma spectrum was measured for 10 minutes by Ge detector with CSS. Levels of Br, Ca, Cl, Cu, I, K, Mg, Mn, Na, and V were analyzed using ⁸⁰Br, ⁴⁹Ca, ³⁸Cl, ⁶⁴Cu, ¹²⁸I, ⁴²K, ²⁷Mg, ⁵⁶Mn, ²⁴Na, and ⁵²V. 2) Another portion of samples was irradiated for 1 hour, and gamma spectrum was measured for 20 minutes after 1 month decay for analyzing Ag, Co, Cr, Cs, Fe, Rb, Sc, Se, and Zn using ^{110m}Ag, ⁶⁰Co, ⁵¹Cr, ¹³⁴Cs, ⁵⁹Fe, ⁸⁶Rb, ⁴⁶Sc, ⁷⁵Se, and ⁶⁵Zn, respectively. NAA method used was validated using NIST SRM 1515 Apple Leaves, NIST SRM 1566b Oyster Tissue, SRM 1573a Tomato Leaves, NIST SRM 1575 Pine Needles, and NRCC-TORT-1 Lobster Hepatopancreas.

Enzymolysis was done by stepwise using α -amylase, protease, and amyloglucosidase to 1 g of food sample, after filtrating the residue, ethanol was added to elute for precipitating the water-soluble fiber. Both of residue and water-soluble fiber are thought to be non-bioavailable portion. Thus, intake of trace elements was estimated by subtracting amounts of elements in non-bioavailable portion from total amount of elements in food samples before enzymolysis.

RESULTS: One of results obtained for food sample are

shown in Fig. 1 as an example. Concentrations were calculated as average and standard deviation for results (n = 2 ~ 5). Fe concentrations differed much between species of trees. Almost all elemental levels except Se were extremely high comparing to food of human beings.

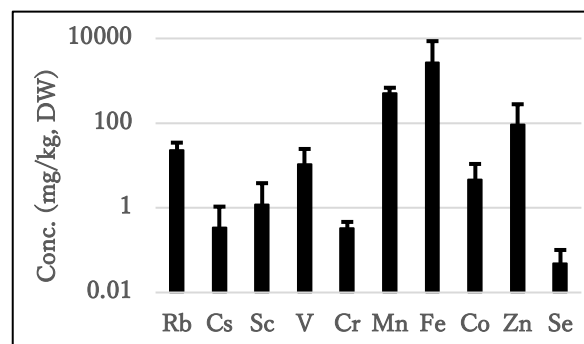


Fig.1 Levels of minor elements in woody leaves (n=2~5) taken by Japanese macaques.

Since Tsuji identified each macaque individual, he could collect fecal samples of identified animals. As an example, we show estimated intake of elements in food and fecal samples for a female individual (body weight: 8 kg) in Table 1.

Table 1 Estimated intake and excretion of elements of one specific female individual of Japanese macaque.

Element	Estimated intake (mg/day)	Excretion (mg/occasion)
Ca	694	233
K	3150	186
Mg	329	64.5
Fe	292	611
Zn	9.9	15.1
Cu	2.4	0.38
Mn	17.7	6.2
I	0.64	Not determined
Se	Not detected	0.36
Cr	0.04	0.88
Rb	5.9	9.4
V	0.44	0.15

The intake did not cover the excretion for Fe, Zn, Cr, and Rb. Further experiments are needed for future for the nutritional information for Japanese macaques.

REFERENCES

- [1] Tsuji *et al.*, *Primates*, **49** (2008) 157-160.
- [2] Tsuji & Takatsuki, *Int. J. Primatol.*, **33** (2012) 489-512.
- [3] Kurihara *et al.*, *Primates*, **61** (2020) 427-442.
- [4] National Research Council (National Academic Press) (2003).

CO6-9 Evaluation of radiation resistance of lens constituent proteins involved in age-related cataract

T. Takata¹ and K. Lampi²

¹ Institute for Integrated Radiation and Nuclear Science, Kyoto University

² Oregon Health & Science University

INTRODUCTION:

The transparency of the lens is maintained by the stable long-lived protein interactions, comprising α -, β -, and γ -crystallin families. A kind of intrinsic damages of lens tissues, such as heat damage, is increased with time. On the other hand, extrinsic damages, such as UV damage, strongly depends on the living environment in the world. Lens contains various protection systems to prevent UV-inducing oxidative stress; however, damaged proteins can still accumulate because these protection systems are lost with aging. The damaged crystallin species have been further subjected to the additional covalent modifications of amino acid residues levels [1]. Those modifications, which are generated by UV light, ionizing irradiation and oxidative stress, are believed lead to the development of age-related cataracts. There are many data on the oxidation “sites” of aged human lens crystallin species, but there are few studies of the oxidation “effects” for each amino acid residue in crystallin. One of oxidative stress inducer, γ -Irradiation generates free radicals and reactive oxygen species (ROS) such as hydroxyl radicals, superoxide, and singlet oxygen, which have been predicted to induce the oxidation of amino acids, as well as the truncation and cross-linking of proteins. Due to COVID-19, the preparation of mouse lens and the timing of irradiation experiment did not match. So, we used our stock aged human lens for targeting the oxidation “sites” for mass spectrometry. As a result, we could find out the oxidation “sites” in human lens β B2-crystallin. The further aim of this study was to investigate that effect of oxidation for β B2-crystallin stabilities.

EXPERIMENTS:

Material Lens from 79 years old was homogenized and fractionated by centrifugation to isolate lens water soluble (WS) fractions. The WS proteins were dissolved and applied for trypsin digestion as previously reported [2]. Recombinantly expressed lens β B2-crystallin wild-type (WT) were prepared and purified as described previously [3]. *In vivo* oxidation candidate sites in β B2-crystallin were mimicked by replacing Tryptophan residues (W) into Phenyl alanine (F) residues by using a QuikChange Mutagenesis kit (Stratagene). The purification was performed as WT.

LC-MS analysis The tryptic peptides from aged lens WS were filtered and injected into LC-MS/MS for modification analysis as previously reported [2]. The oxidation was screened using by Proteome Discoverer™ 1.0 software (ThermoFisher, USA).

CD analysis Circular dichroism measurements in the far-UV range (far-UVCD) were obtained by using a

J-810 spectropolarimeter (JASCO, Tokyo, Japan). For far-UVCD, 0.3 mg/mL of protein sample was prepared, and measured in a cell with a 0.1-cm path length.

RESULTS:

The database search for oxidation of amino acid residues in 79 years old lens showed many modifications in crystallin species. The heavily oxidation of W151 was detected in β B2-crystallin (Fig. 1). There was also heavily acetylation of N-terminal of each protein (data not shown). These data were similar with our previous results that increasing oxidation of tryptophan residues on the β B2-crystallin after γ -Irradiation.

Sequence	Activation Type	Modifications
GEYPRWDSWTSSR	CID	
IILYENPNFTGKK	CID	Y4(Oxidation)
IILYENPNFTGKK	CID	
TDLSLRLPIK	CID	
VQSGTWVGyQYPGyR	CID	W6(Oxidation)...
VQSGTWVGyQYPGyR	CID	Y9(Oxidation)Y...
VQSGTWVGyQYPGyR	CID	Y9(Oxidation)Y...
VQSGTWVGyQYPGyR	CID	Y11(Oxidation)...

Fig. 1. Heavily Oxidation of Trp151 in human β B2-crystallin from aged lens.

Next, to investigate the significance of tryptophan residues in β B2-crystallin, four β B2-crystallin mimic proteins were prepared (wild type, W82F, W85F, and W151F). The CD analysis for four out of four mimics indicated no structural alteration of secondary structure (Fig. 2).

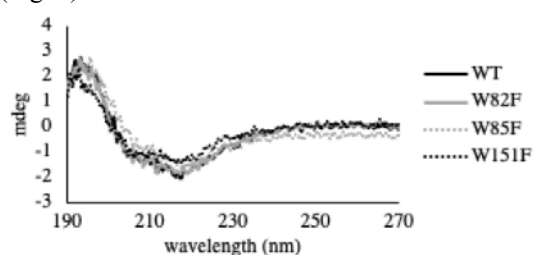


Fig. 2. CD analysis for all β B2-crystallin mimics.

Since the structural differences between W and F is small, the effect for the secondary structure maybe little. However, loss of indole ring should be critical for oxidative stress. To see these effect, β B2-crystallin mimics would be used for γ -irradiation assay.

REFERENCES:

- [1] B. Searle *et al.*, *J Proteome Res*, **4** (2005) 546-554.
- [2] N. Fujii *et al.*, *J. Biol Chem.*, **287** (2012) 663-669.
- [3] K. Lampi *et al.*, *Biochemistry*. **45** (2006) 3146-3153.

CO6-10 Asp racemization/isomerization in shedding products of cell adhesion molecule 1 is potentially involved in the neurodegeneration induced by elevated pressure

A. Yoneshige¹, A. Ito¹ and T. Takata²

¹Department of Pathology, Kindai University

²KURNS

INTRODUCTION: The elevation of internal pressure is often involved in neurodegeneration; intraocular and intraventricular pressure elevations over 20–30 cmH₂O cause glaucoma and hydrocephalus, respectively.

Previously, to investigate the mechanisms by which elevation of intraluminal pressure causes cell or tissue degeneration, we devised a novel two-chamber culture system that enabled us to subject cultured cells to low levels of water pressure (2-50 cmH₂O pressure load) [1,2]. We found that mouse primary neurons degenerated when the water pressure was above 30 cmH₂O, and that ectodomain shedding of synaptic cell adhesion molecule 1 (CADM1) increased in a water pressure-dependent manner [1]. We also discovered that the increase of intracellular product of CADM1 shedding (C-terminal fragment, CADM1-CTF) resulted in decreased neurite density with punctate localization of CADM1 suggesting its aggregation in neurites [1].

CADM1-CTF is rich in Asp residues neighbored by Ala residues, and the conversion of these amino acids to poly-Gly diminished its aggregation state. Since the racemization and isomerization of Asp residues contributes to aggregation of various proteins and it likely occurred when the neighboring residues are small [3,4], these insights led us to hypothesize an involvement of Asp racemization/isomerization in the neurodegeneration induced by internal pressure elevation.

EXPERIMENTS:

(1) Synthetic peptide of internal sequence of CADM1-CTF (GADDAADADTAIINAEGGQNNSEEK) was incubated at 50°C for 0-15 days and applied to LC-MS to identify Asp isomer-containing peptides.

(2) Mouse neuroblastoma cell line Neuro-2a cells with exogenously expressed CADM1-CTF were cultured under 50 cmH₂O and were prepared for LC-MS analysis.

(3) To mimic the human ocular hypertension, mouse retinal explant cultures were prepared to exert water pressure on to the tissues.

RESULTS:

(1) In LC-MS analysis of CADM1-CTF synthetic peptide, multiple peaks were detected after 1 day at pH 6.0 or pH 7.0 indicating that Asp racemization/isomerization could occur under neutral pH.

(2) CADM1-CTF proteins in Neuro-2a cells were solubilized with water, Triton X-100 containing buffer, or SDS containing buffer after 3 days culture under 50 cmH₂O, and CADM1 immunoblot was carried out. CADM1-CTF protein yields (CADM1-CTF / total proteins) were in the order Triton X-100 > SDS > water,

however, the peptide peak was not identified using with LC-MS. To resolve this problem, future experiments are planned for the isolation of CADM1-CTF from cell extracts by immunoprecipitation with the antibody recognize C-terminal of CADM1.

(3) In retinal explant cultures, since PI-positive necrotic cells have begun to appear after 3 days at atmospheric pressure, the cultured retinae were collected at 2 days *in vitro*. The number of TUNEL-positive apoptotic retinal ganglion cells and the degree of GFAP-positive gliosis were analyzed histologically. Those neurodegenerative features were reproduced experimentally in cultured retinae at 50 cmH₂O. Furthermore, we found that Lipocalin-2, an iron binding protein is involved in retinal degeneration both *in vitro* and *in vivo* [5] (Fig.1). Since iron dysregulation induces oxidative stress, further studies exploring the linkage between oxidative stress and Asp racemization/isomerization are needed.

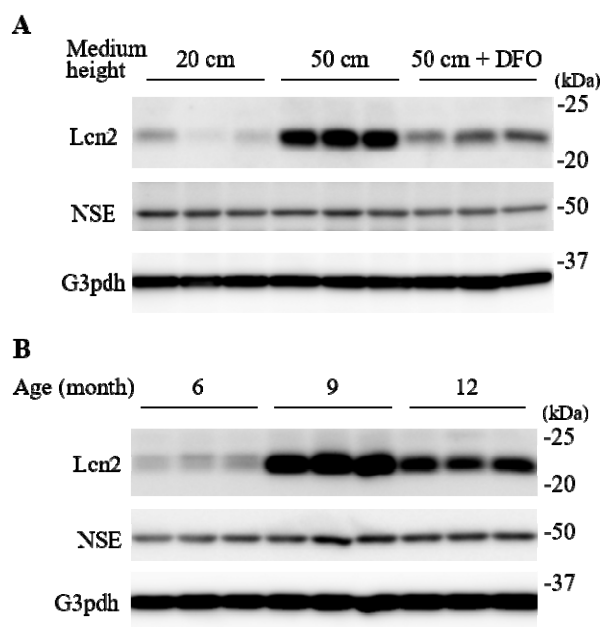


Fig. 1. Lipocalin-2 (Lcn2) upregulation in cultured retinae (A) and in retinae of glaucomatous DBA/2J mice (B). For more information, refer to [5].

REFERENCES:

- [1] A. Yoneshige *et al.*, *Mol. Neurobiol.*, **54** (2017) 6378-6390.
- [2] M. Hagiwara *et al.*, *Front. Physiol.*, **8** (2017) 997.
- [3] N. Fujii *et al.*, *J. Biochem.*, **116** (1994) 663-669.
- [4] T. Takata *et al.*, *Protein Sci.*, **29** (2020) 955-965.
- [5] A. Yoneshige *et al.*, *Front. Cell Dev. Biol.*, **9** (2021) 664327.

CO6-11 The Study of Boron Neutron Capture Therapy (BNCT) for Primary Central Nervous System Lymphoma (PCNSL)

Hideki Kashiwagi¹, Shinji Kawabata¹, Kohei Yoshimura¹, Yusuke Fukuo¹, Takuya Kanemitsu¹, Koji Takeuchi¹, Gen Futamura¹, Ryo Hiramatsu¹, Tsubasa Watanabe², Takushi Takata², Hiroki Tanaka², Minoru Suzuki², Shin-Ichi Miyatake³, Koji Ono³, Masahiko Wanibuchi¹

¹ Department of Neurosurgery, Osaka Medical and Pharmaceutical University

² Institute for Integrated Radiation and Nuclear Science, Kyoto University

³ Kansai BNCT Medical Center, Osaka Medical and Pharmaceutical University

Introduction:

Primary central nervous system lymphoma (PCNSL) is classified as WHO grade IV and accounts for 5% of all brain tumors [1, 2]. Standard care of PCNSL is based on high-dose methotrexate (HD-MTX) chemotherapy followed by whole brain radiation therapy (WBRT), and is the widely recommended initial treatment. This tumor responds well to initial therapy, but relapses after successful treatment are causes of poor prognosis due to the lack of safe and effective treatments for relapse; BNCT may be an effective treatment for PCNSL relapse because it is a highly cell-selective particle therapy. Therefore, we conducted basic experiments of BNCT for PCNSL in order to expand the indication of BNCT for the treatment of recurrent / refractory PCNSL.

Materials and Methods:

A CNS lymphoma model was created by inoculating the Raji human lymphoma cell line into the BALB/c nu-nu mice brain, which has been shown to accumulate boron in tumor cells by exposing to BPA in vitro. The boron compound used for all experiments was boronophenylalanine (BPA), which was administered intraperitoneally and the dose was 500mg/kg b.w. (24 mg Boron/kg). The reactor power of the KUR was 1 MW and the irradiation times were 15 or 30 minutes. The mouse CNS lymphoma models were randomly divided into the following 5 groups for neutron irradiation experiments: untreated control group (Untreated), BPA only control group (BPA control), neutron 30 minutes irradiation control group (Irradiated), BPA administration followed by 15 minutes neutron irradiation group (BNCT 15-min), and BPA administration followed by 30 minutes neutron irradiation group (BPA 30-min). The results were analyzed using Kaplan-Meier survival curves and statistical differences are shown using the log-rank test. [3]

Results:

The results of BNCT study for the mouse CNS lymphoma models divided to 5 groups described above were summarized in Table 1., and the Kaplan-Meier survival curves

were shown in Fig. 1. The median survival time (MST) for each group were as follows: Untreated; 26.5 days [95% confidence interval (CI); 23.5 – 33 days], BPA control; 31.0 days [95% CI; 24 – 33 days], Irradiated; 31.5 days [95% CI; 28 – 33 days], BPA BNCT-15min; 39 days [95% CI; 35.5 – 48.5 days], BPA BNCT-30min; 44.0 days [95% CI; 37 – days]. There were statistically significant differences between the BPA BNCT 15-min and Untreated ($p = 0.02$) and between the BPA BNCT 30-min group and Untreated ($p = 0.007$). [3]

Table 1. The BNCT result for the CNS lymphoma models

Group	n	MST (days)	95% CI (days)
Untreated	6	26.5	23.5-33.0
BPA control	6	31.0	24.0-33.0
Irradiated	8	31.5	28.0-33.0
BPA BNCT 15-min	7	39.0	35.5-48.5
BPA BNCT 30-min	8	44.0	37-

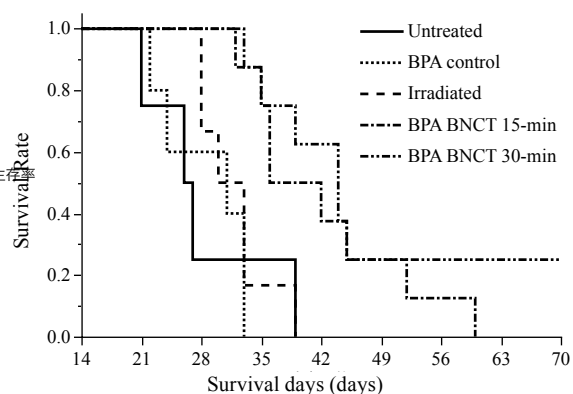


Fig. 1 The Kaplan-Meier survival curves. The BPA-BNCT groups obtained a significant survival advantage over the control group.

Conclusion:

BNCT with BPA was highly effective in an experimental animal model of PCNSL. Some new treatment options for PCNSL are needed and BNCT may be a promising treatment option for PCNSL. The results of this study suggest that future clinical trials exploring the potential of BNCT as a new treatment option for PCNSL may be successful.

References:

- [1] Ostrom, Q.T. *et al.*, *Neuro Oncol*, 21 (2019) v1-v100.
- [2] Villano, J.L. *et al.*, *Br J Cancer*, 105 (2011) 1414-1418.
- [3] K.Yoshimura *et al.*, *Cells*, 10(12) (2021) 3398.

CO6-12 Evaluation of boron neutron capture therapy (BNCT) using brain tumor bearing rats or mice models

Hideki Kashiwagi¹, Shinji Kawabata¹, Ryo Kayama¹, Kohei Yoshimura¹, Yusuke Fukuo¹, Takuya Kanemitsu¹, Koji Takeuchi¹, Gen Futamura¹, Ryo Hiramatsu¹, Kai Nishimura², Kazuki Kawai², Takushi Takata³, Hiroki Tanaka³, Tsubasa Watanabe³, Minoru Suzuki³, Shin-Ichi Miyatake⁴, Hiroyuki Nakamura², Masahiko Wanibuchi¹

¹ Department of Neurosurgery, Osaka Medical and Pharmaceutical University

² Laboratory for Chemistry and Life Science, Institute of Innovative Research, Tokyo Institute of Technology

³ Institute for Integrated Radiation and Nuclear Science, Kyoto University

⁴ Kansai BNCT Medical Center, Osaka Medical and Pharmaceutical University

Introduction:

Boron neutron capture therapy (BNCT), which can be targeted at the cellular level using high-energy particle beams, is a promising treatment for high-grade gliomas (HG). We have demonstrated the BNCT efficacy using maleimide-conjugated *closo*-dodecaborate (MID) bound serum albumin (MID-AC) as a drug delivery system for an F98 rat brain tumor model. MID-AC accumulated in the brain tumor and BNCT using MID-AC produced approximately the same therapeutic effect as BNCT using BPA [1]. Whereas, cyclic RGD peptide is known to bind to integrins that overexpress in many cancer cells including glioma cells. We focused on c(RGDfK), which binds strongly to integrin $\alpha_v\beta_3$. Consequently, the cRGD peptide ligand conjugated serum albumin bound MID (cRGD-MID-AC) has been developed. BNCT using cRGD-MID-AC showed significant tumor growth suppression in the U87MG xenograft subcutaneous tumor models after neutron irradiation [2]. However, the efficacy of BNCT against HG needs to be evaluated in an experimental brain tumor model due to the different nature of subcutaneous and intracerebral tumors, and thus this neutron irradiation experiment was conducted in a rat brain tumor model.

Materials and Methods:

To evaluate the BNCT efficacy at cRGD-MID-AC administration to the rat brain tumor model, an *in vivo* neutron irradiation experiment was performed at KUR. F98 rat glioma cells and Fischer rats were used and created the F98 rat glioma bearing brain tumor model. The result was analyzed using Kaplan-Meier survival curves. The reactor power of KUR was 5 MW and the irradiation time was 20 minutes. The F98 rat glioma models were randomly

divided into the following six groups: untreated control group (Untreated), neutron irradiated control group (Irradiated), neutron irradiation following 2.5 or 8 hours after termination of intravenous administration (*i.v.*) of BPA (BPA 2.5 h or 8 h), and neutron irradiation following 2.5 or 8 hours after termination of *i.v.* of cRGD-MID-AC (cRGD-MID-AC 2.5 h or 8 h).

Results:

The treatment effect was evaluated by using Kaplan-Meier survival curves. Each median survival times (MST) was as follows: Untreated; 30.0 days [95% confidence interval (CI); 26–34 days], Irradiated; 35.0 days [95% CI; 22–40 days], BPA 2.5 h; 42.0 days [95% CI; 39–50 days], BPA 8 h; 40 days [95% CI; 34–48 days], cRGD-MID-AC 2.5 h; 43.0 days [95% CI; 32–47 days], and cRGD-MID-AC 8 h; 38.5 days [95% CI; 27– days]. Significant differences were statistically observed between Untreated and all BNCT groups by the log-rank test. At the case of cRGD-MID-AC 8h, one F98 rat glioma model of them still survived for a long time at 90 days after the F98 rat glioma cells implantation when the other groups have completed their observations.

Table 1. The BNCT result for the F98 rat glioma model

Group	n	MST (days)	95% CI (days)
Untreated	5	30.0	26-34
Irradiated	4	35.0	22-40
BPA 2.5 h	6	42.0	39-50
BPA 8 h	5	40.0	34-48
cRGD-MID-AC 2.5 h	7	43.0	32-48
cRGD-MID-AC 8 h	6	38.5	27-

Conclusion:

The addition of tumor directivity to MID-AC appears to have enabled coverage of a large number of tumor cells due to the albumin-based drug delivery system and integrin-mediated tumor directivity. Based on these results, our research team is currently developing further novel boron compounds. We have previously developed boron compounds that target a folate receptor [3], and we intend to introduce further tumor directivity and a drug delivery system to these compounds in order to develop drugs that are more locally concentrated in tumors.

References:

- [1] H. Kashiwagi *et al.*, Invest New Drugs, 40(2) (2022) 255-264.
- [2] K. Kawai *et al.*, Mol Pharm, 17(10) (2020) 3740-3747.
- [3] T. Kanemitsu *et al.*, Radiat Environ Biophys 58(1) (2019) 59–67.

CO6-13 Establishment of protocol of the preparation of deuterated protein aimed for neutron scattering

R. Inoue, A. Okuda, K. Morishima, M. Shimizu, N. Sato, R. Urade and M. Sugiyama

Institute for Integrated Radiation and Nuclear Science (KURNS), Kyoto University

INTRODUCTION:

One of the noticeable properties associated with neutron scattering is an isotope effect on the neutron scattering length and this effect is especially evident for hydrogen (H). To be more specific, the neutron scattering length of H is significantly different from that of Deuterium (D). Since H atoms are abundantly included in softmatter and biological samples, this property is quite advantageous for studying their structure and dynamics. Let us consider the case for utilization of isotope effect for the structural analysis of protein samples in solution with neutron scattering. The scattering intensity is given by the square of scattering contrast ($\Delta\rho$), which is defined as the difference of neutron scattering length density (SLD) between solute and solvent in the case of biological solution scattering. By setting the value of $\Delta\rho$ to 0, the solute can be “scatteringly invisible”. This technique is quite helpful for the structural analyzes of partial concerned component in the multi-component system or complex with neutron solution scattering. To realize high signal to noise ratio of observable scattering profile, the inverse contrast matching SANS (iCM-SANS) method has been proposed and extensively utilized by our group [1-3]. In this method, both partially deuterated (~75%) and hydrogenated protein are prepared in 100% D₂O. Under this solution condition, partially deuterated are “scatteringly invisible” and hydrogenated protein are “scattering visible”, respectively. The most important procedure is the preparation of partially deuterated protein. We then try to establish the procedure of preparation of partially deuterated protein, which is fitted for iCM-SANS.

EXPERIMENTS:

We prepared three different lots of partially deuterated α B-crystallin (α B) [3]. The cells are cultured in M9 minimal media containing deuterated glucose (1.5 g/L), hydrogenated glucose (0.5 g/L), autoclaved milliQ (250.0 mL), and 99.8% D₂O (750.0 mL). MALDI-TOF Mass Spectrometry 20 (microflexLT: Bruker Daltonics) was used for the determination of degree of deuteration of prepared partially deuterated protein. To check the quality of partially deuterated protein in terms of “scatteringly invisible”, we also performed small-angle neutron scattering measurements on these sample. SANS measurements were performed with QUOKKA installed at the Australian Nuclear Science and Technology Organization (ANSTO, Lucas Heights, NSW, Australia).

RESULTS:

Fig. 1 shows the mass spectra of three different lots of partially deuterated α B (pd- α B) and the degree of deuteration ranged from 70.6 % to 71.7 %. From our preliminary calculation, 73.2% deuterated α B is exactly scatteringly

invisible in 100% D₂O solvent. Hence, it is expected that our prepared all three lots of partially deuterated could be nearly “scatteringly invisible” in 100% D₂O. To validate such an expectation, we concentrated all three lots of pd- α B and finally obtained pd- α B at the concentration of 28.5 mg/mL. Fig. 2 shows the SANS profiles from pd- α B at

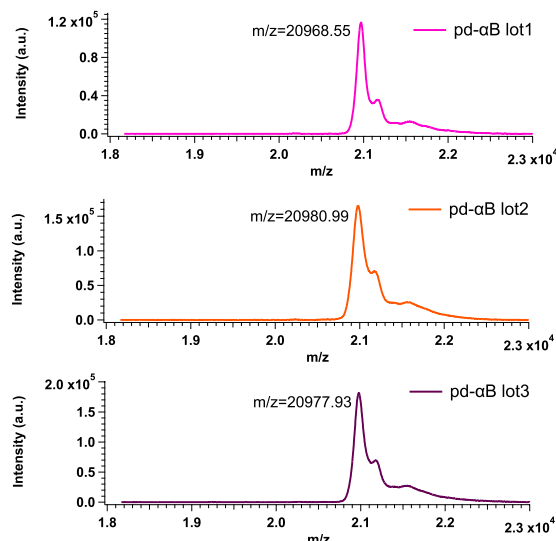


Fig.1 The mass spectra of three different lots of partially deuterated proteins.

28.5 mg/mL and hydrogenated α B (h- α B) at 0.45 mg/mL,

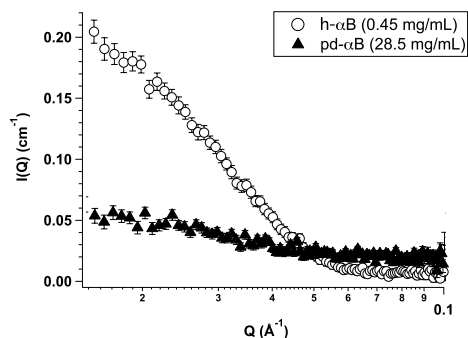


Fig. 2 SANS profiles from partially deuterated α B-cry at 28.5 mg/mL (circle) and hydrogenated α B-cry at 0.45 mg/mL (black triangle).

respectively. Interestingly, the scattering intensity from pd- α B at 28.5 mg/mL is about four time lower than that of h- α B at 0.45 mg/mL. It means that our prepared partially are fulfilled the criteria of “scatteringly invisible” in 100% D₂O even for concentrated protein. It is expected that our protocol would be applicable for other protein samples.

REFERENCES:

- [1] M. Sugiyama *et al.*, *J. Appl. Cryst.* **47** (2014) 430–435.
- [2] M. Sugiyama *et al.*, *Sci. Rep.* **6**, (2016) 35567.
- [3] R. Inoue *et al.*, *Sci. Rep.* **11**, (2021) 2555.

CO6-14 Overall structure of fully assembled cyanobacterial KaiABC circadian clock complex by an integrated experimental-computational approach

H. Yagi¹, Y. Yunoki^{1,2,3}, K. Morishima³, A. Matsumoto⁴, N. Sato³, L. Porcar⁵, A. Martel⁵, R. Inoue³, H. Kono⁴, K. Kato^{1,2} and M. Sugiyama³

¹Graduate School of Pharmaceutical Sciences, Nagoya City University

²Exploratory Research Center on Life and Living Systems, National Institutes of Natural Sciences

³Institute for Integrated Radiation and Nuclear Science, Kyoto University

⁴National Institutes for Quantum and Radiological Science and Technology

⁵Institut Laue-Langevin

INTRODUCTION: The molecular machinery of the cyanobacterial circadian clock comprises three proteins: KaiA, KaiB, and KaiC. Through interactions among the three Kai proteins, the phosphorylation states of KaiC generate circadian oscillations *in vitro* in the presence of adenosine triphosphate (ATP). In this system, KaiA, KaiB and KaiC periodically assemble into a large complex, which is considered to play the key role of the negative feedback loop of circadian rhythm. Recently, the cryo-electron microscopy (EM) structure of the ABC complex has been reported. However, the N-domains of KaiA subunits were poorly resolved due to their missing electron density maps. The whole structure of ABC complex has remained to be elucidated. Herein, for characterization of the overall structure of ABC complex, we conducted integrative techniques using small-angle X-ray scattering (SAXS), inverse contrast-matching small-angle neutron scattering (iCM-SANS) in conjunction with computer simulations.

EXPERIMENTS: X-rays from a high-brilliance point-focused X-ray generator (MicroMAX-007HF, Rigaku, Tokyo, Japan) were focused with a confocal mirror (OptiSAXS) and collimated with a confocal multilayer mirror and two pinholes collimation system with the lower parasitic scattering, “ClearPinhole”. The scattered X-rays were detected with a two-dimensional semiconductor detector (HyPix-6000, Rigaku, Tokyo, Japan). The sample-to-detector distance and wavelength of X-ray used for present work was 1320 mm and 1.542 Å, respectively. For removal of unfavorable aggregates from the sample solution, the laboratory-based SEC-SAXS System (LA-SSS) was employed to measure the SAXS profile in the Q range (0.01 Å⁻¹–0.2 Å⁻¹). The SANS experiments were performed using the D22 instrument installed at the Institut Laue-Langevin (ILL), Grenoble, France. The sample-to-detector distance and wavelength of neutron used for present work was 5600 mm and 6.0 Å, respectively. SEC-SANS system was also utilized for present work.

RESULTS:

Small-angle X-ray and inverse contrast matching

small-angle neutron scatterings coupled with size-exclusion chromatography provided constraints to highlight the spatial arrangements of the N-terminal domains of KaiA, which were not resolved in the previous structural analyses. We computationally built 3D models of the overall structure of ABC complex, which reproduced the SAXS and iCM-SANS profiles. Computationally built 20 million structural models of the complex were screened out utilizing the constraints resulting from scattering data and then subjected to molecular dynamics simulations to examine their stabilities. Our modeling procedure is described Fig. 1.

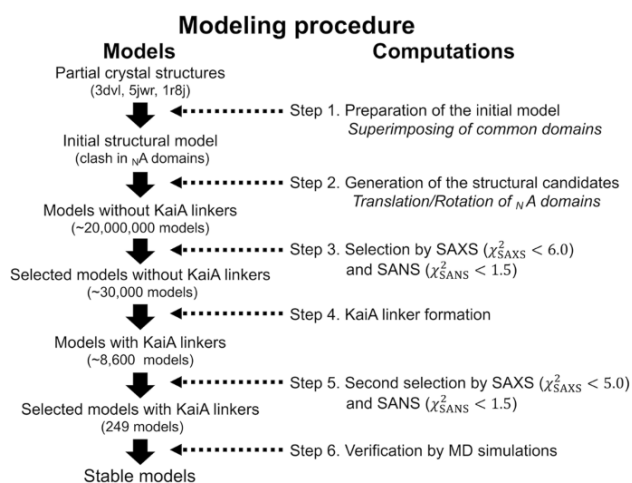


Fig. 1. Modeling procedure of the overall structure of ABC complex.

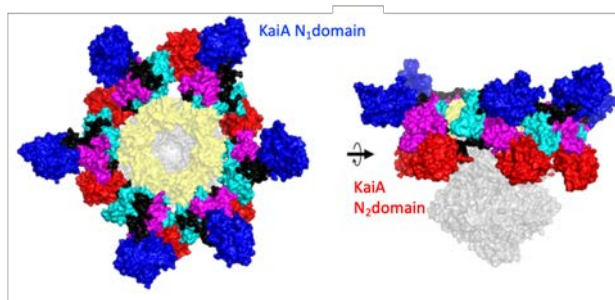


Fig. 2. Top and side view of the ABC complex structure after 100 ns MD simulation

The final model (Fig.2) suggests that, despite large fluctuation of the KaiA N-terminal domains, their preferential positionings mask the hydrophobic surface of the KaiA C-terminal domains, hindering additional KaiA-KaiC interactions.

Thus, our integrative approach provides a useful tool to resolve large complex structures harboring dynamically fluctuating domains.

REFERENCES:

- [1] M. Sugiyama *et al.*, *Sci. Rep.*, **6**:35567 | (2016).
- [2] Y. Yunoki *et al.*, *Commun. Bio.*, **5**:184 | (2022).

CO6-15 Analysis of p53 aggregates for elucidation of aggregation mechanism

E. Hibino, K. Morishima¹, R. Inoue¹, M. Sugiyama¹ and H. Hiroaki.

Graduate School of Pharmaceutical Science, Nagoya University

¹Institute for Integrated Radiation and Nuclear Science, Kyoto University

INTRODUCTION: The tumor suppressor protein p53 is a transcription factor that induces DNA repair proteins when DNA is damaged or induces apoptosis when DNA damage is severe, thereby preventing cells from turning cancerous. In fact, p53 mutations are found in half of all cancers, and preservation of p53 function is important in terms of cancer prevention. However, the development of therapeutic drugs targeting p53 has been challenging. It has been reported that the DNA-binding domain of p53 is aggregation-prone, that the introduction of hot spot mutations common in cancer increases its aggregation, and that the aggregates that form are heterogeneous [1,2].

We recently found that the environments in which amyloid aggregates and amorphous aggregates of p53C tend to form are distinct. They found that high salt and sugar concentrations inhibited amorphous aggregate formation of p53C and suppressed loss of function [3]. However, the mechanisms of p53 aggregation nucleation and elongation remain unresolved, which has been an obstacle in the development of p53-related cancer drugs. The objective of this study is to elucidate the mechanism of aggregation.

EXPERIMENTS: The p53-DNA binding domain (p53C) protein was produced as a GST-fused form in an E. coli expression system. After GST tag affinity purification, the GST tag was cleaved with HRV3C protease and finally purified by size exclusion chromatography. The protein solution was aggregated with the addition of Reagent A, and then sonicated for DLS measurement.

DLS measured by using a system equipped with a 22-mW He-Ne laser, an Avalanche Photo Diode mounted on static/dynamic compact goniometer, ALV/LSE-5003 electronics, and ALV-5000 Correlator. Incident angles were 45°, 60°, 75°, 90°, 105°, 120°, and 135°, and measurements were taken three times at each angle.

RESULTS: We have previously found that p53C becomes predominantly amyloid aggregates when Reagent A is added. p53C aggregate is very difficult to analyze because it is formed as a mixture of amorphous and amyloid aggregates under normal conditions. Thus, we decided to characterize the amyloid aggregates by comparing them without and with Reagent A. Amorphous and amyloid aggregates were sonicated and observed under a microscope, and many small granular aggregates were observed. The granular aggregates were measured by DLS and found to be a mixture of several sizes of aggregates (Fig. 1). Similar profiles were obtained for the amorphous and amyloid aggregates, but the results suggest that the amyloid aggregate

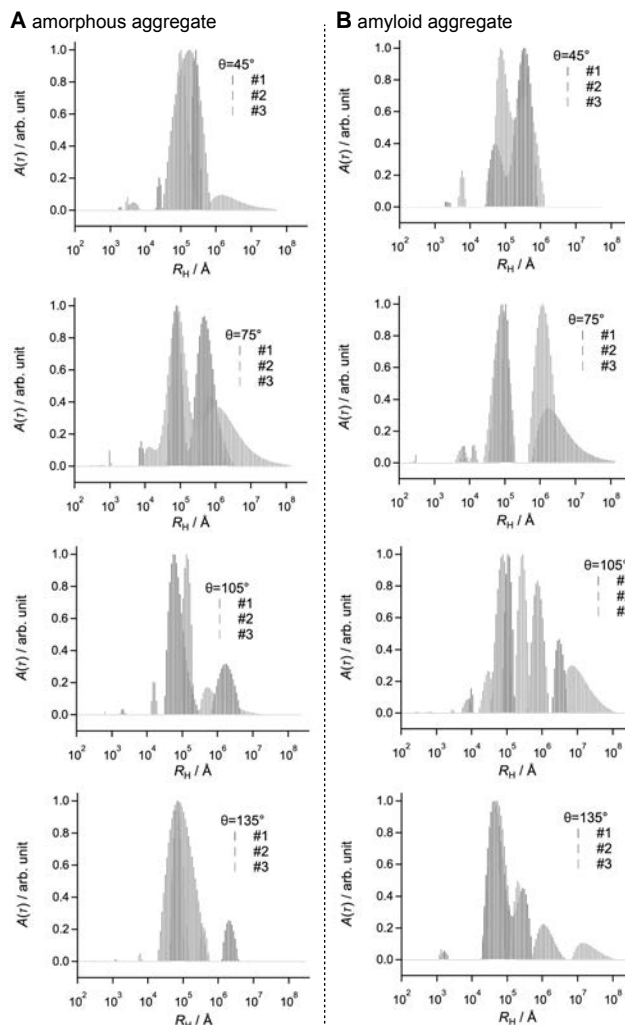


Fig. 1 Overlay of the DLS results of 3 measurements at each angle for amorphous aggregates (A) and amyloid aggregates (B).

exhibits periodicity. Further analysis is needed to characterize specific amyloid aggregates exclusively.

REFERENCES:

- [1] A.P.D.A Bom, L.P. Rangel, D.C.F.Costa, G.A.P. de Oliveira, D. Sanches, C.A. Braga, L.M. Gava, C.H.I. Ramos, A.O.T. Cepeda, A.C. Stumbo, C.V.D.M. Gallo, Y. Cordeiro and J.L. Silva, *J. Biol. Chem.*, **287** (2012) 28152-28162.
- [2] S. Ghosh, S. Salot, S. Sengupta, A. Navalkar, D. Ghosh, R. Jacob, S.D.R. Kumar, N.N.J.S. Sahay, S. Mehra, G.M. Mohite, S.K. Ghosh, M. Kombrabail, G. Krishnamoorthy, P. Chaudhari and S.K. Maji, *Cell Death Differ.* **24** (2017) 1784-1798.
- [3] E. Hibino, T. Tenno and H. Hiroaki, *Biophys. Rev.*, **14** (2022) 267-275.

CO6-16 Development of hydroponics system for wheat cultivation

N. Sato, R. Urade, A. Okuda, K. Morishima, R. Inoue,
and M. Sugiyama

*Institute for Integrated Radiation and Nuclear Science,
Kyoto University*

INTRODUCTION: Wheat flour has been widely served as staple foods in many countries. In most cases, wheat flour is mixed with salts and water and kneaded to produce wheat dough, which is then processed to make various wheat food products: bread, noodles and cookies. The quality of those foods such as the rise of the bread and firm chewiness is much affected by the physical properties of wheat dough. It is well-known that gluten is a key component for determining the physical properties of wheat dough. Gluten is a composite of two major wheat proteins, glutenin and gliadin. Glutenin is high-molecular-weight network polymer protein, which is responsible for elasticity of dough. Gliadin, in contrast, is an aggregated monomeric protein, which is responsible for viscosity of dough. Thus gluten inherits both properties of those two proteins, but it is possible that the composite formation of two proteins brings new properties unique to gluten. Therefore nanoscale structural analysis of the wheat proteins is necessary to make clear how glutenin and gliadin behave in the molecular scale and how they interact in the gluten. However, structural analysis of food materials often becomes a difficult work because they are generally opaque, condensed, disordered, and multicomponent systems. Small-angle scattering technique is one of effective method to overcome this difficulty. It has been utilized for a variety of soft matters including rubber, gels, colloids, and other condensed materials. From this viewpoint, we have been applying small-angle technique to the structural analysis of wheat proteins. In our recent study [1], aqueous solutions and hydrated solids of gliadins have been investigated by small-angle X-ray scattering (SAXS). As a result of this study, we demonstrated that gliadin monomers dispersed isolatedly in low-concentration aqueous solutions, but with increasing concentrations they gradually associate together to form multimolecular domains with interparticle interference. It was also revealed that at much higher concentrations gliadins become insoluble in water to form hydrated aggregates with density fluctuation inside and the correlation length of this fluctuation becomes smaller with increasing gliadin concentrations. To understand the structure of gluten, however, it is insufficient to clarify the structure of gliadin or glutenin alone because gluten consists of a composite of gliadin and glutenin. Several schematic illustrations have been presented so far, the detail of molecular scale structure of gluten is still unknown. We accordingly employ small-angle neutron scattering (SANS) with contrast variation technique to address this problem. Unlike X-ray scattering, neutrons are scattered by nuclei of atoms, and the scattering power depends on isotopes. Deuterium and hydrogen have dif-

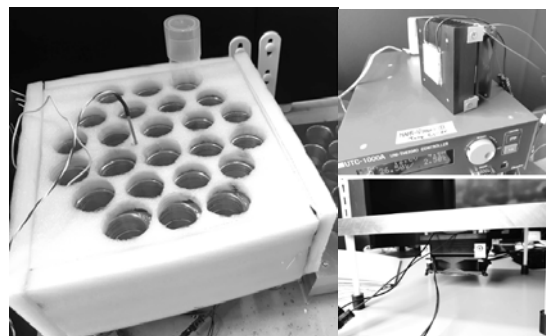


Fig. 1 The hydroponics system for wheat cultivation. (Left) Temperature-controlled container for cultivation vials. (Right top) Peltier device, heatsink, cooling fan and Peltier controller. (Right bottom) Peltier cooling unit installed under the container base.

ferent neutron scattering power. Therefore a part of multicomponent systems are deuterated, it has different contrast compared with the non-deuterated parts. If this fact is applied to the structural analysis of gluten, the structure of gliadin alone is observed in the gluten composite by mixing deuterated gliadin and mixed with non-deuterated glutenin. The largest difficulty of this concept lies on the difficulty of sample preparation. The deuterated proteins are often expressed in *E. coli* grown in heavy water and deuterated carbon sources. However recombinant wheat proteins have not yet been successfully obtained. Thus we planned to grow wheat by hydroponics using heavy water to prepare deuterated gliadin. As a first step, we built a hydroponics system optimized for the cultivation of wheat. Here we report the details of these system.

DESIGN AND FABRICATION: Hydroponics of wheat is planned to conduct by the method reported by Singh and Jenner [2]. First, wheat seeds are grown in planter soil placed in a growth chamber. After the ears emerge, stems are cut and put into water in the cultivation vials. These vials are maintained at 1–2°C until the ears ripens. To keep low temperature, a temperature-controlled vial container with Peltier-cooling system was developed. A Peltier device (TEC1-12706) attached to an aluminum heat sink (30×98×100 mm) and DC fan (92×92×25 mm, 1400 rpm) was driven by a Peltier controller (UTC-1000A, Ampere inc.). A 24-hole vial container made of an aluminum block was manufactured in the factory of KURNS and temperature probe of Peltier controller was inserted into the container.

RESULTS: When the container holding 24 vials filled with 100mL of water was cooled placed in a chamber at 20°C, the container was successfully kept at 1°C for more than two weeks. This result shows that this system can be safely used for hydroponics of wheat.

REFERENCES:

- [1] N. Sato *et al.*, *J. Agric. Food Chem.*, **63** (2015) 8715–8721.
- [2] B. K. Singh and C. F. Jenner, *Aust. J. Plant Physiol.*, **10** (1983) 227–236.

CO6-17 Preparation and Characterization of BPA-uridine conjugate for BNCT

K. Tanabe¹, M. Suzuki², and T. Nishihara¹

¹*Department of Chemistry and Biological Science, College of Science and Engineering, Aoyama Gakuin University*

²*Institute for Integrated Radiation and Nuclear Science, Kyoto University*

INTRODUCTION:

Modified nucleobases are widely used as antitumor agents, and a variety of them have important functions in vivo. Among them, 5-fluorouridine (5FU), 5-fluorodeoxyuridine (FdUrd), and cytarabine are well-known antitumor agents, and their modified derivatives are utilized as stimuli-responsive prodrugs.¹

Recently, we employed uridine with three alcohol units as a solubilizer for poorly soluble compounds and prepared BPA-uridine conjugates for boron neutron capture therapy (BNCT). We found that irradiation in the presence of BPA-uridine markedly enhanced the cytotoxicity of the radiation. In this study, we conducted an in vivo study of BPA-uridine conjugate. Eventually, we confirmed that BPA-uridine showed robust cytotoxic effect on tumor tissue upon thermal neutron irradiation. Thus, uridine seems to be good agents for drug delivery system.

EXPERIMENTS:

Preparation of BPA-uridine conjugate. BPA was added to the aqueous solution of uridine under basic conditions to solubilize the conjugate. After the BPA was dissolved in the aqueous solution, the resulting solution was neutralized and then subjected to in vivo experiments. **Neutron capture therapy to A549 tumor models.** A549 cells in matrigel (1×10^6 cells per mouse) were subcutaneously inoculated into the right thighs of BALB/c nude mice. The tumors were allowed to grow ~1.5 month. The mouse was injected with fructose-BPA or uridine-BPA (250 mg/kg). The mice were placed in acrylic which were secured on a 5-mm-thick thermoplastic plate that contained 40 weight % (wt %) of ⁶LiF (96% ⁶Li) to block thermal neutrons and had a circular hole in the center. The thigh containing the tumor was stretched over the hole, and the tumor was irradiated with epi-/thermal neutrons for 50 min, 1 h after the injection. The tumor size was measured by a caliper, and tumor volume (V) was calculated using the following equation: $V = ab^2/2$, where a and b are the major and minor axes, respectively.

RESULTS:

Conventionally, fructose has been used to solubilize BPA in water for the formation of their complex that showed hydrophilic properties. We expected that the uridine bearing ribose unit formed similar complex with BPA, and thus we combined BPA with uridine and prepared their conjugate. Eventually, we found that BPA-uridine conjugate was smoothly dissolved in water, and then applied them to cellular experiments.

In the research process to date, fructose has been used to

solubilize BPA in water to form a complex that exhibits hydrophilic properties. Therefore, we expected that uridine, which has a ribose unit, would form a similar complex with BPA. Last year, we synthesized the BPA-uridine complex and confirmed that it dissolves smoothly in water. We also applied the complex to cell experiments and found that it exhibited high cytotoxicity under thermal neutron irradiation.

To determine whether the BPA-uridine conjugate is effective in vivo, we administered this conjugate to BALB/cAJcl nude mice with A549 tumors. We administered this conjugate to BALB/cAJcl nude mice with A549 tumors to characterize its efficacy in vivo. A549 cells were transplanted into BALB/cAJcl nude mice ($n = 3$ per group) and allowed to grow until the tumor size was about 100 mm³. The conjugate was then administered subcutaneously and changes in tumor size after thermal-neutron irradiation were recorded.

As shown in Figure 1B, the BPA-uridine conjugate efficiently inhibited tumor growth at the same level as BPA-fructose. These results suggest that BPA-uridine was activated within the tumor upon irradiation conditions and exhibited a cell-killing effect even in vivo.

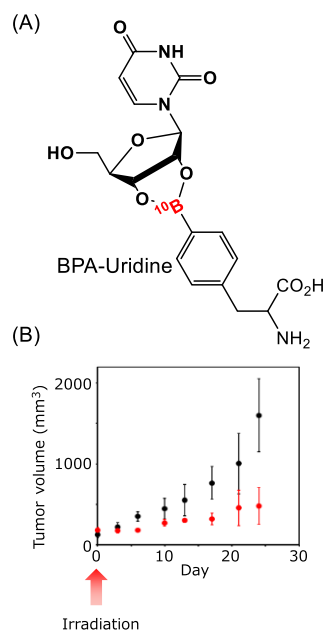


Figure 1. (A) Chemical structure of BPA-Uridine conjugate (B) In vivo evaluation of BPA-uridine as an anti-cancer agent. Tumor volumes of each group (BPA-uridine (+: red, -: black), epi-/thermal neutrons: 50 min).

REFERENCES:

[1] K. Tanabe *et al.*, *Org. Biomol. Chem.* **7** (2009), 651–654.

CO6-18 Analysis of distinct amyloid formation pathways between bovine and human insulin

K. Yuzu, T. Nozaki, K. Morishima¹, A. Okuda¹, R. Inoue¹, M. Sugiyama¹, E. Chatani

Graduate School of Science, Kobe University

¹Institute for Integrated Radiation and Nuclear Science, Kyoto University

INTRODUCTION: Amyloid fibrils are a form of protein aggregates that are associated with various amyloidoses and neurodegenerative diseases. The formation of amyloid fibrils is typically progressed through nucleation and growth phases. The nucleation phase is a rate-limiting step, and once amyloid nuclei are formed, the subsequent rapid elongation of amyloid fibrils is induced. However, much remains unclear about the aggregation mechanisms during the nucleation phase.

In this study, we investigated the fibrillation process of bovine and human insulin, the amino acid sequences of which are slightly different. We previously identified that bovine insulin formed prefibrillar intermediates in early stage of the fibrillation [1, 2]. Here, we performed small-angle X-ray scattering (SAXS) and analytical ultracentrifugation (AUC) measurements to identify and compare the fibrillation process of two species of insulin.

EXPERIMENTS: A sample of 5.0 mg/mL bovine and human insulin dissolved in 25 mM HCl containing 0.1 or 0.5 M NaCl was heated at 75 °C. At different time points, the reaction was instantly stopped with cooling on ice and the samples were subjected to subsequent measurements.

The SAXS profile was collected at 25 °C with a NANOPIX equipped with a HyPix-6000 (Rigaku Corporation, Japan). A Cu K- α line (MicroMAX-007HFMR) was used as a beam source, which was further focused and collimated with a confocal multilayer mirror (OptiSAXS). The camera length was set to 1.33 nm and the range of the scattering vector q was from 0.005 to 0.20 \AA^{-1} .

AUC was conducted with a ProteomeLab XL-I analytical ultracentrifuge (Beckman Coulter, USA). Sedimentation velocity analytical ultracentrifugation (SV-AUC) measurements were performed using Rayleigh interference optics at 40,000 rpm at 20 °C with a 1.5 mm path-length cell. The experimental data were analyzed with SEDFIT software. The density and viscosity of solvent, and partial specific volume of each protein were calculated from their amino acid sequences with SEDNTERP software.

RESULTS: We first performed SAXS measurements to investigate the amyloid formation process of bovine and human insulin (Fig. 1). In both insulin species, the SAXS profiles at 60 min, when the fibrillation was completed, showed the higher scattering intensity especially in lower q region compared to those before the reaction, indicating the fibrillation was successfully observed by SAXS measurements. The slope of the log-log plot at 60 min was close to -1, which is consistent with the rod-like

morphology of amyloid fibrils. Interestingly, the SAXS profile of bovine insulin at 10 min exhibited a scattering pattern intermediate between those before the reaction and at 60 min. These observations indicate the formation of prefibrillar intermediates in the process of amyloid formation of bovine insulin in accordance with our previous observation [2]. On the other hand, the SAXS profile of human insulin at 10 min showed almost the same pattern as that before the reaction, suggesting the absence of prefibrillar intermediates in the fibrillation process of human insulin.

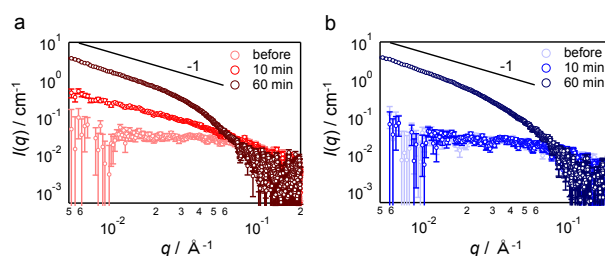


Fig. 1. SAXS profiles of bovine (a) and human insulin (b). The insulin samples heated in the presence of 0.1 M NaCl were subjected to the SAXS measurements.

We further performed SV-AUC measurements to examine the early aggregation process of two species of insulin (Fig. 2). The sedimentation coefficient distribution of bovine insulin showed rapid evolution of aggregates, while those of human insulin showed no significant aggregation. These results indicate that bovine insulin forms oligomers leading to the formation of prefibrillar intermediates immediately after the initiation of the reaction, unlike typical amyloid formation pathway with a lag phase observed in human insulin.

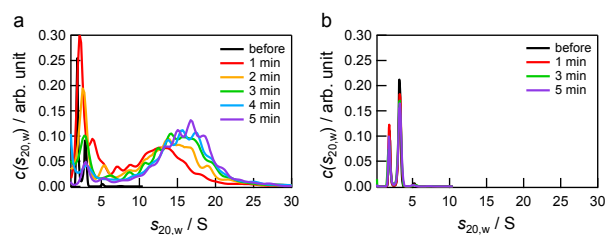


Fig. 2. Sedimentation coefficient distribution of bovine (a) and human insulin (b). The insulin samples heated in the presence of 0.5 M NaCl were subjected to the AUC measurements. For bovine insulin, sample solutions were diluted 2-fold with 25 mM HCl before measurement to suppress flocculation of aggregates induced by cooling.

REFERENCES:

- [1] E. Chatani *et al.*, *J. Biol. Chem.*, **289** (2014) 10399-10410.
- [2] E. Chatani *et al.*, *Sci. Rep.*, **5** (2015) 15485.

CO6-19 Structural analysis of protein complex using analytical ultracentrifugation and small-angle X-ray scattering.

K. Morishima¹, A. Okuda¹, M. Shimizu¹, N. Sato¹, R. Inoue¹, M. Sugiyama¹

¹Institute for Integrated Radiation and Nuclear Science, Kyoto University

INTRODUCTION:

Structural analysis of a protein complex in solution is essential to understanding physiological phenomena in biological systems. Small-angle X-ray scattering (SAXS) is powerful technique which gives three-dimensional structure of a biomacromolecule in solution. To obtain the high-quality structural model, it is crucial to obtain a scattering profile purely corresponding to the target protein complex. On the other hand, because protein complexes and dissociated proteins coexist in the solution under dissociation-aggregation equilibrium, the experimental scattering profile is offered as an ensemble-average of them. Therefore, it is necessary to extract the scattering profile of the concerned protein complex from the ensemble-averaged profile.

Recently, size-exclusion chromatography (SEC)-SAXS attracts an attention to obtain the scattering profile of the concerned component in a multi-component solution. However, SEC-SAXS is unavailable for a weakly-bound complex because they break down in the SEC process.

In this study, we developed the integrated analytical method with analytical ultracentrifugation (AUC) and SAXS, AUC-SAXS, to derive the scattering profile of a weakly-bound complex under dissociation-aggregation equilibrium [1].

EXPERIMENTS:

AUC-SAS was demonstrated for the following two systems:

(i) The complex of the ubiquitin-like domain of the proteasome shuttle factor hHR23b and PUB domain of N-glycanase: The sedimentation equilibrium (SE)-AUC and SAXS was conducted for the mixture (hHR23b + PUB) with equimolar ratio (100 μ M + 100 μ M and 50 μ M + 50 μ M).

(ii) The complex of clock protein KaiA and KaiC: The sedimentation velocity (SV)-AUC and SAXS was conducted for the mixture (KaiA + KaiC) with the ratio of 2 : 6 (5.7 μ M + 17 μ M).

SAXS measurements were carried out with NANOPIX (Rigaku). AUC measurements were conducted with a ProteomeLab XL-I (Beckman Coulter). All measurements were conducted at 25 °C

RESULTS:

Considering the equilibrium to be $A + B \leftrightarrow AB$ for proteins A, B, and complex AB, the scattering profile of the solution under dissociation-aggregation equilibrium is expressed as

$$I(q) = c_A i_A(q) + c_B i_B(q) + c_{AB} i_{AB}(q) \quad (1)$$

Here, q and $I(q)$ are the magnitude of scattering vector

and experimentally obtained scattering intensity, respectively. c_j and $i_j(q)$ are the concentration of component j and scattering intensity per the concentration of component j . In AUC-SAXS, in order to derive the scattering profile of the complex $i_{AB}(q)$, $I(q)$, $i_A(q)$, and $i_B(q)$ are individually measured with SAXS, and c_j s for all components are obtained with AUC.

For the system of hHR23b + PUB, c_j s for all components were calculated with the dissociation constant K_D , which was obtained with SE-AUC. Closed circles in Figure 1 show the scattering profile for the complex of hHR23b and PUB $i_{AB}(q)$. The obtained $i_{AB}(q)$ was not explained by the simple docking model between hHR23b and PUB (gray line in Figure 1). Then, we performed a normal mode analysis using the docking model as an initial structure. Finally, the optimal three-dimensional structure model that reproduces $i_{AB}(q)$ was offered (black line and inset in Figure 1).

With the same procedure, the scattering profile of the complex of KaiA and KaiC was obtained. The three-dimensional structure model that reproduces the scattering profile was revealed with the molecular dynamics simulation.

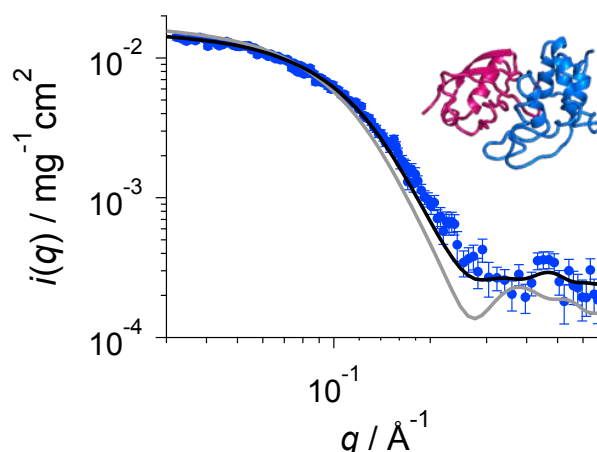


Figure.1. SAXS profile for the complex of hHR23b and PUB $i_{AB}(q)$ (closed circles). Gray and black lines are the profiles calculated from the docking simulation model and the optimized model (inset) with the normal mode analysis.

REFERENCES:

[1] K. Morishima, *et al. Commun. Biol.* **3**, 294 (2020).

CO6-20 Dynamics of copper chaperone for superoxide dismutase studied by small-angle X-ray scattering

M. Shimizu¹, R. Inoue¹, Y. Furukawa², A. Okuda¹, K. Morishima¹, N. Sato¹, R. Urade¹, and M. Sugiyama¹

¹*Institute for Integrated Radiation and Nuclear Science, Kyoto University*

²*Department of Chemistry, Keio University*

INTRODUCTION: Many proteins are composed of multiple structural domains, and function by dynamically changing their domain arrangement. X-ray solution scattering measurement is a useful research technique for structural analysis of such dynamic biomolecules; All molecules with various structures contribute to the scattering data. We have attempted to analyze molecular structures of a multi-domain protein ER-60 based on small-angle X-ray scattering (SAXS) profiles [1].

Here, we focused on a multi-domain protein copper chaperone for superoxide dismutases (CCS) and study its behavior in solution. This protein passes Cu ion to Cu, Zn superoxide dismutases (SOD1), probably via flexible domain dynamics [2]. CCS monomer has three functional domains, and domain II of CCS bind to each other to form CCS homodimer [3]. We studied structure of the CCS dimer in solution by small angle X-ray scattering. In this study, a mutant CCS, which is more likely to maintain its dimeric state than wildtype CCS, was chosen for measurement.

EXPERIMENTS: A mutant human CCS protein was expressed using *Escherichia coli* and purified. Small-angle X-ray scattering (SAXS) was measured by a NANOPIX (Rigaku, Tokyo, Japan). From the raw scattering data, one dimensional SAXS profile was calculated using SAngler [4]. Oligomeric state of CCS in sample solution was examined by analytical ultracentrifugation. The analytical ultracentrifugation was conducted with a ProteomeLab XL-I analytical-ultracentrifuge (Beckman Coulter). The content of each oligomer was calculated using SEDFIT [5]. Both the Small-angle X-ray scattering experiment and analytical ultracentrifugation were performed at 25°C. Scattering profile of dimeric CCS was calculated by combining the SAXS profile and analytical ultracentrifuge data, following a previous report [6]. SAXS profiles of atomistic models were calculated with Pepsi-SAXS [7].

RESULTS: We measured scattering profile of apo-state of the mutant CCS. The profile changed gradually with time; an increase in the radius of gyration of the sample was observed over time. This can be interpreted as the formation of CCS aggregates composed of non-native structure of CCS, which are caused by the radicals produced upon X-ray irradiation. For wild type CCS, it has already been reported that components other than dimeric CCS can contribute significantly to the SAXS profile [8]. Although we utilized a mutant CCS that could potentially suppress the formation of multimers larger than dimers,

the SAXS measurements did not show the expected results. Therefore, we considered the data from the first 10 minutes of the measurement as the SAXS profile of the aggregate-free CCS.

Abundance of each CCS multimer was measured using analytical ultracentrifugation, and SAXS profile of the CCS dimer was calculated using the data.

Subsequently, we examined whether the SAXS profile matched already studied tertiary structures. Currently, a structure of the CCS dimer can be modeled using known crystal structures of CCS [3, 9]. In addition, A theoretical predicted structure of the CCS by AlphaFold are also available [10, 11]. We generated one CCS dimer model from crystal structures, and generated one CCS dimer model from the AlphaFold model. The predicted SAXS profiles of these structures were different from our experimental profile; χ^2 values were 7.71 and 7.39, respectively. This result suggests that the structure of CCS dimer in solution is different from its crystal structure.

Further improvement of the measurement conditions, such as the addition of radical scavengers to the sample buffer, is expected to enable the acquisition of more accurate scattering curves.

REFERENCES:

- [1] A. Okuda *et al.*, *Sci. Rep.*, **11** (2021) 5655.
- [2] P. J. Schmidt *et al.*, *J. Biol. Chem.*, **275** (2000) 33771-33776.
- [3] A. L. Lamb *et al.*, *Biochemistry*, **39** (2000) 1589-1595.
- [4] N. Shimizu *et al.*, *AIP conf. Proc.*, **1741** (2016) 50017.
- [5] M. Sawicki, *Publ. Astron. Soc. Pac.*, **124** (2012) 1208-1218.
- [6] K. Morishima, *Commun. Biol.*, **3** (2020) 294.
- [7] S. Grudin *et al.*, *Acta Cryst.*, **D73** (2017) 449-464.
- [8] G. S. A. Wright *et al.*, *Biochem. J.*, **439** (2011) 39-44.
- [9] F. A. Sala *et al.*, *PLoS Biol.*, **17** (2019) e3000141.
- [10] J. Jumper *et al.*, *Nature*, **596** (2021) 583-589.
- [11] M. Varadi *et al.*, *Nucleic Acids Research*, **D1** (2021) D439-D444.

CO6-21 Structural dynamics of the overlapping di-nucleosome

H. Tanaka¹, M. Nishimura^{1,2}, K. Nozawa¹, K. Morishima³, R. Inoue³, H. Ehara⁴, S. Sekine⁴, M. Sugiyama³, and H. Kurumizaka^{1,2}

¹Laboratory of Chromatin Structure and Function, Institute for Quantitative Biosciences (IQB), The University of Tokyo

²Department of Biological Sciences, School of Science, The University of Tokyo

³Institute for Integrated Radiation and Nuclear Science (KURNS), Kyoto University

⁴RIKEN Center for Biosystems Dynamics Research

INTRODUCTION:

In eukaryotes, the genomic DNA is hierarchically folded as chromatin. The basic repeating unit of chromatin is termed nucleosome, in which approximately 145 base pairs of DNA wrap around an octameric histone core containing two copies of each core histone, H2A, H2B, H3, and H4. In the process of chromatin remodeling, a collision of two adjacent nucleosomes can form an alternative structural unit such as overlapping dinucleosome: OLDN [1]. We have previously reported that the crystal structure of the OLDN, in which the octameric histone core, and the hexameric histone core lacking one copy of H2A-H2B dimer, are tightly associated with each other, and 250 base pairs of DNA are continuously wrapped around it [2]. Subsequent molecular dynamics simulations, small-angle x-ray, and neutron scattering (SAXS and SANS, respectively) analysis suggested that the OLDN adopt a variety of conformations in solution [3]. Here, we combined cryo-electron microscopy (cryo-EM) and analytical ultracentrifuge (AUC) with SAXS to characterize the structural dynamics of the OLDN.

EXPERIMENTS:

The OLDN sample was prepared by the salt dialysis method and purified by nondenaturing gel electrophoresis as previously described [2]. For cryo-EM analysis, OLDN was fixed by the glutaraldehyde crosslinking through the gradient fixation method. The micrographs were acquired using a cryo-EM: Tecnai Arctica transmission electron microscope (FEI), equipped with a K2 summit direct electron detector (Gatan). Single-particle analysis of the OLDN was performed on RELION 3.1 software. SAXS analysis was performed with a NANOPIX instrument (RIGAKU) at the Institute of Radiation and Nuclear Science, Kyoto University. To cover the wide q -range, we employed two sample-to-detector distances: 1,330 mm and 350 mm and combined these data. We performed the standard procedures of transmission correction, buffer solution scattering subtraction, and conversion to an absolute scale with water scattering. We also performed AUC to correct the SAXS data by removing the SAXS profile portion derived from slight aggregates as previously described [4].

RESULTS:

We collected 1737 k particle images from 2833 of micrographs and then removed junk particles throughout the following 2D and 3D classification. Using the 1330 k particles, we performed a 3D classification of OLDN. Consequently, 12 OLDN structures, that exhibit different orientations of the octasome unit and the hexasome unit were observed. We built structural models from four of these classes and determined cryo-EM structures of OLDNs. We then performed AUC-SAS to obtain the refined SAXS profile of the OLDN and plotted the calculated SAXS curves of the four cryo-EM structures with it. Notably, the theoretical SAXS curve derived from the open OLDN configuration fitted to the experimental SAXS curve with the reconstituted OLDN. This result suggests that the various relative orientations between the two histone cores, octasome and hexasome, observed in cryo-EM experiments reflect the structural dynamics of the OLDN in solution.

REFERENCES:

- [1] M. Engholm *et al.*, Nat Struct Mol Biol. **16** (2009) 151-158.
- [2] D. Kato *et al.*, Science. **356** (2017) 205-208.
- [3] A. Matsumoto *et al.*, Biophys J. **118** (2020) 2209-2219
- [4] K. Morishima *et al.*, Commun. Biol. **3** (2020) 294.

CO6-22 ^{11}C medical-isotope production via the $^{12}\text{C}(\gamma,n)^{11}\text{C}$ reaction with carbon nano tube

N. Takahashi^{1,2}, Y. Kosuge^{1,2}, M. Kurosawa¹,
M. Tamura¹, M. Fujiwara^{1,2}, T. Kubota³, N. Abe⁴,
and T. Takahashi⁴

¹Research Center for Nuclear Physics, Osaka University

²Kyoto Medical Technology

³Agency for Health, Safety and Environment, Kyoto University

⁴Institute for Integrated Radiation and Nuclear Science, Kyoto University

INTRODUCTION: L- ^{11}C -Methionine is used as a positron emission tomography (PET) reagent for medical diagnosis of brain tumors [1]. The medical ^{11}C radioisotopes are mostly produced in a cyclotron via the $^{14}\text{N}(p,\alpha)^{11}\text{C}$ reaction by bombarding enriched nitrogen gas with a proton beam [2]. In Japan, Hokkaido University and Osaka University have worked in collaboration with Sumitomo Heavy Industries to obtain the government permission for the PET examination with L- ^{11}C -Methionine for checking the metastasis and recurrence test of the brain tumor patient [3,4].

Instead of producing ^{11}C with the cyclotron, we tried a novel method of producing ^{11}C using the bremsstrahlung γ -rays with a carbon nano tube (CNT) target to get a reasonable number of the ^{11}C specific activity.

Fig. 1 shows a schematic illustration to produce ^{11}C isotopes from a CNT target and to extract them as $^{11}\text{CO}_2$ gas.

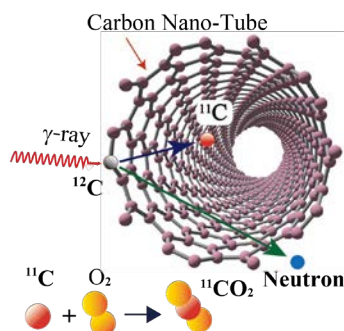


Fig. 1. Scheme of the ^{11}C medical-isotope production via the $^{12}\text{C}(\gamma,n)^{11}\text{C}$ reaction with a CNT target. Neutron and ^{11}C are released from the strong bonding network of CNT after the $^{12}\text{C}(\gamma,n)^{11}\text{C}$ reaction following the nuclear two-body kinematics. Since the recoiled ^{11}C is chemically active, a $^{11}\text{CO}_2$ molecule is produced via the $^{11}\text{C}+\text{O}_2 \rightarrow ^{11}\text{CO}_2$ chemical process.

EXPERIMENTS: We prepare the O_2 gas circulation system, consisting mainly of 1) a CNT target with a nanotube powder, 2) O_2 gas tubes, and 3) molecular sieves. We seal the CNT powders in the Al target vessel with non-woven masks as gas inlet/outlet filter. We trap the $^{11}\text{CO}_2$ using the molecular sieves. The $^{12}\text{C}(\gamma,n)^{11}\text{C}$ reaction experiment has been done using the bremsstrahlung γ -rays generated with a 40 MeV electron beam

at the electron LINAC facility.

Fig. 2 shows the experimental scheme to measure the $^{11}\text{CO}_2$ yields from the $^{12}\text{C}(\gamma,n)^{11}\text{C}$ reaction. The $^{11}\text{CO}_2$ gas flows out from the CNT target and is trapped in two molecular sieve capsules. The radioactive ^{11}C with a half-life of 20 minutes emits a positron. 511-keV γ -rays from positron-electron annihilation are detected using the CdZnTe detectors. Taking into account the incompleteness of trapping $^{11}\text{CO}_2$ gas with molecular sieves, we prepared two molecular sieve capsules to correct for the trapping efficiency.

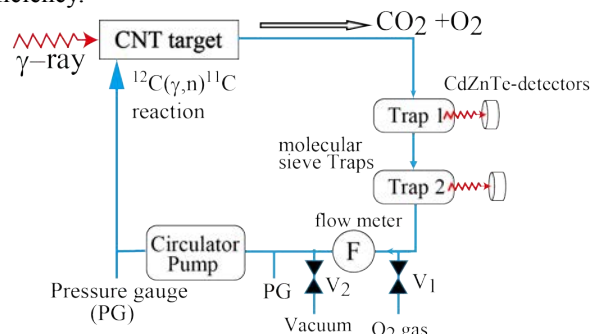


Fig. 2. Experimental scheme to measure the $^{11}\text{CO}_2$ extraction rate.

We confirmed that the $^{11}\text{CO}_2$ flowed out from the CNT target capsules by observing 511-keV γ -rays from $^{11}\text{CO}_2$ trapped in the molecular sieves. The measured decay curve obtained by measuring 511 keV γ -rays as a function of elapsed time was well in agreement with the ^{11}C half-life of 20 minutes. Several forms such as multiwall CNT, single-wall CNT, C60, and graphene were examined to achieve high yields of $^{11}\text{CO}_2$.

RESULTS: We conclude that the extraction rate of $^{11}\text{CO}_2$ from the single-wall CNT target can be as high as 15%. With this extraction rate of 15%, we estimate that we can obtain the ^{11}C activity of 34 GBq when we use a single-wall CNT target under the conditions with 1) a length of 50 cm, 2) weight of 1.13 kg for 0.155 g/cm^3 , 3) a 40 MeV electron beam intensity of $100 \mu\text{A}$ for 40 minute bombardment. This 34 GBq radioactivity is enough amounts for one patient's diagnosis. The detailed report will be published in the near future [5].

REFERENCES:

- [1] Y. Komatsu *et al.*, *Radioisotopes*, **67** (2018) 75.
- [2] T.J. Ruth. A.P. Wolf, *IEEE Trans.*, NS-**26** (1979) 1710.
- [3] M. Kinoshita *et al.*, *J. Neurosurg* **125** (2016) 1136.
- [4] M. Kameyama *et al.*, *Eur. J. Nucl. Med. Mol. Imaging* **43** (2016) 2267.
- [5] M. Kurosawa *et al.*, to be published.

CO6-23 Distribution of the chemical modifications of the amino acid residues in lens structural proteins during development of age-related cataract

S. Matsushita¹, Y. Suzuki¹, A. Nakamura¹ and T. Takata²

¹ Dept of Materials and Applied Chemistry, Nihon University

² Institute for Integrated Radiation and Nuclear Science, Kyoto University

INTRODUCTION:

Imaging mass spectrometry (Imaging MS) is a technique to visualize the localization of a target peptide by scanning mass spectrometry on tissue and superimposing positional information [1]. The method is based on the conventional mass spectrometers, thus depending on the fragmentation of each peptide.

Continuing from the previous year, we tackled to screen the best fragmentation pattern for visualizing the localization of chemical modifications that accumulate in lens structural protein with aging. Now, target modification is the isomerization of Aspartate residues (iso-Asp). Protein-constituting Asp isomerizes spontaneously with aging (four types iso-Asp series: L- α -Asp, L- β -Asp, D- α -Asp, and D- β -Asp) and accumulates with aging [2]. Therefore, identification of iso-Asp is a useful predictor as a new definition of aging.

In previous year, we found out the isomerization of Asp151 in α A-crystallin in the soluble fraction of porcine lens. This Asp is the homologous position of Asp151 in those of human lens α A-crystallin, which was heavily isomerized. We chemically synthesized this target peptide, including Asp151, and a fragmentation pattern was decided using by quadrupole type mass spectrometer. At the next step, we attempted to make a frozen section of the porcine lens on a prep for imaging MS. However, it was technically difficult to prepare the frozen section of lens due to the rich water molecules and high concentrated protein in lens. Therefore, we changed the target peptide in mouse lens, which is easier to handle, and resumed studies.

EXPERIMENTS:

Material Mouse lens was homogenized and fractionated by centrifugation to isolate lens water soluble (WS) fractions. The WS proteins were dissolved and applied for trypsin digestion as previously reported [2]. The peptide, corresponding of the mouse α A-crystallin 169–180 (¹⁶⁹VQSGLDAGHSER¹⁸⁰), was synthesized by Fmoc-based solid-phase peptide synthesis (PSSM-8; Shimadzu). The crude peptides were purified by reverse-phase HPLC using a C18 column (Capcell Pak C18; Shiseido) as previously reported [3].

LC-MS analysis Asp-containing peptides were detected by the multiple reaction monitoring (MRM) method using a triple quadrupole mass spectrometer (LCMS-8060; Shimadzu). Briefly, solutions containing 0.1–1 μ g of peptides was applied into LCMS-8060, then fragmentation pattern was optimized. Then, the HPLC separation

for tryptic peptide of mouse lens WS was carried out (Nexera X2, Shimadzu) using a combination of a C18 column (L-column2 ODS, CERI). The binary mobile phase compositions were 0.1% formic acid/water (mobile phase A) and 0.1% formic acid/acetonitrile (mobile phase B). The linear gradient was 0–45% phase B for 60 min at a flow rate of 0.2 mL/min, and a column temperature of 35°C.

RESULTS:

Prior to analysis, survey for the valid MRM transitions of target peptides of mouse α A-crystallin 169–180 was performed. The MRM method for Asp-containing peptide was created with Lab Solutions software (Shimadzu, Japan). The MRM chromatograms for fragment ions of target peptide was acquired with the transitions as shown in Table 1.

	sequence	MRM transitions for mouse peptide
human	¹⁴⁶ IQTGLDATHAER ¹⁵⁷	1254.30 > 1236.25
pig	¹⁴⁶ VPSGVDAAGHSER ¹⁵⁷	CE: 51.0
mouse	¹⁶⁹ VQSGLDAGHSER ¹⁸⁰	Positive ion mode

Table 1. α A-Crystallin derived peptide sequence and MRM transition for mouse peptide

Next, the isomerization of Asp174 of mouse α A-crystallin was investigated (Fig. 1). AS shown in Fig. 1, we were able to confirm five peaks including the four iso-Asp residues. One more peak may be a peak derived from isomerization of other amino acids, such as Glutamate residue at 179. That result implied the usefulness determination of fragmentation pattern of this peptide was successful. It may still present problem to digest lens tissue on plate, but we could apply this method for frozen section of the mouse lens for imaging MS.

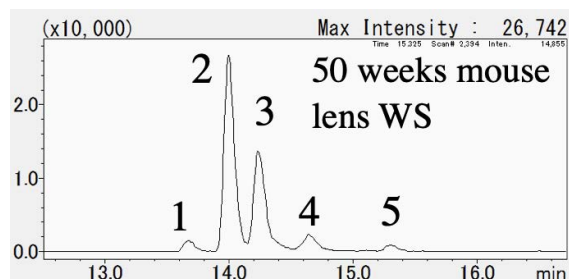


Fig. 1. LC-MS-MRM chromatogram of Asp174 peptide isomers of α A-crystallin in the water soluble fraction derived from the lens of a mouse.

REFERENCES:

- [1] M. Stoeckli *et al.*, Nat. Med., 7 (2001) 493-496.
- [2] N. Fujii *et al.*, J. Biol Chem., 287 (2012) 663-669.
- [3] K. Magami *et al.*, PLoS One., 16 (2021) 0250277.

CO6-24 Molecular dynamics analysis of oxidative folding enzyme ER-60 with solution scattering measurement

A. Okuda, M. Shimizu, K. Morishima, Y. Yunoki, R. Inoue, N. Sato, R. Urade and M. Sugiyama

Institute for Integrated Radiation and Nuclear Science, Kyoto University

INTRODUCTION: ER-60, an oxidative protein folding enzyme that belongs to the PDI family, is a multi-domain protein consisting of four thioredoxin-like domains, **a** and **a'** domains with catalytically active cysteine pairs and chaperone association **b** and **b'** domains in the order **a-b-b'-a'**. The oxidized form of active cysteine pairs (ox) catalyses the oxidation reaction of dithiol on an unfolded protein, while the reduced form (red) catalyses the reduction or isomerization of disulphide bonds. In this process, ER-60 might have the appropriate domain conformations and arrangement in order to function, and it is estimated that the structure fluctuates and changes according to the redox state of active cysteine pairs in the solution [1]. Inverse Contrast Matching Small-Angle Neutron Scattering (iCM-SANS) [2], which takes advantage of the large difference in neutron scattering length between hydrogen and deuterium, is useful for observing the dynamics and structures of such multi-domain proteins in solution.

When hydrogenated and 75% deuterated proteins are in 100% deuterated solvent, the deuterated proteins become scatteringly invisible, and only the scattering of the specific part that is hydrogenated could be observed. Applying this method to multi-domain proteins, the domain motion of the hydrogenated domains could be selectively observed. To achieve this method for multi-domain proteins, the hydrogenated and deuterated domains must be prepared separately and then connected by protein ligation technique.

To reveal the structure-function correlations of ER-60, we aim to analyze selective domain dynamics by iCM-SANS. For this purpose, we connected the hydrogenated and deuterated domains with the ligation enzyme, *OaAEP*.

EXPERIMENTS: Because 75% deuterated recombinant protein requires *E. coli* to be cultured in 75% deuterated M9 medium [3], we examined culture conditions in M9 medium and M9 plus medium [4] in addition to LB broth. Each recombinant protein containing 75% deuterated protein (**a** domain) was purified using a His-tag affinity column and a ion-exchange column. The deuteration rate of 75% deuterated protein was calculated by mass spectrometry with MALDI-TOF MS using a previously reported [3]. The 75% deuterated **a** domain and the hydrogenated **bb'a'** domain were mixed in buffer containing 200 mM Tris-HCl (pH 7.4) / 150 mM NaCl. Then, 0.2 μ M of the ligation enzyme *OaAEP* was added to the mixture, and the protein ligation reaction was performed at 20°C for 64 hours. The results of ligation reactions were confirmed by SDS-PAGE.

RESULTS: **a** domain was more abundant in the M9 medium, so we proceeded to perform 75% deuteration in this medium. In Fig. 1A, expression and purification of the recombinant 75% deuterated **a** domain yielded a highly purified protein sample. The deuteration rate of 75% deuterated **a** domain was calculated to be 73.6% from the increase in mass due to deuteration of un-exchangeable hydrogen obtained from MALDI-TOF MS (Fig. 1B).

The results of the protein ligation reaction are shown in Fig. 2. The band of ligation product, **a-bb'a'**, connecting **a** and **bb'a'** domains was observed, indicating the progress of the protein ligation reaction. Currently, we are investigating conditions to increase the efficiency of the ligation reaction for iCM-SANS, are also carrying out ligation reactions at other ligation sites, and are planning to measure the preliminary structure of them by SAXS.

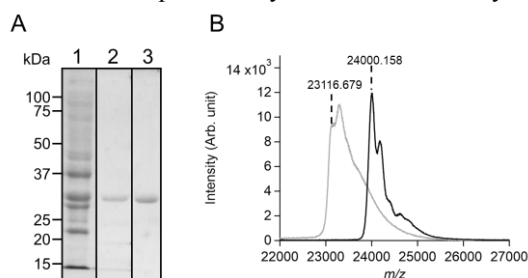


Fig. 1. (A) Expression and purification of recombinant 75% deuterated **a** domain of ER-60. Recombinant **a** domain of ER-60 expressed in *E. coli* in 75% D₂O M9 medium (lane 1) were purified by His-tag column chromatography (lane 2) and ion-exchange chromatography (3). Proteins in each effluent were separated by SDS-PAGE and stained with CBB. (B) Mass spectra of hydrogenated (gray line) and 75% deuterated (black line) **a** domain of ER-60.

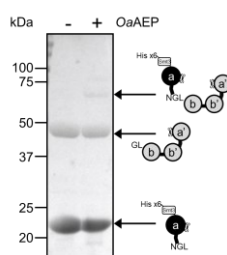


Fig. 2. The ligation product from 75% deuterated **a** domain and hydrogenated **bb'a'** domain of ER-60 by *OaAEP* (reaction times of 64 h at 20°C). Proteins were separated by SDS-PAGE and stained with CBB.

REFERENCES:

- [1] M. Sugiyama *et al.*, *J. Appl. Crystallogr.*, **47** (2014) 430–435.
- [2] A. Okuda *et al.*, *Sci Rep.*, **11** (2021) 5655.
- [3] A. Okuda *et al.*, *Biophys Physicobiol.*, **18** (2021) 16–27.
- [4] M. Cai *et al.*, *J Biomol NMR.*, **66** (2016) 85–91.

CO6-25 Integrative approach using SAXS / SANS and computational science for understanding the structure-function relationship of IDP

T. Oda, R. Oi¹, R. Inoue², K. Morishima², H. Nakagawa³, T. Tominaga⁴, M. Sugiyama², and M. Sato¹

Department of Life science, Rikkyo University

¹*Graduate school of Medical Life science, Yokohama City University*

²*Institute for Integrated Radiation and Nuclear Science, Kyoto University*

³*Materials Sciences Research Center, Japan Atomic Energy Agency*

⁴*Neutron Science and Technology Center, Comprehensive Research Organization for Science and Society (CROSS)*

INTRODUCTION: Intrinsically disordered proteins (IDP), which do not have a rigid folded structure, play important roles in living cells. However, due to its flexibility, it is difficult to understand its function based on its structure. Small-angle X-ray scattering (SAXS) is a useful method to analyze IDP because it provides dynamic structural information of IDP in an aqueous solution. We analyzed a protein Hef involved in the repair of DNA damage. Hef consists of two folded domains (Helicase domain and Nuclease domain), which are connected by an intrinsically disordered region (IDR) [1]. Based on SAXS data, we analyzed the dynamic structure of Hef as an ensemble of computationally generated structures. The ensemble showed that the structure of Hef is slightly more compact rather than that expected to be a random structure, suggesting a relationship with its function. However, in SAXS, the scattering from the two domains and the IDR are all observed as one scattering curve, therefore the interpretation of the ensemble analysis remains arbitrary. When we prepared segmentally deuterated Hef and measure small-angle neutron scattering (SANS), we can obtain structural information of selected region from hydrogenated one utilizing inverse contrast matching SANS (iCM-SANS) [2]. In this study, we prepared segmentally deuterated Hef and checked degree of deuteration and structural integrity. This integrative approach is expected to play a significant role for the analysis of IDP.

EXPERIMENTS:

Preparation of segmentally deuterated Hef- In a conventional contrast matching method, SANS of protein is measured in 40% (v/v) D₂O solvent. In this condition, hydrogenated protein is matched out, and scattering of 100% deuterated protein can be observed. However, under this condition, incoherent scattering from 60% (v/v) H₂O becomes large noise. On the other hand, if we prepare a 75% deuterated protein and measured in a 100% D₂O solvent, the 75% deuterated protein will be matched

out and scattering of only the hydrogenated protein can be observed [2]. Under this condition, incoherent scattering from solvent is significantly lower than 40% D₂O. Therefore, in this study, the deuteration degree was set to ~75%. We prepared two segmentally deuterated Hef. One is (75D)Helicase/(H)IDR-(H)Nuclease and the other is (H)Helicase-(H)IDR/(75D)Nuclease. The (75D)Helicase and the (75D)Nuclease were expressed in *Escherichia coli* cells which is cultured in M9 medium containing 75% (v/v) D₂O, 1.5 g/L of D-body glucose and 0.5 g/L of H-body glucose. After extraction from the cells and purification, the 75D-proteins were ligated to the hydrogenated proteins using a protein ligation enzyme NpuDnaE.

Determination of the degree of deuteration of proteins- The degree of deuteration of proteins were determined using a MALDI-TOF MS. From the peak shift value between ($\Delta m/z$) the 75D- and the H-protein, degree of deuteration was calculated by the following formula [3]; degree of deuteration (%) = $((\Delta m/z)/N)*100$, where N corresponds to a total number of non-exchangeable hydrogen of a protein.

SAXS measurement of segmentally deuterated Hef- The SAXS measurements of segmentally deuterated Hef were performed using a KUR SAXS instrument. Prior to SAXS measurement, samples were dialyzed against 100% D₂O solvent, and the protein concentration was adjusted to 0.8 mg/mL.

RESULTS: We succeeded in preparation of segmentally deuterated Hef. Milligram order of segmentally deuterated Hef, which is enough to use SANS measurement, was obtained. Although the degrees of deuteration of the Helicase and the Nuclease were expected to be 75%, it must be confirmed. Actual degrees of deuteration of the Helicase domain and the Nuclease domain were 79.6% and 70.0% respectively. This information is crucial for fulfilling the precise contrast matching of solvent to the prepared protein and estimate of residual scattering of deuterated region. Prior to SANS analysis, we performed SAXS analysis to check structural integrity of segmentally deuterated Hef in 100% D₂O solvent. The R_g values of (79.6D)Helicase/(H)IDR-(H)Nuclease and (H)Helicase-(H)IDR/(70.0D)Nuclease were $50 \pm 2 \text{ \AA}$ and $48 \pm 1 \text{ \AA}$ respectively. These values are slightly larger than that of non-deuterated Hef in 100% H₂O solvent ($45 \pm 1 \text{ \AA}$). This indicates that these segmentally deuterated Hef contain a small amount of aggregation. Stress during dialysis to the 100% D₂O solvent or transport of sample may have caused sample aggregation. To obtain fine data in SANS, we further have to optimize preparation and transport of sample.

REFERENCES:

- [1] Ishino *et al.*, J. Biol. Chem. 289;31, 21627-21639 (2014).
- [2] Sugiyama *et al.*, J. Appl. Cryst. 47, 430-435 (2014).
- [3] Okuda *et al.*, Biophys Physicobiol 6;18, 16-27 (2021).

CO6-26 Development of New Treatment Method for Epithelioid Sarcoma by BNCT

T. Fujimoto^{1,2}, T. Andoh³, Y. Sakurai⁴, M. Suzuki⁴

¹Department of Orthopaedic Surgery,
Hyogo Cancer Center

²Department of Orthopaedic Surgery, Kobe University
Graduate School of Medicine

³Faculty of Pharmaceutical Sciences,
Kobe Gakuin University

⁴Institute for Integrated Radiation and Nuclear Science,
Kyoto University

INTRODUCTION: Epithelioid sarcoma (ES) is an extremely rare malignant soft tissue tumor that predominates in young adults [1]. Because it is not sensitive to anticancer drugs and radiation therapy, wide surgical excision is the basis of treatment. On the other hand, good therapeutic effects of boron neutron capture therapy (BNCT) on soft tissue sarcoma have been reported [2, 3]. Therefore, in this study, BNCT was performed on ES-bearing animals at the Institute for Integrated Radiation and Nuclear Science, Kyoto University (KURNS), and its antitumor effect was examined.

EXPERIMENTS: Using nude mice, a cancer-bearing animal model was prepared by transplanting a human-derived ES cell line (VA-ES-BJ) [4] into the subcutaneous space of the mouse right thigh. After the tumor grew, tumor volume was calculated from the tumor diameter. Then animals were divided into 3 groups (n=4) of A, B, and C, and the A and B groups were used as controls. In group C (BNCT), 45 minutes after intravenous administration of BPA (500 mg/kg), and in group B without administration of BPA, only the right lower limbs of both groups were irradiated with epithermal neutrons for 10 minutes. The tumor volume of the entire group was measured from the day of irradiation (day 0), and 14 days after irradiation, the tumor tissue was removed and histological examination was performed immediately after expiry.

RESULTS: Fourteen days after irradiation, tumor regression was observed only in group C. Histological examination revealed apoptotic tumor cells in the fibrotic tissue in group C [Fig. 1], while tumor cells in the other groups were still growing [Fig. 2]. The equivalent dose of group C obtained from the dose measurement was 8.7 Gy-Eq for the skin and 20.7 Gy-Eq for the tumor, indicating a selective dose for the tumor.

DISCUSSION: In recent years, it has been suggested that epigenetic-related enzyme EZH2 target inhibitors may improve the therapeutic outcome of advanced ES [5]. Furthermore, here, for the first time, it was clear that ES regressed with only one irradiation by BNCT in this study. Therefore, a new treatment method is expected to be developed in future that combines systemic treatment with drug therapy, local treatment surgery and local treatment with BNCT.

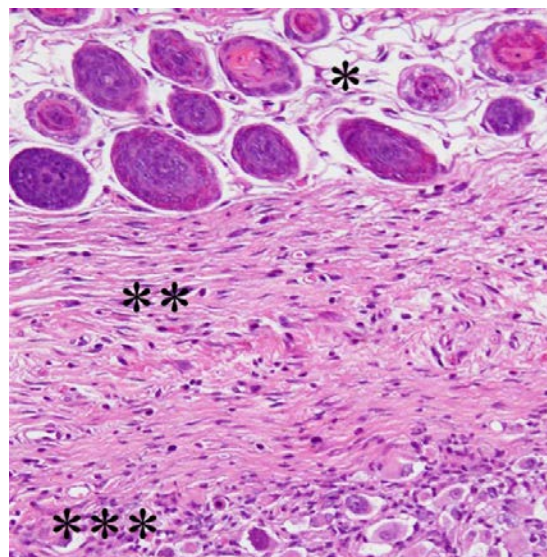


Fig. 1. Histopathological study (HE staining) of group C (BNCT) reveals apoptotic tumor cells (***) are gradually replaced with connective tissue (**). No damage to normal cells was observed on skin or subcutaneous area (*) by BNCT.

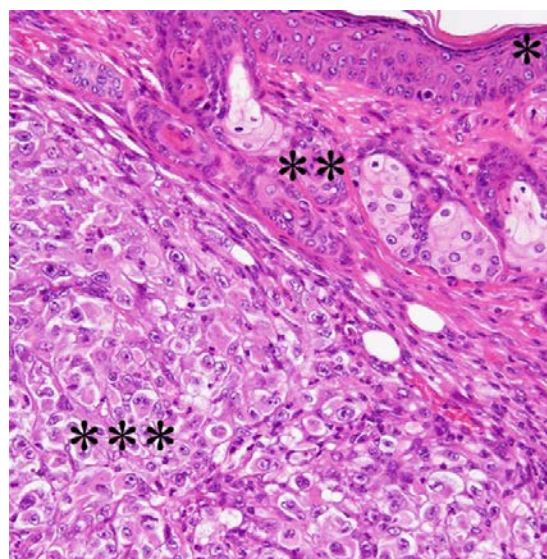


Fig. 2. Histopathological study (HE staining) of group B (hot control) reveals no tumor cells (***) are destroyed, and no normal cells (*, **) are damaged. *, skin; **, subcutaneous space.

REFERENCES:

- [1] AM. Frezza *et al.*, *JAMA Oncol.*, **4** (2018):e180219. doi:10.1001/jamaoncol.2018.0219.
- [2] T. Fujimoto *et al.*, *Appl Radiat Isot.*, **166** (2020). doi: 10.1016/j.apradiso.2020.109324.
- [3] T. Fujimoto *et al.*, *Appl Radiat Isot.*, **169** (2021). doi: 10.1016/j.apradiso.2020.109407.
- [4] C. Helson *et al.*, *Int J Oncol.* **7** (1995). doi: 10.3892/ijo.7.1.51.
- [5] M. Gounder *et al.*, *Lancet Oncol.* **21** (2020). doi: 10.1016/S1470-2045(20)30451-4.

CO6-27 Elucidating the Molecular Basis for the Increased Risk of Nuclear Cataract Development with Global Warming

T. Takata¹ and N. Yamamoto²

¹ Institute for Integrated Radiation and Nuclear Science, Kyoto University

² Research Promotion Headquarters, Fujita Health University

INTRODUCTION:

The transparency of the lens is important for focusing target onto retina. Maintaining the function of lens determines the quality of life. Lens cells contain rich structural proteins, which is called as crystallin. Those stable long-lived crystallin interactions is critical for lens functions. Many past studies have reported about post-translational modifications in crystallin species decreased solubility of crystallins and lead senile cataract formation in aged lens. Those modifications were accumulated under various stresses during life, such as heat and ultraviolet (UV) irradiation. It has also been considered that many factors in addition to UV are the main causes of nuclear cataract (NUC). In order to elucidate those factors, we performed a worldwide epidemiological survey and confirmed that the risk of NUC is significantly higher in residents living in areas where the annual number of days with temperatures of 30°C or higher is higher. Furthermore, in an *in silico* simulation study, the applicant group showed that the incidence of NUC differs within a range of internal temperature differences (35.0-37.5°C). These obvious but new results are currently the focus of worldwide attention. Based on these results, this study aims to clarify the relationship between NUC and environmental temperature. We cultured lens model cells in different temperature and analyzed the modification levels of Aspartate (Asp) in crystallin to verify the mechanism of NUC onset in different temperature.

EXPERIMENTS:

Material Immortalized human lens epithelial cells (iHLEC-NY2) are cultured on different temperature (35.0-37.5°C) and collected by RIPA buffer or PBS. Cell pellets was solubilized by sonication, 6 M Guanidine hydrochloric acid, 8 M Urea or MPEX solution (GL Science). All denaturants were removed by reverse phase spin column, then used for trypsin digestion.

LC-MS analysis After trypsin digestion, each tryptic peptide was injected to LC-MS/MS systems to identify the expressed α A-crystallin in iHLEC-NY2. Each sample was eluted over 60 min with a linear gradient (5%–45%) formed by mixing solvent A (0.1% formic acid aqueous solution) and solvent B (100% acetonitrile containing 0.1% formic acid). The algorithm for the database search was Proteome Discoverer 1.0 (ThermoFisher) as previously reported [1].

D/L analysis Next, the same sample was applied into LC-Q-MS/MS systems to evaluate isomerization levels of Asp58 in α A-crystallin. The mass chromatogram was depicted as previously reported [2].

Western Blotting In order to get intense peptides chromatograms from isolated α A-crystallin, on membrane digestion was considered. To get unique α A-crystallin band on PVDF membrane, electrophoresis for cell extracts and immunoblotting for α A-crystallin was performed with a monoclonal antibody against human α A-crystallin (Santa).

RESULTS:

In the preliminary study phase, the tryptic digestion for the cell extracted by RIPA buffer did not show the chromatograms. Based on the possibility that tryptic digestion was not possible due to the surfactant in RIPA buffer used for collecting cells, we used PBS for collecting cells. We next solubilized cell extracts using by denaturants (guanidine hydrochloric acid or urea). Solubilized samples were diluted for trypsin digestion followed by LC-MS/MS analysis, but no peak was observed. Considering the possibility that denaturants inhibited trypsin digestion, we changed denaturant into to the MPEX solution systems. All preparation included a desalting step before tryptic digestion. While the identification of human α A-crystallin in iHLEC-NY2 was successful, the quantitatively analysis of Asp58 in α A-crystallin was not. The peak on chromatogram was very poor, and not enough to evaluate the peak areas (Fig. 1). Though the molecular weight is specified, there are numerous peaks, although originally four peaks should have been seen even if isomerization was included. It is possible that background is seen due to the low total intensity.

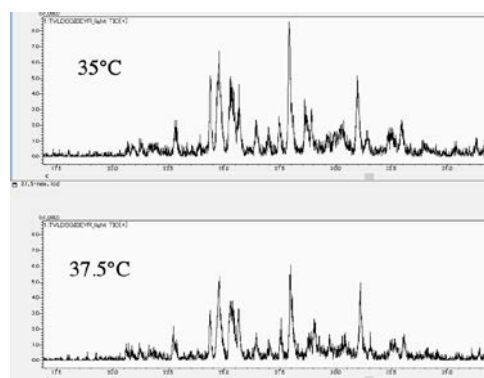


Fig. 1. Modifications on Asp151 of α A-crystallin in iHLEC extracts.

Western blot analysis showed a 20 kDa protein in iHLEC cells, that was strongly immunoreactive with the anti- α A-crystallin antibody (data not shown). The on membrane digestion for quantitative analysis should be in future study.

REFERENCES:

- [1] N. Fujii *et al.*, J. Biol Chem., **287** (2012) 663-669.
- [2] N. Fujii *et al.*, ACS Omega., **5** (2020) 27626-27632.

CO6-28 IL-6 suppresses the increase in cell oxidation through phosphorylation of mTOR and is involved in the acquisition of radiation resistance of the human pancreatic cancer-derived cell line Panc-1.

Y. Tamari^{1,2}, G. Kashino³, M. Suzuki²

¹Department of Radiology, Kyoto Prefectural University of Medicine

²Institute for Integrated Radiation and Nuclear Science, Kyoto University

³RI center, Nara Medical University

INTRODUCTION: Interleukin 6 (IL-6) is a multi-functional cytokine. The detailed mechanism of radiation resistance acquisition by IL-6 has not been elucidated. Our previous studies have revealed that the acquisition of radiation resistance by IL-6 is caused by suppressing mitochondrial-derived oxidative stress after γ -ray irradiation [1]. mTOR exists as a regulator of various phenomena such as cell metabolism, growth, proliferation and survival. It has been reported that mTOR is regulated by the IL-6 signaling pathway [2]. Furthermore, suppression of active oxygen by mTOR has been reported [3], and it was hypothesized that mTOR is involved in the radiation resistance acquisition mechanism through suppression of intracellular oxidation degree by IL-6. Purpose of this study is to investigate the detailed mechanism of radiation resistance acquisition through suppression of oxidative stress by IL-6.

EXPERIMENTS: The human pancreatic cancer derived cell line Panc-1 was used. Recombinant IL-6 (rIL-6) was administered 24 hours prior to 4 Gy X-ray irradiation or analysis. The ELISA method was used to examine the amount of IL-6 produced by Panc-1. In addition, a colony formation assay was performed to investigate the acquisition of radiation resistance by IL-6. Furthermore, the protein expression level downstream of IL-6 was confirmed by Western blotting. At that time, rapamycin was used to investigate the involvement of mTOR in the IL-6 signaling pathway. Fluorescent probes Mitosox Red and JC-1 were treated and fluorescence intensities were measured to measure mitochondrial superoxide levels and membrane potentials, respectively.

RESULTS: As a result of ELISA, Panc-1 produced considerably less IL-6. However, the survival rate after X-ray irradiation was significantly increased when rIL-6 was administered. Activation of STAT3 was shown when rIL-6 was administered, which was suppressed by administration of the mTOR inhibitor rapamycin. The acquisition of radiation resistance by IL-6 in Panc-1 and the involvement of mTOR located downstream of IL-6 were clarified. The amount of active oxygen in mitochondria was increased by X-ray irradiation, but was

suppressed by administration of rIL-6. However, administration of rapamycin neutralized the effects of IL-6. On the other hand, the decrease in mitochondrial membrane potential due to X-ray irradiation was suppressed by rIL-6. Regarding the mitochondrial membrane potential, the effect of IL-6 was canceled by suppressing mTOR.

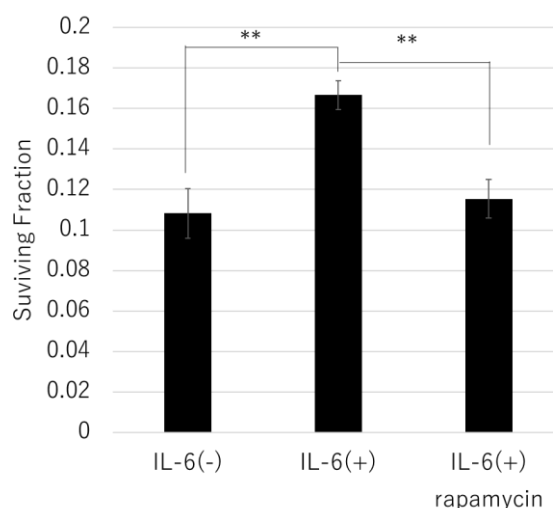


Fig. 1. Effect of mTOR inhibition on radiation resistance acquisition. Mean±SD result are graphed (**p<0.001)

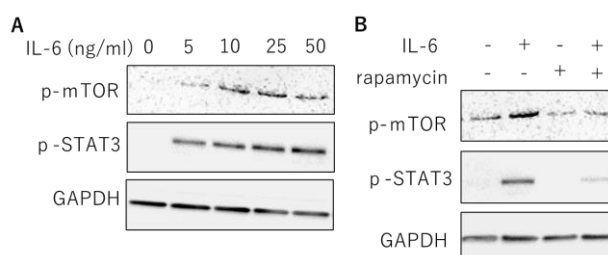


Fig.2. Activation of mTOR and STAT3 by IL-6. (A) Phosphorylation of mTOR and STAT3 depending on the concentration of rIL-6 was observed. (B) Phosphorylation of mTOR and STAT3 was suppressed by rapamycin.

REFERENCES:

- [1] Y. Tamari *et al.*, *J. Radiat. Res.*, **58** (2017)412-420.
- [2] JH. Kim *et al.*, *J. Biol. Chem.*, **283** (2008)708-715.
- [3] J. Hu *et al.*, *Int. J. Biochem. Cell Biol.*, **89** (2017) 42-56.

CO6-29 Production of medical radioisotopes using electron linear accelerator

S. Sekimoto, M. Inagaki and T. Ohtsuki

*Institute for Integrated Radiation and Nuclear Science,
Kyoto University*

INTRODUCTION: A shortage in the supply of ^{99}Mo resulting from the shutdown of reactors used for its production is a global problem. Because ^{99}Mo is an indispensable source of $^{99\text{m}}\text{Tc}$, which is used in nuclear medicine to make diagnoses using techniques such as scintigraphy and single photon emission computed tomography (SPECT), a stable supply of ^{99}Mo is vital. Therefore, production of ^{99}Mo by using neutrons or protons generated in accelerators has been investigated [1–3]. To separate $^{99\text{m}}\text{Tc}$ from ^{99}Mo produced by an accelerator, methods based on sublimation, solvent extraction, and ion-exchange column chromatography have been examined and developed [2,4–6]. In addition, Gopalakrishna et al. have reported the preparation of ^{99}Mo by the $^{100}\text{Mo}(\gamma, n)$ reaction using bremsstrahlung photons [6], followed by conventional solvent extraction using methyl ethyl ketone (MEK) and zirconium (Zr) molybdate gel to separate $^{99\text{m}}\text{Tc}$. According to the regulations of the Japanese pharmacopeia, the extraction using organic materials and the gel method using heavy metal elements such as Zr are not approved for the $^{99\text{m}}\text{Tc}$ -separation methods. Additionally, it is also difficult and impractical to use the sublimation method, which requires complicated and/or large scale devices for the mass-production of pure $^{99\text{m}}\text{Tc}$. Recently, Kaken Inc. developed a new method, known as the “technetium master milk” (TcMM). This technique can produce highly pure $^{99\text{m}}\text{Tc}$ at a maximum activity of 1.85×10^{13} Bq (500 Ci) per batch from ^{99}Mo of low specific activity [7]. We carried out the production of ^{99}Mo by the $^{100}\text{Mo}(\gamma, n)$ reaction using bremsstrahlung photons generated in an electron linear accelerator (LINAC), a technique that has not been investigated significantly in Japan. The amounts of ^{99}Mo produced at several electron energies (E_e) were examined. To separate $^{99\text{m}}\text{Tc}$ from the irradiated target, in this work, the TcMM was applied to the ^{99}Mo produced by LINAC, and the subsequent yield of $^{99\text{m}}\text{Tc}$ was evaluated.

RESULTS: An example of the specifications for a LINAC necessary for the production of a stable supply of ^{99}Mo is now discussed. As mentioned by Gopalakrishna et al. [6], an expansion of ^{99}Mo production to clinical levels requires the scaling up of the specifications for the LINAC, such as E_e , beam current of electrons, amount of target material, irradiation time, and so on. Additionally, to reduce target material costs, the use of $^{\text{nat}}\text{MoO}_3$ is preferable to that of $^{100}\text{MoO}_3$. If $^{\text{nat}}\text{MoO}_3$ is used as the target instead of $^{100}\text{MoO}_3$, the amount of the target material must be increased by one order of magnitude. Therefore, this increase in the quantity of target material necessitates a new system designed to irradiate the bulky target with bremsstrahlung photons effectively.

Here, we show the specification for LINACs where the target ($^{100}\text{MoO}_3$), mean current, and operation time are 10 g, 100 μA , and 20 h, respectively, and E_e is varied from 21 to 41 MeV. The ^{99}Mo activity produced at each E_e and its dependence on operation time and elapsed time are shown in Fig. 1. To efficiently produce ^{99}Mo and reduce the production of radioactive impurities, the E_e must be optimized. Based on the experimental results in this work, the optimized E_e is 35 MeV (see Fig. 1). Therefore, if the LINAC were operated at E_e of 35 MeV, 44.0 GBq of ^{99}Mo would be produced, and if subsequent purification of $^{99\text{m}}\text{Tc}$ by TcMM were carried out more than three times, about 100 GBq of $^{99\text{m}}\text{Tc}$ would be obtained a few days after source irradiation. Because the required activity of $^{99\text{m}}\text{Tc}$ in Japan is about 1000 GBq per day, 30 LINACs with the specifications would be able to supply the Japan’s demand for $^{99\text{m}}\text{Tc}$ in a few days.

The specifications of the LINAC are general and practical. Furthermore, because LINACs can be downsized, it is possible to set up compact LINACs for the production of ^{99}Mo - $^{99\text{m}}\text{Tc}$ in different locations in Japan and even around the world. In the near future, the installation of a new complex using the LINAC ^{99}Mo -production system

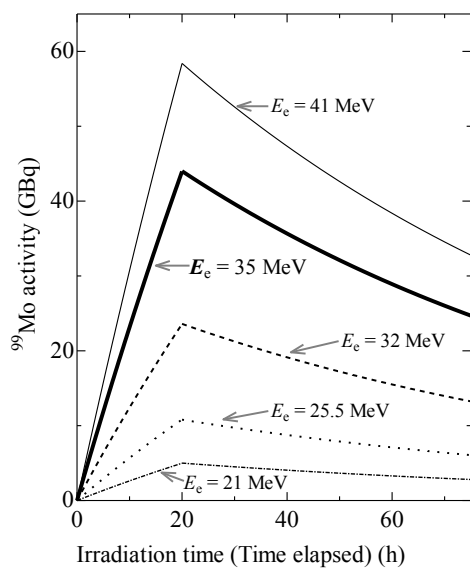


Fig. 1. Estimation of ^{99}Mo -activity based on the LINAC’s specification.

REFERENCES:

- [1] Y. Nagai *et al.*, *J. Phys. Soc. Jpn.*, **82** (2013) 064201.
- [2] Y. Nagai *et al.*, *J. Phys. Soc. Jpn.*, **83** (2014) 083201.
- [3] K. Nakai *et al.*, *Proc. Jpn. Acad. Ser. B* **90** (2014) 413–421.
- [4] M. Kawabata *et al.*, *J. Phys. Soc. Jpn.*, **84** (2015) 023201.
- [5] K. Mang’era *et al.*, *J. Radioanal. Nucl. Chem.*, **305** (2015) 79–85.
- [6] A. Gopalakrishna *et al.*, *J. Radioanal. Nucl. Chem.*, **308** (2016) 431–438.
- [7] K. Tatenuma *et al.*, *Radioisotopes* **63** (2014) 501–513.

and $^{99\text{m}}\text{Tc}$ -separation system by the TcMM would be desirable. Such complexes must be compact and inexpensive to allow their installation at many clinics and hospitals.

CO6-31 Elucidation of the effects of high dose rate radiation on normal and tumor tissues

Tsubasa Watanabe¹, Hiroki Tanaka¹, Minoru Suzuki¹

¹Institute for Integrated Radiation and Nuclear Science, Kyoto University

INTRODUCTION: Recent reports suggest that high-dose-rate irradiation, in which the dose rate is extremely high (1000 times or more) compared to the conventional radiotherapy dose rate (about 0.03 Gy/sec), suppresses side effects better than conventional irradiation and may have the same anti-tumor effect on tumors [1]. If side effects are indeed suppressed at ultra-high dose rates and anti-tumor effects remain unchanged, many conventional radiation therapies, especially X-rays, γ -rays, and proton beams, will be converted to high dose rates, and the position of neutron capture therapy will also change. This research plan will scrutinize the biological effects of ultra-high dose rates and clarify the differences compared to neutron capture therapy, focusing on biological responses and effects on tumors, to consider the future role of neutron capture therapy as a long-term cancer therapy. The goal of this fiscal year is to establish the irradiation environment necessary for this purpose.

EXPERIMENTS: Using an electron accelerator, we irradiate gafchromic films with pulsed electron beams and measure the dose per pulse. We constructed an irradiation system that can irradiate about 8-12 mice at a time.

RESULTS: The dose per pulse was sufficient for biological experiments, proving that experiments with high dose rates are possible. The irradiation system was constructed as shown in the figure (Figure 1 and Figure 2).

Figure1: Irradiation system of mice in a closed system in an acrylic box.



Figure2: The mouse is placed in the irradiation hole in the form of a radial projectile.

REFERENCES:

[1] Andrea Borghini *et al.* Int J Rad Biol 2022;98:127-135.



CO6-32 Theoretical Considerations on Reactor Production of Beta-Emitting Radionuclide ^{177}Lu for Targeted Radionuclide Therapy

K. Washiyama¹, T. Yamamura², T. Tabata², R. Okumura², K. Ogawa³

¹Advanced Clinical Research Center, Fukushima Medical University

²Institute for Integrated Radiation and Nuclear Science, Kyoto University

³Institute for Frontier Science Initiative, Kanazawa University

INTRODUCTION: The medical use of radioisotopes (RIs) has already been applied since the discovery of RIs and radioactivity, and today, [^{18}F]F-FDG and [$^{99\text{m}}\text{Tc}$]Tc-labeled radiopharmaceuticals are recognized as important for nuclear medicine diagnosis. Although research and development of α -particles has been actively conducted in Japan in recent years from both basic and clinical aspects, there has been few research and development of reactor-generated nuclides in Japanese RI production over the past 20 years. For the future development of radionuclide therapy, it is important to conduct research on the development of radiopharmaceuticals based on the production and supply of β -radiopharmaceuticals using domestic nuclear reactors. PDRadiopharma will market ^{177}Lu -DOTATATE, a labeled drug for the treatment of somatostatin receptor-positive neuroendocrine tumors by the end of FY2021, and treatment has been provided to patients, but the supply source of the drug is entirely dependent on overseas countries. In March 2022, Novartis' ^{177}Lu -PSMA-617 was approved by the FDA as a targeted radioligand therapy for the treatment of advanced PSMA-positive metastatic castration-resistant prostate cancer, a disease that affects a large number of patients worldwide, so demand for ^{177}Lu is expected to increase worldwide. However, since the production of ^{177}Lu and the development of ^{177}Lu -labeled radiopharmaceuticals are not so active in Japan, it is possible that future domestic demand will not be fully met.

CONSIDERATIONS: ^{177}Lu can be produced by the $^{176}\text{Lu}(n,\gamma)^{177}\text{Lu}$ reaction using thermal neutrons in a nuclear reactor with ^{176}Lu as a target. ^{176}Lu has a very high thermal neutron activation cross section, so irradiation in a reactor with high neutron flux can produce ^{177}Lu with high specific activity. However, the isotopes of natural ^{176}Lu is only 2.6%, so in practice, ^{176}Lu enriched to 70% or 98.5% is used. When the thermal neutron flux of reactors producing medical RIs, such as BR2 in Belgium and MARIA in Poland, is 3.0×10^{14} [$1/\text{cm}^2/\text{s}$], the specific activity reaches $> 1,000$ GBq/mg after 2 weeks of irradiation if more than 70% ^{176}Lu enriched isotope is also used (Figure 1). This value is close to the specific activity of 4,100 GBq/mg of no carrier added ^{177}Lu and is suitable for the development of antibody-labeled or peptide-labeled radiopharmaceuticals. In contrast, in the case of the hydraulic irradiation holes in the Kyoto University Research Reactor, the neutron flux is 1.6×10^{13} [$1/\text{cm}^2/\text{s}$],

1/20 of BR2, which is less, resulting in a specific activity of > 60 GBq/mg after 2 weeks of irradiation even using more than 70% ^{176}Lu -enriched isotopes. Based on this result, even if ^{176}Lu enriched isotopes are used, Japanese domestic reactors cannot produce ^{177}Lu with high specific activity, limiting its use to drugs that do not require very high specific activity, such as ^{177}Lu -EDTMP, a drug for bone pain palliation.

In contrast, ^{176}Yb can be used to produce ^{177}Lu indirectly by $^{176}\text{Yb}(n,\gamma)^{177}\text{Yb} \rightarrow (\beta^-) \rightarrow ^{177}\text{Lu}$ reaction. Ytterbium and lutetium are rare earth elements, and their chemical properties are similar, but they can still be mutually separated using an extraction chromatography column, and target free ^{177}Lu can be purified. Because the isotope stability is 13.0%, so the use of an enriched isotope of ^{176}Yb is essential for the efficient production of ^{177}Lu even in the indirect production method.

CONCLUSION: This study revealed that a reactor with a high thermal neutron flux is necessary to produce ^{177}Lu with a high specific activity. In the case of domestic research reactors, the $^{176}\text{Lu}(n,\gamma)^{177}\text{Lu}$ reaction cannot be used to produce ^{177}Lu with high specific activity, but the $^{176}\text{Yb}(n,\gamma)^{177}\text{Yb} \rightarrow (\beta^-) \rightarrow ^{177}\text{Lu}$ reaction can be used to produce a target-free ^{177}Lu tracer by combining the chemical separation operation. In the future, for the sustainable production of reactor-generated β -emitters in Japan, development of radiopharmaceuticals, we will actually produce the β -emitting radionuclide ^{177}Lu , understand its production capacity and capability, and optimize the chemical separation technique.

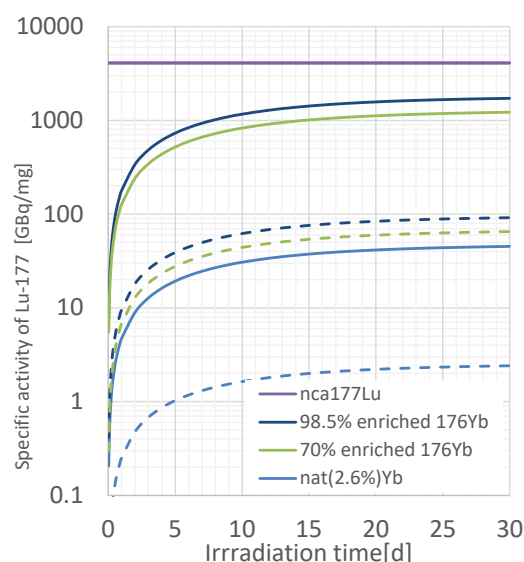


Fig. 1. Specific radioactivity [GBq/mg] of ^{177}Lu produced at $\phi_{th}=3.0 \times 10^{14}$ (solid line) and 1.6×10^{13} (dashed line) [$1/\text{cm}^2/\text{s}$].

REFERENCES:

[1] W. V. Vogel *et al.*, Eur. J. Nucl. Med. Mol. Imaging, **48** (2021) 2329-2335.

CO7-1 Synthesis and evaluation of a novel boron neutron capture therapy agent

H. Kimura¹ and M. Suzuki²

¹ Department of Analytical and Bioinorganic Chemistry, Division of Analytical and Physical Sciences, Kyoto Pharmaceutical University

²Institute for Integrated Radiation and Nuclear Science, Kyoto University

INTRODUCTION:

Only p-dihydroxyboronophenylalanine (BPA) is currently used in BNCT as a boron agent. However, BPA has issues such as low tumor accumulation and selectivity, large single-dose amounts, and water solubility, so there is a need to develop novel agents that show more favorable distribution in the body and higher tumor uptake. Many novel drugs are currently under development, including boron-containing porphyrins, amino acids, peptides, monoclonal antibodies, liposomes, various nanoparticles, boron cluster compounds, and copolymers.

Prostate cancer is the most commonly diagnosed form of cancer and the second leading cause of cancer-related deaths in men in the world. The prostate specific membrane antigen (PSMA) is an attractive target for diagnosis and therapy of prostate cancer because of its high expression in prostate cancer.^{1,2}

PSMA is expressed in normal prostate tissue, primary prostate cancer, and lymph node metastases of prostate cancer,² although PSMA expression in prostate cancer is 10- to 100-fold higher than that in normal prostate tissue.³

PSMA exhibits GCP-II (glutamatecarboxy peptidase-II) activity. Previously, several asymmetric urea compounds (X-CO-Glu) were reported to act as GCP-II inhibitors. We also demonstrated the high affinity of asymmetric urea compounds (maleimido-Cys-CO-Glu) for PSMA *in vivo*.⁴

Given this background, in this study, we designed and synthesized a novel BNCT agent targeting PSMA (BP-1).

EXPERIMENTS:

Synthesis: W-Prep 2XY (Yamazen Corporation, Osaka, Japan) was used for silica gel column chromatography on a Hi Flash silica gel column (40 mm, 60 Å, Yamazen). Silica gel 60 F254, 0.5 mm (Merck KGaA, Darmstadt, Germany), was used for preparative thin layer chromatography (PTLC). A LC-20AD (Shimadzu Corporation, Kyoto, Japan) equipped with a SPD-20A UV detector (ρ ; 220 and 254 nm) (Shimadzu) and a NDW-351 radioisotope detector (Hitachi Aloka Medical, Ltd., Tokyo, Japan) was used for high performance liquid chromatography (HPLC). The eluent consisted of a binary mixture of 0.1% trifluoroacetic acid (TFA) in H₂O (solvent A) and 0.1% TFA in methanol (solvent B). Nanopure water was prepared by MQ Integra15 (Nihon Millipore, Tokyo, Japan). Mass spectra were recorded on a LCMS-2010 EV (Shimadzu). ¹H NMR spectra were recorded on a LNM-AL500 (JEOL) using CDCl₃ or D₂O as the solvent and tetramethylsilane as an internal standard (Euriso-top,

Saint-Aubin, France). Two human prostate carcinoma cell lines were purchased from DS Pharma Biomedical (Osaka, Japan):

Cell culture: LNCaP (PSMA-positive) and PC-3 (PSMA-negative). The cells were cultured as previously reported in Roswell Park Memorial Institute 1640 (RPMI 1640) medium supplemented with 10% fetal bovine serum, glutamine, and antibiotics (penicillin/ streptomycin) in a humidified CO₂ incubator (37°C/5% CO₂).

In vitro assay: BP-1 was administered to the LNCaP (PSMA-positive) and PC-3 (PSMA-negative). Then the cells were incubated for 1hr and irradiated (neutron, 1MW) for 30min at KUR. After irradiation, the colony formation assay was conducted.

RESULTS:

BP-1 containing ¹⁰B could be synthesized in 30-40% total yield. In the absence of neutron irradiation, no cellular damage was observed within the range of drug concentrations tested in this study. However, when neutron irradiation was conducted, cell damage was observed in a drug concentration-dependent manner. The basic usefulness of BP-1 was demonstrated, but further validation, including reproducibility, is needed.

REFERENCES:

- [1] Siegel, R.; Naishadham, D.; Jemal, A. *Cancer Statistics*, 2013. *Ca-Cancer J. Clin.* **2013**, *63*, 11-30.
- [2] Hugosson, J.; Carlsson, S.; Aus, G.; Bergdahl, S.; Khatami, A.; Lodding, P.; Pihl, C.; Stranne, J.; Holmberg, E.; Lilja, H. Mortality Results From the Goteborg Randomised Population-Based Prostate-Cancer Screening Trial. *Lancet Oncol.* **2010**, *11*, 725-732.
- [3] Su, S.; Huang, I.; Fair, W.; Powell, C.; Heston, W. Alternatively Spliced Variants of Prostate-Specific Membrane Antigen RNA - Ratio of Expression as a Potential Measurement of Progression. *Cancer Res.* **1995**, *55*, 1441-1443.
- [4] Harada, N.; Kimura, H.; Ono, M.; Saji, H. Preparation of asymmetric urea derivatives that target prostate-specific membrane antigen for SPECT imaging. *J. Med. Chem.* **2013**, *56*(20), 7890-901.

CO7-2 The evaluation of boron neutron capture therapy (BNCT) to the novel mouse model of pelvic recurrence of colorectal cancer

Jun Arima, MD; Kohei Taniguchi, MD, PhD¹; Masashi Yamamoto, MD, PhD; Tsubasa Watanabe, MD, PhD³; Yusuke Suzuki, MD; Hiroki Hamamoto, MD, PhD; Yosuke Inomata, MD; Hideki Kashiwagi, MD, PhD²; Shinji Kawabata, MD, PhD²; Keitaro Tanaka, MD, PhD; Kazuhisa Uchiyama, MD, PhD, Minoru Suzuki, MD, PhD³ and Sang-Woong Lee, MD, PhD

Department of General and Gastroenterological Surgery, Osaka Medical and Pharmaceutical University, 2-7 Daigaku-machi, Takatsuki, Osaka 569-8686, Japan

¹ Translational Research Program, Osaka Medical and Pharmaceutical University, 2-7 Daigaku-machi, Takatsuki, Osaka 569-8686, Japan

² Department of Neurosurgery, Osaka Medical and Pharmaceutical University, 2-7 Daigaku-machi, Takatsuki, Osaka 569-8686, Japan

³ Department of Particle Radiation Oncology, Institute for Integrated Radiation and Nuclear Science, Kyoto University, 2 Asashiro- Nishi, Kumatori-cho, Sennan-gun, Osaka 590-0494, Japan.

Introduction

Colorectal cancer is the most common cancer worldwide. Surgical resection is the mainstay treatment of colorectal cancer. However, local recurrence still occurs in 5% to 13% of patients after curative resection. When the tumor is unresectable, it needs alternative therapeutic strategy.

In this study, we investigated the effectiveness of boron neutron capture therapy to pelvic colorectal cancer using the mouse model of pelvic recurrence of colorectal cancer.

Material and methods

We used Boronophenylalanine (BPA) as a boron compound. DLD-1 cells were concentrated to $1.0 \times 10^6/100\mu\text{L}$ in 0.1ml of PBS and injected into the pelvic cavity of each mouse. Animals were divided into three groups (nine animals per group); control, neutron irradiation only, BNCT with BPA (i.p.).

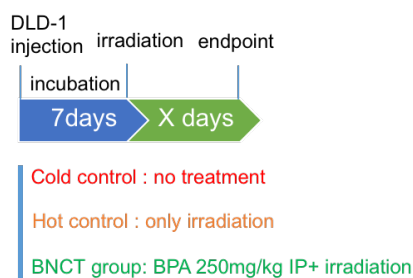
Result

The nine mice were irradiated in the hot control and BNCT groups. BPA was administrated 4 h before irradiation in the group of BNCT. The experiment protocol was shown in **Figure. 1A**. The results showed that animal survival was significantly prolonged in the BNCT group compared with cold and hot control groups. (**Figure. 1B**) (VS. cold control, $P < 0.0001$; VS. hot control, $P < 0.05$) Kaplan-Meier plots also showed that animal survival was significantly prolonged in the hot

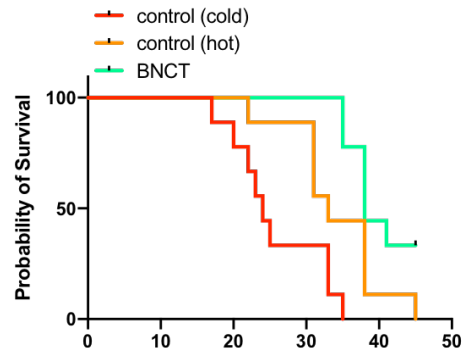
control group compared with cold control. ($P < 0.05$) The cold and hot control group showed a remarkable weight loss compared to the BNCT group. (**Figure. 1C**) These findings suggested that BNCT improved the survival CRC pelvic recurrence condition and no severe side effects of dehydration like diarrhea in the BNCT group.

Figure.1 Overall survival and change in body weight after BNCT.

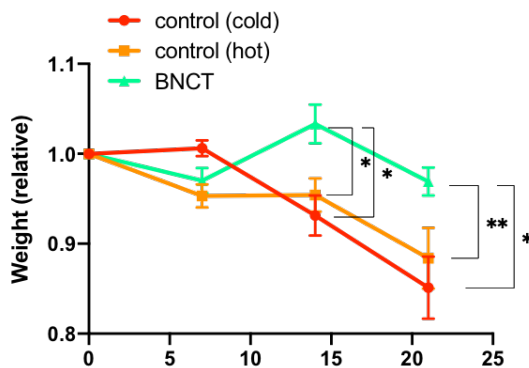
A Experimental protocol



B Overall survival



C Body weight



CO7-3 The abscopal effect as the late influence after the head neutron-irradiation of mice

Y. Kinashi¹, T. Takata¹, Y. Sakurai¹, H. Tanaka¹

¹Institute for Integrated Radiation and Nuclear Science
Kyoto University

INTRODUCTION: It is reported that immune response is activated by partial radiation. The influence on immune organization of the mouse at the time of the head irradiation is not well known. The purpose of this study is to evaluate the relative biological effectiveness in the severe combined immunodeficiency (SCID), so-called SCID mice, those are having well-known high radiation sensitivity following thermal neutron irradiation for mice cranial.

Late effects of radiation are the influence to appear three months later after radiation. Here, I report the abscopal effect as the late influence after the head neutron-irradiation of mice.

EXPERIMENTS: CB17/Icr-Prkdc^{scid}/CrIcrlj (SCID mice) were obtained from Charles River Inc. As a comparison experiment for the SCID mice, Balb/c and C3H/He mice were obtained from Japan Animal Inc.

Neutron irradiation was performed as follows. The Heavy Water Facility of the Kyoto University Research Reactor (KUR) was used. Mice were restrained in a plastic box on a radiation board. Neutron fluence was measured by radioactivation of gold foil and gamma-ray doses by TLD. I set the mouse so that the head part hit an irradiation port in the case of the escape pre-stick and irradiation 1Gy on the head in KUR 1MW. After neutron irradiation by KUR, mice were kept in animal breeding facilities and observed.

RESULTS: As shown in Table 1, the survival rate 12 months after the partial head-irradiation of the neutron by KUR. The partial head-radiation dose was about 1Gy that does not cause the bone-marrow death to a mouse. For example, by the experiment of the acute radiation damage of the SCID mouse, the dose of LD_{50/30} (the dose that 50% die within 30 days after radiation exposure) is reported around 4Gy.

As for the SCID mouse, the death began four months after head irradiation, and the number of deaths became constant 12months from eight months. In case of Balb/c mouse, the death began seven months after head irradiation, and the number of deaths became constant 12months from eight months. With C3H mouse, the death began eleven months after head irradiation, and the number of deaths became the plateau from 12months.

As a result of dissecting a mouse over time, and having observed the internal organs, the involution of the spleen was accepted after irradiation with SCID mouse and Balb/c mouse four months after irradiation. Figure 1 shows that the splenic weight per body weight 4 months after head irradiation by 1MW KUR.

Table1. Survival rate 12months after head irradiation by KUR (1MW,1Gy) .

	C3H (n=20)	Balb/c (n=20)	SCID (n=21)
Survival rate	0.75±0.08	0.67±0.08	0.38±0.04

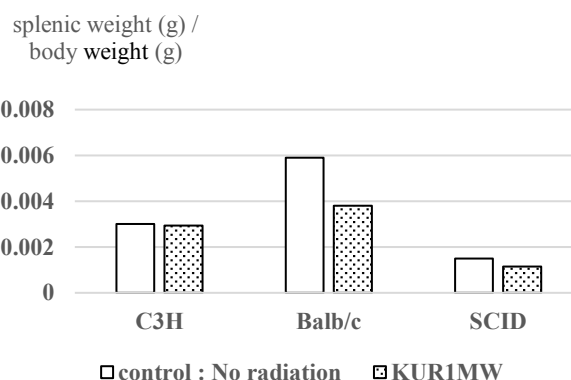


Fig.1 Involution of the spleen. The splenic weight per body weight was compared with no radiation mouse. SCID mice and Balb/c mice shows the involution of the spleen at 4 months after irradiation.

DISCUSSION

In the previous study, I reported that the abscopal effect as the acute influence after the head neutron-irradiation of mice. In experiment of the apoptosis induced in the splenic cells 24 hours after head irradiation, the RBE values of SCID mice was 1.67, comparing the RBE values of C3H/He mice was 2.12. SCID mouse show extreme sensitivity to ionizing radiation, because cells lack functional DNA-dependent protein kinase.

In this study, the radiosensitive SCID mouse had a low survival rate and splenic regression damage, a so-called, the abscopal effect as the late influence after the head neutron-irradiation. It is predicted that the involution of the spleen causes immunodeficiency and death. It is my research theme that details mechanism to explain it in the future study.

CO7-4 A Fundamental Investigation on Correlation Between Important Elements for Activation and Major Elements in Concrete and Cements for Radiation Shielding

K. Kimura, T. Takata¹, Y. Sakurai¹, H. Tanaka¹, and K. Takamiya¹

Fujita Corporation

¹Institute for Integrated Radiation and Nuclear Science, Kyoto University

INTRODUCTION: In several years, we performed neutron activation analyses to more than several hundreds of samples for radiation shield concrete and raw materials by KUR facilities. Based on the above NAA, a little database of important elements for activation for shield concrete and their raw materials were established to perform low activation shielding design for specific facilities [1]-[4]. On the other hand, we have also developed database of shielding materials with analytical major element data for them. The relationship between major elements and elements for activation is discussed in this paper.

DESCRIPTION of FIGURES: Figure 1 is described the correlation between two contents of Cobalt and Europium in concrete and cement. Figure 2 and Figure 3 show the correlation of contents of Cobalt to those of Silicon and Calcium for them. 24 kinds of shield concrete used in radiation facilities in Japan were prepared and irradiated in KUR, focusing to estimate Europium, Cobalt and Cesium (detail procedure was described in past report [4]), which are marked as blue circles in the figures. Nine kinds of cements are also symbolized as black triangles in the figures. Contents of Silicon and Calcium were estimated by x-ray fluorescence analysis (XRF), as well as other elements such as Aluminum, Iron, Sodium.

DISCUSSION: Figure 1 indicates the relatively positive correlation of Europium and Cobalt contents in concrete and cements, which were similar tendency as past works [4]. The relationships between such elements, which are important elements for activation, and major elements in concrete and cements are described in two following figures. Figure 2 indicates the relatively positive correlation between Silicon contents and Cobalt contents in concrete, while Silicon contents and Cobalt contents in cements are uncorrelated. Figure 3 also shows little correlation between Calcium contents and Cobalt contents.

CONCLUSION: Correlations of Silicon and Calcium contents to Cobalt contents are shown, which introduce the discussion of the relationship between major elements and important elements for activation in shield concrete based on material database for concrete and those raw materials.

REFERENCES:

- [1] K. Kimura, *et al.*, Proceedings of 8th International Conference on Radiation Shielding, vol. 1, pp.35-42, ANS inc, Arlington, USA, 1994.
- [2] M. Kinno, *et al.*, ANS Radiation Protection & Shielding Conference, pp.673-678, Spokane, USA, 2002.
- [3] K. Kimura, *et al.*, Proc. of Int. Conf. on Nuclear Engineering Ing (ICONE16), Florida, USA, May 11-15, (2008) 4848.

[4] K. Kimura, *et al.*, KURNS Progress Report 2018–2020.

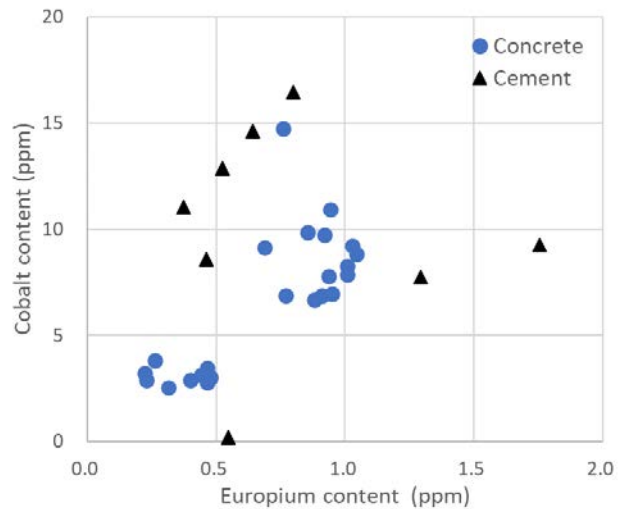


Figure 1 Correlation of Eu and Co in concrete and cement.

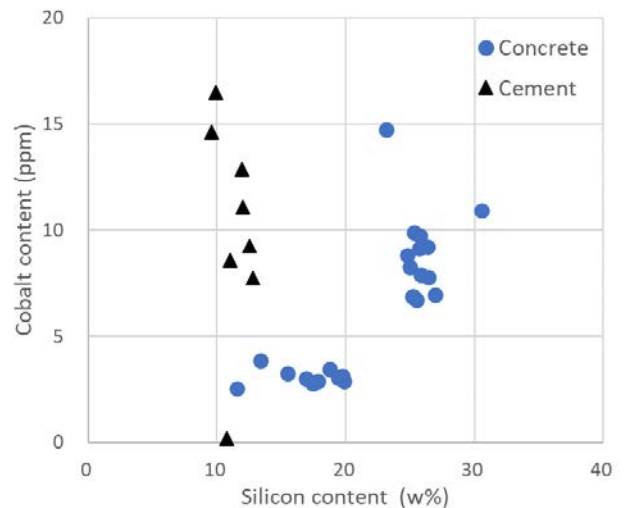


Figure 2 Correlation of Si and Co in concrete and cement.

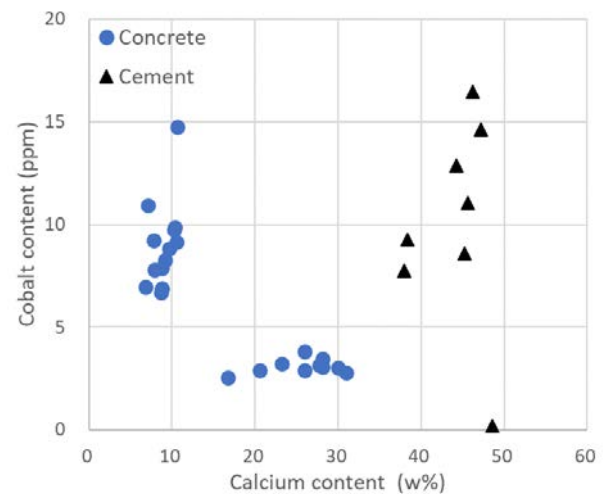


Figure 3 Correlation of Ca and Co in concrete and cement.

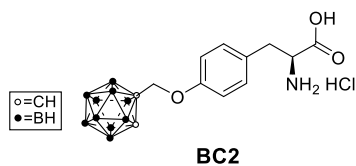
CO7-5 Development of Amino Acid Derivatives Containing ^{10}B -Clusters for BNCT

A. Niitsu¹, S. Kusanagi¹, M. Tsuji¹, Y. Sanada²,
T. Hirayama¹, S. Masunaga², and H. Nagasawa¹

¹ Laboratory of Medicinal & Pharmaceutical Chemistry,
Gifu Pharmaceutical University

² Institute for Integrated Radiation and Nuclear Science,
Kyoto University

INTRODUCTION: Cancer cells alter amino acid and sugar metabolism in order to actively proliferate and metastasize. Proliferating cancer cells increase their uptake of glutamine for energy metabolism, causing glutamine addiction. Glutamine is transported into cells through ASCT2, and the imported glutamine can be used or exchanged through the L-type amino acid transporter (LAT1 or SLC7A5) for hydrophobic or aromatic amino acids such as isoleucine, valine, methionine, tryptophan, and phenylalanine. It is known that these transporters are overexpressed in a variety of tumor cells. Focusing on this characteristic of malignant tumor "glutamine addiction," we have designed, synthesized, and evaluated boron cluster-containing amino acid derivatives to develop boron carriers that can efficiently accumulate ^{10}B atoms in tumors via amino acid transporters that are highly expressed in tumors. As reported previously, **BC2** showed the best cellular uptake among the carborane-containing amino acid derivatives, and we further investigated its uptake process in the present study.



EXPERIMENTS AND RESULTS: Intracellular boron concentrations were examined over time when **BC-2** and L-boronophenylalanine (BPA) were administered to T98G cells at $10\ \mu\text{g}\ ^{10}\text{B}/\text{mL}$. As Fig. 2 shows, the boron concentration reached its maximum at 2 hours was maintained up to 20 hours. Next, the intracellular boron uptake was then measured at different **BC-2** concentrations over a 2-hour uptake time. The intracellular boron uptake was then measured at different **BC-2** concentrations over a 2-hour uptake time. The results showed that the boron concentration at $20\ \mu\text{gB}/\text{mL}$ was $645\ \text{ng B}/10^6\ \text{cells}$, approximately 2.5 times higher than at $10\ \mu\text{gB}/\text{mL}$ ($251\ \text{ng B}/10^6\ \text{cells}$).

Next, to evaluate neutron sensitizing ability of the compounds, T98G cells were treated with 10 or $20\ \mu\text{g}\ ^{10}\text{B}/\text{mL}$ boron carrier for 2 h. Then the cells were washed with PBS, suspended in serum containing medium and aliquoted into Teflon tubes for irradiation. Cells were irradiated using the neutron beam at the Heavy Water Facility of the Kyoto University Research Reactor (KUR) operated at 1 MW power output. The survival rates of the irradiated cells were determined using conventional colony assays. The D_{10} of BNCT was calculated from survival curve shown in Fig 2.

and treated for 20 hours, after which the collected cells were dissolved in nitric acid to be measured the boron concentration by ICP-AES. As a result, intracellular boron uptake was highest in BC-2, with a very high value of about $185\ \text{ng}\ ^{10}\text{B}/10^6\ \text{cells}$, which is more than 10 times higher than BPA (Fig. 2).

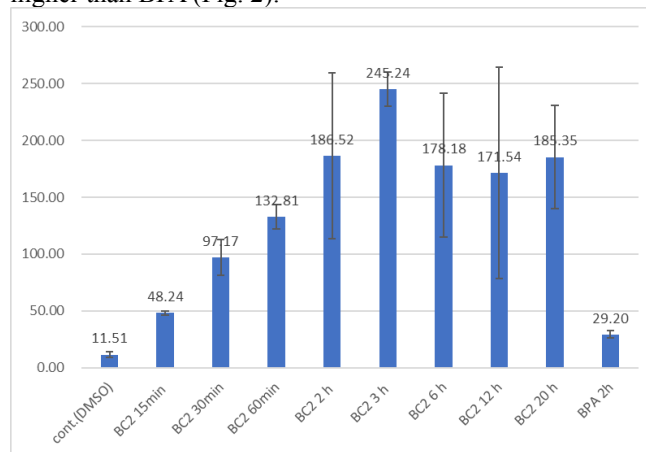
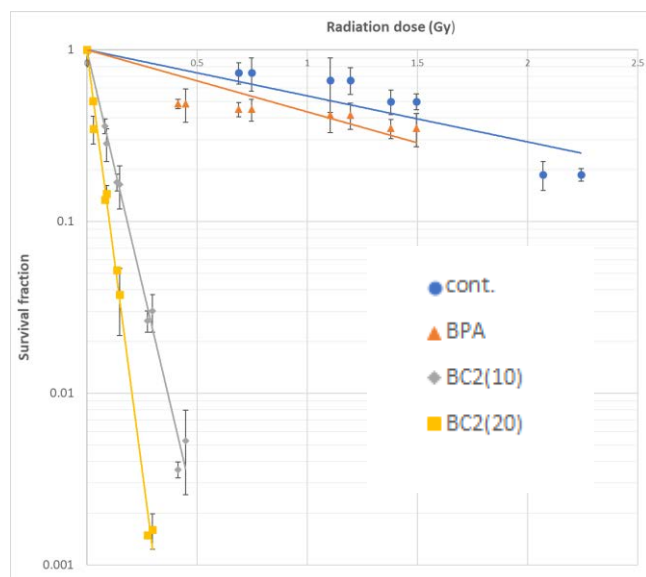


Fig. 1. Uptake of **BC2** in T98 cells.



	DMSO	BPA	BC2(10)	BC2(20)
D10 (Gy)	3.73	2.77	0.18	0.10
ER	0.96	1.29	19.46	34.78

Fig. 2. Survival curves after irradiation on T98G with **BC2**.

The cell-killing effect of neutron irradiation in the presence of **BC-2** was enhanced in a dose-dependent manner. The Enhancement Ratio (ER) of **BC2** ($20\ \mu\text{gB}/\text{mL}$) was 34.8, 30 times that of L-BPA ($10\ \mu\text{gB}/\text{mL}$) (ER=1.29).

CO7-6 Enhancement of the cancer cell-killing effects of boron neutron capture therapy by overexpression of *LAT1* in cancer stem cell-like cells

K. Ohnishi¹, M. Misawa², T. Tani³ and M. Suzuki⁴

Departments of ¹Biology, Ibaraki Prefectural University of Health Sciences

²National Institute of Advanced Industrial Science and Technology

³QST Hospital, National Institutes for Quantum and Radiological Science and Technology

⁴Institute for Integrated Radiation and Nuclear Science, Kyoto University

INTRODUCTION: Outcome from BNCT largely depends on amount of intracellular accumulation of boron compound. L-type amino-acid transporter 1 (*LAT1*) [1], through which boronophenylalanine (BPA) is transported into cells, is frequently expressed in various types of tumor cells including glioblastoma but not in normal cells [2]. We transfected *pCMV/LAT1-GFP* plasmids into a glioblastoma cell line, T98G, and selected several clones. The sensitivity of cancer cells to neutron and γ -ray fluences was well correlated with the expression level of *LAT1* and the level of BPA uptake in the clones [3]. These results suggest that overexpression of *LAT1* in cancer cells results in enhanced anticancer effects of BNCT and BNCT combined with gene therapy is beneficial for tumors with low *LAT1* expression. In this study, we transfected *pCD133-TRE/LAT1-tdTomato/ires/tTA* plasmids including a positive-feedback loop into glioblastoma cell line, T98G. The plasmids were designed to overexpress *LAT1* tagged with tdTomato on cytoplasmic membranes of CD133 expressing cancer cells selectively. We obtained several transfectants which stably overexpress *LAT1* in hypoxic microenvironment of spheroids. We used transfectant spheroids in which *LAT1* is selectively overexpressed in CD133 positive cancer cells. We have already shown that the CD133 positive cancer cells in spheroids are model cells of cancer stem cells [4]. This study examined enhanced effects of *LAT1* overexpression on BNCT in the transfectant spheroids.

EXPERIMENTS: Spheroids formed with T98G/K10 cells (*LAT1*-overexpressed in CD133 positive cell selectively) and T98G/KC6 cells (neo control vector-transfected clone) were treated with medium containing ¹⁰BPA (0, 20, 40 ppm) or PBS for 2 hours. The spheroids in 1.5-ml cryo-tubes were irradiated with the fluences (boron dose 4.8 Gy + γ -rays 0.4 Gy for 20 min irradiation, boron dose 10.0 Gy + γ -rays 0.6 Gy for 40 min irradiation) from KUR. The irradiated spheroids were transferred from the cryo-tubes to non-adherent dishes and then cultured with DMEM for 3 or 7 days. The spheroids were fixed with 10% formalin after the culture of spheroids.

RESULTS: As shown in Fig. 1, volumes of T98G/K10 and T98G/KC6 spheroids treated with PBS (0 ppm) were relatively decreased (approximately 20% reduction) after the irradiation for 20 min or 40 min compared with

non-irradiated spheroids. When T98G/K10 and T98G/KC6 spheroids were treated with 40 ppm ¹⁰BPA, the significant difference in reduction percentage of the volume between T98G/K10 and T98G/KC6 were observed after the irradiation. The reduction percentages in T98G/KC6 spheroids were approximately 20% and 30% after 20 min and 40 min irradiation, respectively. On the other hand, the reduction percentages in T98G/K10 spheroids were approximately 50% and 60% after 20 min and 40 min irradiation, respectively. These results suggest that overexpression of *LAT1* in CD133 positive cells (cancer stem cell-like cells) may result in enhanced sensitivity of spheroids to neutron and γ -ray fluences.

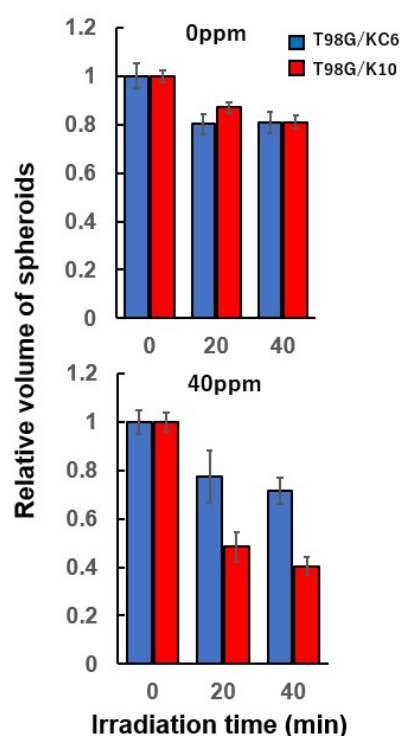


Fig. 1. Sensitivity of spheroids including *LAT1* overexpressed CD133 positive cells to neutrons. Relative volumes of spheroids were measured in ¹⁰BPA- or PBS-treated spheroids after neutron and γ -ray irradiation.

CONCLUSION: This study proposed that overexpression of *LAT1* in cancer stem cells causes enhanced anticancer effects of BNCT. BNCT combined with gene therapy seems to be beneficial for tumors including cancer stem cells resistant to radiation cancer therapy.

REFERENCES:

- [1] Y. Kanai *et al.*, J. Biol. Chem., **273** (1998) 23629-23632.
- [2] K. Kaira *et al.*, Br. J. Cancer, **107** (2012) 632-638.
- [3] K. Ohnishi *et al.*, Radiat. Res., **196** (2021) 17-2.
- [4] K. Ohnishi *et al.*, Biochem. Biophys. Res. Commun., **546** (2021) 150-154.

CO7-7 Effects of overexpression of *LAT1* in cancer stem cell-like cells on suppression of tumor growth by boron neutron capture therapy

K. Ohnishi¹, M. Misawa², T. Tani³ and M. Suzuki⁴

Departments of ¹Biology, Ibaraki Prefectural University of Health Sciences

²National Institute of Advanced Industrial Science and Technology

³QST Hospital, National Institutes for Quantum and Radiological Science and Technology

⁴Institute for Integrated Radiation and Nuclear Science, Kyoto University

INTRODUCTION: Outcome from BNCT largely depends on amount of intracellular accumulation of boron compound. L-type amino-acid transporter 1 (LAT1) [1], through which boronophenylalanine (BPA) is transported into cells, is frequently expressed in various types of tumor cells including glioblastoma but not in normal cells [2]. We transfected *pCMV/LAT1-GFP* plasmids into a glioblastoma cell line, T98G, and selected several clones. The sensitivity of cancer cells to neutron and γ -ray fluences was well correlated with the expression level of LAT1 and the level of BPA uptake in the clones [3]. These results suggest that overexpression of LAT1 in cancer cells results in enhanced anticancer effects of BNCT and BNCT combined with gene therapy is beneficial for tumors with low LAT1 expression. In this study, we transfected *pCD133-TRE/LAT1-tdTomato/IRES/tTA* plasmids including a positive-feedback loop into glioblastoma cell line, T98G. The plasmids were designed to overexpress LAT1 tagged with tdTomato on cytoplasmic membranes of CD133 positive cancer cells selectively. We confirmed several clones which stably overexpress LAT1 in hypoxic microenvironment of spheroids. In this study, we examined enhanced effects of LAT1 overexpression on BNCT using the clones in which LAT1 is selectively overexpressed in CD133 positive cancer cells. We have already shown that the CD133 positive cancer cells in spheroids are model cells of cancer stem cells [4]. We transplanted the clone cells into nude mice and performed neutron irradiation on tumors.

EXPERIMENTS: We transplanted tumors formed with a clone (T98G/K10, *pCD133-TRE/LAT1-tdTomato/IRES/tTA*-transfected, LAT1-overexpressed cells in CD133 positive cell selectively), or a clone (T98G/K4, *pCMV/LAT1-GFP*-transfected, LAT1-overexpressed cells) into femoral region of nude mice. Accumulated amounts of ¹⁰BPA in blood and tumor were measured using prompt gamma-ray assay (PGA) on 1 h after ¹⁰BPA

s.c. injection (100 mg/kg, 1 h before irradiation). The transplanted tumors into mice were irradiated with thermal neutron beam at the fluences of 3.3×10^{12} n/cm² on 1h after the ¹⁰BPA injection.

RESULTS: Averages of the relative tumor volumes in ¹⁰BPA-treated mice and PBS treated mice are shown in Fig. 1. Tumor growth in ¹⁰BPA-treated T98G/K4 (n=6) was strongly suppressed after neutron irradiation compared with that in PBS-treated T98G/K4 (n=6). In contrast to this, tumor growth in ¹⁰BPA-treated T98G/K10 (n=6) was weakly suppressed after neutron irradiation compared with that in PBS-treated T98G/K10 (n=6). The difference in tumor growth rate was observed between ¹⁰BPA-treated T98G/K4 and T98G/K10, but not observed between PBS-treated T98G/K4 and T98G/K10. These results suggest that CD133 expressing cell-selective LAT1 overexpression is effective in ¹⁰BPA-treated cells compared with PBS-treated cells. In further experiments, we plan to compare the effectiveness of CD133 expressing cell-selective LAT1 overexpression between LAT1 non-transfected tumors and T98G/K4 or T98G/K10 tumors.

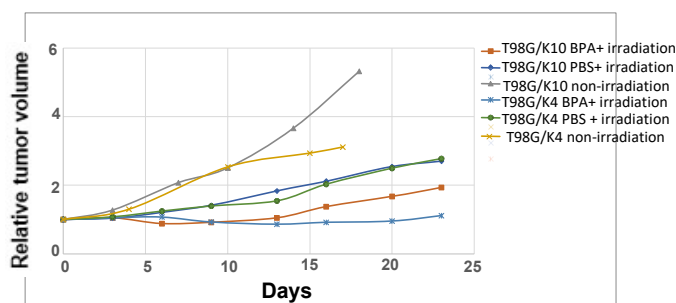


Fig. 1. Tumor growth curves of LAT1 overexpressing tumors (T98G/K4) and CD133 expressing cell selective LAT1 overexpressing tumors (T98G/K10).

CONCLUSION: We obtained preliminary data from this study. On the basis of the data, we plan to perform further detailed experiments in this study.

REFERENCES:

- [1] Y. Kanai *et al.*, J. Biol. Chem., **273** (1998) 23629-23632.
- [2] K. Kaira *et al.*, Br. J. Cancer, **107** (2012) 632-638.
- [3] K. Ohnishi *et al.*, Radiat. Res., **196** (2021) 17-22.
- [4] K. Ohnishi *et al.*, Biochem. Biophys. Res. Communi., **546** (2021) 150-154.

CO7-8 Preliminary Experiment of Tumour Growth Suppression by Intra-Tumoral Injection of Boron-Polyplex/Polymer for Boron Neutron Capture Therapy to Pancreatic Cancer Model *in vivo*

Hironobu Yanagie^{1,2,3}, Xuan Hou⁴, Masashi Yanagawa⁵, Takehisa Matsukawa⁶, Ayano Kubota⁶, Minoru Suzuki⁷, Yoshinori Sakurai⁷, Hiroki Tanaka⁷, Kazuhito Yokoyama⁶, Masayuki Nashimoto³, Jun Nakajima^{2,8}, Minoru Ono^{2,9}, Takumichi Sugihara³, and Hiroyuki Takahashi^{1,2,4}

¹Institute of Engineering Innovation, School of Engineering, Univ of Tokyo, ²Cooperative Unit of Medicine & Engineering, Univ of Tokyo Hospital, ³Niigata Univ of Pharmacy & Applied Life Sciences, ⁴Dept of Bioengineering, School of Engineering, Univ of Tokyo, ⁵Obihiro Univ of Agriculture and Veterinary Medicine, ⁶Dept of Hygiene, Faculty of Medicine, Juntendo University, ⁷Kyoto Univ Institute for Integrated Radiation & Nuclear Science, ⁸Dept. of Pulmonary Surgery, The University of Tokyo Hospital, ⁹Dept. of Cardiac Surgery, The University of Tokyo Hospital, JAPAN

INTRODUCTION:

For effective Boron-neutron capture therapy (BNCT), it is necessary to accumulate Boron atoms into the tumor tissues selectively. We performed the experiments of boron delivery systems for BNCT using boronododecaborane (¹⁰B₁₂ H₁₁SH; ¹⁰BSH) [1, 2, 3]. The ¹⁰BSH is difficult to be kept in the cytoplasm and nucleus in the cancer cells, so we need to develop some functional delivery systems. In this study, we evaluated ¹⁰BSH / hyaluronic acid / protamine-mixed with cationic liposome (¹⁰Boro-plex) or polymer (¹⁰Boro-PEI) as neutron capture therapy agent by *in vivo* experiment on AsPC-1 human pancreatic tumor-bearing mice. We also use electroporation combined cationic liposome / polymer as a method for selective delivery of compound into the cells by open the membrane poles electroporatively in the field of gene therapy and chemotherapy [4, 5].

EXPERIMENTS:

¹⁰Boro-plex were prepared mixed with 1.3mL of ¹⁰BSH(6mg/mL), 0.15mL of a solution of 10mg/mL hyaluronic acid sodium, and 0.05mL of 10mg/mL of protamine incubating at room temperature for 30min, then, these mixing solutions were poured into cationic Liposome; Genetransfer. ¹⁰Boro-PEI were prepared mixed with 1.3mL of ¹⁰BSH(6mg/mL), 0.20mL of a solution of 10mg/mL hyaluronic acid sodium, and 0.10mL of 10mg/mL of protamine incubating at room temperature for 30min, then, these mixing solutions were poured into 0.40mL of Polyethyleneimine(PEI; Exgen). Human pancreatic cancer AsPC-1 cell was used for the *in vivo* anti-tumor effect evaluation. We prepared AsPC-1(5x10⁵) model by transplanting to right lower leg. Electroporation was performed after intra-tumoral injection of 0.1mL of ¹⁰Boro-plex, then, we performed thermal neutron irradiation at Institute for Integrated Radiation and Nuclear

Science, Kyoto University (average neutron fluence of 3.0 × 10¹² n/cm²). The change in tumor growth and survival rate of the mice reflected the anti-tumor effect of ¹⁰Boro-plex. While measuring the size of tumor, the weight change was also recorded for evaluation of the toxicity of these samples.

RESULTS:

The experimental results showed that tumor growth suppression in ¹⁰Boro-plex injected group by NCT was 4.5 times superior compared with non-irradiated group (only ¹⁰Boro-plex injection), and tumor growth suppression in ¹⁰Boro-PEI injected group was 2.3 times superior compared with non-irradiated group (only ¹⁰Boro-PEI injection). No significant weight loss were observed after treatment suggesting low systemic toxicity of this system.

We attempted to enhance of retention of ¹⁰Boron atoms by mixing ¹⁰Boro-plex / ¹⁰Boro-PEI. The mechanism of transfection in ¹⁰Boro-plex and ¹⁰Boro-PEI is thought as endocytosis and proton-sponge effect, respectively. Electroporation is very effective to increase the ratio of transfection of the genes and compounds into the cytoplasm of cancer cells.

It is easily heterogeneous of the concentration of ¹⁰B in the tumor by intratumoral direct injection, so it is thought that combination with the methods of gene delivery system and electroporation was effective to accumulate the ¹⁰B compound into the cancer cells. We hope to apply these techniques including gene therapy and electrochemotherapy actually using in clinical to BNCT for local advanced cancers. We also consider and develop the more safety and stable ¹⁰B delivery systems.

Table1. Tumor growth suppression of by intra-tumoral injection of ¹⁰Boro-plex / ¹⁰Boro-PEI and Electroporation with thermal neutron irradiation on AsPC-1 model *in vivo*

	Tumor growth rate		
	Day8	Day15	Day25
BNCT			
¹⁰ Boro-plex+EP	3.02±0.44	2.71±1.69	3.84±3.68
¹⁰ Boro-PEI+EP	3.14±1.17	4.62±3.28	6.15±5.61
Non NCT			
¹⁰ Boro-plex+EP	5.86±3.35	9.02±5.14	17.35±13.54
¹⁰ Boro-PEI+EP	4.52±1.12	5.79±1.72	13.86±2.86

REFERENCES:

- [1] Yanagie H, *et al.* : Br J Cancer (1997) 75(5):660-5.
- [2] Maruyama K, *et al.* : J Control Release (2004) 98(2):195-207.
- [3] Yanagie H, *et al.* : In Vivo (2021) 35(6):3125-3135.
- [4] Lambricht L, *et al.*: Expert Opin Drug Deliv (2016) 13(2):295-310.
- [5] Trotošek B, *et al.*: World J Gastroenterol (2021)27(48) : 8216-8226.

CO7-9 Enhancement of Tumour Growth Suppression by Electroporation with Intra-Tumoural Injection of Gadolinium-Polyplex for Gadolinium-Neutron Capture Therapy to Pancreatic Cancer Model *in vivo*

Hironobu Yanagie^{1,2,3}, Xuan Hou⁴, Masashi Yanagawa⁵, Yoshiteru Yanagie⁶, Yuriko Sakurai^{1,2,3}, Yasuyuki Morishita⁷, Takehisa Matsukawa⁸, Ayano Kubota⁸, Minoru Suzuki⁹, Yoshinori Sakurai⁹, Hiroki Tanaka⁹, Takeshi Nagasaki¹⁰, Kazuhito Yokoyama⁸, Takefumi Hirata¹¹, Masayuki Nashimoto³, Jun Nakajima^{2,12}, Minoru Ono^{2,13}, Takumichi Sugihara³, and Hiroyuki Takahashi^{1,2,5}

¹Institute of Engineering Innovation, School of Engineering, Univ of Tokyo, ²Cooperative Unit of Medicine & Engineering, Univ of Tokyo Hospital, ³Niigata Univ of Pharmacy & Applied Life Sciences, ⁴Dept of Bioengineering, School of Engineering, Univ of Tokyo, ⁵Obihiro Univ of Agriculture and Veterinary Medicine, ⁶Faculty of Medicine, Teikyo University, ⁷Dept of Human & Molecular Pathology, Graduate School of Medicine, The University of Tokyo, ⁸Department of Hygiene, Faculty of Medicine, Juntendo University, ⁹Kyoto Univ Institute for Integrated Radiation & Nuclear Science, ¹⁰Osaka City University Graduate School of Engineering, ¹¹Geochemical Research Center, School of Science, The University of Tokyo, ¹²Dept. of Pulmonary Surgery, The University of Tokyo Hospital, ¹³Dept. of Cardiac Surgery, The University of Tokyo Hospital, JAPAN

INTRODUCTION:

Gadolinium reacts thermal neutron and offers cytotoxic effect by 1 μ m-range high LET Auger electron, and long-range gamma rays on Gadolinium-neutron capture therapy(GdNCT) [1, 2, 3]. It is necessary to accumulate high concentration of Gadolinium atoms into the tumor tissues selectively for effective GdNCT. Electroporation is an method for selective delivery of compound into the cells by open the membrane poles elcectorically in the field of gene therapy and chemotherapy [4, 5]. In this study, we evaluated the electroporation with intra-tumoral injection of ¹⁵⁷Gadolinium-Polyplex; ¹⁵⁷Gd-plex (gadolinium / hyaluronic acid / protamine-mixed with cationic liposome) by in vivo experiment on AsPC-1 human pancreatic tumor-bearing mice.

EXPERIMENTS:

¹⁵⁷Gd-plex were prepared mixed with 1.5mL of Gadolinium compound "Magnescope" (MW: 753.86), 0.2mL of a solution of 10mg/mL-hyaluronic acid sodium, and 0.1mL of 20mg/mL of protamine incubating at room temperature for 30min, then, these mixing solutions were poured into cationic Liposome; Genetransfer. Human pancreatic cancer AsPC-1 cell was used for the *in vivo* anti-tumor effect evaluation. We prepared AsPC-1(5x10⁵) model by transplanting to right lower leg. Electroporation was performed after intra-tumoral injection of 0.2mL of ¹⁵⁷Gd-plex, then, we performed thermal neutron irradiation at Institute for Integrated Radiation and Nuclear

Science, Kyoto University (average neutron fluence of 2.0 \times 10¹² n/cm²). The change in tumor growth and survival rate of the mice reflected the anti-tumor effect of ¹⁵⁷Gd-plex. While measuring the size of tumor, the weight change was also recorded for evaluation of the toxicity of these samples.

RESULTS:

Thirty percent of tumor growth suppression was achieved in the ¹⁵⁷Gd-plex+EP group in NCT groups compared with non-irradiated group. The tumor growth suppression of the ¹⁵⁷Gd-plex+EP group was superior than the only ¹⁵⁷Gd-plex injected group by NCT.

We attempted enhancement of retention of gadolinium atoms by mixing ¹⁵⁷Gd-plex. The experimental results showed that the tumor growth suppression of ¹⁵⁷Gd-plex+EP group was revealed superiority compared to the group with ¹⁵⁷Gd-plex group after NCT, and no significant weight loss were observed after treatment suggesting low systemic toxicity of this system. We would like to consider the techniques to perform EP in the body. The ¹⁵⁷Gd-plex will become one of the candidates for Gd delivery system on NCT. Moreover, the body weight of the mice did not decrease after the treatments, which indicate the safety of ¹⁵⁷Gd-plex / ¹⁵⁷Gd-plex+EP and the GdNCT.

Table1. Augmentation by electroporation of tumor growth suppression by GdNCT with intra-tumoral injection of ¹⁵⁷Gd-plex on AsPC-1 model *in vivo*

	Tumor growth rate		
	Day8	Day15	Day25
GdNCT			
¹⁵⁷ Gd-plex+EP	1.604 \pm 0.517	2.657 \pm 1.024	4.017 \pm 1.615
¹⁵⁷ Gd-plex	2.217 \pm 0.569	4.034 \pm 1.254	7.522 \pm 1.499
Non NCT			
¹⁵⁷ Gd-plex+EP	3.221 \pm 0.621	7.259 \pm 1.563	12.655 \pm 2.750

Tumor growth suppression in ¹⁵⁷Gd-plex+EP group by NCT was 3times superior compared with non-irradiated group. Tumor growth suppression in ¹⁵⁷Gd-plex+EP group was 1.8times superior compared with ¹⁵⁷Gd-plex group in NCT groups.

REFERENCES:

- [1] Dewi N *et al.*, Biomed & Pharmacother (2013) **67**:451-7.
- [2] Dewi N *et al.*, J Can.Res.Clin.Oncol. (2016) **142**(4):767-75.
- [3] Mi P, *et al.*: J Cont. Release (2014) **174**:63-71.
- [4] Lambricht L, *et al.*, Expert Opin Drug Deliv (2016) **13**(2):295-310.
- [5] Trotošek B, *et al.*, World J Gastroenterol (2021)**27**(48) : 8216-8226.

CO7-10 Identification of host immunostimulatory effects induced by boron neutron capture therapy

Tsubasa Watanabe¹, Hiroki Tanaka¹, Minoru Suzuki¹

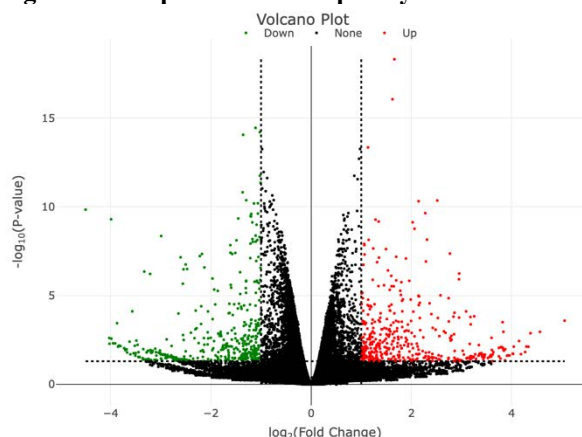
¹Institute for Integrated Radiation and Nuclear Science, Kyoto University

INTRODUCTION: Various tumor immunostimulatory effects have recently been demonstrated following X-ray or gamma irradiation, including an increase in major histocompatibility complex (MHC) molecules on the tumor surface [1], activation of antigen-presenting capacity by dendritic cells [2], and induction of diverse T-cell receptor clones [3]. It has not been clarified whether BNCT has the same immunostimulatory effects as X- or gamma-irradiation. Wet has shown in previous experiments using the reactor until last year that the anti-tumor effect of BNCT is weakened when the immune function of mice is weakened immediately before BNCT. In this fiscal year, we aim to elucidate the specific mechanism of immune activation by BNCT and to clarify the effect of the combination of BNCT and immunotherapy by mouse experiments.

EXPERIMENTS: The spleen was removed from the mice and the splenocytes were collected. The splenocytes were activated and the activated spleen cells were treated with L-BPA followed by neutron irradiation. The subsequent degree of apoptosis of each immune cell was measured using a flow cytometer. Blood was withdrawn from C3H mice in which SCC7 tumor cells were implanted subcutaneously in the lower limbs, or C3H mice without tumor cells, and the blood was dried completely, and the dried blood was irradiated with neutrons. After irradiation, the specimens were subjected to radio-activation analysis. B16 mouse melanoma cells were implanted subcutaneously in C57BL/6 mice and conducted neutron irradiation, BNCT with L-BPA, BNCT with L-BPA combined with anti-PD-1 antibody (immunotherapy). Each tumor tissue was subjected to RNA-seq analysis.

RESULTS: Each immune cell in the splenocytes showed a lower rate of apoptosis after BNCT than the tumor cells such as murine melanoma cell line, B16, and murine squamous cell carcinoma cell line, SCC7. Among the T cells, CD8+ T cells and CD4+ T cells showed a similar rate of apoptosis as the immuno-suppressive regulatory T cells. There was no significant difference in the effect of BNCT on activated T cells compared to the non-activated state. Trace metals, which were expected to change by radio-activation analysis, were not detected in the blood of the carcinoma-bearing mice. RNA-seq results showed that the BNCT group expressed significantly more factors that induce and attract immune cells than the X-rays group.

Fig1. Volcano plot of RNA-seq analysis



The right side of the figure shows the group of genes more expressed in the BNCT group and the left side shows the group of genes more expressed in the X-ray group.

REFERENCES:

- [1] Amit A Lugade *et al.* J Immunol 2008; 180: 3132-3139.
- [2] Youjin Lee *et al.* Blood 2009; 114: 589-595.
- [3] Twyman-Saint Victor C *et al.* Nature 2015; 520: 373-377.

CO7-11 Basic research to expand the indication of neutron capture therapy to non-neoplastic diseases

Tsubasa Watanabe¹, Yoshihide Hattori², Minoru Suzuki¹

¹*Institute for Integrated Radiation and Nuclear Science, Kyoto University*

²*Research Center of BNCT, Osaka Metropolitan University*

INTRODUCTION: In 2020, boron neutron capture therapy (BNCT) using L- BPA (borophalan, trade name: stevoronin) as a boron-based μm -scale cancer treatment with neutron irradiation is covered by insurance to the treatment of head and neck cancer patients in Japan. Clinical trials are currently underway to expand the indications of BNCT other than head and neck cancer including malignant brain tumors and malignant melanoma. The challenges of BNCT are attenuation of thermal neutrons in the body, accumulation of the boron drug in normal tissues, and difficulty in uniformly accumulating the boron drug in the tumor tissue [1]. The first challenge, attenuation of thermal neutrons in the body, can be solved by multi-port irradiation from several directions. The second issue, the accumulation of boron drugs in normal tissues, could be improved by modifying the pharmacokinetics of boron drugs with simultaneous use of pharmacokinetics modifiers. The third problem, the uniform accumulation of boron-based drugs in tumor tissues, is originated to the feature of tumor cells: tumor cells are a population of cells with heterogeneous characteristics. Multiple BNCT irradiations and the use of multiple boron drugs are possible solutions to this problem [2].

The potential of BNCT greatly depends on boron agents. While many new boron agents have been developed and antibody is also tried to be used as a new boron drugs for BNCT, the treatment effect of the antibody-based BNCT had not been enough [3]. One of the big reasons for that is the tumor heterogeneity, one of the challenges of BNCT mentioned above. If we change BNCT target different pathologic cells instead of tumor cells, we may be able to improve morbid conditions using the BNCT principle. This study aims to establish antibody-based BNCT for a new therapeutic strategy for non-tumor diseases, thereby expanding the range of therapeutic indications for BNCT.

EXPERIMENTS: We have created a boronated module using maleimide to bind boron clusters to antibodies. Mice were injected intraperitoneally with β -glucan to induce immunoreactive inflammation (inflammation-induced mouse model). With the boronated module, we developed a boronated antibody targeting immune cells that cause inflammation, administered the boronated antibody to the inflammation-induced model mice, and examined the therapeutic effect of neutron irradiation on the inflammatory site compared to the neutron-alone group.

RESULTS:

Approximately 40 boron per antibody molecule was found to be bound by the maleimide-based method. To investigate the possibility that boronation of antibodies may inhibit the binding of antibodies to their target protein binding, the fluorescent boronated antibody to the CD8a molecule were prepared and co-stained with fluorescent anti-CD8b antibody with CD8+ T cells. Both CD8a and CD8b were well-stained with the antibodies, which shows the target specificity of the boronated antibody was maintained. Inflammation-induced mouse models were treated with the boronated antibody targeting inflammatory cells and irradiated with 5 MW 12-minute neutron locally to the site of inflammation. The intensity of local inflammation was evaluated over time using the inflammation evaluation score compared to the neutron-alone irradiation group. However, no improvement in inflammation was observed. With these results, the boronation module of the antibody was modified to increase the amount of boron that can be bound per antibody molecule.

REFERENCES:

- [1] Rolf F Barth *et al.* *Radiat Oncol* 2012;7:146.
- [2] Kunio Yokoyama *et al.* *J Neurooncol* 2006;78:227-232.
- [3] Weilian Yang *et al.* *Clinical Cancer Res* 2008;14:883-891.

CO7-12 Mechanism of Glioma Resistance After BNCT Conferred by Glioma Niche

N. Kondo¹, E. Hirata², M. Natsumeda³, Y. Sakurai¹, T. Takata¹, T. Kinouchi¹ and M. Suzuki¹

¹ Institute for Integrated Radiation and Nuclear Science, Kyoto University (KURNS)

² Division of Tumor Cell Biology and Bioimaging Cancer Research Institute of Kanazawa University

³ Department of Neurosurgery, Brain Research Institute, Niigata University

INTRODUCTION: Boron Neutron Capture Therapy (BNCT) have been applied to recurrent malignant glioma and even after standard therapy (surgery, chemo-radiation therapy) because of the selective damage to the tumor. Especially, glioblastoma (GBM) is the most miserable cancer, whose patient survival is 14.6 months and remarkably resistant to chemo-radiation and immunotherapy. With BNCT, we achieved better local control and survival benefit in malignant glioma using thermal neutrons produced by the reactor in Kyoto University. However, the recurrence is inevitable after BNCT. Reasons for recurrence after BNCT have not been fully elucidated.

We reported glioma stem cells which are known to be resistant to chemo-radiation therapy, take up a boron compound, *p*-boronophenylalanine (BPA) and can be targeted by BPA-BNCT [1]. In this study, we investigated whether the glioma niche influences the survival of glioma cells after BNCT.

EXPERIMENTS:

Cell culture: We used human GBM cell line, U87MG *delta EGFR* and human microglia cell line, HMC3 as a component of glioma niche. Both cells were cultured in Dulbecco's Modified Eagle Medium (DMEM) containing 10% fetal bovine serum at 37 °C in CO₂ incubator.

Boronophenylalanine (BPA) Treatment and Thermal Neutron Irradiation: We treated U87MG *delta EGFR* cells with medium containing BPA at the concentration of 20 ppm for 30 minutes. The BPA was formulated and its concentration was measured as previously described [2]. After we trypsinized and rinsed the cells, cells were collected in Eppen tubes with DMEM containing BPA at the concentration of 20 ppm and irradiated with thermal neutron for 20 minutes.

Co-culture system: After thermal neutron irradiation, 10E5 U87MG *delta EGFR* cells were disseminated into the bottom dish of 6 well plates. And the same number of HMC3 cells were disseminated into the insert (pore size, 0.4 μm), and co-cultured with U87MG *delta EGFR* cells in 6 well plates. Five days after co-culture, U87MG *delta EGFR* cell numbers were counted and compared with mono-culture of U87MG *delta EGFR* cells.

RESULTS: The cell numbers of non-irradiated mono-culture and co-culture groups were 7.2E5 cells and

4.2E5 cells. While, the cell numbers of BNCT mono-culture and co-culture groups were 2.1E5 cells and 1.0E5 cells (Figure 1). Compared to the mono-culture, cell growth of U87MG *delta EGFR* cells in co-culture system was reduced to 25.3 % in non-irradiated control group and to 27.4 % in BNCT group. In this co-culture system, microglia did not affect glioma cell growth after BNCT. We will further examine the various ways of co-culture system using 3D co-culture, co-culture before and after BNCT etc.

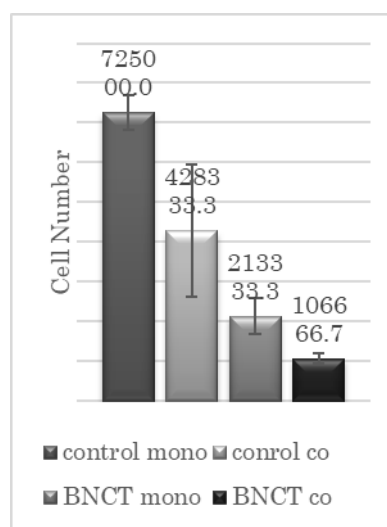


Figure 1. Cell number of U87MG *delta EGFR* cells of non-irradiated control and BNCT groups in mono-culture or co-culture with HMC3 cells 5 days after BNCT.

REFERENCES:

- [1] N. Kondo *et al.*, Cancers, 2020, 12, 3040; doi:10.3390/cancers12103040
- [2] N. Kondo *et al.* Radiat. Environ. Biophys. 55 (2016) 89–94.

CO7-13 Solubilization of All-*Trans*-Retinoic Acid as Macrophage Polarizer by β -1,3-Glucan

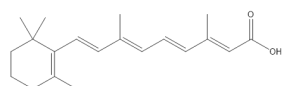
N. Yasukawa¹, K. Bando¹, A. Tabata¹, H. Miyao¹, R. Kawasaki², Y. Sanada³, N. Kondo³, and T. Nagasaki¹

¹Department of Applied Chemistry and Bioengineering, Graduate School of Engineering, Osaka City University

²Program of Applied Chemistry, Graduate School of Advanced Science and Technology, Hiroshima University

³Institute for Integrated Radiation and Nuclear Science, Kyoto University

INTRODUCTION: Boron neutron capture therapy (BNCT) is a potent cancer therapy that exhibits cancer selectivity at the cellular level and has few side effects. However, in many cases, it will not be completely cured due to recurrence/metastasis (distant dissemination). One of the reasons is the involvement of tumor-associated macrophages (TAM) present in the stroma of tumor tissue. It has become a major problem that TAM not only promotes neo-vascularization and tumor regrowth/metastasis, but also enhances antitumor immunity [1]. Since TAM exhibit an M2 phenotype that promotes tumor progression, conversion of M2 TAM toward a tumoricidal M1 phenotype is a promising anti-cancer therapy. Recently Takeya *et al.* reported that natural compounds possessing an inhibitory effect for signal transducer and activator of transcription-3 (STAT3) suppressed M2 polarization [2]. Although all-*trans*-retinoic acid (ATRA) is one of well-known and strong STAT3 inhibitor [3], handling of ATRA is not easy owing to its poor water-solubility. Herein, water-solubilization of ATRA by using β -1,3-glucan is attempted in order to efficiently and selectively deliver the M2→M1 polarizer to M2 macrophages by targeting dectin-1 expressed in M2 macrophages.



Scheme. Chemical structure of ATRA

EXPERIMENTS: β -1,3-glucan was used after purification from black yeast (*Aureobasidium pullulans*). For the preparation of nanogels with excellent blood stability and high efficiency of dectin-1 mediated endocytosis, the molecular weight of β -1,3-glucan was reduced by sonication. The complex nanogel of ATRA with β -1,3-glucan was prepared *via* a dialysis technique based on a supramolecular strategy. The hydrodynamic diameter of the complex was measured using a Zetasizer Nano ZS (Malvern, UK). After lyophilization of aqueous ATRA/ β -1,3-glucan complex solution, the residue was re-dissolved in DMSO. The concentration of ATRA was estimated by molar extinction coefficient of ATRA in DMSO (ϵ , 41500). In rectal cancer transplantation model, pharmacokinetics of ATRA/ β -1,3-glucan complex nanogel was evaluated with co-complexation of Indocyanine Green using *in vivo* imaging system VISQUE[®] InVivo Smart-LF (Vieworks, Korea).

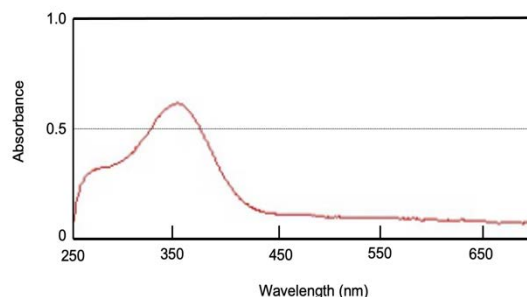


Fig. 1. UV-vis absorption spectrum of ATRA/ β -1,3-glucan nanogel in DMSO.

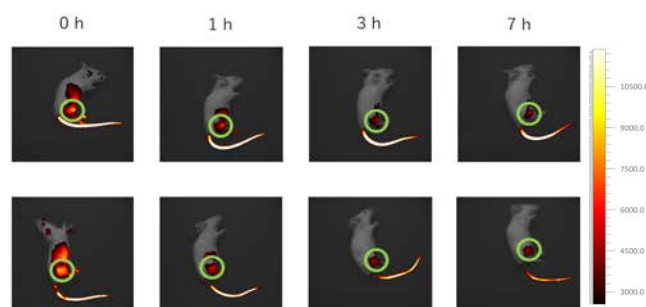


Fig. 2. Pharmacokinetics of ATRA/ β -1,3-glucan nanogel in tumor-bearing mouse. Tumor tissue is marked with circle.

RESULTS: According with Fig. 1, water-solubilization of hydrophobic ATRA by the complexation with β -1,3-glucan was revealed. The concentration of ATRA in aqueous solution was estimated as 1.10 mM. Dynamic scattering measurement revealed ATRA/ β -1,3-glucan complex diameter of 80 nm and a size corresponding to the tumor targeting EPR effect [4].

Tumor tissue accumulation of ATRA/ β -1,3-glucan complex nanogel was immediately confirmed using a mouse rectal cancer transplantation model in a few hours (Fig. 2).

In conclusion, we succeed to prepare the water-soluble ATRA/ β -1,3-glucan nanogel. We will evaluate the effect of the administrating of the macrophage polarizer on the tumor growth inhibitory effect and examine the BNCT sensitizing effect by controlling the polarity of TAM in near future.

REFERENCES:

- [1] M. Takeya and Y. Komohara, *Pathol. Int.*, **66** (2016) 491-505.
- [2] M. Takeya *et al.*, *Can. Sci.*, **102** (2010) 206-211.
- [3] Q. Zhou *et al.*, *Can. Immunol. Res.*, **5** (2017) 547-559.
- [4] H. Maeda *et al.*, *J. Contr. Rel.*, **65** (2000) 271-284.

CO7-14 Carborane bearing pullulan nanogel/boron oxide nanoparticle hybrid for BNCT

R. Kawasaki¹, H. Hirano¹, K. Yamana¹, Y. Sanada², K. Bando³, A. Tabata³, K. Yoshikawa³, H. Azuma³, N. Tarutani¹, K. Katagiri¹, M. Suzuki², T. Takata², Y. Sakurai², K. Tanaka², S. Sawada⁴, Y. Sasaki⁴, K. Akiyoshi⁴, T. Nagasaki³, A. Ikeda¹

¹Program of Applied Chemistry, Graduate School of Advanced Science and Engineering, Hiroshima University

²Institute for Integrated Radiation and Nuclear Science, Kyoto University

³Department of Applied Chemistry and Bioengineering, Graduate School of Engineering, Osaka City University

⁴Department of Polymer Chemistry, Graduate School of Engineering, Kyoto University

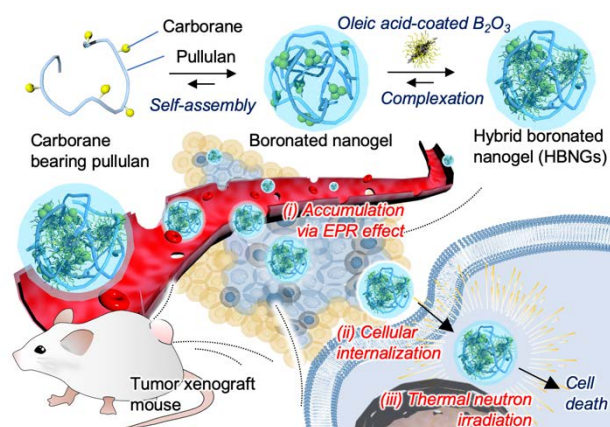


Fig. 1. Schematic illustration of this study. BNCT with hybrid nanogel for cancer therapy.

INTRODUCTION: With noninvasiveness and efficient damage inducibility for genomic DNA, boron neutron capture therapy (BNCT) is one of the most promising modalities for cancer treatment. Cell destruction in BNCT is achieved by energy from the particles which was generated by the nuclear reaction between ^{10}B and low-energy thermal and/or epithermal neutron, that is boron neutron capture reaction, and effective ranges of the energy from these particles are corresponding to the size of a cell ($<10\ \mu\text{m}$), suggesting that accumulation of boron agents toward cancer cells with high specificity is significant to maximize benefits from BNCT. Currently, L-boronophenylalanine (L-BPA) and disodium mercaptoundecahydro-*closo*-dodecaborate (BSH) are clinically available as boron agents for BNCT, however these two types of boron agents have several issues in delivery including short circulation time in blood stream, tumor selectivity, and the leaky feature from cells. For these points of views, delivery platforms for boron agents are urgent requests to expand applicability of BNCT.

In this study, we demonstrated efficient tumor growth suppression using organic-inorganic hybrid nanogels (HBNGs) comprising of carborane bearing pullulan nanogels and hydrophobized boron oxide nanoparticles (Figure 1). Our HBNGs technology is based on a hybrid combination of boron oxide nanoparticles for boron contents with a boronated nanogel carrier. Previously, we showed facile tumor-targeted boron agent delivery based on EPR effect using carborane bearing pullulan nanogel with high boron contents in each nanoparticle. In addition, the nanogels uptaken by cancer cells are accumulated in nuclear membrane, which is advantageous to induce efficient DNA double strand break toward cancer cells.^[1,2] These advantages of carborane bearing pullulan nanogel in BNCT encouraged us to develop the HBNGs systems by coupling carborane bearing pullulan nanogel with hydrophobized boron oxide *via* supramolecular chemistry approach.^[3,4] In the present study, we demonstrated applicability of HBNGs as a boron agent for BNCT *in vitro* and *in vivo*. We then evaluated therapeutic efficacy of BNCT against tumor xenograft mice.

RESULTS AND DISCUSSION: Carborane bearing pullulan nanogels were prepared as previously reported.^[1] To obtain hybrid nanoparticle (HBNGs), the hydrophobized boron oxide nanoparticles were injected to dispersion of nanogels and the boron oxide nanoparticles were encapsulated mainly *via* hydrophobic interaction. Dynamic light scattering measurement revealed that the hydrodynamic diameter of HBNGs is to be 180 nm, which is corresponding to the size for enhanced permeation and retention effect (EPR effect) that is known as passive tumor targeting effect. Transmission electron microscopy revealed that the structures derived from boron oxide nanoparticles agglomerated within nanogels. This feature is ideal to achieve efficient boron neutron capture reaction.

We demonstrated therapeutic efficacy of BNCT *in vitro* using current system. In this study, we employed L-BPA/fructose complex, which is used in clinical, as a comparison. As a result, both systems could induce cell death toward murine colon carcinoma cell line (Colon26) boron concentration dependently. Moreover, IC_{50} value using HBNGs were 6 times lower than that using L-BPA/fructose complex, suggesting our hybrid system are potentially available as a boron agent for BNCT.

In conclusion, our system based on hybrid nanoparticles enabled to induce cell death toward cancer cell lines by irradiating thermal neutron with high efficiency. We will address therapeutic efficacy *in vivo* in the near future.

REFERENCES:

- [1] R. Kawasaki, Y. Sasaki, K. Akiyoshi, *Biochem. Biophys. Res. Commun.*, **483**, 147-153. (2016).
- [2] R. Kawasaki, Y. Sasaki, K. Akiyoshi, *Chem. Lett.*, **46**, 513-515, (2017).
- [3] R. Kawasaki, Y. Sasaki, K. Katagiri, S. Mukai, S. Sawada, K. Akiyoshi, *Angew. Chem. Int. Ed.*, **128**, 11377-11381. (2016).
- [4] R. Kawasaki, Y. Sasaki, T. Nishimura, K. Katagiri, K. Morita, Y. Sekine, S. Mukai, S. Sawada, K. Akiyoshi, *Adv. Healthcare Mater.*, **10**, 2001988, (2021).

CO7-15 Optimization of polymeric BPA for non-clinical studies and basic study on its analogues

T. Nomoto¹, K. Konarita¹, D. Tokura¹, K. Uehara², M. Ishimura², Y. Ishino², A. Sudani², Y. Sakurai³, M. Suzuki³, N. Nishiyama¹

¹Institute of Innovative Research, Tokyo Institute of Technology

²Stella Pharma Corporation

³Institute for Integrated Radiation and Nuclear Science, Kyoto University

INTRODUCTION: Boronophenylalanine (BPA) has been considered as the most powerful drug in boron neutron capture therapy (BNCT). Since BPA can be internalized into cells through LAT1 amino acid transporters expressed on many tumor cells, BPA can accumulate selectively within malignant tumors [1]. Although BPA has proven its promise in clinical studies, it was also reported that intracellular BPA is sometimes exchanged with extracellular amino acids including tyrosine due to the antiport mechanism of the amino acid transporter, leading to short retention time in a target tumor [2]. This unfavorable efflux of intracellular BPA is likely to compromise the ultimate therapeutic effect; thus, it is important to prolong the intracellular retention of BPA.

In this regard, we recently found that polymers possessing multiple hydroxy groups or sugar moieties can form complexes with BPA molecules through boronate esters in aqueous solution and that the polymer-BPA complexes are internalized into cultured tumor cells via LAT1-mediated endocytosis and entrapped mainly in endo-/lysosomes, resulting in prolonged retention in the intracellular compartment by preventing the unfavorable efflux [3, 4]. The polymer-BPA complexes can exhibit the prolonged tumor retention even in *in vivo* condition and significantly enhance the BNCT effects. In particular, poly(vinyl alcohol)-BPA (PVA-BPA) complexes showed the considerably strong BNCT effects in subcutaneous tumor models [3]. Considering the ease of manufacturability PVA-BPA, its clinical translation appears to be promising. Thus, in this study, we prepared PVA-BPA complexes with various compositions and compared their therapeutic effect to optimize the drug formulation for non-clinical studies.

EXPERIMENTS: BALB/c mice bearing subcutaneous CT26 tumors were prepared by subcutaneous injection of the cell suspension. PVA-BPA complexes with various compositions were prepared in aqueous solutions, and they were intravenously injected to the mice at a dose of 10 mg BPA/mouse. As a control, conventional sorbitol-BPA complexes were subcutaneously injected to the mice at a dose of 10 mg BPA/mouse. The thermal neutrons were irradiated to the tumor using KUR 3 h after injection. The tumor volume (V) was calculated using the following equation:

$$V = 1/2 \times a \times b^2$$

where a and b denote major and minor axes of a tumor, respectively.

RESULTS: As shown in Fig. 1, all the PVA-BPA complexes exhibited the enhanced BNCT effects even compared with the conventional sorbitol-BPA that was subcutaneously injected. We are now investigating possible side effects of these complexes and will find out the optimal composition for non-clinical studies.

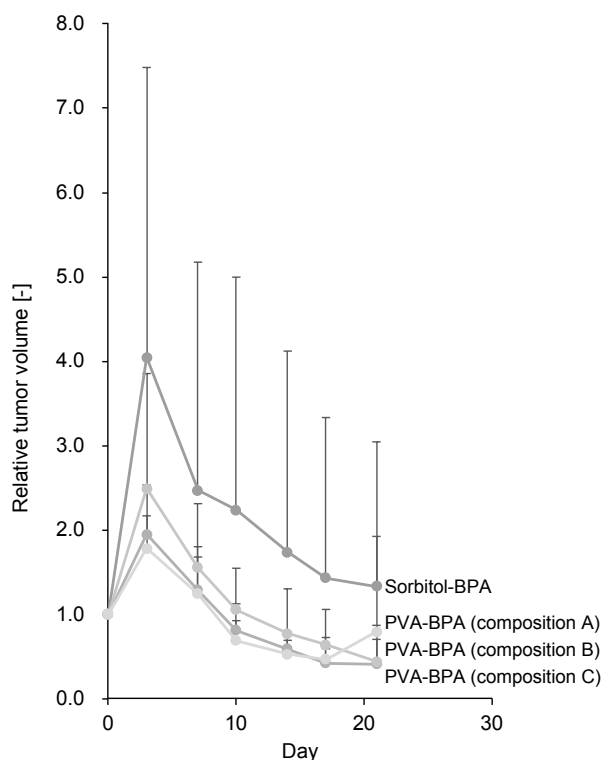


Fig. 1. Antitumor efficacy of sorbitol-BPA and PVA-BPA complexes at various compositions to subcutaneous CT26 tumor models.

REFERENCES:

- [1] P. Wongthai *et al.*, *Cancer Science*, **106** (2015) 279-286.
- [2] A. Wittig, *et al.*, *Radiat. Res.*, **153** (2000) 173-180.
- [3] T. Nomoto *et al.*, *Sci. Adv.*, **6** (2020) eaaz1722.
- [4] T. Nomoto *et al.*, *J. Control. Release*, **332** (2021) 184-193.

CO7-16 Development of Boron-Folic Acid Complex and BNCT Antitumor Effect

K. Nishimura, F. Nakagawa, T. Morita¹, S. Okada¹, K. Miura¹, T. Takada,² M. Suzuki², H. Nakamura¹

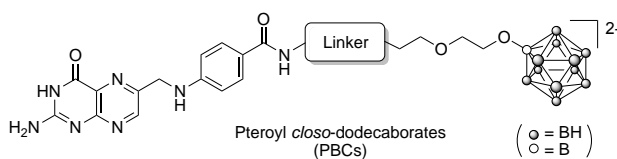
School of Life Science and Technology, Tokyo Institute of Technology

¹Laboratory for Chemistry and Life Science, Institute of Innovative Research, Tokyo Institute of Technology

²Institute for Integrated Radiation and Nuclear Science, Kyoto University

INTRODUCTION: Boron Neutron Capture Therapy (BNCT) is an expecting cancer therapy for the treatment of harsh and un-operatable malignant tumors. The efficiency of boron agent depends highly on tumor selectivity, sufficient amount of boron agent in tumor site, non-toxicity, tumour/normal tissues ratio (>3) and absorption of thermal neutrons by boron. In 2020, accelerator-based BNCT for head and neck cancer using L-BPA was approved by the Pharmaceuticals and Medical Devices Agency in Japan, making BNCT more accessible treatment [1]. L-BPA is known to actively accumulate into tumor cells through L-type amino acid transporter 1 (LAT-1). However, there are still many patients for whom L-BPA is not applicable, thus the development of novel boron carriers applicable to various cancers including L-BPA-negative tumors is required for further development for BNCT.

We focused on folate receptor (FR α). Folate is known to be taken into cells via the folate receptors, that are overexpressed on the surface of many cancer cells [2]. We have developed water-soluble pteroyl-*cis*-dodecaborate conjugates (PBCs) and examined their cell uptake using folate receptor (FR α) positive and negative cells. We found that PBCs showed significant cell uptake by FR α positive cells, especially U87MG glioblastoma cells. In addition, PBCs were found to be adequately low cytotoxic with IC₅₀ values in the range of 1~3 mM toward selected human cancer cells, low enough to use as BNCT boron agents [3].



Compound	Linker
PBC1	—
PBC2	(glutamine)
PBC3	(glycine)
PBC4	(alanine)

Fig. 1. Chemical structures of PBCs

In this study, we examined *in vivo* biodistribution of PBCs in colon 26 tumor-bearing mice.

EXPERIMENTS: Tumor-bearing BALB/c mice (female, 5-6 weeks old) were prepared by injecting subcutaneously (s.c.) a suspension (1.0×10^6 cells/ 50 μ l PBS/ mice) of CT26 cells. The mice were kept on a regular chow diet and water for a week. The tumor-bearing mice were injected *i.v.* with 200 μ l of PBC1, PBC3 or L-BPA-fructose complex solution dissolved in ultrapure (Milli-Q) water at the 1500 ppm [B]. At intervals of 1 hours for 6 h, the mice were lightly anesthetized and blood samples were collected from heart. The mice were then sacrificed by cervical dislocation and dissected. Liver, spleen, kidney, brain, and tumor were excised, washed with saline, and weighted. Each tissue was digested with 1 mL of HNO₃ at 90 °C for 3 h, and then the digested samples were diluted with distilled water. After filtering through a membrane filter (0.5 μ m ϕ , 13JP050AN, ADVANTEC, Japan), boron concentrations were measured by ICP-OES.

RESULTS: As shown in Fig. 2, boron concentrations of PBC 1 and PBC 3 in blood were lower than that of L-BPA. In contrast, accumulations of PBC 3 in liver and kidney were significantly higher compared with those of PBC-1 and L-BPA. A similar accumulation of PBC 1 to L-BPA was observed in tumor at 1 h after injection, however PBC 1 was rapidly cleared from blood after 3 h.

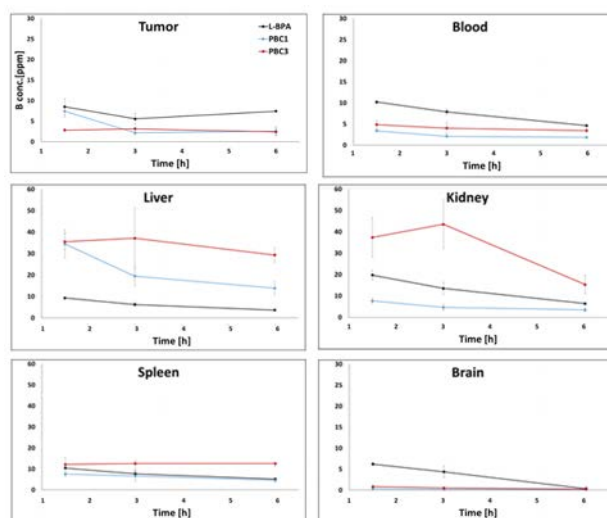


Fig. 2. Time-dependent boron distribution of PBC 1, PBC 2, and L-BPA in CT26 mouse colon tumor-bearing mice. Each boron agent was injected into the mice via the tail vein at a dose of 15 mg[B]/kg. Data are expressed as means \pm SD (n = 3).

REFERENCES:

- [1] H. Kanno *et al.*, The Oncologist, **26** (2021) e1250-e1255.
- [2] LE. Kelemen *et al.*, Int. J. Cancer, **119** (2006) 243-250.
- [3] F. Nakagawa *et al.*, Cells, **9** (2020) 1615.

CO7-17 Development of Gadolinium-Boron Complexes for MRI-Guided BNCT

S. Okada, Q. Ainaya¹, K. Nishimura¹, I. B. Sivaev², K. Miura, T. Takada³, M. Suzuki³, H. Nakamura

Laboratory for Chemistry and Life Science, Institute of Innovative Research, Tokyo Institute of Technology
¹School of Life Science and Technology, Tokyo Institute of Technology

²Russian Academy of Sciences, Russia

³Institute for Integrated Radiation and Nuclear Science, Kyoto University

INTRODUCTION: Boron Neutron Capture Therapy (BNCT) is a promising cancer treatment of harsh and un-operatable malignant tumors. An important condition for effective planning of BNCT treatment of patients is the control of the distribution of the boron-containing drug in the body and its accumulation in tumors. Since the ¹⁰B isotope is non-radioactive, non-invasive measurements in the body are a fairly difficult task and usually require either the introduction of radioactive labels for positron emission tomography (PET) [1].

We focused on the Gd-based magnetic resonance imaging (MRI), one of the most widely used methods of medical diagnostics. The ¹⁵⁷Gd isotope has the highest thermal neutron capture cross section of all stable nuclides in the periodic table, which exceeds the thermal neutron capture cross section of the ¹⁰B isotope by more than 60 times. The reaction of neutron capture by ¹⁵⁷Gd induces complex inner shell transitions that generate prompt γ -emission displacing an inner-core electron, which in turn results in internal-conversion electron emission, and finally in the Auger electron emission, together with soft X-ray and photon emission. Therefore, the synthesis of compounds containing both boron and gadolinium is of particular interest for the further development of neutron capture cancer therapy. We have developed maleimide-functionalized *closo*-dodecaborate (MID) albumin conjugates that demonstrated high and selective accumulation in tumor tissue with no toxicity in the absence of thermal neutrons, hence a promising boron delivery system [2].

In this study, we designed Gd-functionalized MID albumin conjugates aiming MRI-guided BNCT.

EXPERIMENTS: To a solution of bovine serum albumin (BSA) in 10 mM HEPES buffer (pH 7.4) was added Gd-complex ligand. The reaction solution was shaken at 800 rpm for 12 h at room temperature. The reaction solution was subjected to six cycles of ultracentrifugation with a 30 kDa filter to remove excess ligand before the addition of MID. The reaction solution was shaken for another 12 h at 37°C. The final BSA-Gd-MID conjugate was obtained after filtration of excess MID via ultracentrifugation. The concentration of ¹⁰B and Gd was estimated via ICP-OES. The conjugate solution was diluted with PBS for the biodistribution study.

CT26 tumor bearing mice (Balb/cCrSlc nu/nu female, 5–6 weeks old, 16–20 g) were injected via the tail vein

with 200 μ L of MID-BSA or Gd-MID-BSA (25 mg [¹⁰B]/kg). The whole bodies of mice were placed in an acrylic mouse holder and fixed on a 5-mm-thick thermo-plastic plate. At 12 h after administration, the right thighs of mice were irradiated with neutrons in the KUR nuclear reactor. BNCT effects were evaluated on the basis of the changes in tumor volume of the mice.

RESULTS: Previously, we demonstrated that thermal neutron irradiation was performed using the colon 26 tumor-bearing mice injected with MID-BSA in a dose range of 7.5–30 mg [¹⁰B]/kg and observed efficient tumor growth suppression 2 weeks after irradiation [3,4]. Therefore, we compared antitumor effects of Gd-MID-BSA with MID-BSA at a dose of 25 mg [¹⁰B]/kg. The results are shown in Fig. 1. Tumor of cold-control mice grew up very slowly, whereas the tumor growth of mice injected with MID-BSA and Gd-MID-BSA was suppressed. Notably, hot-control mice also suppressed tumor growth similar to the mice injected with MID-BSA and Gd-MID-BSA. These results indicate that complete tumor growth suppressions were observed even in the mice without ¹⁰B injection probably due to the significantly high neutron fluence. Therefore, it is considered necessary to revise the irradiation plan for the next irradiation experiment.

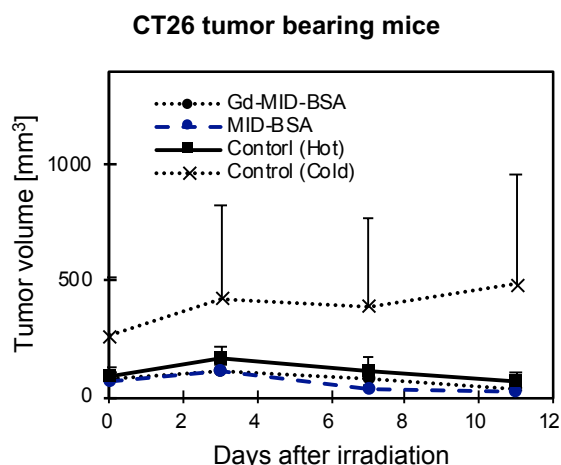


Fig. 1. Antitumor effect in colon 26 (CT26) tumor bearing mice. Gd-MID-BSA and MID-BSA were intravenously injected at a dose of 25 mg [¹⁰B]/kg via the tail vein, and the tumors were irradiated with thermal neutron (hot) for 12 min ($3.0\text{--}4.2 \times 10^{12}$ neutrons/cm²) 3 or 6 hours after injection or without irradiation (cold).

REFERENCES:

- [1] V. Tolmachev *et al.*, *Bioconjugate Chem.*, **10** (1999) 338–345.
- [2] K. Kawai *et al.*, *Mol. Pharm.*, **17** (2020) 3740–3747.
- [3] S. Kikuchi *et al.*, *J. Control. Release*, **237** (2016).
- [4] H. Nakamura *et al.*, *Pure Appl. Chem.*, **90** (2018) 745–753.

CO7-18 Water-soluble dodecaborate-containing pyrazolopyrimidine for BNCT

Y. Hattori, M. Ishimura, I. Nakase¹, M. Kirihata

Research Center of Boron Neutron Capture Therapy,
Osaka Metropolitan University

¹ Graduate School of Science, Osaka Metropolitan University

INTRODUCTION: Recently, boron neutron capture therapy (BNCT) has been recognized as an essential treatment for refractory cancers such as glioma, head and neck cancer, and melanoma. Although many types of boron compounds, including amino acids, peptides, nucleic acids, anticancer drugs, and liposomes have been reported as boron delivery agents for BNCT, only two compounds, *p*-borono-L-phenylalanine (L-BPA, Boropharan-10B, Fig. 1-1) and disodium mercapto-*closo*-undecahydro-dodecaborate (2) ($[B_{12}H_{11}SH]^{2-}2Na^+$, BSH, Fig. 1-2), are clinically used in the treatment of cancer with BNCT. In light of these factors, novel useful boron-pharmaceuticals for BNCT are in high demand.

The translocator protein (TSPO) is an 18 kDa protein composed of at least three subunits. TSPO is localized in the mitochondria and plays important roles in several biological processes, such as cholesterol metabolism, proliferation, and apoptosis. Because TSPO is highly expressed in several disease states, including Alzheimer's disease, Huntington's disease, and cancer, it is a potentially useful drug target. TSPO overexpression has been reported in several cancers, including breast, colorectal, prostate, and ovarian cancer and glioma, and appears to be an indicator of poor prognosis in patients with lymph-node negative breast cancer. Therefore, TSPO ligands labeled with positron emission atoms, such as DPA-713 (Fig. 1-3a), and DPA-714 (Fig. 1-3b), have been reported as potential cancer imaging agents. In particular, pyrazolopyrimidine derivatives DPA-713 and DPA-714 show the high specific affinity for

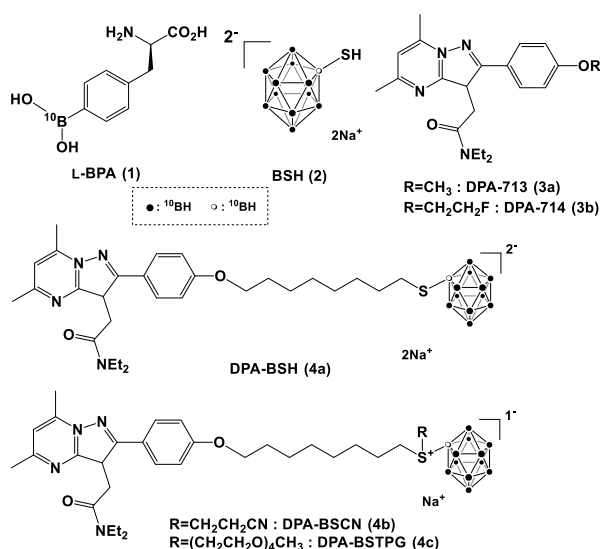


Fig. 1. Boron compounds and TSPO targeted compounds.

TSPO. Arylpyrazolo[1,5- α]pyrimidine acetamide moiety of DPA-714 seem to be important role on TSPO binding affinity, alkyl ether derivatives at the 4'-position of the phenyl ring are reported.

In this study, three novel dodecaborate-containing pyrazolopyrimidine TSPO ligands were developed (Fig. 1): DPA-BSH (4a), DPA-BSCN (4b), DPA-BSTPG (4c). Here, we present the biological evaluation of novel boron compounds 4a-c as boron carrier for BNCT.

RESULTS and Discussion: To evaluate the potential of the dodecaborate-containing DPA derivatives as BNCT agents, we used two breast cancer cell lines, MCF-7 and MDA-MB-231 which exhibit low and high TSPO expression, respectively. We applied equal dosages of boron to the tumor cells *via* treatment with the novel compounds and L-BPA (6.0 Bpm, 0.6mM) as well as a high dosage of L-BPA (20 Bppm, 2.0 mM), and then measured the intracellular boron concentrations by ICP-OES.

As shown in Fig. 2, all three novel dodecaborate-containing DPA derivatives successfully delivered boron to tumor cells, and MDA-MB-231 cells with overexpressed TSPO consistently took up more novel boron compounds than MCF-7 cells. Although DPA-BSH (4a) and DPA-BSCN (4b) delivered moderate levels of boron, DPA-BSTPG (4c) delivered a notably higher level than L-BPA in both MDA-MB-231 and MCF-7 cells. Notably, the MDA-MB-231 intracellular boron concentration achieved by using DPA-BSTPG (4c) was 5-6 times greater than that achieved by using a more highly concentrated dose of L-BPA (DPA-BSTPG: 0.05 mM, BPA: 2.0 mM).

In conclusion, we synthesized novel dodecaborate-containing pyrazolopyrimidine derivatives (Fig. 1-4a-c). The result of the *in vitro* evaluation suggest that these compounds are useful boron carriers targeting TSPO over-expressing cells. DPA-BSTPG (4c), in particular, delivers a large amount of boron to breast cancer cells. The *in vivo* evaluation of DPA-BSTPG is ongoing, and the results will be reported in the near future.

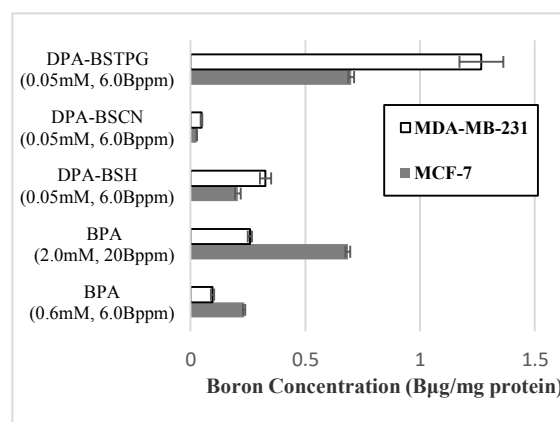


Fig. 2 Cellular uptake of boron in breast cancer cells.

CO7-19 Attempts to sensitize tumor cells by exploiting the tumor microenvironment

Y. Sanada, T. Takata, Y. Sakurai, H. Tanaka and T. Watanabe

Institute for Integrated Radiation and Nuclear Science, Kyoto University

INTRODUCTION: Hypoxia and glucose deprivation have been suggested to play important roles in resistance to radiation [1]. Attempts to sensitize tumor cells by exploiting the tumor microenvironment have been studied. A major mediator of the cellular hypoxic response, hypoxia inducible factor 1 (HIF-1), is a potential target for cancer therapy, because it transcriptionally regulates a number of genes, including those involved in glucose metabolism, angiogenesis and resistance to chemotherapy and radiation therapy [2]. We previously reported that the disruption of Hif-1 α enhanced the sensitivity of murine squamous cell carcinoma (SCC VII) cells to gamma-ray [3]. We have investigated whether the disruption of Hif-1 α affects the sensitivity of SCC VII cells to the boron neutron capture reaction (BNCR) with analysis of early DNA damage response, analysis of the intracellular ^{10}B levels, analysis of SLC7A5 expression profiles, and clonogenic assays. Moreover, we examined whether the disruption of Hif-1 α affects the tumor growth after BNCT.

EXPERIMENTS: Seven-week-old female C3H/He mice were used in the present study. SCC VII and SCC VII Hif-1 α -knockout ($\Delta\text{Hif-1}\alpha$) cells were subcutaneously inoculated into the right hind legs of mice. BPA was subcutaneously administered into nuchal sites in tumor bearing-mice. After 60 min, mice received neutron irradiation for 12 min at 5 MW in the Kyoto University Research Reactor (KUR). Tumor volume and body weight was measured every three days.

RESULTS: In experiments using culture cells and tumor-bearing mice, we found that the survival of SCC VII Hif-1 α -knockout ($\Delta\text{Hif-1}\alpha$) cells was lower than that of SCC VII cells. Hypoxia-treated SCC VII cells exhibited the decreased intracellular concentrations of BPA and the down-regulation of the SLC7A5 protein levels. BPA uptake and the SLC7A5 protein were not decreased in hypoxia-treated $\Delta\text{Hif-1}\alpha$ cells, the survival of which was lower than that of SCC VII cells. More DNA damage was induced in SCC VII $\Delta\text{Hif-1}\alpha$ cells than in SCC VII cells. It was found that the disruption of the Hif-1 α gene enhanced the direct cell-killing effects of BNCT with BPA [4].

Next, tumor growth in the right leg was measured in BNCT-treated and untreated (control) mice. In control groups, tumors continued to grow, regardless of the presence of Hif-1 α gene. Tumor volume was smaller in SCC VII tumor-bearing mice treated with BPA-BNCT in

than in control animals. Furthermore, in SCC VII $\Delta\text{Hif-1}\alpha$ tumor-bearing mice, the tumor volume was decreased and became undetectable at day 6 after BPA-BNCT.

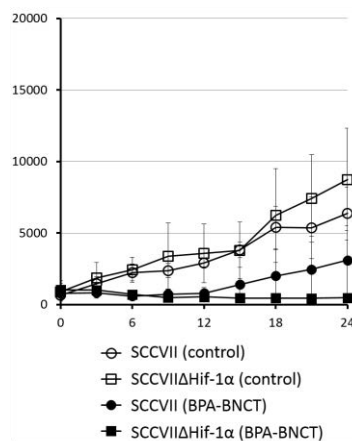


Fig. 1. Mean tumor volume as a function of time after BPA-BNCT. Tumor-bearing animals were administered BPA, followed by neutron irradiation (at day 0). Four to six tumors in each group were used.

REFERENCES:

- [1] S. Masunaga *et al.*, *Int. J. Rad. Biol.* 92 (2016) 187–194.
- [2] Z. Luo *et al.*, *Neuropharmacology.* 89 (2015) 168–174.
- [3] Y. Sanada *et al.*, *Int. J. Rad. Biol.* 94 (2018) 88–96.
- [4] Y. Sanada *et al.*, *Int. J. Rad. Biol.* 97 (2021) 1441–1449.

CO7-20 Establishment of a method for determining position in alpha autoradiography using CR39

Kei NAKAI

Department of Radiation Oncology, faculty of Medicine,
University of Tsukuba.

INTRODUCTION: The biodistribution of boron compounds in the microenvironment is an important factor in the success of boron neutron capture therapy, but an appropriate and simple method for visualizing it has not yet been established. In general, intracellular concentrations are measured by wet ashing of cell samples collected from suspended cell suspensions by plasma luminescence analysis, and the same is true for tissue and blood samples. Therefore, we conducted experiments to establish a measurement system using alpha autoradiography, which requires neutron irradiation but for which materials are relatively easy to obtain.

EXPERIMENTS: CR39 was marked and cut as shown in Fig. 1. A silicon cap was made to fit the 96 wells and sealed to prevent scattering of the radioactive materials during irradiation. Poly-lysine treatment was performed when cells were attached.



Marking was done from the back side of the detection surface and adjusted for laser power that did not penetrate the CR39. The cut CR39 was designed to fit the bottom of the 96-well well and to be easily removed.

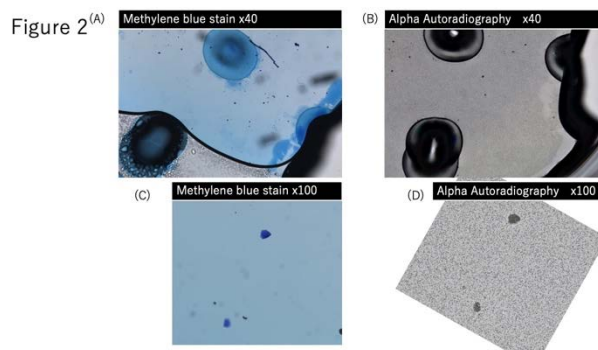
Silicon caps were made by pouring DOWSIL™ 184 into appropriate molds and solidifying at 80°C for 2 hours.

Irradiation was performed at KUR, and this sample was irradiated for 15 minutes using rails.

After irradiation, samples with cellular components were washed, ethanol-fixed, and stored at room temperature. For analysis, as shown in the center of Figure 1, methylene blue staining was performed to obtain microscopic images, which were then etched, and the alpha-ray pits were reapplied to the microscopic images. Etching was performed in a 6N sodium hydroxide solution at 60°C for 60min.

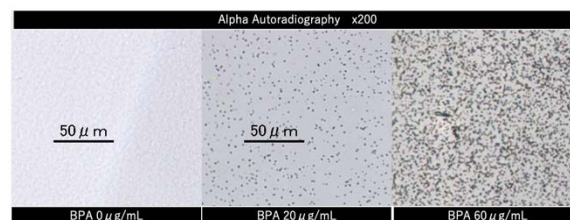
RESULTS: In this case, we analyzed the determination of their location and the acquisition of calibration images. As shown in Fig. 2., the laser-marked points did not change much in size before and after etching, and their relative positions were maintained. Using a sample with cells on it, it was possible to match the positional information before and after etching based on the markers and the

shape of the particles adhering to the surface. It was considered possible to determine the position of the marker alone if the enlarged images were fused together.



(A) and (C) are methylene blue stain image.
(B) and (D) are etched pit image by light microscope.
laser markers were useful for position matching.
alpha particle pathway made pits on image (C) and (D).

Figure 3



alpha pit on the CR39 with Boronophenylalanine solution. boron concentration were 0µg/mL (left), 20µg/mL (middle), 60µg/mL(Right).

Fig. 3. visualizes the alpha-ray range of the boron 10-thermal neutron reaction between the liquid surface (BPA solution) and the solid (CR39) when a solution of boronophenylalanine is placed on CR39. The density of alpha rays increases with concentration.

Discussion: If the staining target is a cell, it is expected that by washing this area thoroughly before etching, more alpha rays will be seen in the cell-attached area on CR39 than in the surrounding liquid phase, if enough boron is incorporated into the area. No other experimental system is capable of irradiating cells in a living state, and it would be possible to evaluate this system for radiobiological studies in terms of visualization of alpha radiation rather than boron. Also, perhaps staining the pits could have applications in absorbance spectrometry and other applications. Although neutron irradiation is required, it may help in a rapid measurement system for boron concentration.

REFERENCES:

- [1] H. Tanaka *et al.*, Applied Radiation and Isotopes. 153-156, **88** (2014).
- [2] H. Yabagie *et al.*, Applied Radiation and Isotopes. 639-646, **61** (2004).

CO7-21 Screening of Boron / Gadolinium Compounds for BNCT of Malignant Brain Tumors, 2021

M. Takagaki, N, Kondoh¹, M. Suzuki¹, RR. Zairov², M, Neikter³, S. Flieger⁴, B Daniel⁴, NS, Hosman⁵

RCNP, Osaka Univ,

¹IIRNS, Kyoto Univ,

²Russian Academy of Science,

³SAKURA exchange program at j-PARC Tokyo

⁴Loyola Univ,

⁵Northern Illinois Univ,

Malignant brain tumor cells infiltrate very quickly, and the tumor cells have already spread widely already at the time of diagnosis, and treatment needs to be performed promptly. However, from our clinical experiences so far, the microdistribution of tumor cells is not visualized at the time of treatment, another words the brain is full of tumor cells. Although it has been excluded from the indication for BNCT in many cases where macroselectivity cannot be clearly expected on MRI images, it still shows recurrence in many indications. Perhaps malignant brain tumor cells might be free to move back and forth in the brain in a variety of ways and forms. In other words, it is no exaggeration to say that the target of malignant brain tumors is not being visible.

The Rocher's theory that cell-selective treatment is possible in BNCT of malignant brain tumors may be achievable microscopically, mainly by devising biological carriers. However, since the physical depth of thermal neutrons is only within 6 cm or less from the brain surface even with intra-operative BNCT and about 4 cm with non-invasive BNCT, the Rocher's theory does not hold in macroselectivity [1]. Therefore, we have conducted therapeutic experiments while improving the micro/macro distribution of thermal neutrons by inserting voids into the brain parenchyma with craniotomy and replacing body fluids with heavy water, but distant recurrence in the brain after BNCT has not been controlled.

Our therapeutic strategies of BNCT for malignant brain tumors are (1) to suppress the infiltration of malignant brain tumor cells, and (2) to investigate the possibility of concomitant use of gadolinium capture reaction. The following is a report on the progress of the experiment last year.

(1) Becker, Flieger and Hosman have already synthesized boron compounds, B1 and B2, and their derivatives using an infiltration inhibitor as a ligand, and confirmed a high BNCT effect in in-vitro experiments in our screening tests. The absorbed dose yielding the D₃₇ (dose used to inhibit 63% colony formation) values were 0.27 Gy for B-1, 0.32

Gy for B-2, 0.82 Gy for BPA and 1.55 Gy for boron-free control. The relative killing effect of R-1 to BPA is 0.82/0.27=3.0, and that of R-2 is 0.82/0.32=2.6. The survival fraction of B-1 and B-2 in a pre-incubation boron concentration at 0.143ppm ¹⁰B and 0.101ppm ¹⁰B respectively were similar, and these result suggest that B-1 and B-2 are actively accumulated and/or attached to the SCCVII cells. In the next, it is necessary to evaluate infiltration suppression and BNCT effect by in-vivo alpha track experiments. Suppression of infiltration of malignant brain tumor cell should be innovative in itself. If suppress of the infiltration of malignant brain tumor cells can be attained by this strategy, it may also improve the clinical malignancy that correlates with invasiveness, so that in that future the indications of another adjuvant treatment options might be able to be reconsidered.

(2) The possibility of gadolinium neutron capture therapy is controversial, but the total range of heavy-charged particles generated by the ¹⁰B (n, α) ⁷Li reaction is local close to the cell diameter, and the total dose distribution is probably too selective. In GdNCT, it is expected that the dose distribution will be improved by higher total kinetic energy of gamma rays, electron beams, Auger electrons, etc., by a single neutron capture reaction of ¹⁶⁷Gd (n, γ) ¹⁶⁸Gd. Zairov and Neikter have prepared gadolinium inclusion nanoparticles and repeated GdNCT experiments in vitro, and confirmed their low toxicity, tumor retention and concentration-dependent GdNCT effect. The figure shows survival fraction of their Gd nano compounds, R1 and R2. The absorbed dose yielding the D₃₇ (dose used to inhibit 63% colony formation) values were 0.55 Gy for B1, 0.56 Gy for B2, and 1.50 Gy for control. We will continue to investigate the possibility of GdNCT.

REFERENCES:

[1] NS. Hosmane, *et al.*, *J Boron and Gadolinium Neutron Capture Therapy for Cancer Treatment*. (ed. NS. Hosmane) World Scientific Publishing, 2012.

CO7-22 The effects of radioactivation of animals on the environment for the BNCT to companion animals.

Y. Wada^{1,2}, T. Takata³ and M. Suzuki².

¹ Veterinary Medical Center, Osaka Prefecture University

²Particle Radiation Oncology Research Center, Institute for Integrated Radiation and Nuclear Science, Kyoto University

³Particle Radiation Medical Physics, Institute for Integrated Radiation and Nuclear Science, Kyoto University

Introduction

In the veterinary medicine field, a few studies have reported the use of BNCT for treatment¹⁾. Because small animals such as dogs and cats have smaller bodies, neutrons can be delivered to deeper portion into organs than that in humans. This is why, many tumors developed in companion animals can be candidate of BNCT. BNCT is expected to expand its application in veterinary medicine in the future.

However, radioactivation of several atoms in the body are generated in the body following thermal or epithermal neutron beams^{2,3)}. Therefore, animals and their excretions after BNCT include radioactive materials, and there are concerns about the effects on owners and the environment around them. Although there are some reports on radio activation of experimental animals after thermal or epithermal neutron beams, no reports on the radioactivation of urine and feces have been reported. In this study, we evaluated the changes in surface doses from rats and their urine and feces activated by neutron irradiation over time.

Experiments

After the neutron irradiation, NaI (TI) scintillation detector (TCS-1172, Hitachi, Tokyo) was used for dose rate measurements at the surface of the abdomen and at ambient 30cm away from rat within 8 days.

Radioactivation of the body was analyzed using an HP-Ge detector. In order to determine the radionuclide, it was necessary to obtain the detection efficiencies of the HP-Ge detector.

Radioactivity in the urine (0.5ml) and stool (0.1g) of irradiated rat was measured with Geiger Mueller counter.

Result

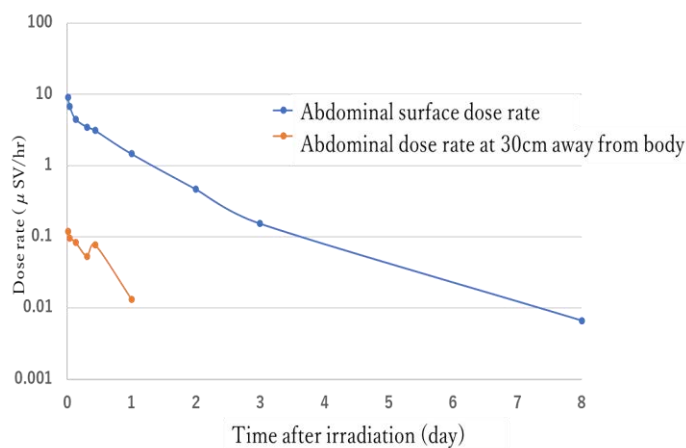
The dose rate on the abdominal surface and the that at 30 cm away from the abdominal surface are shown in Fig1. The surface dose rate decreased to the same level as the background with-

in about 8 days after irradiation, and the 30 cm dose rate decreased to the same level as the background at 1 day after irradiation.

The induced radionuclides were ²⁴Na, ³⁸Cl, ⁵⁶Mn, and ⁴²K from rat after the neutron irradiation.

The half-life of radioactivity in the urine and feces of radioactivated rats was about 14 days. The results suggested that the radionuclide in the urine and stools from the irradiated rats were ³²P.

Fig1. Abdominal surface dose rate and abdominal dose rate at 30cm away from body after irradiation.



Reference

- [1] A.E.Schwint *et al.*, Biology (Basel), **327** (2020).
- [2] S. Nakamura *et al.*, Proc. Jpn. Acad., Ser. B., **93** 821-831 (2017).
- [3] N.Protti *et al.*, Health Phys., **107** 534-541 (2014).

CO7-23 In Vivo Efficacy of BPA-Ionic Liquid as a Novel Compound for BNCT

M. Shirakawa^{1,2}, T. Sakai¹, R. Terada¹, Y. Sato¹, N. Kamegawa³, R. Takeuchi³, H. Hori³, K. Nakai², A. Zaboronok², F. Yoshida², T. Tsurubuchi², T. Sakae², A. Matsumura², T. Takata⁴, N. Kondo⁴, Y. Sakurai⁴, M. Suzuki⁴

¹Department of Pharmaceutical Sciences, Fukuyama University

²Department of Neurosurgery, Faculty of Medicine, University of Tsukuba

³Morita Pharmaceutical Ind., Ltd.

⁴Institute for Integrated Radiation and Nuclear Science, Kyoto University

INTRODUCTION: In 2020, Steboronine® received manufacturing and marketing approval as the world's first BNCT drug. Its medicinal ingredient, p-boronophenylalanine (BPA), shows excellent antitumor effects after thermal neutron irradiation, but is known to require large doses to achieve clinical efficacy because of its low solubility. Therefore, we have been investigating the use of ionic liquids (ILs) as new solvents for BPA. We have already reported that ionic liquids, consisting of meglumine and serine, exhibit high BPA solubility and anti-tumor effects comparable to those of the BPA-fructose complex (BPA-Fru) [1]. Here we advance further and present *in vivo* antitumor effects of BPA-based IL (BPA-IL) after thermal neutron irradiation.

EXPERIMENTS:

1. Synthesis of BPA-IL

BPA-IL used in this study was synthesized using meglumine as a cation and BPA as an anion. Equimolar meglumine and BPA solutions were stirred at room temperature for 24 hours. After that, the water content of the IL was reduced to about 20 wt% by rotary evaporation at 80°C.

2. Anti-tumor effect using BPA-IL by BNCT

Female 3-week-old BALB/cA mice were purchased from CLEA Japan Inc. (Tokyo, Japan). The tumor model was prepared by grafting 2×10^6 of murine colon carcinoma cells (CT26) to the right thigh of mice (4 weeks old, weighing 16-20 g) to develop a tumor of 6-8 mm in diameter.

Ten days later, 40µL of BPA-IL was administrated via intravenous injection before irradiation was delivered at a dose of 24mg¹⁰B/kg. Similarly, 200µL of BPA-Fru was administered. Two hours after injection, thermal neutron irradiation was performed with a flux of $1.2-1.3 \times 10^9$ neutrons/cm²/s over 30 min. The tumor size was measured over time after the irradiation until day 30 and the volume was calculated using the previously applied formula [2].

On the last measurement day, a significant difference between tumor size in each group was calculated using independent t-test. The *p*-values representing significant

differences are marked with the following number of asterisks: *: *p*<0.05, **: *p*<0.01, ***: *p*<0.005, ****: *p*<0.001, and ns: no significant difference.

RESULTS:

As shown in Figure 1, BPA-IL significantly inhibited tumor growth compared to the control group despite the lower dose volume compared to BPA-Fru. As shown in Figure 2, no significant side effects (e.g., weight loss) were observed after using BPA-IL similar to BPA-Fru.

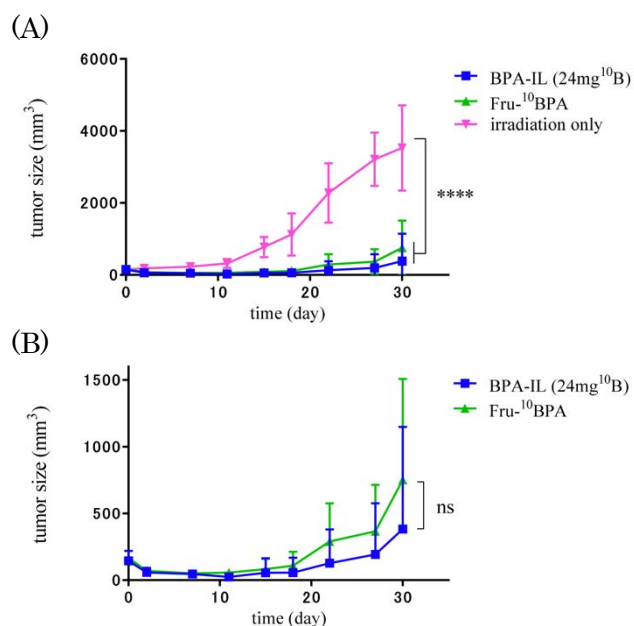


Fig.1) BPA-IL anti-tumor effect after BNCT (n=4). (A) BPA-IL and BPA-Fru vs. irradiation only: **** (B) BPA-IL vs. BPA-Fru: n.s.

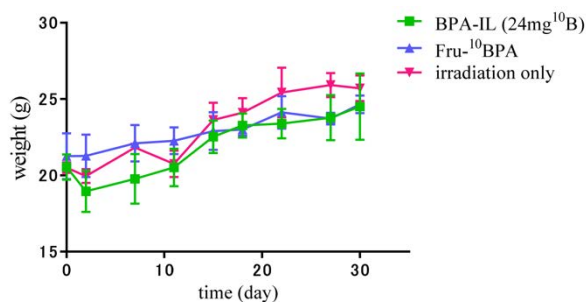


Fig.2) Mice body weight after BPA-IL injection with further neutron irradiation.

REFERENCES:

- [1] M. Shirakawa, *et al.*, Patent application 2020-067196 and patent publication 2021-161093.
- [2] M. Shirakawa, *et al.*, KURRI PROGRESS REPORT 2017, 69 (2018).

ACKNOWLEDGMENTS:

The authors would like to thank Thomas D. Mayers of the MECC, University of Tsukuba, for manuscript revision, for English language revision.

CO7-24 Preliminary study of the anti-tumor effect of BNCT using bubble liposome on the canine hemangiosarcoma model

M. Yanagawa¹, H Xuan^{2,3}, H. Yanagie^{4,5,6},
Y. Sakurai^{5,6}, S. Kageyama⁷, K. Maruyama⁷,
T. Takata⁸, Y. Sakurai⁸, H. Tanaka⁸, M. Suzuki⁸

¹Obihiro Univ of Agriculture and Veterinary Medicine,
²Dept of Nuclear Engineering & Management, School of Engineering, Univ of Tokyo, ³Dept of Bioengineering, School of Engineering, Univ of Tokyo, ⁴Institute of Engineering Innovation, School of Engineering, Univ of Tokyo, ⁵Cooperative Unit of Medicine & Engineering, Univ of Tokyo Hospital, ⁶Niigata Univ of Pharmacy & Applied Life Sciences, ⁷Faculty of Pharma-Science Teikyo Univ ⁸Kyoto Univ Institute for Integrated Radiation & Nuclear Science

INTRODUCTION: Canine hemangiosarcoma is a common malignant tumor derived from vascular endothelial cells. Hemangiosarcoma often occurs in the spleen and liver and has a poor prognosis despite surgery and chemotherapy in veterinary medicine [1,2].

Boron neutron capture therapy (BNCT) is a new treatment that utilizes the nuclear reaction between boron and neutrons. BNCT is an effective treatment for malignant tumors in humans and is expected to be applied to canine malignant tumors. In order to enhance the therapeutic effect of BNCT, it is important to increase the concentration of boron in the tumor.

Recently, drug delivery using a combination of ultrasound and microbubbles has been reported to be effective in increasing drug concentrations [3]. The interaction of microbubbles and US increases the local permeability of blood vessels, allowing the injected drug to move easily out of the vessel and increasing the drug concentration in the tissue. The combination of liposomal doxorubicin, microbubbles, and ultrasound has been reported to inhibit tumors in veterinary medicine. [4].

In this study, we prepared the BSH-encapsulated liposomes and perfluorocarbon microbubbles for selective cancer targeting, and applied the BNCT to the canine hemangiosarcoma model by intravenous injection.

EXPERIMENTS: Canine hemangiosarcoma cell line (Ju-A1) was cultured in RPMI1640 supplemented with 10% FBS, L-glutamate, penicillin and streptomycin. 8×10^5 cells subcutaneously injected into the right hindlimb of nude mice.

BSH-encapsulated liposomes and bubble liposomes were injected via the tail vein, and ultrasound was applied to the tumors.

In vivo evaluation was performed on Ju-A1 tumor-bearing mice irradiated at nuclear reactor facility of Kyoto University Institute for integrated Radiation & Nuclear Science. Antitumor effect was evaluated on the basis of the change in tumor growth.

RESULTS: Tumor growth was suppressed in the group with BSH-encapsulated liposomes, microbubbles, and ultrasound. Tumor growth was significantly suppressed in the Lipo-Bubble-US group than in the non-irradiated control group.

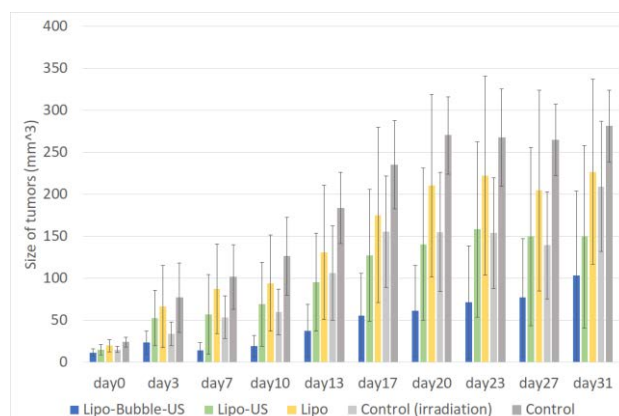


Figure 1. Tumor growth in the canine hemangiosarcoma model.

This preliminary result indicates that drug delivery systems using microbubbles and ultrasound have the potential to be applied to BNCT in canine hemangiosarcoma. In the future, we hope to apply this delivery system to clinical studies of BNCT in veterinary medicine.

REFERENCES:

- [1] JH Kim *et al.*, *Vet Sci.* (2015) 2(4):388-405.
- [2] DM Vail *et al.*, *Withrow & MacEwen's small animal Clinical Oncology 6th* (Elsevier, 2020).
- [3] I. Yokoe *et al.*, *Drug Deliv.* 2021;28(1):530-541.
- [4] I. Yokoe *et al.*, *Cancers* (2020)12(9):2423.

CO7-25 Development of boron-nutritional diagnostics in the plant using a neutron capture reaction

T. Kinouchi

*Institute for Integrated Radiation and Nuclear Science,
Kyoto University*

INTRODUCTION: We are working on elucidating the physiological function of boron in plants using a boron-10 neutron capture (BNC) reaction. This is one of the effective applications of nuclear power in addition to generating electricity. Although boron is an essential nutritional element for all plants, a deficiency or an excess of boron causes various growth disorders. For the numerous and frequent crop disorders arising from boron-toxicity world-wide, noteworthy solutions have yet to be proposed, as a boron analysis method with high resolution has not been well-developed. We still have a poor understanding of the physiological function of boron in plants. In order to collect multidimensional information on how much boron is localized in specific tissue/cell at various stages of plant-growth, *in situ* high-resolution visualization technique capable of detecting the localization of boron is being developed by applying α -autoradiography with solid-state nuclear tracking detector, CR-39[1,2]. We expect that this technique will contribute to the establishment of the nutritional diagnosis method for boron in plants.

Here we report the result from BNC analysis of the boron-distribution in a seed of special tomato cultivar, 'Micro-Tom'.

EXPERIMENTS: Plant materials and growth conditions> Seeds used in analysis were harvested from a dwarf tomato cultivar, 'Micro-Tom' (*Solanum lycopersicum* L). Micro-Tom was originally derived for home gardens as the dwarf cultivar, but is now used as a major material for various plant researches[3]. The original seeds, which were obtained from Inplanta Innovations Inc., seeded on the moderately moisturized vermiculite and cultivated at 23°C under a 16-h light/8-h dark cycle in a 60%-humidified growth chamber. A week later, their seedlings were transferred to the hydroponic media containing major nutrients (1 mM $\text{Ca}(\text{NO}_3)_2$, 0.5 mM KH_2PO_4 , 0.5 mM K_2SO_4 , 1 mM MgSO_4 , and 1.5 mM NH_4NO_3) and micronutrients (75 μM EDTA-Fe, 46 μM $\text{H}_3^{10}\text{BO}_3$, 9 μM MnSO_4 , 0.8 μM ZnSO_4 , 0.3 μM CuSO_4 , and 0.8 μM Na_2MoO_4) under the same condition.

In situ visualization of boron in a Micro-Tom seed using neutron capture radiography> Mounted slice (10- μm thickness) of Micro-Tom seeds onto CR-39 (20 mm \times 30 mm) was irradiated with epithermal neutron for 20 min by applying to the pneumatic tube in the graphite thermal

column (Tc-Pn) of Kyoto University Research Reactor (KUR). The irradiated CR-39 plate was etched in 6 M NaOH solution, and the resulting etch-pits were observed under an optical microscope.

RESULTS: Both Fig. 1(A) and 1(B) show cross sections prepared from the same Micro-Tom seed. Arrowed contents in Fig. 1(A) are the granular starch and embryo, respectively. On the other hand, Fig. 1(B) is a radiograph, which was generated by BNC reaction, and reveals distribution of boron in the cross section. A large number of etch-pits derived from boron-10 were imaged throughout the section as small black spots. Interestingly, the distribution amount of boron in the embryo was almost same as in the granular starch.

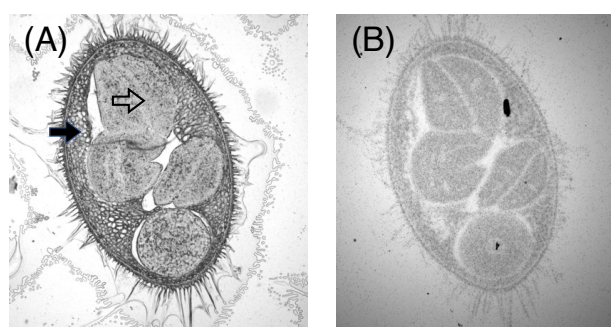


Fig.1 Detection of boron in the Micro-Tom seed using BNC reaction. (A): Optical microscopic images of the cross section of the seed. Black and white arrows indicate granular starch and embryo, respectively. (B): Radiograph.

REFERENCES:

- [1] M. Kobayashi and T. Kinouchi, KURRI Progress Report 2014, 129 (2015)
- [2] T. Kinouchi, KURNS Progress Report 2018, 121 (2019)
- [3] JW. Scott and BK. Harbaugh BK, Florida Agr. Expt. Sta. Circ. 370, 1-6 (1989)

CO7-26 An Evaluation of the Response of Tumor Cells to BNCT

Y. Tong¹, S. Imamichi^{1,2,3,4}, L. Chen^{1,3}, A. B. Myat¹, B. Saraswat¹, T. Onodera^{1,3}, Y. Sasaki^{1,3}, M. Ihara^{1,3}, Y. Sanada⁴, M. Suzuki⁴, S. Masunaga⁴ and M. Masutani^{1,2,3}
 1 Dept. of Molecular and Genomic Biomedicine, Center for Bioinformatics and Molecular Medicine, Nagasaki University Graduate School of Biomedical Sciences
 2 Division of Boron Neutron Capture Therapy, EPOC, National Cancer Center
 3 Central Radioisotope Division and Lab. of Collaborative Research, Division of Cell Signaling, National Cancer Center Research Institute
 4 Institute for Integrated Radiation and Nuclear Science, Kyoto University

INTRODUCTION: Nuclear reactions between thermal neutron and boron-10 generate alpha particle and lithium nuclei of high LET. The analysis of tumor cell response including cell death and various biological reactions as well as the effect on immune regulatory environment is important to consider clinical optimization of boron neutron capture therapy (BNCT). We used cancer cells and xenograft mouse models to analyze the responses to BNCT.

EXPERIMENTS:

Neutron irradiations at KUR reactor was operated at 1 MW in all experiments. We used gold foil activation analysis for the measurement of thermal neutron fluences and thermoluminescence dosimeter (TLD) for the measurement of the γ -ray doses including secondary γ -ray. Total physical dose calculation was carried out using the flux-to-dose conversion factor by the sum of the absorbed doses resulting from $^1\text{H}(n, \gamma)^2\text{D}$, $^{14}\text{N}(n, p)^{14}\text{C}$, and $^{10}\text{B}(n, \alpha)^7\text{Li}$ reactions, as previously described.

The cells were pretreated with ^{110}B -boronophenylalanine fructose complex (BPA) for 1.5-2.0 hrs. The cell survival of human squamous cell line SAS and murine melanoma cell line B16 cells was analyzed by colony formation assay, and cells were harvested at 6 hours and 24 hours with ISOGEN after BNCT. RNA and proteins were also isolated and RNA expression levels were examined using real-time PCR and protein levels were analyzed by ELISA.

For mouse experiment, we used mouse melanoma cell line B16 and B16F10mGM. The C57BL/6J male mice of 5 weeks old were transplanted with either B16 or B16F10mGM cells at bilateral legs 8 days before irradiation. The mice were placed on a board with the head facing out and the feet facing inward, with a circular cutout in the middle as the radiation port, and the left leg of the mouse was irradiated at the same time. Local irradiations to mouse hind legs were operated using ^6LiF containing thermal neutron shield. Mice were injected with BPA at 500 mg/kg bodyweight approximately 30 min or 60 min before irradiation.

RESULTS:

Table 1. Irradiated doses to cells (E-4 rail port) on August 24, 2021. (Cl: Closest, F: Farthest)

Irradiation time [min]	Position	Fluence [μcm^2]		[Gy]					
		Thermal neutron [μcm^2]	Epi-thermal neutron [μcm^2]	Thermal neutron [Gy]	Epi-thermal neutron [Gy]	Fast neutron [Gy]	Gamma-ray [Gy]	Physical Dose [Gy]	B-10** (1ppm)
10	Cl	1.04E+12	1.84E+11	0.14	0.02	0.10	0.12	0.38	0.08
	F	7.76E+11	1.38E+11	0.10	0.01	0.08	0.12	0.31	0.06
60	Cl	6.40E+12	1.10E+12	0.85	0.09	0.63	0.62	2.20	0.47
	F	5.10E+12	9.10E+11	0.68	0.07	0.51	0.62	1.90	0.38
2	Cl	2.30E+11	4.00E+10	0.03	0.00	0.02	0.02	0.08	0.02
4	Cl	4.40E+11	7.80E+10	0.06	0.01	0.04	0.04	0.15	0.03
6	Cl	6.00E+11	1.10E+11	0.08	0.01	0.06	0.09	0.24	0.05
8	Cl	8.60E+11	1.50E+11	0.11	0.01	0.09	0.09	0.30	0.06

Table 2. Irradiated doses for local irradiation of mouse legs (cart, irradiation room) on October 28, 2021. (P: Position, Ce: Center)

Mouse No.	P	Fluence [μcm^2]		[Gy]					
		Thermal neutron	Epi-thermal neutron	Thermal neutron	Epi-thermal neutron	First neutron	γ -ray	Physical dose	B-10** (1ppm)
60	Ce	3.3E+12	5.8E+11	0.44	0.046	0.32	0.23	1.0	0.24
60	Ce	3.2E+12	5.8E+11	0.43	0.046	0.32	0.36	1.2	0.24

Table 3. Irradiated doses for local irradiation of mice (cart, irradiation room) on November 30, 2021. (Cl: Closest, F: Farthest, Ce: Center, V: vial, M: mouse)

Irradiation time [min]	Position	Fluence [μcm^2]		[Gy]					
		Thermal neutron	Epi-thermal neutron	Thermal neutron	Epi-thermal neutron	First neutron	γ -ray	Physical Dose	B-10** (1ppm)
60	Cl	3.0E+12	5.4E+11	0.4	0.043	0.3	0.37	1.1	0.22
	V								
	F	1.5E+12	2.7E+11	0.2	0.022	0.15	0.37	0.75	0.11
	V								
60	Ce	3.8E+12	6.8E+11	0.51	0.054	0.38	0.25	1.2	0.28
	M								
60	Ce	3.9E+12	6.9E+11	0.52	0.055	0.38	0.31	1.3	0.29
	M								

The measurement of thermal neutron fluence and doses are shown in Tables 1-3.

The results from dynamic profiles of RNA and proteins suggested that presence of early responding genes were confirmed after BNCT. A potential role of HMGB1 as a biomarker for evaluation of early *in vivo* response to BNCT was also indicated [1].

REFERENCES:

[1] Imamichi, S, *et al.*, Extracellular Release of HMGB1 as an Early Potential Biomarker for the Therapeutic Response in a Xenograft Model of Boron Neutron Capture Therapy. *Biology* 11: 420, 2022.

CO7-27 Development of ^{10}B -loaded mesoporous silica-based nanoparticles and evaluation in BNCT mouse experiments

F. Tamanoi¹, K. Matsumoto¹, A. Komatsu¹, S. Chin-nathambi¹, M. Laird¹, Y. Higashi¹, A. Kubota and M. Suzuki²

¹Institute for Advanced Study

Institute for Integrated Cell-Materials Sciences, Kyoto University

²Institute for Integrated Radiation and Nuclear Science, Kyoto University

INTRODUCTION: Boron phenylalanine (BPA) has been developed as useful boron compound which is available for Boron neutron capture therapy (BNCT) therapy. We have recently developed a mesoporous silica-based nanoparticle which has biodegradable bond in the framework that are loaded with BPA, named biodegradable periodic mesoporous organosilica (BPMO). These nanoparticles have a large surface area where BPA can be attached for BNCT application. In this study, we intratumor injected BPA-BPMO to mice transplanted with CT26 mouse colon cancer and evaluated the BNCT efficacy.

EXPERIMENTS: BPMO was synthesized by sol-gel synthesis of two precursors, bis[3-(triethoxysilyl) propyl] tetrasulfide and 1, 2-bis(triethoxysilyl) ethane. This resulted in the incorporation of tetrasulfide bonds into the framework of the nanoparticles. BPMO was then processed to modify with GOPTS (3-glycidyloxypropyl trimethoxysilane) that contain epoxy groups. After converting epoxy groups to diols, BPA was mixed with diol-BPMO to graft BPA using a method to chelate boron with diol groups. The synthesized nanoparticles were characterized by using SEM, TEM, FT-IR, nitrogen adsorption-desorption analysis and zeta potential. The amount of boron attached on the nanoparticles was examined by ICP, and boron content was determined.

Mouse model was established by transplanting mouse colon cancer cells CT26 to BALB/c mouse. After injection of BPA-loaded nanoparticles, amount of boron in the tumor was examined by ICP.

Irradiation of mice with neutron beams was carried out by placing mice in specially prepared holders. Irradiation was carried out with thermal neutron for 12 min at an operating power of 5MW. After the irradiation, mice were returned to cage, and tumor size was longitudinally and transversely measured every 2 days for up to 2 weeks.

RESULTS: Nanoparticles synthesized had approximately 80-100 nm of diameter and homogenous shapes examined by SEM and TEM microscopy. FT-IR analysis of BPMO showed diagnostic peaks of typical Si-O-Si, $-(\text{CH}_2)_2-$ and $-\text{CH}_2-$ vibrations. After loading of BPA to BPMO, we analyzed surface charge of BPA-BPMO which was negative due to modification with phospho-

nate. The zeta potential of BPA-BPMO was -41.38 mV.

Boron accumulation in the CT26 tumor was investigated with ICP. We were able to achieve delivery of boron in the tumor but the route of delivery needs to be further investigated. We also observed accumulation of BPA-BPMO in the tumor by confocal microscopy. As seen in Fig.1, the red fluorescence of BPA-BPMO could be observed in the part of the tumor when 6.25 mg/tumor of BPA-BPMO (equivalent to $125 \mu\text{g}$ /tumor of ^{10}B) was injected to tumor.

Investigation of the BNCT efficacy of BPA-BPMO was carried out with Kyoto University Nuclear Reactor and evaluated by measuring tumor size every 2 days for 2 weeks. After mice which was intratumor injected high concentration (6.25 mg/tumor of BPA-BPMO) or low concentration (0.625 mg/mouse of BPA-BPMO) were irradiated with thermal neutron, as seen in Fig.2, BNCT efficacy of BPA-BPMO was resulted in that was lower than that of free BPA, but constant tumor growth inhibition was seen.

We are currently preparing BSH-BPMO instead of BPA-BPMO to transport more boron, and carrying out mouse experiment.

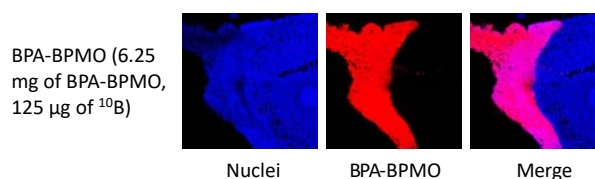


Fig.1 Tumor accumulation of BPA-BPMO by confocal microscopy.

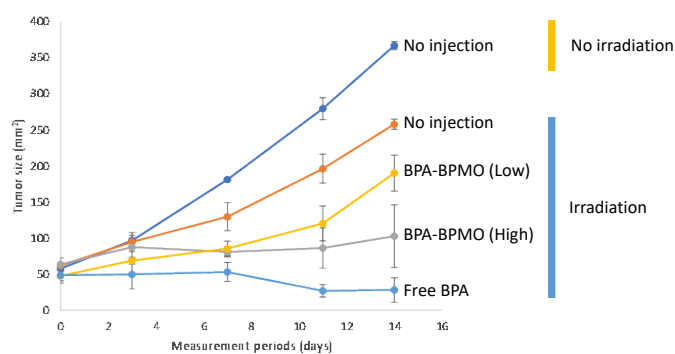


Fig.2 BNCT efficacy of BPA-BPMO.

CO7-28 Conjugation of Phenylboronic Acid Moiety through Multistep Organic Transformations on Nanodiamond Surface for an Anticancer Nanodrug of Boron Neutron Capture Therapy

Masahiro Nishikawa,¹ Heon Gyu Kang,¹ Minoru Suzuki² and Komatsu Naoki¹

¹ Graduate School of Human and Environmental Studies, Kyoto University

² Institute for Integrated Radiation and Nuclear Science, Kyoto University

Detonation nanodiamonds (DNDs) have attracted considerable attention, in particular, in the field of nanomedicine due to its biocompatibility as well as various functionalities imparted by surface modification. Meanwhile, boron neutron capture therapy (BNCT) is an advanced cancer treatment utilizing nuclear fission reaction of ^{10}B upon neutron irradiation. Recently, quite a few boron-containing nanoparticles have been investigated to deliver ^{10}B atoms into cancer tissue selectively and retentively. In this study, we

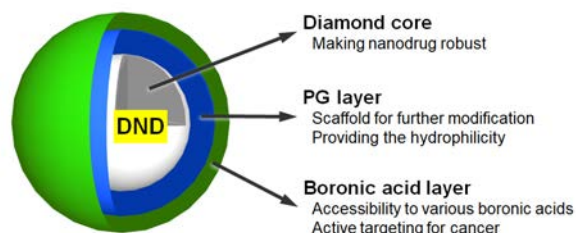


Figure 1. Schematic illustration for design of the three-layered structure of DND-based nanodrug.

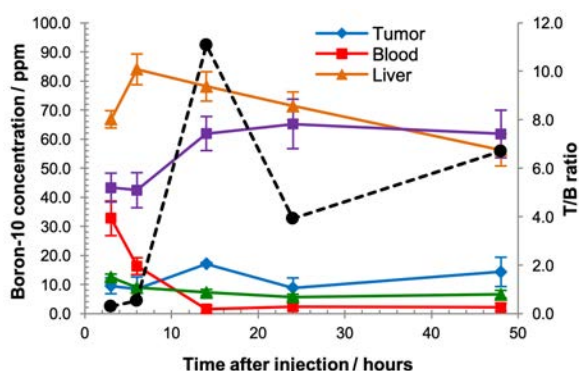


Figure 3. Pharmacokinetic study of DND-PG-PBA-SucMe- ^{10}B ; ^{10}B concentrations in tumor, blood and major organs (solid lines) and the concentration ratio of tumor (T) to blood (B) (T/B ratio, dotted line).

explored boronic acid functionalized DNDs as an anticancer agent for BNCT. Phenylboronic acid (PBA) moiety was introduced to polyglycerol (PG) modified DNDs (DND-PG) through multistep organic transformation (Figure 1 and 2), giving percent order of boron atoms. The process is scalable and reliable by simple covalent chemistry and the resulting product is well dispersed, and stable chemically and physically under physiological conditions. In the *in vivo* experiments, the resulting material was accumulated into the tumor to exert the BNCT efficacy upon neutron irradiation (Figure 3 and 4). These results demonstrate that the PBA functionalized DNDs are a promising candidate as an anticancer nanodrug for BNCT.

Reference: M. Nishikawa, H. G. Kang, Y. Zou, H. Takeuchi, N. Matsuno, M. Suzuki, N. Komatsu* *Bull. Chem. Soc. Jpn.*, 94(9), 2302-2312 (2021).

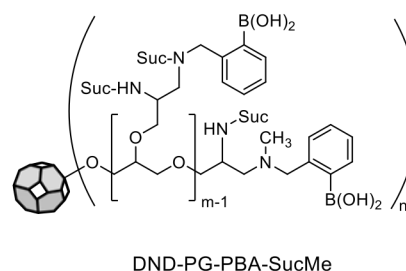


Figure 2. Chemical structure DND-based nanodrug including phenylboronic acid moiety for BNCT.

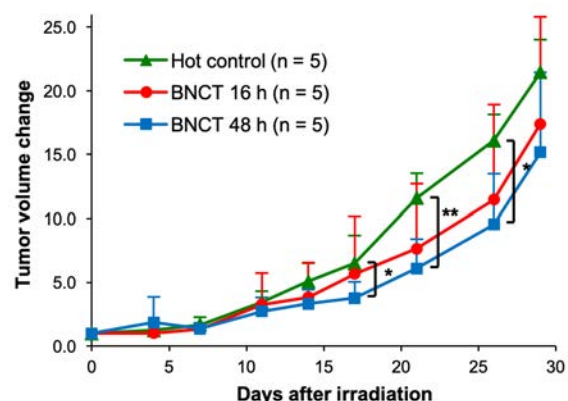


Figure 4. BNCT results of DND-PG-PBA-SucMe- ^{10}B . Relative tumor volume was monitored in BNCT and control groups for 29 days after neutron irradiation. ($n = 5$, the Student's t-test, * $p < 0.05$, ** $p < 0.01$).

CO7-29 The option of BNCT for oral squamous cell carcinomas

K. Igawa¹, R. Ogawara², T. Kusumoto³, A. Sasaki⁴, S. Ibaraki⁴, K. Izumi⁵, M. Suzuki⁶, N. Kondo⁶, Y. Sakurai⁶

¹Neutron Therapy Research Center, Okayama University

²Advanced Research Center for Beam Science, Institute for Chemical Research, Kyoto University.

³National Institute of Radiological Sciences (NIRS), National Institutes for Quantum and Radiological Science and Technology (QST).

⁴Graduate School of medicine, Dentistry and Pharmaceutical Sciences, Okayama University

⁵Graduate School of Medical and Dental Sciences Oral Life, Niigata University

⁶Institute for Integrated Radiation and Nuclear Science, Kyoto University.

INTRODUCTION:

The number of patients with oral and oropharyngeal cancer exceeds 20,000, and both mortality and morbidity rates continue to increase, with approximately 7,000 people currently suffering from oral cancer each year and more than 3,000 people dying in Japan [1]. The most common oral cancer is oral squamous cell carcinoma (OSCC)(90 %), and OSCC has a high potential for nodal metastasis and locoregional invasion, from which over 50% of patients die. As the most common histopathological grading of OSCC, the World Health Organization differentiation criteria, based on the Broders criteria and merely recognizes well-, moderately-, and poorly-differentiated variants of conventional OSCCs, is used for an indicator of prognosis. In consideration of the preservation of organ function, as well as appearance, Boron Neutron Capture Therapy (BNCT) for head and neck cancer is one of the effective treatments instead of surgical procedures, radiotherapy, chemotherapy, and combined therapy [2]. Therefore, the correlation between the tumor differentiation in OSCC and prognosis after BNCT is investigated in this study.

EXPERIMENTS: The HSC-4 (JCRB cell Bank) as well-differentiated OSCC and HSC-3 (JCRB Cell Bank) as poorly-differentiated OSCC were cultured in MEM medium (Gibco, Thermo Fisher Scientific, USA) supplemented with 10 % fetal bovine serum (Sigma -Aldrich, USA) and 100 unit/ml penicillin and 100 mg/ml streptomycin (1% p/s) (Thermo Fisher Scientific, USA) for OSCC mouse model. Each cell lines (1x10⁶ cells) were subcutaneously injected into the left hind legs of 6-week-old female Balb/c nude mice (Clea Japan Inc., Japan). After the injection of L-boronophenylalanine (BPA, Steboronine®, Stella pharma, Japan) to the OSCC mouse, the tumor was resected, centrifuged for 5 mins at 300×g then treated with 60% HNO₃ and heated for 1 hour for measuring the boron concentration by the Inductively Coupled Plasma-Mass Spectrometer (ICP-MS, Agilent technologies 7500cx)[3]. After the administration of BPA, OSCC mice were irradiated by neutron for 40

minutes and the follow-up body weight and the diameter of tumor were measured. The tumor size was calculated according to the following formula.

Tumor volume [mm³] = (Long diameter [mm]) x (Short diameter [mm])² / 2

RESULTS and DISCUSSION:

The results of ICP-MS analysis showed the boron uptake is observed in both OSCC models. However, the boron uptake in poorly-differentiated OSCC is slightly higher than the well differentiated OSCC. After BNCT, the weight loss and the adverse effect were not observed in both OSCC. The tumor had significant growth in non-treatment group, compared to significant shrinkage in BNCT group. The tumor response rate is 84% in poorly differentiated OSCC and 96% in well differentiated OSCC.

These results indicate that BNCT is effective to both OSCC, although there are some slight differences. It was found that it is important to validate not only the boron concentration but also the boron distribution in this study. In 2022, the boron distribution and the boron neutron reaction in the tissue of well- and poorly -differentiated OSCC model would be investigated utilizing neutron induced autoradiography technique with a CR-39[4]. In near future, the multidisciplinary approach including BNCT will proposed for OSCC.

REFERENCES:

- [1]https://ganjoho.jp/reg_stat/statistics/stat/short_pred.ht ml.
- [2]M.Suzuki, *et al.*, Journal of Radiation Research, Volume 55, Issue 1, Pages 146–153, (2014).
- [3]S. Wang, *et al.*, Appl Radiat Isot. 165:109271.(2020).
- [4]R Ogawara *et al.*, Nuclear Instruments and Methods in Physics Research Section B: Beam Interactions with Materials and Atoms, Volume 467, 15, Pages 9-12 (2020).

CO7-30 New boron drug development research targeting pancreatic cancer

H. Michiue¹, T. Fujimoto^{1,2}, N. Kanehira^{1,2}, K. Igawa¹, Y. Sakurai³, N. Kondo⁴, T. Takata³, and M. Suzuki³

¹Neutron Therapy Research Center, Okayama University; 2-5-1, Shikata-cho, Kita-ku, Okayama City, Okayama, Japan.

²Department of Gastroenterological Surgery, Okayama University; 2-5-1, Shikata-cho, Kita-ku, Okayama City, Okayama, Japan.

³Institute for Integrated Radiation and Nuclear Science, Kyoto University, 2-1010, Asashiro-Nishi, Kumatori-cho, Sennan-gun, Osaka, Japan.

INTRODUCTION:

Pancreatic cancer refers to malignant tumors arising from the pancreas, but generally refers to pancreatic ductal carcinoma. Ductal carcinoma originates from the pancreatic duct epithelium and accounts for 80-90% of all neoplastic lesions in the pancreas. According to national statistics, it was the fifth leading cause of death after lung cancer, stomach cancer, colorectal cancer, and liver cancer. Pancreatic cancer in our country has been on the rise in recent years, with more than 30,000 people dying from pancreatic cancer each year.

The number of pancreatic cancer deaths has increased more than eightfold in the past 30 years, and the disease is more common in people in their 60s and slightly more common in men. It has been associated with smoking, family history of pancreatic cancer, diabetes, and chronic pancreatitis.

Pancreatic cancer is difficult to detect in its early stages because there are few subjective symptoms. It is usually noticed after the disease has progressed to a more advanced stage by abdominal pain, weight loss, jaundice, and other symptoms. Therefore, when pancreatic cancer is diagnosed, it is often found in an advanced stage. In addition, although some people worry about pancreatic cancer when they experience back pain, it is not necessarily a characteristic symptom of pancreatic cancer. It is important to note that pancreatic cancer may be present in diabetics when their blood glucose control suddenly deteriorates. Ultrasonography, CT, MRI, endoscopic pancreatography, and angiography are used to diagnose pancreatic cancer. If pancreatic cancer is suspected, the pancreas cannot be seen from the surface of the body, so an ultrasound or CT scan is first performed to check for the presence of a mass in the pancreas. CT scan can also be used to check for metastasis of pancreatic cancer to other organs such as the lungs and liver.

One of the characteristic imaging findings of pancreatic cancer is that the normal pancreas is contrasted without contrasting the pancreatic cancerous area when contrast enhanced CT scan is performed.

Usually, malignant tumors have more pronounced tumor vascular growth than normal tissues due to the rapid development of tumor blood vessels to nourish the tumor. In addition, these tumor vessels maintain a very leaky structure to provide a high degree of oxygen and nutrition to the tumor and are easily detectable using contrast me-

dia. However, pancreatic cancer, despite being a malignant tumor, is characterized by the fact that tumor blood vessels are somewhat scarce compared to normal, and the stroma between tumor cells is hyperplastic, making it difficult to receive the contrast effect of contrast media.

DDS (Drug Delivery System) is a research field that delivers drugs such as anticancer agents to such malignant tumors. It has been reported that when a liposomal formulation containing a drug is administered to a tumor-bearing model, such a macromolecular drug accumulates specifically in the tumor by leaking from the tumor blood vessels. This effect is called the EPR effect (Enhanced Permeability and Retention effect) and has been proposed as a theory that minimizes drug damage to normal tissue and maximizes the effect on tumor tissue.

For pancreatic cancer that does not undergo contrast effect, we believe that it is difficult to use polymeric DDS formulations, which mainly have EPR effect, for future clinical applications. Therefore, we focused on PET (Positron Emission Tomography) using ¹⁸F-FDG, which is used in the diagnosis of pancreatic cancer. FDG is a test reagent of a glucose derivative called fluorodeoxyglucose F18. Glucose is labeled with ¹⁸F, a radionuclide, and is used as a test reagent for various types of cancer. In this study, we focused on glucose metabolism in cancer, and decided to develop a glucose-based boron drug [1].

EXPERIMENTS:

In this study, we decided to develop a boron drug for pancreatic cancer by targeting glucose transporters. In classifying pancreatic cancer, we focused on CA19-9, a tumor marker for pancreatic cancer, which is a type of carbohydrate antigen called carbohydrate antigen 19-9. Pancreatic cancers with high CA19-9 levels are known to have a poor prognosis, and we investigated the relationship between CA19-9 high human pancreatic cancer cell lines and CA19-9 high human pancreatic cancer. To evaluate CA19-9, CA19-9 in the supernatant of cultured cells was measured by ELISA and observed by confocal laser microscopy with cell immunostaining using CA19-9 antibody.

RESULTS:

In this study, we have succeeded in synthesizing a glucose-binding boron drug and have filed a patent application. It was confirmed that the glucose boron drug was efficiently introduced into the cells via glucose transporters highly expressed in pancreatic cancer. The anti-tumor effect of the new drug in pancreatic cancer model mice was demonstrated at Institute for Integrated Radiation and Nuclear Science, Kyoto University with neutron irradiation. The results were further developed and reported as a novel boron drug. We thank many collaborators for their cooperation.

REFERENCES:

[1] Leone RD, *et al.*, *Science*. 2019 Nov 22;366(6468):1013-1021.

CO7-31 Basic research on new BNCT strategies for melanoma

H. Michiue¹, T. Fujimoto^{1,2}, N. Kanehira^{1,2}, K. Igawa¹, Y. Sakurai³, N. Kondo⁴, T. Takata³, and M. Suzuki³

¹Neutron Therapy Research Center, Okayama University; 2-5-1, Shikata-cho, Kita-ku, Okayama City, Okayama, Japan.

²Department of Gastroenterological Surgery, Okayama University; 2-5-1, Shikata-cho, Kita-ku, Okayama City, Okayama, Japan.

³Institute for Integrated Radiation and Nuclear Science, Kyoto University, 2-1010, Asashiro-Nishi, Kumatori-cho, Sennan-gun, Osaka, Japan.

INTRODUCTION:

Melanoma has long been a target of BNCT. In particular, the effectiveness of BNCT has been recognized worldwide as evidenced by the publication of "Treatment of malignant melanoma by single thermal neutron capture therapy with melanoma-seeking 10B-compound" in the *Lancet* in 1989. In the article "Treatment of malignant melanoma by single thermal neutron capture therapy with melanoma-seeking 10B-compound" published in the *Lancet* in 1989, Dr. Mishima et al.[1]

In this report, the world's first successful case of BPA-BNCT for melanoma was reported. It is regarded as the cornerstone of the development of BNCT in Japan. Melanoma is a cutaneous malignancy with an incidence of 1-2 per 100,000 people and is considered a rare cancer. In Australia, the incidence is about 35 per 100,000 people, with regional and racial variation. Surgery is the standard treatment of first choice for localized melanoma, and the prognosis is very good for Stage I melanoma that is unlikely to spread to the regional lymph nodes.

The prognosis, mainly surgery, for localized melanoma is very good, with a 5-year survival rate of 95-100%, and the disease is reported to be curable by surgery. The utility of BNCT for local melanoma is reported to be high for melanoma patients, many of whom are elderly, because there is no pain or functional disability associated with surgery.

The boron drug BAP (p-boronophenylalanine), which was developed to target melanoma, is a derivative of L-phenylalanine, the starting material for melanin synthesis, and has been developed to target malignant melanoma from the beginning, and its concentration in melanoma is It is highly concentrated in melanoma. In recent years, its use in malignancies other than melanoma has been progressing, and its incorporation into various malignant tumors via LAT1, an amino acid transporter that is highly expressed in cancers, has been reported.

Immunotherapy for advanced-stage melanoma has been in the spotlight in recent years. For many years, the therapeutic efficacy of immunotherapy was considered limited, but the development of immune checkpoints and inhibitors by Professor Honjo Tasuku and his colleagues, who received the 2018 Nobel Prize in Physiology or Medicine, has established immunotherapy as a fourth

therapeutic approach alongside surgery, chemotherapy and radiation therapy, immunotherapy has been established as a fourth therapeutic modality alongside surgery, chemotherapy, and radiation therapy.

Immune cells in our body are quick to attack invading foreign substances such as viruses. On the other hand, they cannot easily attack cancer cells generated from our own cells because they are our own cells, even if they proliferate in our body. They discovered that the reason why immune cells are unable to attack cancer cells is due to the binding between an immune checkpoint molecule called PD-1, which exists on the surface of cytotoxic T cells, and a molecule called PD-L1 on the surface of cancer cells.

Furthermore, by developing a drug that inhibits the mechanism by which cancer cells escape from the immune mechanism, the foundation of immunotherapy that enables immune cells to smoothly kill cancer cells has been completed. This drug is called an immune checkpoint inhibitor. The efficacy of this immune checkpoint inhibitor was confirmed in patients with advanced-stage melanoma, marking the start of immunotherapy.

We believe that it would be very useful for the future development of BNCT to investigate the direction of combined immunotherapy using anti-PD-1 antibody, which has good results in melanoma, and BPA-BNCT, which is compatible with melanoma, and to verify the effectiveness of this combination through basic research using animal models.

EXPERIMENTS:

We purchased the B16-F10 mouse melanoma cell line to create a melanoma model, as B16-F10 has high melanin synthesis capacity and has a large amount of black melanin pigment even in cultured cells. Since B16-F10 originated from C57BL/6 mice, we used these mice as a melanoma model. Animal experiments were conducted after strict approval by the ethics committees of Okayama University and Kyoto University.

Melanoma model mice were created at Okayama University and then transported to t Institute for Integrated Radiation and Nuclear Science, Kyoto University, where BNCT treatment experiments were conducted and subsequent experiments were performed.

RESULTS:

We used BPA as an effective boron agent for melanoma and confirmed the anti-tumor effect of neutron irradiation. The results were favorable, and are useful for the development of BPA-BNCT for melanoma in the future

We would like to express our deepest gratitude to the many collaborators who assisted in this project..

REFERENCES:

[1] Y. Mishima et al., *Lancet* **334**, 388-9 (1989).

CO7-32 Quantitative analysis of the contribution of tumor vascular damage to the antitumor effect of X-ray using BNCR

K. Ono¹, T. Watanabe², H. Tanaka², T. Takata², S. Suzuki²

¹BNCT Joint Clinical Institute, Osaka Medical Pharmaceutical University

²Institute for Integrated Radiation and Nuclear Science, Kyoto University

INTRODUCTION: Tumor tissue consists of tumor cells and stroma, especially the vasculature that supplies the cells with oxygen and nutrients. The antitumor effect in BNCT is almost specific to cells accumulating boron compounds. In this study, we compare the effect of this tumor cell-specific BNCT with the effect of X-rays that has no tumor cell specificity and quantitatively elucidate the effect of damage caused in the vascular system on the overall antitumor effect. This is the purpose of this research.

In FY2021, data from a previous paper using SCCVII tumors were re-analyzed to determine whether the effect of BNCT on solid tumors can be explained solely by its cellular-level killing effect.

EXPERIMENTS: The main mechanism of radiation-induced cell death is double-strand breaks in DNA. Unrepaired breaks therefore appear as micronuclei in the cytoplasm after nuclear division. Addition of cytochalasin B to the culture medium of irradiated cells does not inhibit nuclear division but does inhibit cell division, so that cells which have undergone post-irradiation division are identified as binuclear cells. The decrease in the proportion of cells without micronuclei is equal to the α value of the cell survival curve analyzed by the LQ model; the particles released from the BNCR are high-LET particles and cell survival can only be expressed in terms of α values. Therefore, if the distribution of the boron compound is non-uniform, the lines obtained from both the micronucleus and colony formation assays should bend in the middle. Conversely, if the boron drug is not taken up by the cells and is distributed almost uniformly in the extracellular space, the two curves after BNCT should overlap perfectly. The relationship between neutron fluence and cell survival at the level determining cure can be estimated from the neutron fluence and cure rate curves in tumor cure experiments. Combining these two neutron fluence and cell survival curves, and assuming a reasonable tumor cell count based on tumor size, the relationship between cell survival and neutron fluence can be estimated for the range from pre-neutron irradiation to the neutron fluence at which cure is achieved.

RESULTS and DISCUSSION: As shown in Figure-1, for BSH, which is not taken up by cells and is mostly present in the intercellular space, the cell survival curve showed an exponential decrease concerning neutron fluence, and the micronucleus test curve completely overlapped on cell survival curve. On the other hand, for BPA-BNCT, cell survival showed an exponential decrease to the 10^{-3} level, but the micronucleus test curve bent in the middle. This was thought to be due to heterogeneous accumulation of BPA in the cells. This discrepancy also suggests that the colony formation rate of cells which did not take up BPA was significantly lower than that of cells. Figure-2 shows the estimated slope of the cell survival curve at the level at which tumor cure is achieved in BNCT cure experiments with BSH and BPA. Combining the results of figures -1 and -2, the estimated cell survival curve in the full fluence range is shown in figure-3. From this, the tumor-forming potential of SCCVII tumor cells in mice was estimated to be between 10^{-3} and 10^{-4} . TD50 has not been determined but is considered to be an approximately reasonable figure based on transplantation experience. As can be seen from the present analysis, most of the anti-tumor effects of BPA-BNCT but also BSH-BNCT with higher blood boron concentrations, can be explained by the direct effect of BNCT on tumor cells and the contribution of vascular damage to tumor cure is estimated very small if present.

crease to the 10^{-3} level, but the micronucleus test curve bent in the middle. This was thought to be due to heterogeneous accumulation of BPA in the cells. This discrepancy also suggests that the colony formation rate of cells which did not take up BPA was significantly lower than that of cells. Figure-2 shows the estimated slope of the cell survival curve at the level at which tumor cure is achieved in BNCT cure experiments with BSH and BPA. Combining the results of figures -1 and -2, the estimated cell survival curve in the full fluence range is shown in figure-3. From this, the tumor-forming potential of SCCVII tumor cells in mice was estimated to be between 10^{-3} and 10^{-4} . TD50 has not been determined but is considered to be an approximately reasonable figure based on transplantation experience. As can be seen from the present analysis, most of the anti-tumor effects of BPA-BNCT but also BSH-BNCT with higher blood boron concentrations, can be explained by the direct effect of BNCT on tumor cells and the contribution of vascular damage to tumor cure is estimated very small if present.

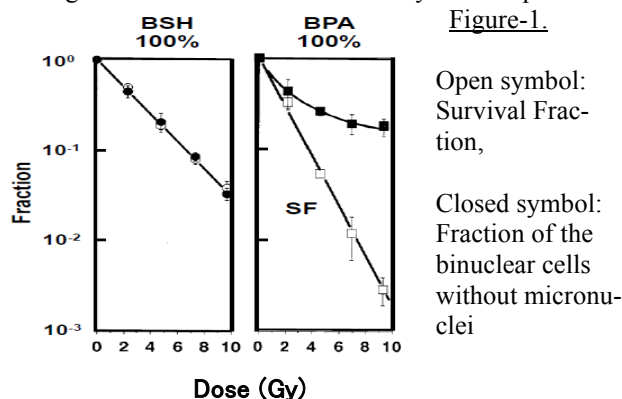


Figure-1.

Open symbol: Survival Fraction,

Closed symbol: Fraction of the binuclear cells without micronuclei

Figure-2

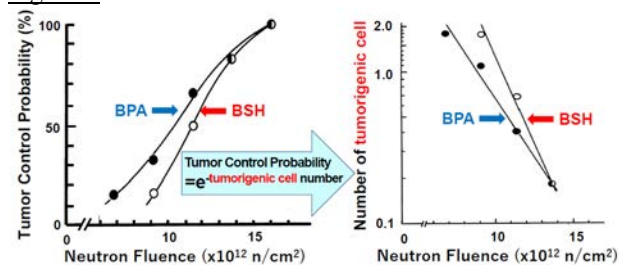
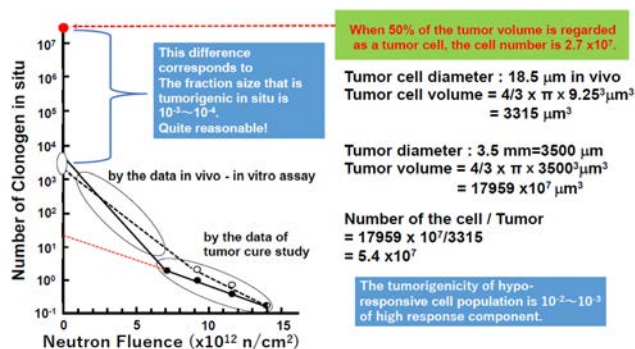


Figure-3



CO7-33 Study on Intracellular Protein Destruction by Boron Neutron Capture Reaction

Hiroki Kakuta¹, Yuta Takamura¹, Rui Nozaki¹, Kazuyo Igawa², Tamon Kusumoto³, Ryo Ogawara⁴, Natsuko Kondo⁵, Yoshinori Sakurai⁵.

¹ Division of Pharmaceutical Sciences, Okayama University Graduate School of Medicine, Dentistry and Pharmaceutical Sciences.

² Neutron Therapy Research Center, Okayama University.

³ National Institute of Radiological Sciences (NIRS), National Institutes for Quantum and Radiological Science and Technology (QST).

⁴ Advanced Research Center for Beam Science, Institute for Chemical Research, Kyoto University.

⁵ Institute for Integrated Radiation and Nuclear Science, Kyoto University.

INTRODUCTION: Boron neutron capture therapy (BNCT) is a cancer treatment based on the nuclear reaction between boron-10 (¹⁰B) and neutron. The high-energy particle beam after neutron capture by ¹⁰B is reported to break the double-stranded DNA of cancer cells and induce apoptosis. However, the effect of the particle beam on intracellular organelles has not been investigated in detail. In this study, we investigate whether protein cleavage based on neutron irradiation occurs using the retinoid X receptor (RXR), one of nuclear receptors, and a boron-containing RXR ligand.

EXPERIMENTS: The compounds shown in Figure 1A and bexarotene were synthesized by the authors. The RXR ligand binding domain (RXR-LBD) was kindly gifted by Prof. Nakano, University of Shizuoka. RXR-LBD binding assay and reporter gene assay were performed according to references 1 and 2. Neutron beam was irradiated at 5 MW for 30–60 minutes. The irradiated sample (100 μL) was prepared as below; RXR-LBD (10 μM), CBTF-EE-BSH (200, 100, 50 μM, converted to ¹⁰B concentration 24, 12, 6 ppm), bexarotene (20 μM or not), buffer (10 mM HEPES, 150 mM NaCl, 2 mM MgCl₂, 5 mM DTT, 5% DMSO). The irradiated sample was diluted 10 times with above buffer and mixed with BPB-containing buffer in a 4:1 composition, and electrophoresed at 250 V, 20 mA for 70 minutes. The concentration of RXR-LBD was estimated using CBB staining.

RESULTS: We have reported CBTF-EE (**1a**) as an RXR antagonist.^[1] Also, it has been confirmed that CBTF-EE-BODIPY (**1b**), which was designed by inducing a fluorescent group at the end of the alkoxy chain of **1a**, functions as an RXR antagonist.^[2] Thus, we designed and synthesized CBTF-EE-BSH (**1c**), which has ¹⁰B cluster molecule BSH, and evaluated whether **1c** will function as an RXR ligand (Figure 1A). As a result of RXR-LBD binding assessment, it has been revealed that a *K_i* value of **1c** was 3.31 μM (Figure 1B). Then, neutron irradiation was performed on each solution in which **1c** and RXR-LBD coexisted, and in which bexarotene, which is an RXR agonist and inhibits the binding of **1c** to RXR-LBD, was further

added. After irradiation, the amount of RXR-LBD was estimated by SDS-PAGE, which can evaluate the migration distance according to the molecular weight of the protein, and CBB staining. Irradiation with 2.98×10^{13} /cm² as thermal neutrons and 5.53×10^{12} /cm² as extrathermal neutrons did not show (Figure 1C). Interestingly, NATIVE-PAGE, which can evaluate the three-dimensional structure of the protein, indicated that the binding of bexarotene becomes dominant by neutron irradiation (Figure 1D).

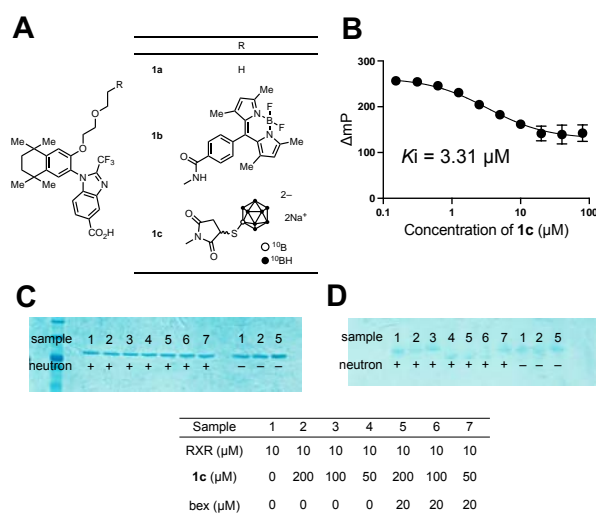


Figure 1. (A) Chemical structures of **1a–1c**. (B) Binding ability of **1c** toward RXR-LBD. Evaluation of RXR-LBD concentration by SDS-PAGE (C), and the 3D structure of RXR-LBD by NATIVE-PAGE (D).

DISCUSSIONS AND FUTURE PLAN: The neutron irradiation to the combination of **1c** and RXR-LBD could not induce RXR-LBD degradation. On the other hand, NATIVE-PAGE revealed that neutron irradiation induced the structural change of **1c** and the dominant binding of bexarotene to RXR-LBD, when **1c** and bexarotene coexisted. It remains whether this phenomenon is caused by BNCR. Irradiation of gamma ray or electron beams is a subject for future study.

In recent years, various fields have been challenging to produce boron delivery agents which could replace L-boronophenylalanine (BPA). Given that the BNCT targets tumor DNA cleavage, it is of interest to use nuclear receptor ligands as boron delivery agents. The reporter gene assay revealed that **1c** functions as an RXR antagonist. In the future, we will investigate the intracellular translocation ability of **1c** in detail and aim to provide insights into the availability of nuclear receptor ligands as intracellular ¹⁰B delivery agents.

REFERENCES:

- [1] M. Watanabe *et al.* *J. Med. Chem.*, **2021**, *64*, 430–439.
- [2] M. Takioku *et al.* *ACS Med. Chem. Lett.*, **2021**, *12*, 1024–1029.

CO7-34 Observation of Intracellular Boron Neutron Capture Reaction with a Novel Boron Compound

Hiroki Kakuta¹, Rui Nozaki¹, Yuta Takamura¹, Kazuyo Igawa², Takanori Sasaki², Tamon Kusumoto³, Natsuko Kondo⁴, Yoshinori Sakurai⁴.

¹ Division of Pharmaceutical Sciences, Okayama University Graduate School of Medicine, Dentistry and Pharmaceutical Sciences.

² Neutron Therapy Research Center, Okayama University.

³ National Institute of Radiological Sciences (NIRS), National Institutes for Quantum and Radiological Science and Technology (QST).

⁴ Institute for Integrated Radiation and Nuclear Science, Kyoto University.

INTRODUCTION: Boron neutron capture therapy (BNCT) is a cancer treatment based on the nuclear reaction between boron-10 (¹⁰B) and neutron. Since this therapeutic effect depends on the collision of ¹⁰B with neutron, the concentration of boron in the cancer tissue is an important factor. However, for borofalan (4-boronophenylalanine), currently the only drug approved for BNCT, the boron concentration in cancer tissue is estimated from the blood concentration. Thus, we aimed to create a new BNCT agent whose boron concentration in cancer tissue is measurable.

Since BNCT agents are used in large doses, we focused on iodine contrast agents for X-ray CT, which are also used in similar large doses, and enable quantify iodine concentration noninvasively by X-ray CT. We hypothesized that this principle could be used to measure boron concentration in tissues. To test the above hypothesis, we designed and synthesized **1** (Figure 1A), and investigated the intercellular transferability, X-ray CT imaging ability, and boron neutron capture reaction (BNCR) in cancer cell B16BL6.

EXPERIMENTS: After obtaining iodine-containing boron compound **1**, the intracellular transferability was determined by following the steps as below. Cells were cultured in 35 mm petri dishes submerged 2 cm squares of CR-39 and exposed to medium containing the **1** for 2 h. The cells were then washed with PBS and the cell lysates were prepared. Then, the concentration of **1** was measured using LC-MS/MS. And the CR-39 was irradiated with neutrons at KUR. Neutron irradiation conditions were at E-3 for 2 hours, 1 MW for 10, 20 minutes, or 5 MW for 10, 20 minutes, respectively. Sample conditions; were as follows: blank, BSH (500 μM), **1** (500 μM), **1** (500 μM) + A6K (100 μM). After neutron irradiation, the samples were treated according to the literature [1] and imaged using an optical microscope (BZ-X700). X-ray CT scan was performed using Eminence STARGATE in aqueous solutions with iodine concentrations of 4000, 2000, 1000, and 500 ppm.

RESULTS: Chemical structure of **1** contains a boron cluster BSH, and two iodines for X-ray CT. The intracellular translocation of each condition was measured

in B16BL6 cells, and 2-hour exposure at 500 μM of **1** gave an intracellular approximately 20-fold higher boron concentration than that of BSH, and a combination with A6K, which promotes intracellular delivery of BSH [2], approximately 100-fold higher boron concentration than that of BSH.

X-ray CT imaging of aqueous solutions of **1** was performed, and the correlation between the iodine concentration of **1** and the CT values was obtained. It was found that the iodine concentration which enables to quantify was more than 800 ppm.

B16BL6 cells seeded on CR-39, which can quantify BNCR, were irradiated with neutrons at KUR, and the trajectory of alpha particle on CR-39 was analyzed. As a result, while no etch pits were observed even after 2 hours of irradiation in E-3, a boron concentration-dependent number of etch pits was detected after 20 minutes of irradiation at 1 MW (thermal neutron fluence 2.22×10^{12} cm⁻²). The BNCR on CR-39 after irradiation was quantified as etch pits (Table 1). The results showed a high correlation with the intracellular boron concentration (Table 1) calculated by LC-MS/MS ($R^2 = 0.968$, Figure 1B).

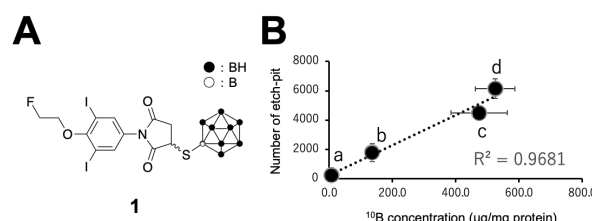


Figure 1. (A) The Chemical structure of **1**. (B) Correlation between BNCR generated on CR-39 and intracellular boron concentration.

Table 1. Comparison of conditions a–d, number of etch pits on CR-39 and intracellular boron concentration

compounds	concentration (μM)	¹⁰ B concentration (μg/mg protein)	etch-pit (quantity/field)
a	blank	-	248.2
b	BSH	500	1785.6
c	1	500	4498.0
d	1 /A6K	500/100	6148.2

DISCUSSIONS AND FUTURE PLAN: In this study, **1** was created and found to permeate B16BL6 cells in combination with A6K peptide, whose concentration is expected to be detectable by X-ray CT imaging. We are planning to perform CT imaging in tumor-bearing mouse. In addition, **1** was found to exhibit intracellular BNCR using CR-39. In accordance with the previous report [3], colony assays will be planned.

REFERENCES:

- [1] T. Kusumoto *et al.*, *Radiat. Res.*, **2019**, *191*, 460–465.
- [2] H. Michiue *et al.*, *J. Control Release.*, **2021**, *330*, 788–796.
- [3] S. Masunaga *et al.*, *Springerplus.*, **2014**, *3*, 128.

CO7-35 Development of immune function targeted boron neutron capture therapy using novel nanoparticles

Tsubasa Watanabe¹, Minoru Suzuki¹

¹*Institute for Integrated Radiation and Nuclear Science,
Kyoto University*

INTRODUCTION: Recent studies have shown that irradiation of tumors with X-rays has various tumor immunostimulatory effects, and this is a new aspect of the antitumor effects of radiation therapy. Boron neutron capture therapy (BNCT) is a type of radiation therapy that uses the interaction of neutrons and boron nuclei (¹⁰B) to emit heavy particles with high cell-killing effects at a micro-level range [1]. In this study, we aim to develop boron neutron capture therapy targeting immune functions by creating boron-containing nanoparticles that target immune functions and cell populations that have negative effects on anti-tumor immunity.

EXPERIMENTS: We attempted to develop BNCT using novel nanoparticles that target immunosuppressive cells by encapsulating the boron drug BSH in liposomes and binding proteins targeting immunosuppressive cells to their outer surface. Ligands were bound to BSH-encapsulated liposomes targeting CD25 and CD11b. The prepared boron drug was cultured with suppressor T cells and myeloid-derived suppressor cells (MDSCs), and the uptake capacity of the boron drug was evaluated using ICP-AES.

RESULTS: Contrary to expectations, the boron drug created did not accumulate on suppressive T cells and MDSCs.

REFERENCES:

[1] Rolf F Barth *et al.* *Radiat Oncol* 2012;7:146.

CO7-36 Basic Experiment of Boron Neutron Capture Therapy(BNCT) for a Rat Model of Malignant Spinal Cord Glioma

R. Kayama, S. Kawabata, K. Sakai, H. Kashiwagi, T. Kanemitsu, R. Hiramatsu, T. Watanabe¹, T. Takata¹, H. Tanaka¹, M. Suzuki¹, S-I. Miyatake², T. Takami, M. Wanibuchi.

Department of Neurosurgery, Osaka Medical and Pharmaceutical University

¹*Institute for Integrated Radiation and Nuclear Science, Kyoto University*

²*Kansai BNCT Medical Center, Osaka Medical and Pharmaceutical University*

INTRODUCTION

Boron neutron capture therapy (BNCT) is a particle irradiation which can destroy tumor cells with selectivity. Owing to this merit, BNCT has been expected to be adjuvant therapy for invasive or unresectable cancers. Actually, BNCT using BPA has been covered by insurance for head and neck cancer since 2020. At our institution, we have clinically applied BNCT since 2002 as an experimental adjuvant therapy for intracranial malignant gliomas using nuclear reactor as a neutron source.

Intramedullary spinal cord tumors (IMSCT) are rare neoplasms, accounting for 4% of central nervous system tumors, and for 15% of all primary spinal cord tumors. High-grade spinal cord gliomas make up 10% of them [1]. Due to such rarity, optimal management strategy remains controversial despite its poor prognosis. Imitating management of intracranial gliomas, intervention for IMSCT actually include surgical resection, radiation therapy, and chemotherapy. However, it is often difficult to obtain gross total removal for high-grade spinal cord glioma, and sometimes surgical complications are inevitable. Furthermore, in previous reports, extent of removal makes no statistical difference in prognosis [2]. Similarly, adjuvant therapy is not estimated to prolong survival [3,4].

The objective is exploring the possibility that BNCT have antitumor effect against malignant spinal cord glioma, which is often unresectable and resistant to conventional adjuvant therapy.

MATERIAL AND METHOD

Experimental design

Twelve Fisher 344 rats received intramedullary injection containing 100,000 F98 rat glioma cells in 5 μ l Dulbecco's Modified Eagle Medium (DMEM). They were randomized into following 3 groups.

<Group1> untreated control group (n=4)

<Group2> neutron irradiation only (n=2)

<Group3> neutron irradiation 2 hours after BPA administration by intravenous injection (n=6)

Animals in group 3 received intravenous injection of BPA with dose of 250mg/kg b.w. (12mg B/kg) 2 hours before irradiation. A week after inoculation of F98 cells into a rat spinal cord, rats of group2 and group3 were irradiated at reactor power of 5 MW for twenty minutes. After irradiation, the animals were observed in KURNS. Euthana-

sia was performed when Basso, Bresnahan and Beattie (BBB) score (functional testing scale of hindlimb) was less than or equal to 5, or severe bladder and rectal obstruction was observed. The survival time since tumor cell implantation was calculated

Production of spinal cord tumor model

Animals were anesthetized with intraperitoneal injection of following anesthetics: medetomidine (ZENOAQ, Fukushima, Japan) (0.4mg/kg), midazolam (SANDOZ, Yamagata, Japan) (2.0mg/kg), and butorphanol (Meiji Seika, Tokyo, Japan) (5.0mg/kg). Placed prone on sterile field, their backs were sterilized and shaved. Longitudinal skin incision was made on the level of Th8 to Th10. The underlying paravertebral muscles were retracted, spinous process and lamina of Th9 was removed, and finally spinal cord was revealed. Cell implantation was performed at the median of bare spinal cord with a 28gauge Hamilton syringe. The needle was proceeded to a depth of 3mm from the dorsal surface of the spinal cord. Wounds were sutured with 3-0 silk braided.

RESULTS

Median survival of each group (untreated, irradiation only, irradiation after BPA i.v) was 15.8 \pm 0.5 days, 18.5 \pm 0.5 days, and 22.5 \pm 2.0 days. There was significant difference between survival time of group 1 and group 3 ($p = 0.0071$, log-rank test). But, comparison between group 1 and group 2, group 2 vs group 3 shows no statistical difference ($p = 0.0439$, $p = 0.1489$ respectively).

DISCUSSION

This experiment resulted in a significant difference in survival time between the untreated group and BNCT group. None of the irradiated rats improved their BBB scores and eventually died, suggesting that therapeutic effect of BNCT was limited to retard the progression of tumor.

Although the irradiation and boron compound contribution followed previous experimental protocol for the rat brain tumor model, we consider it is necessary to optimize the experimental method for the spinal cord tumor model. Future assignment is unrevealing biodistribution of boron especially in normal spinal cord and spinal cord tumors to determine optimal conditions for boron compound administration. Besides, evaluation of the histopathology is indispensable to assess the antitumor effect and the presence of radiation necrosis.

CONCLUSION

It was suggested that BNCT is effective treatment for malignant spinal cord glioma.

REFERENCES

- [1] A. Raco, V. Esposito, J. Lenzi, *et al.*, *Neurosurgery* 56: 972-981, 2005.
- [2] H. Adams, J. Avendano, SK. Raza, *et al.*, *Spine* 37: E727-735, 2012.
- [3] MC. Chamberlain, SK. Johnston., *J Neurooncol* 102:427-432, 2011.
- [4] T. Seki, K. Hida, *et al.*, *Asian SpineJ* 9: 935-941, 2015.

CO8-1 Demonstration experiment of nuclear material detection using a low-cost assay system

M. Komeda¹, Y. Toh¹, Y. Kitamura², T. Misawa² and K. Tanabe³

¹Nuclear Science and Engineering Center, Japan Atomic Energy Agency

²Institute for Integrated Radiation and Nuclear Science, Kyoto University

³National Research Institute of Police Science

INTRODUCTION: A compact and low-cost non-destructive assay system to detect hidden nuclear material is required in the fields of nuclear security. We have therefore developed an innovative nuclear material detection method by using a neutron source of Californium-252. In this method, a neutron source is rotated at a speed of thousands of rpm nearby a measurement object. Meanwhile, it is possible to detect nuclear materials by confirming the deformation of the time-distribution spectrum obtained by a neutron detector near the object. The machine to rotate the neutron source is quite compact that its width, depth, and height is approximately 60 cm each. In the previous studies, we have accomplished following two objectives. One is that this new method was verified with a neutron detector bank composed of He-3 proportional counters. Another is that a low-cost assay system setup was completed with the rotation machine and water Cherenkov detector. The water Cherenkov detector is much lower in cost than He-3 counters. The purpose of this year was to detect nuclear materials by using the low-cost assay system in KUCA.

EXPERIMENTS: Figure 1 shows the experimental setup of the low-cost assay system and a measurement object. The water Cherenkov detector basically consists of four PMTs (Photomultiplier tube) and an aquarium (30x25x30cm). The back of the aquarium is covered with PTFE diffuse reflective sheets.

Black sheet and boron sheet are covered with the surface in order to prevent light and thermal neutrons. The aquarium is filled with the gadolinium aqueous solution of approximately 0.5wt%. The gadolinium was added in order to increase the amount of the Cherenkov light. To detect more Cherenkov light emission, a wavelength converter is added. Since high energy gamma ray also causes the Cherenkov light in water, we discriminate neutron signal by pulse height difference. A measurement object is put between the aquarium and the rotation machine. In this experiment, we used approximately 60 g of U-235 surrounded by polyethylene blocks. Measurements of the neutron time distribution were performed by a multi-channel scaler (MCS) that is synchronized with

the disc rotation. The rotation machine can rotate a neutron source at a rotation speed between 0 and 4000 rpm. The neutron source was installed at the outer periphery of the disc of 32 cm diameter.

RESULTS: Figure 2 shows an example of experimental results of a sample including uranium when the rotation speed is 3000 rpm. The left edge near 6000 micro seconds is higher than the right edge near 11000 micro seconds due to the geometric condition. Comparing the deformation of the time-distribution spectrum at 3000 rpm with that at 600 rpm, it was observed that the integrated value after the center, which is near 9000 micro-seconds, increased while the integrated value did not increase in the case not containing nuclear materials. We have confirmed detecting nuclear material by using the low-cost assay system composed of the rotation machine and water Cherenkov detector.



Fig. 1 Arrangement of the assay system: The water Cherenkov detector (left), measurement object containing uranium (middle) and the rotation machine (right).

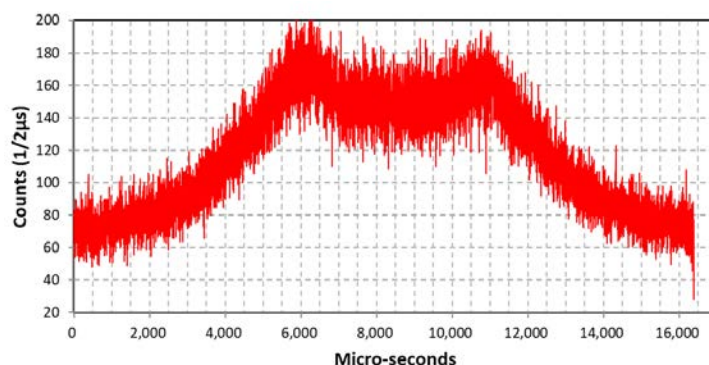


Fig. 2 Neutron events distribution of the uranium sample. The measurement time was 15 minutes with the rotation speed of 3000 rpm.

CO8-2 Neutron efficiency of a GEM-based detector

H. Ohshita, H. Endo, T. Seya, Y. Yasu, S. Matoba,
M. Hino¹, T. Oda¹

*Institute of Materials Structure Science, KEK
¹Institute of Integrated Radiation and Nuclear Science,
Kyoto University*

INTRODUCTION: A two-dimensional neutron detector with a gas electron multiplier (GEM) has been developed [1]. The GEM-based detector is called “nGEM” [2]. The nGEM is a gas-flow radiation detector having a 7:3 gas mixture of Ar and CO₂. It has a compact body (52 × 25 × 5 cm) that includes a gas chamber and onboard electronics. In the onboard electronics, an application-specific integrated circuit for pulse shaping and a field-programmable gate array for online processing are also installed. The measurement data are transferred directly to a computer through a network. The data transfer capability is limited by the Gigabit Ethernet. The hit information, such as time of flight (TOF), hit position, and pulse width, is included in the 8-byte data format. The active area is 100 × 100 mm. For neutron detection, nGEM can be used to measure the number of charged particles originating from the $n(^{10}\text{B}, \alpha)^7\text{Li}$ nuclear reaction. The thermal neutron efficiency of nGEM depends on the thickness of the enriched-boron layer on cathode aluminum plate. The thermal neutron efficiency simulated by Geant4 [3] is shown in Figure 1. The maximum neutron efficiency is expected to be approximately 5% with a 2–3- μm -thick ^{10}B layer. Above the thicker layer region, the charged particles cannot come out from the ^{10}B layer because the particles from the $n(^{10}\text{B}, \alpha)^7\text{Li}$ nuclear reaction have a shorter range. Therefore, the thermal neutron efficiency decreases. In the thinner layer region, because it is difficult to control the layer thickness, the film formation accuracy becomes worse. To perform absolute measurements in some neutron experiments, neutron detectors must first evaluate the neutron efficiencies. In this article, the experimental results of neutron efficiency for nGEM are described. The neutron irradiation test was carried out using CN-3 [4] at the Kyoto University Reactor (KUR).

EXPERIMENTS AND RESULTS: The neutron efficiency of nGEM was studied through a comparison with the measurement data of helium-3 proportional counter (^3He -PC). ^3He -PC covered with B₄C resin shield was used to measure the TOF. The counter had a gas mixture of ^3He and CO₂ (99:1), and the total pressure was 1003.19 kPa. The counter was cylindrical with a 1-inch diameter. The opening area of the B₄C resin shield was 10 × 10 mm. A disk chopper was operated at 30 Hz to obtain the neutron wavelength dependence. Neutrons from 1.5 to 6 Å passed through the disk chopper. The ^3He -PC was set downstream at a distance of 2.154 m from the disk chopper. After the operation condition of the ^3He -PC was defined, the beam center was scanned using CN-3. The relationship between the TOF and de-

tector position was measured by moving the detector position. The neutron intensity in CN-3 was derived from the measurement data of the ^3He -PN with the absorption correction of the SUS detector housing. After the estimation of the absorption correction with Geant4, the measurement data were converted to the neutron intensity. The expected neutron intensity at CN-3 with a KUR beam power of 5 MW was approximately 2016.1 ± 1.4 neutrons/s·cm². Furthermore, the counting rate of nGEM was measured by replacing ^3He -PC.

The neutron efficiency is defined as the ratio of the nGEM counting rate and the expected neutron intensity in CN-3. The neutron efficiency of nGEM is shown in Figure 2. The results show that the nGEM has a thermal neutron efficiency of approximately 0.3%. The Geant4 simulation result with a 0.07- μm -thick ^{10}B layer is indicated as a blue line in the aforementioned figure. Because the measurement data are consistent with the simulation result, it can be concluded that the ^{10}B layer thickness is close to 0.07 μm .

This work was carried out in part with the support of JSPS KAKENHI, Grant Numbers JP20K12503 and JP20H04462.

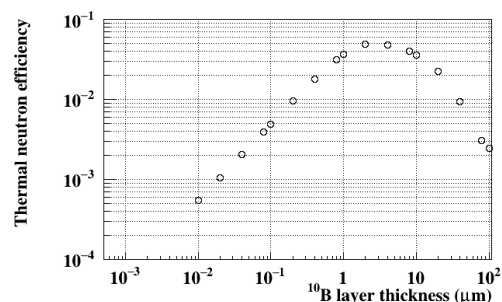


Figure 1. Thermal neutron efficiency with Geant4.

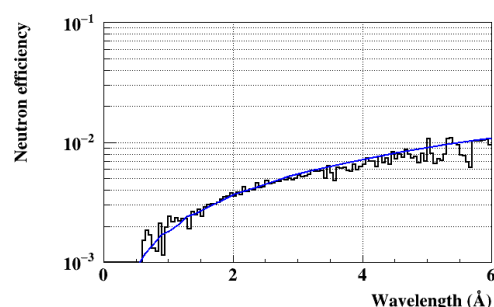


Figure 2. Neutron efficiency of nGEM.

REFERENCES:

- [1] F. Sauli, Nucl. Instr. and Meth. A, **386** (1997) 531.
- [2] H. Ohshita *et al.*, JPS Conf. Proc., **8** (2015) 036019.
- [3] S. Agostinelli *et al.*, Nucl. Instr. and Meth. A, **506** (2003) 250.
- [4] M. Hino *et al.*, Annu. Rep. Res. Reactor Inst. Kyoto Univ., **27** (1994) 196.

CO8-3 Establishment of a novel mutation breeding using Boron Neutron Capture Reaction (BNCR)

M. Kirihata, S. Segami¹, Y. Hattori, T. Kinouchi,
Y. Kinashi²

Research Center of BNCT, Osaka Prefecture University

¹Research Institute of Environment, Agriculture and Fisheries, Osaka Prefecture

²Institute for Integrated Radiation and Nuclear Science, Kyoto University

INTRODUCTION: Boron Neutron Capture Reaction (BNCR) is based on the nuclear reaction of ¹⁰B atom with thermal/epithermal neutron already applied to cancer treatment (BNCT) [1, 2]. As a new utilization method of BNCR, the purpose of this study is to establish a novel mutation breeding using BNCR.

The method attempts to mutagenesis by immersing plant seeds in a ¹⁰B-enriched boron compound, re-drying, and then irradiating the seeds with thermal neutrons to induce BNCR. Its mutagenic effect depends on chemical and physical factors such as ¹⁰B concentration, thermal neutron intensity, and irradiation time. In previous experiments, rice seeds were treated with ¹⁰B-enriched *p*-boronophenylalanine (BPA) [3] or BPA-fructose complexes (BPA-Fc) at concentrations of 10-1000 ppm for 16, 24, or 48 hours, irradiated with thermal neutrons, and then examined for germination rate to evaluate mutagenicity. As a result, no decrease in germination rate was observed under these conditions; considering the solubility of BPA, 1000 ppm is considered to be the upper limit, and as for the immersion time, no relationship with BNCR was observed for the 48h treatment, and simply the immersion time decreased the germination rate, indicating that 48h or longer is not appropriate. In other words, it was difficult to achieve a stronger treatment with BPA. In order to investigate a stronger treatment method that would confirm a decrease in germination rate, the experiment was conducted this time by changing the boron compound used to ¹⁰B-enriched boric acid (H₃¹⁰BO₃).

EXPERIMENTS: The experimental material used *Oryza sativa* L. cv. Nipponbare. The dry seeds were immersed into different concentrations (0, 1, 10, 50, 100 mM) of ¹⁰B-enriched boric acid for 24 h and 100mM H₃¹⁰BO₃ for 36 h. Solvent was PBS buffer. The samples were washed with water and re-dried. The seeds in 6-mL tubes were irradiated with thermal neutron for 90 minutes in the Kyoto University Research Reactor (KUR). The irradiated seeds were sown in cell trays on May 13, 2021, germinated in a germination machine, grown outdoors, and the germination and survival rate was examined 14 and 21 days after sowing. As a control experiment, seeds that were only treated with H₃¹⁰BO₃ immersing and not irradiated with thermal neutrons were sown on petri-dishes with continual moistening of filter paper to check germination rate after 7 days.

RESULTS: Germination rate decreased in a H₃¹⁰BO₃ concentration-dependent manner (Fig. 1). This concentration-dependent decrease in germination rate was not observed in seeds that were not irradiated with thermal neutrons, suggesting that it was not due to immersion in H₃¹⁰BO₃ solution, but rather to BNCR. As mentioned above, no reduction in germination rate was observed in previous experiments using BPA, so it is assumed that this result is due to differences in ¹⁰B uptake in plant seeds caused by differences in boric acid compounds. This is an interesting finding regarding the uptake of boron by plant seeds. Based on the results of this study, the germination and survival rates of the 10B boric acid treatment were less than 50% after 24h treatment at 50 ppm, suggesting that 24h and 10 ppm is the most efficient treatment for mutagenesis. In the future, we would like to confirm the phenotype of M₁ and M₂ generations, evaluate the mutation spectrum, and conduct genetic analysis to discover the effectiveness of this method as mutation breeding.

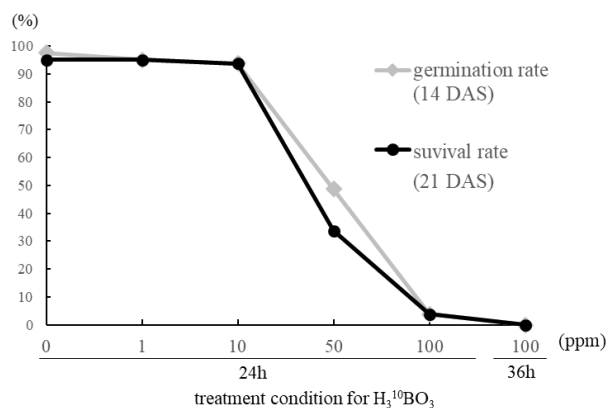


Fig.1 Relationship between treatment conditions and germination and survival rates.

*DAS : day after sowing

REFERENCES:

- [1] H. A. Soloway *et al.*, Chem. Rev., **98** (1998), 1515-1562.
- [2] B. Farhood, *et al.*, Rep. Pract. Oncol. Radiother: **23** (2018), 462-473.
- [3] H. R. Snyder, *et al.*, J. Am. Chem. Soc. **80** (1958), 835-838.

CO9-1 Nuclides sorption onto rock samples in the presence of humic acid

T. Sasaki, Q. Zhao, T. Saito¹, R. Tonna, N. Sato², A. Kirishima², D. Akiyama², K. Takamiya¹, T. Kobayashi, S. Sekimoto¹

Graduate School of Engineering, Kyoto University

¹ Institute for Integrated Radiation and Nuclear Science, Kyoto University

² Institute of Multidisciplinary Research for Advanced Materials, Tohoku University

INTRODUCTION: Safer handling of high-level radioactive wastes (HLW) produced from nuclear recycling is a major scientific and engineering challenge. Although the possibility of early failure of HLW packages after repository closure is low, the radionuclides (RNs) could leach to the biosphere. The sorption reaction of RNs onto host rock would be exploited as an effective barrier to inhibit the migration. Simulation-, field-, and laboratory-based studies have demonstrated that the sorption of RNs would be significantly affected by natural organic matters, such as humic acid (HA) molecules in groundwater, by complexation or colloidal formations [1,2]. In addition, the gamma rays stemming from the decay of RNs penetrate through the steel canisters of HLW with a long-term gamma irradiation field will be generated near the packages. The gamma irradiation would affect the chemical properties of HA, subsequently leading to interactions between HA and RN. Nevertheless, the effect of gamma-irradiated HA on the sorption of RN has not been clarified yet.

This study was aimed at elucidating the dependence of gamma-irradiated HA solutions on the sorption of RNs. It can enable the prediction of radionuclide migration and help establish a sorption coefficient database. For this purpose, this research was conducted on investigating the impact of gamma irradiation on the complexation of HA with non-radioactive Cs and Eu, including the apparent formation constant and the complexation affinity in terms of molecular-weight fractions.

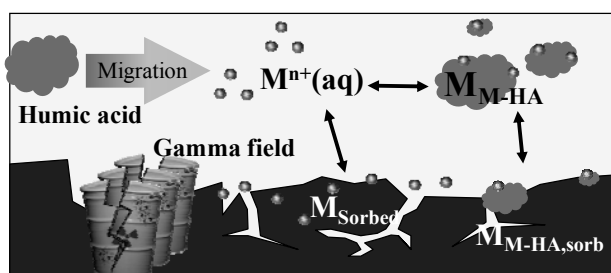


Fig. 1 Typical sorption and complexation of RNs (M) in the presence of humic acid and a groundwater systems.

EXPERIMENTS: The pH of the irradiated HA solution was adjusted to around 8. Stock metal solution was added to the HA solution to obtain an initial metal con-

centration of ca. 10^{-8} mol/dm³. The rock powder was put into a polycarbonate tube. The metal-HA solutions were either not aged or aged for a few months prior to the following process, named as the co-sorption and pre-contact systems. Samples were placed horizontally and shaken gently at room temperature. After a contact time of 1 month, the supernatant was filtered through a membrane filter with a pore size of 0.20 μ m. The filtrates were analyzed using a total organic carbon analyzer and ICP-MS for TOC and metal concentrations, respectively. For comparison, the metal concentration was also measured by using a 10 kDa pore size filter. Recovery experiments were also carried out for the loss of HA and metal ions in the metal-HA system using a 0.20 μ m pore size filter under the same experimental conditions [3].

RESULTS: Batch sorption experiments were performed to evaluate the effect of gamma-irradiated HA on the sorption reactions of Cs and Eu at neutral pH. The purified Aldrich HA in solution was irradiated by a ⁶⁰Co source at KURNS of gamma rays up to 100 kGy. The irradiation reduced the sorption coefficients of the HA molecules.

In the absence of HA, the sorption coefficient of trivalent Eu ions was as high as the reported values. In the presence of non-irradiated HA, the sorption of Eu complexed with HA was suppressed owing to the formation of neutral or negatively charged complexes in aqueous phase. Although the ratio of HA- and non-complexed species was more than 10, the ratio in the solid phase was less than 1. The ratio was evaluated based on the difference in metal and TOC concentration solutions filtered by a different pore size filter. The result indicated the ratios decreased with dose, suggesting that the metal complexation affinity of the decomposed fragments of HA was lower than that of the non-irradiated one.

On the other hand, the Cs sorption was not affected by HA and the gamma irradiation dose, probably due to a weak complexation ability of monovalent cation with HA. And, it indicates an insignificant contribution of HA to Cs sorption onto the rock surface. This new method to evaluate the molecular-weight distribution of species in liquid and solid would provide more quantitative findings of the impact of HA on the sorption of metal ions onto rock sample. Further experimental investigation of the sorption mechanism will provide more detailed insight into the different impacts of HA on RNs.

REFERENCES:

- [1] J.F. McCarthy *et al.*, T.C.J. Yeh, Water Resour. Res. 32 (1996), 1223–1238.
- [2] J.F. McCarthy *et al.*, Hydrol. 30 (1998), 49–77.
- [3] Qi Zhao *et al.*, J. Hazard. Mater., Vol. 428, 128211, 2022.

CO9-2 Solid phase transformation of lanthanide oxide to hydroxide in aqueous solutions

T. Kobayashi, R. Nanjo, Y. Sato, T. Sasaki, R. Motokawa¹, S. Sekimoto², K. Mori², K. Takamiya²

Graduate School of Engineering, Kyoto University

¹ Japan Atomic Energy Agency

² Institute for Integrated Radiation and Nuclear Science, Kyoto University

INTRODUCTION: For the safety assessment of high-level radioactive waste disposal, it is important to establish a robust prediction of the migration behavior of radionuclides under relevant disposal conditions. Actinides with long-half-lives behave as polyvalent metal ions and easily hydrolyzed to form amorphous hydroxide precipitates at neutral pH of groundwater. The sparingly soluble amorphous hydroxides are considered to play as solubility-limiting solid phases to dominate the migration behavior of actinides [1]. However, due to decay heat from the high-level waste, the amorphous hydroxides are possibly transformed into more thermodynamically stable solid phases during the long-time migration scenario. On the other hand, some of crystalline oxides known as stable solid phases are reported to be partly converted to hydroxides in aqueous solutions under certain conditions [2]. Although it is necessary to elucidate the stable state of solid phase in long-term disposal system, there are still some open questions on the stability of hydroxide-oxide solid phases in aqueous solutions. In the present study, we focus on the trivalent lanthanum oxide-hydroxide solid phases as chemical analogous of trivalent americium and curium. Lanthanum crystalline oxide was prepared and aged in aqueous solutions at 90 °C. After given aging periods, the solid phases were investigated by X-ray and neutron diffraction techniques.

EXPERIMENTS: Lanthanum oxide (La_2O_3) were purchased from the manufacturer and heat at 1000 °C for 2 hours to remove possible residual hydroxides. Then given amount of La_2O_3 was added in a sample solution. The sample solution was prepared by D_2O and the initial pH was adjusted to pH 8 by DCI/NaOD with small portion of pH buffer (TAPS). The ionic strength (I) was set to $I = 0.1$ by adding appropriate amount of NaClO_4 . After the sample solution with the solid phase was heated at 90 °C for 1, 3, 7 hours, the solid phase was separated and dried. In order to prevent the possible contamination of proton (H) and possible transformation by atmospheric H_2O , preparation of sample solution, aging, and drying were performed in an Ar glove box. The X-ray diffraction patterns were collected by Smartlab (Rigaku), The neutron diffraction pattern was collected by the versatile compact neutron diffractometer (VCND) located at the B-3 beam port of the Kyoto University research reactor (KUR) [3]. A Cu monochromator with 40 mm diameter was used to monochromatize the neutron wavelength of 1.0Å. The beam size was approximately 10 mm in width and 30 mm in height. The beam flux was 1.3×10^5 n/s·

cm^2 during the operation at the power of 5 MW on KUR.

RESULTS: Figure 1 shows the X-ray and neutron diffraction patterns of initial La_2O_3 and the solid phase after aging at 90 °C for 1 hour. The X-axis represent the lattice plane spacing d ($d = \lambda/2 \sin \theta$, $\lambda = 1.54$ Å for X-ray diffraction and $\lambda = 1.0$ Å for neutron diffraction). By comparing the XRD patterns before and after the aging, peaks corresponding to La_2O_3 disappeared and those corresponding to $\text{La}(\text{OH})_3$ appeared. This indicated that the initial La_2O_3 almost completely converted to crystalline $\text{La}(\text{OH})_3$ even after 1 hour. The XRD patterns of the solid phases after 3 and 7 hours aging were found to show no significant difference to that after 1 hour. Figure 1 also shows the neutron diffraction patterns of before and after the aging. The pattern seems to include both peaks corresponding to La_2O_3 and $\text{La}(\text{OH})_3$. Further confirmation is needed by the measurement of longer aging periods.

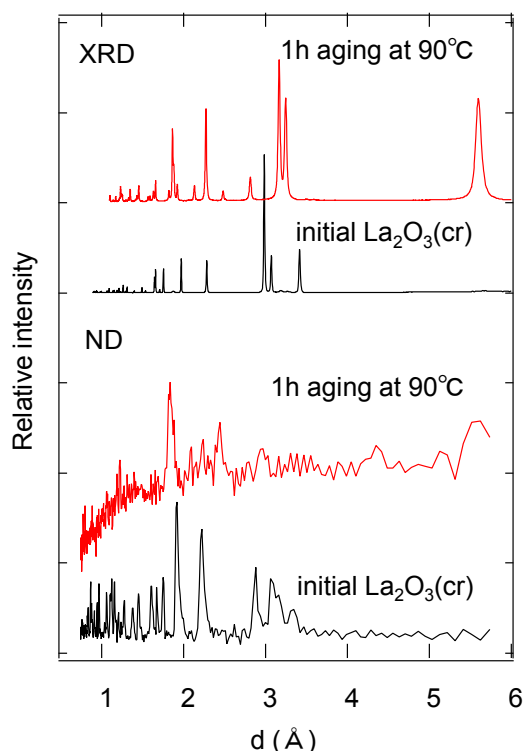


Fig. 1. X-ray and neutron diffraction patterns of initial La_2O_3 and the solid phase after aging at 90 °C for 1 hour.

REFERENCES:

- [1] 包括的技術報告:わが国における安全な地層処分の実現—適切なサイトの選定に向けたセーフティケースの構築—, NUMO-TR-20-03 (2021).
- [2] Md.Moniruzzaman *et al.*, J. Nucl. Radiochem. Sci., 20,32-42 (2020).
- [3] K. Mori *et al.*, JPS Cnf.Proc., 33, 011093 (2021).

CO9-3 Electrochemical U dissolution from U-Ru alloy in LiCl-KCl-UCl₃ melt

T. Murakami¹, Y. Sakamura¹, K. Uozumi¹ and K. Takamiya²

¹Central Research Institute of Electric Power Industry

²Institute for Integrated Radiation and Nuclear Science, Kyoto University

INTRODUCTION: Electrochemical dissolution of actinides in molten chloride salt is performed in electrorefining process of spent metallic fuels. Since part of actinides exists as alloys with noble metal fission products in spent metallic fuels [1], for the purpose of achieving a high dissolution ratio of actinides from the spent metallic fuels, it is necessary to accumulate the basic knowledge on the actinide dissolution from actinide-noble metal alloys. As one of actinides-noble metal alloys, this study focused on U-Ru alloy and electrochemical dissolution of U from U-Ru alloy was investigated in LiCl-KCl-UCl₃ melt.

EXPERIMENTS: All experiments were performed in an Ar atmosphere glove box. Cyclic voltammetry, one of the electrochemical measurements, was performed using a Ru metal plate and a W wire as the working electrode in LiCl-KCl eutectic salt containing 0.16 mol% UCl₃ at 723, 773 and 823 K. The counter electrode was a glassy carbon rod. The reference electrode was Ag/AgCl electrode which was composed of a Ag wire immersed in LiCl-KCl-AgCl melt loaded in a pyrex glass tube.

RESULTS: Since W forms no alloy with U, a cathodic current, c1, and the corresponding anodic current, a1, observed at around -1.4 V (vs. Ag/AgCl) in Fig. 1 were ascribed to U metal deposition and the dissolution of the deposited U metal (reaction 1), respectively,



Another cathodic and anodic current couple (c2 and a2) was seen at around -0.2 V, corresponding to the U³⁺/U⁴⁺ redox reaction (U⁴⁺ + e⁻ = U³⁺).

Fig. 2 shows cyclic voltammograms of the Ru plate electrode in the melt at 723, 773 and 823 K. In addition to the cathodic and anodic current couples ascribing to U metal deposition and dissolution (c1 and a1) and U³⁺/U⁴⁺ redox reaction (c2 and a2), several cathodic and anodic currents were observed. Taking into account that five alloy phases, U₂Ru, URu, U₃Ru₄, U₃Ru₅ and URu₃, exist in U-Ru binary system [2], it was considered that the cathodic currents corresponded to U³⁺ reduction on the Ru plate to form U-Ru alloys and the anodic currents were due to the U dissolution from the formed U-Ru alloys (reaction 2),



The results of Fig. 2 also indicated that most part of U could be anodically dissolved from U-Ru alloy by keeping the anode potential at more positive potential than -1.0 V at the electrorefining process. As the future study, it is necessary to investigate the anodic dissolution behavior of U from U-noble metal fission products alloys other than U-Ru alloy to evaluate the electrolysis condition of electrorefining process with a high dissolution

ratio of U from spent metallic fuels.

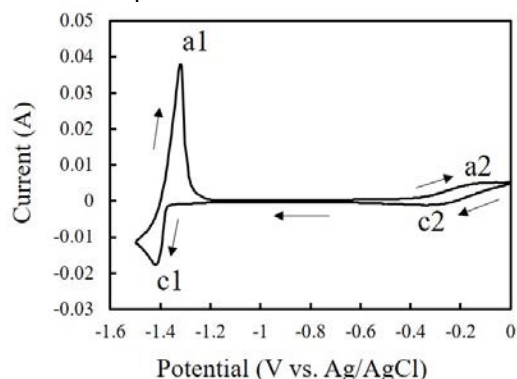


Fig. 1 Cyclic voltammogram of the W wire electrode (1 mmφ, immersion depth of 7 mm into the melt) in LiCl-KCl-0.16mol%UCl₃ melt at 773 K. Scan rate was 50 mVs⁻¹.

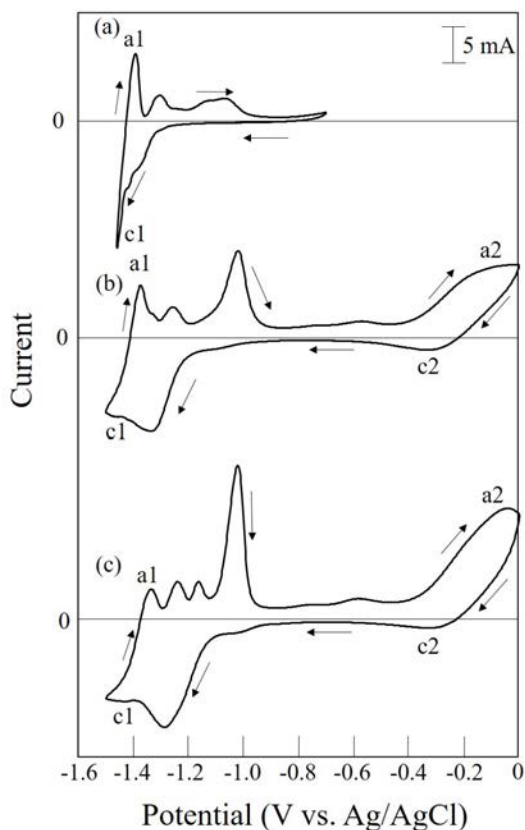


Fig. 2 Cyclic voltammograms of the Ru plate electrode in LiCl-KCl-0.16mol%UCl₃ melt at (a) 723 K, (b) 773 K and (c) 823 K. Scan rate was 20 mVs⁻¹. The effective electrode dimension was (a) 1×2×7 mm, (b) and (c) 1×2×8 mm.

REFERENCES:

- [1] K. Inagaki *et al.*, Trans. Am. Nucl. Soc., **110** (2014) 786-787.
- [2] T. B. Massalski ed., BINARY ALLOY PHASE DIAGRAMS SECOND EDITION, ASM International, Materials Park, OH (1990).

CO9-4 The solvent extraction behavior of Eu and Tb in nitric acid solution using TDdDGA

M. Ikeno, C. Saiga, S. Takahashi, C. Kato, T. Matsumura¹, H. Suzuki¹, S. Fukutani² and T. Fujii

Graduate School of Engineering, Osaka University

¹Nuclear Science and Engineering Center, Japan Atomic Energy Agency

²Institute for Integrated Radiation and Nuclear Science, Kyoto University

INTRODUCTION: For the long-term use of nuclear power plants, it is essential to make further progress in the technology for the processing of radioactive waste contained in the spent nuclear fuel. In response to this situation, JAEA has developed the “SELECT process” as a part of the technology for separation and transmutation of radioactive nuclides from radioactive liquid waste [e.g. 1]. In this process, several extractants suitable for different applications have been considered for the extraction of minor actinides (MAs) and rare earth elements (REEs) from radioactive liquid waste. More detailed studies to expand knowledge of the chemical extraction behavior between these extractants and radioactive elements are needed. We focused on europium (Eu), which is a radioactive element contained in the spent nuclear fuel. Europium concentration in the spent nuclear fuel can be up to ~0.52 g/L [2] and the isotopes ¹⁵⁴Eu and ¹⁵⁵Eu have a half-life of 8.6 years and 4.8 years respectively [3] posing as a threat to the recycling process. In order to understand its chemical behavior during the extraction reaction, a new extractant, *N,N,N',N'*-tetradodecyl diglycolamide (TDdDGA) was used to with the solvent extraction method to determine its chemical properties. In addition, terbium (Tb), which is also a lanthanide and has similar properties to Eu, was studied and the results were compared.

EXPERIMENTS: For the HNO₃ concentration dependency, TDdDGA was used as the extractant and a mixed solution of n-Dodecane and 1-Octanol was used as solvents to adjust the TDdDGA concentration to 0.01, 0.02, 0.04 and 0.10 M. For the aqueous phase, 1 ppm of Eu or Tb was added to HNO₃ 1.5 M. Both phases were stirred for 30 mins to reach equilibrium. The solution was separated by centrifugation and the aqueous phase was exchanged with a 0.1 M HNO₃ solution and back extraction was performed. The Eu and Tb concentrations of the aqueous phase before and after both extractions were measured by Inductively Coupled Plasma Quadrupole Mass Spectrometry (ICP-QMS) at Kyoto University, and the distribution ratios were determined. Furthermore, fluorescence spectra were measured to observe the com-

plex structure in the organic solutions after fore extraction. All experiments were carried out at room temperature.

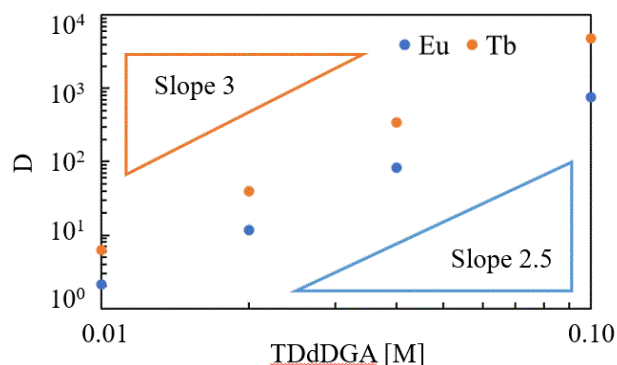


Fig 1. Dependence of D on TDdDGA for Eu and Tb. Tb has a higher D compared to Eu.

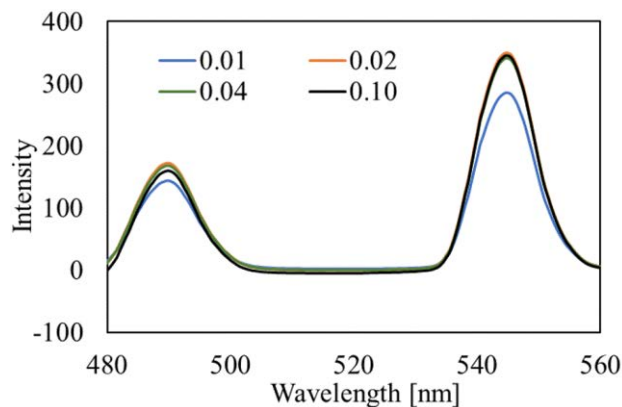


Fig 2. Fluorescence spectra of Tb with various TDdDGA concentrations.

RESULTS AND DISCUSSIONS: The solvent extraction and fluorescence spectra results are shown in Figs 1 and 2. Terbium was consistently up to 10 times higher in distribution ratios at all extractant concentrations compared to Eu. From the extraction reaction and slope analysis, it is suggested that a TDdDGA : Eu = 3 : 1 complex had formed and the complex structure did not change with the increase in extractant concentration. For Tb, it was also suggested that a complex of TDdDGA : Tb = 3 : 1 formed. However, since the fluorescence spectra intensity increased between TDdDGA 0.01 M and above, this indicates the existence of multiple complex structures can be formed with Tb and that there is a distinct difference between 0.01 M and 0.02 M or higher.

REFERENCES:

- [1] T. Matsumura., *Kino Zairyo* **40** 60-71 (2020).
- [2] JAEA-Review, 2008-037 (2008).
- [3] G. Audi. *et al.*, *Nucl. Phys. A*, **729** 3-128 (2003).

CO9-5 Solid-liquid extraction of Ca, Sr, Ba, Ra with crown ether toward the chemical study of nobelium

E. Watanabe,^{1,2} Y. Kasamatsu,^{1,2} R. Nakanishi,^{1,2}
S. Otaka,^{1,2} K. Takamiya³ and A. Shinohara^{4,5}

¹Graduate School of Science, Osaka University

²RIKEN Nishina Center for Accelerator-Based Science

³Institute for Integrated Radiation and Nuclear Science,
Kyoto University

⁴Institute for Radiation Science, Osaka University

⁵Osaka Aoyama University

INTRODUCTION: Nobelium (No) is an actinide element with atomic number 102. While other f-block elements are stable at +3 or higher valence states in aqueous solutions, No is considered to form +2 valence state stably because of its electronic configuration $[Rn]5f^{14} 7s^2$. Previous ion-exchange experiments have reported that No exhibits similar chemical behavior to that of Ca^{2+} and Sr^{2+} [1]. Our group has recently suggested that No^{2+} shows different behavior from alkaline earth metal ions, in the samarium hydroxide coprecipitation [2]. Further systematic studies are needed on the No^{2+} comparing with group II elements from the viewpoint of molecular structure in the solution and its electronic structure.

We focus on solid-liquid extraction using crown ether. Sr resin, commercially available crown-ether supported resin, has extraction selectivity for alkaline earth ions, and this selectivity is sensitive to change by type of acid of a liquid phase and its concentration [3,4].

This study aims to investigate the extraction behavior of No^{2+} in the Sr resin system and the bonding properties of No^{2+} -crown complexes. To obtain a distribution coefficient (K_d) of ^{255}No , which has a half-life of 3.5 min, chemical reaction in the extraction systems must rapidly reach chemical equilibrium. In this study, solid-liquid extraction experiments of ^{47}Ca , ^{85}Sr , ^{133}Ba , and ^{226}Ra were conducted to investigate the applicability of Sr resin extraction system for ^{255}No experiments.

EXPERIMENTS: 0.5-2 mL of HNO_3 or HCl solutions containing the radiotracers ^{47}Ca , ^{85}Sr , ^{133}Ba , and ^{226}Ra were contacted with 50-500 mg of Sr resin and shaken for 1-1440 minutes. ^{47}Sr , ^{85}Ba , and ^{133}Ra are produced by AVF cyclotron at RIKEN Nishina Center and had no carrier (no matrix elements), while ^{47}Ca was produced by neutron irradiation to ^{nat}CaO powder at KURNS and had carrier about 1 mg / mL Ca dissolved. After extraction experiments, only the liquid phase was taken by centrifugation, and the γ rays of each nuclide were measured with a Ge semiconductor detector. A sample without resin was also prepared. K_d was calculated by the equation

$$K_d = (A_{STD} - A_s)V / A_s w,$$

where A_s and A_{STD} are radioactivities of the aqueous phase of the extraction sample and the control sample, respectively; V is the volume of the aqueous phase (mL);

and w is the mass of the dry resin (g). The A values for each nuclide were appropriately corrected considering their respective half-lives.

RESULTS: Figure 1 shows the K_d values in 3.5 M HNO_3 as a function of shaking time. For Sr, Ba, and Ra, the extraction equilibrium was reached within 1 min. On the other hand, it took about 5 minutes for Ca to reach chemical equilibrium. This difference may be caused by the fact that only the Ca sample contained a macro amount of carriers. It is important to examine the change in the K_d values of ^{255}No for shaking times 1-5 min.

In both nitric and hydrochloric acid systems, the K_d values of Ca are significantly lower than that of Sr, Ba, and Ra. Since ionic radius and available coordination number of Ca^{2+} is small, the extracted species, $Ca^{2+}(NO_3)_2$ -crown, may have lower stability.

We will obtain the K_d values of ^{255}No in Sr resin system using the batch-type solid-liquid extraction apparatus developed in our previous study [5]. We also plan to conduct an X-ray absorption spectroscopy study to obtain the detailed molecular structure of the extracted Ca^{2+} -crown complexes.

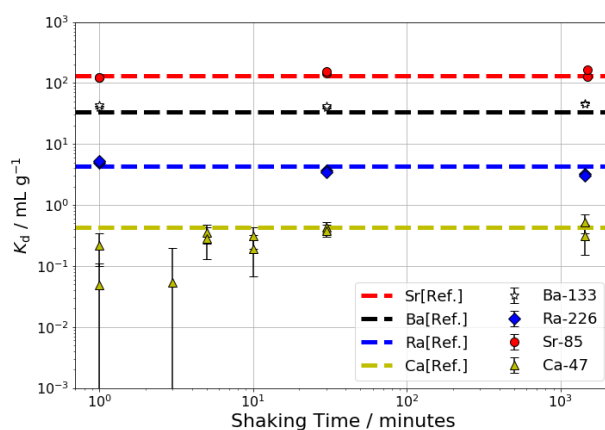


Figure 1. The K_d values of ^{47}Ca , ^{85}Sr , ^{133}Ba , ^{226}Ra in Sr resin / 3.5 M HNO_3 system (dashed lines indicate the values obtained in reference [3]).

REFERENCES:

- [1] R. Silva *et al.*, *Inorg. Chem.*, **13** (1974) 2233.
- [2] H. Ninomiya, Master thesis, Osaka University (2019).
- [3] E. P. Horwitz *et al.*, *Solv. Extr. Ion Exch.*, **10** (1992) 313.
- [4] D. V. Filosofov *et al.*, *Solv. Extr. Ion Exch.*, **33** (2015) 496.
- [5] Y. Kasamatsu *et al.*, *Radiochim. Acta*, **103** (2015) 513.

CO9-6 Determination of Uranium in Fallout Using Fission-Track Analysis

K. Takamiya, N. Toe, M. Inagaki, S. Sekimoto, Y. Oki and T. Ohtsuki

Institute for Integrated Radiation and Nuclear Science, Kyoto University

INTRODUCTION: A large amount of radioactive materials were released to the environment by the severe accident of Fukushima Daiichi Nuclear Plant in 2011. One of the major radioactive components of the released materials are radio-caesium, but there contained a small amount of uranium [1]. Insoluble radioactive particles which is one of the important chemical forms of fallout materials were found in the environment, and a part of them also contain uranium component [2]. The radioactivity of uranium in fallouts is so large to affect human health, but the uranium is an important fingerprint of melted nuclear fuel of the power plant. In the case of radio-caesium, the quantity in insoluble particles can be determined by measurement of gamma-ray spectrum, but it is difficult to determine the uranium component because of their low radioactivity. Fission track method is one of the useful techniques to determine a small amount of fissile materials [3]. In the present work, a standard environmental sample which contains uranium were subjected to the fission-track analysis to investigate experimental conditions for determination of the uranium in fallout materials.

EXPERIMENTS: The standard environment sample of IAEA-384 which contains comparable amount of uranium as soils in Japan has been irradiated by neutrons to produce fission tracks on a polycarbonate detector (BARYOTRAK, Fukubi Chemical Industry). Several mg of the fine particles of the sample were scattered on the detector surface and wrapped by a paraffin film to fix particles on the detector. Samples with detectors were irradiated by neutrons using TC-Pn irradiation facility at the power of 1 MW on KUR. The irradiation time varies from 1 to 60 min. After the irradiation, sample particles were removed from the detector together with the film. Fission tracks were etched in the detector with a solution of 8 mol/L sodium hydroxide at 70°C for 1 hour. Detectors were washed by pure water and the etched tracks were observed by using optical microscope.

RESULTS: Examples of image of fission tracks are shown in Fig. 1. The upper and lower panels indicate the images obtained by irradiation for 10 and 60 min, respectively. Fission tracks were produced all over the surface of both detectors. There found several clusters of tracks in both images but not in the image of 1-min irradiation. The clusters might indicate existence of highly concentrated uranium. Because the concentration of uranium in fallout materials released from the nuclear power plant is expected to be higher than that of the sample used in the present work, it was found that the fallout materials con-

taining uranium can be clearly identified from soil and other natural particles by fission-track analysis. In the case of identification of fallout materials from the nuclear power plant, the irradiation time shorter than 10 min might be effective because cluster of tracks can be produced by only the fallouts but not by soil and other natural particles.

In the near future, we will try to determine the uranium concentration in fallout materials using fission-track analysis. And this method could be applied to detection of insoluble particles produced by nuclear incident such as explosion of an atomic bomb.

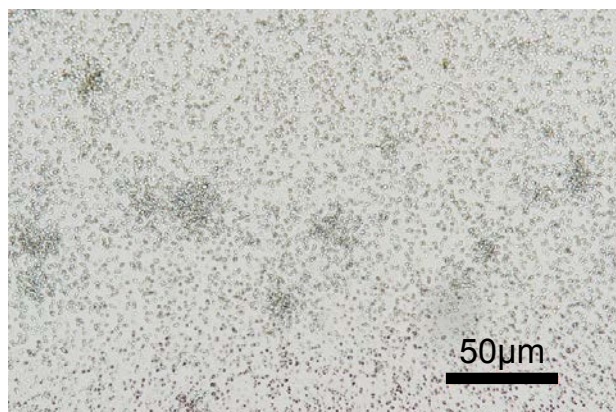
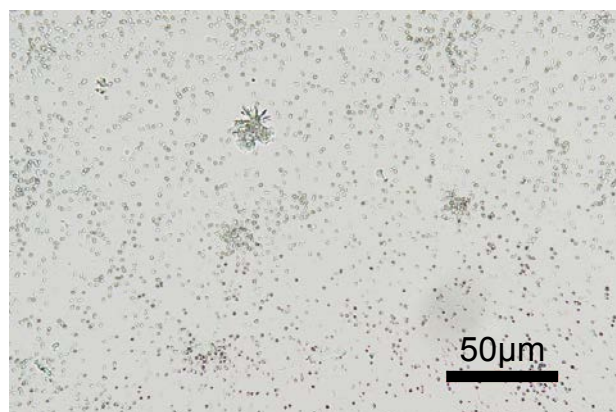


Fig. Tracks produced on the surface of the detector by irradiation of IAEA-384. Upper and lower panels show images observed by irradiations for 10 and 60 min, respectively.

REFERENCES:

- [1] Y. Shibahara *et al.*, *J. Radioanal. Nucl. Chem.* **303**, 1421-1424 (2015).
- [2] Y. Abe *et al.*, *Analytical Chemistry* **86**, 8521-8525 (2014).
- [3] F. Esaka *et al.*, *Analytical Chemistry* **87**, 3107-3113 (2015).

CO9-7 Measurement of X-ray of Pd-103 with a CdZnTe semiconductor detector

T. Kubota¹, S. Fukutani², and Y. Shibahara²

¹Agency for Health, Safety and Environment, Kyoto University

²Institute for Integrated Radiation and Nuclear Science, Kyoto University

INTRODUCTION: Palladium-107 is one of long half-life nuclides in high level radioactive waste. It undergoes only beta decay with a half-life is 6.5×10^6 y. Its migration in the environmental and the following inner exposure is a concern for safety assessment [1]. In the assessment with radiochemical methods, Pd-103 would be used as a tracer with an appropriate length of half-life; however, its low gamma ray emission rate is unfavorable. Nevertheless, the emission rate of X-ray around energy of 20 keV from Pd-103 is much higher, which provides the possibility to make quantitative analysis. The acquisition of photon energy spectra is usually used by a Ge(Li) semiconductor detector. However, it cannot measure such low energy region. In this report the photon spectrum of Pd-103 was acquired with a CdZnTe (CZT) semiconductor detector which can detect low-energy photon.

EXPERIMENTS: Pd-103 was produced from Pd-104 through photo nuclear reaction. The powder of PdCl₂ was encapsulated in a quartz tube under vacuum [2]. The PdCl₂ sample was irradiated with high-energy photons generated from the bombardment of platinum with electrons of 30 MeV at KURNS-LINAC. The CZT detector, GR1TM from Kromek Ltd, can be used without cooling and its detector size was 1cm³ [3]. The calibration of the detector was conducted with reference sources containing Am-241, Cd-109, Co-57, Co-60, and Cs-137.

RESULTS: Figure 1 shows the photon spectrum of the reference sources. The CZT detector can measure the low energy photon of 10 keV without interfere by noise. The energy resolution was 1.6 % at 662 keV of Cs-137. The high peak of X-ray from Am-241 and Cd-109 was shown around 20 keV and is overlapped with a small peak probably from Cs-137. This spectrum yields an energy calibration curve in Figure 2, showing its high linearity in a wide energy range. Figure 3 shows the photon spectrum of PdCl₂ two weeks after irradiation. The peak of 357 keV of Pd-103 was hardly shown in the spectrum due to its low emission rate. The large peak shown around 300 keV was identified as Rh-101m of 307 keV produced from Pd-102 through photo nuclear reaction. The large peak shown around 20 keV can be considered as mixed X-ray from Pd-103 and Rh-101m. The purification of Pd-103 from Rh-101m can provide the X-ray source of Pd-103, suitable for radiochemical tracer.

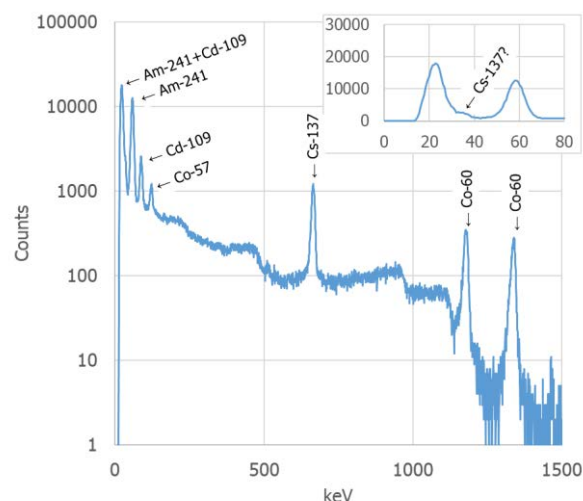


Figure 1 Photon spectrum obtained from mixed reference sources.

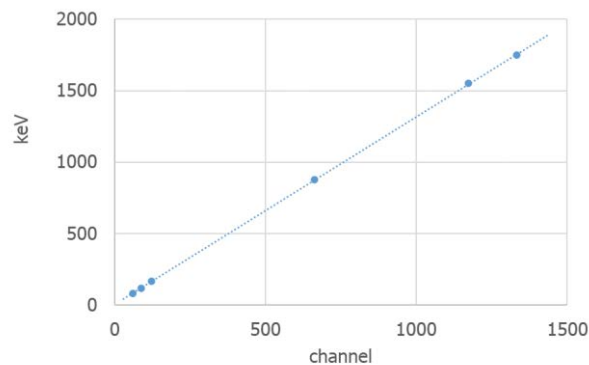


Figure 2 Energy calibration curve evaluated with mixed reference sources.

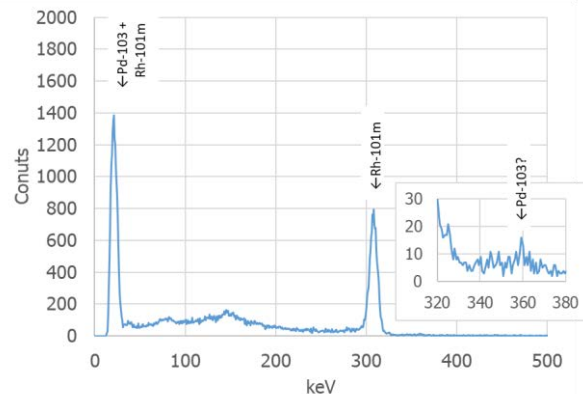


Figure 3 Photon spectrum obtained from irradiated palladium.

REFERENCES:

- [1] K. Iwata *et al.*, Proc. 18th Workshop on Environmental Radioactivity, (2017) 163-166.
- [2] T. Kubota *et al.*, KURNS Progress Report (2018) 209.
- [3] M. Kowatari *et al.*, Radiation Protection Dosimetry (2015), Vol. 167, pp. 348-352.

CO9-8 Effect of Coexistence of Adsorptive Metal Ions on γ -Ray Irradiation for Crown Ether Resin in HNO_3

M. Nogami¹, M. Katsuyama¹, M. Yokota¹, and N. Sato²

¹Faculty of Science and Engineering, Kindai University

²Institute for Integrated Radiation and Nuclear Science, Kyoto University

INTRODUCTION: We have been investigating the applicability of crown ether resins to radioactive liquid wastes treatment. In our earlier study, silica-supported resins consisting of dibenzo-18-crown-6 (DB18C6) (Fig. 1) has been found to adsorb e.g. Pd(II) and Ag(I) in nitric acid media[1]. It has also been revealed that γ -ray irradiation to DB18C6 resin in HNO_3 caused opening of crown ether ring (Fig. 2), resulting in the formation of structure obtaining plural hydroxyl groups without selectivity to the above-mentioned metal ions[2]. These results suggest that coexisting adsorptive metal ions on γ -ray irradiation for crown ether resins may suppress the ring opening, because these metal ions would be captured by DB18C6 resin in a manner of getting stuck in the crown ether ring. In the present study, therefore, γ -ray irradiation behavior to DB18C6 resin in HNO_3 containing Pd(II) and Ag(I), respectively, was investigated.

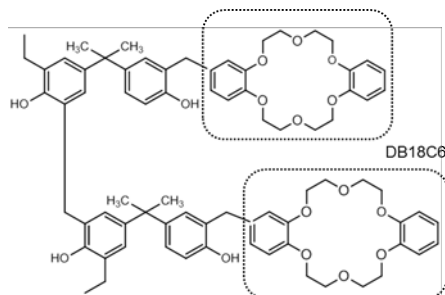


Fig. 1. Chemical structure of DB18C6 resin

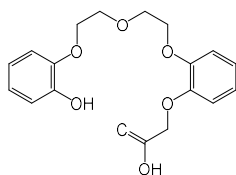


Fig.2. An expected ring opening of DB18C6 by irradiation in HNO_3

EXPERIMENTS: DB18C6 resin was synthesized by following the earlier study[1]. 0.5 mol/dm^3 (=M) HNO_3 containing 10 mM Pd(II) or Ag(I), and 0.5 M HNO_3 as the reference were used as the sample solutions followed by the preparation of in total four irradiation samples shown below :

- (i) DB18C6 resin + 10mM Pd(II) in 0.5 M HNO_3
- (ii) DB18C6 resin + 10mM Ag(I) in 0.5 M HNO_3
- (iii) DB18C6 resin + 0.5 M HNO_3
- (iv) silica support + 10mM Ag(I) in 0.5 M HNO_3

where solid/liquid ratio for every sample was 1 g/5cm^3 . γ -Ray irradiation was carried out similarly to the earlier study (max. 54 kGy)[3]. The irradiated samples underwent solid-liquid separation and concentrations of metal ions for supernatant liquid of samples (i), (ii) and (iv) were measured using ICP-OES. Adsorptivities were evaluated by the distribution ratio, K_d .

RESULTS: In this study, phenomena of interest except irradiation procedure itself were observed for the relationship between DB18C6 resin and metal ions. For Sample (ii), white turbidity was generated in the glass sample tube after preparation of the solution. Afterwards, the turbid compounds were precipitated and white lumps were deposited on the dark brown DB18C6 resin. The concentration of Ag in the supernatant after deposition of white lumps was found to be 0.8 M, meaning that more than 90 % of Ag disappeared from the liquid phase before irradiation. Such a precipitation was not observed in our earlier study, and it is probably because the initial concentration of Ag(I) was 10 times lower (1 mM) than that of this study[1]. On the other hand, such a precipitation was not seen in Sample (iv), either. These results indicate that a precipitation reaction occurred between DB18C6 resin and Ag(I). Ag has been expected to be adsorbed onto DB18C6 resin in the form of Ag(I). However, the expectation should be re-evaluated.

Eventually, the concentration of Ag in the supernatant of Sample (ii) after irradiation was decreased to 0 mM. The result can be expressed as ∞ by evaluating by K_d . K_d value of neat DB18C6 resin for Ag(I) at 0.5 M HNO_3 was ca. 9[1]. Although the direct comparison is impossible because the experimental conditions were not completely identical, it is likely that the irradiated DB18C6 resin still captures Ag in a certain chemical form.

For Sample (i), the concentration of Pd in the supernatant after irradiation was found to be 2.7 mM, which is equivalent to $K_d \approx 13$. K_d value of neat DB18C6 resin for Pd(II) at 0.5 M HNO_3 was ca. 75[1]. Although the direct comparison is impossible due to the similar reason for Ag(I), adsorptivity of DB18C6 resin for Pd(II) is found decreased after irradiation. These results suggest that the opening of crown ether ring by irradiation takes place even under coexistence of Pd(II).

REFERENCES:

- [1] M. Nogami *et al.*, J. Radioanal. Nucl. Chem., **303** (2015) 1549-1553.
- [2] M. Oya *et al.*, ICIE2018, Yogyakarta, Indonesia (2018) ADS-2P.
- [3] N. Miyata *et al.*, KURRI Progress Report 2010 (2011) 258.

CO9-9 Fundamental study on reactor production and separation and purification of β -radioactive materials including Ce-141 for nuclear medicine therapy

T. Yamamura¹, K. Washiyama², C. Tabata¹, R. Okumura¹, K. Ogawa³

¹Institute for Integrated Radiation and Nuclear Science, Kyoto University

²Advanced Clinical Research Center, Fukushima Medical University

³Pharmaceutical Sciences Department, Kanazawa University,

(B-1) ¹⁴⁶Nd (17.2%) (n, γ) ¹⁴⁷Nd (11.0d) \rightarrow ¹⁴⁷Pm (2.6y), ¹⁴⁸Nd (5.8%) (n, γ) ¹⁴⁹Nd (1.73h) \rightarrow ¹⁴⁹Pm(53.1h), (B-2) ¹⁶⁸Er (26.8%) (n, γ) ¹⁶⁹Er (9.4d), ¹⁷⁰Er (14.9%) (n, γ) ¹⁷¹Er (7.5h) \rightarrow ¹⁷¹Tm (1.9y) are possible.

We need several discussions with researchers in this community and trial-error-based experiments of ¹⁷⁷Lu production was put ahead of the present study. The experimental study will be executed in the next KUR machine time.

INTRODUCTION:

Recent investigations on the targeted alpha therapy (TAT) revealed its efficacy in the case of ²²⁵Ac [1] and also the difficulty in the production of ²²⁵Ac. Depending on the target disease and patient's condition, cancer drugs based on β -ray emitting radionuclides (RI's) such as ¹⁷⁷Lu is still competitive in the efficacy of ²²⁵Ac [2]. However, Japan is also very far behind in the production of β -ray emitting RI's that can be produced by neutron irradiation reactions. The author has taken part in the IAEA International Conference "Technical Meeting on State of the Art Research Reactor Based Radioisotope and Radiopharmaceutical Production" on March 22-26, 2021 as the only Japanese participant [2]. It was a valuable opportunity to share best practices in each country, especially information on the production and supply of ¹⁷⁷Lu and the recent ¹⁶⁶Ho radiopharmaceuticals, in addition to the traditional ⁹⁰Y.

For irradiation using the present KUR and the forthcoming Fukui reactor, several requirements holds on the (n, γ) reaction candidates. The reaction have a certain neutron absorption cross section, the isotope abundance ratio of the target nuclide in nature be large, the β -ray energy available for therapy be large, and the half-life be in the range of several days to 20 days. The target and nuclide combinations that satisfy these conditions (Table 1) are (A) ¹⁴⁰Ce(88.5%)(n, γ) ¹⁴¹Ce ($T_{1/2}$ = 32.5d), ¹⁴²Ce(11.1%)(n, γ) ¹⁴³Ce (33.0h) \rightarrow ¹⁴³Pr(13.6d). If the conditions (4) allow for the lifetime of the daughter nuclide to be 1-2 years, then

EXPERIMENTS:

The experiments planned were as follows: RI production using a hydraulic transport tube, which has the highest neutron flux in the reactor at the Combined Research Laboratory of Kyoto University. Ce (50 μ g), Nd (50 μ g), and Er (50 μ g) of atomic absorption standard solutions are dropped into a small quartz beaker, evaporated and dried under an IR lamp, sealed in a polyethylene bag, and placed in an Al irradiation vessel. During the 1-week cooling period, (A) ¹⁴³Pr and (B-1) ¹⁴⁹Pm are produced and are separated from the target by chemical manipulation and purified as carrier-free material. On the other hand, since (A) ¹⁴¹Ce and (B-2) ¹⁶⁹Er have half-lives in the good range in spite of not carrier-free, the amount produced and radioactivity be checked.

REFERENCES:

- [1] Clemens Kratochwil, *et al.*, J. Nucl. Med., 57 (2016) 1941; doi.org/10.2967/jnumed.116.178673
- [2] Richard P. Baum, *et al.*, J. Nucl. Med., 57 (2016) 1006. https://doi.org/10.2967/jnumed.115.168443
- [3] T. Yamamura, RI production for medical applications in Japanese Research Reactors, JRR-3, KUR and future reactor, Technical Meeting on State of the Art Research Reactor Based Radioisotope and Radiopharmaceutical Production, IAEA EVT1904823 (2021) .

Table 1 Classifications of RI's based on several requirements on the (n, γ) reaction candidates.

Classification based on half-life	Elements	Starting nuclide		Product nuclide				Side / Following reactions
		Nuclide	σ [barn]	Nuclide (Mass number)	γ [keV]	β [MeV]	Half-life	
Objective of this study (moderate;10-40 d)	Ce	140 (88.5%)	0.58	141	145	0.4, 0.6	32.5 d	Ce-138 (0.25%) \rightarrow Ce-139 (137.6d)
		142 (11.1%)	0.95	143	293, 57	1.1, 1.4 \rightarrow 0.9	33 h \rightarrow 13.57d	Ce-143 \rightarrow Pr-143
	Nd	146 (17.19%)	1.4	147	91, 531	0.8, 0.9	10.98 d	
		Er	168 (26.8%)	169	169	110	0.3	9.40 d
	170 (14.9%)		6	171	308, 296, 112	1.1, 1.5	7.52 h	
Too short (<3d) #	La	139 (99.9%)	9.0	140	1596, 487	1.4, 2.2	40.2 h	
	Y	89 (100%)	1.25	90	?	2.3	64.1 h	
Too long (>40d)	Tb	159 (100%)	23.1	160	879, 299, 966	0.6, 1.7	72.3 d	
	Tm	169 (100%)	105	170	84	1.0	128.6 d	
	Sc	45 (100%)	15	46	889, 1121	0.4	83.82 d	

CO10-1 Effective Measures on Safety, Security, Hygiene and Disaster Prevention in Laboratories

T. Iimoto¹, M.M. Hasan¹, H. Koike¹, Q. Jin¹, S. Sho¹, K. Fukuda¹, T. Takahashi²

¹ *The University of Tokyo*

² *Institute for Integrated Radiation and Nuclear Science, Kyoto University*

INTRODUCTION: Important aspects of the study can be found in the following keywords, such as safety, security, hygiene and disaster prevention. Nuclear research reactor is one of representative facilities together with these keywords under their operation. It is effective to investigate the latest status on practical measures on these keywords in various facilities including nuclear research reactors, to compare each other among facilities, and to discuss more optimized ones for our positive safety management. Through this process, it is also essential to investigate the latest international and/or national regulations and the movement of revision of them. In addition, development of human resource and public literacy on nuclear science and technology is also within the scope of the research. The total discussion contents and their fruits are directly useful for all relating laboratories.

RESEARCH APPROACH:

General research approach is as follows.

- Measures of safety management during operation or standstill status of the real facilities would be investigated. This information would be used for our research discussion on the positive and more optimized safety management.
- It would not be a single year research, but maybe two to three years research for one theme.
- Information source of facilities would not be only KUR, KUICA or the other facilities in Kyoto University, but also the Kindai university research nuclear reactor or the facility of National Institute of Fusion Science, etc. This research is an active joint-research with these relating facilities and positive researchers on safety management.
- One of the distinctive features of this research is to involve office staffs as cooperators as well as researchers and technical staffs. In The University of Tokyo, most of the members in Division for Environment, Health and Safety are office staffs who knows real situation of safety management in laboratories very well.

Concrete discussion target in FY of 2021 was determined as following two; “local safety management rule for exempted radioactive sources” and “developing a set of educational videos for safety managers and workers in

universities on X-ray application”. IAEA safety standards recommend that nuclear regulators use a graded approach in their oversight of nuclear installations – that is, they adapt the rigorousness of their oversight to the likelihood that something could go wrong with the regulated facility or activity, and the severity of consequences should that happen. Our discussion and research fruits are following the strategy and concept fully.

LOCAL SAFETY MANAGEMENT RULE FOR EXEMPTED RADIOACTIVE SOURCES

The radiation risk of exempted radioactive sources is extremely low, therefore the rule of safety management for them should be followed as graded approach basis. The rule determined in The University of Tokyo is;

1. Procedures for receiving, discharging, and disposing of radiation sources should be performed by the department's radiation control personnel.
2. Departmental radiation control personnel should perform the administrative procedures for transferring and receiving radiation sources.
3. The use and storage of radiation sources should be in accordance with the instructions attached to the sources. In the absence of such instructions, the person in charge of radiation control should check them with Japan Radioisotopes Association (JRIAS).
4. The storage location radiation sources should be determined after appropriate consideration based on the circumstances of the department.
5. The person in charge of radiation control in the department should establish a system to periodically check the actual radiation sources.
6. When a radiation source is disposed of, it should be returned and passed to JRIAS.

DEVELOPING EDUCATIONAL VIDEOS IN UNIV. FOR X-RAY APPLICATION:

Safety education system for managers and users of X-ray has been discussed to standardize it in universities. Based on the discussion results, we developed a set of new safety educational videos, which is 10-15 min for each; (1) Laws and regulations concerning X-rays and the university's management system, (2) Methods of managing research x-ray equipment and electron microscopes, (3) Internal inspection methods for X-Ray Generators, and (4) New management methods for very low-hazard X-ray generators. Especially the contents of (4) was prepared as the local rule of The University of Tokyo, based on the graded approach in an optimized safety management concept. These videos will be opened and used from FY 2022 in The University of Tokyo.

CO10-2 Investigation of a method for analyzing chlorine and bromine in volatile liquid samples in neutron activation analysis

K. Ito¹, T. Fujimori², K. Oshita¹, S. Fukutani³, K. Shiota¹, M. Takaoka¹, S. Takahashi⁴

¹Department of Environmental Engineering, Graduate School of Engineering, Kyoto University

²Faculty of Advanced Science and Technology, Ryukoku University

³KURNS

⁴Graduate School of Agriculture, Ehime University

INTRODUCTION: Among organochlorine and bromine compounds, persistent organic pollutants (POPs) are subject to international regulation, but the number of POPs is increasing year by year, so extractable organochlorine (EOCl) and extractable organobromine (EOBr) have attracted attention as a comprehensive risk assessment including related and alternative substances [1]. However, from a safety perspective, it is necessary to volatilize the liquid content of volatile liquid samples and measure them as solid samples [2]. However, the large chlorine and bromine content of filter paper, which is used as a medium to attach components to, has limited the quantification of EOCl and EOBr. Therefore, the objective of this study was to investigate alternative materials to the filter paper used in sample preparation. Empty samples were prepared using various materials to determine the amount of chlorine and bromine as background, and the ability of those to attach components was compared using extracts of sediment samples.

EXPERIMENTS: Material was prepared in a polyethylene (PE) bag for background measurements (in Table1), binding it with a sealer, and then sealing it with a double PE bag. The weight of the materials was not standardized among the materials, but they were placed in the bags so that they were almost the same in volume. The sediment samples were Soxhlet extracted with toluene and inorganic halogens were removed using sodium sulfate solution, dropped into a PE bag containing materials, allowed to dry and solidify for 12 hours at room temperature and pressure, then

Sample	Contents
No Materials	Only PE Bag
PE Sheet	PE Bag + Cut up PE sheet
Glass Wool	PE Bag + Glass Wool
Washed Filter	PE Bag + Washed Filter Paper ^a
Filter Paper(1/8)	PE Bag + 1/8 size cut Filter Paper
Filter Paper(1/4)	PE Bag + 1/4 size cut Filter Paper

Table1. Prepared sample names and their contents. ^a Filter Paper which washed by ultra pure water and hexane and dried.

bound with a sealer, and further sealed with a double PE bag. As a standard sample, a mixed aqueous solution of ammonium chloride and ammonium bromide was dropped onto filter paper (1/8, unwashed) in a PE bag. Samples were irradiated for 15 min with a thermal neutron flux of $2.0\text{--}2.4 \times 10^{13} \text{ cm}^{-2} \cdot \text{s}^{-1}$ at KURNS. ³⁸Cl ($t_{1/2} = 37.18 \text{ min}$, $E_{\gamma} = 1642, 2168 \text{ keV}$) and ⁸⁰Br ($t_{1/2} = 17.6 \text{ min}$, $E_{\gamma} = 616 \text{ keV}$) were measured by using a Ge semiconductor detector for 300 sec. Concentrations in the sediment samples were calculated using the comparison method between those and standard samples minus the amount of chlorine and bromine from the PE bag and each material.

RESULTS: Figure1(A) shows the results of the background measurement and Figure1(B) shows the results of the concentration measurement of the sediment. In Figure1(A), filter paper contains more chlorine and bromine than other materials, and the use of filter paper more than doubles the amount of chlorine and bromine of background-origin, so it is better to use other materials. Figure1(B) shows that there was no significant difference in the sediment concentration of about 5 $\mu\text{g/g}$ for any of the materials. Note that the filter paper (1/4 size) has a higher sediment concentration of 9.2 $\mu\text{g/g}$, but this data includes the effect of background chlorine (especially from filter paper) because the calculation method has not been improved. The results indicate that there is no significant difference in the role of each material in "attracting" extracted components, and it is clear that sediment concentration can be obtained without the inclusion of any media. In addition, the standard error of the sediment concentration showed a large variation when quartz cotton was used.

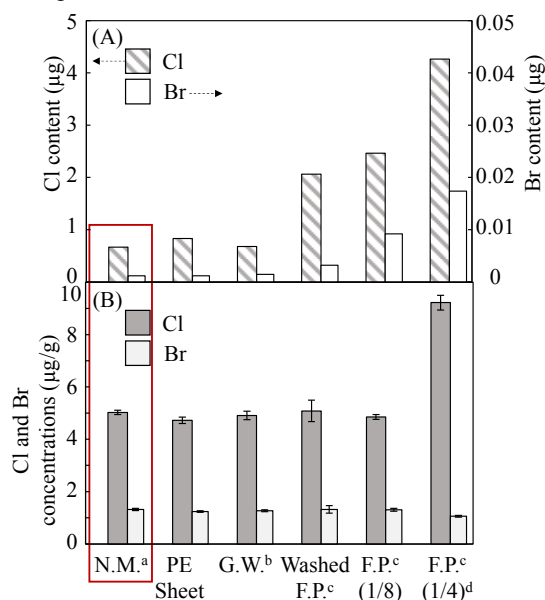


Figure1. (A) is the Cl and Bromine content ($\mu\text{g/g}$) as backgrounds in each samples. (B) is the concentrations of EOCl and EOBr in the sediment samples. ^aN.M. means No Materials, ^bG.W. means Glass wool, ^cF.P. means Filter Paper.

This study aimed to find an alternative material to filter paper, and it became clear that the most appropriate method was to drop only the extracted solution directly into a PE bag without any contents; the PE bag alone would also serve as a medium for the extracted components, minimizing the amount of chlorine and bromine of background-origin, thus allowing for low-concentration samples to be more accurate calculations can be made. On the other hand, the filter paper was used in the standard sample, and it is desirable to investigate the same method can be applied to aqueous solution in the future.

REFERENCES:

[1], [2] Mukai *et al.* (2021) Science of the Total Environment. 756, 143843.

CO10-3 Development of the Evaluation Method of Dose Reduction Effects by Reverse Tillage in the Forest Using the Point-Kernel Integration Method

Y. Sogabe¹, M. Yoneda¹, Y. Shimada¹, S. Fukutani², M. Ikegami²

¹Graduate School of Engineering, Kyoto University

²Institute for Integrated Radiation and Nuclear Science, Kyoto University

INTRODUCTION: Decontamination of forests contaminated by the Fukushima Daiichi Nuclear Power Plant accident in March 2011 is required. In this study, we considered decontamination using the reverse tillage method as a method to reduce the radiation dose in the air without generating soil to be removed. In this method, the upper layer of soil with a high concentration of radioactive Cs is replaced with the lower layer with a low concentration to decrease the radiation dose in the air. Therefore, we develop a calculation method using QAD-CGGP2R, a direct ray calculation code based on the point-kernel integration method, and G33-GP2R, a sky shine calculation code, as a method for evaluating air dose that also takes land use classification and forest topography conditions into account. Using the developed calculation method and data obtained in actual forests in Fukushima Prefecture for the implementation of our KURNS Collaboration Research, we evaluate the reduction effect of air dose when the reverse tillage is implemented in those forests.

CALCULATION METHOD: The following procedure is used to evaluate the dose reduction effect of the reverse tillage in the forests. 1) Conduct a field survey to measure the density of trees, distribution of Cs concentration in the soil, and distribution of air dose in the forest. 2) Determine the area to be evaluated for radiation dose. In order to calculate the radiation dose in this area, it is necessary to calculate the radiation dose from outside the assessment area, and in determining this calculation area, it is necessary to include sufficiently distant locations that will not have much effect on the calculated air dose in the assessment area. 3) The forest to be calculated is modeled as a collection of rectangular bodies. Determine the spacing of the point sources for splitting the volume sources and the spacing of the scattering points for calculating skyshine. In determining the size of the rectangular bodies for modeling these fields and the spacing, set them as large as possible to save computation time, to the extent that they do not affect the calculated doses at the dosimetry points too much. 4) To perform calculations using existing calculation codes, an input file describing the settings of the above calculation conditions is required. However, because it is difficult to input these settings for each calculation, we developed a program to automatically create the necessary input files and perform the calculations.

The calculation code expresses the area as a collection of rectangles, but the following innovations were made to algorithmize the calculation method and shorten

the calculation time. First, we used data from the National Land Information System (NLDIS) as the elevation, and classified land types by visually classifying google earth photos into rough land types, and created a program that automatically identifies which land type each mesh for the calculation is included in. Next, in order to reduce the total amount of calculation while maintaining the accuracy of the calculation in the evaluation target area, the elevation mesh to represent the field and the source mesh to represent the distribution of radiation sources were made larger the further they were from the evaluation target area. Furthermore, for the radioactivity distribution in the subsurface direction, we considered the equivalent depth as the depth at which the calculated value of the dose at the evaluation point is the same whether the radioactivity distribution in the depth direction is taken into account or the total radioactivity in the depth direction is concentrated at a single point. This reduces the number of vertical rectangles and point sources. Then, calculations were performed based on measured data at the site, and the calculation accuracy was verified by comparing it with the measured data of air dose. In this study, we evaluated the dose reduction effects of several construction scenarios, in which the depth, extent, and percentage of the construction work to be done by the reverse tillage were varied. The percentage of construction means the percentage of the construction area that could actually be constructed, because it is difficult to completely construct a certain area due to the presence of tree roots and other factors.

RESULTS: The results of the analysis showed that the error between the measured and calculated values ranged from -38 to 54% (average -4.8%). The main cause of this error was considered to be that the calculation was performed assuming that the distribution of radioactivity in the soil was uniform over the entire area, and the accuracy of the calculation could be improved if the horizontal distribution of radioactivity concentration in the soil was taken into account. The construction scenarios evaluated in this study were the following four patterns. (1) 17m x 20m, with the upper layer (2cm organic layer + 0-20cm soil layer) and the lower layer (20-40cm soil layer) turned over
(2) 17m x 20m with upper layer (2cm organic layer + 0-20cm soil layer) and lower layer (20-50cm soil layer)
(3) 30.6m x 28m, with the upper layer (2cm organic layer + 0-20cm soil layer) and the lower layer (20-50cm soil layer)
(4) 17m x 20m, 80% of upper layer (2cm organic layer + 0-20cm soil layer) and lower layer (20-40cm soil layer) are returned over, and 20% are not turned over. The calculations resulted in air dose reductions of 32-70 (average 57)% for (1), 6-77 (average 63)% for (2), 38-80 (average 70)% for (3), and 29-65 (average 53)% for (4) within the construction area.

CO10-4 Application of KURAMA-II to Radiation Monitoring of Public Facilities in Fukushima Prefecture

A. Maekawa, K. Kusakabe, H. Inoue and M. Tanigaki¹

Fukushima Prefectural Centre for Environmental Creation
¹Institute for Integrated Radiation and Nuclear Science,
 Kyoto University

INTRODUCTION: KURAMA (Kyoto University Radiation Mapping system)-II is a radiation measurement system characterized by its compactness, autonomous operation, and acquisition of pulse-height spectrum data (Fig. 1) [1]. KURAMA-II measures ambient dose equivalent rate (hereafter referred to as air dose rate) and GPS position and automatically transmits them to a dedicated cloud server. We evaluated the effectiveness of a backpack style KURAMA-II (Fig. 2) for the radiation monitoring of public facilities in Fukushima prefecture by comparing it with a NaI(Tl) scintillation survey meter conventionally used in radiation monitoring.

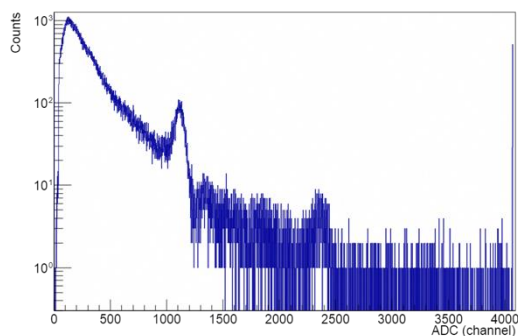


Fig. 1. A typical example of pulse-height spectrum obtained by KURAMA-II measurement.

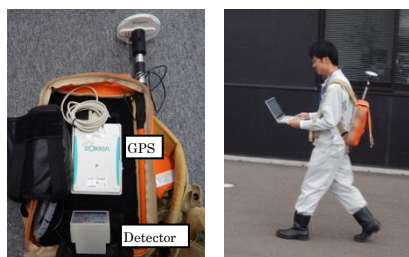


Fig. 2. KURAMA-II in a backpack.

EXPERIMENTS: From 2020 to 2021, the air dose rates of five public facilities were measured by walking with a KURAMA-II in a backpack. The situation of the sites is as follows.

Site A: School grounds and surrounding road

Site B: Gymnasium grounds and surrounding road

Site C: Community center grounds and surrounding road

Site D: School grounds and surrounding road

Site E: Park in the forest

A CsI(Tl) scintillation detector (C12137-01, Hamamatsu Photonics) was used for measurement. The air dose rate and GPS position were measured every 3 seconds. About

400 data sets were obtained at each site. Air dose rates at 10-14 points in each site were measured by a NaI(Tl) scintillation survey meter (TCS-172B, Hitachi) for validity confirmation. Additionally, the air dose rate owing to artificial radionuclide was separately evaluated from the pulse-height spectrum data obtained by KURAMA-II [2].

RESULTS: As shown in Fig.3 and 4, there was no large difference between KURAMA-II results and those by NaI(Tl) survey meter. The dose ratio (artificial/total) was 0.43-0.67 in 2020 and 0.38-0.61 in 2021. From 2020 to 2021, no clear decreasing trend in air dose rate was observed, suggesting that the contribution of short-lived radionuclides could be ignored at the time of 10 years after the accident. Based on the observed pulse height spectra, ¹³⁷Cs ($T_{1/2} = 30.1$ y) was estimated to be the dominant artificial radionuclide.

In conclusion, KURAMA-II showed sufficient performance for the radiation monitoring of public facilities.

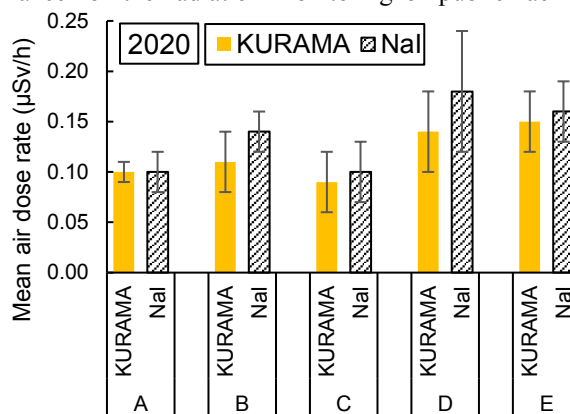


Fig. 3. The result at each site in 2020. Error bars indicate the standard deviation of the measured data.

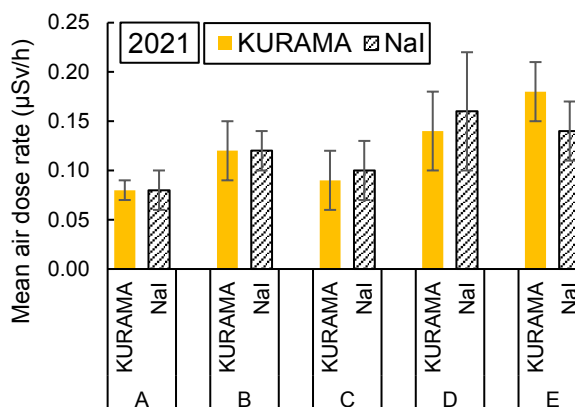


Fig. 4. The result at each site in 2021. Error bars indicate the standard deviation of the measured data.

REFERENCES:

- [1] M. Tanigaki *et al.*, Nucl. Instrum. Meth. Phys. Res. **781** (2015) 57–64.
- [2] M. Andoh *et al.*, T. J. At. Energy Soc. Jpn., **16**[2] (2017) 63-80 [in Japanese].

CO10-5 Study of FP contamination behavior on structural materials using neutron activation analysis – Study of penetration and elution behavior of Cs -

K. Kondo¹, K. Yoneyama¹, I. Sato¹, E. Suzuki²

¹Tokyo City University

²Japan Atomic Energy Agency

INTRODUCTION: In order to contribute to the elucidation of the mechanism of radioactive contamination, which is one of the issues of NDF6, penetration and elution tests of Cs were conducted on concrete as a structural material in the containment vessel of a nuclear reactor. INAA, PIXE, and ICP-MS were used for quantitative analysis of Cs in these experiments.

EXPERIMENTS: Mortar samples (ordinary portland cement, W/C=0.37, size: 20 mm ×20 mm ×20 mm) were used in the experiments. Acrylic resin was applied to 5 of the 6 surfaces to permit penetration to one surface. Then, (1): mortar penetrated in 10⁻²M CsOH solution for 10 days and (2): mortar eluted with water for 1 day after (1) were ground 0.5mm ×4 times in depth direction and analyzed by PIXE for each powder obtained during grinding. In addition, (3): Mortar penetrated in 10⁻³M CsOH solution for 10 days and (4): Mortar eluted with water for 1 day after (3) were ground in the same manner, and the powder was analyzed using INAA.

RESULTS: The Cs that penetrated into the mortar eluted 39.0%, 80.9%, 51.6%, and 4.0%, in order from the surface side, and 48.8% for the entire sample. Regarding the penetration behavior, it could be considered that the greater the penetration depth, the harder it is to penetrate. On the other hand, if the migration of Cs was considered to be proportional to the concentration gradient, it could be presumed that the solution in contact with the mortar surface would change from CsOH solution to water containing no Cs, resulting in a larger concentration gradient, and then the Cs concentration profile could be changed like in the red line in Fig. 2. However, it did not exhibit such behavior. This may be due to sites in the cement where Cs is strongly adsorbed, which may complicate diffusion phenomena during the elution. To analyze this elution behavior, it would be important to analyze the distribution of sites where Cs is strongly adsorbed and their ability to adsorb Cs at different depths in the cement. As to the difference in data due to the difference in analysis method, the Cs elution rate on the mortar surface determined by INAA was 29.6%, although the value determined by PIXE was 39.0% as mentioned above. Considering that INAA detects Cs in the entire sample while PIXE detects Cs on the sample surface, INAA, which can detect Cs in the entire powder

obtained during, is considered to be more accurate in determining the elution rate.

In these experiments, only the Cs elution rate at the mortar surface was analyzed by INAA. Next year, we would like to analyze the elution rate in the depth direction to obtain more accurate results.

CONCLUSION: Penetration and elution tests for Cs were conducted on concrete, a structural material, in the reactor containment vessel. The elution behavior of Cs from mortar indicates that analysis may need to take into account the diversity of Cs adsorption sites in mortar.

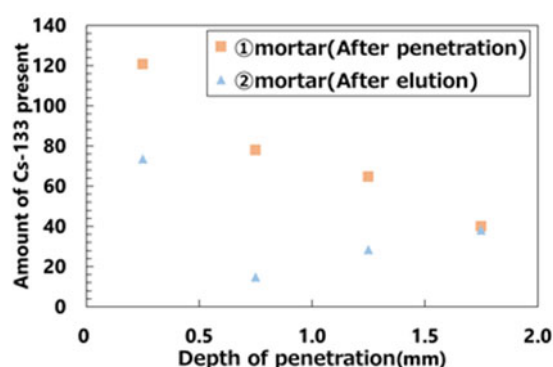


Fig.1 Amount of Cs present at each mortar depth.

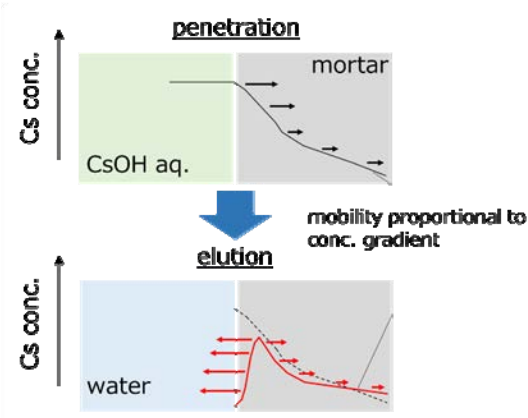


Fig.2 Elution behavior according to concentration gradient (a predicted diagram) .

REFERENCES:

- [1] T.Akimoto (2016), *The Molecular Simulation Society of Japan*, Vol.18, No.3, 136.
- [2] K.Yoneyama, ICONE28, Virtual Conference, Online, August 4th – August 6th , 2021

CO12-1 Determination of natural cobalt content as impurity in iron cyclotron yokes

G. Yoshida, K. Nishikawa¹, K. Takahashi, H. Nakamura, H. Yashima², M. Inagaki², S. Sekimoto², T. Miura, A. Toyoda, H. Matsumura, and K. Masumoto

Radiation Science Center, KEK

¹ Quantum Life and Medical Science Directorate, QST

² Institute for Integrated Radiation and Nuclear Science, Kyoto University

INTRODUCTION: In Japan, the number of establishment of accelerator facility had increased rapidly since the 1990s. Most of them are cyclotrons for Positron Emission Tomography (PET) drug production and are expected to be decommissioned in the near future, considering their useful life. When the decommissioning of accelerators, the generation of radioactive waste resulting from activation and their disposal become significant issue. Therefore, it is important to quantify the degree of activation in the whole facility, and it can predict the amount of generated radioactive waste accurately in order to facilitate decommissioning.

We focused on the iron yoke of PET cyclotron which accounts for a large amount of weight in the facility, and developed the activation estimation tool using Monte Carlo simulation. In this method, 3D-model which can reproduce the actual cyclotron is established and the rate of nuclear reactions for each modeling element is calculated by PHITS [1]. As a pilot study for this method, we performed the calculation for the PET cyclotron at the Nishina Memorial Cyclotron Center (NMCC) in the Takizawa Research Institute of the Japan Radioisotope Association in Takizawa City, Iwate Prefecture. The calculated reaction rate gradient agreed well with the radioactivity depth gradient of the actual yoke determined by the core boring method. However, we could not discuss whether the absolute values of radioactivity are consistent or not because the concentration of cobalt which content as impurity in the iron yoke has not been quantified.

In this study, we analyzed trace element concentrations in some iron and steel samples with neutron activation analysis (NAA) which suitable for trace element analysis of ppm order. We have been used NAA for quantification of trace elements in accelerator facility concretes [2], though this is the first time to apply this method for metallic materials. The feasibility of NAA for determination of trace elements in the steel sample was also verified in this study.

EXPERIMENTS: Irradiation samples were prepared from iron yoke of PET-cyclotron in NMCC. Chips were taken from the surface layer where no activation was observed, using a drill. Iron chips were washed with boiled water twice and with acetone, then dried and weighed by 100 mg as an irradiation sample. Japanese iron and steel certified reference materials (JSS001-8, JSS003-7, JSS050-8, JSS651-16, JSS-652-16) distributed by the

Japan iron and steel federation were employed as references and prepared in the same way. For analysis of short-lived nuclides generated by neutron irradiation, samples were irradiated at Pn-3 with 1 MW during 10 s, and measured with a Ge detector immediately after irradiation. Next day of 10s irradiation, samples were irradiated at Pn-2 with 5 MW during 3000 s, and measured with a Ge detector after short lived nuclides were attenuated.

RESULTS: The results of the 10s irradiation showed ⁵⁶Mn and ²⁸Al peaks in the γ -ray spectra of all samples. Relative value of radioactivity was consistent with the nominal values of manganese and aluminum in the standard sample. We measured the 3000s irradiated samples with a Ge detector one month after irradiation. The result of the long time irradiation showed ⁵⁹Fe and ⁶⁰Co peaks in the γ -ray spectra of all samples, though that in some samples the ⁵⁹Fe peak was too large and masked the ⁶⁰Co peak. Remeasurement of these samples after the ⁵⁹Fe had decay enough are mandatory.

The cobalt concentration in the iron yoke of the NMCC cyclotron was estimated to be approximately 40 μ g/g. From this value and the ⁶⁰Co reaction rate, the radioactivity distribution was derived as shown in Fig.1 and agreed very well with the actual radioactivity depth distribution. In conclusion, it was found that aluminum, manganese, and cobalt in iron samples in an accelerator can be determined accurately using NAA.

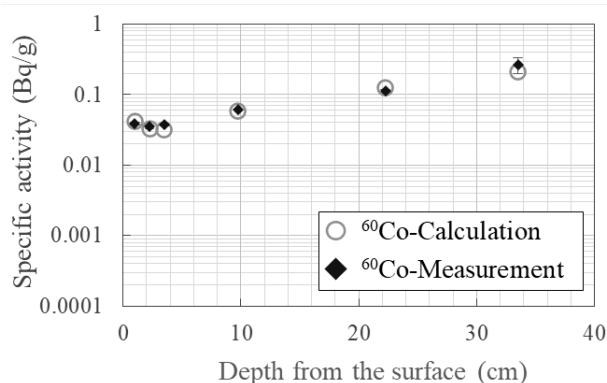


Fig. 1. Depth distribution of ⁶⁰Co activity in the iron yoke of PET-cyclotron at NMCC.

REFERENCES:

- [1] G. Yoshida, H. Matsumura *et al.*, The 3rd JSRM / JHPS Joint Conference (IC5-4), online, 1-3. Dec. 2021.
- [2] G. Yoshida, K. Nishikawa *et al.*, J.Radioanal. Nucl.Chem. **325** (2020) 801-806.

CO12-2 Neutron Resonance Spectrometry for Nuclear Security and Safeguards Education

J. Kawarabayashi, R. Sasaki, R. Watanabe, A. Miura, T. Takeuchi, D. Ibuki and J. Hori¹

Department of nuclear safety engineering, Tokyo City University

¹ KURNS

INTRODUCTION: In order to support nuclear facility regulations in Japan for safe use, it is necessary to develop educational training course with broad knowledge associated with nuclear engineering. Nuclear facilities include reprocessing, nuclear fuel factories, research facilities, etc. in addition to nuclear power plants, it is important to teach not only the knowledge of radiation, reactor physics, but also the physics of nuclear material itself at each stage of the nuclear fuel cycle. The knowledge of physical and chemical properties of nuclear material is also needed for effective regulation. As a part of this human resource development, we have proposed an isotope ratio measurement training program with uranium using pulsed neutron spectrometry as a candidate for the nuclear regulatory educational course to deepen the understanding of the nuclides in nuclear fuel cycle. Observation of the neutron resonance absorption phenomena of natural, enriched and depleted uranium will develop the understanding of the isotope itself and the properties of the nucleus of uranium. In this fiscal year, as the pandemic of Covid-19 limited our student to travel to Kyoto University, we tried to establish an online experiment to acquire neutron resonance absorption spectra of various samples.

EXPERIMENTS: Samples of six different elements (Ag, In, Mn, Co, Cd, U) were irradiated at KURNS-LINAC to record neutron transmission spectrum. A ³He proportional counter followed by a multiple-stop time spectrometer (ORTEC EASY-MCS) was located behind the sample at 13m experimental room and generated timing signal of neutron detection. A signal from the accelerator was used as the start signal of the time spectrometer. The timing calibration between start signal and output signal of the ³He proportional counter was performed with an oscilloscope by gamma-flash signal generated at the Ta target of the accelerator. The sample of Uranium was arranged at in front of the neutron irradiation port and time spectra of neutron transmission were recorded. Five students participated in the experiment over computer network by Zoom meeting software.

RESULTS: As shown in left part of Fig. 1, a resonance dip of ¹⁰⁹Ag was clearly observed in the time spectrum with the sample of silver plate (thickness: 1.0 mm) successfully, with measurement of 60,000 sweeps and 20 msec. range. The accelerometer was running at 50Hz with pulse-width of 4 micro sec. per pulse. The time spectrum was recorded within about 20 minutes. The energy of this dip was estimated to be 5.3 eV derived

from the source-detector distance of 12 m and dip position of 0.377 msec. The first energy level of ¹⁰⁹Ag is 5.19 eV [1]. There is a good agreement between the experimental result and literature value. In right part of Fig. 1, time spectrum with In plate (thickness: 1 mm) were obtained. There were three resonance dips corresponding to ¹¹⁵In. We confirmed the dips corresponded to resonant absorption energies of 1.46 eV, 3.85 eV, 9.07eV[1]. Fig. 2 shows the time spectrum of natural Uranium (left) and enriched Uranium (right, ²³⁵U amount of 0.416 g) samples. We can observe three clear resonant dips corresponding to the first, second and third levels of ²³⁸U nucleus in the left part of Fig. 2. In the observed time spectrum of enriched U, we can see the first resonance wide dip of ²³⁵U around 0.3 eV at TOF of 1.5 msec. and several weak resonance dips at 0.29 msec. and 0.34 msec. The screen of the PC acquiring these spectra was shared with online students through Zoom-meeting software. The online students were able to observe the acquisition of neutron transmission spectra in real time. The experimental system and conditions were explained online with a video taken in the morning of the day when the experiment was carried out. Interviews with students after training showed that the content of the experiment could be understood online.

CONCLUSION: We proposed pulsed neutron spectrometry as a candidate for the nuclear regulatory educational course to deepen the understanding of the nuclides in nuclear fuel cycle and performed online training program. The results showed that online program was able to support for students to understand the difference of the cross-sections of ²³⁵U and ²³⁸U for low energy neutron.

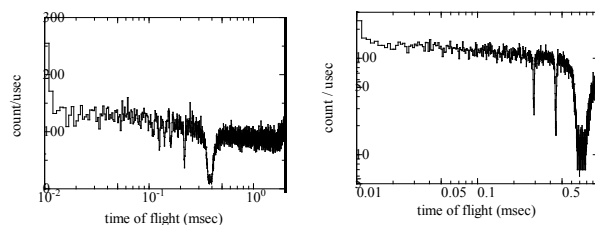


Fig. 1. ToF spectrum of Ag (left) and In (right).

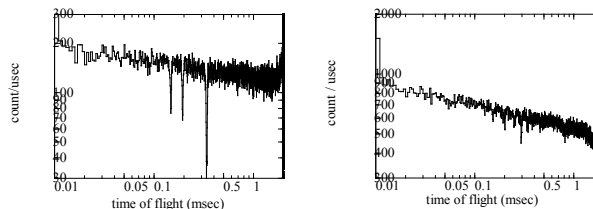


Fig. 2. ToF spectrum of natural U (left) and enriched U (right).

REFERENCES:

[1] S. F. Mughabghab, Atlas of Neutron Resonances.

CO12-3 Structural Analysis of Additives in Lubricants by Small-Angle X-ray Scattering

T. Hirayama, S. Nambo¹, W. Yagi¹, Y. Takashima², N. Sato³ and M. Sugiyama³

Graduate School of Engineering, Kyoto University

¹*Graduate School of Engineering, Kyoto University*

²*Idemitsu Kosan Co., Ltd.*

³*Institute for Integrated Radiation and Nuclear Science, Kyoto University*

INTRODUCTION: Tribology is a research field that deals with friction, wear, and lubrication techniques on mechanical sliding surfaces, and many efforts have been made to reduce friction. In recent years, some researchers have proposed the use of fullerenes (C60) in lubricants to reduce the friction between two surfaces, and their effectiveness has been verified. In fact, several research groups have reported that fullerenes are effective in reducing friction when mixed at relatively high concentrations of 1000 ppm or more, and fullerenes are highly anticipated as a lubricant additive in the near future. However, there are reports that the size of the effect varies depending on the base oil, and it is assumed that the effect depends largely on the dispersion form of fullerenes in the base oil, but the actual state remains unclear. In this study, the dispersion morphology of fullerenes in various base oils are investigated using small-angle X-ray scattering (SAXS).

EXPERIMENTS: SAXS analysis was performed to understand the dispersion morphology of fullerenes in lubricant under various temperature conditions. A SAXS spectrometer with Cu radiation source installed at the Institute for Integrated Radiation and Nuclear Science, Kyoto University, was used for the analysis. First, fullerenes were dissolved in polyalphaolefin (PAO4) at a concentration of 1000 ppm, which was used as the target sample. The temperature conditions were 25°C and 100°C. The radius of gyration R_g of fullerenes in PAO was estimated from the obtained scattering profiles.

RESULTS: The obtained scattering curve is shown in Fig. 1, and its transformation into a Guinier plot is shown in Fig. 2. The radius of gyration of the fullerenes in PAO was found to be 0.78 nm at 25°C and 0.96 nm at 100°C, respectively. No aggregation of fullerenes was observed in PAO. Since the outer diameter of a fullerene is approximately 1.4 nm, the radius of gyration of fullerene in PAO is almost the same as the original size. It remains to be verified whether this is due to the fact that the fullerenes are covered with PAO molecules, but at least it was confirmed that the radius of gyration and the aggregation form of the fullerenes in the base oil can be estimated by SAXS analysis.

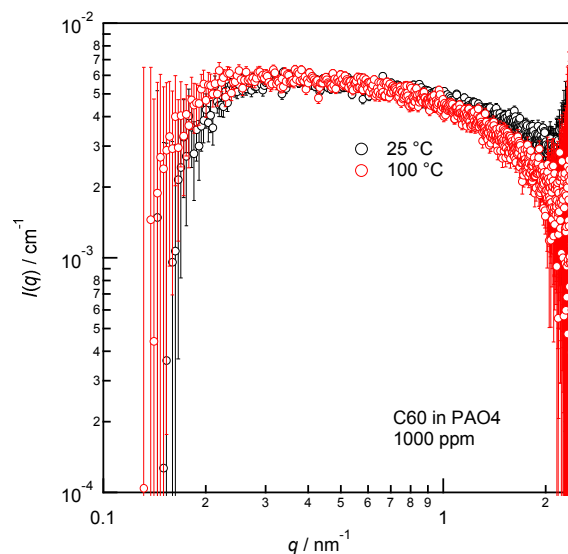


Fig. 1 $I(q)$ profiles of C60 in PAO at 25 and 100°C.

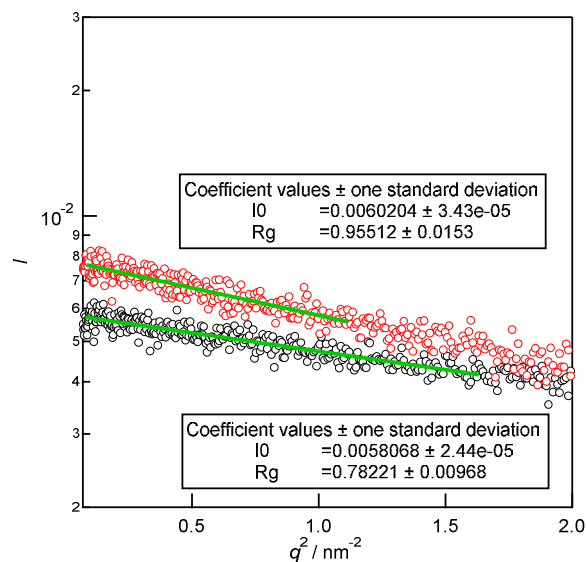


Fig. 2 Guinier plots transformed from Fig. 1.

CO12-4 Visualization of Lubricant Behavior in Machine Elements by Neutron Phase Imaging

T. Hirayama, L. Sun¹, Y. Seki², T. Shinohara³, M. Hino⁴ and R. Nakamura⁴

Graduate School of Engineering, Kyoto University

¹*Graduate School of Engineering, Kyoto University*

²*Institute of Multidisciplinary Research for Advanced Materials, Tohoku University*

³*J-PARC center, Japan Atomic Energy Agency*

⁴*Institute for Integrated Radiation and Nuclear Science, Kyoto University*

INTRODUCTION: Engineering related to friction, wear, and lubrication on mechanical sliding surfaces have been studied intensively in the field of tribology. In particular, the formation of oil film has a great influence on the tribological properties of sliding surfaces, and since the friction coefficient of a sliding surface varies greatly depending on the presence or absence of oil film, it is extremely important to predict the state of lubrication of sliding surfaces. In the field of tribology, the Reynolds equation is generally used to predict the state of oil film formation. However, when the Reynolds equation is applied to sliding bearings, for example, the boundary condition of atmospheric pressure at the end of the sliding bearing is often used. On the other hand, it is difficult to understand the behavior of the gas-liquid boundary at the end of machine elements such as sliding bearings because they are often made of metal and are difficult to visualize.

In this study, we attempted to understand the shape of the gas-liquid boundary at the end of a sliding bearing by using neutron phase imaging. The main reasons for using neutron phase imaging are as follows.

1. The high penetrability of neutron beams enables direct observation of the gas-liquid boundary.
2. The contrast of the area to be observed can be adjusted arbitrarily by deuterating a part of the liquid.

EXPERIMENTS: In this study, we used the cold neutron beamline CN-3 at Institute for Integrated Radiation and Nuclear Science, Kyoto University. Neutron phase imaging is a new visualization technique that uses a Talbot-Lau interferometer to detect the phase change of the neutron beam after it penetrates an object and to obtain an image of the waveform. The visibility image obtained by this method is particularly suitable for this study because it can map the microscopic inhomogeneous state of size and density of molecules in the target field.

A bearing model used in the experiment is shown in Fig. 1, and the tapered shape of the sliding bearing end is also shown in Fig. 1.

RESULTS: The transparent contrast image, differential phase contrast image, and visibility contrast image obtained from the experiment are shown in Fig. 2. In this experiment, polyalphaolefin (PAO), a common machine

oil, was used as the sample oil. It can be said that the numerical calculation of the images obtained by the phase imaging method enabled us to obtain images focusing on the information we expected to obtain.

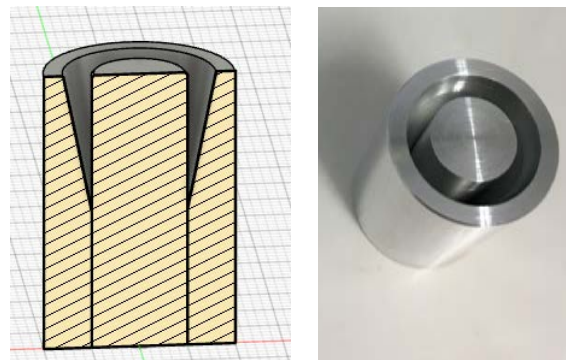


Fig. 1 Sliding bearing model with taper seal at the bearing end made from Aluminum.

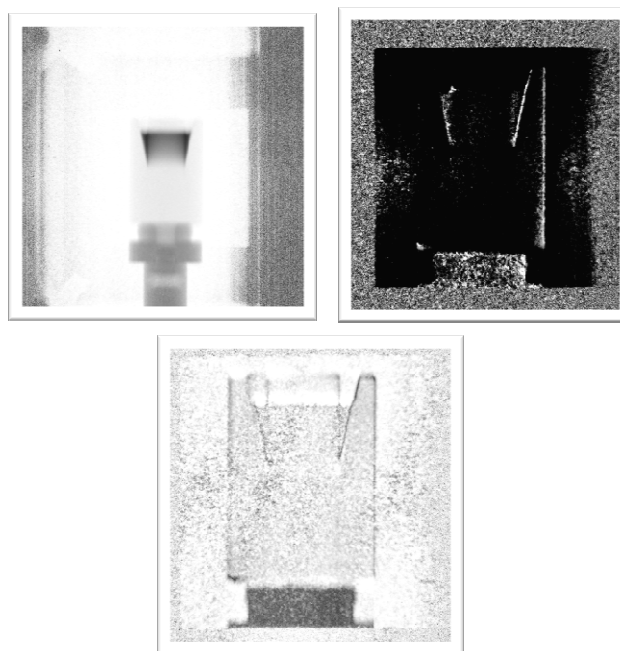


Fig. 2 Obtained images; transparent contrast image (upper left), differential phase contrast image (upper right), and visibility contrast image (lower).

CO12-5 Neutron Activation Analysis of Neodymium Oxide

T. Miura¹, S. Sekimoto², R. Okumura², H. Yoshinaga², Y. Iinuma²

¹National Metrology Institute of Japan, AIST

²Institute for Integrated Radiation and Nuclear Science, Kyoto University

INTRODUCTION: National Metrology Institute of Japan (NMIJ) is responsible for developing certified reference materials and for establishing the traceability of SI (The International System of Units) on chemical metrology in Japan. To establish SI traceability, the primary method of measurements should be applied to the characterization of the certified reference materials. Neutron activation analysis using comparator standard is recognized as a potential primary ratio method [1]. Despite the potential of neutron activation analysis as primary ratio method, the evaluation the measurement capability and the measurement uncertainty are required in any analysis. In general, there are three main components of uncertainty in neutron activation analysis, that is, sample preparation uncertainty, neutron flux homogeneity, and gamma ray measurement uncertainty. Usually, flux monitor is used to correct the neutron flux heterogeneity. However, although the flux monitor can correct the neutron flux variation using the count rate of the known amount of the monitor nuclide, it does not reflect the neutron flux of the actual sample. The most practical method to eliminate neutron flux heterogeneity to improve gamma ray measurement uncertainty is an internal standard method [2, 3]. For the development of primary inorganic standard solution as national standard, the purity of starting material has to be determined. The high purity neodymium oxide was candidate starting material for preparation of Nd standard solution as national standard of Japan. The several trace analytical methods including neutron activation analysis, were used for purity determination of the high purity neodymium oxide. In this work, we presented that capability of instrumental neutron activation analysis for determination of Sc, La, Pr, Sm, Eu, Gd, Tb, Dy, Ho, Er, Yb, and Lu as impurity about rare earth elements in the neodymium oxide.

EXPERIMENTS: The high purity neodymium oxide (Alfa Aesar, Reacton) purchased from FUJIFILM Wako Pure Chemical Corporation. The informative purity value of the neodymium oxide was 99.999 %. NIST SRM single element standard solutions (3148a Sc, 3127a La, 3142a Pr, 3147a Sm, 3117a Eu, 3118a Gd, 3157a Tb, 3115a Dy, 3123a Ho, 3116a Er, 3160a Tm, 3166a Yb, 3130a Lu) were used for calibration standard in impurity analysis of the neodymium oxide, respectively. The standard solutions were added on filter paper to prepare the calibration standard in the analysis. The prepared calibration standards were heat sealed into polyethylene bags. Ten mg of the neodymium oxide samples were used for impurity analysis. The neutron irradiations performed

by KUR Pn2 (thermal neutron flux: $5.5 \times 10^{12} \text{ cm}^{-2}\text{s}^{-1}$) for 5 min, Pn3 (thermal neutron flux: $4.7 \times 10^{12} \text{ cm}^{-2}\text{s}^{-1}$) for 1 min and TcPn (thermal neutron flux: $8.0 \times 10^{10} \text{ cm}^{-2}\text{s}^{-1}$) for 12 h. The irradiated samples were cooled appropriately. The gamma rays from irradiated samples were measured using Canberra GC4070-7500 Ge detector with Laboratory Equipment Corporation MCA 600. The measure radioactive isotopes were ⁴⁶Sc, ¹⁴⁰La, ¹⁴¹Ce, ¹⁴²Pr, ¹⁵³Sm, ^{152m}Eu, ¹⁵⁹Gd, ¹⁶⁰Tb, ¹⁶⁵Dy, ¹⁶⁶Ho, ¹⁷¹Er, ¹⁷⁰Tm, ¹⁷⁵Yb and ¹⁷⁷Lu.

RESULTS: Analytical results of the high purity neodymium oxide were shown in Table 1. In this measurement, Sc, Pr, Sm, Eu, Gd, Tb, Dy, Ho, Er, Yb, and Lu in the neodymium sample could not be detected by instrumental neutron activation analysis. Therefore, the detection limits for these elements were estimate from the count rate of energy region of gamma rays emitted by induced radioactive nuclides. The estimated detection limits were also presented on Table 1.

Table 1. Analytical results of the high purity neodymium oxide

	Measured values, mg/kg
Sc	< 0.3
La	0.4 ± 0.16
Pr	< 4
Sm	< 1
Eu	< 0.04
Gd	< 40
Tb	< 8
Dy	< 0.7
Ho	< 4
Er	< 11
Yb	< 6
Lu	< 2

REFERENCES:

- [1] R. Greenberg, P. Bode, E. De Nardi Fernandes (2011) Spectrochim. Acta B, 66, 193-241.
- [2] T. Miura, K. Chiba, T. Kuroiwa, T. Narukawa, A. Hioki, H. Matsue (2010) Talanta, 82, 1143-1148.
- [3] T. Miura, R. Okumura, Y. Iinuma, S. Sekimoto, K. Takamiya, M. Ohata (2015) J. Radioanal. Nucl. Chem., 303, 1417-1420.
- [4] NuDat 2, National Nuclear Data Center in Brookhaven National Laboratory, <https://www.nndc.bnl.gov/nudat2/index.jsp>.

CO12-6 Observation of Superposition of Coherent Transition Radiation Using an Extra Ring Resonator

N. Sei, and T. Takahashi¹

Research Institute for Measurement and Analytical Instrumentation, National Institute of Advanced Industrial Science and Technology

¹Institute for Integrated Radiation and Nuclear Science, Kyoto University

INTRODUCTION: A coherent radiation generated by a relativistic electron beam, which was observed for the first time in Japan [1], becomes high power in the terahertz-wave region. Therefore, many light sources using the coherent radiation have been developed at various electron linac facilities. Using an L-band linac at Kyoto University Institute for Integrated Radiation and Nuclear Science (KURNS-LINAC) [2], we have also demonstrated a new radiation principle that is superior to coherent transition radiation (CTR) in radiation power [3]. However, the development of the new radiation principle is not the only effective means to obtain intense terahertz waves. By matching phases of multiple terahertz-wave sources, higher power terahertz waves can be obtained [4]. Then, we proposed that coherent radiation generated by a pulse train of electron bunches was confined in a ring resonator and superimposed with the same phase. In the initial experiments, it was confirmed that a CTR beam was amplified by using a ring-type optical cavity installed in the electron beam orbit. However, it was difficult to adjust a cavity length of the optical cavity because it was installed in a vacuum chamber. Therefore, in order to adjust the cavity length, the optical cavity was set in the experimental room to guide the CTR beam into it. An amplification depending on the cavity length was successfully observed.

EXPERIMENTS: The CTR beam extracted from the coherent radiation beamline to the atmosphere in the experimental room was adjusted to a parallel beam with a diameter of 42 mm using two concave mirrors. It was guided to a Cyclo Olefin Polymer (COP) substrate with a thickness of 3 mm in the ring-type optical cavity, and a part of the CTR beam reflected on the surface of the COP substrate accumulated in the optical cavity. The optical cavity consisted of two parabolic mirrors with a focal length of 508 mm and two plane mirrors, and the cavity length was 922 mm, which corresponded to four electron micropulse intervals. The COP had a refractive index of 1.531 and its absorption coefficient was negligible in the terahertz-wave region [5]. Approximately 8% of the CTR beam accumulated in the optical cavity was emitted to the outside of the optical cavity by reflection from both sides of the COP substrate per circumference of the optical cavity. The emitted CTR beam was synchronized with the CTR beam transmitted through the COP substrate without entering the optical cavity. These CTR beams were focused by a parabolic mirror with a focal length of 101

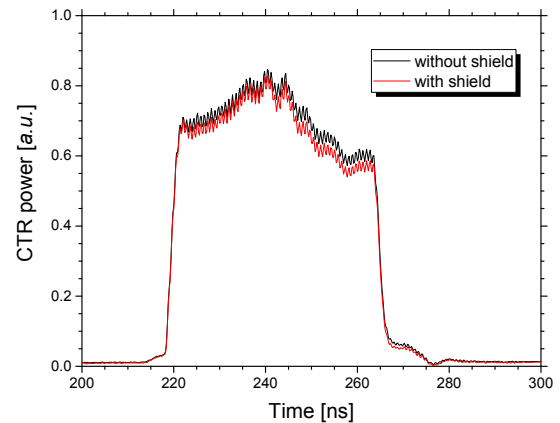


Fig. 1 Measured CTR power emitted from the optical cavity with (red line) and without (black line) an absorber in the optical cavity.

mm and detected by a D-band diode detector (Millitech Inc., DXP-06) with an antenna [6]. The output signal of the diode detector was measured by an oscilloscope with the frequency band less than 350 MHz.

RESULTS: We conducted experiments using the KURNS-LINAC electron beam with the electron energy of 41 MeV and the current of 2.4 μ A. The duration of the electron-beam macropulse was set to be 47 ns. Figure 1 shows the measured powers of the CTR beams emitted from the optical cavity with and without an absorber in the optical cavity. The difference between two lines in this figure represents the presence of the CTR beam accumulated in the optical cavity. It is noted that the resonated CTR beam increased with the time in the macropulse. Because the power of the resonated CTR beam depended on the cavity length, it is considered that the CTR power was amplified by superimposing the each CTR pulse orbiting the ring-type optical cavity.

In the next experiment, we plan to install the optical cavity in the electron beam orbit to clarify the relationship between the cavity length and the amplification of the CTR power.

REFERENCES:

- [1] T. Nakazato *et al.*, Phys. Rev. Lett., **63** (1989) 1245-1248.
- [2] T. Takahashi and K. Takami, Infrared Phys. Technol., **51** (2008) 363-366.
- [3] N. Sei and T. Takahashi, Sci. Rep. **7** (2017) 17440.
- [4] N. Sei and T. Takahashi, Sci. Rep. **10** (2020) 7526.
- [5] http://www.tydexoptics.com/pdf/THz_Materials.pdf.
- [6] N. Sei *et al.*, J. Phys. D: Appl. Phys. **46** (2013) 045104.

CO12-7 Another Trial to Analyze the Texture of Roof-tile: Toward Detailed Provenancial Studies of Excavated Ceramics by INAA

M. Tomii, K. Takamiya¹, H. Yoshii, M. Kidachi², A. Ito, and Y. Chiba

Graduate School of Letters, Kyoto University

¹*Institute for Integrated Radiation and Nuclear Science, Kyoto University*

²*College of Letters, Ritsumeikan University*

INTRODUCTION: Following the last year trial, in order to establish the procedures to archaeologically identify local groups for production of ceramics in Japan, 16 pieces of the roof-tiles with stamp impression from the same collection as the one in last year are analyzed. They were excavated from the archaeological site in Kyoto in 1992, where the garrison from the *Tosa* domain had occupied in the mid-19th century. The normal type of roof-tiles in the collection is almost exclusively composed of the ones having the stamp impressions of Chinese characters which indicate the name of maker/atelier of the tile. 24 kinds of stamp impression have been recognized in this collection, and 23 stamp impression groups of the 24 suggest the makers in *Tosa* region at that time [1].

Despite the difference in potter's names written in the impressions, it has been improbable to divide pieces in the whole collection into groups in terms of size and production technique. This study thus tries to check whether the groups based on the difference in stamp impressions, suggesting different production groups, corresponds with the groups of tile texture in detail.

EXPERIMENTS: Conventional INAA was applied to determine the elemental composition of samples of the tiles, each of which had been drilled into a fine powder as a sample by Maria Shinoto (Universität Heidelberg), and the same was also done by Johannes Sterba (Technische Universität Wien) at the Atominstitut in Wien (Vienna) for comparison [2]. In KURNS, 16 pieces of the roof-tile of normal type, composed of three stamp impression groups, were chosen; seven were from the "AKIBUN" group, another seven from "AKIKANE" group, and the rest two, each of which had two samples for double measurement, respectively, from "SUMIKAWARA" group. Each 18 samples, enclosed in a polyethylene bag, was neutron-irradiated, firstly at Pn-3 of KUR (1 MW) for 90 seconds to detect short-lived nuclides, and then at Hyd (1MW for 23 hours and successively 5 MW for 6 hours) to determine long-lived nuclides. The comparative standards (JR-3, JB-1b) were irradiated with the same condition. Around 20 mg was used for Pn-3 and around 30 mg for Hyd, in each sample.

The gamma-ray spectrometry of the irradiated samples for short-lived nuclides had been performed four times based on the last year experience; just after the irradiation, after 15 minutes, 40 minutes, and around 20 hours. The photo-peak analysis for short-lived nuclides was performed by using FitzPeaks [3]. Concentrations of elements

included in the samples were estimated by comparison of the intensity of gamma-rays between the comparative standard and tile samples.

RESULTS: Concentrations of nine elements (Na, Mg, Al, K, Mn, Ga, La, Sm and Th) in every sample were determined. Samples irradiation by Hyd for determination of long-lived nuclides could not be recovered because of adhesion of plastic bags for sample sealing during irradiation. Before the comparison with the result in Atominstitut, which analyzed exactly the same roof-tiles, estimation of the elemental concentrations for long-lived nuclides is inevitably required at KURNS to apply the Mahalanobis Distance for quantitative investigation into the 16 tiles. Nevertheless the following two results can be pointed out;

- a) both two sets for double measurement suggest that two elements (Al and Mg) have a wider range of value of concentration (table 1).

Table 1 Concentration ($\mu\text{g/g}$) of two elements determined for the roof-tiles "KS92-466" and "KS92-693".

Tile	Al	Mg
KS92-466	$4.36\text{E}+04 \pm 8.94\text{E}+02$	$5.27\text{E}+02 \pm 1.21\text{E}+02$
KS92-693	$6.79\text{E}+04 \pm 1.30\text{E}+03$	$7.97\text{E}+02 \pm 1.77\text{E}+02$
	$5.65\text{E}+04 \pm 1.12\text{E}+03$	$6.59\text{E}+02 \pm 1.47\text{E}+02$

- b) two elements (Na and Mn) show a clear difference in concentration to divide 18 samples into two groups, respectively, and the concentrations combination of the two suggests the three groups, which fully correspond with the stamp groups (Fig.1).

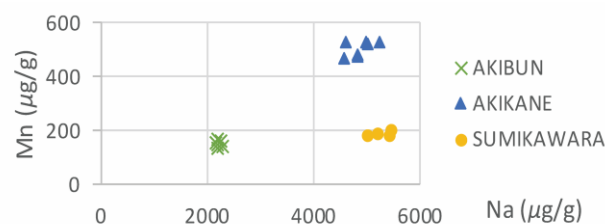


Fig 1 Distribution of 18 samples on the concentrations combination of Na with Mn.

ACKNOWLEDGEMENT

We would like to thank Dr Johannes Sterba and Dr Maria Shinoto for performing the sampling procedures on the sherds according to the workflow established in Vienna.

REFERENCES:

- [1] Y. Chiba *et al.*, *Annual Report of Archaeological Researches in KU sites for 1992*. (1995) 65-125.
- [2] J. Sterba, *J. Radio. Nucl. Chem.*, **316** (2018) 753-759
- [3] J. Fitzgerald, FitzPeaks Gamma Analysis and Calibration Software, <https://www.jimfitz.co.uk/fitzpeak.htm>

CO12-8 Development of high-count rate two-dimensional neutron detector system

S. Sato, K. Mori¹, Y. Yoshino¹, T. Seya, T. Otomo, H. Oshita

High Energy Accelerator Laboratory, KEK

¹ *Institute for Integrated Radiation and Nuclear Science, Kyoto University*

INTRODUCTION: Most of the neutron detectors currently in use are ³He gas detectors, and some neutron scintillator detectors are used to obtain a high counting rate and high position resolution. In this study, the LiTA system [1] has been developed as a high counting rate two-dimensional detector system. However, it is expensive and difficult to use, and it has been not widely used. Therefore, we have developed an ADCnet64 system at last year as a low-cost, simple using, and high-counting-rate two-dimensional neutron detector system instead of the LiTA system. The performance of the ADC net64 system had been evaluated using the B3 port of KUR continuously.

EXPERIMENTS: The ADCnet64 system is a readout circuit for high-speed scintillators. It has 64-channel high-speed analog to digital converters (ADCs) with 10 bits 80 MHz sampling rate to read a 5 cm square 8 × 8 multi-anode type photomultiplier tube. Although the ADCnet64 system is inferior to the LiTA system in performance, similar data are obtained with fewer circuits and easy way.

This year, we used a 1 mm thickness of ⁶Li and explored ways to achieve better position resolution and higher detection efficiency with the B3 port.

Since the ADCnet64 system uses a photo-multiplier tube with 64 anodes spaced 6 mm apart, it was found that a single threshold value did not give good characteristics. Figure 1 shows the single threshold data, which has good position resolution but poor detection efficiency. It is only 57 % more efficient than Figure 2. Figure 2 shows the data with a low hardware threshold and a high software threshold, which proved to have both good position resolution and detection efficiency.

RESULTS: We have developed the ADCnet64 system with a low-cost, simple, high-counting-rate, and two-dimensional neutron detector. We have evaluated its performance using the B3 port at KUR.

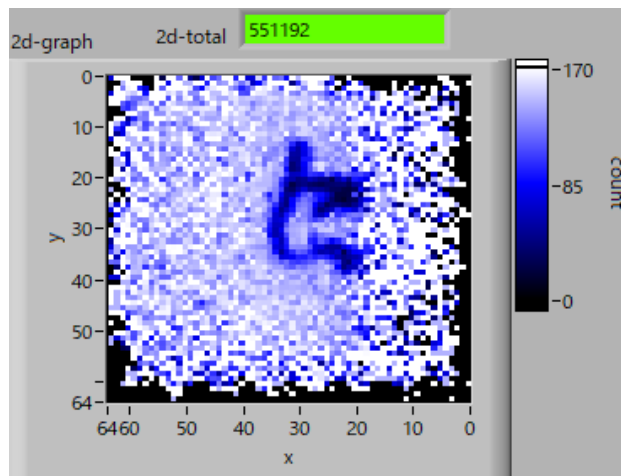


Fig. 1. Two-dimensional graph using ⁶Li glass in 1 mm thickness by the single threshold.

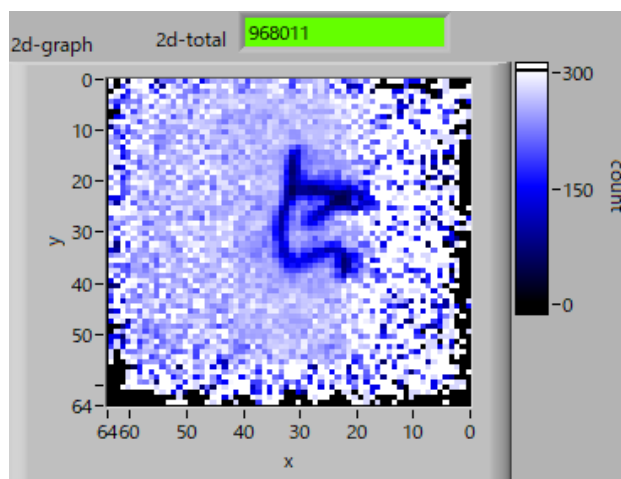


Fig. 2. Two-dimensional graph using ⁶Li glass in 1 mm thickness by the two thresholds.

REFERENCES:

- [1] S. Satoh, UCANS-V 2015, DOI 10.1393/ncc/i2015-15197-7.

CO12-9 Study for activity measurement technique of radioactive noble gases using a plastic scintillator

Takahiro Yamada^{1,3}, Tatsuya Yamada², Ken-ich Mori³ and Hiroshi Yashima⁴

Kindai University

¹Atomic Energy Research Institute

²Faculty of Science and Engineering

³Graduate school of Science and Engineering

⁴Institute for Integrated Radiation and Nuclear Science, Kyoto University

INTRODUCTION: In order to calibrate monitors used for measuring radioactive noble gases in nuclear power plants or reprocessing facilities, use of activity reference measurement standard gases shall be required. A β -ray counting technique using a set of multiple ventilated proportional counters having different lengths is generally used to determine activity concentration of standard gases [1]. In this study, a method based on the $4\pi\beta\text{-}\gamma$ spectroscopic method using a plastic scintillator (PS) as a β -detector was carried out to measure activity of ^{41}Ar absolutely as an alternative approach.

EXPERIMENTS: ^{41}Ar gas was produced via $^{40}\text{Ar}(n,\gamma)^{41}\text{Ar}$ reaction. Pure argon gas was filled into the small crystal glass container having 10 ml with atmospheric pressure and was irradiated for 60 s at the bottom of KUR-SLY under operating at 1 MW thermal output. Around 300 kBq of ^{41}Ar was produced with $7.84 \times 10^{11} \text{ n}^{-1}\text{s}^{-1}\text{cm}^{-2}$ of the nominal flux of the thermal neutron. The radioactive gas was transferred to a large volume container and diluted with stable argon gas. In the present study 5 kBq of ^{41}Ar produced at UTR-KINKI was also used without dilution.

A small acrylic gas container with internal dimensions of $\phi 60 \text{ mm} \times 40 \text{ mm}$ (113 ml) was used as the β -detection part of the measurement system. The entire inner wall of the container was lined with 1 mm thick of PS. In addition, to observe β -spectra from each PS set on three different positions (top, bottom and side) of the inner wall separately, a series of measurements using a gas container lined with 1 mm PS on the top, bottom or side was also carried out. The container was covered with aluminum tape on the sides and white tape on the top as a reflector, and a photomultiplier tube (PMT) was connected to the top of the container and stored in a light-shielded case. The β -detector was placed directly onto the Ge detector, and the signal outputs from the β - and γ -detectors were fed to the signal inputs of a multi-channel analyzer (MCA) capable of acquiring data in list mode to obtain list data consisting of the pulse height from each detector and a time stamp of the detection time. ^{41}Ar emits γ -ray ($E_\gamma=1293 \text{ keV}$) following disintegration by beta minus decay to excited levels of ^{41}K with branching ratio of 0.9917 [2]. In order to obtain the β - γ coincidence spectrum from the time-stamped pulse height data, the γ -signals derived within $4.5\mu\text{s}$ from the β -detection time stamps were considered as true coinci-

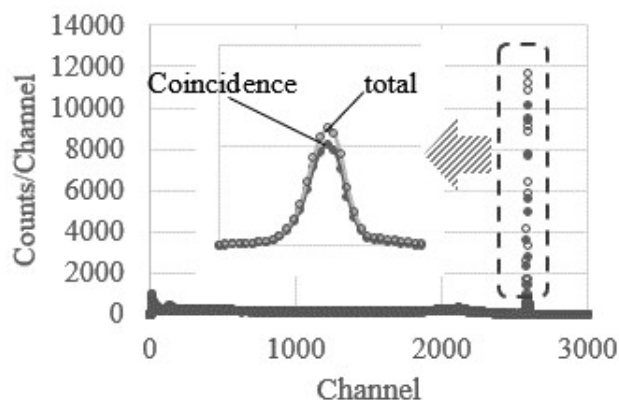


Fig. 1. Coincidence- and γ -spectra obtained from the present measurement using ^{41}Ar .

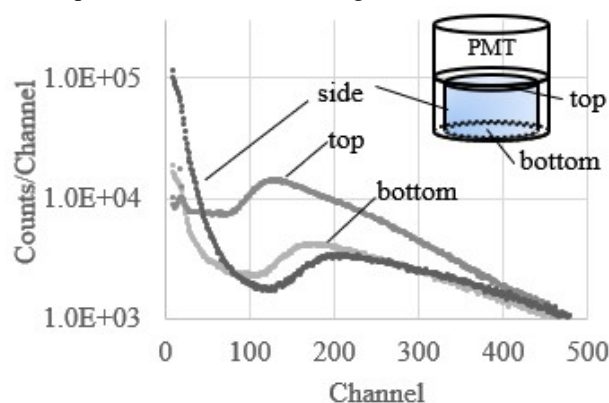


Fig. 2. β -spectra observed by a set of measurements using a gas container lined with 1 mm PS on the top, bottom or side.

dences. β -counting efficiency ε_β is determined as the ratio of net peak area in the coincidence spectrum n_c to the net peak area n_γ in the γ -spectrum.

RESULTS: Figure 1 shows the coincidence and γ -ray spectra obtained in the present experiment. β -counting efficiency determined as n_c / n_γ was 0.872 ± 0.001 . The β -spectra observed by a set of measurements using a gas container lined with 1 mm PS on the top, bottom or side were shown in Fig. 2. As shown in this figure, the spectra obtained from the PS on the side or the bottom were significantly degraded as compare with a spectrum obtained from the PS on the top, where is closest to the PMT, indicating that the difference in light collection at each position of scintillator was considered to be one of the reasons for the counting efficiency decrease of more than 10 %.

REFERENCES:

- [1] A. Yunoki, T. Yamada and H. Yashima, KURNS Progress Report 2019, ISSN 2434-9488, CO12-5 (31059).
- [2] Bé, M., 2011. Table of Radionuclides. http://www.nucleide.org/DDEP_WG/DDEPdata.htm

CO12-10 Fiber-reading Radiation Monitoring System with an Optical Fiber and Red-emitting Scintillator at the ^{60}Co Radiation Facility II

S. Kurosawa^{1,2}, C. Fujiwara², A. Yamaji^{1,2}, H. Tanaka³

¹New Industry Creation Hatchery Center, Tohoku University

²Institute for Materials Research Tohoku University

³Institute for Integrated Radiation and Nuclear Science, Kyoto University

INTRODUCTION: Decommissioning reactors at the nuclear power plant with safety is an important issue in Japan, and a real-time dose-rate monitor in the extremely high radiation dose condition is required for the above application.

Cs_2HfI_6 (CHI) has a high light output (over 60,000 photons/MeV), high effective-atomic number (over 60), red and infrared emission (600 – 800 nm) and no after-glow (less than 1% within 1s), and this material is available for such dose monitors. On the other hand, this material cannot be applied to alpha-ray detection due to the package for the hygroscopic nature[1,2].

Since the size of the scintillation sample should be small as well as a few mm^3 due to the fiber diameter and space limitation in the power plant, a high effective gamma-ray efficiency and no package against the hygroscopic nature are required. One of the candidate materials is Yb-doped $\text{La}_2\text{Hf}_2\text{O}_7$ (Yb:LHO), because this atomic number is 64. Moreover, Yb-doped samples are expected to have an infrared sharp peak around 970 nm originating from Yb^{3+} of 4f-4f transition. Although Yb:LHO has a high melting point of over 2400°C, we grew this crystal by the Core-Heating (CH) method, which we have developed as a novel crystal-growth technique in 2020[3].

Last year, we reported the intensity of Yb:LHO has lower intensity (1% of CHI) than those of Cr: α - Al_2O_3 (10% of CHI), and the dose-rate dynamic range was narrow than the others. In this year, we evaluated the signal-noise-to ratio, precisely.

EXPERIMENTS: We fabricated a Yb:LHO sample grown by the CH method, and the demonstration was performed at the ^{60}Co Gamma-ray Irradiation Facility with an activity of ~ 70 TBq. The monitor and setup were the same as that last year; and an optical fiber (S.600/600B, Fujikura) had a length of 20 m and a pure SiO_2 with a core diameter of $600 \pm 30 \mu\text{m}$. The scintillation light was transmitted through the fiber and measured with a CCD spectrometer (Blue-UVNb, StellarNet). We defined the signal-to-noise ratio as shown in Fig. 1; The integral range was over 10% peak value in the wavelength region as signal and noise.

RESULTS: We succeeded in growing the transparent Yb:LHO sample, and the sample and fiber were assembled. The assembly was irradiated with gamma rays from the ^{60}Co source, and the emission spectrum was obtained as

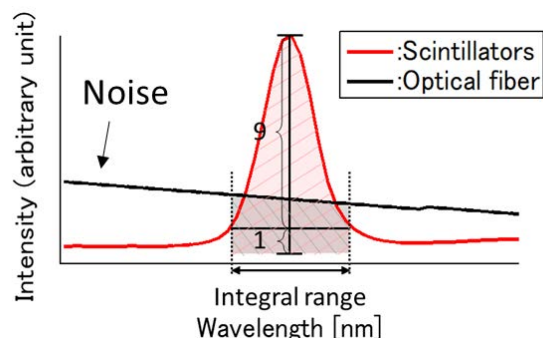


Fig. 1 Definition of integrating zone.

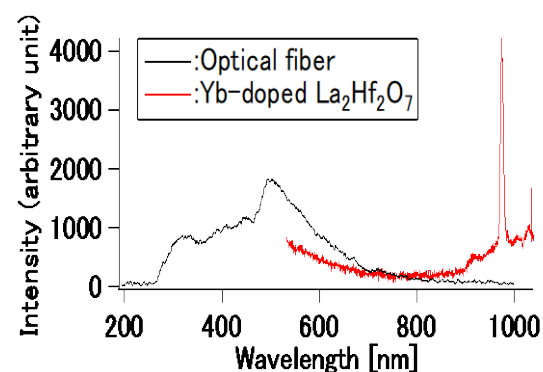


Fig. 2 Emission spectra of Yb:LHO+optical fiber and only fiber irradiated with gamma rays from the ^{60}Co source

shown in Fig.2. Here, this spectrum included optical fiber noise, and sharp peaks around 974 nm was originating from Yb^{3+} 4f-4f transition.

Moreover, the fiber was also irradiated without Yb:LHO to measure background noise (Fig. 2), and signal-to-noise ratio was calculated. When the scintillator and optical fiber were under 0.18 and 0.87 kSv/h, for instance, the ratio was evaluated to be 0.63 ± 0.2 . On the other hand, CHI has that of 0.55 ± 0.2 . Although Yb:LHO had smaller emission intensity than that of CHI, Yb:LHO had the good ratio compared to CHI due to longer emission wavelength.

As future works, we developed novel scintillators with high emission intensity at 800 – 1000 nm, which is the region of low background level.

REFERENCES:

- [1] S. Kodama *et al.*, Appl. Phys. Express, **13** (2020) 047002.
- [2] S. Kodama *et al.*, Radiat. Meas., **124**, (2019) 54.
- [3] <https://www.tohoku.ac.jp/japanese/2021/01/press20210122-01-core.html>

CO12-11 Size Measurement of Radioactive Aerosol Particles Using a Diffusion Battery and Imaging Plates in an Electron LINAC Facility

Y. Oki, K. Takamiya, M. Inagaki, S. Sekimoto

*Institute for Integrated Radiation and Nuclear Science,
Kyoto University*

INTRODUCTION: Recently mA-class accelerators have been developed for isotope production and medical use. Target melting accidents, such as the J-PARC accident in 2013, could happen easily by mis-handling of high-intensity beam. The nature of radioactive species in air of the accelerator rooms is very important information to estimate behavior of radionuclides emitted from the accidents in addition to ordinary radiation safety control.

During machine operation the accelerator room is filled with radiation-induced aerosol particles in the size range of several nm to ca. 100 nm in addition to radioactive gases. The size for the radioactive particles was often measured using a wire screen technique in accelerator facilities. Convenient size measurement techniques are needed for radiation protection in accelerator facilities. A combination technique with imaging plate (IP) was employed in a proton accelerator facility [1].

In this work, continuing from FY2020, an attempt was made to measure the size of ^{13}N -bearing aerosol particles using the combination technique of screen-type diffusion battery (SDB) and IPs in an electron linear accelerator facility. Nitrogen-13 is a principal radionuclide ($T_{1/2} = 9.965$ min) produced in air of accelerator rooms in electron LINACs.

EXPERIMENTS:

Measurement method: The SDB employed in this work consists of 40 pieces of 500-mesh stainless steel wire screen and a backup filter (PTFE membrane filter). After collection of the aerosol particles with the SDB, selected screens and the backup filter were measured with an IP.

Principle of SDB: When very fine aerosol particles pass through a stack of wire screens, a part of the particles is deposited on the wire surface of the screens by their diffusion according to their particle size. The loss by the screens is expressed as a function of particle size, coarseness and number of screens, and flow rate of particles. The radioactivity-based size distribution of the aerosol particles can be calculated by measuring the penetration ratio (A/A_0), where A_0 and A are activity of the nuclide of the aerosol particles before and after penetrating screens, respectively.

Formation and collection of radiation-induced aerosols: Aerosol-free air was irradiated with an electron beam air-irradiation experiment was carried out in the 46-MeV electron LINAC of the Institute for Integrated Radiation and Nuclear Science, Kyoto University (KURNS). An

irradiation chamber was placed at a rear position of a platinum target in the target room. During the irradiation, aerosol-free air was introduced to the chamber from the experiment room next to the target room. The target was bombarded with a 30-MeV electron beam to produce bremsstrahlung. The bremsstrahlung ionizes air and produces the radiation-induced aerosol. The beam current was ca. 100 μA . The irradiated air was sampled with the SDB at the measurement station in the experiment room.

Estimation of size distribution of radioactive aerosol particles: The IP image of the selected screens and the backup filter was simultaneously taken using a single large IP (Size: 43 x 35 cm). The penetration ratio for the i -th screen was calculated by the dividing total activity of the screens downstream of the i -th screen and the backup filter by the total activity of all screens and the backup filter. In this calculation, the activity of each 500-mesh screen was estimated by fitting of the intensity of photostimulated luminescence (PSL) of the measured 500-mesh screens.

RESULTS AND DISCUSSION: During the sampling the number-based particle size distribution was repeatedly measured using an SMPS (Scanning Mobility Particle Sizer). It was confirmed that the number-based particle size showed a stable lognormal distribution. The curve of the penetration ratios was successfully fitted to a theoretical function [2] for lognormal distributions to obtain the geometric mean and geometric standard deviation of particle diameter.

The preliminary result of the size was found to be in the range of 40 to 60 nm in diameter, which coincided with the particle size previously reported by another SDB method [3]. The activity-based particle size was always larger than the number-based particle size. The radioactive aerosol particles (the radionuclide-bearing radiation-induced aerosol particle) are formed by incorporating a radionuclide atom into the radiation-induced non-radioactive aerosol particle. The activity-based particle size can be simply compared with the number-based size without any correction. Because the number concentration of radiation-induced aerosol particles is several orders of magnitude greater than the activity concentration of radionuclides formed in accelerator air, the possibility of incorporation of plural radioactive atoms into a single the non-radioactive particle is negligible.

REFERENCES:

- [1] Y. Oki *et al.*, J. Radiat. Prot. Res., **41** (2016) 216-221.
- [2] Y.S. Cheng and H.C. Yeh, J. Aerosol Sci., **11** (1980) 313-320.
- [3] Y. Oki, KURNS Prog. Rep., (2019) CO10-7.

CO12-12 Study of Isotope Separation via Chemical Exchange Reaction

R. Hazama, T. Yoshimoto, A. Rittirong, Y. Sakuma¹, T. Fujii², T. Fukutani³, Y. Shibahara³, A. Sunaga³

Graduate School of Human Environment, Osaka Sangyo University

¹Laboratory for Advanced Nuclear Energy, Tokyo Institute of Technology,

²Graduate School of Engineering, Osaka University

³Institute for Integrated Radiation and Nuclear Science, Kyoto University

INTRODUCTION: Chemical isotope separation for calcium and lithium has been studied by liquid-liquid extraction (LLE) with DC18C6 crown-ether [1, 2]. This report describes the change of separation factor (α) for the total of six times multistage process of LLE in terms of different solvent of water and 12M HCl.

EXPERIMENTS: Chemical Isotopic exchange occurs according to the following chemical exchange reaction:

$$^{40}\text{Ca}^{2+}_{(\text{aq})} + ^{48}\text{CaL}^{2+}_{(\text{org})} \rightarrow ^{48}\text{Ca}^{2+}_{(\text{aq})} + ^{40}\text{CaL}^{2+}_{(\text{org})} \quad (1)$$
, where L represents macrocyclic polyether(18-crown-6). Calcium chloride solution (30% w/w CaCl_2 (aq), and CaCl_2 (12M HCl)) was mixed in an Erlenmeyer flask with 0.07M DC18C6 in chloroform, by the volume ratio of 5/100 mL (aq/org), for 1 minute. The mixture solution was put in the separating funnel for 10 minutes before separation. The loaded solvent was removed with 10 mL pure water for back-extraction.

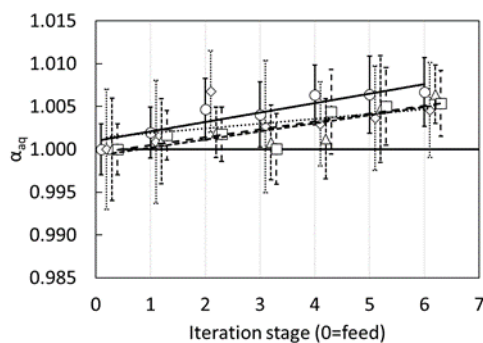


Fig 1. The separation factor (α) of Ca isotope over the iteration stage with 12M HCl acid solvent: Preliminary.

$\bigcirc = ^{48}\text{Ca}/^{40}\text{Ca}$ (—), $\diamond = ^{48}\text{Ca}/^{42}\text{Ca}$ (···),
 $\triangle = ^{48}\text{Ca}/^{43}\text{Ca}$ (-----), $\square = ^{48}\text{Ca}/^{44}\text{Ca}$ (- - -)

The same procedure was iterated using the recovered solution from the previous extraction for six iterations by the new 100 mL organic phase. The calcium concentration was measured by AAS (Shimadzu AA-6800). The isotopic composition was measured by reaction-cell ICP-MS (Agilent 7900: H_2 gas) (Fig 1, 2). It is noted that

our measured isotope ratios of reaction-cell ICP-MS were checked to give the same magnitude by the measurement of TIMS (TRITON and MAT261) by the help of TIT [3].

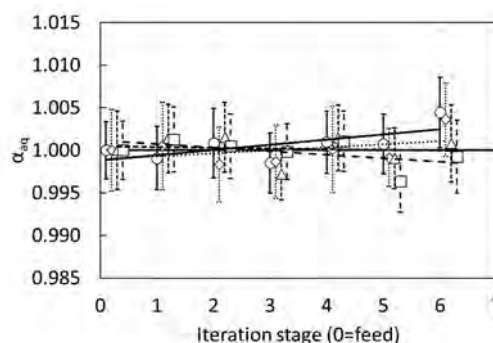


Fig 2. The separation factor (α) of Ca isotope over the iteration stage with aqueous solvent: Preliminary.

$\bigcirc = ^{48}\text{Ca}/^{40}\text{Ca}$ (—), $\diamond = ^{48}\text{Ca}/^{42}\text{Ca}$ (···),
 $\triangle = ^{48}\text{Ca}/^{43}\text{Ca}$ (-----), $\square = ^{48}\text{Ca}/^{44}\text{Ca}$ (- - -)

RESULTS: Multistage iteration using HCl solvent increased the calcium absorption to the crown-ether [2]. Therefore, the recovery of calcium is lower than the aqueous solvent (25.6% and 50.4% for HCl and aqueous solvent at the sixth iteration, respectively). The separation factor (α) ($^{48}\text{Ca}/^{40}\text{Ca}$) of the recovered calcium was 1.007 ± 0.004 and 1.004 ± 0.004 for HCl solvent and an aqueous solvent, respectively (Fig 1, 2). This finding indicated the enrichment feasibility of ^{48}Ca via liquid-liquid extraction under the presence of HCl acid, which can be compared with the chromatographic method [4]. It is noted that the recovery of cation content significantly influences a scale-up on mass production progress of isotope enrichment. Regardless of the calcium recovery, the required iteration to achieve ten-time enrichment of ^{48}Ca was 2112 and 3793 for HCl solvent and an aqueous solvent, respectively. The result shows that the mass production of calcium enrichment is possible via isotope exchange using crown-ether. Moreover, the LLE could be applied to other lighter elements, such as lithium [1, 2, 3], which is widely used in a nuclear reactor.

REFERENCES:

- [1] R. Hazama *et al.*, KURRI Progress Report 2020, 227.
- [2] A. Rittirong *et al.*, J. Phys.: Conf. Ser. 2022, 2147, 012015.
- [3] A. Rittirong, Doctor Thesis, OSU (2022).
- [4] S. Nemoto *et al.*, Journal of Nuclear Science and Technology 2012, 49.4: 425.

CO12-13 Beam Test of a Micro-Cell MWPC for a Muon-Electron Conversion Search Experiment, DeeMe

M. Aoki, N. Abe¹, K. Hase², Y. Higashino, H. Natori³, Y. Seiya², K. Sugita, T. Takahashi¹, N. Teshima², T. Uematsu², and K. Yamamoto²

School of Science, Osaka University

¹KURNS

²Faculty of Science, Osaka City University

³Institute of Materials Structure Science, KEK

INTRODUCTION: The charged-lepton flavor violation (CLFV) process such as the muon-electron conversion has never been observed for unknown reasons. Based on this fact, the charged-lepton flavor is assumed to be conserved a priori in the Standard Model of particle physics (SM). However, it is rather natural to introduce the CLFV processes in the frameworks of many models beyond SM (BSM). Any discoveries or improvements of upper limits on the rate of CLFV processes provide very important information to elucidate BSM. DeeMe is one of experiments to search for the μ -e conversion in nuclear field [1]. It uses high-power high-purity pulsed proton beam from J-PARC RCS and the detector of DeeMe should be operational after an order of micro second from a burst of prompt particles (100 GHz/mm²). We successfully developed a multi-wire proportional-chamber (MWPC) with such a novel feature by introducing high-voltage switching technique [2] and have been performing various R&D for further improvements of overall spectrometer performance.

EXPERIMENTS: The MWPC performance with gas mixtures of Ar : i-C₄H₁₀ (isobutane) : C₃H₈O₂ (methylal) was tested. Addition of methylal is expected to reduce delayed false MWPC-pulses observed for longer than 10 μ s after irradiation of burst electrons (10⁷ electrons/200-ns). Since methylal comes in a liquid state, it must be evaporated to gas by a precisely controlled manner. Such a gas mixture system is rather complicated and we were able to run the system stably after some struggles.

MWPC output-signal gains were measured using low-rate DC electrons from the LINAC, while the amount of delayed false pulses was investigated by injecting burst electrons to MWPC. MWPC output signals were recorded using a fast-FADC system [3].

We also coated a part of MWPC cathode strip with graphite and checked the effect on the MWPC gains. The cathode is made of aluminum, while graphite has a larger work function than aluminum by about 20%. If the delayed false pulses originate from electron emission at the cathode electrode caused by positive ions hitting it, graphite coating could reduce them.

As an extension of our spectrometer system, we are considering a plastic scintillation fiber-tracker system which can provide additional timing information. We tried to investigate responses of a plastic-scintillation fiber with SiPM readout to burst electrons. We newly developed a special circuit to switch bias voltages from the forward direction to reverse direction according to the burst timing

to see any effects on the slow recovery from the saturation due to burst injection.

RESULTS: Fig. 1 shows delayed false-pulse rate versus gain for a gas mixture of Ar : isobutane : methylal = 75 : 15 : 15. The case of mixing R-134a gas instead of methylal is also included for comparison of which data were taken in previous beam tests. It is seen that methylal is much more effective to reduce false-pulse rates compared to R-134a. The effect of delayed false pulses to momentum measurement is also estimated. For the same gas mixture and HV of 1460 V, the number of false tracks reconstructed from false pulses is expected to be about 0.01 for one year of data taking period and is confirmed to be small enough.

The effect of painting graphite on the aluminum cathode strip on the gains was found to be small, about a 5% level of reduction. As a longer-term plan, we would like to investigate signal-to-noise ratios and explore the possibility of coating the cathode surface with an appropriate material.

As to the response of the fiber-SiPM system with applying switching bias voltages, it was found that the state change of the SiPM due to switching the bias voltages from the forward direction to the reverse direction took rather a long time (about 40 μ s) which was too slow for our application. We need to investigate some more details of time evolution of semi-conductor states resulting from bias voltage switching.

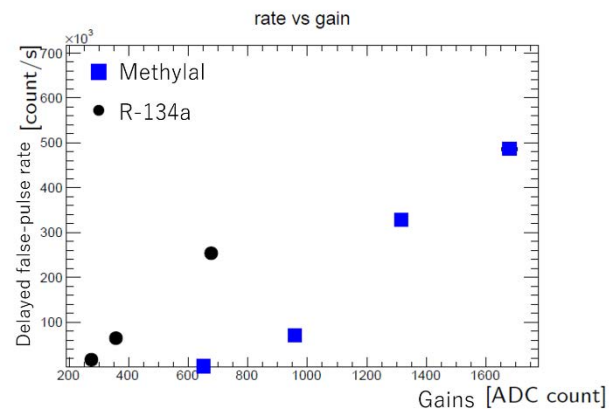


Fig. 1 Relation between the gain and the delayed false-pulse rate.

REFERENCES:

- [1] N. Teshima on behalf of the DeeMe Collaboration, “DeeMe experiment to search for muon to electron conversion at J-PARC MLF”, in proceedings of NUFACT conference PoS (NuFact2017) 109 (2018).
- [2] H. Natori, *et al.*, “A fast high-voltage switching multi-wire proportional chamber”, Prog. Theor. Exp. Phys. 2017(2) 023C01 (2017).
- [3] N.M. Truong, *et al.*, “Real-Time Lossless Compression of Waveforms Using an FPGA”, IEEE Trans. Nucl. Sci. 65 2650 (2018).

CO12-14 Determination of Impurity Metals in the Uranium Oxide by ICP-MS

T. Miura¹, K. Takamiya², Y. Iinuma², H. Yoshinaga²

¹National Metrology Institute of Japan, AIST

²Institute for Integrated Radiation and Nuclear Science, Kyoto University

INTRODUCTION: National Metrology Institute of Japan (NMIJ) is responsible for developing certified reference materials and for establishing the traceability of SI (The International System of Units) on chemical metrology in Japan. To establish SI traceability, the starting material of inorganic standard solution should be characterized and measured impurities by sensitive analytical method. In this study, the impurity metals in the uranium oxide reagent were measured by inductively coupled plasma mass spectrometry (ICP-MS) for assist the development of precise titration method for uranium.

EXPERIMENTS: The 0.2 g of uranium oxide reagent was weighed in the 200 mL borosilicate glass beaker. The weighed uranium oxide sample was dissolved by 5 mL of 69 % HNO₃. After dissolution of the uranium oxide reagent, the solution was diluted by 1 % HNO₃ and transfer to the 100 mL PFA (Perfluoroalkoxy alkane) bottle. Two samples (1.0 g and 0.98 g) were taken from the prepared sample solution. The sample solutions were evaporated to dryness using hot plate. After evaporation, the residue was dissolved with 20 mL 4 mol dm⁻³ HNO₃. The sample solutions were loaded on eichrom U/TEVA extraction chromatographic resin column (bed volume; 2 mL) that had been previously washed with 10 mL of 4 mol dm⁻³ HNO₃. The U/TEVA resin [1] column was then washed with 10 mL 4 mol dm⁻³ HNO₃ and 20 mL 5 mol dm⁻³ HCl. The Al, Mn, Fe, Bi, etc. on the U/TEVA resin column were eluted out with 10mL 4M nitric acid as the first washing solution, and then Th was eluted from the U/TEVA resin column with 20mL 5 mol dm⁻³ HCl as the second washing solution. The effluent at sample loading solution, 1st washing solution (10 mL 4 mol dm⁻³ HNO₃) and 2nd washing solution (20 mL 5 mol dm⁻³ HCl) combined and evaporated to dryness using hot plate. Then the residue was dissolved with 1 % HNO₃. The sample solutions were transferred to 50 mL polypropylene bottles. The sample solutions were introduced to determine the impurity metals by Analytic-jena PlasmaQuant ICP-MS. The operating conditions for the ICP-MS were shown in Table 1.

Table 1 Operating conditions for the ICP-MS

	ICP source operation parameters
RF power	1.2 kW
Plasma gas flow	9.0 L/min
Auxiliary gas flow	1.5 L/min
Nebulizer gas flow	1.0 L/min
Nebulizer	Borosilicate glass concentric

The NIST SRM standard solutions (Sc, La, Ce, Nd, Pr, Sm, Eu, Gd, Tb, Dy, Ho, Er, Tm, Yb, and Lu), SPEX XSTC-7, SPEX XSTC-22, SPEX XSTC-331 were used for calibration of the ICP-MS.

RESULTS: The analytical results of impurity metals were shown in Table 2. The

Table 2 Analytical results of metallic impurity elements in the uranium oxide reagent

	Analytical results		Analytical results
Sc	< 50 mg/kg	Pr	< 9 mg/kg
V	< 70 mg/kg	Nd	< 10 mg/kg
Cr	< 15 mg/kg	Sm	< 4 mg/kg
Mn	< 1 g/kg	Eu	< 2 mg/kg
Fe	< 0.1 g/kg	Gd	< 5 mg/kg
Co	< 12 mg/kg	Tb	< 4 mg/kg
Zn	< 35 mg/kg	Dy	< 8 mg/kg
Ga	< 19 mg/kg	Ho	< 14 mg/kg
Sr	< 11 mg/kg	Er	< 30 mg/kg
Y	< 6 mg/kg	Tm	< 9 mg/kg
Zr	< 50 mg/kg	Yb	< 2 mg/kg
Mo	< 11 mg/kg	Lu	< 10 mg/kg
Pd	< 23 mg/kg	Hf	< 3 mg/kg
Cd	< 9 mg/kg	Pt	< 16 mg/kg
Sn	< 40 mg/kg	Tl	< 7 mg/kg
Ba	< 6 mg/kg	Pb	< 0.5 g/kg
La	< 5 mg/kg	Bi	< 2 mg/kg
Ce	< 10 mg/kg	Th	< 16 mg/kg

REFERENCES:

[1] E. P. Horwitz *et al.*, Anal. Chim. Acta, 266, 25-37, 1992.

CO12-15 Neutron activation of medicines for development of new imaging methodology

A. Toyoshima, N. Koshikawa¹, Y. Kadonaga², A. Omata¹, M. Masubuchi¹, K. Tokoi³, A. Imada⁴, K. Takamiya⁵, and J. Kataoka¹

Institute for Radiation Sciences, Osaka University

¹*Graduate School of Advanced Science and Engineering, Waseda University*

²*Graduate School of Medicine, Osaka University*

³*Graduate School of Science, Osaka University*

⁴*School of Science, Osaka University*

⁵*Institute for Integrated Radiation and Nuclear Science, Kyoto University*

INTRODUCTION: In the drug delivery system, it is desired to obtain high therapeutic effects with no side-effect by direct transportation of medicine to lesion. At present, it is impossible to simultaneously evaluate the accumulation of administrated medicine in a targeted organ and its therapeutic effect without incision. Imaging of radiations emitted from activated medicine, however, makes it possible to visualize the pharmacokinetics without incision. In our group, an advanced imaging camera available for a wide energy range of X- and γ -rays has been already developed [1]. In this study, therefore, we activated gold nano-particle (AuNP), platinum nano-particle (PtNP), Cisplatin, and Gadoteridol by thermal neutron to produce short-lived radioisotopes suitable for imaging: ^{198}Au (half-life = 2.69 d), ^{159}Gd (18.48 h), and ^{197}Pt (18.3 h). This study is our first approach to develop a novel methodology of the radioactivated medicine imaging.

EXPERIMENTS: For AuNP, PtNP, and Gadoteridol, dried samples were separately prepared by evaporation of their commercial products on filter papers which were then enclosed in small plastic bags. For Cisplatin, its powder was enclosed in a plastic bag. The prepared AuNP (0.3 mg), Gadoteridol (1 mg), PtNP (2 mg), and Cisplatin (5 mg) samples were irradiated by thermal neutron using the Pn-2 pneumatic transport system of KUR for 1 min, 10 min, 20 min, and 20 min, respectively. After the irradiation, these were transported to Osaka University. Experiments of PtNP and Cisplatin were carried out 1 day after the irradiation for the decay of simultaneously produced detection-hindering radioisotope ^{199}Pt with a shorter half-life (30.8 min). Gamma rays from the samples were measured using a high purity Ge detector. For AuNP and PtNP, purification by filtration was made after suspension. For Gadoteridol and Cisplatin, HPLC analysis/separation was carried out after dissolution. After the separation, measurement for the purified samples was also conducted using the imaging camera [1].

RESULTS: In the measurements using the Ge detector, γ -rays of ^{198}Au (412 keV), ^{159}Gd (364 keV), ^{197}Pt (77 keV) were identified in the AuNP, Gadoteridol, and both PtNP and Cisplatin samples, respectively. In Fig. 1, γ -ray

spectrum of AUNP is showed as an example. Two γ -peaks of ^{198}Au and characteristic X-rays from Hg after the β^- decay of ^{198}Au are clearly seen. This means that the irradiated AuNP was activated as intended. For the activated samples, the amounts of the radioisotopes at the γ -ray measurements were determined to be approximately 100 kBq for ^{198}Au in AuNP, 70 kBq for ^{159}Gd in Gadoteridol, 15 kBq for ^{197}Pt in PtNP, and 70 kBq for ^{197}Pt in Cisplatin. Results on the purification of AuNP and PtNP, HPLC analysis of Gadoteridol and Cisplatin, and imaging of the activated samples are under analysis.

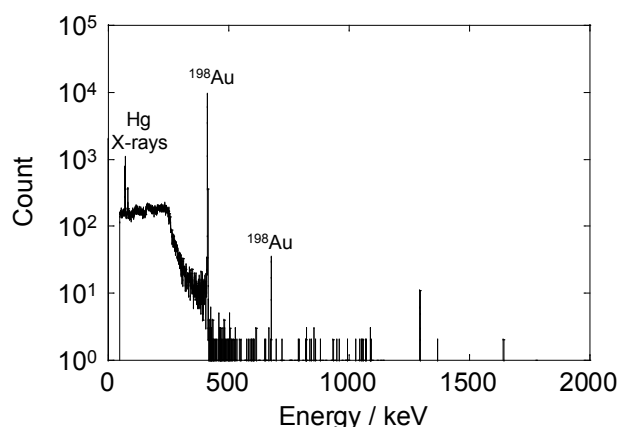


Fig. 1. Gamma ray spectrum of the activated AuNP measured with a high purity Ge detector.

REFERENCE:

[1] A. Omata *et al.*, *Sci. Reports*, **10** (2020), 14604.

CO12-16 Evaluation Test of Quantitative 3-D Measurement of Gamma Dose in the Reactor Building by ETCC

T.Tanimori¹, S.Sonoda¹, A.Takada¹, M.Tsuda¹,
K.Tahara¹, K.Kobayasi¹, H.Nagai², T.Sato²,
H.Nakayama², M.Tanigaki³, A.Taniguchi³

¹Graduate School of Science, Kyoto University

²Nuclear Science and Engineer Center, JAEA

³Institute for Integrated Radiation and Nuclear Science, Kyoto University

INTRODUCTION: We have developed an electron track detecting Compton camera (ETCC) that can uniquely determine the direction of arrival of MeV gamma rays. The ETCC is the unique gamma ray camera that can acquire linear images by bijective method as well as an optical camera, and thus can measure 3-D dose rates distribution from at least two directions simultaneously. On the other hand, conventional Compton cameras or multi-pinhole cameras cannot measure such quantitative 3D dose distribution due to their nonlinear images.

To demonstrate this, 3D measurements of the 1F (1st Fukushima Nuclear Power Plant) reactor building was scheduled in 2021 in the project of “Nuclear Energy Science & Technology and Human Resource Development Project” supported by JAEA. However, due to the coronal disaster, it has been impossible to carry out the measurement in 1F by the end of December 2021, when the project was to be terminated. Therefore, we proposed the 3D dose rate measurement in the reactor facility of this institute, which is the only facility in Japan that can be used jointly.

Method

The ETCC was set on the second-floor catwalk of the reactor building looking down on the reactor and measuring the reactor from four directions, 70 to 120 degrees apart in Fig.1. The average dose on the catwalk at 5 MW output is about 2 μ Sv/h. The 20 cm diameter ETCC to be used in this experiment has a detection efficiency of about 0.02% for 662 eV gamma radiation after noise reduction by analy-



Fig. 1 20cmETCC set on catwalk.

sis. Therefore, at this dose rate, 5 counts of gamma rays of which direction is determined completely per second can be obtained. To obtain a 3D dose distribution with an accuracy of 5 degrees cubic in space, we need at least 50,000 gamma rays per direction, which means that 2-4 hours observation at one direction is needed. Considering the operation time of 6hours at 5MW operation in one day, 3 days observation are needed.

EXPERIMENTS AND RESULTS:

The experiment was done at 5 WM output on December 2, 9, and 16. We measured the reactor from four different directions and obtained gamma-ray images with the energy range from 0.1 to 5 MeV. The data are currently being analyzed. It is already well known that when the reactor power is increased to 5 MW, the air inside the reactor is irradiated and ⁴¹Ar was produced. Then, a small amount of ⁴¹Ar was emitted outside the reactor. ⁴¹Ar emits 1290 keV γ -rays with a half-life of 110 minutes. Because the dose of ⁴¹Ar is so small, the details of how it exits from the reactor have long been unknown. From the catwalk in front of the control room, we measured the image of 1290 keV gammas after 10:00 a.m., when ⁴¹Ar was

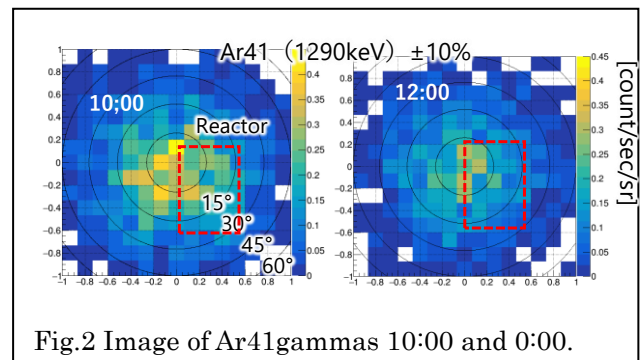


Fig.2 Image of Ar41gammas 10:00 and 0:00.

strongest, and at 12:00 a.m., when the half-life had elapsed, as shown in Fig.2, ⁴¹Ar was clearly measured to be decreasing. In fact, changes of ⁴¹Ar at intervals of 7 minutes were also captured, and we succeeded in capturing the diffusion of ⁴¹Ar as an animation. Currently, we are seeking the distribution of gamma rays in other energy regions and their three-dimensional distributiona.

II. PUBLICATION LIST
(APRIL 2021 – MARCH 2022)

1. Slow Neutron Physics and Neutron Scattering

Papers

Overscreening Induced by Ionic Adsorption at the Ionic Liquid/Electrode Interface Detected Using Neutron Reflectometry with a Rational Material Design

Nishi Naoya, Uchiyashiki Junya, Oda Tatsuro, Hino Masahiro, Yamada Norifumi L.

Bulletin of the Chemical Society of Japan **94(12)** (2021) **2914-2918** (doi) 10.1246/bcsj.20210328

Direct observation of magnetic Friedel oscillation at Fe(001) surface

Mitsui Takaya, Sakai Seiji, Li Songtian, Ueno Tetsuro, Watanuki Tetsu, Kobayashi Yasuhiro, Masuda Ryo, Seto Makoto, Akai Hisazumi

Hyperfine Interactions **242** (2021) **37** (doi) 10.1007/s10751-021-01772-0

Muon-Induced Single-Event Upsets in 20-nm SRAMs: Comparative Characterization with Neutrons and Alpha Particles

Kato Takashi, Tampo Motonobu, Takeshita Soshi, Tanaka Hiroki, Matsuyama Hideya, Hashimoto Masanori, Miyake Yasuhiro

IEEE Transactions on Nuclear Science **68(7)** (2021) **1436-1444** (doi) 10.1109/TNS.2021.3082559

Pure Nuclear Bragg Reflection due to Combined Magnetic and Quadrupole Interaction in Fe₃O₄

Nakamura Shin, Mitsui Takaya, Kurokuzu Masayuki, Shimomura Susumu

Journal of the Physical Society of Japan **90(10)** (2021) **104713** (doi) 10.7566/JPSJ.90.104713

Element-specific magnetic hysteresis loops observed in hexagonal ErFeO₃ thin films

Yokota Hiroko, Kobori Yu, Jitsukawa Shunsuke, Sakai Seiji, Takeda Yukiharu, Mitsui Takaya, Kobayashi Yasuhiro, Kitao Shinji

Materials Research Express **8(8)** (2021) **086402** (doi) 10.1088/2053-1591/ac1aa9

Quasielastic Neutron Scattering for Analyzing Transport Dynamics of Chemically-Bound Hydrogen in Minerals Takuo OKUCHI

Nihon Kessho Gakkaishi **2** (2021) **129-134** (in Japanese) (doi) 10.5940/jcrsj.63.129

Double-focusing geometry for phase correction in neutron resonance spin-echo spectroscopy

Funama F., Tasaki S., Hino M., Oda T., Endo H.

Nuclear Instruments and Methods in Physics Research Section A: Accelerators, Spectrometers, Detectors and Associated Equipment **1010** (2021) **165480** (doi) 10.1016/j.nima.2021.165480

Phase correction method in a wide detector plane for MIEZE spectroscopy with pulsed neutron beams

Oda Tatsuro, Endo Hitoshi, Ohshita Hidetoshi, Seya Tomohiro, Yasu Yoshiji, Nakajima Taro, Hino Masahiro, Kawabata Yuji

Nuclear Instruments and Methods in Physics Research Section A: Accelerators, Spectrometers, Detectors and Associated Equipment **1012** (2021) **165616** (doi) 10.1016/j.nima.2021.165616

Neutron flat-panel detector using In–Ga–Zn–O thin-film transistor

Fujiwara Takeshi, Miyoshi Hiroaki, Mitsuya Yuki, Yamada Norifumi L., Wakabayashi Yasuo, Otake Yoshie, Hino Masahiro, Kino Koichi, Tanaka Masahito, Oshima Nagayasu, Takahashi Hiroyuki

Review of Scientific Instruments **93(1)** (2022) **013304** (doi) 10.1063/5.0066557

Neutron reflectometry-based in situ structural analysis of an aligning agent additive for the alignment of nematic liquid crystals on solid substrates

Nemoto Fumiya, Yamada Norifumi L., Hino Masahiro, Aoki Hiroyuki, Seto Hideki

Soft Matter **18(3)** (2021) **545-553** (doi) 10.1039/d1sm01355f

Proceedings

Conceptual design of neutron source driven by the proton cyclotron at Institution for Integrated Radiation and Nuclear Science, Kyoto University.

Riichiro Nakamura, Masahiro Hino, Hiroki Tanaka, Yasutoshi Kuriyama, Yoshihisa Iwashita

Proceedings of the 56th KURNS Scientific Meeting, Online (Feb. 9-10, 2022) **25** (in Japanese)

Present Status of Source Development of Various-Element Mössbauer Spectroscopy using KUR and LINAC at KURNS

Shinji Kitao, Yasuhiro Kobayashi, Masayuki Kurokuzu, Makoto Seto, Hiroyuki Tajima, Hiroyuki Yamashita, Taku Fujihara, Takumi Kubota

Proceedings of the 56th KURNS Scientific Meeting, Online (Feb. 9-10, 2022) 34 (in Japanese)

Structural Analysis of Additives in Lubricants by Means of Small Angle X-Ray Scattering

Tomoko Hirayama, Shoei Nanbo, Wataru Yagi, Yoriyuki Takashima, Nobuhiro Sato, Masaaki Sugiyama

Proceedings of the 56th KURNS Scientific Meeting, Online (Feb. 9-10, 2022) 38 (in Japanese)

Structural analysis of DLC films using positron, soft x-ray and high energy ion beams

Kazuhiro Kanda, Tomohiro Mishima, Fuminobu Hori, Atsushi Yabuuchi, Atsushi Kinomura

Proceedings of the 56th KURNS Scientific Meeting, Online (Feb. 9-10, 2022) 41 (in Japanese)

Understanding relationship between structure and property in disordered materials via topological analyses

Yohei Onodera

Proceedings of the 56th KURNS Scientific Meeting, Online (Feb. 9-10, 2022) 64-66 (in Japanese)

Improvement of Spectral Resolution for β -NMR Spectroscopy in Liquids

M. Mihara, K. Matsuta, M. Fukuda, R. Wakabayashi, Y. Otani, Y. Kimura, M. Fukutome, G. Takayama, T. Minamisono, D. Nishimura, H. Takahashi, T. Izumikawa, T. Ohtsubo, N. Noguchi, M. Ogose, M. Sato, K. Takatsu, S. Momota, A. Ozawa, T. Nagatomo, A. Kitagawa, and S. Sato

Proceedings of the Specialists' Meeting on "Nuclear Spectroscopy and Condensed Matter Physics Using Short-Lived Nuclei VIII" Online, (Jan. 15, 2021) 41-44 (in Japanese)

Others

中性子の波紋と超高分解能写真フィルム(原子核乾板)で重力を撮る

Naotaka Naganawa

名古屋大学アイソトープ総合センターTracer 71 (2022) 3-8 (in Japanese)

2. Nuclear Physics and Nuclear Data

Papers

Tritium release behavior from neutron-irradiated FLiNaBe mixed with titanium powder

Kubo Kaito, Katayama Kazunari, Oya Makoto, Tsukahara Katsuya, Fukada Satoshi, Tanaka Teruya, Sagara Akio, Yagi Juro, Inuma Yuto

Fusion Engineering and Design 171 (2021) 112558 (doi) 10.1016/j.fusengdes.2021.112558

Proton radiation hardness of x-ray SOI pixel sensors with pinned depleted diode structure

Hayashida Mitsuki, Hagino Kouichi, Kohmura Takayoshi, Kitajima Masatoshi, Yarita Keigo, Oono Kenji, Negishi Kousuke, Tsuru Takeshi G., Tanaka Takaaki, Uchida Hiroyuki, Kayama Kazuho, Kodama Ryota, Mori Koji, Takeda Ayaki, Nishioka Yusuke, Hida Takahiro, Yukumoto Masataka, Arai Yasuo, Kurachi Ikuo, Kitamura Hisashi, Kawahito Shoji, Yasutomi Keita

Journal of Astronomical Telescopes, Instruments, and Systems 7(3) (2021) 036001

(doi) 10.1117/1.JATIS.7.3.036001

Measurements of the neutron capture cross section of ^{243}Am around 23.5 keV

Kodama Yu, Katabuchi Tatsuya, Rovira Gerard, Kimura Atsushi, Nakamura Shoji, Endo Shunsuke, Iwamoto Nobuyuki, Iwamoto Osamu, Hori Jun-ichi, Shibahara Yuji, Terada Kazushi, Nakano Hideto, Sato Yaoki

Journal of Nuclear Science and Technology 58(11) (2021) 1159-1164 (doi) 10.1080/00223131.2021.1943557

Thermal-neutron capture cross-section measurement of Tantalum-181 using graphite thermal column at KUR

Nakamura Shoji, Shibahara Yuji, Endo Shunsuke, Kimura Atsushi

Journal of Nuclear Science and Technology 58(10) (2021) 1061 (doi) 10.1080/00223131.2021.1908187

Nuclear Resonance Vibrational Spectroscopic Definition of the Fe(IV)_2 Intermediate Q in Methane Monooxygenase and Its Reactivity

Jacobs Ariel Benjamin, Banerjee Rahul, Deweese Dory Ellen, Braun Augustin, Babicz Jeffrey Thomas, Gee Leland Bruce, Sutherland Kyle David, Böttger Lars Hendrik, Yoda Yoshitaka, Saito Makina, Kitao Shinji, Kobayashi Yasuhiro, Seto Makoto, Tamasaku Kenji, Lipscomb John D., Park Kiyoungh, Solomon Edward I.
Journal of the American Chemical Society **143(39)** (2021) **16007-16029** (doi) 10.1021/jacs.1c05436

Development of All-in-one Phantom Dosimeter to Measure Multidimensional Dose Distribution for Co-60 Radiotherapy Unit

H. Y. Shin, J. H. Kim, S. W. Song, J. H. Kim, B. Lee, J. H. Moon and C. H. Pyeon

JOURNAL OF THE KOREAN PHYSICAL SOCIETY **78** (2021) **829-836**

(doi) 10.1007/s40042-021-00129-8

Neutron beam filter system for fast neutron cross-section measurement at the ANNRI beamline of MLF/J-PARC
Rovira Gerard, Kimura Atsushi, Nakamura Shoji, Endo Shunsuke, Iwamoto Osamu, Iwamoto Nobuyuki, Katabuchi Tatsuya, Terada Kazushi, Kodama Yu, Nakano Hideto, Hori Jun-ichi, Shibahara Yuji

Nuclear Instruments and Methods in Physics Research Section A: Accelerators, Spectrometers, Detectors and Associated Equipment **1003** (2021) **165318** (doi) 10.1016/j.nima.2021.165318

Effect of neutron-photon converter materials (Cd, Gd, and Sm) on the positron production in a reactor-based slow positron beamline

Atsushi Yabuuchi

Nuclear Instruments and Methods in Physics Research Section B: Beam Interactions with Materials and Atoms **513** (2022) **44-49** (doi) 10.1016/j.nimb.2021.12.008

Enhancement of the parity-violating energy difference of H₂X₂ molecules by electronic excitation

Kuroda Naoya, Oho Takumi, Senami Masato, Sunaga Ayaki

Physical Review A **105(1)** (2022) **12820** (doi) 10.1103/PhysRevA.105.012820

Enforced stripping of negative muons from μHe^+ ions to stimulate muon-catalyzed fusion by cyclotron resonance acceleration

Yoshiharu Mori

Progress of Theoretical and Experimental Physics **2021(9)** (2021) **093G01** (doi) 10.1093/ptep/ptab111

Proceedings

⁶¹Ni Mössbauer Spectroscopy for Hofmann-like Coordination Polymers

T. Kitazawa, H. Okada, D. Ueda, Y. Kobayashi, S. Kitao, T. Kubota and M. Seto

Proceedings of the Specialists' Meeting on "Nuclear Spectroscopy and Condensed Matter Physics Using Short-Lived Nuclei VII" Online, (Jan. 15, 2021) 10-15 (in Japanese)

Development of Time- and Energy-Resolved Mössbauer Spectroscopy

S. Kitao, R. Masuda, H. Taniguchi, H. Tajima, Y. Yoda, and M. Seto

Proceedings of the Specialists' Meeting on "Nuclear Spectroscopy and Condensed Matter Physics Using Short-Lived Nuclei VII" Online, (Jan. 15, 2021) 1-3 (in Japanese)

Mössbauer spectroscopy in Fe-Ag Hofmann-type SCO complex

K. Kitase, M. Takahashi and T. Kitazawa

Proceedings of the Specialists' Meeting on "Nuclear Spectroscopy and Condensed Matter Physics Using Short-Lived Nuclei VII" Online, (Jan. 15, 2021) 4-9 (in Japanese)

Observation of Dynamic Behavior of Indium Doped SrTiO₃ Studied by Means of the Perturbed Angular Correlation Method

S. Komatsuda, W. Sato, and Y. Ohkubo

Proceedings of the Specialists' Meeting on "Nuclear Spectroscopy and Condensed Matter Physics Using Short-Lived Nuclei VII" Online, (Jan. 15, 2021) 49-53 (in Japanese)

Synchrotron-Radiation-Based Mössbauer Spectroscopy on High-Energy Resonant Nuclei using a He-free Cryostat

S. Tsutsui

Proceedings of the Specialists' Meeting on "Nuclear Spectroscopy and Condensed Matter Physics Using Short-Lived Nuclei VII" Online, (Jan. 15, 2021) 16-21 (in Japanese)

Experimental plan for displacement damage cross sections using 120-GeV protons at Fermi National Accelerator Laboratory

Yosuke IWAMOTO, Makoto YOSHIDA, Shin-ichiro MEIGO, Katsuya YONEHARA, Taku ISHIDA, Keita NAKANO, Shin-ichiro ABE, Hiroki IWAMOTO, T. SPINA, K. AMMIGAN, N. MOKHOV, Atsushi YABUUCHI, and Toshimasa YOSHIIE

Symposium on Nuclear Data 2020 (SND2020) Wako, Japan, (Jan. 26-27, 2020) 138-143

Books

Measurements of Displacement Cross Section of Tungsten under 389-MeV Proton Irradiation and Thermal Damage Recovery

Iwamoto Yosuke, Yoshida Makoto, Matsuda Hiroki, Meigo Shin Ichiro, Satoh Daiki, Yashima Hiroshi, Yabuuchi Atsushi, Shima Tatsushi

Materials Science Forum Vol. 1024

Prof. Kenji Kikuchi

Trans Tech Publications, Ltd. (2021) (doi) 4028/www.scientific.net/MSF.1024.95

Others

Neutron filtering system for fast neutron cross-section measurement at ANNRI

G. Rovira, O. Iwamoto, A. Kimura, S. Nakamura, N. Iwamoto, S. Endo, T. Katabuhi, K. Terada, Y. Kodama, H. Nakano, J. Hori, Y. Shibahara

JAEA-conf20211 (2022)

Thermal-neutron capture cross-section measurement of ^{237}Np using graphite thermal columnS.

Nakamura, S. Endo, A. Kimura, Y. Shibahara

KURNS Progress Report 2020 (2021) 94

3. Reactor Physics and Reactor Engineering

Papers

Rapid Discrimination of Extracellular Vesicles by Shape Distribution Analysis

Ryuzaki Sou, Yasui Takao, Tsutsui Makusu, Yokota Kazumichi, Komoto Yuki, Paisrisarn Piyawan, Kaji Noritada, Ito Daisuke, Tamada Kaoru, Ochiya Takahiro, Taniguchi Masateru, Baba Yoshinobu, Kawai Tomoji

Analytical Chemistry 93(18) (2021) 7037-7044 (doi) 10.1021/acs.analchem.1c00258

Application of dynamic mode decomposition to exponential experiment for spatial decay constant determination
Yamamoto Toshihiro, Sakamoto Hiroki

Annals of Nuclear Energy 162 (2021) 108506 (doi) 10.1016/j.anucene.2021.108506

First demonstration experiment of the neutron rotation method for detecting nuclear material

Komeda M., Toh Y., Tanabe K., Kitamura Y., Misawa T.

Annals of Nuclear Energy 159 (2021) 108300 (doi) 10.1016/j.anucene.2021.108300

Novel Method of Search for Transparent Optical Materials with Extremely High Melting Point

Kurashima Yutaro, Kurosawa Shunsuke, Murakami Rikito, Yamaji Akihiro, Ishikawa Shiori, Pejchal Jan, Kamada Kei, Yoshino Masao, Toyoda Satoshi, Sato Hiroki, Yokota Yuui, Ohashi Yuji, Yoshikawa Akira

Crystal Growth & Design 21(1) (2021) 572-578 (doi) 10.1021/acs.cgd.0c01396

SiC p+n Junction Diodes Toward Beam Monitor Applications

Kishishita Tetsuichi, Kosugi Ryoji, Fujita Yowichi, Fukao Yoshinori, Kojima Kazutoshi, Masumoto Keiko, Nishiguchi Hajime, Tanaka Manobu M., Tanaka Yasunori

IEEE Transactions on Nuclear Science 68(12) (2021) 2787-2793 (doi) 10.1109/TNS.2021.3118788

Role of Al Substitution in the Enhancement of High-Temperature Thermoelectric Properties of ZnO Compound
Pilasuta Panida, Paengson Supasit, Singsoog Kunchit, Seetawan Tosawat

Integrated Ferroelectrics 222(1) (2022) 28-37 (doi) 10.1080/10584587.2021.1961513

Flow regime and void fraction predictions in vertical rod bundle flow channels

Han Xu, Shen Xiuzhong, Yamamoto Toshihiro, Nakajima Ken, Sun Haomin, Hibiki Takashi

International Journal of Heat and Mass Transfer 178 (2021) 121637

(doi) 10.1016/j.ijheatmasstransfer.2021.121637

Evaluation of Gas Entrainment Flow Rate by Free Surface Vortex

TORIKAWA Tomoaki, ODAIRA Naoya, ITO Daisuke, ITO Kei, SAITO Yasushi, MATSUSHITA Kentaro, EZURE Toshiki, TANAKA Masaaki

JAPANESE JOURNAL OF MULTIPHASE FLOW 36(1) (2022) 63-69 (in Japanese)

(doi) 10.3811/jjmf.2022.004

Pressure Drop of Single-/Two-Phase Flow in Fin-Type Heat Sink

ZHANG Huanran, ODAIRA Naoya, TO Daisuke, ITO Kei, SAITO Yasushi, SHINOZAKI Masaru

JAPANESE JOURNAL OF MULTIPHASE FLOW 36(1) (2022) 37-46 (in Japanese) (doi) 10.3811/jjmf.2022.001

Exact Monte Carlo calculation method for K-eigenvalue change using perturbation source method

Yamamoto Toshihiro, Sakamoto Hiroki

Journal of Nuclear Science and Technology 58(8) (2021) 886-898 (doi) 10.1080/00223131.2021.1883144

KeV-neutron capture cross-section measurement of ¹⁹⁷Au with a Cr-filtered neutron beam at the ANNRI beamline of MLF/J-PARC

Rovira Gerard, Kimura Atsushi, Nakamura Shoji, Endo Shunsuke, Iwamoto Osamu, Iwamoto Nobuyuki, Katabuchi Tatsuya, Kodama Yu, Nakano Hideto, Sato Yaoki, Hori Jun-ichi, Shibahara Yuji, Terada Kazushi

Journal of Nuclear Science and Technology 59(5) (2021) 647-655 (doi) 10.1080/00223131.2021.1997666

Monte Carlo Analyses of Light-Water-Moderated and Light-Water-Reflected Cores with Highly-Enriched Uranium Fuel at Kyoto University Critical Assembly

C. H. Pyeon and K. Morioka

Journal of Nuclear Science and Technology 59 (2022) 257-265 (doi) 10.1080/00223131.2021.1961636

Uncertainty Quantification of Lead and Bismuth Sample Reactivity Worth at Kyoto University Critical Assembly

C. H. Pyeon, M. Yamanaka and M. Fukushima

Journal of Nuclear Science and Technology 195(8) (2021) 877-889 (doi) 10.1080/00295639.2020.1870861

Thermal-hydraulic characteristics of upward two-phase flows in vertical large size square channels

Hibiki Takashi, Katono Kenichi, Shen Xiuzhong

Nuclear Engineering and Design 384 (2021) 111490 (doi) 10.1016/j.nucengdes.2021.111490

Comparison of Theoretical and Machine Learning Models to Estimate Gamma Ray Source Positions using Plastic Scintillating Optical Fiber Detector

J. H. Kim, S. H. Kim, S. W. Song, J. H. Park, J. H. Kim, T. S. Lim, C. H. Pyeon and B. Lee

Nuclear Engineering and Technology 53(10) (2021) 3431-3437 (doi) 10.1016/j.net.2021.04.019

Development of a multiwire proportional chamber with good tolerance to burst hits

Teshima N., Aoki M., Higashino Y., Ikeuchi H., Komukai K., Nagao D., Nakatsugawa Y., Natori H., Seiya Y., Truong N.M., Yamamoto K.

Nuclear Instruments and Methods in Physics Research Section A: Accelerators, Spectrometers, Detectors and Associated Equipment 999 (2021) 165228 (doi) 10.1016/j.nima.2021.165228

Applicability of Dynamic Mode Decomposition to Estimate Fundamental Mode Component of Prompt Neutron Decay Constant

F. Nishioka, T. Endo, A. Yamamoto, M. Yamanaka and C. H. Pyeon

Nuclear Science and Engineering 196 (2022) 133-143 (doi) 10.1080/00295639.2021.1968225

Experimental Analyses of ²⁴³Am and ²³⁵U Fission Reaction Rates at Kyoto University Critical Assembly

C. H. Pyeon, A. Oizumi and M. Fukushima

Nuclear Science and Engineering 195 (2021) 1144-1153 (doi) 10.1080/00295639.2021.1932220

Gamma-ray Spectroscopy using Inorganic Scintillator Coated with Reduced Graphene Oxide in Fiber-Optic Radiation Sensor

J. H. Kim, S. H. Kim, S. W. Song, T. S. Lim, J. H. Park, J. H. Kim, C. H. Pyeon, S. W. Hwang, B. S. Lee

Photonics 12 (2021) 543-543 (doi) 10.3390/photonics8120543

Deterministic and stochastic methods for sensitivity analysis of neutron noise
Yamamoto Toshihiro, Sakamoto Hiroki
Progress in Nuclear Energy 145 (2022) 104130 (doi) 10.1016/j.pnucene.2022.104130

Proceedings

Characteristics of Two-Phase Flow in Packed Bed Systems
Yasugi Noriaki, Fujitsu Akito, Odaira Naoya, Ito Daisuke, Ito Kei, Saito Yasushi
2021 28th International Conference on Nuclear Engineering, Online (Aug. 4-6, 2021) V004T14A066
(doi) 10.1115/ICONE28-64955

COMPARISON OF NEUTRON NOISE SOLVERS BASED ON NUMERICAL BENCHMARKS IN A 2-D SIMPLIFIED UOX FUEL ASSEMBLY

P.Vinai, H. Yi, A. Mylonakis, C. Demaziere B. Gasse, A. Rouchon, A. Zoia, A. Vidal-Ferrandiz, G. Verdu, T. Yamamoto

Proceedings of International Conference on Mathematics and Computational Methods Applied to Nuclear Science and Engineering (M&C2021) Online (Jan. 3-7, 2021)

Evaluation of Gas Entrainment Flow Rate by Free Surface Vortex
Tomoaki Torikawa, Naoya Odaira, Daisuke Ito, Kei Ito, Yasushi Saito
Proceedings of the 56th KURNS Scientific Meeting, Online (Feb. 9-10, 2022) 18 (in Japanese)

Evaluation of interfacial area concentration for gas-liquid two-phase flow in coolant flow channels of MTR-type fuel assembly

Xiuzhong Shen, Toshihiro Yamamoto, Takashi Hibiki
Proceedings of the 56th KURNS Scientific Meeting, Online (Feb. 9-10, 2022) 46 (in Japanese)

Measurement of current induced on triaxial cables under gamma-ray irradiation
Yasuhito Gotoh, Nobuhiro Sato, Yasuki Okuno, Masafumi Akiyoshi, Mitsuru Imaizumi, Tomohiro Kobayashi, Tamotsu Okamoto
Proceedings of the 56th KURNS Scientific Meeting, Online (Feb. 9-10, 2022) 17 (in Japanese)

Pressure drop of two-phase flow in fin-type heat sink
Huanran Zhang, Naoya Odaira, Daisuke Ito, Kei Ito, Yasushi Saito
Proceedings of the 56th KURNS Scientific Meeting, Online (Feb. 9-10, 2022) 35 (in Japanese)

Reviews

Issues on Criticality Safety Control of Fuel Debris
Ken Nakajima
Insights Concerning the Fukushima Daiichi Nuclear Accident 2 (2021) 191-198

Issues for regulatory compliance for nuclear fuel and RI facilities at universities
Mitsuru Uesaka, Masami Uno, Takumi Saito, Sato Nobuaki, Tatsuya Suzuki, Takehiko Tsukahara, Ken Nakakjima, Toshiaki Hiyama, Hiroaki Muta
Journal of the Atomic Energy Society of Japan 63(4) (2021) 353-357 (in Japanese)

Task and recommendation for nuclear fuel and RI facilities at universities
Masami Uno, Kozo Katsuyama, Takumi Saito, Nobuaki Sato, Tatsuya Suzuki, Takehiko Tsukahara, Ken Nakakjima, Toshiaki Hiyama, Fiminori Honda, Hiroaki Muta, Tomoo Yamamura
Journal of the Atomic Energy Society of Japan 64(2) (2022) 110-114 (in Japanese)

Books

Part V 原子力教育・人材育成 (分担執筆)
中島健(計 63 名による共著)
The Nuclear Almanac 2022
山脇道夫(「原子力年鑑 2022」編集委員会)
日刊工業新聞社 (2021) (in Japanese)

Others

事故耐性の高い軽水炉用制御棒の開発(4)京大炉による新型中性子吸収材の照射試験
太田 宏一, 中村 勤也, 佐野 忠史, 高橋 佳之
日本原子力学会 2021 年春の年会 2K03 (2021) (in Japanese)

4. Material Science and Radiation Effects

Papers

Enhancement of Thermoelectric Properties of n-Type $\text{Bi}_2\text{Te}_{3-x}\text{Se}_x$ by Energy Filtering Effect
Kawajiri Yuhei, Tanusilp Sora-at, Kumagai Masaya, Ishimaru Manabu, Ohishi Yuji, Tanaka Junya, Kurosaki Ken
ACS Applied Energy Materials 4(10) (2021) 11819-11826 (doi) 10.1021/acsaem.1c02560

Flexible Thermoelectric Paper and Its Thermoelectric Generator from Bacterial Cellulose/ Ag_2Se Nanocomposites
Palaporn Dulyawich, Mongkolthanasak Wiyada, Faungnawakij Kajornsak, Kurosaki Ken, Pinitsoontorn Supree
ACS Applied Energy Materials 5(3) (2022) 3489-3501 (doi) 10.1021/acsaem.1c04042

A simple method for fabricating flexible thermoelectric nanocomposites based on bacterial cellulose nanofiber and Ag_2Se
Dulyawich Palaporn, Wiyada Mongkolthanasak, Sora-at Tanusilp, Ken Kurosaki, and Supree Pinitsoontorn
Applied Physics Letters 120 (2022) 073901-1-073901-7 (doi) 10.1063/5.0077137

Effect of silica-nanoparticle fillers on the Johari-Goldstein- β process in polymer nanocomposites
Saito Makina, Mashita Ryo, Kanaya Toshiji, Kishimoto Hiroyuki, Yoda Yoshitaka, Seto Makoto
Hyperfine Interactions 242 (2021) 58 (doi) 10.1007/s10751-021-01784-w

Mössbauer spectroscopy with polarized synchrotron beams at Fe/Au (111) interface
Okabayashi Jun, Li Songtian, Sakai Seiji, Kobayashi Yasuhiro, Fujiwara Kosuke, Mitsui Takaya, Mitani Seiji
Hyperfine Interactions 242(1) (2021) 59 (doi) 10.1007/s10751-021-01788-6

Crystallographic hydride phase analysis and hydrogenation properties of Gd_2Co_7 with Ce_2Ni_7 - and Er_2Co_7 -type structures
Iwase Kenji, Ishida Shuhei, Mori Kazuhiro
International Journal of Hydrogen Energy 45(51) (2021) 27413-27420 (doi) 10.1016/j.ijhydene.2020.07.045

Anisotropy and stability of the mechanical properties of the W alloy plate reinforced with Y-Zr-O particles and prepared by a wet chemical method
Zhao Zhi-Hao, Yao Gang, Luo Lai-Ma, Zan Xiang, Xu Qiu, Wu Yu-Cheng
International Journal of Refractory Metals and Hard Materials 99 (2021) 105597
(doi) 10.1016/j.ijrmhm.2021.105597

Gamma-ray irradiation effects on CdTe solar cell dosimeter
Okamoto Tamotsu, Igari Tomoya, Fukui Takahiro, Tozawa Ryuto, Gotoh Yasuhito, Sato Nobuhiro, Okuno Yasuki, Kobayashi Tomohiro, Imaizumi Mitsuru, Akiyoshi Masafumi
Japanese Journal of Applied Physics 60 (2021) SBBF02-1-SBBF02-5 (doi) 10.35848/1347-4065/abd6d8

Effects of dislocations and hydrogen concentration on hydrogen embrittlement of austenitic 316 stainless steels
Ye Fengjiao, Zhu Te, Mori Kazuhiro, Xu Qiu, Song Yamin, Wang Qianqian, Yu Runsheng, Wang Baoyi, Cao Xingzhong
Journal of Alloys and Compounds 876 (2021) 160134 (doi) 10.1016/j.jallcom.2021.160134

Influence of hydrogen behaviors on tensile properties of equiatomic FeCrNiMnCo high-entropy alloy
Zhu T., Zhong Z.H., Ren X.L., Song Y.M., Ye F.J., Wang Q.Q., Ngan Alfonso H.W., Wang B.Y., Cao X.Z., Xu Q.
Journal of Alloys and Compounds 892 (2022) 162260 (doi) 10.1016/j.jallcom.2021.162260

Investigation of irradiation resistance characteristics of precipitation strengthened high-entropy alloy (CoCrFeNi)
 $_{95}\text{Ti}_1\text{Nb}_1\text{Al}_3$ using slow positron beam
Xu Q., Zhu T., Zhong Z.H., Cao X.Z., Tsuchida H.
Journal of Alloys and Compounds 888 (2021) 161518 (doi) 10.1016/j.jallcom.2021.161518

Controlled thermal expansion and thermoelectric properties of Mg₂Si/Si composites
Fu Jiahui, Tanusilp Sora-at, Kumagai Masaya, Ohishi Yuji, Kurosaki Ken
Journal of Applied Physics **130(3)** (2021) 035105 (doi) 10.1063/5.0057137

Change in nanoindentation hardness of polycrystalline tungsten irradiated with Fe ions or electrons by hydrogen gas charging
Sato Koichi, Kasada Ryuta, Kiyohara Atsushi, Hirabaru Masashi, Nakano Kenichi, Yabuuchi Kiyohiro, Hatakeyama Masahiko, Xu Qiu
Journal of Nuclear Materials **560** (2022) 153483 (doi) 10.1016/j.jnucmat.2021.153483

Effect of He on the irradiation resistance of equiatomic CoCrFeMnNi high-entropy alloy
Huang S.S., Guan H.Q., Zhong Z.H., Miyamoto M., Xu Q.
Journal of Nuclear Materials **561** (2022) 153525 (doi) 10.1016/j.jnucmat.2022.153525

Evaluating surface damage behavior of W-(Y_{0.9}La_{0.1})₂O₃ composites during spark plasma sintering process improvement
Yao Gang, Liu Xue-Peng, Zhao Zhi-Yuan, Zhao Zhi-Hao, Luo Lai-Ma, Cheng Ji-Gui, Zan Xiang, Xu Qiu, Wu Yu-Cheng
Journal of Nuclear Materials **558** (2021) 153322 (doi) 10.1016/j.jnucmat.2021.153322

Radiation-enhanced diffusion of copper in iron studied by three-dimensional atom probe
Toyama T., Zhao C., Yoshiie T., Yamasaki S., Uno S., Shimodaira M., Miyata H., Suzudo T., Shimizu Y., Yoshida K., Inoue K., Nagai Y.
Journal of Nuclear Materials **556** (2021) 153176 (doi) 10.1016/j.jnucmat.2021.153176

Tensile fracture behavior and texture evolution of a hot-rolled W–Y₂ (Zr)O₃ alloy
Zhao Zhi-Hao, Yao Gang, Luo Lai-Ma, Zan Xiang, Xu Qiu, Wu Yu-Cheng
Journal of Nuclear Materials **554** (2021) 153080 (doi) 10.1016/j.jnucmat.2021.153080

The superior thermal stability and irradiation resistance capacities of tungsten composites synthesized by simple second-phase particle component modulation
Yao Gang, Chen Hong-Yu, Zhao Zhi-Hao, Luo Lai-Ma, Ma Yong, Cheng Ji-Gui, Zan Xiang, Xu Qiu, Wu Yu-Cheng
Journal of Nuclear Materials **561** (2022) 153522 (doi) 10.1016/j.jnucmat.2022.153522

Neutron capture and total cross-section measurements and resonance parameter analysis of niobium-93 below 400 eV
Endo Shunsuke, Kimura Atsushi, Nakamura Shoji, Iwamoto Osamu, Iwamoto Nobuyuki, Rovira Gerard, Terada Kazushi, Meigo Shin-ichiro, Toh Yosuke, Segawa Mariko, Maeda Makoto, Tsuneyama Masayuki
Journal of Nuclear Science and Technology **59(3)** (2021) 318-333 (doi) 10.1080/00223131.2021.1970040

Electrochemical, Thermal, and Structural Features of BaF₂–SnF₂ Fluoride-Ion Electrolytes
Mori Kazuhiro, Mineshige Atsushi, Emoto Takuro, Sugiura Maiko, Saito Takashi, Namba Kaoru, Otomo Toshiya, Abe Takeshi, Fukunaga Toshiharu
Journal of Physical Chemistry C **125(23)** (2021) 12568-12577 (doi) 10.1021/acs.jpcc.1c03326

Electron and hole capture processes in Cu-doped glass exhibiting radiophotoluminescence
Hashikawa Ryo, Takada Yuya, Nishi Yusaku, Kinomura Atsushi, Saito Takeshi, Okada Arifumi, Wakasugi Takashi, Kadono Kohei
Journal of Physics: Condensed Matter **34(2)** (2021) 025701 (doi) 10.1088/1361-648X/ac2fd5

Structure of disordered materials under ambient to extreme conditions revealed by synchrotron x-ray diffraction techniques at SPring-8-recent instrumentation and synergic collaboration with modelling and topological analyses
Ohara Koji, Onodera Yohei, Murakami Motohiko, Kohara Shinji
Journal of Physics: Condensed Matter **33(38)** (2021) 383001 (doi) 10.1088/1361-648X/ac0193

Dynamic properties on ⁹⁹Mo adsorption and ^{99m}Tc elution with alumina columns
Fujita Y, Seki M, Sano T, Fujihara Y, Suzuki T, Yoshinaga H, Hori J, Suematsu H, Tsuchiya K
Journal of Physics: Conference Series **2155** (2022) 012018 (doi) 10.1088/1742-6596/2155/1/012018

Effect of Fe Content on Steady-State Grain Size in Ni–Fe Alloys
Sato H., Tasaki A., Fujita R., Adachi N., Todaka Y., Kobayashi Y.

Journal of the Japan Institute of Metals and Materials 86(3) (2022) 43-51 (in Japanese)
(doi) 10.2320/jinstmet.J2021047

X-ray Crystal Structure Analysis of Magnetoelectric Metal UNi₄B
Tabata Chihiro, Sagayama Hajime, Saito Hiraku, Nakao Hironori, Amitsuka Hiroshi
Journal of the Physical Society of Japan 90(6) (2021) 064601 (doi) 10.7566/JPSJ.90.064601

Effects of He-D Interaction on Irradiation-Induced Swelling in Fe₉Cr Alloys
Wu Haibiao, Wang Zhen, Zhu Te, Xu Qiu, Wang Baoyi, Xiao Detao, Cao Xingzhong
Materials 14(21) (2021) 6669 (doi) 10.3390/ma14216669

Excellent performance of W–Y₂O₃ composite via powder process improvement and Y₂O₃ refinement
Yao Gang, Liu Xuepeng, Zhao Zhihao, Luo Laima, Cheng Jigui, Zan Xiang, Wang Zumin, Xu Qiu, Wu Yucheng
Materials & Design 212 (2021) 110249 (doi) 10.1016/j.matdes.2021.110249

Damage evolutions of completely recrystallized W–Y₂O₃ composite evaluated using the dual effects of electron beam thermal shock and helium ion irradiation
Yao Gang, Zhao Zhi-Hao, Luo Lai-Ma, Cheng Ji-Gui, Zan Xiang, Xu Qiu, Wu Yu-Cheng
Materials Chemistry and Physics 271 (2021) 124947 (doi) 10.1016/j.matchemphys.2021.124947

Age-hardening mechanisms of heterogeneous-nanostructured SUS316LN stainless steel fabricated by heavy cold rolling
Miura Hiromi, Watanabe Chihiro, Aoyagi Yoshiteru, Oba Yojiro, Kobayashi Masakazu, Yoshinaga Naoki
Materials Science and Engineering: A 833 (2022) 142531 (doi) 10.1016/j.msea.2021.142531

Ultrafast olivine-ringwoodite transformation during shock compression
Okuchi Takuo, Seto Yusuke, Tomioka Naotaka, Matsuoka Takeshi, Albertazzi Bruno, Hartley Nicholas J., Inubushi Yuichi, Katagiri Kento, Kodama Ryosuke, Pikuz Tatiana A., Purevjav Narangoo, Miyanishi Kohei, Sato Tomoko, Sekine Toshimori, Sueda Keiichi, Tanaka Kazuo A., Tange Yoshinori, Togashi Tadashi, Umeda Yuhei, Yabuuchi Toshinori, Yabashi Makina, Ozaki Norimasa
Nature Communications 12(1) (2021) 4305 (doi) 10.1038/s41467-021-24633-4

X-ray study of ferroic octupole order producing anomalous Hall effect
Kimata Motoi, Sasabe Norimasa, Kurita Kensuke, Yamasaki Yuichi, Tabata Chihiro, Yokoyama Yuichi, Kotani Yoshinori, Ikhlas Muhammad, Tomita Takahiro, Amemiya Kenta, Nojiri Hiroyuki, Nakatsuji Satoru, Koretsune Takashi, Nakao Hironori, Arima Taka-hisa, Nakamura Tetsuya
Nature Communications 12(1) (2021) 5582 (doi) 10.1038/s41467-021-25834-7

Stability of scattered hydrogen signals from a-C:H films during He-induced elastic recoil detection analysis
Kinomura A., Nakao S., Suzuki K., Kuzuya Y., Nakajima M., Yasuda K.
Nuclear Instruments and Methods in Physics Research Section B: Beam Interactions with Materials and Atoms 502 (2021) 54-58 (doi) 10.1016/j.nimb.2021.05.019

Iron nitride, α' -Fe₁₆N₂, around interstitial type dislocation loops in neutron-irradiated iron
Yoshiie T., Inoue K., Yoshida K., Toyama T., Satoh Y., Nagai Y.
Philosophical Magazine 101(10) (2021) 1202-1213 (doi) 10.1080/14786435.2021.1891317

Large anharmonicity and low lattice thermal conductivity of thermoelectric Sn(SbTe₂)₂
Sora-at Tanusilp, Masaya Kumagai, Yuji Ohishi, Naoki Sadayori, and Ken Kurosaki
Phys. Status Solidi RRL 16(1) (2022) 2100482-1-2100482-5 (doi) 10.1002/pssr.202100482

Hugoniot equation-of-state and structure of laser-shocked polyimide C₂₂H₁₀N₂O₅
Katagiri K., Ozaki N., Murayama D., Nonaka K., Hironaka Y., Inubushi Y., Miyanishi K., Nakamura H., Okuchi T., Sano T., Seto Y., Shigemori K., Sueda K., Togashi T., Umeda Y., Yabashi M., Yabuuchi T., Kodama R.
Physical Review B 105(5) (2022) 054103 (doi) 10.1103/PhysRevB.105.054103

Microscopic observation of hidden Johari-Goldstein- β process in glycerol
Saito Makina, Kurokuzu Masayuki, Yoda Yoshitaka, Seto Makoto
Physical Review E 105(1) (2022) L012605 (doi) 10.1103/PhysRevE.105.L012605

Liquid Structure of Tantalum under Internal Negative Pressure

K. Katagiri, N. Ozaki, S. Ohmura, B. Albertazzi, Y. Hironaka, Y. Inubushi, K. Ishida, M. Koenig, K. Miyanishi, H. Nakamura, M. Nishikino, T. Okuchi, T. Sato, Y. Seto, K. Shigemori, K. Sueda, Y. Tange, T. Togashi, Y. Umeda, M. Yabashi, T. Yabuuchi, and R. Kodama

Physical Review Letters **126**(17) (2021) **175503** (doi) 10.1103/PhysRevLett.126.175503

Relationship between Viscosity and Acyl Tail Dynamics in Lipid Bilayers

Nagao Michihiro, Kelley Elizabeth G., Faraone Antonio, Saito Makina, Yoda Yoshitaka, Kurokuzu Masayuki, Takata Shinichi, Seto Makoto, Butler Paul D.

Physical Review Letters **127**(7) (2021) **78102** (doi) 10.1103/PhysRevLett.127.078102

The influence of Gd₂O₃ on shielding, thermal and luminescence properties of WO₃-Gd₂O₃-B₂O₃ glass for radiation shielding and detection material

E. Kaewnuam, N. Wantana, S. Tanusilp, K. Kurosaki, P. Limkitjaroenporn, and J. Kaewkhao

Radiation Physics and Chemistry **190** (2022) **109805-1-109805-9** (doi) 10.1016/j.radphyschem.2021.109805

Relationship between diffraction peak, network topology, and amorphous-forming ability in silicon and silica

Kohara Shinji, Shiga Motoki, Onodera Yohei, Masai Hirokazu, Hirata Akihiko, Murakami Motohiko, Morishita Tetsuya, Kimura Koji, Hayashi Kouichi

Scientific Reports **11**(1) (2021) **22180** (doi) 10.1038/s41598-021-00965-5

Structure of alumina glass

Hashimoto Hideki, Onodera Yohei, Tahara Shuta, Kohara Shinji, Yazawa Koji, Segawa Hiroyo, Murakami Motohiko, Ohara Koji

Scientific Reports **12**(1) (2022) **516** (doi) 10.1038/s41598-021-04455-6

Vacancy migration energies in CrMnFeCoNi, CrFeCoNi, and CrFeNi alloys and their effect on atomic diffusion

Sugita Kazuki, Ogawa Ryusei, Mizuno Masataka, Araki Hideki, Yabuuchi Atsushi

Scripta Materialia **208** (2022) **114339-1-114339-5** (doi) 10.1016/j.scriptamat.2021.114339

Gamma-ray induced photo emission from ZnO single crystal wafer: Comparison with GaN

Nakamura Toshihiro, Nishimura Tomoaki, Kuriyama Kazuo, Nakamura Tohru, Kinomura Atsushi

Solid State Communications **336** (2021) **114413** (doi) 10.1016/j.ssc.2021.114413

Synthesis and thermoelectric properties of Si-YbSi₂ nanocomposite sintered pack

Akinori Nishide, Sora-at Tanusilp, Yuji Ohishi, Hiroaki Muta, Jun Hayakawa, Ken Kurosaki

The Journal of the Thermoelectrics Society of Japan **17**(3) (2022) **127-133** (in Japanese)

Highly Swollen Adsorption Layer Formed by Polymeric Friction Modifier Providing Low Friction at Higher Temperature

Yamashita Naoki, Hirayama Tomoko, Yamada Norifumi L., Watanabe Honami, Onodera Ko, Sato Takehisa

Tribology Letters **69**(2) (2022) **65** (doi) 10.1007/s11249-021-01443-9

Proceedings

Advancement of materials irradiation and defect characterization

Atsushi Kinomura, Koji Inoue, Koichi Sato, Toshihiro Nakamura, Tomoaki Nishimura, Masafumi Akiyoshi, Kazuhiro Kanda and Setsuo Nakao

Proceedings of the 56th KURNS Scientific Meeting, Online (Feb. 9-10, 2022) 56-59 (in Japanese)

Experimental Study on planetary materials under high pressure conditions using laser shock technique

Yuhei Umeda, Norimasa Okazaki, Tosinori Sekine, Alessandra Benuzzi-Mounaix, Marco Guarguaglini, Yuichi Inubushi, Keiya Fukui, Nobuki Kamimuram Kento Katagiri, Ryosuke Kodama, Takesih Matsuoka, Kohei Miyanishi, Alessandra Ravasio, Takayoshi Sano, Keiichi Sueda, Tadashi Togashi, Makina Yabashi, Toshinori Yabuuchi, Takuo Okuchi

Proceedings of the 56th KURNS Scientific Meeting, Online (Feb. 9-10, 2022) 53-55 (in Japanese)

Interaction of defects with hydrogen and helium in SUS316L

Yutaro Suzuki, Hidetsugu Tsuchida, Qiu Xu

Proceedings of the 56th KURNS Scientific Meeting, Online (Feb. 9-10, 2022) 11 (in Japanese)

Synthesis and characterization of base metal alloy nanoparticles by irradiation reduction method
Kemeng Zhu, Tomoko Yamada, Toshiyuki Matsui, Akihiro Iwase, Noboru Taguchi, Shingo Tanaka, Fuminobu Horii

Proceedings of the 56th KURNS Scientific Meeting, Online (Feb. 9-10, 2022) 20 (in Japanese)

Non-destructive identification of chemical state for iron compounds by muon

K. Ninomiya, M. Kajino, A. Nanbu, M. Inagaki, T. Kudo, K. Terada, A. Sato, D. Tomono, Y. Kawashima, Y. Sakai, T. Takayama and A. Shinohara

Proceedings of the Specialists' Meeting on "Nuclear Spectroscopy and Condensed Matter Physics Using Short-Lived Nuclei VII" Online, (Jan. 15, 2021) 24 (in Japanese)

Present status of nuclear spectroscopic experiments using KISS and MRTOF

Y. Watanabe

Proceedings of the Specialists' Meeting on "Nuclear Spectroscopy and Condensed Matter Physics Using Short-Lived Nuclei VII" Online, (Jan. 15, 2021) 28-30 (in Japanese)

Probing the Open Spaces in MOFs with Positronium Lifetime Spectroscopy

Daiki Ueda, Kiminori Sato, and Takafumi Kitazawa

Proceedings of the Specialists' Meeting on "Nuclear Spectroscopy and Condensed Matter Physics Using Short-Lived Nuclei VII" Online, (Jan. 15, 2021) 25-27 (in Japanese)

Temperature dependence of spin-lattice relaxation time of ^{19}O in oxide fuel cell material YSZ

Y. Otani, M. Mihara, K. Matsuta, M. Fukuda, R. Wakabayashi, N. Okimoto, M. Fukutome, Y. Kimura, G. Takayama, T. Izumikawa, N. Noguchi, M. Ogose, Y. Sato, K. Takatsu, T. Ohtsubo, D. Nishimura, H. Takahashi, S. Sugawara, A. Gladkov, A. Kitagawa, S. Sato, S. Momota, H. Okumura, T. Moriguchi, and A. Ozawa

Proceedings of the Specialists' Meeting on "Nuclear Spectroscopy and Condensed Matter Physics Using Short-Lived Nuclei VII" Online, (Jan. 15, 2021) 45-48 (in Japanese)

Trial productions of β -detector for a 4π clover detector and On-Line experiment using KUR-ISOL Y. Ishikawa, Y. Irie, M. Kanaji, M. Shibata and A. Taniguchi

Proceedings of the Specialists' Meeting on "Nuclear Spectroscopy and Condensed Matter Physics Using Short-Lived Nuclei VII" Online, (Jan. 15, 2021) 31-36 (in Japanese)

Reviews

Investigations on Adsorption of Inorganic Ions in Aqueous Solution to Some Metal Oxides, Hydroxides and a Carbonate by the X-Ray Spectroscopic Method

OHASHI Hironori, YONEZU Kotaro, KAWAMOTO Daisuke, YOKOYAMA Takushi

Analytical Sciences 37(10) (2021) 1321-1330

Direct Observation of Magnetic Friedel Oscillation at the Fe (001) Surface

Takaya Mitsui, Seiji Sakai, Makoto Seto, and Hisazumi Akai

Butsuri 77(1) (2022) 23-28 (in Japanese)

New Glasses Exhibiting Radiophotoluminescence for Dosimeter

Kadono Kohei

Cchemical Industry 72(6) (2021) 367-372 (in Japanese)

ガラス構造のトポロジカル解析—無秩序に潜む秩序抽出へのデータ駆動型アプローチ

Y. Onodera

Ceramics Japan 57 (2022) 171-177 (in Japanese)

Structure and dynamics of hydrogen in materials of Earth and planetary interiors

Takuo OKUCHI

Japanese Magazine of Mineralogical and Petrological Sciences 50(2) 31-42 (2021) (in Japanese)

Quasielastic Neutron Scattering for Analyzing Transport Dynamics of Chemically-Bound Hydrogen in Minerals
Takuo Okuchi

Nihon Kessho Gakkaishi 63(2) (2021) 129-134 (in Japanese)

Laboratory planetary sciences using high-power lasers
Takuo OKUCHI, Norimasa OZAKI
Optronics 41(1) (2022) 61-66 (in Japanese)

Understanding diffraction patterns of disordered materials
S.Kohara, Y.Onodera, O.Sakata
SPring-8 Research Frontiers 2020 (2021) 44-45

Ultrafast in-situ Measurement of Crystal Structure Transformation during Hypervelocity Collisions of Asteroids
OKUCHI Takuo
SPring8/SACLAI Information 26(4) (2021) 341-348 (in Japanese)

Ultrafast In-Situ Analysis of Shock-Compressed Planetary Materials
Takuo OKUCHI, Norimasa OZAKI
The Review of High Pressure Science and Technology 31(3) (2021) 166-171 (in Japanese)

Others

金属間化合物合金における空孔型欠陥と水素原子の相互作用に関する研究
堀史説
九州大学応用力学研究所共同利用研究成果報告書 24 (2021) 117 (in Japanese)

事故耐性の高い軽水炉用制御棒の開発 (6) 新型中性子吸収材と炭化ケイ素の高温共存性
中村勤也, 太田宏一
日本原子力学会 2022 春の年会 3J11 (2022) (in Japanese)

照射還元を用いた卑金属系合金ナノ微粒子合成制御およびその特性評価
朱科蒙, 山田智子, 松井利之, 堀史説, 徐虬, 田中慎吾, 田口昇
2021 年度放射線施設共同利用報告書 (2021) 7 (in Japanese)

鉄系合金における水素捕獲挙動に対する電子線照射効果
大友彦卓, 大林浩也, 金野泰幸, 堀史説, 徐虬
2021 年度放射線施設共同利用報告書 (2021)17 (in Japanese)

5. Geochemistry and Environmental Science

Papers

Relationship of ¹³⁷Cs with Fungal Spore Tracers in the Ambient Aerosols from Fukushima after the 2011 Nuclear Accident, East Japan
Kawamura Kimitaka, Kunwar Bhagawati, Kita Kazuyuki, Hayashi Naho, Igarashi Yasuhito
Atmosphere 13(3) (2022) 413 (doi) 10.3390/atmos13030413

Reassessment of the radiocesium resuspension flux from contaminated ground surfaces in eastern Japan
Kajino Mizuo, Watanabe Akira, Ishizuka Masahide, Kita Kazuyuki, Zaizen Yuji, Kinase Takeshi, Hirai Rikuya, Konnai Kakeru, Saya Akane, Iwaoka Kazuki, Shiroma Yoshitaka, Hasegawa Hidenao, Akata Naofumi, Hosoda Masahiro, Tokonami Shinji, Igarashi Yasuhito
Atmospheric Chemistry and Physics 22(2) (2022) 783-803 (doi) 10.5194/acp-22-783-2022

Determination of halogens in geological reference materials using neutron irradiation noble gas mass spectrometry
Kobayashi Masahiro, Sumino Hirochika, Saito Takehiko, Nagao Keisuke
Chemical Geology 582 (2021) 120420 (doi) 10.1016/j.chemgeo.2021.120420

Tumor microenvironment and radioresistance
Suwa Tatsuya, Kobayashi Minoru, Nam Jin-Min, Harada Hiroshi
Experimental & Molecular Medicine 53(6) (2021) 1029-1035 (doi) 10.1038/s12276-021-00640-9

Ab initio and steady-state models for uranium isotope fractionation in multi-step biotic and abiotic reduction
Sato Ataru, Bernier-Latmani Rizlan, Hada Masahiko, Abe Minori
Geochimica et Cosmochimica Acta **307 (2021) 212-227** (doi) 10.1016/j.gca.2021.05.044

Investigation of the source region of the lunar-meteorite group with the remote sensing datasets: Implication for the origin of mare volcanism in Mare Imbrium
Nagaoka Hiroshi, Ohtake Makiko, Shirai Naoki, Karouji Yuzuru, Kayama Masahiro, Daket Yuko, Hasebe Nobuyuki, Ebihara Mitsuru
Icarus **370 (2021) 114690** (doi) 10.1016/j.icarus.2021.114690

Cretaceous to Miocene NW Pacific Plate Kinematic Constraints: Paleomagnetism and Ar–Ar Geochronology in the Mineoka Ophiolite Mélange (Japan)
Ganbat Ariuntsetseg, Pastor-Galán Daniel, Hirano Naoto, Nakamura Norihiro, Sumino Hirochika, Yamaguchi Yuji, Tsujimori Tatsuki
Journal of Geophysical Research: Solid Earth **5 (2021) e2020JB021492** (doi) 10.1029/2020JB021492

Transfer of ^{137}Cs to web-building spiders, *Nephila clavata*, and its pathways: a preliminary study using stable carbon and nitrogen isotope analyses
Tanaka Sota, Kakinuma Hotaru, Adati Tarô, Atarashi-Andoh Mariko, Koarashi Jun
Journal of Nuclear Science and Technology **58(4) (2021) 507-514** (doi) 10.1080/00223131.2021.1894255

Multiple shock events recorded in the Northwest Africa 2139 LL6 chondrite: Implications for collisional histories of the LL chondrite parent body
Takenouchi Atsushi, Sumino Hirochika, Shimodate Karin, Yamaguchi Akira
Meteoritics & Planetary Science **56(12) (2021) 2230-2249** (doi) 10.1111/maps.13768

Petrology, geochemistry, and geochronology of plutonic rocks from the present Southwest Indian Ridge: Implications for dropstone distribution in the Indian Ocean
Sato Hiroshi, Machida Shiki, Senda Ryoko, Sato Keiko, Kumagai Hidenori, Hyodo Hironobu, Yoneda Shigekazu, Kato Yasuhiro
Polar Science **29 (2021) 100725** (doi) 10.1016/j.polar.2021.100725

Atmospheric resuspension of insoluble radioactive cesium-bearing particles found in the difficult-to-return area in Fukushima
Tang Peng, Kita Kazuyuki, Igarashi Yasuhito, Satou Yukihiro, Hatanaka Koutarou, Adachi Kouji, Kinase Takeshi, Ninomiya Kazuhiko, Shinohara Atsushi
Progress in Earth and Planetary Science **9(1) (2022) 17** (doi) 10.1186/s40645-022-00475-6

Temporal change of $^{236}\text{U}/^{238}\text{U}$ and $^{235}\text{U}/^{238}\text{U}$ isotopic ratios in atmospheric deposition in Tokyo and Akita from 1963 to 1979
Ohno Takeshi, Sato Naoki, Shikimori Junko, Ijichi Yuta, Fukami Yusuke, Igarashi Yasuhito
Science of The Total Environment **810 (2022) 151292** (doi) 10.1016/j.scitotenv.2021.151292

Proceedings

Mass balance trend of organochlorine in a sediment core from Beppu Bay
Ito. K., Fujimori. T., Mukai. K., Anh. H.Q., Fukutani. S., Takaoka. M., Takahashi. S.
29th Symposium on Environmental Chemistry, Osaka, Japan (Jun. 1-3, 2021)

Mass balance trend of organobromine in a sediment core from Beppu Bay, Japan
Ito. K., Fujimori. T., Mukai. K., Anh. H.Q., Fukutani. S., Takaoka. M., Takahashi. S.
DIOXIN2021, Tianjin, China (Jan. 8-11, 2021)

Estimation of trace elements in foods and amounts of intake of wild monkey (*Macaca fuscata*)
Michiko Fukushima, Yamato Tsuji, and Yuto Iinuma
Proceedings of the 56th KURNS Scientific Meeting, Online (Feb. 9-10, 2022) 32 (in Japanese)

Long term change in soil elements of the atmospheric coarse particle observed at Sakai, Osaka
Norio Ito and Akira Mizohata
Proceedings of the 56th KURNS Scientific Meeting, Online (Feb. 9-10, 2022) 21 (in Japanese)

Decontamination of Radioactive Cesium and the Redox State of Iron in the Soil

S. Nakashima, T. Basuki, and K. Inada

Proceedings of the Specialists' Meeting on "Nuclear Spectroscopy and Condensed Matter Physics Using Short-Lived Nuclei VII" Online, (Jan. 15, 2021) 22-23 (in Japanese)

Design of Veterinary Epidemiological Survey to Understand Disaster-Related Deaths

Masahiko Takahagi

Proceedings of the Symposium on the expansion of boron neutron capture therapy to the field of veterinary medicine.-Challenges and potential for interdisciplinary research- Online, (Mar. 4, 2021) 96-99 (in Japanese)

Reviews

Activity Report of the Task Group on Parameters Used in Biospheric Dose Assessment Models for Radioactive Waste Disposal

TAKAHASHI Tomoyuki, FUKAYA Yukiko, IIMOTO Takeshi, UNI Yasuo, KATO Tomoko, SUN Siyi, TAKEDA Seiji, NAKAI Kunihiro, NAKABAYASHI Ryo, UCHIDA Shigeo, TAGAMI Keiko, HIRAYAMA Makoto

Japanese Journal of Health Physics 56(4) (2021) 288-305 (in Japanese)

Inexpensive in-situ Filtration Systems: Biological Filtration Utilizing Iron Bacteria, Soil Percolation, and Filtration with Fibrous Material

Yoko Fujikawa

Journal of environmental conservation engineering 50(4) (2021) 186-189 (in Japanese)

Theory of Deep Filtration From Iwasaki

Hiroaki Ozaki, Yoko Fujikawa

Journal of environmental conservation engineering 50(4) (2021) 180-185 (in Japanese)

環境の分析技術・データ解析・モデル化講座Ⅱ. 環境のデータ解析・モデル化－R によるデータ加工とグラフ作成の自動化

Yoko Fujikawa

Journal of environmental conservation engineering 50(3) (2021) 166-171 (in Japanese)

水のろ過－古典的なろ過から最新のろ過まで－

Yoko Fujikawa

Journal of environmental conservation engineering 50(4) (2021) 179 (in Japanese)

Books

2.4.2 安全でおいしい水のための浄水技術 鉄バクテリア法

Yoko Fujikawa

Encyclopedia of Water Environment

Japan Society on Water Environment

朝倉書店 (2021) (in Japanese)

6. Life Science and Medical Science

Papers

Characterization of a Conformation-Restricted Amyloid β Peptide and Immunoreactivity of Its Antibody in Human AD brain

Kageyama Yusuke, Irie Yumi, Matsushima Yuka, Segawa Tatsuya, Bellier Jean-Pierre, Hidaka Kumi, Sugiyama Hiroshi, Kaneda Daita, Hashizume Yoshio, Akatsu Hiroyasu, Miki Kunio, Kita Akiko, Walker Douglas G., Irie Kazuhiro, Tooyama Ikuo

ACS Chemical Neuroscience 12(18) (2021) 3418-3432 (doi) 10.1021/acchemneuro.1c00416

TLC-based MS Imaging Analysis of Glycosphingolipids and Glycerin Fatty Acid Esters after 1,2-Dichloroethane Washing

MATSUSHITA Shoko, HASEGAWA Takuma, HIRAOKA Marina, HAYASHI Aki, SUZUKI Yusuke

Analytical Sciences 37(11) (2021) 1491-1495 (doi) 10.2116/analsci.21C009

Terahertz Imaging for Formalin Fixed Malignant Liver Tumors Using Two-Band Beamline at the Accelerator Facility of Nihon University

Kawashima Yusuke, Masaaki Suemitsu, Kuyama Kayo, Sakai Takeshi, Hayakawa Yasushi, Kaneda Takashi, Sei Norihiro

Applied Sciences 12(4) (2022) 2229 (doi) 10.3390/app12042229

Dynamic interactions in the l-lactate oxidase active site facilitate substrate binding at pH4.5

Furubayashi Naoki, Inaka Koji, Kamo Masayuki, Umena Yasufumi, Matsuoka Takeshi, Morimoto Yukio

Biochemical and Biophysical Research Communications 568 (2021) 131-135

(doi) 10.1016/j.bbrc.2021.06.078

Tumor-targeting hyaluronic acid/fluorescent carborane complex for boron neutron capture therapy

Yamana Keita, Kawasaki Riku, Sanada Yu, Tabata Anri, Bando Kaori, Yoshikawa Kouhei, Azuma Hideki, Sakurai Yoshinori, Masunaga Shin-ichiro, Suzuki Minoru, Sugikawa Kouta, Nagasaki Takeshi, Ikeda Atsushi

Biochemical and Biophysical Research Communications 559 (2021) 210-216

(doi) 10.1016/j.bbrc.2021.04.037

Conformational dynamics of a multidomain protein by neutron scattering and computational analysis

Nakagawa Hiroshi, Saio Tomohide, Nagao Michihiro, Inoue Rintaro, Sugiyama Masaaki, Ajito Satoshi, Tominaga Taiki, Kawakita Yukinobu

Biophysical Journal 120(16) (2021) 3341-3354 (doi) 10.1016/j.bpj.2021.07.001

APOE ε4 allele advances the age-dependent decline of amyloid β clearance in the human cortex

Saito Atsushi, Kageyama Yusuke, Pletnikova Olga, Rudow Gay L., An Yang, Irie Yumi, Kita Akiko, Miki Kunio, Li Ling, Southall Pamela, Irie Kazuhiro, Troncoso Juan C.

bioRxiv (2021) (doi) 10.1101/2021.04.07.438832

Overall structure of fully assembled cyanobacterial KaiABC circadian clock complex by an integrated experimental-computational approach

Yunoki Yasuhiro, Matsumoto Atsushi, Morishima Ken, Martel Anne, Porcar Lionel, Sato Nobuhiro, Yogo Rina, Tominaga Taiki, Inoue Rintaro, Yagi-Utsumi Maho, Okuda Aya, Shimizu Masahiro, Urade Reiko, Terauchi Kazuki, Kono Hidetoshi, Yagi Hirokazu, Kato Koichi, Sugiyama Masaaki

Communications Biology 5(1) (2022) 184 (doi) 10.1038/s42003-022-03143-z

Design and Synthesis of Supramolecular Phosphatases Formed from a Bis(Zn²⁺-Cyclen) Complex, Barbitol-Crown-K⁺ Conjugate and Cu²⁺ for the Catalytic Hydrolysis of Phosphate Monoester

Rahman Akib Bin, Okamoto Hirokazu, Miyazawa Yuya, Aoki Shin

European Journal of Inorganic Chemistry 13 (2021) 1213-1223 (doi) 10.1002/ejic.202001009

Synthesis and Anticancer Properties of Bis- and Mono(cationic peptide) Hybrids of Cyclometalated Iridium(III) Complexes: Effect of the Number of Peptide Units on Anticancer Activity

Haribabu Jebiti, Tamura Yuichi, Yokoi Kenta, Balachandran Chandrasekar, Umezawa Masakazu, Tsuchiya Koji, Yamada Yasuyuki, Karvembu Ramasamy, Aoki Shin

European Journal of Inorganic Chemistry 2021(18) (2021) 1796-1814 (doi) 10.1002/ejic.202100154

Mefloquine, a Potent Anti-severe Acute Respiratory Syndrome-Related Coronavirus 2 (SARS-CoV-2) Drug as an Entry Inhibitor in vitro

Shionoya Kaho, Yamasaki Masako, Iwanami Shoya, Ito Yusuke, Fukushi Shuetsu, Ohashi Hirofumi, Saso Wakana, Tanaka Tomohiro, Aoki Shin, Kuramochi Kouji, Iwami Shingo, Takahashi Yoshimasa, Suzuki Tadaki, Muramatsu Masamichi, Takeda Makoto, Wakita Takaji, Watashi Koichi

Frontiers in Microbiology 12 (2021) 651403 (doi) 10.3389/fmicb.2021.651403

Isorhamnetin Promotes 53BP1 Recruitment through the Enhancement of ATM Phosphorylation and Protects Mice from Radiation Gastrointestinal Syndrome

Nishiyama Yuichi, Morita Akinori, Tatsuta Shogo, Kanamaru Misaki, Sakaue Masahiro, Ueda Kenta, Shono Manami, Fujita Rie, Wang Bing, Hosoi Yoshio, Aoki Shin, Sugai Takeshi

Genes 12(10) (2021) 1514 (doi) 10.3390/genes12101514

- Synthesis and antiproliferative activity of novel organometallic cobalt(III) complex encapsulated in polydiacetylene-phospholipid nanoformulation
Mounica Arangasamy, Balachandran Chandrasekar, Gopalakrishnan Durairaj, Sivasakthi Pandiyan, Prakash Muthuramalingam, Aoki Shin, Ganeshpandian Mani
Inorganica Chimica Acta **530** (2022) **120701** (doi) 10.1016/j.ica.2021.120701
- Oligomeric Structural Transition of HspB1 from Chinese Hamster
Kurokawa Nina, Midorikawa Rio, Nakamura Manami, Noguchi Keiichi, Morishima Ken, Inoue Rintaro, Sugiyama Masaaki, Yohda Masafumi
International Journal of Molecular Sciences **22(19)** (2021) **10797** (doi) 10.3390/ijms221910797
- Evaluation of sodium orthovanadate as a radioprotective agent under total-body irradiation and partial-body irradiation conditions in mice
Nishiyama Yuichi, Morita Akinori, Wang Bing, Sakai Takuma, Ramadhani Dwi, Satoh Hidetoshi, Tanaka Kaoru, Sasatani Megumi, Ochi Shintaro, Tominaga Masahide, Ikushima Hitoshi, Ueno Junji, Neno Mitsuru, Aoki Shin
International Journal of Radiation Biology **97(9)** (2021) **1241-1251** (doi) 10.1080/09553002.2021.1941377
- Potential anti-COVID-19 agents, cepharanthine and nelfinavir, and their usage for combination treatment
Ohashi Hirofumi, Watashi Koichi, Saso Wakana, Shionoya Kaho, Iwanami Shoya, Hirokawa Takatsugu, Shirai Tsuyoshi, Kanaya Shigehiko, Ito Yusuke, Kim Kwang Su, Nomura Takao, Suzuki Tateki, Nishioka Kazane, Ando Shuji, Ejima Keisuke, Koizumi Yoshiki, Tanaka Tomohiro, Aoki Shin, Kuramochi Kouji, Suzuki Tadaki, Hashiguchi Takao, Maenaka Katsumi, Matano Tetsuro, Muramatsu Masamichi, Saijo Masayuki, Aihara Kazuyuki, Iwami Shingo, Takeda Makoto, McKeating Jane A., Wakita Takaji
iScience **24(4)** (2021) **102367** (doi) 10.1016/j.isci.2021.102367
- SPINK1 as a plasma marker for tumor hypoxia and a therapeutic target for radiosensitization
Suwa Tatsuya, Kobayashi Minoru, Shirai Yukari, Nam Jin-Min, Tabuchi Yoshiaki, Takeda Norihiko, Akamatsu Shusuke, Ogawa Osamu, Mizowaki Takashi, Hammond Ester M., Harada Hiroshi
JCI Insight **6(21)** (2021) **e148135** (doi) 10.1172/jci.insight.148135
- Structural and thermodynamical insights into the binding and inhibition of FIH-1 by the N-terminal disordered region of Mint3
Ten Tensho, Nagatoishi Satoru, Maeda Ryo, Hoshino Masaru, Nakayama Yoshiaki, Seiki Motoharu, Sakamoto Takeharu, Tsumoto Kouhei
Journal of Biological Chemistry **297(5)** (2021) **101304** (doi) 10.1016/j.jbc.2021.101304
- A Novel RNA Synthesis Inhibitor, STK160830, Has Negligible DNA-Intercalating Activity for Triggering A p53 Response, and Can Inhibit p53-Dependent Apoptosis
Morita Akinori, Ochi Shintaro, Satoh Hidetoshi, Ujita Shohei, Matsushita Yosuke, Tada Kasumi, Toyoda Mihiro, Nishiyama Yuichi, Mizuno Kosuke, Deguchi Yuichi, Suzuki Keiji, Tanaka Yoshimasa, Ueda Hiroshi, Inaba Toshiya, Hosoi Yoshio, Aoki Shin
Life **11(10)** (2021) **1087** (doi) 10.3390/life11101087
- Cyclometalated Iridium(III) Complex–Cationic Peptide Hybrids Trigger Paraptosis in Cancer Cells via an Intracellular Ca²⁺ Overload from the Endoplasmic Reticulum and a Decrease in Mitochondrial Membrane Potential
Balachandran Chandrasekar, Yokoi Kenta, Naito Kana, Haribabu Jebiti, Tamura Yuichi, Umezawa Masakazu, Tsuchiya Koji, Yoshihara Toshitada, Tobita Seiji, Aoki Shin
Molecules **26(22)** (2021) **7028** (doi) 10.3390/molecules26227028
- Isomerization of Asp is essential for assembly of amyloid-like fibrils of α A-crystallin-derived peptide
Magami Kosuke, Hachiya Naomi, Morikawa Kazuo, Fujii Noriko, Takata Takumi
PLOS ONE **16(4)** (2021) **e0250277** (doi) 10.1371/journal.pone.0250277
- Direct coordination of pterin to Fe^{II} enables neurotransmitter biosynthesis in the pterin-dependent hydroxylases
Iyer Shyam R., Tidemand Kasper D., Babicz Jeffrey T., Jacobs Ariel B., Gee Leland B., Haahr Lærke T., Yoda Yoshitaka, Kurokuzu Masayuki, Kitao Shinji, Saito Makina, Seto Makoto, Christensen Hans E. M., Peters Günther H. J., Solomon Edward I.
Proceedings of the National Academy of Sciences **118(15)** (2021) **e2022379118** (doi) 10.1073/pnas.2022379118

Formation of clustered DNA damage in vivo upon irradiation with ionizing radiation: Visualization and analysis with atomic force microscopy

Nakano Toshiaki, Akamatsu Ken, Tsuda Masataka, Ujimoto Ayane, Hirayama Ryoichi, Hiromoto Takeshi, Tamada Taro, Ide Hiroshi, Shikazono Naoya

Proceedings of the National Academy of Sciences 119(13) (2022) e2119132119

(doi) 10.1073/pnas.2119132119

Pro108Ser mutation of SARS-CoV-2 3CL^{pro} reduces the enzyme activity and ameliorates the clinical severity of COVID-19

Abe Kodai, Kabe Yasuaki, Uchiyama Susumu, Iwasaki Yuka W., Ishizu Hirotsugu, Uwamino Yoshifumi, Takenouchi Toshiki, Uno Shunsuke, Ishii Makoto, Maruno Takahiro, Noda Masanori, Murata Mitsuru, Hasegawa Naoki, Saya Hideyuki, Kitagawa Yuko, Fukunaga Koichi, Amagai Masayuki, Siomi Haruhiko, Suematsu Makoto, Kosaki Kenjiro,

Scientific Reports 12(1) (2022) 1299 (doi) 10.1038/s41598-022-05424-3

Proceedings

Radioresistance mechanism of Escherichia coli acquired by adaptive evolution using gamma rays as a selective pressure

Takeshi Saito

Proceedings of the 56th KURNS Scientific Meeting, Online (Feb. 9-10, 2022) 42 (in Japanese)

A study of small neutron source using proton accelerator for generation of intensity collimated neutron beam

Masahiro Hino, Riichiro Nakamura, Yutaka Abe

Proceedings of the 56th KURNS Scientific Meeting, Online (Feb. 9-10, 2022) 14 (in Japanese)

Deuterated/undeuterated positions in denatured/refolded hen egg lysozyme

Akiko Kita and Yukio Morimoto

Proceedings of the 56th KURNS Scientific Meeting, Online (Feb. 9-10, 2022) 31 (in Japanese)

Dynamics of a multi-domain protein studied by small angle X-ray scattering and molecular dynamics simulations
Masahiro Shimizu, Aya Okuda, Ken Morishima, Yasuhiro, Yunoki, Rintaro Inoue, Nobuhiro Sato, Reiko Urade, Masaaki Sugiyama

Proceedings of the 56th KURNS Scientific Meeting, Online (Feb. 9-10, 2022) 48(in Japanese)

Hydrogen trapping in Fe-Al Intermetallic Compounds with supersaturated vacancies

Hikotaku Otomo, Yasuyuki Kaneno, Akihiro Iwase, Kazuhito Ohsawa, Qiu Xu, Masaki Maekawa, Atsuo Kawasuso and Fuminobu Hori

Proceedings of the 56th KURNS Scientific Meeting, Online (Feb. 9-10, 2022) 15 (in Japanese)

Integrated approach for structural analysis of protein in polydisperse solution with small angle scattering and analytical ultracentrifugation (AUC-SAS)

Ken Morishima, Rintaro Inoue, Yasuhiro Yunoki, Masahiro Shimizu, Aya Okuda, Nobuhiro Sato, Reiko Urade, Masaaki Sugiyama

Proceedings of the 56th KURNS Scientific Meeting, Online (Feb. 9-10, 2022) 16 (in Japanese)

Overall structure of a fully assembled complex in the cyanobacterial circadian clock analyzed by an integrated biophysical and computational approach

Hirokazu Yagi, Yasuhiro Yunoki, Atsushi Matsumoto, Ken Morishima, Rintaro Inoue, Koichi Kato, Hidetoshi Kono, and Masaaki Sugiyama

Proceedings of the 56th KURNS Scientific Meeting, Online (Feb. 9-10, 2022) 22 (in Japanese)

Preparation of deuterated wheat proteins for small-angle neutron scattering measurements

Nobuhiro Sato, Reiko Urade, Aya Okuda, Yasuhiro Yunoki, Masahiro Shimizu, Ken Morishima, Rintaro Inoue and Masaaki Sugiyama

Proceedings of the 56th KURNS Scientific Meeting, Online (Feb. 9-10, 2022) 33 (in Japanese)

Solution structure of multi-domain protein ER-60

Aya Okuda

Proceedings of the 56th KURNS Scientific Meeting, Online (Feb. 9-10, 2022) 8-9 (in Japanese)

Structural analysis of GATA3-nucleosome complex in solution
Hiroki Tanaka, Yoshimasa Takizawa, Aya Okuda, Ken Morishima, Nobuhiro Sato, Rintaro Inoue, Masaaki Sugiyama, Hitoshi Kurumizaka
Proceedings of the 56th KURNS Scientific Meeting, Online (Feb. 9-10, 2022) 44 (in Japanese)

Structural analysis of water-soluble vitamin K2 derived from *Bacillus subtilis* natto
Toshiyuki Chatake, Yasuhide Yanagisawa, Aya Okuda, Ken Morishima, Rintaro Inoue, Masaaki Sugiyama
Proceedings of the 56th KURNS Scientific Meeting, Online (Feb. 9-10, 2022) 13 (in Japanese)

The molecular machine KaiC hexamer regulates circadian clock system
Yasuhiro Yunoki, Atsuji Kodama, Maho Yagi, Ken Morishima, Nobuhiro Sato, Aya Okuda, Yasuhiro Shimizu, Rintaro Inoue, Reiko Urade, Yasukazu Yagi, Koichi Kato, Masaaki Sugiyama
Proceedings of the 56th KURNS Scientific Meeting, Online (Feb. 9-10, 2022) 26 (in Japanese)

SHORT PULSED BEAM EXTRACTION IN KURNS FFAG
Tomonori Uesugi, Yoshihiro Ishi, Yasutoshi Kuriyama, Yoshiharu Mori
Proceedings of the 18th Annual Meeting of Particle Accelerator Society of Japan, Online (Aug. 9-10, 2021)
(in Japanese)

Combinatorial Construction of Metallosupramolecular Complexes to Mimic Natural Alkaline Phosphatases by the Self-assembly of Functionalized Building Block
Shin Aoki, Hirokazu Okamoto, Akib Bin Rahman, and Mohd Zulkefli
Thai Journal of Pharmaceutical Sciences (TJPS), Special Issue Malaysia, online (Sep. 28-29, 2021) 13-14

Design and Synthesis of Poly(2,2'-bipyridyl) Ligands Directed toward Chelation Therapy of Cancer
Masumi Hirose, Jun-Jie Zhu, Chandrasekar Balachandran, Tomohiro Tanaka, Yosuke Hisamatsu, Yasuyuki Yamada, and Shin Aoki
Thai Journal of Pharmaceutical Sciences (TJPS), Special Issue Malaysia, online (Sep. 28-29, 2021) 14-15

Design, Synthesis, and Anticancer Activity of Amphiphilic Anticancer Agents Having Cationic Peptides for the Induction of Programmed Cell Death in Cancer Cells
Kohei Yamaguchi, Kenta Yokoi, and Shin Aoki
Thai Journal of Pharmaceutical Sciences (TJPS), Special Issue Malaysia, online (Sep. 28-29, 2021) 11-12

Design, Synthesis, and Biological Evaluation of 2-Pyrolone Derivatives as Radio Protectors Regulating p53 Discovered in Phenotypic Screening
Hidetoshi Satoh, Shintaro Ochi, Kosuke Mizuno, Shohei Ujita, Miyu Toyoda, Yuichi Nishiyama, Kasumi Tada, Yosuke Matsushita, Yuichi Deguchi, Keiji Suzuki, Yoshimasa Tanaka, Hiroshi Ueda, Toshiya Inaba, Yoshio Hosoi, Akinori Morita, and Shin Aoki,
Thai Journal of Pharmaceutical Sciences (TJPS), Special Issue Malaysia, online (Sep. 28-29, 2021) 11

One-pot Synthesis of Cyclic Oligosaccharides by Means of Thioglycoside Donor/Acceptor Units
Gota Ishigami, Takehito Seki, Hidehisa Someya, Yasuyuki Yamada, and Shin Aoki,
Thai Journal of Pharmaceutical Sciences (TJPS), Special Issue Malaysia, online (Sep. 28-29, 2021) 11

Reviews

Recent Advances in Cataract Research Using D-Amino Acids as a Molecular Marker
Takumi Takata
Journal of The Japanese Society for Cataract Research 33(1) (2021) 59-61 (in Japanese)

The Post-Translational Modifications of Amino Acid in Crystallin and Their Contributions to Aged Lens
Noriko Fujii
Journal of The Japanese Society for Cataract Research 33(1) (2021) 12-24 (in Japanese)

トリプル四重極質量分析計を用いた抗体医薬品の新しい品質管理指標に関する研究
Takumi Takata, Toshiya Matsubara, Tsuyoshi Nakanishi, Tetsuo Tanigawa
SHIMADZU Application Notes 71 (2021) 1-5 (in Japanese)

Post-complexation functionalization によるシクロメタレート型イリジウム(III)錯体の機能化と生命科学および材料科学への応用—金属錯体をビルディングブロックとする機能性分子の創製—

青木伸, 横井健汰, Chandrasekar Balachandran, 久松洋介
有機合成化学協会誌 79 (2021) 1113-1124 (in Japanese)

Books

Gota Ishigami, Takehito Seki, Hidehisa Someya, Yasuyuki Yamada, and Shin Aoki
薬学演習 I (スタンダード薬学シリーズ II-9) P195-200, P287-291, P479-480
日本薬学会
東京科学同人 (2021) (in Japanese)

Others

Transfer of silver, cesium, and rubidium from nutrient solution to radish (*Raphanus sativus* var. *sativus*)
T. Kubota, S. Fukutani, Y. Shibahara
KURNS Progress Report 2020 (2021) 152

Nanostructural Analysis of Hydrated Food Protein Assembly by Ultra-Small-Angle X-ray Scattering towards
Development of Novel Functional Foods
Nobuhiro Sato, Reiko Urade, Masaaki Sugiyama
SPring-8/SACLA Research Report (2022) 64-66 (in Japanese) (doi) 10.18957/rr.10.1.64

理科大の化学と生物学の研究力を活かした新型コロナウイルス治療薬の開発
倉持幸司, 渡士幸一, 大橋啓史, 青木伸, 田中智博
理大科学フォーラム 422 (2021) 10-13 (in Japanese)

7. Neutron Capture Therapy

Papers

Dodecaborate Conjugates Targeting Tumor Cell Overexpressing Translocator Protein for Boron Neutron Capture
Therapy
Hattori Yoshihide, Ishimura Miki, Ohta Youichirou, Takenaka Hiroshi, Kawabata Shinji, Kirihata Mitsunori
ACS Medicinal Chemistry Letters 13(1) (2022) 50-54 (doi) 10.1021/acsmchemlett.1c00377

Development of a real-time neutron beam detector for boron neutron capture therapy using a thin silicon sensor
Takada Masashi, Nunomiya Tomoya, Masuda Akihiko, Matsumoto Tetsuro, Tanaka Hiroki, Nakamura Satoshi,
Endo Satoru, Nakamura Masaru, Aoyama Kei, Ueda Osamu, Narita Masataka, Nakamura Takashi
Applied Radiation and Isotopes 176 (2021) 109856 (doi) 10.1016/j.apradiso.2021.109856

Extracellular Release of HMGB1 as an Early Potential Biomarker for the Therapeutic Response in a Xenograft
Model of Boron Neutron Capture Therapy
Imamichi Shoji, Chen Lichao, Ito Tasuku, Tong Ying, Onodera Takae, Sasaki Yuka, Nakamura Satoshi, Mauri
PierLuigi, Sanada Yu, Igaki Hiroshi, Murakami Yasufumi, Suzuki Minoru, Itami Jun, Masunaga Shinichiro,
Masutani Mitsuko
Biology 11(3) (2022) 420 (doi) 10.3390/biology11030420

Salvage Boron Neutron Capture Therapy for Malignant Brain Tumor Patients in Compliance with Emergency
and Compassionate Use: Evaluation of 34 Cases in Taiwan
Chen Yi-Wei, Lee Yi-Yen, Lin Chun-Fu, Pan Po-Shen, Chen Jen-Kun, Wang Chun-Wei, Hsu Shih-Ming, Kuo
Yu-Cheng, Lan Tien-Li, Hsu Sanford P. C., Liang Muh-Lii, Chen Robert Hsin-Hung, Chang Feng-Chi, Wu Chih-
Chun, Lin Shih-Chieh, Liang Hsiang-Kuang, Lee Jia-Cheng, Chen Shih-Kuan, Liu Hong-Ming, Peir Jinn-Jer, Lin
Ko-Han, Huang Wen-Sheng, Chen Kuan-Hsuan, Kang Yu-Mei, Liou Shueh-Chun, Wang Chun-Chieh, Pai Ping-
Ching, Li Chih-Wei, Chiek Daniel Quah Song, Wong Tai-Tong, Chiou Shih-Hwa, Chao Yee, Tanaka Hiroki,
Chou Fong-In, Ono Koji
Biology 10(4) (2021) 334 (doi) 10.3390/biology10040334

Development of an irradiation method for superficial tumours using a hydrogel bolus in an accelerator-based
BNCT

Sasaki Akinori, Tanaka Hiroki, Takata Takushi, Tamari Yuki, Watanabe Tsubasa, Hu Naonori, Kawabata Shinji, Kudo Yoshihiro, Mitsumoto Toshinori, Sakurai Yoshinori, Suzuki Minoru

Biomedical Physics & Engineering Express **8(1)** (2021) **015015** (doi) 10.1088/2057-1976/ac3d73

Conjugation of Phenylboronic Acid Moiety through Multistep Organic Transformations on Nanodiamond Surface for an Anticancer Nanodrug for Boron Neutron Capture Therapy

Nishikawa Masahiro, Kang Heon Gyu, Zou Yajuan, Takeuchi Hidekazu, Matsuno Naoyoshi, Suzuki Minoru, Komatsu Naoki

Bulletin of the Chemical Society of Japan **94(9)** (2021) **2302-2312** (doi) 10.1246/bcsj.20210200

A Novel Boron Lipid to Modify Liposomal Surfaces for Boron Neutron Capture Therapy

Shirakawa Makoto, Zaboronok Alexander, Nakai Kei, Sato Yuhki, Kayaki Sho, Sakai Tomonori, Tsurubuchi Takao, Yoshida Fumiyo, Nishiyama Takashi, Suzuki Minoru, Tomida Hisao, Matsumura Akira

Cells **10(12)** (2021) **3421** (doi) 10.3390/cells10123421

Carboxyboranyl-amino ethanol: unprecedented discovery of boron agents for neutron capture therapy in cancer treatment

Zhu Yinghui, Cai Jianghong, Hosmane Narayan S., Suzuki Minoru, Uno Kazuko, Zhang Yingjun, Takagaki Mao

Chemical Communications **79** (2021) **10174-10177** (doi) 10.1039/d1cc03034e

Suppression of Tumor Growth in a Rabbit Hepatic Cancer Model by Boron Neutron Capture Therapy With Liposomal Boron Delivery Systems

Yanagie Hironobu, Yanagawa Masashi, Morishita Yasuyuki, Shinohara Atsuko, Dewi Novriana, Nonaka Yasumasa, Furuya Yoshitaka, Mizumachi Ryouji, Murata Yuuji, Nakamura Hiroyuki, Suzuki Minoru, Sakurai Yoshinori, Tanaka Hiroki, Masunaga Shinichiro, Ono Koji, Sugihara Takumichi, Nashimoto Masayuki, Yamauchi Haruo, Ono Minoru, Nakajima Jun, Takahashi Hiroyuki

In Vivo **35(6)** (2021) **3125-3135** (doi) 10.21873/invivo.12607

HIF-1 α affects sensitivity of murine squamous cell carcinoma to boron neutron capture therapy with BPA

Sanada Yu, Takata Takushi, Tanaka Hiroki, Sakurai Yoshinori, Watanabe Tsubasa, Suzuki Minoru, Masunaga Shin-ichiro

International Journal of Radiation Biology **97(10)** (2021) **1441-1449** (doi) 10.1080/09553002.2021.1956004

Prevention and early management of carotid blowout syndrome for patients receiving head and neck salvage boron neutron capture therapy (BNCT)

Lan Tien-Li, Chang Feng-Chi, Wang Chun-Wei, Igawa Kazuyo, Wu Szu-Hsien, Lo Wen-Liang, Chen Yi-Wei

Journal of Dental Sciences **16(3)** (2021) **854-860** (doi) 10.1016/j.jds.2020.12.013

Measurement of spatial fluence distribution of neutrons and gamma rays using MAGAT-type gel detector doped with LiCl for BNCT at Kyoto University Reactor

Tanaka Kenichi, Kajimoto Tsuyoshi, Mitsuyasu Aruma, Ito Yuto, Hayashi Shin-ichiro, Sakurai Yoshinori, Tanaka Hiroki, Takata Takushi, Bengua Gerard, Endo Satoru

Journal of Physics: Conference Series **2167** (2022) **012006** (doi) 10.1088/1742-6596/2167/1/012006

Technical note: Optical imaging of lithium-containing zinc sulfate plate in water during irradiation of neutrons from boron neutron capture therapy (BNCT) system

Yamamoto Seiichi, Yabe Takuya, Hu Naonori, Kanai Yasukazu, Tanaka Hiroki, Ono Koji

Medical Physics **49(3)** (2021) **1822-1830** (doi) 10.1002/mp.15424

Dodecaborate-Encapsulated Extracellular Vesicles with Modification of Cell-Penetrating Peptides for Enhancing Macropinocytotic Cellular Uptake and Biological Activity in Boron Neutron Capture Therapy

Hirase Shiori, Aoki Ayako, Hattori Yoshihide, Morimoto Kenta, Noguchi Kosuke, Fujii Ikuo, Takatani-Nakase Tomoka, Futaki Shiroh, Kirihata Mitsunori, Nakase Ikuhiko

Molecular Pharmaceutics **19(4)** (2022) **1135-1145** (doi) 10.1021/acs.molpharmaceut.1c00882

Reactor-based boron neutron capture therapy for 44 cases of recurrent and refractory high-grade meningiomas with long-term follow-up

Takai Satoshi, Wanibuchi Masahiko, Kawabata Shinji, Takeuchi Koji, Sakurai Yoshinori, Suzuki Minoru, Ono Koji, Miyatake Shin-Ichi

Neuro-Oncology **24(1)** (2022) **90-98** (doi) 10.1093/neuonc/noab108

Accelerator-based BNCT for patients with recurrent glioblastoma: a multicenter phase II study
Kawabata Shinji, Suzuki Minoru, Hirose Katsumi, Tanaka Hiroki, Kato Takahiro, Goto Hiromi, Narita Yoshitaka, Miyatake Shin-Ichi
Neuro-Oncology Advances 3(1) (2021) vdab067 (doi) 10.1093/nojnl/vdab067

Fluorescent boron carbide quantum dots synthesized with a low-temperature solvothermal approach for boron neutron capture therapy
Singh Paviter, Kaur Manjot, Singh Kulwinder, Meena Ramovatar, Kumar Manjeet, Yun Ju-Hyung, Thakur Anup, Nakagawa Fumiko, Suzuki Minoru, Nakamura Hiroyuki, Kumar Akshay
Physica E: Low-dimensional Systems and Nanostructures 132 (2021) 114766
(doi) 10.1016/j.physe.2021.114766

First measured optical image of Cerenkov-light in water during irradiation of neutron beam from boron neutron capture therapy (BNCT) system
Yabe Takuya, Yamamoto Seiichi, Hu Naonori, Kanai Yasukazu, Tanaka Hiroki, Ono Koji
Radiation Measurements 146 (2021) 106633 (doi) 10.1016/j.radmeas.2021.106633

Evaluation of a treatment planning system developed for clinical boron neutron capture therapy and validation against an independent Monte Carlo dose calculation system
Hu Naonori, Tanaka Hiroki, Kakino Ryo, Yoshikawa Syuushi, Miyao Mamoru, Akita Kazuhiko, Isohashi Kayako, Aihara Teruhito, Nihei Keiji, Ono Koji
Radiation Oncology 16(1) (2021) 243 (doi) 10.1186/s13014-021-01968-2

First optical observation of ^{10}B -neutron capture reactions using a boron-added liquid scintillator for quality assurance in boron neutron capture therapy
Nohtomi Akihiro, Maeda Hideya, Sakamoto Naoya, Wakabayashi Genichiro, Takata Takushi, Sakurai Yoshinori
Radiological Physics and Technology 15(1) (2022) 37-44 (doi) 10.1007/s12194-021-00645-z

Chronic pathophysiological changes in the normal brain parenchyma caused by radiotherapy accelerate glioma progression
Tsuji Yuichiro, Nonoguchi Naosuke, Okuzaki Daisuke, Wada Yusuke, Motooka Daisuke, Hirota Yuki, Toho Taichiro, Yoshikawa Nobuhiko, Furuse Motomasa, Kawabata Shinji, Miyatake Shin-Ichi, Nakamura Hiroyuki, Yamamoto Ryohei, Nakamura Shota, Kuroiwa Toshihiko, Wanibuchi Masahiko
Scientific Reports 11 (2021) 22110 (doi) 10.1038/s41598-021-01475-0

Thermal Neutron Measurements Using Thermoluminescence Phosphor Cr-doped Al_2O_3 and Cd Neutron Converter
Oh Ryoken, Yanagisawa Shin, Tanaka Hiroki, Takata Takushi, Wakabayashi Genichiro, Tanaka Masaya, Sugioka Natsumi, Koba Yusuke, Shinsho Kiyomitsu
Sensors and Materials 33(6) (2021) 2129-2135 (doi) 10.18494/sam.2021.3328

Proceedings

Feasibility study on energy-dependent neutron flux monitor using multi-core SOF detector
M. Ishikawa, R. Ogawara, K. Baba, S. Ishiguri, H. Handa,
Proceedings of 19th International Congress of Neutron Capture Therapy, Granada, Spain (Sep. 5-10, 2021)

Development of ionization chamber for fast neutron monitoring in accelerator-based BNCT
Nishiki Matsubayashi, Akinori Sasaki, Takushi Takata, Yoshinori Sakurai, Hiroki Tanaka
Proceedings of the 56th KURNS Scientific Meeting, Online (Feb. 9-10, 2022) 43 (in Japanese)

Development and experimental verification of dose calculation algorithm for boron neutron capture therapy
Mai Nojiri, Takushi Takata, Yoshinori Sakurai, Hiroki Tanaka
Proceedings of the 56th KURNS Scientific Meeting, Online (Feb. 9-10, 2022) 24 (in Japanese)

Experimental verification of Absolute Epi-thermal and Fast Neutron Flux Intensity Detectors for BNCT
Shoya Tada, Kazushi Aoki, Daisuke Hatano, Shingo Tamaki, Sachie Kusaka, Hiroki Tanaka
Proceedings of the 56th KURNS Scientific Meeting, Online (Feb. 9-10, 2022) 12 (in Japanese)

Study on improvement of neutron distribution by overlapping of irradiation fields using intensity modulators in accelerator-based BNCT

Akinori Sasaki, Takushi Takata, Naonori Hu, Nishiki Matsubayashi, Mai Nojiri, Yoshinori Sakurai, Minoru Suzuki, Hiroki Tanaka

Proceedings of the 56th KURNS Scientific Meeting, Online (Feb. 9-10, 2022) 30 (in Japanese)

The effect of boron neutron capture therapy on normal tissues

Minoru Suzuki

Proceedings of the 56th KURNS Scientific Meeting, Online (Feb. 9-10, 2022) 2 (in Japanese)

Advanced veterinary care at Hokkaido University veterinary teaching hospital and collaboration between human medicine and veterinary medicine

Mitsuyoshi Takiguchi

Proceedings of the Symposium on the expansion of boron neutron capture therapy to the field of veterinary medicine.-Challenges and potential for interdisciplinary research-, Online (2021 Mar. 4) 86-95 (in Japanese)

Boron Neutron Capture Therapy

Minoru Suzuki

Proceedings of the Symposium on the expansion of boron neutron capture therapy to the field of veterinary medicine.-Challenges and potential for interdisciplinary research-, Online (2021 Mar. 4) 1-5 (in Japanese)

Collaboration of Radiation Research between Medical and Veterinary Science at Gifu University

Masayuki Matsuo

Proceedings of the Symposium on the expansion of boron neutron capture therapy to the field of veterinary medicine.-Challenges and potential for interdisciplinary research-, Online (2021 Mar. 4) 71-85 (in Japanese)

Current status of cyclotron-based neutron source for BNCT

Hiroki Tanaka

Proceedings of the Symposium on the expansion of boron neutron capture therapy to the field of veterinary medicine.-Challenges and potential for interdisciplinary research-, Online (2021 Mar. 4) 6-13 (in Japanese)

Current status of PET medical care in small animals

Masahiro Natsuhori

Proceedings of the Symposium on the expansion of boron neutron capture therapy to the field of veterinary medicine.-Challenges and potential for interdisciplinary research-, Online (2021 Mar. 4) 52-62 (in Japanese)

Examination of route of boron administration to brain tumor for BNCT-Looking for clinical usefulness of the intracerebroventricular injection of BPA to brain tumor for rat-

Sachie Kusaka

Proceedings of the Symposium on the expansion of boron neutron capture therapy to the field of veterinary medicine.-Challenges and potential for interdisciplinary research-, Online (2021 Mar. 4) 100-103 (in Japanese)

Importance of ¹⁸F-FBPA PET in BNCT

Kayako Isohashi

Proceedings of the Symposium on the expansion of boron neutron capture therapy to the field of veterinary medicine.-Challenges and potential for interdisciplinary research-, Online (2021 Mar. 4) 14-25 (in Japanese)

Radiation Therapy in Veterinary Medical Center in Yamaguchi University

Munekazu Nakaichi

Proceedings of the Symposium on the expansion of boron neutron capture therapy to the field of veterinary medicine.-Challenges and potential for interdisciplinary research-, Online (2021 Mar. 4) 41-51 (in Japanese)

The past, present and future of comparative oncology aimed at overcoming cancer in humans and animals

Kohji Maruo

Proceedings of the Symposium on the expansion of boron neutron capture therapy to the field of veterinary medicine.-Challenges and potential for interdisciplinary research-, Online (2021 Mar. 4) 63-70 (in Japanese)

Translational and clinical-veterinary studies of Boron Neutron Capture Therapy for Head and Neck cancer

Mandy Schwint

Proceedings of the Symposium on the expansion of boron neutron capture therapy to the field of veterinary medicine.-Challenges and potential for interdisciplinary research-, Online (2021 Mar. 4) 26-40

Reviews

Current Status of Accelerator-Based Boron Neutron Capture Therapy (BNCT)

Hiroki Tanaka

Japanese Journal of Medical Physics (Igakubutsuri) 41(3) (2021) 117-121 (in Japanese)

Realization of the World's First Accelerator BNCT System Using a Cyclotron

Hiroki Tanaka, Toshinori Mitsumoto, Koji Ono

Journal of the Particle Accelerator Society of Japan 17(2) (2021) 81-85 (in Japanese)

DOI: (doi) 10.50868/pasj.17.2_81

Activities on neutron measurement standards for BNCT

Akihiko Masuda, Tetsuro Masuda, Harano Hideki

JSAP Annual Meetings Extended Abstracts 46 (2021) 72-76 (in Japanese)

Progress of Boron Neutron Capture Therapy and Biological Problems

Natuko Kondo, Yoshinori Sakurai, Takushi Takata, Hiroki Tanaka, Minoru Suzuki

Radiation Biology Research Communications 57(1) (2022) 63-70 (in Japanese)

ポリビニルアルコールに秘められた可能性: ホウ素送達システムへの応用

Takahiro Nomoto

The Japanese Society for Biomaterials (JSB) 39(2) (2021) 128-129 (in Japanese)

放射線医学 頭頸部腫瘍に対するホウ素中性子捕捉療法の現状

Minoru Suzuki

医学のあゆみ 277(2) (2021) 182-183 (in Japanese)

8. Neutron Radiography and Radiation Application

Papers

Application of Machine Learning Methods to Neutron Transmission Spectroscopic Imaging for Solid-Liquid Phase Fraction Analysis

Kamiyama Takashi, Hirano Kazuma, Sato Hiroataka, Ono Kanta, Suzuki Yuta, Ito Daisuke, Saito Yasushi

Applied Sciences 11(13) (2021) 5988 (doi) 10.3390/app11135988

Efficacy of Boron Neutron Capture Therapy in Primary Central Nervous System Lymphoma: In Vitro and In Vivo Evaluation

Yoshimura Kohei, Kawabata Shinji, Kashiwagi Hideki, Fukuo Yusuke, Takeuchi Koji, Futamura Gen, Hiramatsu Ryo, Takata Takushi, Tanaka Hiroki, Watanabe Tsubasa, Suzuki Minoru, Hu Naonori, Miyatake Shin-Ichi, Wanibuchi Masahiko

Cells 10(12) (2021) 3398 (doi) 10.3390/cells10123398

Proof-of-principle Experiment of ^4He Excimer Cluster Generation via Neutron- ^3He Absorption Reaction for Visualization of Velocity Fields in Superfluid ^4He

Matsushita T., Sonnenschein V., Iguchi T., Ito D., Kitaguchi M., Kiyonagi Y., Guo W., Saito Y., Shinohara T., Shimizu H.M., Suzuki S., Tsuji Y., Tomita H., Hayashida H., Hishida M., Hiroi K., Hirota K., Maruyama T., Waki S., Wada N.

Hamon 30(4) (2021) 192-196 (in Japanese) (doi) 10.5611/hamon.30.4_192

Density Functional Study on Compounds to Accelerate the Electron Capture Decay of ^7Be

Yoshida Akira, Abe Minori, Hada Masahiko

Journal of Physical Chemistry A 125(29) (2021) 6356-6361 (doi) 10.1021/acs.jpca.1c01491

Proceedings

Effects of water accumulation in the proton exchange membrane and the gas diffusion layer on the power generation performance of PEFC

K. Mine, H. Murakawa, K. Sugimoto, H. Asano, D. Ito and Y. Saito

International Conference on Power Engineering2021, Online (Jan. 17-21, 2021) C224

Beam quality determination of a boron neutron capture therapy irradiation system using microdosimetry

Naonori Hu

Proceedings of the 56th KURNS Scientific Meeting, Online (Feb. 9-10, 2022) 50 (in Japanese)

Direct Observation of Lubricant Behaviour in Machine Elements by Means of Neutron Phase Imaging Tomoko Hirayama, Sun Lin, Yoshichika Seki, Takenao, Shinohara, Masahiro Hino, Riichiro Nakamura

Proceedings of the 56th KURNS Scientific Meeting, Online (Feb. 9-10, 2022) 49 (in Japanese)

Effect of Internal Moisture Movement on Spalling for High-strength Concrete Exposed to High Temperature

Azusa Miyabe, Yuhei Nishio, Masamichi Tamura, Daisuke Ito, Kanematsu Manabu

Proceedings of the Concrete Structure Scenarios, JSMS 21 (Jan. 2021) 413-418 (in Japanese)

Verification of the Applicability of Water Cherenkov Detector to Active Neutron Method and Development of a Prototype Detector

K. Tanabe, M. Komeda, Y. Toh, Y. Kitamura, T. Misawa, H. Sagara

The 2021 IEEE Nuclear Science Symposium and Medical Imaging Conference, Yokohama, Japan (Jan. 16-23, 2021) (in Japanese)

Frost Deposition Distribution Estimated by X-ray and Neutron Cooperative Imaging

R. Kuroda, T. Makihara, Y. Oda, R. Matsumoto, N. Odaira, D. Ito, Y. Saito

The Second Asian Conference on Thermal Sciences, 2nd ACTS, Online (Jan. 3-7, 2021) ACTS-1314

Others

複合ラジオグラフィによる熱交換器の着霜評価

黒田 陸斗, 松本 亮介, 小田 豊, 榎原 拓郎, 斎藤 泰司, 伊藤 大介, 大平 直也

2021 年度日本冷凍空調学会年次大会講演論文集 (2021) A122 (in Japanese)

9. TRU and Nuclear Chemistry

Papers

Coprecipitation with samarium hydroxide using multitracer produced through neutron-induced fission of ^{235}U toward chemical study of heavy elements

Y. Kasamatsu, M. Nagase, H. Ninomiya, E. Watanabe, Y. Shigekawa, N. Kondo, K. Takamiya, T. Ohtsuki, N. Shiohara, A. Shinohara

Applied Radiation and Isotopes 179 (2022) 110006 (doi) 10.1016/j.apradiso.2021.110006

Supercritical hydrothermal synthesis of UO_{2+x} : stoichiometry, crystal shape and size, and homogeneity observed using ^{23}Na -NMR spectroscopy of $(\text{U}, \text{Na})\text{O}_{2+x}$

Tabata Chihiro, Shirasaki Kenji, Sunaga Ayaki, Sakai Hironori, Li Dexin, Konaka Mariko, Yamamura Tomoo

CrystEngComm 23(48) (2021) 8660-8672 (doi) 10.1039/d1ce00996f

Phase transformation of mixed lanthanide oxides in an aqueous solution

Md. Moniruzzaman, T. Kobayashi, T. Sasaki

Journal of Nuclear and Radiochemical Sciences 21 (2021) 15-27

Solubility of Mixed Lanthanide Hydroxide and Oxide Solid Solutions

Md. Moniruzzaman, T. Kobayashi, T. Sasaki

Journal of Nuclear Fuel Cycle and Waste Technology 19(3) (2021) 353-366

Solubility of $\text{PuO}_2(\text{am,hyd})$ and the Formation of $\text{Pu}(\text{IV})$ Carbonate Complexes in Carbonate Solutions Containing $0.1\text{--}5.0 \text{ mol}\cdot\text{dm}^{-3} \text{ NaNO}_3$

Kobayashi Taishi, Fellhauer David, Sasaki Takayuki

Journal of Solution Chemistry 50(4) (2021) 443-457 (doi) 10.1007/s10953-021-01080-9

Towards highly accurate calculations of parity violation in chiral molecules: relativistic coupled-cluster theory including QED-effects

Sunaga Ayaki, Saue Trond

Molecular Physics 119 (21-22) (2021) SI (doi) 10.1080/00268976.2021.1974592

Hydrofluorocarbon Diluent for CMPO Without Third Phase Formation: Extraction of Uranium(VI) and Lanthanide(III) Ions

Tabata Chihiro, Nakase Masahiko, Harigai Miki, Shirasaki Kenji, Sunaga Ayaki, Yamamura Tomoo
Separation Science and Technology 57(7) (2022) 1097-1110 (doi) 10.1080/01496395.2021.1970767

Proceedings

Crystal structure and magnetism of uranium phthalocyanine complex

Chihiro Tabata

GIMRT Joint International Symposium on Radiation Effects in Materials and Actinide Science (GIMRT-REMAS2020) Sendai, Japan, Online (Sep. 30- Oct. 3, 2020)

Isotope fractionation behavior of molybdenum in saturated calcium chloride solution

Kota Suzuki, Chizu Kato, Takeshi Ohno, Satoshi Fukutani, Toshiyuki Fujii

Proceedings of the 56th KURNS Scientific Meeting, Online (Feb. 9-10, 2022) 45 (in Japanese)

Development of measurement method for gas-liquid two-phase flow in a packed bed of spheres

Noriaki Yasugi, Naoya Odaira, Daisuke Ito, Kei Ito, Yasushi Saito

Proceedings of the 56th KURNS Scientific Meeting, Online (Feb. 9-10, 2022) 28 (in Japanese)

Study of Isotope Separation via Chemical Exchange Reaction

Ryuta Hazama, Takaaki Yoshimoto, Anawat Rittirong, Yoichi Sakuma, Toshiyuki Fujii, Satoshi Fukutani, Yuji Shibahara, Ayaki Sunaga

Proceedings of the 56th KURNS Scientific Meeting, Online (Feb. 9-10, 2022) 44-47 (in Japanese)

Chemical and electronic properties of Actinide compounds and their applications

Tomoo Yamamura, Chihiro Tabata, Yoshinori Haga, Tsuyoshi Yaita, Hiroshi Yamagami, Hiroshi Amitsuka, Kenji Ishida, Fusako Kon, Yuma Kaneko, Eikai Hayasaka, Tatsuya Suzuki, Z. Ma, F. H. Ikhwan, Rin Murayama, Irvin Mardongan, Yuji Shibahara, Satoshi Fukutani, Kenji Shirasaki, Hidetoshi Kikunaga, Kohshin Washiyama, Atsushi Shinohara, Takashi Yoshimura, Masanobu Nogami, Yokota Masayoshi, Kita Daiki, Minoru Abe, Masahiko Hada, Ayaki Sunaga, Ataru Sato, Rei Yoshida, Hiroki Shishido, Hidetoshi Hashizume, Masahiko Nakase, Miki Harigai, Hidetaka Nakai, Tohru Kobayashi

Proceedings of the 56th KURNS Scientific Meeting, Online (Feb. 9-10, 2022) 3-7 (in Japanese)

Effect of iron on dissolution behavior of pentavalent uranium solid phase

Ryutaro Tonna, Takayuki Sasaki, Taishi Kobayashi, Shun Sekimoto

Proceedings of the 56th KURNS Scientific Meeting, Online (Feb. 9-10, 2022) 39 (in Japanese)

Effect of oxalic acid on vanadium redox

Naoya Wada, Hideyuki Sugihara, Akihiro Uehara, Satoshi Fukutani, Chizu Kato, Toshiyuki Fujii

Proceedings of the 56th KURNS Scientific Meeting, Online (Feb. 9-10, 2022) 37 (in Japanese)

Revealing the origins of volatile elements in CAIs from Zn isotopes

Chizu Kato Frédéric Moynier, Toshiyuki Fujii

Proceedings of the 56th KURNS Scientific Meeting, Online (Feb. 9-10, 2022) 19 (in Japanese)

Solid-liquid extraction experiment of Group 2 elements using crown ether toward the chemical study of nobelium.
Eisuke Watanabe, Yoshitaka Kasamatsu, Nakanishi Ryohei, Saki Otaka, Koichi Takamiya, and Atsushi Shinohara

Proceedings of the 56th KURNS Scientific Meeting, Online (Feb. 9-10, 2022) 10 (in Japanese)

Solvent extraction characteristics of tin from nitric acid solution

Shin Takahashi, Chizu Kato, Satoshi Fukutani, Tatsuro Matsumura, Hideya Suzuki, Toshiyuki Fujii

Proceedings of the 56th KURNS Scientific Meeting, Online (Feb. 9-10, 2022) 23 (in Japanese)

Review

アルファ線核医学治療のための薬剤開発の考察—その 5—IAEA Technical Meeting 報告: α 線核種ならびに TAT 薬剤の最新動向—

矢野恒夫, 長谷川功紀, 山村朝雄, 渡部直史, 巽光朗, 佐藤達彦, 角永悠一郎, 樺山一哉, 深瀬浩一, 平林容子, 藤井博史, 米倉義晴

Pharmaceutical and Medical Device Regularoty Science 52(2) (2021) 85-106 (in Japanese)

アルファ線核医学治療のための薬剤開発の考察(その 6)

矢野恒夫, 長谷川功紀, 石井明子, 渡部直史, 巽光朗, 角永悠一郎, 樺山一哉, 深瀬浩一, 米倉義晴, 平林容子, 佐藤達彦, 藤井博史

PharmTechJapan 37(11) (2021) 85-94 (in Japanese)

アルファ線核医学治療のための薬剤開発の考察(その 7)

矢野恒夫, 長谷川功紀, 石井明子, 渡部直史, 巽光朗, 角永悠一郎, 樺山一哉, 深瀬浩一, 米倉義晴, 平林容子, 佐藤達彦, 藤井博史

PharmTechJapan 38(1) (2022) 85-94 (in Japanese)

10. Health Physics and Waste Management

Papers

Behaviour of Fossil and Biogenic Carbon in Sewage Sludge Treatment Processes and Their Impacts on Greenhouse Gas Emissions

Liu C., Oshita K., Takaoka M., Fukutani S.

Chemical Engineering Transactions 89 (2021) 97-102

EXISTENCE FORMS OF RADIOACTIVE CS CONSIDERING SOIL PROPERTIES AND VERTICAL DISTRIBUTION IN FOREST SOIL

Maiko Ikegami, Satoshi Fukutani, Yoko Shimada, Tomoyuki Takahashi, Shu SATO, Minoru YONEDA

Journal of Japan Society of Civil Engineers, Ser. G (Environmental Research) 77(7) (2022) III_277 -III_284 (in Japanese) (doi) 10.2208/jscejer.77.7_III_277

Fluorescence pulses derived from thin poly (ethylene terephthalate) in response to charged particles

Nakamura Hidehito, Mori Kazuhiro, Shirakawa Yoshiyuki

Physica Scripta 96(12) (2021) 125307 (doi) 10.1088/1402-4896/ac237f

ANALYSES OF H*(10) DOSE RATES MEASURED IN ENVIRONMENT CONTAMINATED BY RADIOACTIVE CAESIUM: CORRECTION OF DIRECTIONAL DEPENDENCE OF SCINTILLATION DETECTORS

Tsuda S, Tanigaki M, Yoshida T, Okumura R, Saito K

Radiation Protection Dosimetry 193(3-4) (2021) 228-236 (doi) 10.1093/rpd/ncab060

Proceedings

X-ray and neutron diffraction measurements of trivalent and tetravalent metal hydroxide solid phases

Reo Nanjo, Taishi Kobayashi, Takayuki Sasaki, Kazuhiro Mori

Proceedings of the 56th KURNS Scientific Meeting Online (2022 Feb. 9-10) 29 (in Japanese)

Reviews

Thoron and NORM for Past 30 Years in Japan

Takeshi Iimoto, Shinji Tokonami, Hidenori Yonehara, Sadaaki Furuta, Michikuni Shimo

Radiation Environment and Medicine 10(2) (2021) 55-66

11. Accelerator Physics

Papers

Technical Note: Range verification of pulsed proton beams from fixed - field alternating gradient accelerator by means of time - of - flight measurement of ionoacoustic waves

Nakamura Yuta, Takayanagi Taisuke, Uesaka Tomoki, Unlu Mehmet Burcin, Kuriyama Yasutoshi, Ishi Yoshihiro, Uesugi Tomonori, Kobayashi Masanori, Kudo Nobuki, Tanaka Sodai, Umegaki Kikuo, Tomioka Satoshi, Matsuura Taeko
Medical Physics **48(9)** (2021) **5490-5500** (doi) 1002/mp.15060

Proceedings

Instrumentation R&D for the studies of SRF thin-film structures at KEK and Kyoto University
Y. Iwashita, Y. Kuriyama, H. Tongu, Y. Fuwa, H. Hayano
2021 International Conference on RF Superconductivity (SRF2021) Virtual Conference (Jun. 28 - Jly. 2, 2021)

Development of a Hybrid Detector for Simultaneous Measurement of Thermal Neutron Flux and γ -ray Dose Rate for Therapeutic
Hiroaki Kato, Nishiki Matsubayashi, Takushi Takata, Tetsuya Mukawa, Keita Suga, Yoshinori Sakurai, Hiroki Tanaka
Proceedings of the 56th KURNS Scientific Meeting Online (Feb. 9-10, 2022) **37** (in Japanese)

Evaluation of Radiation-Induced Demagnetization of Permanent Magnets using KUR
Yasuhiro Fuwa, Yasutoshi Kuriyama, Yoshihisa Iwashita, Koichi Takamiya, Tomohiro Takayanagi
Proceedings of the 56th KURNS Scientific Meeting Online (Feb. 9-10, 2022) **40** (in Japanese)

次世代粒子加速器に向けた多角的研究
Yasutoshi Kuriyama
Proceedings of the 56th KURNS Scientific Meeting Online (Feb. 9-10, 2022) **60-63** (in Japanese)

Towards an accelerator driven neutron source facility using a 30 MeV Cyclotron
Yasutoshi Kuriyama, Riichiro Nakamura, Hiroki Tanaka, Yoshihisa Iwashita, Masahiro Hino
Proceedings of the 56th KURNS Scientific Meeting Online (Feb. 9-10, 2022) **36** (in Japanese)

Development of a Small Beta-NMR System Using Halbach Array Permanent Magnet
Y. Kimura, M. Mihara, K. Matsuta, M. Fukuda, Y. Otani, G. Takayama, T. Izumikawa, N. Noguchi, M. Ogose, Y. Sato, K. Takatsu, T. Ohtsubo, H. Takahashi, S. Momota, H. Okumura, T. Moriguchi, A. Ozawa, A. Kitagawa, and S. Shinji
Proceedings of the Specialists' Meeting on "Nuclear Spectroscopy and Condensed Matter Physics Using Short-Lived Nuclei VII", Online, 37-40 (2021 Jan. 15) (in Japanese)

12. Other

Papers

Nonlinear effects of hydration on high-pressure sound velocities of rhyolitic glasses
Gu Jesse T., Fu Suyu, Gardner James E., Yamashita Shigeru, Okuchi Takuo, Lin Jung-Fu
American Mineralogist **106(7)** (2021) **1143-1152** (doi) 10.2138/am-2021-7597

Microtremor surveys based on rotational seismology: theoretical analysis with focus on separation of Rayleigh and Love waves in general wavefield of microtremors
Cho I, Yoshida K, Uebayashi H
Geophysical Journal International **228(1)** (2022) **589-603** (doi) 10.1093/gji/ggab358

Isotope separation by DC18C6 crown-ether for neutrinoless double beta decay of ^{48}Ca
Rittirong A, Yoshimoto T, Hazama R, Kishimoto T, Fujii T, Sakuma Y, Fukutani S, Shibahara Y, Sunaga A
Journal of Physics: Conference Series **2147** (2022) **012015** (doi) 10.1088/1742-6596/2147/1/012015

TORSIONAL VIBRATION CHARACTERISTICS OF A SEISMICALLY-ISOLATED BUILDING CONSTRUCTED ON AN INCLINED BEARING LAYER INFERRED FROM RECORDED MOTIONS AND RESPONSE ANALYSES
TAKAHIRA Tomohiro, TOBITA Yoshinori, NISHIURA Ryo, UEBAYASHI Hiroto, WANG Xin, NAGANO Masayuki

Journal of Structural and Construction Engineering (Transactions of AIJ) 86(783) (2021) 706-716 (in Japanese) (doi) 10.3130/aijs.86.706

Chemical effect on muonic atom formation through muon transfer reaction in benzene and cyclohexane samples
Inagaki Makoto, Ninomiya Kazuhiko, Nambu Akihiro, Kudo Takuto, Terada Kentaro, Sato Akira, Kawashima Yoshitaka, Tomono Dai, Shinohara Atsushi

Radiochimica Acta 109(4) (2021) 319-326 (doi) 10.1515/ract-2020-0112

Proceedings

Design and Construction of an Intense Terahertz-Wave Source Based on Coherent Cherenkov Radiation Matched to Circle Plane Wave

N. Sei, K. Hayakawa, Y. Hayakawa, K. Nogami, H. Ogawa, T. Sakai, Y. Sumitomo, T. Takahashi, Y. Takahashi, T. Tanaka

12th International Particle Accelerator Conference, Online (May. 24-28, 2021) 2751-2754

Development of an AR Training Construction System Using Embedded Information in a Real Environment
Harazono Yuki, Tamura Taichi, Omoto Yusuke, Ishii Hirotake, Shimoda Hiroshi, Tanaka Yoshiaki, Takahashi Yoshiyuki

13th International Conference, VAMR 2021, Held as Part of the 23rd HCI International Conference, Online (Jly. 24-29, 2021) 614-625 (doi) 10.1007/978-3-030-77599-5_42

The FM(C)T - When And How To Realize It?

Hirokazu Kumekawa, Hiroshi Tsuboi and Hironobu Unesaki

INMM & ESARDA Joint Annual Meeting 2021, Web Online meeting (Aug. 23- Sep. 1, 2021) 1-10

Materials Informatics -development and applications of a large scale materials databases-

Masaya Kumagai

Proceedings of the 56th KURNS Scientific Meeting, Online (Feb. 9-10, 2022) 51-52 (in Japanese)

Reviews

Discussion of visions for nuclear energy in 2050 among the young experts

Murakami Kenta, Terada Kazushi, Takeda Satoshi, Hagura Naoto

Journal of the Atomic Energy Society of Japan 63(9) (2021) 665-668 (in Japanese)

Electron-Bunch Shape Unveiled by Coherent Edge Radiation

N. Sei

Journal of the Particle Accelerator Society of Japan 18(2) (2021)72-80 (in Japanese)

Ten years of the collaborative research in Fukushima prefecture since the Great East Japan Earthquake

Ueda Yoshikatsu, Sugiyama Akifumi, Tokuda Yomei, Nihei Naoto, Tanigaki Minoru

Sustainable Humanosphere 17 (2021) 1-15 (in Japanese)

Foreword

Takuo OKUCHI

The Review of High Pressure Science and Technology 31(1) (2021) 1-2 (in Japanese)

KURNS Progress Report 2021

Issued in July 2022

Issued by the Institute for Integrated Radiation and Nuclear Science,
Kyoto University
Kumatori-cho, Sennan-gun, Osaka 590-0494 Japan

Tel. +81-72-451-2300

Fax. +81-72-451-2600

In case that corrections are made, overwrite the modified version
in the following webpage:

<https://www.iri.kyoto-u.ac.jp/PUB/report/PR/ProgRep2021/ProgRep2021.html>

Publication Team

ABE, Naoya
INOUE, Rintaro (Chief)
ISHI, Yoshihiro
KONDO, Natsuko
NAKATANI, Maki
NAKAYAMA, Chiyoko
PYEON, Cheol Ho
SAKURAI, Yoshinori (Subchief)
SANO, Hiroaki
TOMINAGA, Yuta
UMEDA, Yuhei
YOKOTA, Kaori
